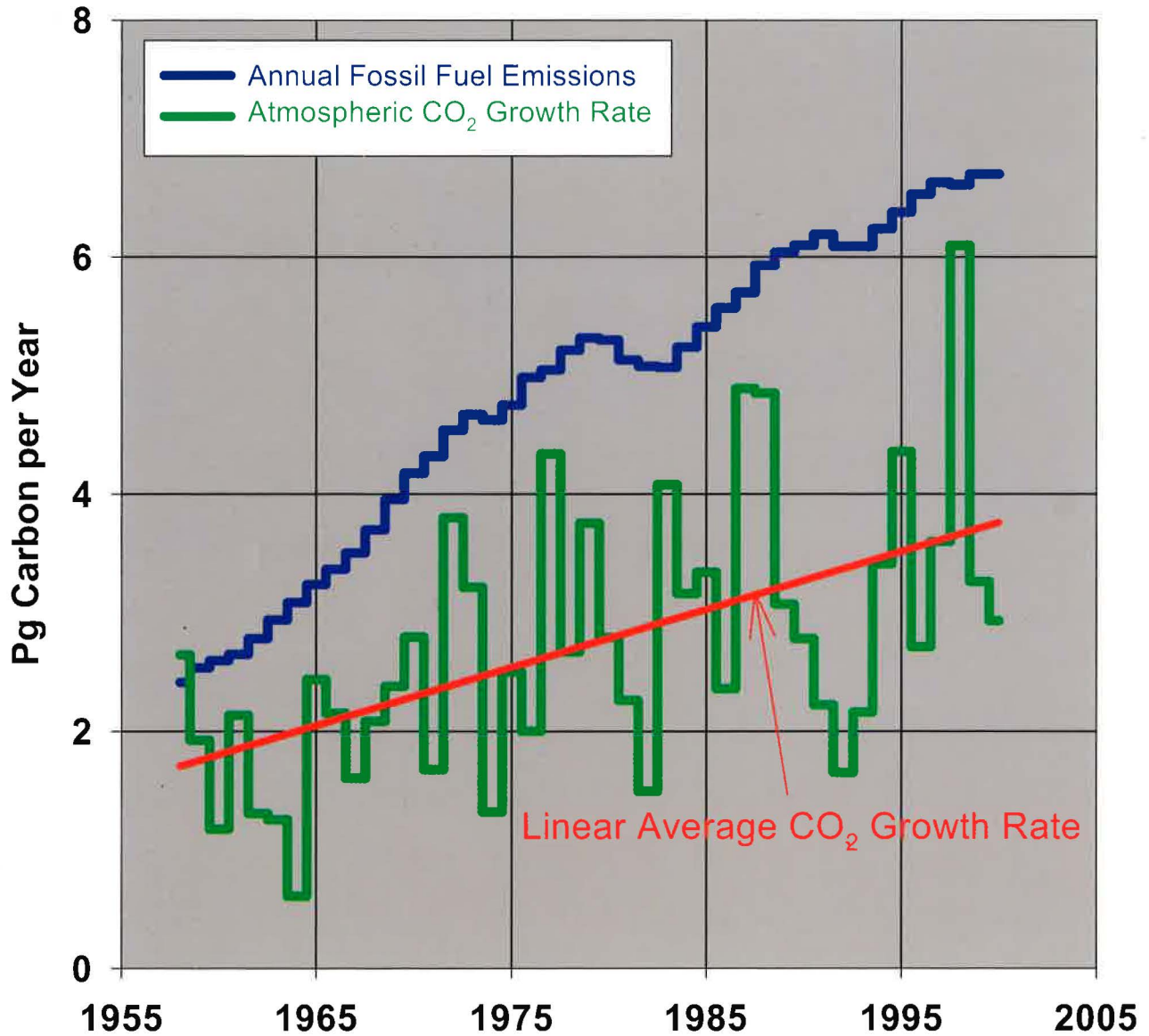# Climate Monitoring and Diagnostics Laboratory
Summary Report No. 26
2000-2001

U.S. Department of Commerce
National Oceanic and Atmospheric Administration
Oceanic and Atmospheric Research

Climate Monitoring and Diagnostics Laboratory Summary Report No. 26

2000-2001

Daniel B. King, Editor
Russell C. Schnell, Editor
Rita M. Rosson, Assistant Editor
Christine Sweet, Assistant Editor

Boulder, Colorado

March 2002

NOTICE

Mention of a commercial company or product does not constitute an endorsement by NOAA Office of Oceanic and Atmospheric Research. Use for publicity or advertising purposes of information from this publication concerning proprietary products or the tests of such products is not authorized.

Preface

The Climate Monitoring and Diagnostics Laboratory (CMDL) is located in Boulder, Colorado, with Baseline Observatories in Barrow, Alaska; Mauna Loa, Hawaii; Cape Matatula, American Samoa; and South Pole, Antarctica. It is one of twelve research components within the Office of Oceanic and Atmospheric Research (OAR) of the National Oceanic and Atmospheric Administration (NOAA). CMDL conducts research related to atmospheric constituents that are capable of forcing change in the climate of the Earth through modification of the atmospheric radiative environment, for example, greenhouse gases and aerosols, and those that can cause depletion of the global ozone layer, for example, chlorine- and bromine-containing compounds.

This report is a summary of CMDL activities for calendar years 2000 and 2001. It is the 26th consecutive report issued by this organization and its Geophysical Monitoring for Climatic Change predecessor since formation in 1972. From 1972 through 1993 (numbers 1 through 22), reports were issued annually; thereafter, the reports were issued on a biennial basis. At CMDL's Internet home page (www.cmdl.noaa.gov) you will find information about our major groups and Observatories, latest events and press releases, publications, data availability, and personnel. Numerous data graphs and ftp data files are available. Information (program descriptions, accomplishments, publications, plans, data access, etc.) on CMDL parent organizations can best be obtained via the Internet (OAR: www.oar.noaa.gov; NOAA: www.noaa.gov).

This report is organized into the following major sections:

1. Observatory, Meteorology, and Data Management Operations
2. Carbon Cycle
3. Aerosols and Radiation
4. Ozone and Water Vapor
5. Halocarbons and other Atmospheric Trace Species
6. Cooperative Programs

These are followed by a list of CMDL staff publications for 2000-2001.

Inquiries and/or comments should be addressed to:

Director, R/CMDL
NOAA/Climate Monitoring and Diagnostics Laboratory
325 Broadway
Boulder, CO 80305-3328
(303) 497-6074

or

Russell.C.Schnell@noaa.gov

Judy Pereira
Years of Service: 1966-1999

John Chin
Years of Service: 1960-1962; 1964-1966; 1968-2000

Together, Judy Pereira and John Chin were a unique team that helped to make the Mauna Loa Observatory the world-class institution it is today. One cannot think of Mauna Loa Observatory without being reminded of their dedication, service, and outstanding personalities.

Judy Pereira

In 1966, Judy, the reigning "Miss Aloha Hawaii" and a student at the University of Hawaii, Hilo, joined Mauna Loa as a part-time worker. She soon became the permanent secretary and served as the heart and soul of Mauna Loa until her retirement in December 1999 after a 33-year association with the observatory. Over those years she worked for eight different directors, or rather eight directors worked with her, as she often knew much more about MLO history and daily operations than they did. She ran the observatory office in an efficient and professional manner with dashes of Hawaiian Island flavor and local culture mixed in. Because she was related to a large percentage of the people in the Hilo area, Judy could usually get repairs and services completed any time of the week, often free as a favor to a "family member." And, any member of the Mauna Loa staff was considered part of this extended family, with the requisite invitations to weddings, first-year birthday parties, Christmas celebrations, and family luaus.

Judy's ready smile, enthusiasm, empathy, friendliness, and knowledge made her memorable to all she met. She continued her role as the official greeter for Mauna Loa and Hilo throughout all her years of service. Visitors and scientists who came to Mauna Loa from around the world remained her friends for life. Often these people would come back to the Big Island decades later just to renew her acquaintance and to introduce their spouses and children to her, a living embodiment of the "Aloha" spirit.

John Chin

John joined the Mauna Loa Observatory, U.S. Weather Bureau Research Station, in 1960 to work on the Scripps Institution of Oceanography (SIO) CO_2 program. He left in 1962 to broaden his skills at NASA and Lockheed before returning to Mauna Loa in 1964 to again conduct the SIO atmospheric CO_2 monitoring program along with other observatory duties. In 1966, John left for a brief time to work at Cloud Physics, University of Hawaii, studying warm rain projects. In 1968, he rejoined Mauna Loa and Federal service. In 1974 he helped in the expansion of the NOAA carbon cycle programs at MLO. As a physicist he continued to operate both SIO and NOAA CO_2 programs, in addition to many other observatory duties, through to his retirement in December 2000, completing 37 years of service at Mauna Loa.

It has been calculated that during his tenure, John made at least 6000 round trips on the Mauna Loa Road, which is equivalent to driving around the Earth 25 times at the equator.

John is known for his reliability and predictability. He always arrived for work within 2 minutes of a set time, and his weekly lunch menu never varied. For 37 years, his lunch always consisted of a sandwich, tuna or chicken, a banana, carrot or celery sticks, and a small box of raisins that he ate exactly at 12 noon.

When John first entered service at Mauna Loa Observatory in 1960, the annual mean atmospheric CO_2 concentration was 316 ppm. The annual mean was 370 ppm in the year he retired. The MLO CO_2 curve is recognized around the world as one of the longest and most important geophysical records in existence; John can be proud that he was instrumental in helping make it so.

Contents

CMDL Organization, 2001

The CMDL organization structure features five research areas organized according to scientific discipline as follows: (1) Carbon Cycle; (2) Halocarbons and other Atmospheric Trace Species; (3) Ozone and Water Vapor; (4) Aerosols and Radiation; and (5) Observatory Operations. At the end of 2001, the laboratory staff consisted of 50 Civil Service personnel (excluding part-time student assistants), 26 CIRES/University of Colorado personnel, and 2 NOAA Corps officers, as well as several visitors and people on special appointments.

Director, CMDL
David Hofmann
(303) 497-6966

Program Management Specialist	Physical Science Administrator	Budget Analyst
Ann Thorne	Russell C. Schnell	Brenda Seader
(303) 497-6074	(303) 497-6733	(303) 497-6070

Carbon Cycle

Pieter Tans
(303) 497-6678

Halocarbons and other
Atmos. Trace Species

James W. Elkins
(303) 497-6224

Ozone and Water Vapor

Samuel Oltmans
(303) 497-6676

Observatory Operations
and Data Management

Russell C. Schnell
(303) 497-6733

Aerosols and Radiation
John Ogren
(303) 497-6210
Ellsworth Dutton
(303) 497-6660

Barrow Observatory	Mauna Loa Observatory	Samoa Observatory	South Pole Observatory
Daniel J. Endres	John Barnes	Joel Michalski	Pauline Roberts
(907) 852-6500	(808) 933-6965	(684) 622-7455	(303) 497-6655

CMDL Staff, 2001

Director's Office

David J. Hofmann, Director
Russell C. Schnell, Phys. Sci. Admin.
Ann Thorne, Pgm. Management Specialist
Brenda Seader, Budget Analyst
Linda Sachetti, Admin. Assistant
Rita Rosson, Editorial Assistant

Special Projects

Lori Bruhwiler, Physical Scientist
Eric Hackathorn, Computer Specialist

Aerosols and Radiation

Ellsworth Dutton, Meteorologist
John Ogren, Physical Scientist
Connie Craig, Secretary
Elizabeth Andrews, CIRES
Gail Anderson, USAF
Greg Bland, Student
Barry Bodhaine, Meteorologist
David Jackson, Electronic Technician
Anne Jefferson, CIRES
David Longenecker, CIRES
Donald Nelson, Meteorologist
Katie O'Gara, CIRES Student
Patrick Sheridan, Physical Scientist
Robert Stone, CIRES
Renee Tatusko, Physical Scientist
James Treadwell, Electronic Technican
James Wendell, Electronic Technician
Norman Wood, CIRES

Ozone and Water Vapor

Samuel Oltmans, Physicist
Beverly O'Donnell, Secretary
Gloria Carbaugh, Physical Scientist
Dan Chao, Phys. Science Aid
Mark Clark, CIRES
Robert Evans, Research Scientist
Joyce Harris, Research Physical Scientist
Bryan Johnson, Research Chemist
Michael O'Neill, CIRES
Dorothy Quincy, CIRES
Eric Rice, CIRES Student
David Sherman, CIRES
Brian Vasel, CIRES
Holger Vömel, CIRES
Brooke Walsh, Student

Carbon Cycle

Pieter Tans, Senior Scientist
Connie Craig, Secretary
Peter Bakwin, Physicist
Thomas Conway, Research Chemist
Ed Dlugokencky, Research Chemist
Sara Fletcher, CIRES Grad. Res. Asst.
Douglas Guenther, CIRES
Michael Hahn, CIRES
Duane Kitzis, CIRES
Patricia Lang, Physical Scientist
Kenneth Masarie, Research Physicist
John Miller, CIRES Grad. Res. Asst.
Anthony Nepomuceno, Phys. Science Aid
Paul Novelli, Research Chemist
Karen Partak, CIRES
Natalie Paynter, CIRES
Britt Stephens, CIRES
Kirk Thoning, Physicist
Michael Trudeau, CIRES
Conglong Zhao, CIRES

Halocarbons and other Atmospheric Trace Species

James Elkins, Supervisory Physicist
Debra Hansen, Secretary
James Butler, Research Chemist
Geoffrey Dutton, CIRES
Brad Hall, Physical Scientist
Dale Hurst, CIRES
Daniel King, CIRES
Eric Kline, CIRES
Debbie Mondeel, CIRES
Steve Montzka, Research Chemist
Fred Moore, CIRES
David Nance, CIRES
Karen Pietruszka, Student
Pavel Romashkin, CIRES
Thayne Thompson, Physicist

Observatory Operations

Russell C. Schnell, Phy. Sci. Admin.
Debra Hansen, Secretary
Andrew Clarke, Chemist
Thomas Mefford, CIRES
Donald Neff, Physicist

Daniel Endres, Physicist,
  Station Chief, **Barrow**
Glen McConville, Electronic Technician

John Barnes, Physicist,
  Director, **Mauna Loa**
Leslie Pajo, Office Automation Clerk
Paul Fukumura-Sawada, Electronic Engineer
Darryl Kuniyuki, Electronic Engineer
Steven Ryan, Physical Scientist
Robert Uchida, Electronic Technician
Alan Yoshinaga, Chemist

Joel Michalski, NOAA Corps,
  Station Chief, **Samoa**
Malcom Gaylord, Electronic Engineer

Pauline Roberts, NOAA Corps,
  Station Chief, **South Pole**
Eric Sandberg, Electronic Engineer
Scott Wingerter, NOAA Corps
Loreen Lock, Chemist

CMDL Station Information

Name:	**Barrow (BRW)**	**Mauna Loa (MLO)**
Latitude:	71.323°N	19.539°N
Longitude:	156.609°W	155.578°W
Elevation:	8 m	3397 m
Time Zone:	GMT – 9	GMT – 10
Office Hours:	8:00 am-5:00 pm	8:00 am-5:00 pm
Telephone		
Office hours:	(907) 852-6500	(808) 933-6965
Fax:	(907) 852-4622	(808) 933-6967
Postal Address:	Officer in Charge	U.S. Dept. of Commerce
	NOAA/ERL/CMDL	NOAA - Mauna Loa Observatory, Rm. 202
	Pouch 888	P.O. Box 275
	Barrow, AK 99723	Hilo, HI 96721
Freight Address:	Officer in Charge	U.S. Dept. of Commerce
	NOAA/ERL/CMDL	NOAA - Mauna Loa Observatory
	617 Cunningham	154 Waianuenue Ave.
	Barrow, AK 99723	Hilo, HI 96720-2452

Name:	**Samoa (SMO)**	**South Pole (SPO)**
Latitude:	14.232°S	89.997°S
Longitude:	170.563°W	102.0°E
Elevation:	77 m	2837 m
Time Zone:	GMT – 11	GMT + 12
Office Hours:	8:00 am-5:00 pm	8:00 am-5:00 pm
Telephone:		
Office hours:	011 (684) 622-7455	Relayed through CMDL Boulder
After hours:	011 (684) 258-2847	
Fax:	011 (684) 622-7455	
Postal Address:	Officer in Charge	Officer in Charge
	U.S. Dept. of Commerce	NOAA/CMDL Clean Air Facility S-257
	NOAA - CMDL Samoa Observatory	South Pole, Antarctica
	Pago Pago, American Samoa 96799	PSC 468 Box 402
		FPO AP 96598-5402
Freight Address:	Same as above	Same as above

1. Observatory, Meteorology, and Data Management Operations

1.1. MAUNA LOA OBSERVATORY

J. BARNES, J. CHIN, P. FUKUMURA-SAWADA, D. KUNIYUKI,
L. PAJO, S. RYAN, B. UCHIDA, AND A. YOSHINAGA

1.1.1. OPERATIONS

The most noticeable change to the Mauna Loa Observatory (MLO), Hawaii, was moving the Jet Propulsion Laboratory (JPL) ozone lidar from the trailers into the Network for the Detection of Stratospheric Change (NDSC) building in March 2001. This move was long awaited and went smoothly. The trailers were moved to the upper parking lot for equipment removal and will be returned to JPL in the future. After the trailers were moved, construction was started in August 2001 on a new lidar building to house a Doppler lidar built by Michigan Aerospace to measure wind from the ground through the troposphere. The project is being funded by NOAA and managed by the University of New Hampshire. The old radiation platform above the Keeling building was modified for new mercury detection equipment installed by the Environmental Protection Agency (EPA) in August 2000. The top section of the platform was removed and the lower part reinforced.

U.S. Army contractors installed a new pole for the Army's radio repeater antenna. The pole is downslope from MLO and should solve a previous electrical noise problem with the National Institute of Water and Atmospheric Research/ultraviolet (NIWA/UV) spectrometer. The contractors also began modifying the visitor building to house the radio equipment. A scientific drilling group for the Hawaii Volcano Observatory (HVO), U.S. Geological Survey (USGS), drilled a 140-m (400-ft) well for the placement of a seismometer and strain gauge for monitoring Mauna Loa volcano. The instruments and telemetry are solar powered and located on the edge of the helicopter pad.

Observatory use by visiting groups for short-term calibrations of their instruments (of a few weeks duration) continued to increase. There were many repeat visits as well as several new groups. For the most part, the instruments are for various solar radiation measurements of varying complexity. One Japanese group left an instrument running unattended for several weeks, returning to pack and ship the instrument back to Japan. Computer network connections were added to the visitor building to accommodate them.

John Chin, who retired after more than 30 years of service at MLO, was replaced by an electrical engineer with experience at Pearl Harbor with the Department of Defense and with telescopes on Mauna Kea.

Outreach

Requests to visit the observatory continued, many through the Internet. Several classes from the University of Hawaii at Hilo toured MLO, and several lectures were given by the station chief on campus. A National Aeronautics and Space Administration/Earth Observing System (NASA/EOS)/Aqua Satellite educational webcast was transmitted through MLO's Internet connection in May 2000. MLO personnel were filmed and interviewed, and participated in the online discussions with the elementary schools that were logged on.

The MLO station chief lectured on climate change and pollution to a group of 60 senior citizens in Kona and to about 20 at an Aloha Exchange Club meeting. He also judged the Hawaii County Science Fair and presented awards for environmentally related projects. Two high school summer students were mentored each summer on short data analysis projects for part of the University of Hawaii at Hilo's Upward Bound project. Two university students also worked summers on the lidar program, one from the University of Pennsylvania and the other from the University of Hawaii at Hilo.

A MLO scientist received the Department of Commerce bronze medal for his work with the Hawaii schools Volcano Gas observatory Network (VOGNET). The VOGNET program began its sixth year in 2001. A prototype PC-operated continuous condensation nuclei (CN) counter was developed and tested in the summer of 2000 at MLO. This CN counter can be built by students for $450 with readily available parts. Hawaii Preparatory Academy (HPA) received a grant from the local electric company to fund a network of these instruments at schools around the Big Island. In spring 2001 students and teachers at six schools began assembling their CN counters, which were then tested and calibrated at MLO/Hilo in August-September 2001. At the end of 2001, the instruments, connected to the central HPA data archival computer by modem, were collecting continuous data at the schools. A web page developed and run by HPA students will provide the public with near-real-time information on the levels of volcanic pollution around the island.

Computers/Network

The networks at the Hilo office and at portions of the mountain site have been changed from the older coax type to the 10 base-T type. The Hilo office was upgraded further by installating fast Ethernet devices running at 100 megabits on its Local Area Network (LAN). The router in the Hilo office, three computers, and two network printers were obtained from excessed census equipment. More network hubs were added at various locations at the observatory to accommodate increased visiting projects requiring Internet access. Most of the computers and network devices are now on some type of uninterruptible power supply (UPS). At the end of 2001 MLO had 51 computers at its site. Three additional racks were installed to provide a more efficient use of space.

MLO's domain name was changed at the Hilo site from "mlo.hawaii.gov" to "mlo.noaa.gov" and is officially registered in the NOAA database. This allows the staff access to NOAA sites to obtain data and programs without a fee. It affects only the MLO Hilo addresses. The U.S. Fish and Wildlife Service still retains the "mlo.hawaii.gov" address, and the mountain site remains at "mtn.noaa.gov". MLO's new web address is "www.mlo.noaa.gov". In June the High Altitude Observatory (HAO) installed its own 56-K line at the observatory. HAO is now independent from the

TABLE 1.1. Summary of Measurement Programs at MLO in 2000-2001—continued

Program/Measurement	Instrument	Sampling Frequency
Meteorology		
Air temperature	Aspirated thermistor, 2-, 9-, 37-m heights*	Continuous
	Max.-min. thermometers, 2.5-m height	1 day⁻¹, weekdays
Air temperature (30-70 km)	Lidar	1 profile wk⁻¹
Temperature gradient	Aspirated thermistors, 2-, 9-, 37-m heights*	Continuous
Dewpoint temperature	Dewpoint hygrometer, 2-m height*	Continuous
Relative humidity	TSL, 2-m height*	Continuous
Pressure	Capacitance transducer*	Continuous
Wind (speed and direction)	8.5-, 10-, and 38-m heights*	Continuous
Precipitation	Rain gauge, 20-cm diameter	5 wk⁻¹
	Rain gauge, 20-cm diameter‡	1 wk⁻¹
	Rain gauge, tipping bucket*	Continuous
Total precipitable water	Foskett IR hygrometer*	Continuous
Precipitation Chemistry		
pH	pH meter	1 wk⁻¹
Conductivity	Conductivity bridge	1 wk⁻¹
Cooperative Programs		
CO₂ (SIO)	Applied Physics IR analyzer*	Continuous
CO₂, ¹³C, N₂O (SIO)	5-L evacuated glass flasks§	1 pair wk⁻¹
CO₂, CO, CH₄, ¹³C/¹²C (CSIRO)	Pressurized glass flask sample	3 pair mo⁻¹
O₂ analyses (SIO)	5-L glass flasks through tower line and pump unit§	3 (2 mo)⁻¹
Total suspended particulates (DOE)	High-volume sampler	Continuous (1 filter wk⁻¹)
Ultraviolet radiation (CSU and USDA)	Multi-wavelength radiometer (direct, diffuse, shadow band)	Continuous
Radionuclide deposition (DOE)	Ion-exchange column	Quarterly sample
Aerosol chemistry (Univ. of Calif., Davis)	Programmed filter sampler	Integrated 3-day sample, 1 continuous and 1 downslope sample (4 days)⁻¹
Hg°, Hg⁻², Hgᵖ (EPA/NERL)	Tekran 2537A, 1130 and 1135p (began 7/01)	Continuous
Particulate 2.5-10 μm (EPA/NERL)	Dichotomous Partisol-Plus Model 2025 (began 8/01)	1 downslope sample wk⁻¹
Sulfate, nitrate, aerosols (Univ. of Hawaii)	Filter system	Daily, 2000-0600 LST
Radon (ANSTO)	Aerosol scavenging of Rn daughters; two-filter system*	Continuous; integrated 30-min samples
AERONET sunphotometers (NASA Goddard)	Automated solar-powered sunphotometers	Continuous
Global Positioning System (GPS) Test Bed (FAA and Stanford University)	GPS-derived column water vapor profiles	Continuous
Earthquakes (HVO-USGS Menlo Park)	Seismometer	Continuous
Earthquakes (Northwestern University)	Seismometer (ended 6/01)	Continuous
CO isotopes (SUNY)	1000 psi cylinder	1 wk⁻¹
Cosmic dust (CALTECH)	Magnetic collector	1 wk⁻¹ (ended 1/01); 1 (2 wk)⁻¹ (began 1/01)
Volcanic activity (HVO)	Seismic and expansion instrument in 370-ft-deep well	Continuous
Network for the Detection of Stratospheric Change (NDSC)		
Ultraviolet radiation (NOAA and NIWA)	UV spectroradiometer (285-450 nm), 0.8-nm resolution*	Continuous
Stratospheric O₃ profiles, 20-66 km (Univ. of Mass., Amherst)	Millitech Corp., 110.8-GHz microwave ozone spectroscopy	3 profiles h⁻¹
Stratospheric water vapor profiles, 40-80 km, 10-15 km resolution (NRL)	Millimeterwave spectrometer	Continuous
Stratospheric O₃ profiles (15-55 km), temperature (20-75 km), aerosol profiles (15-40 km) (JPL)	UV lidar*	3-4 profiles wk⁻¹
NO₂ (NIWA and NOAA)	Slant column NO₂ spectrometer	Continuous, daytime
BrO (NIWA and NOAA)	Column BrO spectrometer	Continuous, daytime
Column O₃, UVB (AES, Canada)	Two Brewer spectrophotometers	Daily
Solar spectra (Univ. of Denver)	FTIR spectrometer, automated*	5 days wk⁻¹

All instruments are at MLO unless indicated.
*Data from this instrument recorded and processed by microcomputers.
†Kumukahi only.
‡Kulani Mauka.
§MLO and Kumukahi.

remained on line. The Chromatograph for Atmospheric Trace Species (CATS) GC had a new computer installed in January 2001. In April 2001 all halon fire extinguishers were removed from all buildings at MLO at the request of Boulder. This alleviated a noisy background trace that had existed for a while. In August 2001 the RITS and CATS units were shut down because the calibration tanks and valve replacement parts did not arrive. Normal operation resumed the next month when tanks and parts were received. The last remaining channel (B) on RITS was shut down in December 2000 as the last few intercomparisons were completed.

Aerosols

The Atmospheric Sampling System, installed in April 2000, is a new automated system for measuring aerosol light scattering as a function of wavelength, aerosol light absorption, and condensation nuclei. Two particle impactors are used to measure these properties for aerosol sizes less than 1 and 10 μm. The main components are a Thermo Systems Incorporated (TSI) three-wavelength nephelometer (model 3563), a Radiance Research particle soot absorption photometer (PSAP), and a TSI condensation nucleus counter (CNC; model 3760). The system measures the following parameters: total and backward scattering coefficient time series at 450-, 550-, and 700-nm wavelengths in two size ranges; absorption coefficient time series at 565 nm in two size ranges; and CN concentration time series. From the measurements the following parameters can be calculated: single scattering albedo at about 550 nm in two size ranges; Ångström coefficient; and hemispheric backward scattering fraction in two size ranges.

Condensation nuclei. The old TSI unit was shipped to Boulder in May 2001 after a year of comparison with the new TSI unit. The Pollak CNC is no longer in use and was moved to the Hilo office to calibrate the VOGNET continuous CNCs.

Aerosol light scattering. The three-wavelength nephelometer measuring at 450, 550, and 700 nm was shipped to Boulder in May 2001 after a year of comparison with the replacement nephelometer.

Aerosol light absorption. The aethalometer was found to be non-Y2K compliant. When a lengthy power failure occurs, the instrument's year resets to 1994. MLO staff must manually reset the date to the current year. In August 2000 the roller mechanism had to be repaired, which caused the unit to be down for 5 days. In July 2001 the instrument was sent to Magee Scientific to be upgraded. In October a new seven-wavelength spectrum aethalometer was installed at the observatory.

Stratospheric and upper tropospheric aerosols. Weekly observations continued with the Nd:YAG lidar throughout 2000 and 2001. The background period continued, and no stratospheric aerosol was conclusively measured from a volcanic eruption. Raman water vapor measurements were initiated in 2000 and improved with the purchase of new photomultiplier tubes optimized for the red part of the spectrum. The telescope optical support structure was extended to accommodate one of the 74-cm-diameter (long-focal-length) mirrors that had never been used. At that time the ruby telescope was remounted for testing. A proposal to

NASA was funded to validate water vapor measurements from the Atmospheric Infrared Sounder (AIRS) instrument on the Aqua satellite. A computer power supply for the expansion chassis failed and was replaced in August 2001. Other maintenance consisted of flashlamp and cooling water changes for the laser.

Solar Radiation

The Physikalisch-Meteorologisches Observatorium Davos (PMOD) three-wavelength (380, 500, and 778 nm) sunphotometer was removed from service in April 2001 because of degraded filters. The normal incidence pyrheliometer (the data go back to 1958) is calibrated periodically against an active-cavity radiometer. Seven of these comparisons were done in 2000 and three in 2001. The active-cavity radiometer was sent to Boulder for intercomparisons in May 2001. Mauna Loa Observatory is also used to calibrate handheld sunphotometers by the Langley technique; two instruments were calibrated in 2000 and 14 were calibrated in 2001. The observatory is used to calibrate CMDL's Yankee UVB instruments; three were calibrated in 2000 and none were calibrated in 2001. SP01-A and SP02 instruments (four-channel tracking sunphotometers) were installed temporarily in the tracking dome for calibrations and comparisons with the precision filter radiometer. Two SP01-A instruments were installed in 2000, and two SP02 instruments were installed in 2001. A data line and a pressure sensor were connected to the HP data acquisition system, and a temperature controller was installed in the dome to support the SP02 installations.

Meteorology

A computer-based "New Met System" measures station pressure, temperatures at the 2-, 9-, and 37-m levels, dewpoint temperature at the 2-m level, and wind speeds and directions at the 8.5-, 10-, and 38-m levels of the MLO Observation Tower. Precipitation is measured with a tipping bucket rain gauge. This new system continues to operate unaltered and with high reliability.

Precipitation Chemistry

The MLO modified program of precipitation chemistry collection and analyses continued throughout 2000-2001 within the basic MLO operational routine. This program consists of collections of a weekly integrated precipitation sample from the Hilo NWS station and the collection of precipitation event samples at MLO. These samples are analyzed in the Hilo laboratory for pH and conductivity.

Cooperative Programs

MLO cooperative programs are listed in Table 1.1. New programs and changes not discussed in the NDSC section (next) are presented here.

In July 2001 two scientists from the U.S. EPA National Exposure Research Laboratory (NERL) arrived at MLO to install a mercury analyzer and dichotomous partisol sampler and train MLO staff on its operation and maintenance. On July 31, 2001, the mercury analyzer was placed on line. The system continuously measures elemental mercury (Hg°), reactive gaseous mercury (Hg^{+2}), and particulate mercury (Hg^p). On August 23, 2001, the particle sampler was activated. The State of Hawaii Health Department will

weigh the filters from the partisol sampler. Filters are collected only during downslope conditions, and one filter sample is collected each week.

The Australian Nuclear Science and Technology Organization (ANSTO) has measured radon continuously at MLO since 1989. A new data logger and computer were installed in March 2000, and a new flow meter was installed in May 2001.

For the University of California, Davis, particulate special-event projects, the Asian Pacific Regional Aerosol Characterization Experiment (ACE-Asia)-MLO Collabora-tion, multistage drum units and hi-vol filters were installed/exposed in March 2000, March 2001, and August 2001 for approximately 6 weeks each and then shipped back to the University of California, Davis. The State University of New York (SUNY) CO isotope sample compressor failed in June 2001. The California Institute of Technology (CALTECH) cosmic dust collector continued to operate, although the weekly sampling was changed to biweekly in January 2001.

Network for the Detection of Stratospheric Change (NDSC)

All NDSC instruments from previous years continued observations. The NOAA lidar, ozonesonde, and Dobson operations, which are also part of the MLO NDSC facility, are described in other sections of this report.

Ultraviolet/Visible (UV/VIS) absorption spectroradiometer. The UV instrument began operation in the MLO NDSC building in November 1997. The UV spectroradiometer uses a double monochromator grating spectrometer to measure the UV spectrum between 285 and 450 nm with a resolution of 0.8 nm. Measurements are taken at 5° solar zenith angle intervals throughout the day. The instrument is calibrated weekly with a mercury lamp and a 45-W quartz lamp. An absolute-standard 1000-W FEL lamp calibration is performed twice each year. In August 2001 NIWA installed a new calibration lamp unit and a precision power supply unit. The power supply unit is programmable and maintains and controls the output current automatically during weekly calibrations.

Microwave ozone and water vapor spectroscopy systems. The University of Massachusetts microwave instrument measures the vertical profile of ozone from 20 to 66 km with a vertical resolution of 10 km or less up to 40 km, degrading to 17 km at 60 km. The ozone altitude distribution is retrieved from the details of the pressure-broadened line shape. The Naval Research Laboratory (NRL) operates a similar water vapor system that measures vertical profiles typically from 40 to 80 km. Both systems received the usual maintenance and continued operations in 2000 and 2001.

UV lidar. In March 2001 the JPL ozone lidar was moved out of the trailers and into the NDSC building. The move took about 6 weeks. A new Nd:YAG laser replaced one of the excimer lasers for better reliability for all-night operation during campaigns. JPL also used the opportunity offered by the move to extend the range of its measurements to lower altitudes by redesigning some of the optics and adding channels. The additional space has made the lidar easier to operate and maintain.

NO₂, BrO spectrometers. Since July 9, 1996, stratospheric NO_2 has been measured at MLO by the twilight-zenith technique with a NIWA UV/VIS spectrometer. Two additional spectrometers were added in December 1999 for column measurements of NO_2 and BrO. The BrO spectrometer is used to measure stratospheric bromine monoxide, an important species in current attempts to model future nonpolar ozone trends. The instruments can be operated over the Internet by NIWA in Lauder, New Zealand.

Brewer spectrophotometer. The measurements of O_3 and UVB radiation with a single monochromator Brewer instrument are supplemented by all-sky images recorded every 10 minutes to assist in the analysis of the UVB data. Overviews of the automatic operation of the instrument and data retrievals are carried out remotely from Atmospheric Environment Service (AES), now called Meteorological Service, in Toronto over the Internet. The data are archived at the World Ozone and Ultraviolet Data Centre (WOUDC) in Toronto. Up-to-date preliminary data are available over the Internet from AES. Publication of new results is planned after thorough analysis of a longer data record. This program continued throughout 2000-2001. Annual maintenance and calibration checks and other instrumentation calibrations were carried out in March 2000.

Solar Fourier transform infrared (FTIR) spectrometer. The University of Denver FTIR spectrometer routinely monitors HCl, HNO_3, O_3, N_2O, HCFC-22, HF, CH_4, NO, HCN, CO, C_2H_2, and C_2H_6. Because of the automatic nature of the instrument, the program is able to look at diurnal variations in the species. Data are not collected on Sundays or Monday mornings unless special operators are on site to add liquid nitrogen into the instrument.

1.2. BARROW OBSERVATORY

D. ENDRES AND G. MCCONVILLE

1.2.1. OPERATIONS

Begun in January 1973, operations at Barrow Observatory (BRW), Barrow, Alaska, have grown from a small program to one that now touches upon, or supports components of, almost every major climate change study in the U.S. Arctic. In addition to a full suite of CMDL measurements, programs include research activities from several U.S. government agencies and a broad selection of universities in the United States and other countries. As the Arctic becomes recognized as the location where global climate warming will probably be observed first and where the effects of the warming will be relatively easy to detect, BRW measurements and facilities are becoming ever more in demand.

In 2001 a new garage with greater square footage than the main laboratory was constructed to house observatory vehicles and up to 100 large compressed gas cylinders. There is also room for a small workshop and storage. The ability to park vehicles in a warm garage will save on vehicle maintenance and will allow for a safe and dry environment to unload, pack, and unpack shipments. Compressed gas cylinders were previously stored at the Air Force Long

Range Radar Site, formerly the Distant Early Warning (DEW) Line site, in an unheated storage building one-half mile from the Barrow station or at the station on the tundra in summer mud or under snow in the winter. All the small, old buildings on site were removed as part of the garage-building program; this has resulted in a much-improved overall appearance.

Construction on the BRW access road was essentially completed at the end of summer 2000, and it was graded in 2001. By summer 2002 the road will be settled to the point that the final gravel coating can be applied. The road was passable to wheeled vehicles most of winter 2000-2001 for the first time ever, with only minor interruptions from drifting snow.

From 1994 to 2000 there were no personnel changes at BRW. In 2000 the station chief completed 16 years at BRW and the electronics technician 6 years. In July 2000 the technician transferred to the CMDL American Samoa Observatory (SMO) and was replaced with a technician who had previously worked at BRW. This technician left in December 2000 and will be replaced by a technician who formerly wintered at the CMDL South Pole Observatory (SPO).

The station staff continues to be involved with the Barrow Arctic Science Consortium (BASC), and the station chief is a member of the Barrow Environmental Observatory Management Committee. The station chief will travel to Nome, Alaska, in January 2002 to help train five native students and two teachers from villages along the Bering Sea coast of Russia in techniques for the collection of snow samples for later analysis of the mercury content. The chief will similarly train a number of native students and teachers from the North Slope of Alaska. The project is a 5-yr effort funded by the U.S. State Department and the U.S. Environmental Protection Agency (EPA) through BASC to determine the extent and severity of mercury pollution in Bering Sea coastal areas of Alaska and Russia. Mercury found in the milk of native subsistence hunter mothers is believed to have its origins in power plant plumes flowing into the Arctic from lower latitudes.

In the middle of 2001 Internet service to BRW, supplied by the U.S. Department of Energy (DOE) Atmospheric Radiation Measurement (ARM) program, was reduced from T-1 to 256K service when the cost of a T-1 connection increased 560%. As a consequence, access to many web pages needed for efficient station operation is no longer possible. A return to T-1 connectivity is being pursued.

In 2000-2001, 232 visitors to BRW signed the guest book, including the acting administrator of NOAA and documentary television crews from England and Japan. The community of Barrow hosted the Alaska Presswomen convention in 2001, which brought reporters from around the United States to Barrow. A group of journalists from the meeting visited BRW to gather information for their local newspapers and magazines. For one of many resulting articles, BRW was featured on the cover of *Biology Digest*.

The Y2K problem turned out to be a non-event for BRW. All data computers passed through the change of the year with no problems. One old office computer experienced some difficulties, signaling that it was in need of replacement.

1.2.2. PROGRAMS

Table 1.2 lists programs for 2000-2001 at BRW as well as cooperative programs that operated in 2000-2001 and that are approved for 2002. Highlights of the programs are as follows:

Gases

Carbon dioxide. The CO_2 system continues to have problems associated with aging components. The Siemens Ultramat 5-E analyzer is showing signs of a temperature-dependent signal. The solution has been to leave the door to the rack open for better airflow around the instrument.

Flask samples. Flask samples were collected as available and as scheduled with no major problems. Isotopic composition measurements of CO_2 continue, and data from this program can be found elsewhere in this report.

Methane. The HP-6890 gas chromatograph (GC) continues to run with very few problems. Data show a clearly defined annual frequency, with higher values occurring in the winter months and lower values in the summer.

Total column ozone. Dobson spectrophotometer no. 91 ran well the entire period with no major problems. Regular calibrations were performed to maintain data quality at a high standard. A noisy bearing will be repaired when the BRW instrument is sent to Boulder in winter 2002 for recalibration. Dobson measurements are not possible during the winter months because of the lack of sunlight, so no measurements will be missed during the recalibration of the instrument. Column ozone values as high as 400 Dobson units (DU) and values as low as 290 DU were recorded over the past 2 years.

Carbon monoxide. A Trace Analytical GC has been the station instrument since 1991 and continues to run with minimal maintenance. The major work to the system this past year was replacement of the Hg scrubber and the UV lamp.

Halocarbons and other atmospheric trace species. The Chromatograph for Atmospheric Trace Species (CATS) ran well with only minor problems. Fourteen compounds are measured in situ with the CATS system. The most notable problem over the past 2 years was an inoperative water trap that produced poor data on one of the four channels for a short period of time. After the trap was replaced, the instrument has run properly. A flash heater for the cryo-cooler was replaced when the old one burned out.

Halocarbon flask samples were collected on a routine schedule and provide a comparison for in situ instrument performance. They also enable analysis of chemical species that are not measured in the field.

Aerosols

Arctic haze, air pollution from Eurasia, continues to dominate the springtime aerosol measurements at BRW. The haze concentrations build up over winter followed by declines in late spring/early summer when persistent cloudiness returns to the North Slope. The aerosol equipment ran well for the entire 2000-2001 period with only minor problems. Personnel from Boulder performed annual maintenance and system calibrations. All data from

TABLE 1.2. Summary of Measurement Programs at BRW in 2000-2001

Program/Measurement	Instrument	Sampling Frequency
Gases		
CO$_2$	Siemens Ultramat 5-E analyzer	Continuous
	3-L glass flasks	1 pair wk^{-1}
	0.5-L glass flasks, through analyzer	1 pair wk^{-1}
CO$_2$, CH$_4$, CO, and ^{13}C/^{12}C and ^{18}O/^{16}O of CO$_2$	0.5-L glass flasks, P^3 pump unit	1 pair wk^{-1}
CH$_4$	Carle automated GC	1 sample (12 min)$^{-1}$
Surface O$_3$	Dasibi ozone meter	Continuous
Total O$_3$	Dobson spectrophotometer no. 91	3 day^{-1}
CO	Trace Analytical GC	1 sample (6 min)$^{-1}$
N$_2$O, CFC-11, CFC-12, CFC-113, CH$_3$CCl$_3$, CCl$_4$, SF$_6$, HCFC-22, HCFC-21, HCFC-124, HCFC-141b, HCFC-142b, HCFC-152a, CH$_3$Br, CH$_3$I, CH$_3$Cl, CH$_2$Cl$_2$, CHCl$_3$, CH$_2$Br$_2$, CHBr$_3$, C$_2$Cl$_4$, H-1301, H-1211, HFC-134a, C$_6$H$_6$, COS	850-mL, 2.5-L, or 3-L stainless-steel flasks	1 pair wk^{-1}
CFC-11, CFC-12, CFC-113, N$_2$O, CH$_3$CCl$_3$, CCl$_4$, CH$_3$Br, CH$_3$Cl, H-1211, SF$_6$, HCFC-22, HCFC-142b, CHCl$_3$, COS	Automated CATS GC	1 sample h^{-1}
Aerosols		
Condensation nuclei	Pollak CNC	1 day^{-1}
	TSI CNC	Continuous
Optical properties	Three-wavelength nephelometer	Continuous
	Radiance Research PSAP	Continuous
Black carbon	Aethalometer	Continuous
Solar Radiation		
Global irradiance	Eppley pyranometers with Q and RG8 filters	Continuous
Direct irradiance	Tracking pyrheliometer	Continuous
	Eppley pyrheliometer with Q, OG1, RG2, and RG8 filters	Discrete
Albedo	Eppley pyranometer	Continuous
Ultraviolet B irradiance	NILU radiometer	Continuous
	Yankee UVB radiometer	Continuous
Ultraviolet spectral irradiance	Biospherical five-wavelength photometer	Continuous
Aerosol optical depth	Carter-Scott four-wavelength sunphotometer	Continuous
Terrestrial (IR) Radiation		
Upwelling and downwelling	Eppley pyrgeometers	Continuous
Meteorology		
Air temperature	Thermistor, two levels	Continuous
	Max.-min. thermometers	1 day^{-1}
Dewpoint temperature	Dewpoint hygrometer	Continuous
Pressure	Capacitance transducer	Continuous
	Mercurial barometer	Discrete
Wind (speed and direction)	R.M. Young aerovane	Continuous
Precipitation	Rain gauge, tipping bucket	Continuous
Cooperative Programs 2000-2001		
Total surface particulates (DOE)	High-volume sampler (1 filter wk^{-1})	Continuous
Precipitation gauge (USDA)	Nipher shield, Alter shield, two buckets	1 mo^{-1}
Magnetic fields (USGS)	Three-component fluxgate magnetometer and total field proton magnetometer	Continuous
	Declination/inclination magnetometer sample	6 sets mo^{-1}
CO$_2$, ^{13}C, N$_2$O (SIO)	5-L evacuated glass flasks (3 flasks set^{-1})	1 set wk^{-1}
CH$_4$ (Univ. of Calif., Irvine)	Stainless-steel flasks	1 set (3 mo)$^{-1}$
O$_2$ in air (Princeton)	3-L glass flasks	1 pair wk^{-1}
CO$_2$ flux (San Diego State Univ.)	CO$_2$ and H$_2$O infrared gas analyzer and sonic anemometer	Continuous, check site 1 wk^{-1}

TABLE 1.2. Summary of Measurement Programs at BRW in 2000-2001—continued

Program/Measurement	Instrument	Sampling Frequency
Cooperative Programs 2000-2001—continued		
Magnetic fields (NAVSWC)	^{3}He sensors	Continuous
Magnetic micropulsations (Univ. of Tokyo)	Magnetometer and cassette recorder	1 (3 wk)$^{-1}$
UV (NSF)	UV spectrometer	1 scan (0.5 h)$^{-1}$
Thaw depth in permafrost (SUNY)	Temperature probe	Continuous
Total VOC and heavy metals (Hokkaido Univ.)	Filter samples	1 h^{-1}
Atmospheric mercury (EPA)	Mercury vapor monitors	Continuous, spring
Atmospheric mercury (NOAA/ARL)	Mercury vapor monitors	Continuous
Arctic coastal ice characteristics (Univ. of Washington, Seattle) (began 2001)	Optical sensors	Continuous
POES satellite transmission downlink (NESDIS) (began 2001)	3-m dish and receiver	Continuous
Eider duck migration patterns (Univ. of Alaska, Fairbanks) (began 2001)	Radar and optical observations	Seasonal
Soil organic matter (Univ. of Alaska, Fairbanks) (began 2001)	Vegetation samples	Discrete
Organochlorine contaminants (Oregon State Univ.) (began 2001)	Air samples	Discrete weekly
Snow radiation (JMA/MRI, Japan) (began 2001)	Albedo and reflections from snow	Continuous
Mercury in snow (Univ. of Michigan) (began 2001)	Snow samples	Winter season
Cooperative Programs Approved for 2002		
Persistent organic pollutants (Battelle-Northwest Labs.)	High-volume pump	Continuous
SuomiNet GPS meteorology station (Univ. of Alaska, Fairbanks)	GPS water vapor measuring station	Continuous
NOAA Climate Reference Network Station	Global climate reference station	Continuous
Dimethyl sulfide (Univ. of Alaska, Fairbanks)	Gas chromatograph	Continuous
Removal mechanisms of Arctic haze (Wayne State Univ.)	Aerosol samples	Continuous, weekly filter change
Optical properties of Arctic ecosystems (California State Univ.)	Multispectral optical sensors	Continuous

JMA/MRI, Japan Meteorological Agency/Meteorological Research Institute.

the aerosol system are monitored directly from Boulder in real time via the Internet except the aethalometer black carbon measurements that are first collected on floppy disks before being transferred to the aerosol program computer.

Solar Radiation

Several new solar radiation instruments were installed over the 2000-2001 period to specifically measure ultraviolet B (UVB) radiation. One such instrument from Norway, the Norwegian Institute for Air Research (NILU) UVB irradiance radiometer, was found to be less than satisfactory for conditions in BRW. A Yankee UVB radiometer installed about the same time is operating up to design specifications. A third UVB spectral irradiance photometer, from Biospherical Inc., also appears to operate

well. A new sunphotometer, the SP0-1 manufactured by Carter-Scott, was installed in summer 2000 for testing. It was sent to Boulder for calibration during the winter and was subsequently replaced with the SP0-2 in spring 2001. The SP0-2 had a few problems with water leaking into the data/control cable connector, but otherwise it worked well.

In October 2001 a new albedo rack was installed in the clean-air sector, moving the sensors from 1.2 m (4 ft) above ground level to 3.7 m (12 ft). This affords a broader field of view for the sensors.

The majority of data quality issues in the solar radiation program during 2000-2001 came from instrument grounding problems that produced noisy data. Complete replacement of grounding lines on a number of instruments fixed the problems.

Meteorology

The meteorology system had some problems with the Metrabyte modules during 2000-2001. One module lost its program and had to be reinitialized. There were some problems with the dewpoint sensor due to corrosion, and the sensor head was replaced. All other sensor probes were calibrated and adjusted as needed.

Cooperative Programs

The largest new program was a study funded by the NOAA Arctic Research Office and undertaken by the NOAA Air Resources Laboratory (ARL) and CMDL to continuously measure mercury concentrations in air and the flux of mercury into and out of snow. This program entailed installation and maintenance of instrumentation along with mounting of sensors on the roof of the main building. The program will continue to operate through 2002 and possibly much longer. For 2 months each in spring 2000 and 2001, the U.S. EPA operated complementary mercury in air and mercury flux studies at BRW.

The newest cooperative program at BRW comes from the NOAA National Environmental Satellite, Data, and Information Service (NESDIS) and consists of a satellite downlink antenna (3-m diameter) to collect data from the Polar Operational Environmental Satellite (POES) series of polar-orbiting satellites. This is not a cooperative science program in the traditional sense, but the BRW station now has near-real-time access to polar views of cloud, ice, and coastal conditions that will aid in the interpretation of data and the planning of measurement timetables. If this program proves to be of high value to NOAA/NESDIS, a feasibility study will be conducted to determine if a 13-m dish could be installed at BRW to control the POES satellites. The installation of the NESDIS facilities will eventually necessitate T-1 or T-3 data transmission lines to the BRW site. This will benefit CMDL in that the added Internet transmission capabilities will be made available for BRW observatory use.

A number of relatively short cooperative programs operated at Barrow, such as a University of Alaska study of eider duck migration with a radar device mounted at the BRW facility; a soil organic and winter CO_2 flux study, also from the University of Alaska; Arctic vegetation studies by the University of Colorado; and mercury in snow sampling by a scientist from the University of Michigan.

An unprecedented number of cooperative programs will be coming to BRW in 2002 and many of them have required the construction of new infrastructure in 2001. For instance, a NOAA/ARO-funded project to measure persistent organic pollutants (POPs) in the atmosphere, to be conducted by Battelle-Northwest Laboratories, Richland, Washington, necessitated construction of an extension to the filter platform and a small, enclosed filter-changing room. The platform extension required the insertion of four pilings 5.5 m (18 ft) into the permafrost. Another piling was installed to support a Global Positioning System (GPS) antenna for an University of Alaska water vapor monitoring program, also to begin in spring 2002. Three more pilings were inserted to support instrumentation for a Climate Reference Network (CRN) site to be installed by the NOAA National Climatic Data Center (NCDC), also in spring 2002.

The long-term stability of BRW made the site an ideal place for CRN instruments. Instrumentation from the University of Alaska to measure dimethyl sulfide in a continuous mode will be installed in late spring 2002, and a program from Wayne State University to measure radiochemicals in Arctic haze will also begin in late spring 2002.

1.3. SAMOA OBSERVATORY

J. MICHALSKI, M. GAYLORD, AND E. SANDBERG

1.3.1. OPERATIONS

American Samoa is located in the middle of the South Pacific Ocean, about midway between Hawaii and New Zealand. The island is characterized by year-round warmth and humidity, lush green mountains, and the strong Samoan culture. Many changes occurred at the American Samoa Observatory (SMO) during 2000-2001.

During the first half of 2000 the entire station was cleaned and organized. Truckloads of trash, including broken instruments, out-of-date spare parts and manuals, 7000 pounds of leaking lead acid batteries, and a cabinet full of mostly unidentified, corroding hazardous materials, were hauled to the appropriate disposal areas. Both the batteries and hazardous materials were disposed of by the local Environmental Protection Agency (EPA) office.

Data collection was made more reliable with the institution of weekly File Transfer Protocol (FTP) data transfers and weekly data backups. New daily check sheets, modeled after those at Barrow and South Pole, were created for all instruments.

Basic station maintenance was completed, including painting the new Dobson dome, and painting and weatherproofing the roof, which fixed the leaks. A new wood crown on the parapet was installed and painted. New window glass replaced the old, yellowing Plexiglas in the main laboratory. The old meteorological scaffolding tower was dismantled and removed.

Improvements in air sampling were made with the movement of all instruments previously on the old scaffolding tower to the new Blue Sky mobile phone tower. The new tower provides higher sample positions for the CMDL Halocarbon and other Atmospheric Trace Species (HATS) group and Advanced Global Atmospheric Gases Experiment (AGAGE) gas chromatograph (GC) intakes, and better positions for the meteorological wind and temperature sensors. The Miami Sea-Air Exchange Experiment South Pacific Aerosol Network (SEASPAN) filter apparatus also was relocated to the top of the new tower. All data and power cables were protected inside conduit connecting the Hudson building to the top of the tower.

To further complete the scientific improvements, all computers were networked with modern 10 base-T cabling, and a data link between the Hudson building and the main laboratory was installed. All computers can now share and copy files, making it much easier to back up data throughout the laboratory.

During 2001 facilities were significantly improved with the completion of some major projects. The old, rotting

carport was demolished and replaced with a new, three-stall port. The new carport has the dual purpose of shading parked cars and supporting the rehabilitated solar photovoltaic (PV) array. The PV array, which was dormant for the last decade, was rehabilitated with a grant from the U.S. Department of Energy (DOE) through the American Samoa Government's Territorial Energy Office (TEO), a local agency supporting island-wide energy conservation and alternative energy sources. With the help of people at TEO and the local Community College, all the solar panels were refurbished and a grid-tied inverter was installed, which puts the solar power directly into the station's main breaker panel. The solar-electric power supplements the electricity demand whenever the Sun is shining and can provide up to 30% of daytime electricity demand. Along with the new carport and solar project, the old and disintegrating cedar shake on the station awning was replaced with corrugated roofing material, matched to the color of the new carport.

The last link for state-of-the-art scientific data collection at SMO is a real-time connection to the Internet. During 2001 significant progress was made in developing an agreement with the Pan-Pacific Education and Communication Experiments by Satellite (PEACESAT) program to connect to its island-wide Internet education network. The agreement has been finalized and only needs to be signed and enacted. It is realistic to plan on real-time Internet service to the laboratory by the end of the second quarter of 2002.

Finally, the chief's and technician's houses were completely gutted and remodeled. The chief's house was remodeled by island contractors, supervised by the Army Corps of Engineers. The technician's house was remodeled by the technician, and a new kitchen, bath, laundry, utility, bedroom, computer room, and living room were added. Two new trucks, Ford Rangers with extended cabs, were acquired for observatory operations. The old Toyota and Mitsubishi trucks were sold in a government auction. The new houses and station vehicles will make for a much more enjoyable lifestyle for employees working at SMO.

For the near future, areas that need immediate attention include replacement of the stairs down to the point and rehabilitation of the underside of the observatory roof where the concrete is severely flaking off.

1.3.2. PROGRAMS

Table 1.3 summarizes the programs at SMO for 2000-2001. Operational highlights follow:

Gases
Carbon dioxide. In situ monitoring and AIRKIT sampling continued without interruption during this reporting period.
Surface ozone. In situ monitoring with the Thermo Environmental Instruments (TEI) ultraviolet (UV) photometric ozone analyzer continued uninterrupted throughout the reporting period.
Total ozone. The Dobson spectrophotometer continued to operate reliably during 2000-2001. In October 2001 it

was sent to Christchurch, New Zealand, for an intercomparison and calibration.
Ozonesonde balloons. Weekly ozonesonde flights continued during this reporting period with the National Weather Service (NWS) balloon inflation facility at the Tafuna airport.
Halocarbons and other atmospheric trace species. The Chromatograph for Atmospheric Trace Species (CATS) operated throughout this reporting period, and the Radiatively Important Trace Species (RITS) system was retired on September 29, 2000.

Aerosols
The only aerosol-measuring instrument at Samoa is a Pollak condensation nucleus counter (CNC). Daily Pollak observations were conducted in 2000-2001, although a significant valve leak prevented observations in late 2001, pending arrival of replacement parts.

Solar Radiation and Meteorology
The solar radiation and meteorological instruments continued to operate throughout the reporting period. In early 2000 the meteorological instruments were repositioned on the new mobile phone tower after the old meteorology scaffolding tower was removed.

Cooperative Programs
A complete list of SMO cooperative projects is given in Table 1.3. All operated without significant problems during 2000-2001. One new project was added in May 2001, the U.S. Geological Survey (USGS) Evapotranspiration Study, which is designed to measure the combined loss of water from the Earth via evaporation and transpiration. For this program a small monitoring station was set up on the grounds of the observatory and will remain there until May 2002.

1.4. SOUTH POLE OBSERVATORY

D. NEFF, P. ROBERTS, A. CLARKE, J. MICHALSKI,
E. SANDBERG, AND B. HALTER

1.4.1. OPERATIONS

The CMDL South Pole Observatory (SPO) is located at the geographic south pole on the Antarctic plateau at an elevation of 2838 m above sea level. The majority of CMDL SPO projects are housed within the Atmospheric Research Observatory (ARO), a National Science Foundation (NSF) facility that is used in support of scientific research related to atmospheric phenomena and is part of the overall Amundsen-Scott South Pole Station. The CMDL SPO projects were previously located at the now demolished Clean Air Facility (CAF), and the CMDL observatory at ARO is still often referred to as the CAF.

Amundsen-Scott South Pole Station is an integral part of the U.S. Antarctic Program (USAP), which is funded and managed by NSF. Most of the administrative, logistical, and operational support for USAP is provided by private business under contract to NSF. The current prime support contractor is Raytheon Polar Services (RPS). Antarctic

TABLE 1.3. Summary of Measurement Programs at SMO in 2000-2001

Program/Measurement	Instrument	Sampling Frequency
Gases		
CO_2	Siemens Ultramat-5E analyzer	Continuous
CO_2, CH_4	0.5-L glass flasks, through analyzer	1 pair wk^{-1}
CO_2, CH_4, CO, and ^{13}C, ^{18}O of CO_2	2.5-L glass flasks, AIRKIT	1 pair wk^{-1}
Surface O_3	TEI UV photometric ozone analyzer	Continuous
Total O_3	Dobson spectrophotometer no. 42	4 day^{-1}
O_3 profiles	Balloonborne ECC sonde	1 wk^{-1}
N_2O, CFC-11, CFC-12, CFC-113,	2.5-L glass flasks, AIRKIT	2 pairs mo^{-1}
CH_3CCl_3, CCl_4, SF_6, HCFC-22,	850-mL, 2.5-L, or 3.0-L stainless-steel flasks	1 pair wk^{-1}
HCFC-141b, HCFC-142b, HCFC-21,		
HCFC-124, HFC-134a, HFC-152a, CH_3Br,		
CH_3Cl, CH_3I, CH_2Cl_2, $CHCl_3$, C_2Cl_4,		
H-1301, H-1211, $CHBr_3$, CH_2Br_2,		
C_6H_6, COS		
CFC-11, CFC-12, CFC-113, N_2O, CCl_4,	CATS four-channel automated GC	1 sample h^{-1}
H-1211, CH_3CCl_3, SF_6, HCFC-22,		
CH_3Cl, CH_3Br, COS, HCFC-142b, $CHCl_3$		
N_2O	Shimadzu automated GC (ended 9/00)	1 sample h^{-1}
Aerosols		
Condensation nuclei	Pollak CNC	1 day^{-1}
Solar Radiation		
Global irradiance	Eppley pyranometers with Q and RG8 filters	Continuous
Direct irradiance	Eppley pyrheliometer with Q filter	Continuous
	Eppley pyrheliometer with Q, OG1,	Discrete
	RG2, and RG8 filters	
Diffuse irradiance	Eppley pyranometers with shading disk and Q filter	Continuous
Terrestrial (IR) Radiation		
Downwelling	Eppley pyrgeometer	Continuous
Meteorology		
Air temperature	Thermistors (3)	Continuous
Dewpoint temperature	Polished mirror	Continuous
Pressure	Capacitance transducer	Continuous
	Mercurial barometer	1 wk^{-1}
Wind (speed and direction)	R.M. Young Windbird	Continuous
Precipitation	Rain gauge, tipping bucket	Continuous
	Rain gauge, plastic bulk	1 day^{-1}
Cooperative Programs		
CO_2, ^{13}C, N_2O (SIO)	5-L evacuated glass flasks	1 trio wk^{-1}
CO_2, O_2, N_2 (SIO)	5-L glass flasks	2 trios mo^{-1}
CH_4, N_2O, $CHCl_3$, CFC-11, CFC-12,	HP5890 Series II 3 channel gas chromatograph	3 h^{-1}
CFC-113, CCl_4, CH_3CCl_3 (NASA-AGAGE)		
Total suspended particulates (DOE)	High-volume filter sampler	Continuous (1 filter wk^{-1})
Total suspended particulates (SEASPAN)	High-volume filter sampler	Continuous (1 filter wk^{-1})
Light hydrocarbons (Univ. of California, Irvine)	1-L evacuated stainless steel flasks	3-4 flasks qtr^{-1}
O_2 (Princeton Univ.)	2.5-L glass flasks	1 pair wk^{-1}
H_2O budget (USGS, Samoa EPA)	Evapotranspiration pan	Continuous

SIO, Scripps Institution of Oceanography.

Support Associates (ASA) was the prime contractor from April 1990 through March 2000.

The ARO facility is located approximately 500 m grid east-northeast of the new elevated station, physically separated and generally upwind of all other station facilities. (Grid north, grid 0°/360°, is defined as parallel to and in the direction of the prime meridian from the South Pole; Greenwich is situated grid north of South Pole Station.) The ARO building is located at the vertex of an obtuse angle, with sides aligned to grid 340° and grid 110°, which define the Clean Air Sector (CAS). The prevailing winds at South Pole are from the CAS more than 90% of the time.

The CAS was established to preserve the unique atmospheric and terrestrial conditions from South Pole Station influences. Except for special circumstances, access to the CAS is prohibited, allowing for nearly continuous measurement of trace constituents of the atmosphere in a location remote from anthropogenic sources and sinks.

CMDL's stratospheric ozonesonde program is conducted from the Balloon Inflation Facility (BIF), which is located grid south (generally downwind) of the new elevated station. This facility is shared with the RPS meteorology staff and occasionally with other research groups.

There are, for practical purposes, two distinct "seasons" at South Pole Station. The austral summer season (November through January) and the austral winter season (February through October). Current staffing at the station exceeds 200 persons during the summer season and is reduced to approximately 50 "winterovers" during the winter season.

The only USAP transportation to and from South Pole Station is on one of more than 300 "routine" Lockheed Martin LC-130 Hercules aircraft flights during the austral summer season. These flights, currently flown by the 109th Airlift Wing of the New York Air National Guard, typically take place from late October to mid-February (station opening to station closing) each year. Occasional USAP-contracted de Havilland DH-6 Twin Otter aircraft flights are made to the station, mostly using South Pole as a stopover during special programs.

South Pole Station, including CMDL's observatory, is physically isolated from the rest of the world during the austral winter season. During this period, temperatures are generally too low, the weather too unpredictable, and the risk to hydraulic systems too great for aircraft to operate safely. An unprecedented Twin Otter "medevac" flight was made to the station in April 2001, but this capability cannot be relied on in general.

Due to the 9-mo isolation, air samples taken during the austral winter cannot be returned for analysis until the station reopens the following November. However, communications and data access via satellite (including Internet connectivity) are available for several hours each day throughout the year. Data collected in situ are transmitted regularly via the Internet to locations around the world.

During the austral summer season the CAF usually receives a large number of Distinguished Visitors (DVs). Typical DVs are members of Congress and their staff, U.S. and N.Z. Embassy officials, U.S. military delegations, U.S. Executive Branch delegations, members of the National Science Board, ex-astronauts, and members of numerous news organizations.

The summer season at South Pole Station is marked by a variety of activities, relatively "warm" temperatures (about –30°C average and sometimes as warm as –15°C), and constant sunlight. The average temperature during the winter season is about –60°C, but temperatures can drop below –75°C on occasion. The Sun sets toward the latter part of mid-March, twilight is generally significant through the middle of April, and the winter night begins in earnest toward the end of April. The first faint signs of light from the Sun are clearly visible again in early August, preceding sunrise in the latter part of mid-September. Station life generally runs at a slower pace during the winter season.

ARO Electrical

South Pole Station power is generally reliable, but outages and other problems occasionally do occur. ARO and BIF are equipped with uninterruptable power supplies (UPS) for some of the more sensitive equipment. However, in recent seasons, the buildings' UPS systems have not been reliable, and individual UPS systems have been installed for most of the CMDL experiments.

The ARO first-floor UPS system failed in December 2000. A replacement was installed within 2 months, but it also failed prior to carrying an electrical load. Several smaller UPS systems were shipped from CMDL in the interim while NSF and Raytheon worked to provide generalized UPS systems for ARO. The ARO second-floor UPS system has been inoperable for several seasons and continues to be unusable. A 30-kVA transformer was installed in February 2001 within ARO to supply power to temporary buildings occupied throughout the year by other atmospheric scientists.

Station Network/Communications

Voice and Internet access to/from South Pole Station are available for several hours each "day" dependent on satellite coverage, equipment, and weather. Detailed technical information is provided on the RPS website (www.rpsc.raytheon.com) and on the NSF website (www.nsf.gov). The ARO Local Area Network (LAN) is connected to the station-wide system, which is managed by RPS for NSF. Selected ARO computers are connected to this system for remote login and data retrieval. CMDL data retrieval is conducted through satellite connections, when available.

Outreach

Unofficial visitors at South Pole Station are rare, but outreach is possible through Internet connections and to some extent through the mail. School groups frequently write, curious about the lifestyle and the science at the station.

The number of visitors (official USAP and "non-governmental") on record at ARO for the three reported seasons are 20 for the 1999 season, 57 for the 2000 season, and 40 for the 2001 season.

The actual numbers are slightly higher, because visitors occasionally slip through without signing the CMDL guest book.

1.4.2. PROGRAMS

Table 1.4 summarizes the programs at SPO for 2000 and 2001 austral seasons. Operational highlights follow for the 1999, 2000, and 2001 seasons. Items mentioned refer to all three seasons except where otherwise noted. For specific operational details, refer to the monthly SPO station reports and the individual equipment checksheets and digital logs available from the CMDL Observatory Operations office.

Gases

Carbon Cycle. The Siemens continuous carbon dioxide analyzer ran with very few significant problems. The analyzer's chopper lamp was replaced with a "mini-maglite"

TABLE 1.4. Summary of Measurement Programs at SPO in 2000 and 2001 Austral Seasons

Program/Measurement	Instrument	Sampling Frequency
Gases		
CO_2	Siemens non-dispersive IR analyzer (ended 2001)	Continuous
	LI-COR system (began 2001)	Continuous
CO_2, CH_4, CO, H_2, N_2O, SF_6, $^{13}C/^{12}C$ of CH_4, and $^{13}C/^{12}C$, $^{18}O/^{16}O$ of CO_2	2.5-L glass flasks, through analyzer	1 pair wk^{-1} (2 mo^{-1} in 2001)
	2.5-L glass flasks, MAKS pump unit	1 pair wk^{-1}
Surface O_3	Dasibi and TEI surface ozone analyzers	Continuous
Total column O_3	Dobson spectrophotometer no. 80	3 sets day^{-1}
Ozone vertical profiles	Balloonborne ECC sonde	~3 wk^{-1}, spring/early summer; ~1 wk^{-1}, remainder of year
CFC-11, CFC-12, CFC-113, HCFC-21, HCFC-22, HCFC-124, HCFC-141b, HCFC-142b, HFC-134a, HFC-152a, H-1211, H-1301, CH_3Cl, CH_2Cl_2, $CHCl_3$, CCl_4, CH_3CCl_3, C_2Cl_4, CH_3Br, CH_2Br_2, $CHBr_3$, CH_3I, N_2O, SF_6, COS, C_6H_6	0.85-L, 2.5-L, or 3.0-L stainless-steel flasks	2 pair mo^{-1} (~1st and 15th)
	2.5-L glass flasks, pump unit	1 pair mo^{-1} (~15th)
CFC-11, CFC-12, CCl_4, CH_3CCl_3, N_2O	Two RITS Shimadzu GCs (ended 12/00)	1 sample h^{-1}
CFC-11, CFC-12, CFC-113, HCFC-22, HCFC-142b, H-1211, CH_3Cl, $CHCl_3$, CCl_4, CH_3CCl_3, CH_3Br, N_2O, SF_6, COS	Automated CATS GC	1 sample h^{-1}
Aerosols		
Condensation nuclei	Pollak CNC	2 set day^{-1}
	TSI CNC	Continuous
Optical properties	Four-wavelength nephelometer	Continuous
Solar Radiation		
Global (total) irradiance	Eppley pyranometer with Q filter	Continuous, summer
	Eppley pyranometer with RG8 filter	Continuous, summer
Direct irradiance	Eppley pyrheliometer with Q and RG8 filters (tracking NIP)	Continuous, summer
	Eppley pyrheliometer with Q, OG1, RG2, and RG8 filters (manual filter-wheel NIP)	~3 sets day^{-1}, summer
Diffuse irradiance	Eppley pyranometer with shading disk and Q filter	Continuous, summer
Albedo	Eppley pyranometer with Q filter (downward facing)	Continuous, summer
	Eppley pyranometer with RG8 filter (downward facing)	Continuous, summer
	Eppley pyranometer with Q filter (on tower/downward facing)	Continuous, summer
Optical depth	SP01-A multiwavelength aureole sunphotometer	Continuous, summer
Terrestrial (IR) Radiation		
Upwelling and downwelling	Two Eppley pyrgeometers	Continuous
Meteorology		
Air temperature (2- and 20-m heights)	Logan platinum resistance probe	Continuous
Pressure	Setra capacitive pressure transducer	Continuous
	Mercurial barometer	1 wk^{-1}
Wind (speed and direction at 10-m height)	R.M. Young wind monitor	Continuous
Frost-point temperature	TSL dewpoint hygrothermometer	Continuous
Cooperative Programs		
CO_2, ^{13}C, N_2O (SIO)	5-L evacuated glass flasks	2 trios mo^{-1} (~1st and 15th)
O_2/N_2, CO_2 (SIO)	Pump unit, 5-L glass flasks	2 trios mo^{-1} (~1st and 15th)
Surface Air Sampling Program (DOE/EML) (natural and anthropogenic radionuclides)	High-volume pump and filters	Continuous (4 filters mo^{-1})
Interhemispheric $^{13}C/^{12}C$ (CSIRO) (CO_2, CH_4, CO, H_2, N_2O, and $^{13}C/^{12}C$, $^{18}O/^{16}O$ of CO_2)	Pump unit, 0.5-L and 5-L flasks	2 pairs mo^{-1} (~1st and 15th)
H_2O_2 (Univ. of Arizona)	Surface snow sample collection	2 wk^{-1}
TFA (Univ. of Arizona)	Surface snow sample collection (2001 only)	1 mo^{-1}
Oxygen isotopes (UCSD)	High-volume pump and filters (2001 only)	Continuous (1 wk^{-1})
Sulfur compounds (ISCAT)	High-volume pump and filters	Continuous (1 mo^{-1})
	1-L flasks (2001 only)	Periodically

lamp from early March to late October 2000 in lieu of a standard spare. The zero-gas flow was reduced in early April 2000 to conserve the supply, and old working-gas cylinders were used in lieu of zero gas from early May 2000 onward. In November 2000 the mini-maglite lamp was replaced with a new chopper lamp. The Siemens analyzer began to develop intermittent noise problems and voltage fluctuations early in 2001 and was replaced with a new LI-COR system at that time.

Sample flasks were filled through the analyzer twice per month during the 1999 and 2001 seasons and once per week during the 2000 season. Flasks were also filled once per week with the Martin and Kitzis Sampler (MAKS) portable pump unit. An external 12-V battery was connected to the MAKS unit in May 1999 to replace the standard internal battery that had failed.

Ozone and water vapor. The Dasibi surface ozone analyzer operated continuously with no significant problems during the reported seasons. A second analyzer, manufactured by Thermo Environmental Instruments (TEI), was installed in December 1999 and operated well. Preliminary results indicate the two instruments showed close agreement through the 2001 season.

Routine measurements of total column ozone were taken three times daily during the austral summer months with a Dobson total ozone spectrophotometer. Whenever possible, total ozone values were obtained in the austral winter with the Dobson and the full moon as the light source.

The balloonborne stratospheric ozonesonde program continued to run well. During the annual austral spring/early summer stratospheric ozone depletion, ozone profiles up to about 30 km were obtained about three times per week and up to once per day during the total ozone minimum. Profiles were obtained once per week during the remainder of the year. Several special ozonesonde intercomparison flights were completed in January 1999. These flights were part of a larger ozonesonde intercomparison program.

Halocarbons and other atmospheric trace species. The custom-built Chromatograph for Atmospheric Trace Species (CATS) gas chromatograph (GC) and the existing Radiatively Important Trace Species (RITS) GCs were operated side by side throughout the 1999 and 2000 seasons. All instrumentation operated continuously except for the occasional repair or replacement of failed components. Routine maintenance and gas cylinder replacements caused very few interruptions of GC measurements. Ultra-high purity (UHP) air was used in lieu of calibration (CAL 1) gas from early November 1999 until the new CAL 1 cylinder arrived in the middle of February 2000. The RITS GCs were removed, and the CATS gas select valves were replaced in December 2000.

Sample flasks were filled twice per month with the Halocarbons and other Atmospheric Trace Species (HATS) group flask pump. In addition, during austral winter 2000, glass flasks were filled once per month to be compared with the typical samples collected in stainless-steel flasks. Some species can be analyzed from air samples stored in glass flasks that cannot be measured reliably from air stored in stainless-steel flasks.

Aerosols

The four-wavelength nephelometer suffered through a spate of problematic filter wheel motors, and except for the replacement of an electronics board and consequent reference calibrations, the instrument operated without major problems during the 1999 season. The nephelometer operated continuously with no significant problems during the entire 2000 season. During the 2001 season the nephelometer was again problematic, and data collection was intermittent for most of the season even after extensive repairs. Routine condensation nuclei (CN) measurements were carried out both seasons with the Pollak instrument.

The Thermo Systems Incorporated (TSI) CN counter (CNC) operated with no major problems during the 1999 season although several minor repairs were necessary. The TSI CNC operated continuously with no significant problems during the entire 2000 season. A replacement TSI output module board was installed in May 2001 to address discrepancies found between the TSI CNC front-panel readout and the corresponding value recorded by the Campbell Scientific Inc. (CSI) acquisition module.

Solar and Terrestrial Radiation

The instrumentation ran with no significant problems during the reported seasons, though occasional noise in the signal lines remained an issue. The majority of instrumentation is disconnected during the winter months, May to September, but the terrestrial radiation instruments are typically left operational year-round. The instrumentation was connected to a single-point electrical ground during the 2001 season to address problems with noise pickup.

The albedo rack was raised in December 1999. A new precision spectral pyranometer (PSP) was installed on a boom suspended from the NOAA meteorology tower in January 1999. Several scheduled instrument replacements were made during austral summers 1999-2001. The SP01-A aureole sunphotometer was operated at SPO from late December 1999 to late January 2000, from mid-November 2000 to late March 2001, and again from late September 2001 through mid-November 2001.

Meteorology

The meteorology instrumentation operated continuously with no significant problems. Daily weather observations were recorded, and special observations were taken, when possible, if conditions changed significantly.

The temperature and wind sensors on the tower were raised in early February 2000 and again in February 2001 to maintain the WMO-recommended height specifications above the ever-rising snow surface. The sensors were calibrated and inspected during the February 2000 maintenance.

Cooperative Programs

Scripps Institution of Oceanography (SIO). Sample flasks were filled twice per month for later analysis at SIO.

U.S. Department of Energy/Environmental Measurements Laboratory (DOE/EML). The Surface Air Sampling Program (SASP) pump ran continuously without significant

problems. Sample filters were changed once per week, and a sample blank was collected monthly.

Commonwealth Scientific and Industrial Research Organization (CSIRO). Sample flasks were filled twice per month for later analysis by CSIRO.

University of Arizona. Snow samples were obtained and snow heights were measured from a "sampling grid" inside the Clean Air Sector weekly during the 1999 season. Groups of surface snow samples were obtained approximately seven times each month during the 2000 and 2001 seasons. Snow samples were also collected monthly during the 2001 season for trifluoroacetate analysis.

University of California, San Diego (UCSD). Weekly rooftop filter samples were collected during the 2001 season beginning in February 2001.

Investigation of Sulfur Chemistry in the Antarctic Troposphere (ISCAT). Forty-eight air samples were collected in metal sampling cans periodically throughout the 2001 season. Rooftop filter samples were collected weekly until February 2001. A significant number of air samples were also collected during the 1999 and 2000 seasons, though no filter samples were collected then.

1.5. METEOROLOGICAL MEASUREMENTS

T. MEFFORD

1.5.1. METEOROLOGY OPERATIONS

Introduction

The climatology of surface meteorological observations at the four CMDL observatories is based on hourly average measurements of the prevailing wind direction and speed, barometric pressure, ambient and dewpoint temperatures, and precipitation amounts. The meteorological sensors in use were selected for their high accuracy as well as their ability to withstand the extreme conditions of both the tropics and polar regions. Data is recorded as 1-min averages so that the variability within the hourly averages can be determined. To the extent that is possible, World Meteorological Organization (WMO) siting standards [*WMO*, 1969] are followed. Thermometers are also positioned at the top of the sampling towers at the Barrow Observatory (BRW), Mauna Loa Observatory (MLO), and South Pole Observatory (SPO) to measure the temperature gradient and to determine the stability of the surface boundary layer.

Peterson and Rosson [1994] give a detailed description of the PC-based data acquisition system. Table 1.5 describes the CMDL instrument deployment as of December 31, 2001.

Data Management

The meteorological data acquisition system gathers data from sensors that operate continuously at each of the four CMDL observatories. Data are transferred from the observatories to Boulder daily via the Internet, except for the Samoa Observatory (SMO), whose data are transferred to Boulder weekly. Preliminary hourly averages of prevailing wind direction and speed, barometric pressure, ambient and dewpoint temperatures, and precipitation

amounts are sent to the stations daily, except for SMO, which are sent weekly.

A comparison of the number of data points recorded against that expected for the year was used to monitor each system's performance. Table 1.6 shows the performance for each station in 2000 and 2001. On average, the meteorological data acquisition system combined for the four observatories operated 92.65% and 91.92% of the time for 2000 and 2001, respectively. Because of the remoteness of the observatories, power outages are common and are the main reason for data loss. Hardware failure, system restarts, and system maintenance are the other reasons. At BRW, during the winter, rime ice and snow occasionally build up on the sensors and have to be removed manually.

1.5.2. STATION CLIMATOLOGIES

The 25-yr station climatologies are an important record for the interpretation of measured values of aerosols, trace gases, atmospheric turbidity, and solar radiation, and the long-term changes in the records themselves, and they serve to outline periods of local contamination.

Barrow

In Figure 1.1, wind roses of hourly average prevailing wind direction and wind speed (WS) at BRW are presented in 16 direction classes and 3 speed classes. Winds from the "clean air" sector, north-northeast to southeast, occurred 62.6% of the time in 2000 and 64.0% in 2001 compared with 61.4% for the 23-yr period from 1977 through 1999 (Figure 1.2). Wind speeds in excess of 10 m s^{-1} in 2000 (11.4%) were more frequent than for the 23-yr climatology (10.8%), whereas in 2001 (7.1%) they were less frequent than in the 23-yr climatology. The average wind speeds of 5.8 m s^{-1} in 2000 and 5.5 m s^{-1} in 2001 (Table 1.7) were slightly below the long-term average (6.0 m s^{-1}).

The average air temperatures of −11.5°C in 2000 and −11.7°C in 2001 (Table 1.7) were both warmer than the climatological average of −12.2°C. The barometric pressure in 2000 was 0.5 hPa above the 23-yr average of 1014.1 hPa, and the average for 2001 was 0.4 hPa below the climatological average. May and August 2000 recorded new record-high barometric pressure readings for the respective months. The summertime precipitation amounts for 2000 (63 mm) and 2001 (57 mm) were above the long-term average of 39 mm.

Mauna Loa

The climatology of MLO is best understood when it is considered in two distinctive wind regimes, the night (downslope) period of 1800-0559 Hawaiian Standard Time (HST) and the day (upslope) period of 0600-1759 HST. The 23-yr (1977-1999) night and day wind charts illustrate the two distinct wind regimes (Figure 1.3).

For the night regime at MLO, the 23-yr wind rose (Figure 1.3) shows that 89.9% of all winds observed had a southerly component. The percentage occurrence of southerly winds was 89.4% in 2000 (Figure 1.4) and 90.1% in 2001 (Figure 1.5). Pressure-gradient-controlled winds (WS $\geq$ 10 m s^{-1}) from predominantly westerly and southeasterly directions, occurred 5.0% of the time in 2000 and 4.7% in 2001, both

TABLE 1.5. CMDL Meteorological Sensor Deployment December 31, 2001

Sensor	BRW Serial No.	Elevation* (m)	MLO Serial No.	Elevation* (m)	SMO Serial No.	Elevation* (m)	SPO Serial No.	Elevation* (m)
Primary anemometer†	14584	10.5	23186	10.2	15945	22.9	14583	10.3
Secondary anemometer†			15946	38.2				
Pressure transducer‡	374199	9.5	374198	3398.4	374200	78.5	358960	2841.0
Mercurial barometer	641	9.5	278	3398.4	961	78.5	1215A	2841.0
Air temperature A§		2.4		2.0		18.9		1.6
Air temperature B§¶		15.7		37.4		18.9		22.0
Air temperature C**		2.9		2.0		18.9		2.0
Dewpoint temperature	G0001	2.9	G0004	2.0	G0008	18.9	G0007	2.0
Rain gauge		~4		0.8		~4		

*Heights are in meters above surface, except for the pressure transducer and mercurial barometer, which are with respect to mean sea level (MSL).
†Propeller anemometer, model no. 05103, R. M. Young Company, Traverse City, Michigan.
‡Pressure transducer, model no. 270, Setra Systems, Acton, Massachusetts.
§Platinum resistance probe, Logan 4150 Series, Logan Enterprises, Liberty, Ohio.
¶Thermometer, positioned at the top of the local sampling tower to facilitate an estimation of boundary layer stability, except at SMO where both sensors were at the same height.
**Hygrothermometer, model no. 1088-400, Technical Services Laboratory, Fort Walton Beach, Florida.

TABLE 1.6. CMDL Meteorological Operations Summary

Station	Expected Number of Data Points	Data Capture (%)	Number of Missing Data Points
2000			
BRW	4,216,320	98.36	68,959
MLO	6,851,520	91.55	579,028
SMO	4,216,320	83.95	676,523
SPO	4,216,320	96.74	137,395
Average		92.65	
2001			
BRW	4,204,800	97.34	111,693
MLO	6,832,800	86.82	900,727
SMO	4,204,800	93.43	276,424
SPO	4,204,800	90.10	416,135
Average		91.92	

of which were below the 23-yr average of 6.9%. The annual average wind speeds for 2000 and 2001 were both below the long-term average (Tables 1.8 and 1.9). The upslope, or northerly component, winds (north-northwest through east-northeast) that occurred 4.8% of the time in 2000 and 3.9% in 2001 are the result of the daytime upslope flow extending into the early evening hours.

For the day regime at MLO, the 2000 and 2001 wind roses (Figures 1.4 and 1.5) indicate that winds from the west-northwest through east-southeast occurred 72.6% of the time in 2000 and 71.5% of the time 2001, compared with 60.2% for the 23-yr climatology (Figure 1.3). Pressure-gradient-controlled winds (WS ≥ 10 m s^{-1}) occurred 3.6% of the time in 2000 and 2001, both of which

were lower than the climatological average of 6.9%. In 2000 and 2001 the pressure gradient winds, which are usually associated with storms, followed the expected pattern of fewer occurrences during the day regime. The day wind chart is more uniformly distributed in the light-wind classes than the night wind chart. This is due to the occurrence of variable wind directions during the transition periods at dawn and dusk, most of which are included in the day regime.

The average ambient temperature for 2000 (Table 1.8), combining both day and night regimes, was 7.1°C, which equals the long-term average of 7.1°C, whereas the 6.7°C in 2001 (Table 1.9) was below the long-term average. The average barometric pressure for 2000 (680.1 hPa) was below the climatological average of 680.5 hPa, whereas for 2001 (680.4 hPa) it was near the climatological average. June 2000 tied the record minimum pressure value for the month, and January 2001 set a new maximum barometric pressure record for the month. The total precipitation amount in 2000 (212 mm) was considerably below the long-term average of 352 mm, whereas in 2001 (359 mm) it was slightly above the long-term average.

Samoa

A comparison of SMO's 2000 and 2001 wind roses (Figure 1.6) to the wind rose of the 23-yr period (Figure 1.7) shows a considerably higher percentage of "clean air" sector winds (north-northwest through southeast) in 2000 (77.6%) and 2001 (73.4%) than the long-term average of 58.5%. The occurrence of winds in the 10 m s^{-1} or greater class was 9.8% in 2000 and 14.0% in 2001, whereas the expected occurrence based on the climatological average is 5.0%. The annual average wind speeds for 2000 (5.9 m s^{-1}) and 2001 (6.0 m s^{-1}) (Table 1.10) were both above the long-term average of 5.0 m s^{-1}. No wind data are available for January-March 2000 because of instrument problems.
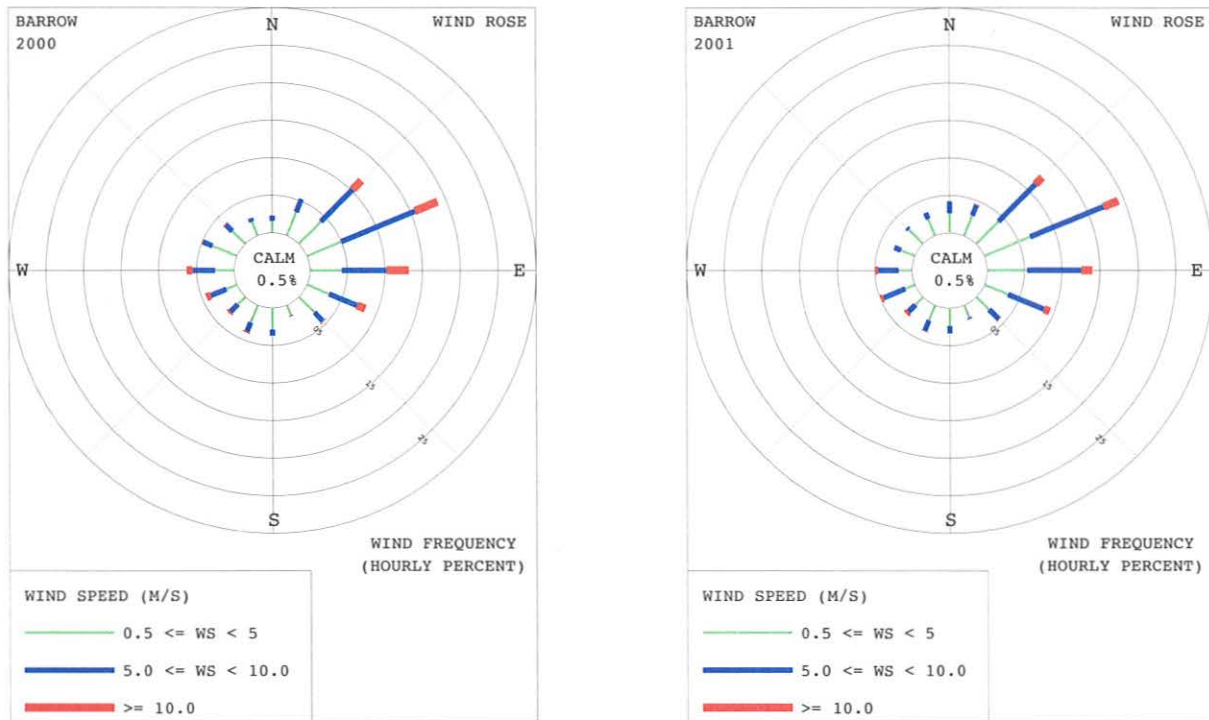
Fig. 1.1. Wind roses of the surface winds at BRW for 2000 (left) and 2001 (right). The distributions of prevailing wind direction and speed are given in units of percent occurrence for 16 direction classes and 3 wind speed (WS) classes. Percent frequency of calm winds (WS < 0.5 m s⁻¹) is indicated on the graphs.
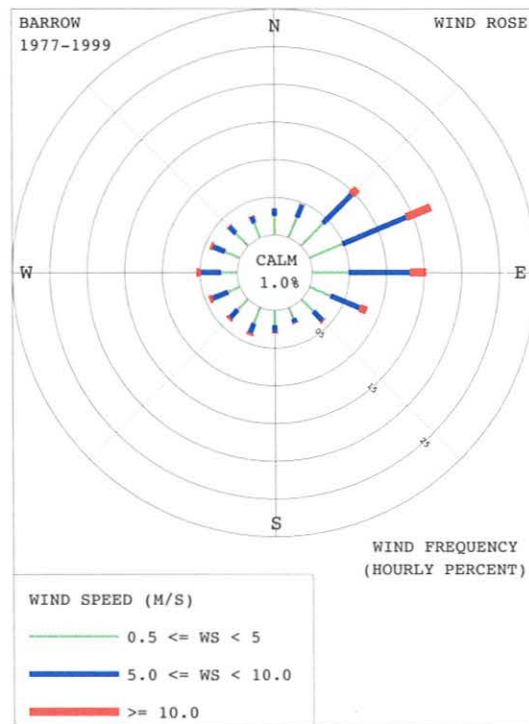

Fig. 1.2. Wind rose of surface winds at BRW for 1977-1999. The distributions of prevailing wind direction and speed are given in units of percent occurrence for the 23-yr period for 16 direction classes and 3 speed classes. Percent frequency of calm winds (WS < 0.5 m s⁻¹) is indicated on the graph.

TABLE 1.7.   BRW 2000 and 2001 Monthly Climate Summary

	Jan.	Feb.	March	April	May	June	July	Aug.	Sept.	Oct.	Nov.	Dec.	Year
							2000						
Prevailing wind direction	W	ENE	ENE	E	ESE	ESE	ENE	E	ESE	NE	ENE	ENE	ENE
Average wind speed (m s^{-1})	5.1	5.1	7.4	5.2	4.0	4.2	5.3	6.3	5.1	6.1	7.4	7.9	5.8
Maximum wind speed* (m s^{-1})	14.7	11.8	14.3	14.5	9.0	13.5	15.2	21.9	13.2	14.5	20.6	18.3	21.9
Direction of max. wind* (deg.)	270	54	82	55	113	230	238	251	346	77	74	89	251
Average station pressure (hPa)	1011.9	1014.6	1017.7	1022.2	1017.3	1011.0	1010.1	1013.6	1008.6	1008.9	1014.9	1024.3	1014.6
Maximum pressure* (hPa)	1036.4	1032.1	1037.4	1037.6	1041.1	1029.6	1027.9	1035.8	1025.2	1022.3	1034.4	1035.7	1041.1
Minimum pressure* (hPa)	979.6	997.6	1001.6	1004.8	1003.7	995.0	995.6	996.3	994.4	992.3	996.6	1009.2	979.6
Average air temperature (°C)	-25.0	-26.6	-24.5	-17.9	-9.5	1.5	2.9	3.2	0.3	-7.2	-16.3	-19.8	-11.5
Maximum air temperature* (°C)	-11.9	-9.3	-15.0	-4.6	-0.4	16.2	19.3	15.3	12.7	0.3	-6.1	-10.0	19.3
Minimum air temperature* (°C)	-39.2	-41.1	-35.7	-29.5	-22.5	-5.1	-2.2	-1.6	-7.1	-18.3	-28.5	-31.4	-41.1
Average dewpoint temperature (°C)	-28.1	-29.7	-27.8	-20.5	-11.4	-0.1	1.6	0.3	-1.8	-9.1	-18.6	-22.4	-14.7
Maximum dewpoint temperature* (°C)	-13.4	-10.6	-18.4	-5.5	-1.7	10.0	12.6	6.9	7.9	-0.1	-7.6	-11.4	12.6
Minimum dewpoint temperature* (°C)	-43.3	-45.9	-40.0	-33.0	-24.8	-7.6	-2.6	-3.0	-9.8	-20.1	-31.9	-35.3	-45.9
Precipitation (mm)	0	0	0	0	2	11	31	14	5	0	0	0	63
							2001						
Prevailing wind direction	ENE	ENE	ENE	ENE	E	ESE	ENE	E	E	NE	ENE	ENE	ENE
Average wind speed (m s^{-1})	7.7	6.4	6.3	5.6	4.0	5.0	5.2	5.7	5.1	5.4	5.7	4.4	5.5
Maximum wind speed* (m s^{-1})	21.3	16.2	13.2	12.6	10.1	11.9	10.7	12.4	11.7	11.8	13.5	12.1	21.3
Direction of max. wind* (deg.)	61	278	48	67	142	235	237	256	87	42	83	252	61
Average station pressure (hPa)	1009.7	1014.7	1023.4	1016.0	1017.3	1016.7	1011.5	1007.7	1006.7	1016.9	1013.1	1011.0	1013.7
Maximum pressure* (hPa)	1029.8	1043.9	1046.9	1036.9	1031.2	1029.7	1024.5	1024.1	1017.8	1033.4	1032.0	1039.9	1046.9
Minimum pressure* (hPa)	981.6	988.8	997.0	997.6	1006.6	1001.6	995.3	992.0	991.7	994.0	990.2	990.6	981.6
Average air temperature (°C)	-23.3	-18.9	-26.5	-16.7	-10.9	0.8	2.3	1.7	0.1	-11.9	-16.4	-21.9	-11.7
Maximum air temperature* (°C)	-10.2	-5.1	-15.8	-6.8	1.2	11.1	19.9	11.7	13.0	-2.4	-5.8	-5.3	19.9
Minimum air temperature* (°C)	-33.2	-33.5	-35.8	-32.4	-24.3	-4.1	-2.4	-2.0	-7.8	-24.5	-26.9	-31.6	-35.8
Average dewpoint temperature (°C)	-25.4	-20.9	-29.3	-19.1	-12.8	-0.6	0.3	-0.5	-1.2	-13.9	-18.9	-24.8	-14.2
Maximum dewpoint temperature* (°C)	-12.0	-6.2	-18.0	-8.8	-0.5	5.9	12.8	7.0	6.0	-3.5	-7.0	-7.1	12.8
Minimum dewpoint temperature* (°C)	-35.7	-36.3	-39.3	-35.2	-27.3	-5.7	-3.9	-4.0	-10.8	-27.3	-30.5	-36.0	-39.3
Precipitation (mm)	0	0	0	0	0	2	30	20	5	0	0	0	57

Instrument heights: wind, 10.5 m; pressure, 9.5 m (MSL); air temperature, 2.9 m; dewpoint temperature, 2.9 m. Wind and temperature instruments are on a tower 25 m northeast of the main building.

*Maximum and minimum values are hourly averages.
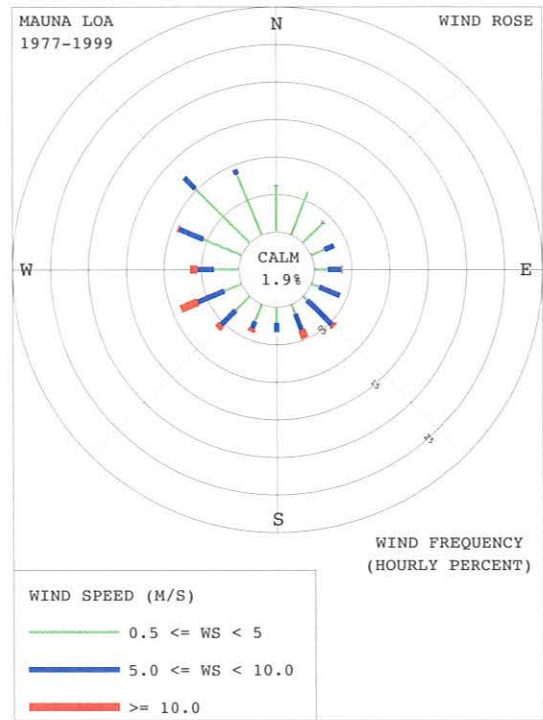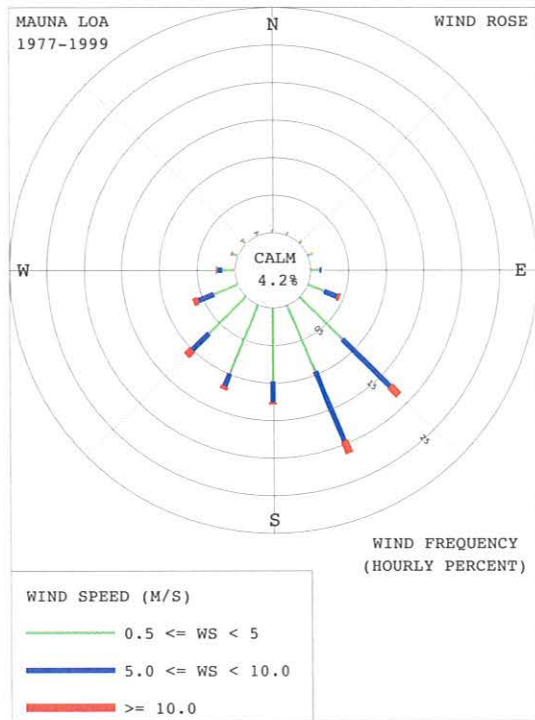
Fig. 1.3. Wind roses of the surface winds at MLO for 1997-1999 night (left) and day (right). The distributions of prevailing wind direction and speed are given in units of percent occurrence for the 23-yr period for 16 direction classes and 3 speed classes. Percent frequency of calm winds (WS < 0.5 m s^{-1}) is indicated on the graphs.
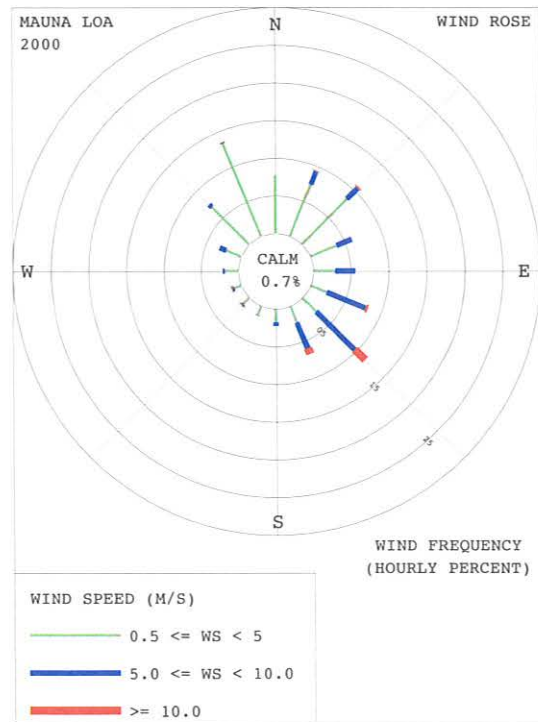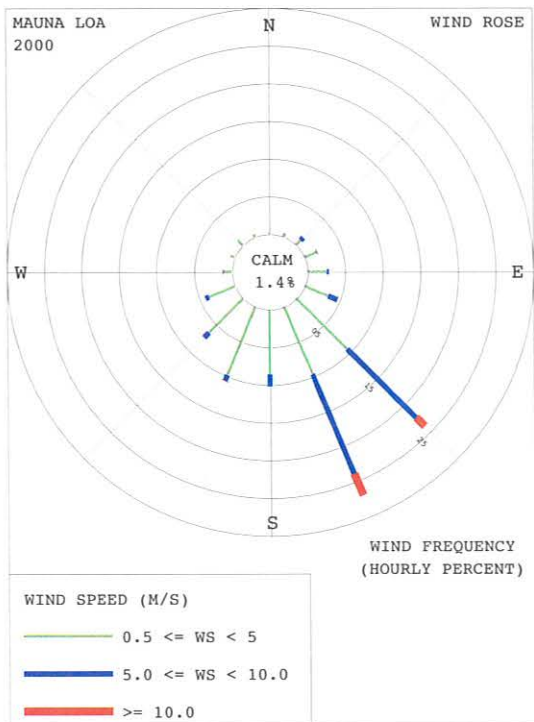
Fig. 1.4. Wind roses of the surface winds at MLO for 2000 night (left) and day (right). The distributions of prevailing wind direction and speed are given in units of percent occurrence for 16 direction classes and 3 speed classes. Percent frequency of calm winds (WS < 0.5 m s^{-1}) is indicated on the graphs.
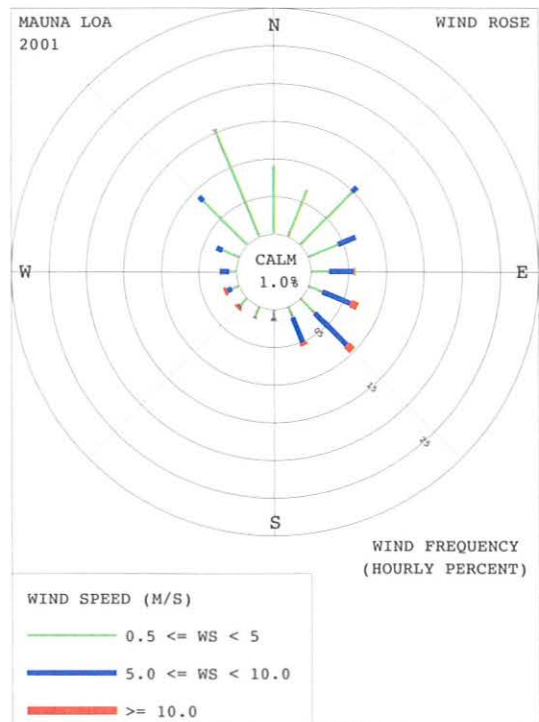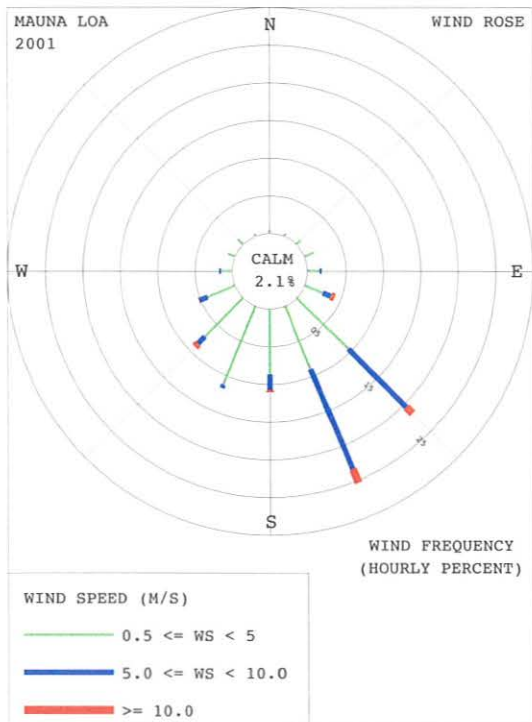
Fig. 1.5. Wind roses of the surface winds at MLO for 2001 night (left) and day (right). The distributions of prevailing wind direction and speed are given in units of percent occurrence for 16 direction classes and 3 speed classes. Percent frequency of calm winds (WS < 0.5 m s^{-1}) is indicated on the graphs.

Fig. 1.6. Wind roses of the surface winds at SMO for 2000 (left) and 2001 (right). The distributions of prevailing wind direction and speed are given in units of percent occurrence for 16 direction classes and 3 speed classes. Percent frequency of calm winds (WS < 0.5 m s^{-1}) is indicated on the graphs.

TABLE 1.8. MLO 2000 Monthly Climate Summary

	Jan.	Feb.	March	April	May	June	July	Aug.	Sept.	Oct.	Nov.	Dec.	Year
							Night						
Prevailing wind direction	SE	SSE	SE	SSE	SSE	E	SSE	SE	SE	SE	SSE	SSE	SSE
Average wind speed (m s^{-1})	4.4	5.6	6.2	5.5	4.5	4.0	3.9	4.2	3.0	4.2	4.4	4.3	4.5
Maximum wind speed* (m s^{-1})	13.8	16.8	15.2	13.0	12.1	13.6	12.5	9.2	9.1	12.6	11.1	13.6	16.8
Direction of max. wind* (deg.)	154	154	155	158	170	157	155	140	152	152	239	153	154
Average station pressure (hPa)	678.3	680.9	679.7	679.9	680.8	680.1	680.7	680.4	680.3	680.1	679.7	679.9	680.1
Maximum pressure* (hPa)	683.0	683.9	682.5	683.2	684.5	683.1	683.5	682.3	683.2	682.6	681.8	683.0	684.5
Minimum pressure* (hPa)	673.7	678.5	676.2	675.3	677.6	676.7	678.0	677.5	677.1	677.8	677.0	676.5	673.7
Average air temperature (°C)	2.1	4.3	3.3	4.9	6.9	6.9	6.4	6.7	6.7	5.3	3.3	4.5	5.1
Maximum air temperature* (°C)	7.9	10.2	9.9	11.0	12.1	13.7	13.1	12.3	11.2	10.9	7.7	9.3	13.7
Minimum air temperature* (°C)	-2.6	-0.5	-1.8	-2.3	2.7	0.6	3.2	2.5	1.9	1.7	-1.0	-0.1	-2.6
Average dewpoint temperature (°C)	-12.8	-15.3	-16.9	-19.3	-13.5	-16.1	-7.0	-11.4	-6.7	-8.6	-8.6	-16.9	-12.8
Maximum dewpoint temperature* (°C)	3.1	3.8	1.9	2.7	3.1	6.2	6.9	7.8	7.7	7.1	5.5	6.5	7.8
Minimum dewpoint temperature* (°C)	-30.8	-33.8	-30.5	-35.9	-29.3	-30.8	-19.4	-31.5	-27.0	-28.1	-25.8	-30.5	-35.9
Precipitation (mm)	1	0	0	0	0	0	0	2	2	0	22	0	27
							Day						
Prevailing wind direction	NNW	SE	SE	SE	NNE	NNE	NNW	NNW	NE	NNW	SE	NNW	NNW
Average wind speed (m s^{-1})	4.3	5.0	6.1	5.2	4.9	4.1	4.1	3.4	2.6	3.5	3.8	3.3	4.2
Maximum wind speed* (m s^{-1})	13.3	13.0	14.8	11.8	11.6	10.5	11.4	8.6	7.9	12.2	11.7	10.0	14.8
Direction of max. wind* (deg.)	152	141	143	148	186	36	148	131	156	141	245	141	143
Average station pressure (hPa)	678.2	680.9	679.7	680.0	680.8	680.2	680.8	680.6	680.3	680.0	679.6	679.8	680.1
Maximum pressure* (hPa)	682.9	683.6	683.2	682.6	684.0	682.6	683.4	682.7	682.9	682.4	681.9	683.3	684.0
Minimum pressure* (hPa)	673.4	678.4	676.3	675.4	678.2	677.5	678.4	677.6	677.3	677.8	676.7	677.3	673.4
Average air temperature (°C)	5.2	8.6	7.5	9.3	11.5	10.9	10.7	10.2	10.7	9.0	7.0	8.3	9.1
Maximum air temperature* (°C)	11.6	15.0	14.3	16.5	16.5	18.2	16.0	16.5	16.2	15.4	12.5	14.0	18.2
Minimum air temperature* (°C)	-2.3	0.2	-1.4	-1.4	4.8	2.5	4.2	2.9	3.3	1.9	-1.2	-0.4	-2.3
Average dewpoint temperature (°C)	-8.2	-12.3	-11.9	-13.0	-8.0	-6.0	-1.0	-2.4	-0.7	-3.7	-6.1	-9.8	-7.0
Maximum dewpoint temperature* (°C)	8.0	5.3	5.6	5.3	5.4	7.2	9.5	8.4	9.6	8.1	7.4	9.4	9.6
Minimum dewpoint temperature* (°C)	-31.2	-29.7	-29.4	-34.2	-27.8	-28.9	-19.1	-31.4	-27.2	-26.8	-25.5	-30.2	-34.2
Precipitation (mm)	4	7	0	0	0	2	0	28	30	47	67	0	185

Instrument heights: wind, 10.2 m; pressure, 3398.4 m (MSL); air temperature, 2.0 m; dewpoint temperature, 2.0 m. Wind and temperature instruments are on a tower 15 m southwest of the main building.
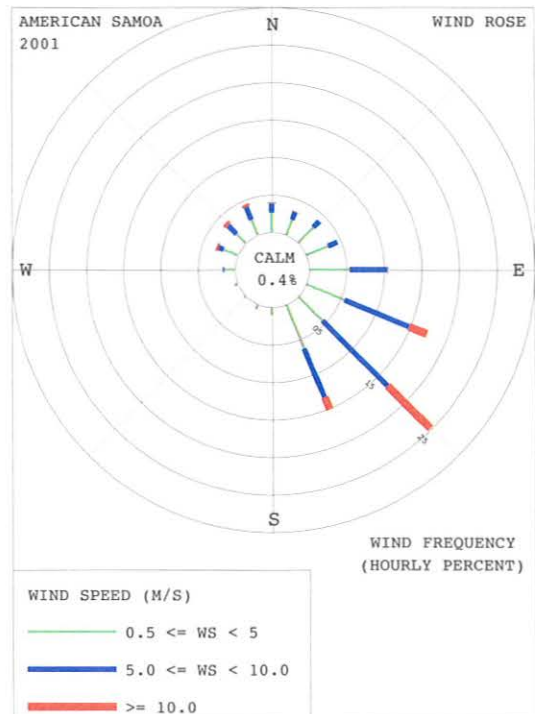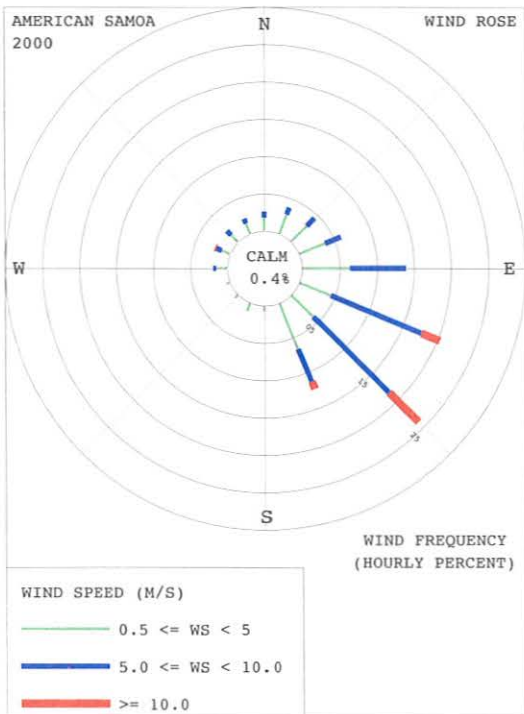*Maximum and minimum values are hourly averages.

TABLE 1.9. MLO 2001 Monthly Climate Summary

	Jan.	Feb.	March	April	May	June	July	Aug.	Sept.	Oct.	Nov.	Dec.	Year
							Night						
Prevailing wind direction	SSE	SE	SE	SSE	SSE	S	SE	SSE	SE	SE	SSE	SSE	SSE
Average wind speed (m s^{-1})	5.5	4.7	4.2	3.1	3.0	2.9	3.2	4.4	3.6	4.1	4.4	8.4	4.3
Maximum wind speed* (m s^{-1})	11.9	11.4	10.3	10.2	8.6	8.1	11.3	10.7	11.4	12.0	15.7	16.7	16.7
Direction of max. wind* (deg.)	157	158	158	159	155	164	165	117	156	154	173	151	151
Average station pressure (hPa)	680.7	678.2	679.3	680.2	680.5	680.4	680.9	681.5	681.0	680.4	681.3	679.5	680.3
Maximum pressure* (hPa)	684.3	681.6	684.4	682.8	683.1	683.2	682.8	684.7	683.6	683.9	684.1	682.6	684.7
Minimum pressure* (hPa)	676.7	671.8	675.1	676.5	677.5	677.4	678.5	679.2	677.9	677.2	675.2	675.3	671.8
Average air temperature (°C)	4.5	2.6	2.9	3.8	4.6	5.2	6.6	6.6	6.1	5.4	5.8	4.2	4.8
Maximum air temperature* (°C)	10.7	8.4	11.1	8.9	11.3	11.5	12.4	12.2	11.1	9.8	11.1	8.3	12.4
Minimum air temperature* (°C)	-0.5	-0.9	-1.7	-0.8	-0.3	0.4	1.9	1.5	1.3	1.0	0.9	-1.0	-1.7
Average dewpoint temperature (°C)	-18.2	-10.3	-19.7	-14.5	-11.6	-8.4	-10.9	-8.7	-9.5	-9.8	-11.2	-15.0	-12.6
Maximum dewpoint temperature*(°C)	4.9	1.7	2.9	4.7	4.4	6.1	5.9	8.0	7.2	7.0	5.5	4.9	8.0
Minimum dewpoint temperature* (°C)	-37.0	-33.7	-35.7	-30.2	-27.9	-29.4	-26.9	-24.5	-26.3	-27.5	-30.1	-31.6	-37.0
Precipitation (mm)	0	17	0	0	0	0	0	0	6	8	69	67	167
							Day						
Prevailing wind direction	SE	NNW	NE	NNW	NE	NNW	NNW	NE	NNW	NW	NNW	SE	NNW
Average wind speed (m s^{-1})	4.7	4.1	3.8	3.1	2.9	3.0	3.3	4.2	3.1	4.1	3.4	7.3	3.9
Maximum wind speed* (m s^{-1})	11.1	10.5	9.8	9.9	6.4	12.4	10.6	14.7	11.1	11.7	12.6	14.8	14.8
Direction of max. wind* (deg.)	120	181	141	155	116	174	168	121	156	142	156	125	125
Average station pressure (hPa)	680.7	678.2	679.3	680.3	680.6	680.6	681.2	681.8	681.0	680.5	681.3	679.5	680.4
Maximum pressure* (hPa)	685.6	681.9	684.3	682.6	682.7	683.0	683.9	684.8	683.5	684.7	684.8	682.7	685.6
Minimum pressure* (hPa)	676.4	672.1	675.0	677.1	677.5	677.7	678.8	679.4	678.4	677.1	675.3	675.4	672.1
Average air temperature (°C)	8.5	5.8	7.0	7.7	8.9	8.9	10.5	10.6	9.8	9.1	9.1	7.6	8.6
Maximum air temperature* (°C)	16.7	12.5	12.7	13.0	15.8	15.6	15.8	15.7	15.8	14.0	16.6	14.0	16.7
Minimum air temperature* (°C)	-0.2	-0.7	-0.8	0.0	1.6	2.4	3.3	3.0	2.5	2.5	1.3	-0.8	-0.8
Average dewpoint temperature (°C)	-11.9	-6.1	-11.5	-5.7	-5.0	-2.9	-4.4	-2.1	-2.7	-3.3	-6.4	-13.0	-6.4
Maximum dewpoint temperature* (°C)	8.1	4.8	4.2	4.4	6.8	7.2	7.6	9.5	8.8	7.4	9.1	6.9	9.5
Minimum dewpoint temperature* (°C)	-37.1	-26.4	-34.7	-29.5	-26.4	-27.7	-24.5	-23.2	-23.9	-25.3	-27.8	-29.5	-37.1
Precipitation (mm)	0	20	1	5	9	25	0	6	13	0	69	44	192

Instrument heights: wind, 10.2 m; pressure, 3398.4 m (MSL); air temperature, 2.0 m; dewpoint temperature, 2.0 m. Wind and temperature instruments are on a tower 15 m southwest of the main building.

*Maximum and minimum values are hourly averages.

TABLE 1.10. SMO 2000 and 2001 Monthly Climate Summary

	Jan.	Feb.	March	April	May	June	July	Aug.	Sept.	Oct.	Nov.	Dec.	Year
							2000						
Prevailing wind direction	---	---	---	ESE	ESE	SE	SSE	SE	SE	ESE	ESE	WNW	SE
Average wind speed (m s^{-1})	---	---	---	4.5	5.2	7.9	6.3	6.6	6.4	6.5	5.2	4.5	5.9
Maximum wind speed* (m s^{-1})	---	---	---	11.3	11.6	15.6	15.1	13.3	13.5	13.9	11.6	11.5	15.6
Direction of max. wind* (deg.)	---	---	---	118	121	128	139	133	127	131	131	297	128
Average station pressure (hPa)	1000.1	1001.8	1001.2	1001.3	1002.2	1002.9	1002.8	1002.5	1003.8	1001.5	1000.6	998.7	1001.6
Maximum pressure* (hPa)	1005.4	1006.5	1005.3	1005.3	1006.0	1006.7	1007.5	1006.2	1007.3	1005.4	1004.9	1003.2	1007.5
Minimum pressure* (hPa)	993.1	996.8	996.1	997.6	997.8	998.1	998.4	998.5	999.8	996.0	995.4	993.5	993.1
Average air temperature (°C)	27.1	27.1	26.9	27.3	26.8	26.6	25.7	25.6	26.2	26.1	26.8	27.3	26.6
Maximum air temperature* (°C)	28.4	28.7	28.7	29.1	29.2	29.1	27.7	27.0	27.7	27.4	28.0	29.6	29.6
Minimum air temperature* (°C)	23.2	23.1	22.8	23.0	22.4	23.3	23.2	22.8	22.8	22.8	23.3	24.5	22.4
Average dewpoint temperature (°C)	22.9	23.0	23.2	23.3	22.7	22.5	21.1	22.4	22.4	22.6	23.3	23.2	22.7
Maximum dewpoint temperature* (°C)	24.3	24.6	24.4	24.5	24.7	24.5	23.7	24.4	23.8	24.1	24.6	25.5	25.5
Minimum dewpoint temperature* (°C)	19.9	20.5	21.5	21.5	17.0	17.8	15.4	19.4	20.5	20.4	18.5	20.6	15.4
Precipitation (mm)	364	189	166	200	172	156	93	33	93	256	168	220	2110
							2001						
Prevailing wind direction	E	E	NW	ESE	SE	ESE	SSE	SE	SE	SE	SE	SE	SE
Average wind speed (m s^{-1})	4.6	4.4	5.1	4.0	6.0	5.8	5.3	8.2	8.7	7.6	7.7	4.9	6.0
Maximum wind speed* (m s^{-1})	11.0	12.8	15.2	11.6	14.0	11.9	12.6	13.5	17.0	16.7	16.0	14.9	17.0
Direction of max. wind* (deg.)	319	92	322	132	152	126	148	142	140	137	127	330	140
Average station pressure (hPa)	1001.1	999.0	1000.1	1000.4	1001.3	1000.8	1002.2	1002.2	1002.9	1001.3	1000.8	996.9	1000.8
Maximum pressure* (hPa)	1004.4	1002.7	1004.2	1003.7	1005.7	1005.1	1005.8	1006.5	1007.3	1005.6	1005.0	1000.8	1007.3
Minimum pressure* (hPa)	997.7	995.0	993.5	997.1	996.7	997.4	996.2	995.8	999.4	996.3	996.8	992.8	992.8
Average air temperature (°C)	27.5	27.2	27.3	27.3	27.0	26.7	26.3	25.9	25.8	26.0	26.6	26.9	26.7
Maximum air temperature* (°C)	28.9	28.7	28.8	29.2	28.9	27.8	28.1	27.4	27.4	27.6	27.8	28.6	29.2
Minimum air temperature* (°C)	23.4	23.3	23.8	23.9	24.7	24.0	22.8	23.7	23.4	22.5	23.9	23.3	22.5
Average dewpoint temperature (°C)	23.1	23.1	23.9	23.8	23.3	24.0	22.6	22.5	22.9	23.2	23.7	23.9	23.3
Maximum dewpoint temperature* (°C)	24.8	24.5	25.2	25.2	25.8	25.5	25.6	25.0	25.1	25.2	25.3	25.7	25.8
Minimum dewpoint temperature* (°C)	21.3	21.4	21.7	20.7	16.6	22.0	15.8	17.5	17.7	19.6	19.2	19.9	15.8
Precipitation (mm)	137	132	---	104	220	226	134	48	141	233	210	451	2036

Instrument heights: wind, 22.9 m; pressure, 78.5 m (MSL); air temperature, 18.9 m; dewpoint temperature, 18.9 m. Wind and temperature instruments are on Lauagae Ridge, 110 m northeast of the main building.
*Maximum and minimum values are hourly averages.

AMERICAN SAMOA
1977-1999

N

WIND ROSE

W

CALM
2.4%

E

S

WIND FREQUENCY
(HOURLY PERCENT)

WIND SPEED (M/S)

——— 0.5 <= WS < 5

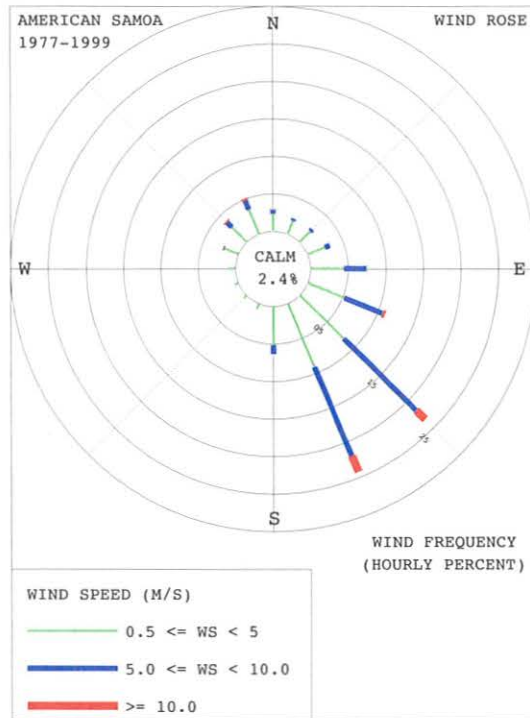——— 5.0 <= WS < 10.0

——— >= 10.0

Fig. 1.7. Wind rose of surface winds at SMO for 1977-1999. The distributions of prevailing wind direction and speed are given in units of percent occurrence for the 23-yr period for 16 direction classes and 3 speed classes. Percent frequency of calm winds (WS < 0.5 m s^{-1}) is indicated on the graph.
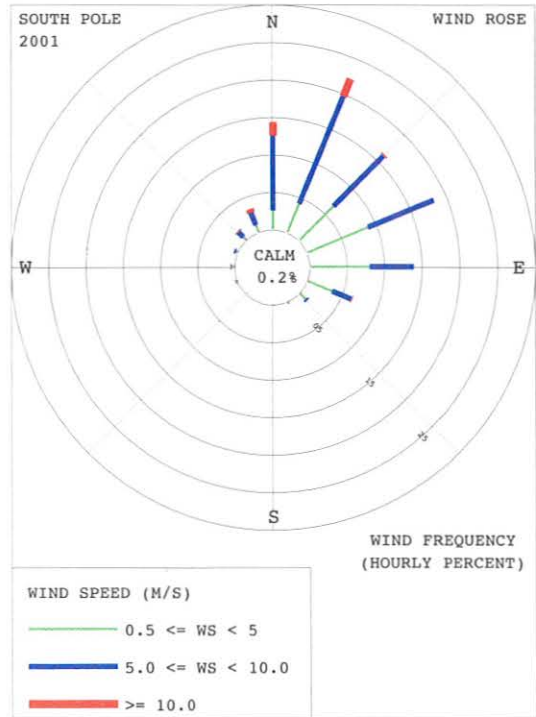

SOUTH POLE
2000

N

WIND ROSE

W

CALM
0.2%

E

S

WIND FREQUENCY
(HOURLY PERCENT)

WIND SPEED (M/S)

——— 0.5 <= WS < 5

——— 5.0 <= WS < 10.0

——— >= 10.0

SOUTH POLE
2001

N

WIND ROSE

W

CALM
0.2%

E

S

WIND FREQUENCY
(HOURLY PERCENT)

WIND SPEED (M/S)

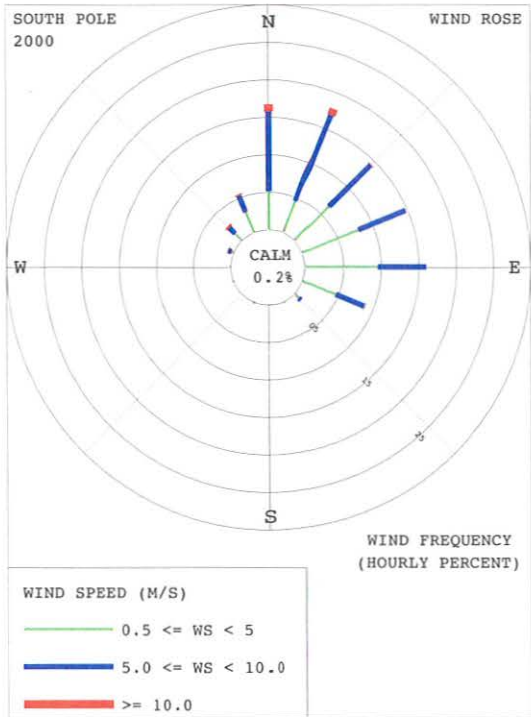——— 0.5 <= WS < 5

——— 5.0 <= WS < 10.0

——— >= 10.0

Fig. 1.8. Wind roses of surface winds at SPO for 2000 (left) and 2001 (right). The distributions of prevailing wind direction and speed are given in units of percent occurrence for 16 direction classes and 3 speed classes. Percent frequency of calm winds (WS < 0.5 m s^{-1}) is indicated on the graphs.

TABLE 1.11. SPO 2000 and 2001 Monthly Climate Summary

	Jan.	Feb.	March	April	May	June	July	Aug.	Sept.	Oct.	Nov.	Dec.	Year
							2000						
Prevailing wind direction	NNE	E	E	ENE	E	E	N	NE	NE	N	NNE	NNE	NNE
Average wind speed (m s^{-1})	4.4	4.1	4.7	5.5	5.4	5.8	6.2	5.5	6.0	5.7	6.7	4.1	5.4
Maximum wind speed* (m s^{-1})	10.1	10.3	16.0	11.6	14.3	11.6	12.2	11.0	11.4	12.5	14.9	7.7	16.0
Direction of max. wind* (deg.)	353	354	318	107	15	27	3	347	114	358	289	11	318
Average station pressure (hPa)	681.1	680.6	681.3	679.8	676.3	681.3	677.1	676.9	678.6	672.5	687.4	691.5	680.3
Maximum pressure* (hPa)	690.4	694.2	695.0	692.4	695.7	701.3	697.3	694.4	702.8	682.1	697.8	699.9	702.8
Minimum pressure* (hPa)	672.4	670.7	668.7	666.5	663.2	665.6	664.9	662.7	659.9	660.2	668.7	681.3	659.9
Average air temperature (°C)	-30.2	-42.7	-54.7	-61.4	-59.3	-59.1	-60.1	-59.2	-60.4	-50.4	-33.4	-27.4	-50.1
Maximum air temperature* (°C)	-23.4	-29.1	-35.4	-45.7	-40.1	-41.0	-41.5	-42.8	-41.8	-34.2	-24.0	-24.0	-23.4
Minimum air temperature* (°C)	-38.7	-57.1	-69.7	-71.0	-71.1	-74.7	-74.1	-73.4	-74.8	-63.6	-51.8	-31.1	-74.8
Average dewpoint temperature (°C)	-33.3	-47.1	-58.8	-65.6	-62.9	-63.1	-64.5	-63.3	-64.5	-54.2	-36.9	-30.8	-53.7
Maximum dewpoint temperature* (°C)	-25.5	-32.6	-38.1	-49.7	-43.3	-44.6	-45.3	-46.2	-45.0	-37.5	-27.4	-27.1	-25.5
Minimum dewpoint temperature* (°C)	-42.7	-61.9	-74.3	-75.0	-74.9	-79.4	-78.8	-78.2	-79.6	-68.1	-56.2	-34.8	-79.6
Precipitation (mm)	0	0	0	0	0	0	0	0	0	0	0	0	0
							2001						
Prevailing wind direction	NE	N	NNE	E	NNE	NNE	ENE	NNE	N	ENE	ENE	NNE	NNE
Average wind speed (m s^{-1})	4.0	4.1	6.2	5.8	6.0	6.7	6.3	6.8	6.4	6.2	5.8	5.3	5.8
Maximum wind speed* (m s^{-1})	7.5	8.5	13.2	11.5	14.6	13.4	14.7	12.2	13.3	12.4	12.6	9.5	14.7
Direction of max. wind* (deg.)	23	328	28	11	2	27	16	5	8	23	349	11	16
Average station pressure (hPa)	687.7	688.4	678.7	675.4	680.5	677.6	679.2	669.7	677.5	672.9	681.3	683.2	679.3
Maximum pressure* (hPa)	695.3	696.1	692.4	686.9	697.7	692.3	694.3	689.5	697.8	686.9	690.4	697.5	697.8
Minimum pressure* (hPa)	681.0	676.8	669.6	662.0	667.6	666.5	662.3	654.0	660.8	652.2	671.1	670.8	652.2
Average air temperature (°C)	-29.2	-38.5	-55.7	-59.6	-57.9	-57.3	-60.6	-63.4	-56.4	-53.2	-34.8	-26.3	-49.6
Maximum air temperature* (°C)	-23.3	-25.9	-38.6	-44.7	-40.2	-41.4	-39.8	-40.6	-33.2	-30.4	-22.4	-21.6	-21.6
Minimum air temperature* (°C)	-36.1	-53.4	-64.6	-70.9	-70.8	-69.8	-73.2	-76.0	-72.1	-69.6	-42.7	-34.4	-76.0
Average dewpoint temperature (°C)	-32.7	-42.5	-58.6	-63.8	-62.0	-61.1	-64.6	-67.6	-60.0	-57.3	-39.0	-29.8	-53.6
Maximum dewpoint temperature* (°C)	-26.0	-29.0	-41.8	-48.1	-43.2	-44.6	-43.3	-44.1	-36.4	-33.7	-25.2	-24.7	-24.7
Minimum dewpoint temperature* (°C)	-40.3	-58.1	-69.3	-75.7	-75.7	-75.3	-78.2	-80.7	-76.1	-73.6	-47.2	-38.1	-80.7
Precipitation (mm)	0	0	0	0	0	0	0	0	0	0	0	0	0

Instrument heights: wind, 10.3 m; pressure, 2841 m (MSL); air temperature, 2.0 m; dewpoint temperature, 2.0 m. Wind and temperature instruments are on a tower 91.4 m grid north-northwest of the Atmospheric Research Observatory.

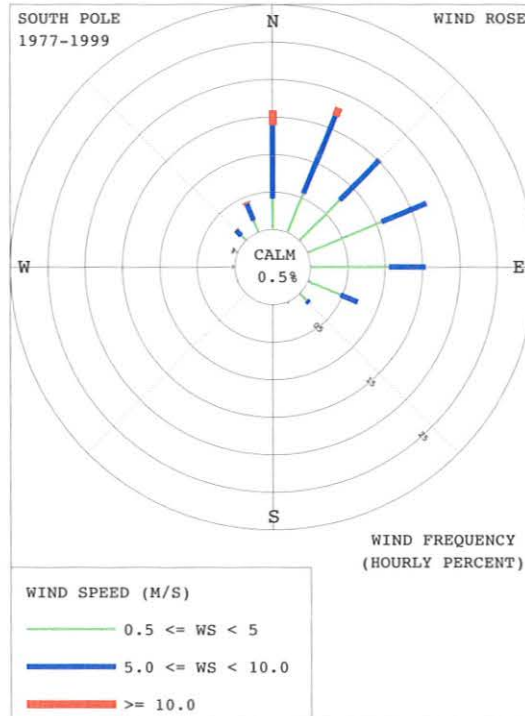*Maximum and minimum values are hourly averages.

Fig. 1.9. Wind rose of surface winds at SPO for 1977-1999. The distributions of prevailing wind direction and speed are given in units of percent occurrence for the 23-yr period for 16 direction classes and 3 speed classes. Percent frequency of calm winds (WS < 0.5 m s^{-1}) is indicated on the graph.

The average ambient temperatures for 2000 (26.6°C) and 2001 (26.7°C) (Table 1.10) were both cooler than the 23-yr average of 27.0°C. The average barometric pressure for 2000 (1001.6 hPa) was higher than the 23-yr average of 1000.9 hPa, whereas for 2001 (1000.8 hPa) it was slightly below the climatological average. Low-pressure records were tied in both January and February 2000. The precipitation amounts in both 2000 (2110 mm) and 2001 (2036 mm) were higher than the climatological average of 1754 mm.

South Pole

The distributions of the surface wind directions in 2000 and 2001 (Figure 1.8) show percentages of "clean air" sector (grid north-northwest through east-southeast) winds of 93.8% in 2000 and 94.3% in 2001, similar to the 23-yr average of 93.8% (Figure 1.9). The percentage of winds in the 10 m s^{-1} or greater class was 2.7% in 2000 and 5.3% in 2001, compared with 4.0% for the long-term average. The annual average wind speed for 2000 (5.4 m s^{-1}) equaled the climatological average wind speed

of 5.4 m s^{-1}, whereas the wind speed for 2001 (5.8 m s^{-1}) was higher than the climatological average.

The average temperatures for 2000 (−50.1°C) and 2001 (−49.6°C) (Table 1.11) were both colder than the long-term average of −49.3°C. January and February 2000 both set new record minimum temperatures for the month. The minimum temperature in 2000 of −74.8°C occurred in September. The minimum temperature in 2001 of −76.0°C occurred in August. The annual average barometric pressure for 2000 (680.3 hPa) was 1.1 hPa higher than the 23-yr average of 679.2 hPa, whereas for 2001 (679.3 hPa) it was slightly above average.

1.6. REFERENCES

Peterson, J.T., and R.M. Rosson (Eds.), *Climate Monitoring and Diagnostics Laboratory No. 22 Summary Report 1993*, 152 pp., NOAA Environ. Res. Labs., Boulder, CO, 1994.

WMO (World Meteorological Organization), *Guide to Meteorological Instrumentation and Observing Practices, WMO No. 8, Tech. Paper 3*, 347 pp., Geneva, 1969.

2. CARBON CYCLE

P.P. TANS (EDITOR), P.S. BAKWIN, L. BRUHWILER, T.J. CONWAY, E.J. DLUGOKENCKY, D.W. GUENTHER,
D.R. KITZIS, P.M. LANG, K.A. MASARIE, J.B. MILLER, P.C. NOVELLI, K.W. THONING,
B.H. VAUGHN*, J.W.C. WHITE*, AND C. ZHAO

2.1. OVERVIEW

The goal of the Carbon Cycle Greenhouse Gases group (CCGG) is to improve the understanding of the factors that determine the atmospheric burdens of major trace gases influencing the Earth's climate, in particular CO_2, CH_4, and CO. Since 1997 N_2O and SF_6 have also been measured. The anthropogenic impact on each of these species is large, but natural cycles are involved as well, except for SF_6. The continuing international climate change negotiations highlight the fact that the world has tentatively started to take steps to control the steadily increasing climate forcing by anthropogenic greenhouse gases. Two of the requirements for effective policies are a reliable method to track the atmospheric changes of each of these gases and a quantitative understanding of what controls the atmospheric concentrations.

The main tool for studying the global budgets of the trace gases is the measurement of atmospheric spatial concentration patterns and their changes over time. Two methods have been employed from the start of the Geophysical Monitoring for Climatic Change program, the forerunner of CMDL: continuous measurements are made in remote clean-air locations, namely the four CMDL observatories; and weekly pairs of discrete flask samples are obtained, also at remote clean-air locations, and analyzed in Boulder. Initially the samples were analyzed only for CO_2, but gradually more species have been added (Table 2.1). The isotopic ratio measurements are being carried out at the Institute for Arctic and Alpine Research (INSTAAR) of the University of Colorado (CU), in close cooperation with CCGG. Anomalous [17]O enrichments were measured in some of the flasks by scientists at the University of California at San Diego. A California Institute of Technology scientist started to measure D/H of H_2 in a small subset of flasks in fall 2001. The global air samples provide a unique resource for narrowing uncertainties of greenhouse gas budgets as well as other atmospheric problems. CCGG continues to investigate the feasibility of additional measurements. CCGG also collaborates with a scientist from Kyrgyzstan in a project of the International Science and Technology Center, Moscow, comparing spectroscopic absorption measurements of the total column abundances of CO_2 and other species to the CCGG network data.

Information on sources and sinks of the trace gases is obtained from their rates of change and from their spatial distributions. The quantitative link is provided by numerical models of atmospheric transport, operating in both two and three dimensions. The method used is to work "backward" from observed concentrations to the sources

TABLE 2.1. Species Analyzed in Samples of the Global Cooperative Air Sampling Network

Species	Start Date	Method*	Precision (1σ)	Collaborators
CO_2	1976	NDIR	0.05 ppm (0.02%)	
CH_4	1983	GC/FID	<1 ppb (0.07%)	
CO	1988	GC/HgO	0.5 ppb (0.5-1%)	
H_2	1988	GC/HgO	2 ppb (0.4%)	
CO_2, [13]C	1990	IRMS	0.01‰	CU/INSTAAR
CO_2, [18]O	1990	IRMS	0.03‰	CU/INSTAAR
N_2O	1996	GC/ECD	0.2 ppb (0.07%)	HATS group
SF_6	1996	GC/ECD	0.03 ppb (1%)	HATS group
CO_2, [17]O	1997	IRMS	0.03‰	UC San Diego
CH_4, [13]C	1998	GC/IRMS	0.06‰	CU/INSTAAR

*NDIR, non-dispersive infrared analyzer; GC, gas chromatograph; FID, flame ionization detector; IRMS, isotope ratio mass spectrometer; ECD, electron capture detector.

causing them, and therefore it is in the class of so-called inverse problems. The greatest limitation is sparseness of data, especially in regions close to important sources and sinks. Therefore the spatial coverage of the cooperative air sampling network has been gradually expanded. Isotopic analyses have been added because different sources/sinks may be characterized by different isotopic "signatures."

To overcome the limitation of having only measurements from the remote marine boundary layer, two new approaches were initiated. The first is to continuously measure a number of chemical species and atmospheric physical parameters at different heights on very tall towers. Mole fractions (also called mixing ratios) in the continental boundary layer are highly variable, making them more difficult to interpret and requiring much more auxiliary data than the traditional marine air samples. The second new approach is to obtain discrete air samples from low-cost airplanes in automated fashion from the boundary layer up to about 8-km altitude. These samples are then sent back to the laboratory in Boulder for analysis. It is hoped that the combination of continuous CO_2 and flask sampling can be greatly expanded on aircraft, especially over North America, to provide significant regional-scale constraints on the budgets of the gases measured.

Because the global coverage of CMDL's sampling network is unmatched, it plays an active role in bringing together the measurements from many different laboratories around the world. Toward this end, measurements of standard reference gases as well as actual field samples are being compared. For CO_2 and CO, CMDL provides cali-

---

*Institute for Arctic and Alpine Research, University of Colorado

brated reference gas mixtures under the auspices of the World Meteorological Organization (WMO). CMDL assembles a common global database for CO_2, called GLOBALVIEW-CO_2, which is currently based on the measurements from laboratories in 13 countries, and in which an attempt is made to avoid significant calibration or methodological inconsistencies. Its intended use is for three-dimensional (inverse) modeling. Its first release took place in 1996, and it has been updated once a year since then, around August (http://www.cmdl.noaa.gov/ccgg/global-view/co2/index.html). A similar database was assembled for methane, GLOBALVIEW-CH_4. The first release occurred in 1999, and a second release took place in December 2001 [*GLOBALVIEW-CH₄*, 2001].

Full individual data records and monthly means can be obtained for each species for each site from the CMDL World Wide Web page (http://www.cmdl.noaa.gov); from the ftp file server's "pub" directory (ftp.cmdl.noaa.gov); from the WMO World Data Center for Greenhouse Gases in Tokyo, Japan; and from the Carbon Dioxide Information Analysis Center in Oak Ridge, Tennessee.

2.2. CARBON DIOXIDE

2.2.1. IN SITU CARBON DIOXIDE MEASUREMENTS

The mole fraction of atmospheric CO_2 was measured with continuously operating non-dispersive infrared (NDIR) analyzers at the four CMDL observatories during 2000 and 2001, as in previous years. Monthly and annual mean CO_2 concentrations are given in Table 2.2. These values are provisional, pending final calibrations of reference gas standards. Preliminary selected hourly average CO_2 mole fractions for 2000 and 2001 are plotted for the four observatories in Figure 2.1.

Except at the South Pole Observatory (SPO), the CO_2 in situ analyzers performed without any major problems. At SPO, the Siemens Ultramat 5F CO_2 analyzer experienced some mechanical problems in March 2000. An incandescent light bulb that is used to detect the rotational speed of the chopper wheel inside the analyzer burned out. A replacement bulb, not of the original type, was installed to allow the analyzer to continue working. However, this change resulted in a change in the characteristics of the analyzer, such as reduced sensitivity and reduced output. Although the measurements resulting from the analyzer appeared to be normal, further inspection of the data showed some small offsets on the order of several tenths of a part per million (ppm) compared with flask data taken at SPO. There was also evidence of changes in the analyzer characteristics whenever the output signal of the analyzer was modified. This can be seen in December 2000 when a shift in the data of about 0.5 ppm occurred after the analyzer output was shifted upward. The analyzer was replaced on February 14, 2001, with a LI-COR Model 6251 CO_2 analyzer. Until the old Siemens analyzer can be returned to the CMDL Boulder laboratory for testing, and until all reference gases used in 2000 and 2001 are returned, the data from SPO must be considered very preliminary and subject to change.

TABLE 2.2. Provisional 2000 and 2001 Monthly and Annual Mean CO_2 Mole Fractions from Continuous Analyzer Data (μmol mol^{-1}, Relative to Dry Air), for the Four CMDL Observatories

Month	BRW	MLO	SMO	SPO
	2000			
Jan.	374.76	369.05	368.39	366.36
Feb.	376.48	369.34	368.20	366.21
March	374.54	370.35	368.60	366.15
April	375.42	371.77	368.02	366.22
May	375.88	371.32	367.64	366.35
June	372.34	371.53	367.37	366.69
July	365.98	369.75	368.16	367.15
Aug.	360.77	368.20	368.36	367.63
Sept.	363.07	366.86	368.07	367.84
Oct.	368.62	366.94	368.73	367.84
Nov.	370.97	368.28	369.06	367.75
Dec.	373.03	369.62	368.99	367.99
Year	370.99	369.42	368.30	367.01
	2001			
Jan.	375.64	370.46	369.42	367.83
Feb.	376.36	371.44	369.80	367.54
March	376.29	372.38	369.78	367.48
April	377.41	373.33	369.30	367.75
May	377.49	373.78	368.41	368.01
June	375.27	373.09	369.73	368.26
July	367.71	371.51	370.30	368.69
Aug.	361.05	369.48	369.93	369.19
Sept.	363.58	368.12	369.97	369.47
Oct.	368.81	368.59	370.08	369.71
Nov.	373.94	369.74	370.24	369.77
Dec.	376.19	371.10	370.51	369.58
Year	372.48	371.08	369.79	368.61

μmol mol^{-1} is abbreviated as ppm.

2.2.2. FLASK SAMPLE CARBON DIOXIDE MEASUREMENTS

The CMDL Global Cooperative Air Sampling Network (Figure 2.2) is the most extensive and representative network in existence for the measurement of climatically important trace gases. Samples are currently collected approximately weekly at 47 fixed locations. The samples are measured at CMDL for CO_2, CH_4, CO, H_2, N_2O, and SF_6, and at INSTAAR for ^{13}C and [18]O of CO_2. In 2000, 7400 samples were analyzed, and in 2001, 7000 were analyzed. Samples from seven sites are measured for ^{13}C of CH_4 at INSTAAR; samples from three sites are measured for [17]O of CO_2 at the University of California at San Diego; and samples from one site are measured for [2]H (deuterium) in H_2 at the California Institute of Technology. The mole fraction and isotopic measurements are used to quantify global and regional carbon budgets by inverse techniques or to constrain source/sink estimates obtained from process-based models.

Several changes to the network occurred during 2000-2001. Sampling began at Moody, Texas (WKT), in 2001 as part of the new tall-tower project there. After resumption of
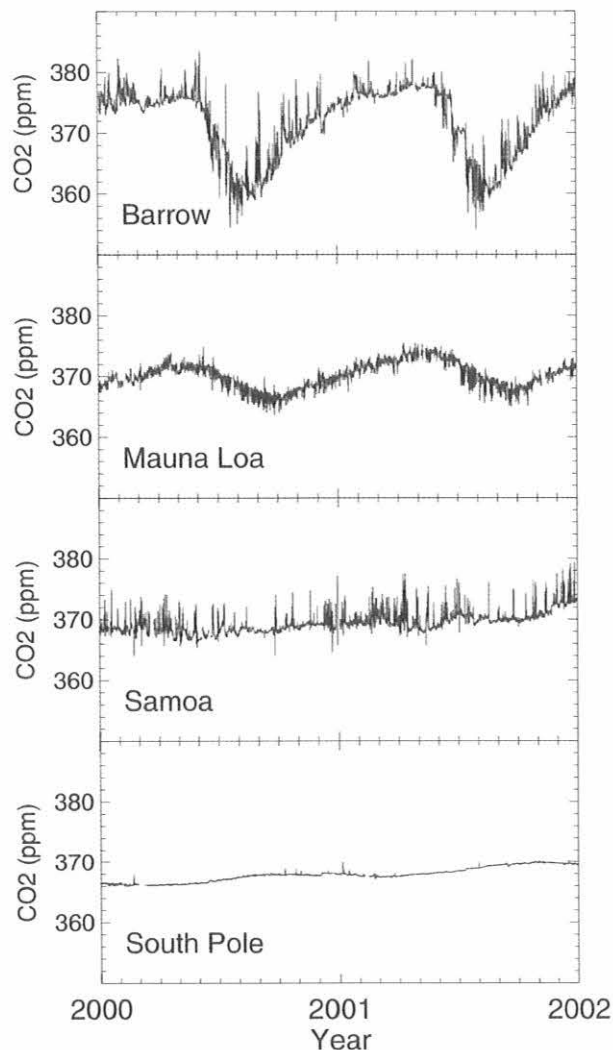
Fig. 2.1. Hourly mean CO_2 mole fractions in dry air, expressed in µmol mol^{-1} (ppm, parts per million) measured at the four CMDL observatories during 2000 and 2001. Data were not selected for background conditions. Only hours with instrument malfunctions were omitted.

regular sampling at Christmas Island (CHR) in 1998, logistical problems again interrupted sampling in 2001. Resumption of sampling at CHR or another island (Palmyra) in the region is planned. Sampling was discontinued at the Kaashidhoo Climate Observatory (KCO) when the observatory closed; Gozo, Malta, was discontinued due to lack of sampling; and the WITN tall-tower site in Grifton, North Carolina (ITN), was discontinued when the tower project there ended.

The last CCGG shipboard sampling program in the Pacific Ocean ended when the *Argentina Star* completed its route in 2001. Although modeling studies have shown the importance of the data obtained from the Pacific Ocean and the previously interrupted South China Sea cruises, these programs could not be continued.

One component of the ongoing effort to assure the quality of the flask network data is the measurement each analysis day of test flasks filled with air of known composition. The test-flask CO_2 results for 1998-2001 are plotted in Figure 2.3a. The symbols represent the difference between the measured value of each flask and the value assigned to the high-pressure cylinder from which the flasks are filled. The larger scatter observed prior to 1999 (asterisks) was reduced in early 1999 when a new person started filling the test flasks. Since that change, careful adherence to the filling procedure has produced a test-flask record (plus symbols) that can be used to investigate instrument performance and sources of uncertainty in the CO_2 measurements.

The red curve in Figure 2.3a is a smooth fit to the data, showing significant long-term variations in the test-flask differences. One possible explanation of these long-term variations is that the CO_2 mole fractions of the flask analysis reference gases are changing over time. The black lines in Figure 2.3a show the drifts in the flask analysis reference gases relative to their initial assigned values determined by periodic recalibrations during their lifetimes. Test-flask differences based on data corrected for reference gas drifts are plotted in Figure 2.3b. Much less long-term signal is seen in the drift-corrected results. The standard deviation of the test-flask differences is 0.08 ppm, which is a good approximation of the analytical precision of an individual flask measurement. This value is the sum of several sources of imprecision. The uncertainty arising from the high-frequency (1-Hz) noise of the NDIR instrument is ~0.02 ppm (1 standard error of the 30-s average). Additional lower frequency noise is observed in the variability of the three reference gases used to calibrate the instrument several times during each analysis day. The red squares in Figure 2.3b represent the difference between the value assigned to the mid reference gas and the value calculated (linearly) for mid using the high and low reference gases. The offset from zero is due to the instrument nonlinearity (which is accounted for in the determination of actual flask values), and the variability is measurement noise resulting from pressure and temperature variations, and possible regulator or other gas-handling effects, which are not accounted for by the calibration scheme. This source contributes 0.04 ppm to the overall imprecision. Based on this analysis, the remaining 0.07 ppm (uncertainties are summed in quadrature) of the test-flask imprecision likely occurs during the filling of the test flasks or results from interaction of the test gas with the flask between filling and analysis.

During 1999 and 2000 there was no significant offset in the test-flask measurements. In 2001 there is an as-yet-unexplained offset of ~0.05 ppm. Reliable test-flask data, as shown in Figure 2.3b, are useful in the interpretation of results from interlaboratory flask intercomparison experiments (discussed in section 2.7). The stability of the CMDL CO_2 analytical apparatus demonstrated by the test flasks makes it hard to postulate a CMDL analytical problem as the cause for the significant differences observed when CMDL and the Meteorological Service of Canada (MSC) measure air from the same flasks.

The 2000 and 2001 annual mean CO_2 mole fractions (mixing ratios) calculated from smooth curves fitted to the
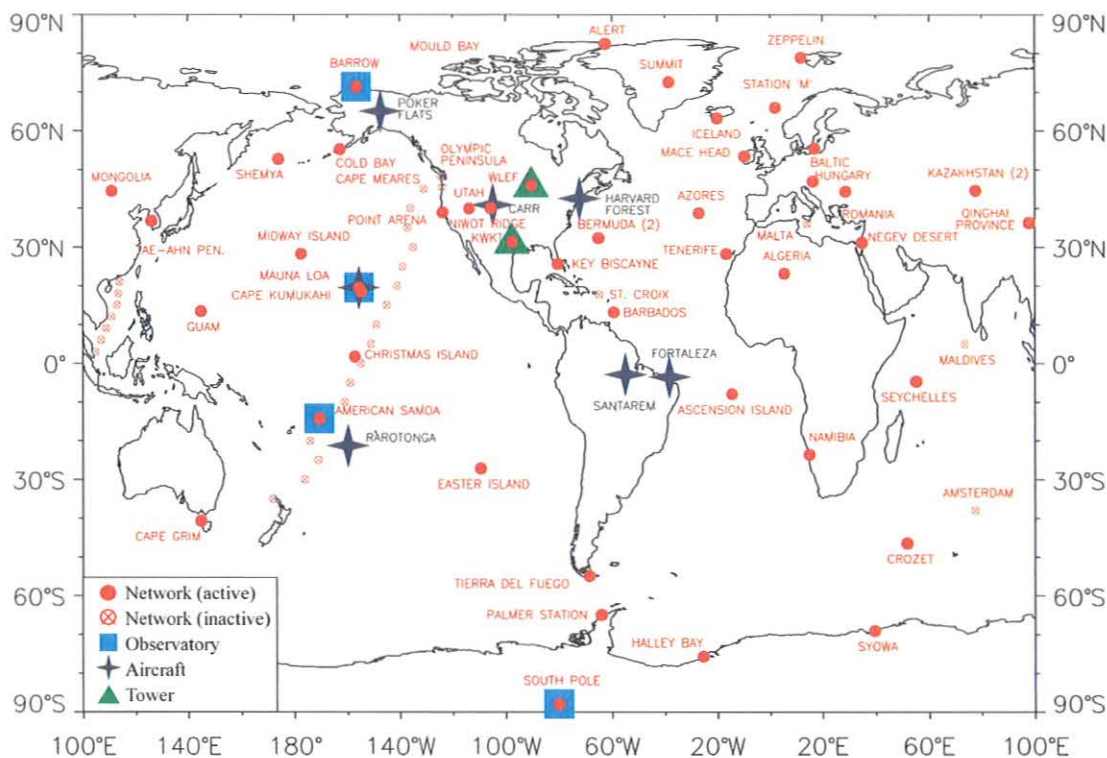
Fig. 2.2. Locations of the CCGG measurement programs, including the baseline observatories (squares), Global Cooperative Air Sampling Network (circles), discontinued sites of same (open circles with cross), aircraft vertical profiles (stars), and the very tall tower sites (triangles).

data for 47 sites in the CMDL/CCGG Global Cooperative Air Sampling Network are given in Table 2.3. The globally averaged CO_2 mole fraction and long-term trend (seasonal cycle filtered out) are shown as smooth curves in Figure 2.4a. In 2001 the globally averaged CO_2 mole fraction was 370.2 compared with the pre-industrial value of ~280 ppm in 1880. The CO_2 increase from 1999 to 2001 was 1.35 ppm yr^{-1}, slightly lower than the 1979-2001 average growth rate of 1.5 ppm yr^{-1} and about half of the 1997-1998 increase of 2.7 ppm yr^{-1}. The globally averaged CO_2 growth rate as a function of time is shown in Figure 2.4b.

2.2.3. CARBON DIOXIDE STANDARDS AND REFERENCE GAS CALIBRATIONS

The 15 primary WMO standards, ranging in CO_2 mole fraction from approximately 250 to 520 µmol mol^{-1}, were calibrated at regular intervals of slightly more than 1 year by CMDL's manometric system [Zhao et al., 1997]. The function of the primary standards is to provide continuity to the WMO scale, as well as a quality control check on the performance of the manometric system. From September 1996 through August 2001, 237 individual manometric determinations were made of the CO_2 mole fractions in these cylinders. The results of the analyses are summarized in Table 2.4. For comparison, the CO_2 mole fractions

measured by the Scripps Institution of Oceanography (SIO) by infrared absorption relative to the WMO X93 mole fraction scale, maintained by SIO, are also shown in Table 2.4. The mean precision of an individual manometric measurement by CMDL, indicated in Table 2.4 as the standard deviation, has been about 1 part in 3200. The mole fractions analyzed by CMDL are lower than by SIO at the low end of the scale and higher at the high end, while in the atmospheric CO_2 concentration range of 340 to 400 µmol mol^{-1} SIO is on average 0.10 µmol mol^{-1} less than CMDL. To maintain and propagate the WMO scale, the assigned values of the WMO primary standards have been based on both the SIO and CMDL measured values. The assigned values as of January 2000 are indicated in Table 2.4 as "old scale." Contrary to plans described in the previous CMDL report [Tans et al., 2001], it was decided to wait a bit longer before basing the assignments of the WMO primary standards on the CMDL manometric measurements alone. CMDL recently received from SIO revisions of its earlier reported IR measurements of the WMO primary standards (not incorporated in Table 2.4), and an assessment and revision of the WMO scale, to be named X2002, will be described in detail in a future publication.

Because the goal is to maximize the useful life span of the primary standards, the primary calibration scale is transferred via NDIR measurements, approximately twice a
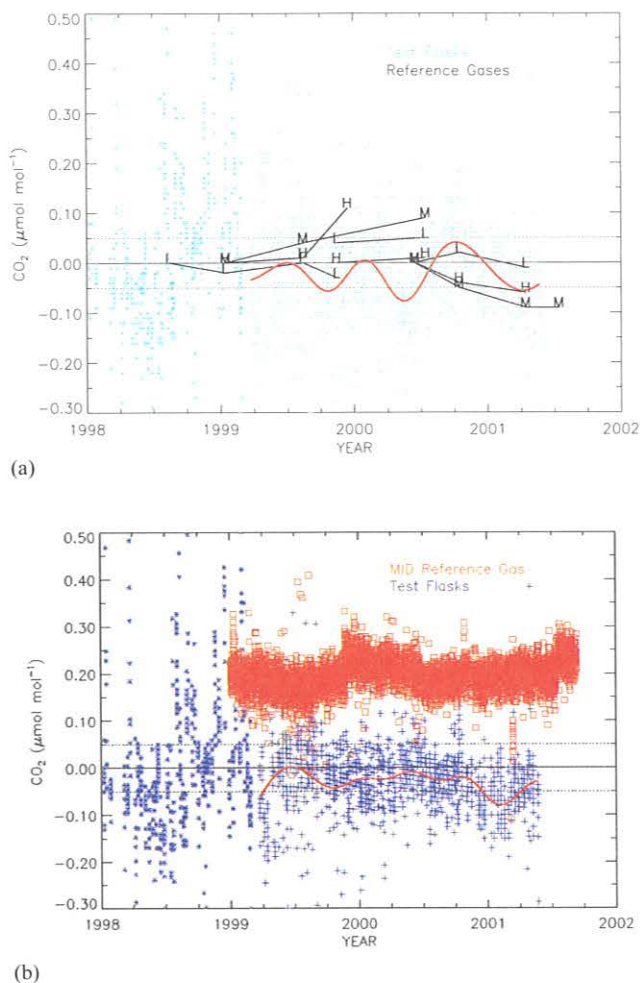
(a)

(b)

Fig. 2.3. (a) Comparison of the measurements of test flasks filled from cylinders having well-calibrated concentrations with the assigned concentration of those cylinders. Drifts of high, mid, and low (H, M, and L) reference gases are used in the measurements of the test flasks (and all other flasks). The red curves are smooth fits to the test-flask data. (b) Same as (a) after correction for drift of H, M, and L. Squares are the measured values of reference cylinder M based on linear interpolation of measurements of H and L, plotted as the difference from the assigned value of M.

year, to a set of secondary standards. The secondary standards, which typically have a useful lifespan of 3 to 4 years, are in turn used to calibrate all other cylinders, in which each cylinder is always compared with a set of four bracketing secondary standards. During 2001 about 600 cylinders were assigned a value on the WMO Mole Fraction Scale in this way. The reproducibility, in the range between 250 and 520 μmol mol^{-1}, has generally been better than 0.05 μmol mol^{-1}. In the range of 325-425 μmol mol^{-1}, the reproducibility (1σ) has been 0.014 μmol mol^{-1} [*Kitzis and Zhao*, 1999].

On request, calibrations can be performed with the manometric system well outside of the range of atmospheric

CO_2 values. Because there has been some demand for calibrations well above 520 μmol mol^{-1}, new primary CO_2 standards were created at the high end of the range, at approximately 600, 700, 1000, 1500, 2000, 2500, and 3000 μmol mol^{-1}. The standards will allow CO_2 calibrations to be performed by the comparative infrared absorption technique rather than the time-consuming manometric determinations.

Cylinders prepared by CMDL with a specified CO_2 concentration undergo the following procedures at its clean-air pumping station at high elevation on Niwot Ridge, 30 km west of Boulder:

New or recently hydrotested cylinder: (1) The cylinder is vented and then pressurized twice with dry natural air to about 20 atm (300 psi) and vented again. (2) The cylinder is filled to about 34 atm (510 psi) with dry natural air and stored for several weeks. (3) Before the final fill, the cylinder is first vented and then spiked with either 10% or zero CO_2-in-air, depending on the desired final mixing ratio. (4) The final fill is made with ambient and dried natural air to 135 atm (2000 psi), during which the ambient CO_2 mixing ratio is monitored. (5) The water vapor content of the filled cylinder is measured; it must be less than 5 ppm and is usually less than 1 ppm. Drying is accomplished with magnesium perchlorate, $Mg(ClO_4)_2$. The pump is a RIX oil-less diving compressor.

Previously used cylinder: Steps 1 and 2 are replaced by one vent and one fill with dry natural air to a pressure of 20 atm. Other trace gases, such as CH_4 and CO, can be targeted to specified values in the same cylinders.

2.2.4. MEASUREMENTS OF STABLE ISOTOPES OF ATMOSPHERIC CO_2

The Stable Isotope Laboratory (SIL) at the Institute of Arctic and Alpine Research at the University of Colorado has, for the past decade, worked closely with CCGG to measure stable isotope ratios of atmospheric greenhouse gases. Currently $\delta^{13}C$ and $\delta^{18}O$ of atmospheric CO_2 are measured in nearly all of the NOAA Global Cooperative Air Sampling Network, including flask sites, tall towers, and aircraft. Samples from 13 sites are also analyzed for $\delta^{13}C$ of atmospheric CH_4, with plans to expand this measurement to the full network when funding permits. A system to measure δD in atmospheric CH_4, as well as isotopes in water vapor extracted from the NOAA flasks, is also in the testing phase. Planned future analyses include isotopes of atmospheric CO and N_2O.

$\delta^{13}C$ of Atmospheric CO_2
A current "flying carpet" plot of $\delta^{13}C$ of CO_2 is shown in Figure 2.5. These data are key to the separation of fluxes of atmospheric CO_2 between the terrestrial biosphere and the ocean. Plants discriminate against $^{13}CO_2$ during photosynthesis by about −18 per mil (‰). This is a relatively large effect compared with the few-per-mil fractionation that occurs when CO_2 goes into and out of the surface ocean. A reconstruction of net terrestrial biospheric and oceanic fluxes is shown in Figure 2.6 from the CCGG two-dimensional (latitude, height) transport model [*Tans et al.*, 1989]. Several key observations can be made from this figure. The temperate latitudes of the northern hemisphere,

TABLE 2.3. Provisional 2000 and 2001 Annual Mean Mixing and Isotopic Ratios
from the Global Cooperative Air Sampling Network

Site		CO_2 (µmol mol^{-1})		CH_4 (nmol mol^{-1})		CO (nmol mol^{-1})		N_2O (nmol mol^{-1})		SF_6 (pmol mol^{-1})		$\delta^{13}CO_2$ (‰)		$\delta^{13}CH_4$ (‰)	
Code	Location	2000	2001	2000	2001	2000	2001	2000	2001	2000	2001	2000	2001	2000	2001
ALT	Alert, Nunavut, Canada	370.6	372.0	1829.0	1829.7	126.1	124.8	315.5	316.2	4.44	4.64	-8.20	-8.18	[ ]	-47.47
ASC	Ascension Island	367.8	369.6	1717.2	1714.3	72.1	67.0	315.0	315.7	4.38	4.59	-7.98	-7.97	[ ]	[ ]
ASK	Assekrem, Algeria	369.8	371.4	1779.3	1779.7	102.9	103.3	315.8	316.6	4.57	4.77	-8.09	-8.09	[ ]	[ ]
AZR	Terceira Island, Azores	369.9	[ ]	1801.8	[ ]	111.6	[ ]	315.7	[ ]	4.63	[ ]	-8.08	[ ]	[ ]	[ ]
BAL	Baltic Sea	374.6	[ ]	1861.3	[ ]	176.9	[ ]	316.5	[ ]	4.75	[ ]	-8.35	[ ]	[ ]	[ ]
BME	Bermuda (east coast)	370.6	371.6	1799.6	1796.0	119.3	118.2	315.8	316.4	4.65	4.83	-8.20	-8.13	[ ]	[ ]
BMW	Bermuda (west coast)	370.5	371.7	1806.8	1798.6	125.3	118.1	315.8	316.4	4.65	4.85	-8.15	-8.16	[ ]	[ ]
BRW	Barrow, Alaska	370.8	372.2	1840.8	1837.6	125.4	126.7	315.2	315.9	4.63	4.82	-8.22	-8.18	-47.43	-47.53
BSC	Black Sea, Romania	377.7	377.7	1905.1	1909.0	239.3	233.1	316.7	317.3	4.70	4.87	-8.46	-8.39	[ ]	[ ]
CBA	Cold Bay, Alaska	[ ]	372.1	1825.6	1826.4	125.3	125.2	315.8	316.2	4.64	4.82	-8.33	-8.20	[ ]	[ ]
CGO	Cape Grim, Tasmania	366.9	368.5	1708.1	1706.2	49.1	48.7	314.3	314.9	4.34	4.54	-7.97	-7.95	-46.94	[ ]
CHR	Christmas Island, Kiribati	370.0	[ ]	1736.0	[ ]	74.6	[ ]	315.9	[ ]	4.45	[ ]	-7.99	[ ]	[ ]	[ ]
CRZ	Crozet Island	366.8	[ ]	1706.3	[ ]	51.4	[ ]	314.4	[ ]	4.33	[ ]	-8.00	[ ]	[ ]	[ ]
EIC	Easter Island	366.2	368.1	1708.1	1705.4	59.4	64.2	314.7	315.1	4.36	4.54	-7.95	-7.87	[ ]	[ ]
GMI	Mariana Islands, Guam	369.3	371.0	1753.9	1756.1	78.9	88.3	315.7	316.4	4.51	4.72	-8.03	-8.04	[ ]	[ ]
HBA	Halley Bay, Antarctica	366.7	[ ]	1706.2	[ ]	49.2	[ ]	314.1	[ ]	4.32	[ ]	-7.98	[ ]	[ ]	[ ]
HUN	Hegyhatsal, Hungary	374.2	[ ]	1872.8	[ ]	194.8	[ ]	316.9	[ ]	4.79	[ ]	-8.30	[ ]	[ ]	[ ]
ICE	Heimaey, Iceland	370.1	371.7	1824.6	1828.5	121.5	125.7	315.7	316.4	4.64	4.84	-8.17	-8.19	[ ]	[ ]
IZO	Izaña Obs., Tenerife	370.2	371.7	1782.2	1780.0	99.8	101.8	315.8	316.4	4.58	4.77	-8.08	-8.12	[ ]	[ ]
KEY	Key Biscayne, Florida	371.2	373.2	1794.0	1789.0	112.6	111.1	315.8	316.5	4.62	4.80	-8.10	-8.16	[ ]	[ ]
KUM	Cape Kumukahi, Hawaii	369.9	371.4	1775.2	1776.0	94.6	100.6	315.7	316.4	4.57	4.77	-8.07	-8.08	-47.16	-47.53
KZD	Sary Taukum, Kazakhstan	371.5	373.3	1845.1	1845.3	146.7	[ ]	316.0	316.5	4.64	4.83	-8.23	-8.23	[ ]	[ ]
KZM	Plateau Assy, Kazakhstan	369.1	371.2	1816.4	1816.2	131.5	127.4	315.9	316.5	4.62	4.81	-8.06	-8.14	[ ]	[ ]
LEF	Park Falls, Wisconsin	373.1	374.4	1865.8	1856.5	143.4	142.3	315.9	316.4	4.71	4.85	-8.30	-8.24	[ ]	[ ]
MHD	Mace Head, Ireland	370.0	371.8	1820.2	1819.8	120.9	128.4	314.3	315.7	4.65	4.86	-8.12	-8.12	[ ]	[ ]
MID	Sand Island, Midway	369.5	371.5	1786.2	1788.4	105.0	109.1	315.7	316.3	4.59	4.80	-8.08	-8.08	[ ]	[ ]
MLO	Mauna Loa, Hawaii	369.6	371.2	1762.9	1764.3	89.2	93.4	315.7	316.3	4.52	4.73	-8.06	-8.06	-47.09	-47.20
NMB	Gobabeb, Namibia	[ ]	[ ]	[ ]	[ ]	[ ]	[ ]	[ ]	[ ]	[ ]	[ ]	[ ]	[ ]	[ ]	[ ]
NWR	Niwot Ridge, Colorado	370.3	372.4	1790.1	1793.9	111.2	119.2	315.7	316.3	4.60	4.79	-8.10	-8.13	-47.14	-47.23
PSA	Palmer Station, Antarctica	366.9	368.6	1707.2	1706.3	47.3	48.3	314.5	315.0	4.32	4.52	-8.00	-8.00	[ ]	[ ]
PTA	Point Arena, California	[ ]	376.8	[ ]	1809.0	[ ]	126.3	[ ]	317.3	[ ]	4.85	[ ]	-8.42	[ ]	[ ]
RPB	Ragged Point, Barbados	369.1	371.2	1770.8	1767.0	91.9	93.0	315.7	316.4	4.56	4.75	-8.02	-8.01	[ ]	[ ]
SEY	Mahé Island, Seychelles	368.3	[ ]	1725.6	[ ]	77.9	[ ]	315.3	[ ]	4.41	[ ]	-7.98	[ ]	[ ]	[ ]
SHM	Shemya Island, Alaska	370.5	372.3	1824.2	1827.2	129.5	132.6	315.9	316.5	4.63	4.84	-8.20	-8.19	[ ]	[ ]
SMO	American Samoa	368.2	369.8	1714.5	1712.4	54.7	58.6	315.1	315.7	4.40	4.58	-7.95	-7.97	-47.02	-47.18
SPO	South Pole, Antarctica	366.8	368.6	1706.9	1705.8	45.9	48.4	314.2	314.8	4.33	4.52	-7.99	-8.00	-46.96	[ ]
STM	Ocean Station M	370.6	371.8	1828.6	1828.3	129.0	128.2	315.6	316.3	4.66	4.85	-8.18	-8.17	[ ]	[ ]
SUM	Summit, Greenland	[ ]	[ ]	[ ]	[ ]	[ ]	[ ]	[ ]	[ ]	[ ]	[ ]	[ ]	[ ]	[ ]	[ ]
SYO	Syowa Station, Antarctica	366.9	[ ]	1706.3	[ ]	46.7	[ ]	314.3	[ ]	4.32	[ ]	-8.00	[ ]	[ ]	[ ]
TAP	Tae-ahn Pen., Rep. of Korea	373.3	376.4	1855.7	1851.9	219.1	207.8	316.5	317.0	4.70	4.87	-8.31	-8.40	[ ]	-47.45
TDF	Tierra del Fuego, Argentina	366.8	[ ]	1707.5	[ ]	48.4	[ ]	314.5	[ ]	4.35	[ ]	-7.98	[ ]	[ ]	[ ]
UTA	Wendover, Utah	371.3	372.2	1799.2	1802.5	120.9	120.7	315.9	316.5	4.65	4.82	-8.17	-8.18	[ ]	[ ]
UUM	Ulaan Uul, Mongolia	371.2	372.4	1830.7	1829.7	148.9	154.6	315.9	316.4	4.64	4.84	-8.16	-8.16	[ ]	[ ]
WIS	Negev Desert, Israel	371.2	372.7	1827.0	1823.8	149.0	146.2	316.0	316.8	4.66	4.88	-8.17	-8.15	[ ]	[ ]
WLG	Mt. Waliguan, P.R. of China	370.3	[ ]	1807.8	[ ]	133.0	[ ]	315.9	[ ]	4.66	[ ]	-8.14	[ ]	[ ]	[ ]
WKT	Moody, Texas	[ ]	[ ]	[ ]	[ ]	[ ]	[ ]	[ ]	[ ]	[ ]	[ ]	[ ]	[ ]	[ ]	[ ]
ZEP	Ny-Ålesund, Svalbard	371.2	372.5	1831.4	1835.3	127.5	127.3	315.7	316.4	4.66	4.84	-8.20	-8.24	[ ]	[ ]

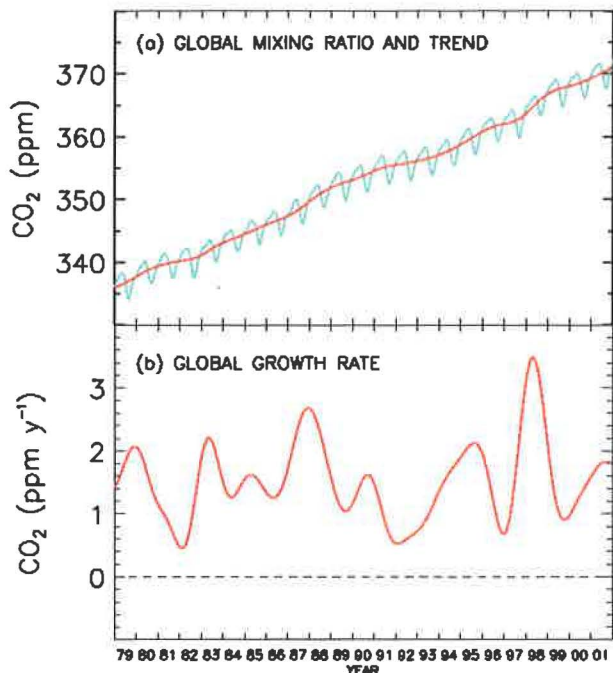Square brackets indicate insufficient data to calculate the annual mean.

Fig. 2.4. (a) Globally averaged mixing ratio and long-term trend and (b) growth rate of atmospheric CO_2 as measured by the CMDL Global Cooperative Air Sampling Network.

a land-dominated region, are always a sink of carbon for both ocean and land, with the land sink larger than the ocean sink. In the tropics, both land and ocean are almost always a source of carbon. The land source is over-estimated and the ocean source underestimated in this analysis because conversion of C-3 forests to C-4 pastures

is not included in the model. Plants with the C-3 photo-synthetic pathway (the majority of plants) discriminate against $^{13}CO_2$, whereas C-4 plant discrimination is much smaller and thus more oceanlike in its effect on isotopic ratios. When this land conversion effect is included, the net land curve will be near zero. Importantly, this implies that there must be a sink of CO_2 in the living tropical biosphere because deforestation is clearly contributing to a source of CO_2. The impact of land conversion on the isotope record is the subject of one of CCGG's recent publications [*Townsend et al.*, 2002].

A key challenge to keeping these data useful for the modeling community is maintaining a stable and precise isotopic scale over time. Measurement precision needs to be extremely high, at least ±0.01‰ (1σ), in order to keep the global uncertainty in the above deconvolutions to less than 0.5×10^{14} moles of carbon. This requires constant calibrations and the maintenance of a large suite of calibrated cylinders that are measured periodically to detect and distinguish between any observed instrument drift and possibly long-term change occurring in the suite of calibrated cylinders. In addition, the laboratory maintains several closely monitored intercomparison projects with other laboratories in which both laboratories analyze the same air-flask sample. Intercomparison projects are important because they can alert laboratories to analytical problems that can be addressed in near-real time. SIL also plays a key role along with laboratories in Japan, Australia, United States, and Germany in an ongoing effort to establish an international standard for isotopes in atmos-pheric greenhouse gases.

Spatial and Temporal Patterns of Terrestrial Discrimination

Measurements of CO_2 and $\delta^{13}C$ are used to deduce meridional patterns in oceanic and terrestrial CO_2 uptake in a simple two-dimensional inverse model. The input to the

TABLE 2.4. Summary of Measurements of the WMO Primary CO_2 Standards Expressed as μmol mol^{-1} in Dry Air (ppm), September 1996-August 2001

Cylinder Serial Number	N	CMDL		SIO		Old Scale (ppm)	Difference (mano − old)* (ppm)
		(ppm)	(1σ)	(ppm)	(1σ)		
110	12	246.68	0.10	246.82	0.52	246.78	−0.10
102	17	304.39	0.11	304.43	0.18	304.41	−0.02
111	19	324.01	0.15	324.04	0.13	324.03	−0.02
130	13	337.27	0.10	337.29	0.12	337.28	−0.01
121	11	349.39	0.08	349.35	0.12	349.36	0.03
103	18	353.35	0.10	353.18	0.12	353.24	0.11
139	14	360.90	0.06	360.82	0.14	360.84	0.06
105	16	369.38	0.12	369.32	0.16	369.34	0.04
136	15	381.34	0.12	381.24	0.17	381.26	0.08
146	15	389.54	0.11	389.47	0.20	389.49	· 0.05
101	17	396.35	0.15	396.17	0.20	396.22	0.13
106	13	412.09	0.14	411.91	0.25	411.96	0.13
123	15	423.06	0.16	422.88	0.29	422.93	0.13
107	21	453.13	0.19	452.76	0.40	452.90	0.23
132	21	521.39	0.16	520.99	0.80	521.10	0.29

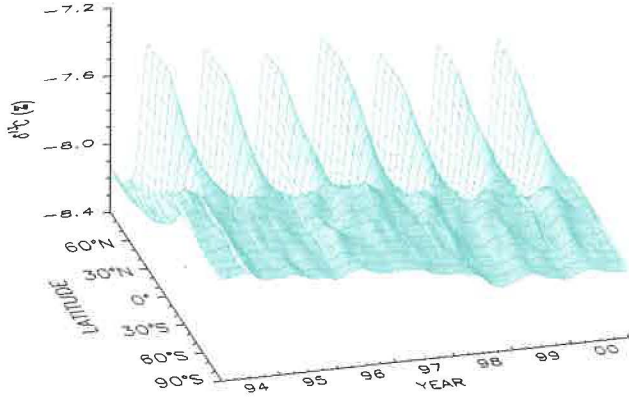*Difference between CMDL manometric values and values determined with the old scale.

Fig. 2.5. Three-dimensional representation of the latitudinal distribution of the carbon isotopic composition of atmospheric carbon dioxide in the marine boundary layer. The measurements of stable isotope ratios were made at the University of Colorado INSTAAR on air samples provided by the CMDL Global Cooperative Air Sampling Network. The surface represents data smoothed in time and latitude. The isotope data are expressed as deviations of the carbon-13/carbon-12 ratio in carbon dioxide from the VPDB-CO₂ standard in per mil (parts per thousand).

Fig. 2.6. Reconstructions of net CO_2 fluxes between the atmosphere and the terrestrial biosphere (green) and the ocean (blue) as well as the total net flux between the atmosphere and the Earth's surface from pCO₂ (red), in major latitude zones. Dashed lines represent source/sink reconstructions using values for terrestrial discrimination that are consistent with CCGG observations.

model is smoothed over time and does not include high-frequency variability that exists in the data. This allows correlation of the high-frequency variations in CO_2 and $\delta^{13}C$ in order to check model-derived patterns of surface discrimination. In a manner similar to that of *Bakwin et al.* [1998b], changes in CO_2 and $\delta^{13}C$ are related to isotopic discrimination of a source or sink using a time-varying background of CO_2 and $\delta^{13}C$. The observed CO_2 mole fraction is defined to be the sum of contributions from some regional background concentration and regional fluctuations due to biospheric sources and sinks and fossil fuel emissions. A similar equation is defined for ^{13}C using the product of CO_2 and $\delta^{13}C$, which, to a good approximation, is conserved [*Tans et al.*, 1993].

$$C = C_{bg} + C_{ff} + C_{bio} , \quad (1)$$

$$\delta C = (\delta C)_{bg} + (\delta C)_{ff} + (\delta C)_{bio} , \quad (2)$$

where C refers to CO_2 mole fraction and δ refers to $\delta^{13}C$. The subscript *bg* refers to background, *ff* to fossil fuel, and *bio* to terrestrial biological contribution. Terms with no subscript refer to the observed atmospheric values. For each sampling site, the data are fitted with a curve consisting of a second-order polynomial and two harmonic functions [*Thoning et al.*, 1989]. This "smooth curve" represents a regional average for either CO_2 or $\delta^{13}C \times CO_2$, so the background components in equations (1) and (2) are defined by the smooth-curve fits. Then, if the molar emission ratio (R) of CO to CO_2 for fossil fuels is known, C_{ff} can be determined according to equations (3) and (4):

$$CO = CO_{bg} + CO_{ff} , \quad (3)$$

$$C_{ff} = (CO - CO_{bg})/R . \quad (4)$$

As with CO_2, CO_{bg} is defined to be the smooth-curve fit to the CO data. With this model, changes in CO due to OH photochemistry and biomass burning are neglected. However, *Bakwin et al.* [1998b] showed that changes in CO:CO_2 emission ratios of 15% and the inclusion of OH consumption had very little effect on the calculation of δ_{bio}. A value for R of 20 ppb CO/ppm CO_2 is assumed. Values for δ_{ff} are taken from a zonally and annually averaged data set of $\delta^{13}C$ of fossil fuel emissions for 1992 [*Andres et al.*, 1996]. For a given site, values from the four nearest 1° zonal bands are averaged to calculate δ_{ff}. Equations (1), (2), and (4) are then combined to give equation (5):

$$(\delta C)^R - \delta_{ff} CO^R/R = \delta_{bio} (C^R - CO^R/R) . \quad (5)$$

Superscript R denotes the residual difference between the data and smooth curve. The right-hand side of equation (5) is plotted against the left such that the slope of the line is δ_{bio}.

Figure 2.7 shows δ_{bio} for the subset of continental sites with more than 3 years of data available for May, June,

July, August, and September. Fluctuations in summertime data are more likely to be related to biospheric fluxes, and thus calculated discrimination values are less sensitive to the fossil fuel correction. Analysis was restricted to continental sites because they are the most likely to satisfy the assumptions implicit in equations (1)-(5). Specifically, the equations do not account for fluctuations about the smooth curve resulting from oceanic exchange processes. At the continental sites used here it is likely that most oceanic fluxes have been mixed into the atmosphere to the extent that they are captured by variations in the smooth curve, and the remaining fluctuations are mainly a result of terrestrial processes. Note that other sites, during certain times, may also satisfy the assumptions of equations (1)-(5).

δ_{bio} varies from about −30 to −24‰ (Figure 2.7). The average of the 14 sites used is −26.0 ± 1.9‰ (1σ between sites). When data from all continental sites are binned as one site, δ_{bio} = −24.5 ± 0.2‰. This second average is heavier than the first because sites with more data, and especially those with larger residuals, like the tall tower sites ITN, HUN, and LEF, are given more weight. These values of δ_{bio} correspond to isotopic discrimination values of 18.0 and 16.5‰, respectively, for the 14 sites and all continental sites.

Fung et al. [1997], using a Simple Biosphere Model (SiB2) coupled to a general circulation model (GCM), found that discrimination changed from 10 to 20‰ between 30° and 50°N. *Lloyd and Farquhar* [1994] used a different approach to calculate discrimination values ranging only between 15 and 16.5‰ over the same latitudes. The map of discrimination used in this study to calculate the terrestrial carbon flux from CMDL atmospheric observations [*Ciais et al.*, 1995a] ranges between 18 and 19‰ over the same latitudes. The average discrimination values CCGG inferred from observations are less than the *Ciais et al.* [1995a] model, although about half the sites agree quite
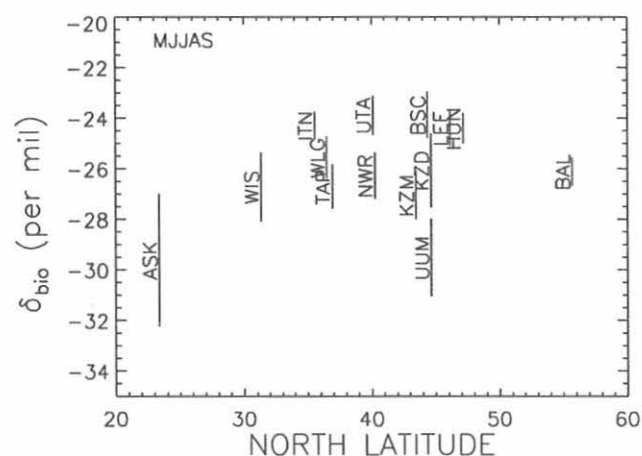
well. The data show no meridional gradient in contrast to the *Fung et al.* [1997] result. About half the sites studied also agree reasonably well with the *Lloyd and Farquhar* [1994] model, with the other sites showing higher discrimination. In the CCGG analysis, the origin of the air sampled has not been accounted for, which may explain some of the discrepancy between the models and CCGG calculations.

A Global Data Set for $\delta^{18}O$ of Atmospheric CO_2

The $\delta^{18}O$ of atmospheric CO_2 has great potential as a tool to separate net photosynthetic and respiratory fluxes of CO_2 by land plants. The oxygen of CO_2 can exchange with oxygen in leaf water and in soil water. Because leaf water is typically enriched in ^{18}O relative to ^{16}O due to evaporation of water from leaves, the $\delta^{18}O$ of atmospheric CO_2 that has been in contact with leaf water (the photosynthetic flux) is enriched relative to $\delta^{18}O$ of atmospheric CO_2 that has been in contact with soil water (the respiratory flux). Several papers have recently explored the potential of this tracer technique using GCMs with isotope physics included in the carbon and water cycles [*Yakir et al.*, 1994; *Miller et al.*, 1999; *Peylin et al.*, 1999]. One major hurdle to the further development of this tracer is that air samples collected "wet," that is, when the air is not dried during the sampling process, may experience post-sampling equilibration of oxygen in CO_2 with oxygen in the water vapor in the flask. It was demonstrated that this can occur when air humidities are high [*Gemery et al.*, 1996]. In the past, all flask data for $\delta^{18}O$ of atmospheric CO_2 between the latitude bands of 30°N and 30°S have been flagged as bad. CCGG has known that this approach eliminates some good data but has been unable to discern which samples were good data and which were not. With the addition of several AIRKITs at tropical sites, which are sampling systems that dry air during sampling, data needed to compare sampling systems and generate a data set of $\delta^{18}O$ of atmospheric CO_2 with global coverage are now available. An example of this is shown in Figure 2.8, which compares sampling systems used in parallel at Cape Kumukahi, Hawaii. Note that evacuated flasks compare well with the dried flasks, an important observation because the Pacific Ocean shipboard flasks are evacuated flasks. Multiyear records of $\delta^{18}O$ of atmospheric CO_2 at dried sites also allow assessment of the range of the expected variability in moist, tropical sites and selection of the evacuated and undried data accordingly. The new, filtered data are shown in Figure 2.9 as annual means for each site plotted as a function of latitude.

2.3. METHANE

2.3.1. IN SITU METHANE MEASUREMENTS

Quasi-continuous measurements of atmospheric methane continued at Mauna Loa and Barrow observatories at a frequency of four ambient measurements each hour. The relative precision is 0.07%. Details of the measurement techniques and analysis of the in situ data through early 1994 were published in 1995 [*Dlugokencky et al.*, 1995]. Daily averaged methane mole fractions (in 10^{-9} mol mol^{-1},
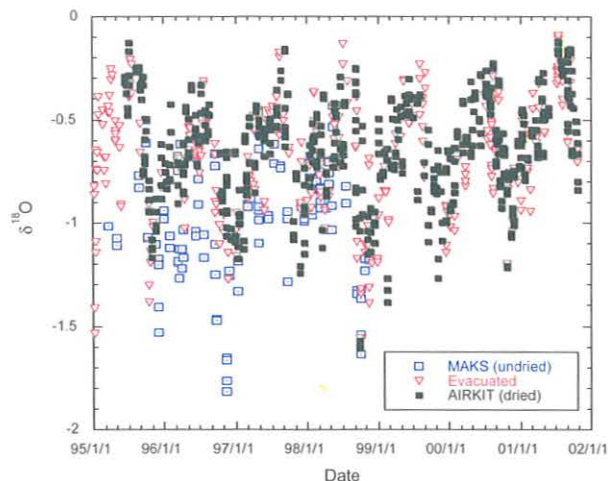

Fig. 2.7. Isotopic composition of biospheric sources at the continental stations of the CMDL Global Cooperative Air Sampling Network for May through September. Bars to the right of the symbols (site codes) denote estimated uncertainty.

Fig. 2.8. Comparison of $\delta^{18}O$ of atmospheric CO_2 from three different sampling systems at Cape Kumukahi, Hawaii: dried, evacuated, and undried.
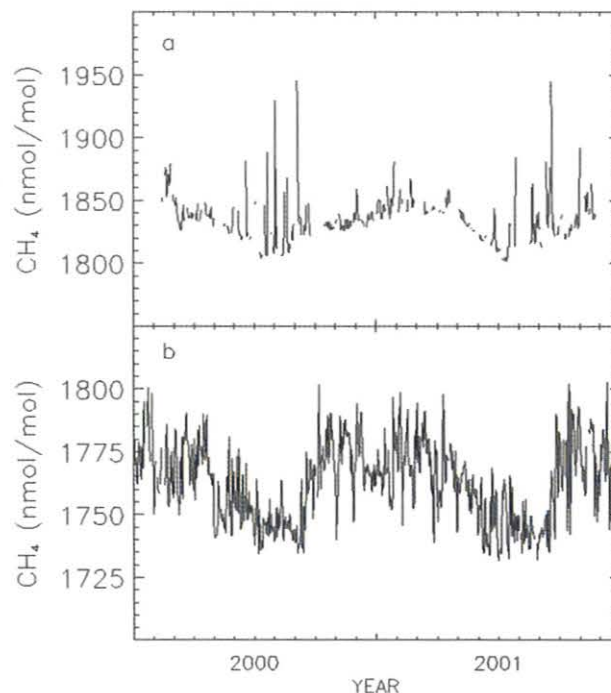

Fig. 2.10. Daily mean CH_4 mole fractions (in nmol mol^{-1}) for (a) Barrow and (b) Mauna Loa, for 2000 and 2001. The data are constrained for wind regime (see text), and they have undergone a quality control step to ensure that the analytical instrument was working optimally when they were obtained [*Masarie et al.*, 1991].

nmol mol^{-1}) for 2000-2001 are plotted in Figure 2.10 for BRW and MLO. The data were edited for instrument malfunction using a rule-based expert system [*Masarie et al.*, 1991], and they were selected for meteorological conditions. Briefly, the BRW data are constrained to the clean-air sector, which includes wind directions of 20°-110°, and wind speeds >1 m s^{-1}. MLO data are constrained to 0000-0659 local time, which is typically a period with downslope winds. In situ data are available at hourly, daily, and monthly time resolution from the CMDL World Wide Web page (www.cmdl.noaa.gov) or ftp file server's "pub" directory (ftp.cmdl.noaa.gov).

2.3.2. MEASUREMENTS OF METHANE IN DISCRETE SAMPLES

During 2000-2001 the determination of the global distribution of atmospheric methane continued from 47 sampling sites of the CCGG Global Cooperative Air Sampling Network. Sampling was started at one new site during this 2-yr period. A new tower measurement and sampling program on the KWKT television transmitter tower in Moody, Texas, began in February 2001. North-south sampling transects of the Pacific Ocean (and in the South China Sea) by ship have been suspended. Because of the importance of these measurements in studies of the global methane cycle, it is hoped that sampling can begin again in the future. Sampling also ended in 1999 at Maldives (KCO) and Malta (GOZ). Provisional annual mean values for 2000 and 2001 are given in Table 2.3. Complete data records and monthly means can be obtained through 2001 for each site from the CMDL World Wide Web page (www. cmdl.noaa.gov) or ftp file server's "pub" directory (ftp.cmdl.noaa.gov).

Globally averaged CH_4 dry-air mole fractions are plotted in Figure 2.11a for the period 1983.5 through 2001 (see *Dlugokencky et al.* [1994a] for details on calculation of global and zonal averages). During this time, CH_4 increased from about 1615 nmol mol^{-1} to about 1750 nmol mol^{-1}. The instantaneous growth rate for globally averaged

Fig. 2.9. Latitude distribution of $\delta^{18}O$ of atmospheric CO_2 from NOAA data. Annual averages from sites where samples are collected "dry" are shown as solid red squares. Annual averages from the Pacific Ocean and South China Sea shipboard samples collected in 3-L flasks are shown as solid blue circles and green triangles, respectively. The latitude distribution for each year shown is represented by a curve fitted to "dry" records only.
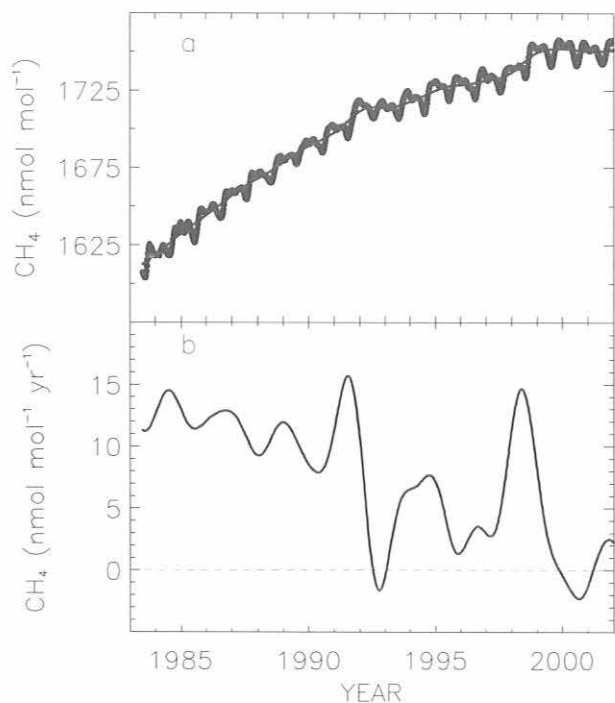
Fig. 2.11. (a) Globally averaged methane mole fractions. The solid line is a deseasonalized trend curve. (b) Instantaneous CH₄ growth rate for the global averages. The growth rate is calculated as the derivative of the solid curve in (a).

CH₄ is plotted in Figure 2.11b; it has decreased from about 14 nmol mol⁻¹ yr⁻¹ at the start of the record to approximately zero in 2000 and 2001, with significant interannual variability. An attempt has been made to explain the large variations in growth rate. The increased global growth rate in 1991 appears to have been driven by CH₄ sink chemistry in the tropics after the eruption of Mt. Pinatubo in July 1991. *Dlugokencky et al.* [1996] showed that SO₂ emitted during the eruption, and subsequent sulfate aerosol produced by oxidation of the SO₂, affected tropical photochemistry, which temporarily decreased the photo-chemical CH₄ destruction rate. The decreased global growth rate during 1992 was driven by a decrease of 0.3 ± 0.8 nmol mol⁻¹ in the northern hemisphere. *Dlugokencky et al.* [1994b] suggested that the decreased growth rate in 1992 could, only in part, be explained by decreased emissions from natural wetlands. B. Walter (personal communication, 2000) used a process-based model to show that lower-than-normal temperatures and precipitation in high northern wetland regions during 1992 resulted in decreased CH₄ emissions from wetlands. Such a change in wetland emissions would have been temporary; there is now evidence in the measurements that a separate step-like decrease in high northern emissions occurred during 1992 (see later in this section). During 1998, there was a large positive anomaly in global growth rate that corresponded to an increase in the imbalance between sources and sinks of 24 Tg CH₄ (1 Tg = 10¹² g). *Dlugokencky et al.* [2001]

attributed this to increased emissions from wetlands in the high-northern and southern-tropical latitudes resulting from warmer and wetter-than-normal conditions. *Walter* [1998] and *Walter and Heimann* [2000] used an adaptation of a process-based model that included soil-temperature and precipitation anomalies to calculate decreased emissions for 1998 of 11.6 Tg CH₄ from wetlands north of 30°N and 13 Tg CH₄ for tropical wetlands compared with the average emissions calculated for 1982-1993. Nearly all (11.5 Tg CH₄) of the tropical emission anomaly was in the southern tropics (equator to 30°S).

The observed long-term decrease in growth rate is consistent with our previous suggestion that atmospheric CH₄ is approaching steady state [*Dlugokencky et al.*, 1998], if it is assumed that the CH₄ lifetime has been constant over the time period of the measurements. In Figure 2.12a annual global CH₄ emissions are plotted for the period 1984-2000. They were calculated using the measured global CH₄ burden and rate of increase with a constant lifetime of 9 years [*Montzka et al.*, 2000] in a mass-balance equation [*Dlugokencky et al.*, 1998]. Other recent studies, though, suggest that the CH₄ lifetime may not be constant. *Krol et al.* [1998] and *Karlsdóttir and Isaksen* [2000] suggested that global hydroxyl radical (OH) is increasing, with a resulting decrease in CH₄ lifetime of about 0.5% yr⁻¹ during this measurement period. If confirmed, CH₄ emissions must be increasing, also by 0.5% yr⁻¹. Contrary
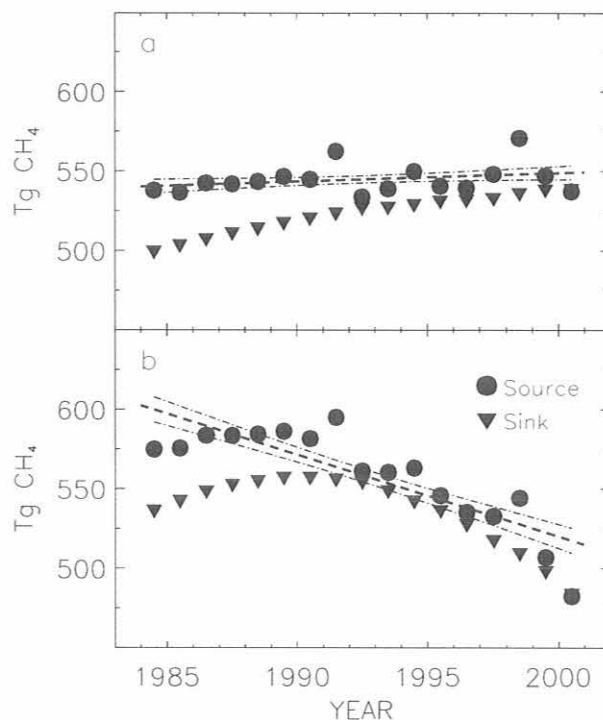

Fig. 2.12. Global annual emissions (circles) and sinks (triangles) for methane calculated using (a) a constant lifetime of 9 years and (b) smoothly varying lifetime determined by *Prinn et al.* [2001]. The dashed lines are linear fits to the emissions with 1σ confidence limits.

to these studies, *Prinn et al.* [2001] suggest that global OH has decreased by an average rate of 0.64 ± 0.60% yr^{-1} over the period 1978 to 2000. Further, they state that OH increased by 15 ± 22% from 1979 to 1988, and then decreased to levels in 2000 that were 10 ± 24% lower than those in 1979. The impact of the *Prinn et al.* [2001] OH changes on CH$_4$ lifetime is quite large, and the resulting changes in global CH$_4$ emissions are plotted in Figure 2.12b. CCGG has not yet determined what combination of changes in sources could explain the nearly 100 Tg CH$_4$ decrease in global emissions between 1991 and 2000.

Figure 2.12a suggests that a potentially huge change has occurred in the global CH$_4$ budget; that is, in 2000 it is observed that for the first time in the CCGG record the global sink was larger than global emissions. This indicates a net decrease in the global burden of CH$_4$. No one can yet explain, even qualitatively, the changes in CH$_4$ source-sink imbalance that have occurred over the past decade to cause a net decrease in global CH$_4$ burden. Without an understanding of the processes causing this change, it is not possible to guess, much less predict, what will happen to the CH$_4$ growth rate in the future.

One possible change that may have tipped the balance to a net global CH$_4$ decrease is in emissions of CH$_4$ from the fossil fuel sector in the former Soviet Union (FSU). In *Schnell et al.* [2001, pp. 33-34], a speculative scenario is described that may have contributed to the observed decreasing burden of atmospheric methane. Evidence for this scenario comes from two recent studies of CH$_4$ emissions from Russia. *Reshetnikov et al.* [2000] estimated 24-40 Tg CH$_4$ emissions from the Russian gas industry during the late 1980s and early 1990s. *Dedikov et al.* [1999], using measurements from an extensive program in 1996 and 1997 to determine losses from Russian gas production and transmission facilities, estimated a 3.6 Tg yr^{-1} CH$_4$ emission during that time. The dramatic decrease in emissions suggested by these studies is not supported by CCGG measurements, but an abrupt decrease in emissions from high northern latitudes is consistent with changes in the observed CH$_4$ latitudinal gradient. Differences in CH$_4$ calculated for polar latitudes (53.1°-90°N = PNH; 53.1°-90°S = PSH) are plotted in Figure 2.13. From 1984 through 1991, the difference in zonal average increased. In 1992, there was a downward step change in the difference of about 10 nmol mol^{-1}, which continued downward after 1992. It is unlikely that this step change is due to a natural source such as wetland emissions or a permanent change in the sink. It is almost certainly an anthropogenic source that can be altered quickly; fossil fuel exploitation is the most likely source. During 2000, the FSU produced 28% of the world's natural gas and about 10% each of coal and oil. Coal, oil, and natural gas production relative to 1990 for the FSU are plotted as a function of time in Figure 2.14. Between 1991 and 1997, production of natural gas decreased by 15%, or about 60 Tg CH$_4$. Combined with the large decreases in oil and coal production, it is conceivable (but not proved) that these changes are responsible for atmospheric CH$_4$ sources and sinks coming to steady state.

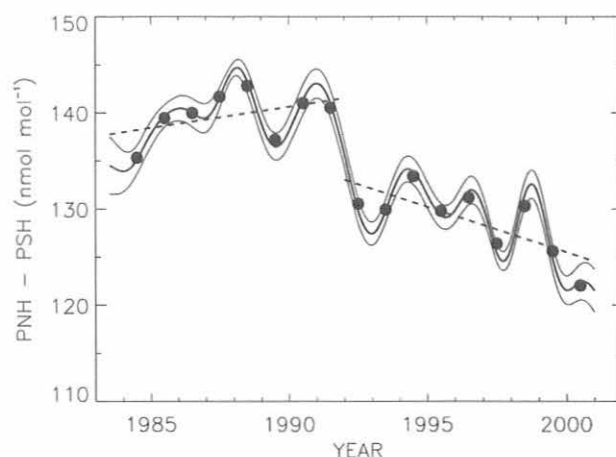Fig. 2.13. Annual (filled circles) and weekly (solid curve with 1σ confidence limits) differences in zonally averaged CH$_4$ mole fractions in the latitude zones 53.1°-90°N (PNH) and 53.1°-90°S (PSH). Trends in the differences are plotted for two periods as dashed lines: 1983.5-1991 (0.44 ± 0.36 nmol mol^{-1} yr^{-1}) and 1992-2000 (−0.94 ± 0.32 nmol mol^{-1} yr^{-1}). The mean difference for the entire period is 133.9 nmol mol^{-1}.

2.3.3. ATMOSPHERIC δ^{13}CH$_4$ SINCE 1998

INSTAAR's SIL has been measuring δ^{13}C in atmospheric CH$_4$ at 6 sites since 1998, and has recently increased that number to 13 sites. Partitioning atmospheric CH$_4$ into its sources and sinks is possible through global measurements of its stable carbon isotopic ratio, δ^{13}CH$_4$, in addition to its

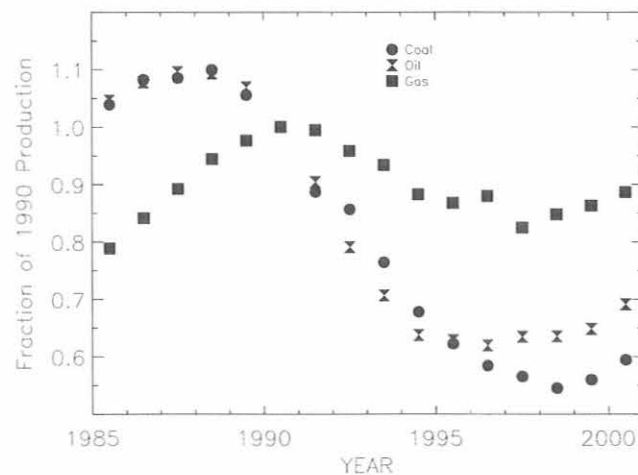Fig. 2.14. Production of coal, natural gas, and oil in the former Soviet Union relative to 1990. Production in 1990 was 332 × 10^6 tonnes oil equivalent for coal, 684.6 × 10^6 tonnes oil equivalent for natural gas, and 570.5 × 10^6 tonnes oil.

atmospheric mole fraction. Biological sources, such as wetlands, have a characteristic isotopic composition (typically −60‰) that is more depleted in the heavy isotope, ^{13}C, than thermal sources like natural gas (−40‰), which in turn, are more depleted than biomass burning sources (−25‰). The measured isotopic ratio of atmospheric CH_4 (−47‰) is a composite of these sources, but it is also influenced by the enrichment in ^{13}C content (+5‰) that results from the destruction of methane by OH, which is slightly more rapid for $^{12}CH_4$ than for $^{13}CH_4$.

An automated system was designed for the analysis of ^{13}C in atmospheric methane [*Miller et al.*, 2002]. Since January 1998, pairs of flasks were analyzed on a weekly basis from six sites (SPO, CGO, SMO, MLO, NWR, and BRW) of the Global Cooperative Air Sampling Network (see Table 2.3 for site acronym definitions). In January 2001, a new automated flask manifold with a capacity of 16 flasks and multiple reference tanks was built and installed. This has allowed an expansion of the number of sites measured from 6 to 13. The new sites are ALT, ASC, AZR, KUM, MHD, TAP, and WLG. The CCGG standard scale is linked to a scale maintained by the University of California, Irvine (UCI). Air tanks calibrated at UCI are used to establish the CCGG suite of working reference tanks. A program whereby both CCGG and the UCI laboratories measure $\delta^{13}C$ in small cylinders collected at NWR commenced in summer 2000. Preliminary analysis indicates good agreement between the laboratories.

Figure 2.15 shows the seasonal variations of $\delta^{13}C$ and CH_4 at BRW. The seasonal minima for $\delta^{13}C$ at BRW occur during September or October and are curiously offset in time from either the seasonal CH_4 maxima or minima. The timing of the seasonal cycle of CH_4 indicates that it is driven, in large part, by seasonal variations in OH, the primary sink for CH_4 in the atmosphere. The seasonal cycle of $\delta^{13}C$, on the other hand, is driven most strongly by

emissions from wetlands. The growth rate of $\delta^{13}C$ during the summer is negative, which is consistent with the addition of isotopically light CH_4 (more negative $\delta^{13}C$) that is characteristic of wetlands emissions. This occurs despite the increasing activity of OH during the summer, which, in the absence of other processes, would result in a positive $\delta^{13}C$ growth rate. The late summer minima in $\delta^{13}C$ are probably the combined result of OH concentrations that are reduced relative to the middle of summer and wetlands emissions that are still significant.

During 1998 at BRW the CH_4 minimum was less pronounced than in other years, and the minimum in $\delta^{13}C$ was more pronounced (see the smooth-curve fits in Figure 2.15). *Dlugokencky et al.* [2001] hypothesized that the growth rate anomaly in CH_4 associated with the higher-than-normal seasonal minimum was a result of two factors: increased CH_4 emission from boreal wetlands in Canada and Siberia, and large emissions of CH_4 from peatland fires in Siberia. With a two-box model of the atmospheric CH_4, this hypothesis was tested against the CH_4 and $\delta^{13}C$ observations. It was found that the combination of anomalous wetland emissions and fire emissions fitted the observations better than either emission anomaly on its own.

2.4. CARBON MONOXIDE

2.4.1. MEASUREMENTS OF CARBON MONOXIDE

During 2000-2001 the study of the global distribution of CO in the lower troposphere continued using air samples collected through the CMDL Global Cooperative Air Sampling Network, in situ measurements at BRW and MLO, and air samples collected as part of the Measurement of Pollution in the Troposphere (MOPITT) validation program. Rates of drift in CMDL CO standards were quantified, and procedures for revision of the data were developed and implemented. In the air sampling network, the conversion on the last flasks to glass pistons with Teflon O-rings allowed CO to be measured at all active sites in the network. In situ measurements at BRW and at MLO each had unique problems. Improvements to the ruggedness of the air sampling units used aboard aircraft provided much greater success in vertical profiles at remote sites. The four vertical air sampling sites established for the validation of MOPITT provided monthly to biweekly profiles. Profiles were also determined over southern Africa as part of the Southern Africa Fire-Atmosphere Research Initiative 2000 (SAFARI 2000).

Flask Measurements

Provisional annual mean CO mole fractions for 2000 and 2001 are presented in Table 2.3. These values represent a correction to the CMDL CO scale (described in section 2.4.2). As discussed previously [*Novelli et al.*, 1998a], a high degree of interannual variation occurs in tropospheric CO (Figure 2.16). The sharp decline in global CO during 1992 has been attributed to the effects of the June 1991 eruption of Mt. Pinatubo [*Bekki et al.*, 1994], and as the effects of the eruption diminished in 1993, CO returned to
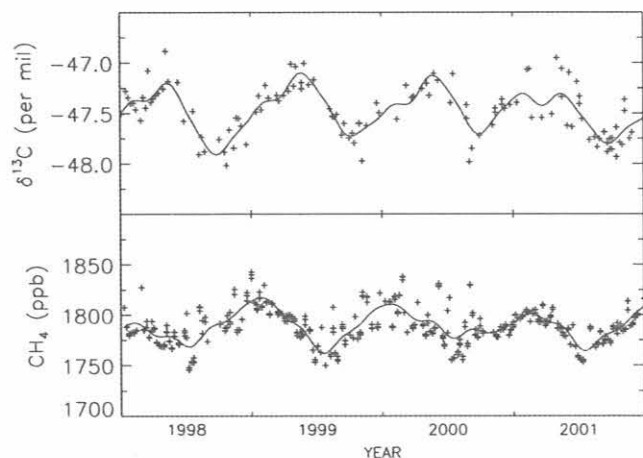

Fig. 2.15. $\delta^{13}C$ (top panel) and mole fraction (bottom panel) of atmospheric CH_4 at Barrow, Alaska (BRW), from 1998 to 2001. Pluses are averages of sample pairs collected sequentially on the same day. The solid curves are smooth fits to the data [*Thoning et al.*, 1989].
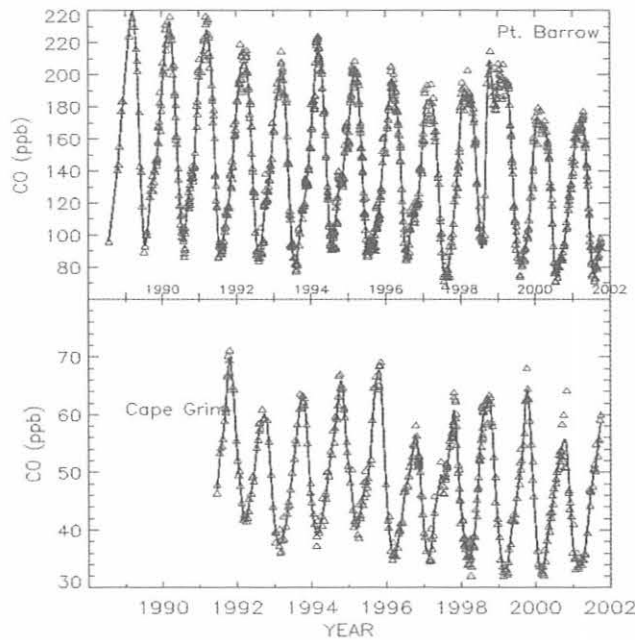
Fig. 2.16. Time series of tropospheric CO mixing ratios from Pt. Barrow, Alaska, and Cape Grim, Tasmania. Triangles are the mean of a pair of flasks; the solid curves are smooth fits to the data.

previous levels. CO mole fractions determined in flask samples showed strong enhancements beginning late 1997 through 1998. In the southern hemisphere the anomaly was largely confined to the tropics during late 1997, when strong fires in Indonesia burned agricultural areas, forests, and peat swamps. In the northern hemisphere a weak summer minimum in 1998 was followed by high CO values throughout the fall. The enhanced CO is attributed to extreme and widespread forest burning during the summer and fall of 1998. Fires in Siberia detected by Advanced Very High Resolution Radiometer (AHVRR) burned late into the autumn. Interannual variations in the CO time series are probably related to variations in large-scale biomass burning. *Wotawa et al.* [2002] reported that two-thirds of the interannual CO variability in the extratropical northern hemisphere can be explained by boreal biomass burning. Measurements from the air sampling network show that after the high CO observed during 1997 and 1998, mixing ratios returned to pre-1998 levels in 2000 and 2001 (Figure 2.16).
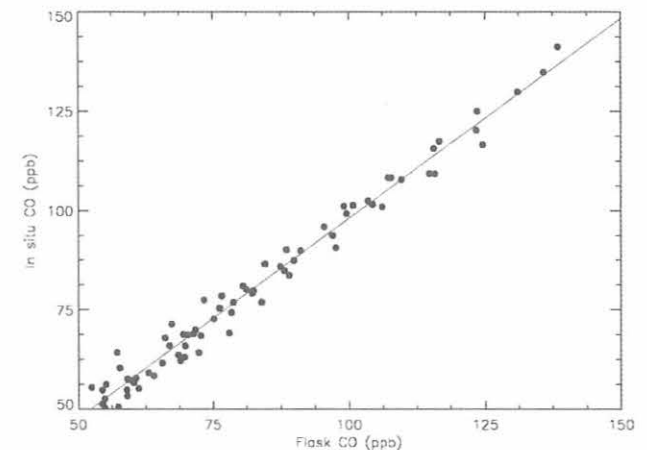
In Situ Measurements

Quasi-continuous measurements of CO (3-4 samples per hour) continued at BRW and MLO. Both sites had minor problems. The instrument at BRW was off line during mid-September-November 2000 because of a loss of standards during shipping. Measurements at MLO were hindered by a series of bad Hg lamps in the instrument, which often limited acceptable data to 1-2 samples per hour. In spite of these problems, CO determined from the in situ instruments agreed well with flask samples. At MLO the annual mean CO mole fractions determined from flask measurements and

from the in situ instrument (selected for downslope conditions) agreed well, even during periods when the instrument's Hg lamp was marginal. High correlation between the flask and in situ measurements was found at both sites, and there is no significant offset between the two measurements (Figure 2.17). However, the scatter is greater at MLO than at BRW ($r = 0.973$ and 0.997, respectively).

The residuals from a function approximating the annual oscillations and trend [*Thoning et al.*, 1989] were used to examine CO at BRW. Using a transport model and estimates of emissions from fires burning in eastern Russia, *Bruhwiler et al.* (in preparation, 2002) showed that the high levels of CO seen at BRW during fall 1988 are consistent with the transport of emissions from fires in eastern Russia.
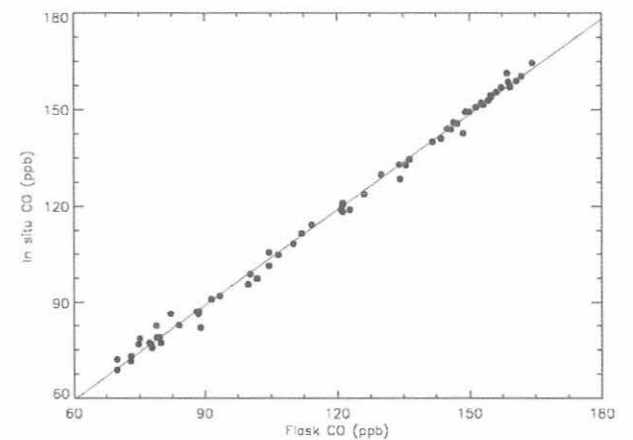
(a)

(b)

Fig. 2.17. Comparison of flask to in situ measurements at (a) Pt. Barrow and (b) Mauna Loa. The relationship between these measurements is defined with an orthogonal linear regression. BRW: $y = 0.087 (\pm 0.987) + 0.989 (\pm 0.008) x$; MLO: $y = -2.583 (\pm 1.485) + 1.006 (\pm 0.017) x$.

Vertical Profiles

With funding from the NASA Earth Enterprise System (formally the Earth Observing System), CMDL established four sites where the vertical profiles of CO and CH_4 are determined on a regular basis (Table 2.5). The measurement program has two goals: (1) It will provide vertical distributions of CO and CH_4 for the validation of MOPITT radiances and mixing ratios. MOPITT is a nadir-viewing, gas filter correlation radiometer that determines the column distribution and total abundance of CO and column abundance of CH_4. (2) It will use these data to better understand the distributions of trace gases above the boundary layer and provide additional constraints on trace gas budgets. The data collected by this program provide a unique view of CO and other trace gases as a function of altitude.

The portable air sampling equipment developed at CMDL is used on chartered aircraft to collect air samples at altitudes of up to 8 km above sea level once or twice per month. Flights are scheduled such that the aircraft is about halfway through its descent as the satellite passes overhead. Analysis in Boulder includes the suite of gases measured by CCGG: CO and CH_4, and also CO_2, H_2, N_2O, and SF_6. In addition to the long-term sites, profiles were measured over South Africa, Botswana, and the western Indian Ocean as part of the SAFARI 2000 campaign. Preliminary comparison of the CMDL profiles with the MOPITT retrievals are within the MOPITT specifications. Other flights in Colorado, Oklahoma, California, and South Africa were used to validate measurements made by two MOPITT simulators developed at the University of Toronto and at the National Center for Atmospheric Research/Atmospheric Chemistry Division (NCAR/ACD). More than 110 flights were conducted as part of this program. Regular sampling at the four MOPITT sites builds time series that define the trends and seasonal cycles of CO and the other trace gases at altitude (Figure 2.18).

2.4.2. CO REFERENCE GASES

Nine CO standards were prepared by CMDL using gravimetric methods during late 1999 and early 2000. Mole fractions assigned to CMDL working standards referenced
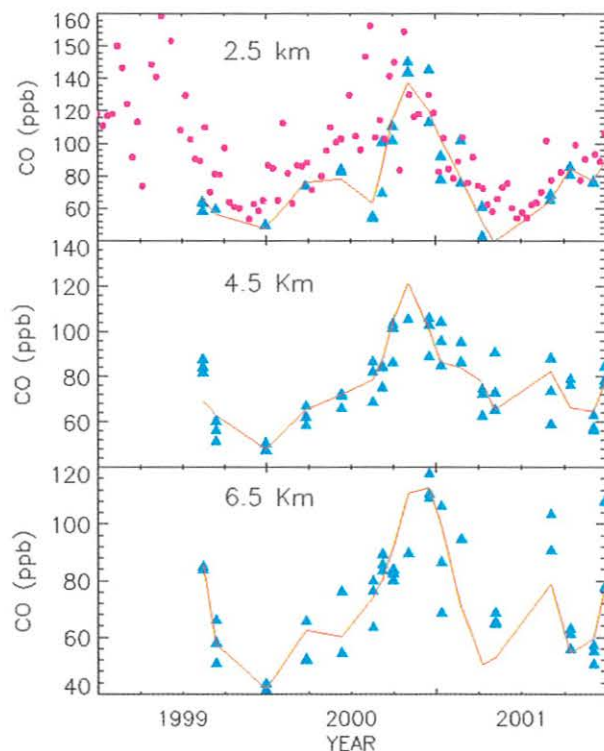

Fig. 2.18. CO time series from Molokai, Hawaii, binned for each 1000 ± 500 m altitude (typically 2-3 samples; each sample is plotted as a solid triangle). In the top panel, open circles are the flask results from MLO.

against the new gravimetrics were significantly larger than those previously assigned based upon the original CMDL CO scale [Novelli et al., 1991, 1994]. Mole fractions assigned to the working standards using dynamic dilution of a National Institute of Standards and Technology (NIST) 9.7-ppm standard in 2000 confirmed the higher CO levels in the new standards. Although frequent intercomparison of a suite of standards maintained at CMDL did not suggest drift in the standards, comparison of calibrations of working standards referenced to three sets of gravimetric standards (prepared in 1989/1992, 1996, and 1999/2000) did indicate a change over time. A re-evaluation of the CO scale, extending back to the first set of gravimetric standards, plus confidence in both the original scale and the 1999/2000 gravimetric standards, lead to the belief that both the secondary and working standards have changed over time. Calculation of linear drift rates of ±0.3 ppb yr^{-1} between 1992 and 1999/2000 are consistent with the results from a set of gravimetric standards prepared in 1996, and with comparisons with several other laboratories [Novelli et al., 1998b; Masarie et al., 2001]. Thus, there is consistent evidence that many of the CMDL standards have drifted upward.

Calibration procedures were based upon the analysis of six to eight standards with mixing ratios between 50 and 200 ppb; calibration curves were generated using area response and the CO mixing ratio assigned to the standards. Their relationship was defined using both a quadratic and

Table 2.5. MOPITT Validation Sites

Site	Latitude/ Longitude	Maximum Altitude (km)	Environment
Poker Flats, AK	65.1°N/147.5°W	7.5	HNH background continental
Harvard Forest, MA	42.5°N/71.2°W	7.9	NH polluted continental
Molokai, HI	21.4°N/157.2°W	7.9	Background NH oceanic
Rarotonga, Cook Islands	21.2°S/159.8°W	5.0	Background SH oceanic
Southern Africa*	20–30°N/22–35°E	8.4	SH background and polluted oceanic and continental

*SAFARI 2000 campaign (not a permanent site).

third-order polynomial curve [*Novelli et al.*, 1998a]. The original set of working standards used between 1990 and mid-1997 were all calibrated against the 1992 and the 1999/2000 gravimetric standards, and in many cases also against the gravimetric standards prepared in 1996. From calibrations, a rate of change in the working standard was determined. These rates were then applied to the mole fraction assigned to each standard in 1992, and new calibration curves were generated. Combined with the archived sample area responses, each sample analyzed through June 1997 was assigned a new mole fraction. (In mid-1997 the CO analytical system was changed to the Measurements of Atmospheric Gases Influencing Climate Change (MAGICC) system, and a second set of working standards was installed.)

All CO calibrations for high-pressure cylinders (standards), which were also made against the original set of working standards, required revision. A similar approach to that described above for flask measurements was used for the cylinders. First, the calibration curves were re-calculated based upon the corrected standard CO values. Archived responses from the calibrations were then combined with the revised curves to assign new CO mole fractions to the standards. The set of working standards used on MAGICC were corrected, and the sample CO value was recalculated. Table 2.6 compares revised mole fractions of several standards (calculated as described above) to mole fractions determined by direct calibration using the 1999/2000 gravimetric standards as the reference. A histogram of the differences between mixing ratios assigned to a number of tanks during 2000 and mixing ratios calculated by the correction procedure (Figure 2.19) shows that the calculated CO mixing ratios determined by the correction are generally somewhat greater than those measured. The mean bias of the corrected mole fractions is −0.9% (0.8 ppb) relative to the measured mole fractions. The tendency toward more negative differences is shown in the negative skewness (−0.71). This offset suggests that the rates of drift assigned to the working standards may, in general, have been overestimated by 0.1-0.2 ppb yr^{-1}.

2.5. NITROUS OXIDE AND SULFUR HEXAFLUORIDE

Measurements of N_2O and SF_6 from all sites in the CCGG Global Cooperative Air Sampling Network continued during 2000 and 2001 on the MAGICC analysis system. Annual mean mole fractions are given in Table 2.3 for N_2O and SF_6.

TABLE 2.6. Comparison of Measured and Revised CO Mixing Ratios

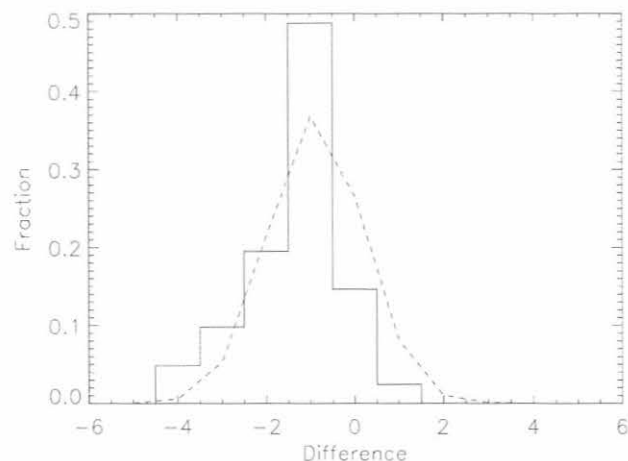| Tank ID	Measured CO (ppb)	Calculated CO (ppb)
104208	49.1 (0.4)	49.5 (0.5)
01790	54.0 (0.7)	54.7 (0.8)
01783	69.2 (1.0)	71.2 (0.8)
71607	140.8 (0.8)	141.7 (1.3)
68734	167.4 (0.6)	168.5 (0.8)
38734	200.6 (1.1)	202.4 (1.7)

Values in parentheses are 1σ of the mean.

Fig. 2.19. Histogram of the difference between CO mole fractions assigned to standards by measurement and the 1999/2000 gravimetric standards and mole fractions assigned by the data revision procedure. CMDL working standards used in the correction are not included. The dashed curve is a Gaussian fit to the data.

2.6. MEASUREMENTS ON TALL TOWERS

The CCGG tall-towers program began measurements of CO_2 mole fractions on a 610-m-tall TV transmitter tower in North Carolina (NC, site code ITN) in June 1992. CCGG observations at this site were discontinued in June 1999 due to loss of the lease with the tower owner. Measurements were started on a 447-m-tall TV tower in Wisconsin (WI, site code LEF) in October 1994 and are ongoing. Site characteristics and data from the ITN and LEF were discussed by *Bakwin et al.* [1998a]. In February 2001 measurements were begun on a 505-m-tall TV tower near Moody, Texas (TX, site code WKT). Surface winds often indicate transport of air into the interior of the eastern United States from the Gulf of Mexico, especially in summer, so the WKT site may represent an upwind end member for samples obtained over the eastern United States during many periods.

The time series of daily mean CO_2 mixing ratios at the highest measurement level on each of the towers is shown in Figure 2.20. Of note is the very weak drawdown of CO_2 in summer at WKT compared with ITN and LEF. WKT is in a region of relatively dry grazing lands with very hot summers. July-August 2001 was particularly hot and dry: at Waco high temperatures in excess of 34°C were recorded each day from July 3 through August 26, with only 25 mm of rain recorded during this period. This weather condition affected a large region of the southwest United States and apparently resulted in low activity by vegetation and soils in the area. This is reflected in the diurnal cycle of CO_2 measured at WKT (Figure 2.21). During August 2001 the accumulation of CO_2 in the shallow nighttime stable layer at TX was much less than at WI, and during the daytime the vertical gradient of CO_2 from 9 m to 457 m at TX was negligible.
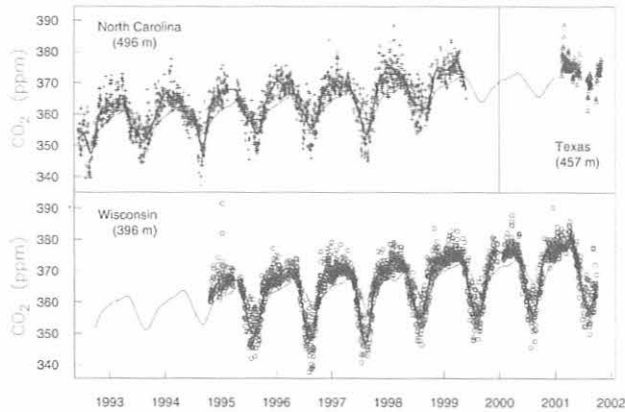
Fig. 2.20. Daily mean CO$_2$ mole fractions at the top measurement levels on the North Carolina, Texas, and Wisconsin towers. Heavy lines show smooth curve fits to the NC and WI tower data [*Thoning et al.*, 1989], and thin lines show MBL reference curves [*GLOBALVIEW-CO$_2$*, 2001] for the latitudes of the NC and WI towers.

Fig. 2.22. Growth rate from smooth-curve fits [*Thoning et al.*, 1989] to daily mean CO$_2$ mole fractions at the North Carolina and Wisconsin towers and the CCGG flask site at Ulaan Uul, Mongolia, and from the MBL reference curve for 40°N [*GLOBALVIW-CO$_2$*, 2001].

Variations in the growth rates of CO$_2$ at the ITN and LEF towers generally lead those in the marine boundary layer (MBL) and display slightly greater amplitude (Figure 2.22). Growth rate variations at the U.S. tower sites are more similar to the MBL curve than are those at the CCGG flask sampling site in Mongolia, suggesting that vegetation changes on the North American continent had a greater influence on MBL growth rates during the period of observations than did those in Eurasia.

One aim of the tower program is to provide data that can be used to test and refine models of the carbon cycle at global and continental scales. A key finding from recent global model studies has been the existence of a "rectifier effect" by which covariance between atmospheric transport and surface fluxes of CO$_2$ lead to mean horizontal and vertical gradients of CO$_2$ mixing ratios [*Denning et al.*, 1995]. In order to balance the global atmospheric CO$_2$ budget, models that have a strong rectifier effect require a northern hemisphere CO$_2$ sink that is larger than seems reasonable based on current understanding of the global carbon cycle [*Law and Simmonds*, 1996; *Denning et al.*, 1999]. At ITN surface exchange of CO$_2$ is measured [*Berger et al.*, 2001; K.J. Davis et al., The annual cycles of CO$_2$ and H$_2$O exchange over a northern mixed forest as observed from a very tall tower, submitted to *Global Change Biology*, 2002], as well as the dynamics of the atmospheric boundary layer (ABL) [*Yi et al.*, 2001]. Therefore the strength of the rectifier forcing for this site can be evaluated. The observations are compared with output from the global tracer transport model of *Denning et al.* [1995], which exhibits a strong rectifier effect. The model underestimates the diurnal covariance and the resulting difference between ABL and free troposphere (FT) CO$_2$ when compared with the observations. At seasonal time scales, however, the model overestimates the covariance and ABL-FT CO$_2$ difference. The seasonal covariance is responsible for the bulk of the predicted rectifier forcing on the global scale. Hence, the rectifier forcing in the model appears to be too strong. There are uncertainties in this analysis regarding seasonality of transport between the continental and marine boundary layers, representativeness of the single observing site, and a bias toward fair-weather observing conditions. This work has been submitted for publication (C. Yi et al., Is the simulated forcing of the CO$_2$ rectifier effect too strong?, submitted to *Geophysical Research Letters*, 2002).

In collaboration with scientists at Colorado State University, CCGG has made progress in the use of the tower data to constrain regional-scale carbon cycle simulations. The work couples a revised version of the Simple Biosphere Model (SiB2.5) with a nested-grid regional transport model, the Regional Atmospheric

Fig. 2.21. Mean diurnal cycles for each measurement level on the Wisconsin and Texas towers for August 2001. For each day the average value for the top measurement level (plotted as a number) has been subtracted from all data in order to remove synoptic variability.
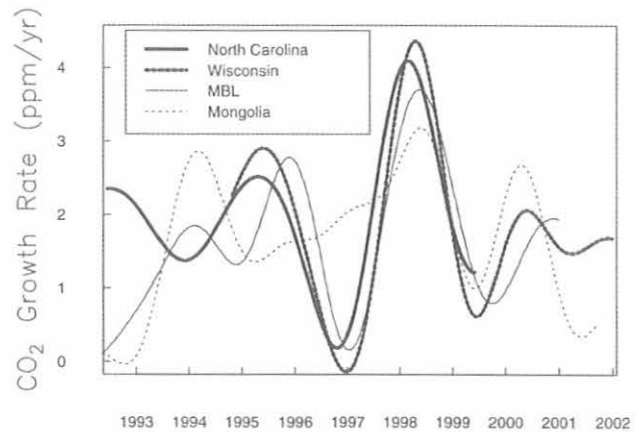
Modeling System (RAMS). Physiological properties of the vegetation and phenology were specified from satellite imagery. Encouraging results have been submitted for publication (I. Baker et al., Simulated and observed fluxes of sensible and latent heat and CO_2 at the WLEF-TV tower using SiB2.5, submitted to *Global Change Biology*, 2002; A.S. Denning et al., Simulated and observed variations in atmospheric CO_2 over a Wisconsin forest, submitted to *Global Change Biology*, 2002). This work represents the first step toward an inverse modeling scheme for the regional-scale carbon cycle.

2.7. DATA INTEGRATION (GLOBALVIEW)

The Cooperative Atmospheric Data Integration Project for carbon dioxide, established in 1995, continues its effort to improve the temporal and spatial coverage of atmospheric CO_2 observations by integrating existing observations made by different laboratories into a cooperative global network. Twenty laboratories in 13 countries now participate in this activity, contributing their up-to-date, high-precision CO_2 records from land-surface, aircraft, ship, and tower sites (see http://www.cmdl.noaa.gov/ccgg/globalview/co2). Data from this cooperative network are used to derive GLOBALVIEW-CO_2, a globally consistent data product for use with carbon cycle modeling studies [GLOBALVIEW-CO_2, 2001]. GLOBALVIEW-CO_2, which is updated annually, contains no actual data. The product consists of smoothed time series derived directly from observations as well as statistical summaries of atmospheric variability, and average diurnal and seasonal patterns. Since it was first introduced in 1996, more than 2500 Internet requests (~37 per month) for the data product have been made from more than 50 countries. Interest in GLOBALVIEW-CO_2 continues to increase (Figure 2.23). In 1997 the average number of accesses per month was 14. In 2000 the average increased to 53 per month, and in 2001 it increased again to more than 70 inquiries per month.
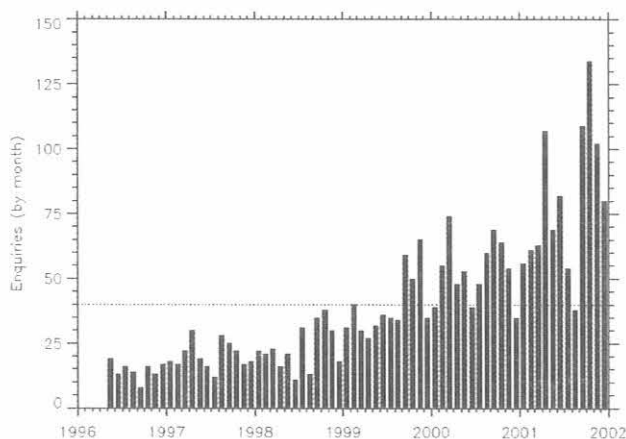

Fig. 2.23. Number of Internet requests for the GLOBALVIEW-CO_2 data product. The dotted line is the overall average since 1996.

Assessing the level of comparability among actual observations made by different laboratories continues to be a primary focus of this activity. The challenge is to ensure that spatial and temporal patterns among observations from the cooperative global network are due to CO_2 sources and sinks as affected by atmospheric mixing and transport and not due to inconsistencies among internal calibration scales and potential systematic errors introduced when sampling the atmosphere. The level of traceability of each laboratory's internal CO_2 calibration scale to the absolute WMO CO_2 mole fraction scale must be determined to properly assess comparability. Periodic cylinder-air ("round-robin") intercomparison experiments endorsed by the WMO and International Atomic Energy Agency (IAEA) are used to make this assessment. Participating laboratories compare their measurements of CO_2 and other trace species and isotopes in dry air made on a set of circulating high-pressure cylinders. These experiments are critical for the assessment of each laboratory's ability to make high-precision measurements and maintain their internal calibration scales. Results from the 1995/1996 cylinder-air comparison suggest that measurements made by laboratories contributing to GLOBALVIEW-CO_2 are comparable to within 0.2 μmol mol^{-1} with respect to calibration [*Peterson et al.*, 1999]. Preliminary results from the most recent round-robin experiment (1999/2000) suggest a slight improvement in the number of laboratories with agreement at the 0.1 μmol mol^{-1} level. Current scientific objectives require a global network precision of 0.1 μmol mol^{-1} among northern hemisphere observations and 0.05 μmol mol^{-1} among southern hemisphere observations [*WMO*, 1981]. Attaining this level of comparability among atmospheric observations with existing technology requires laboratories to maintain a level of traceability to the WMO scale significantly better than 0.05 μmol mol^{-1}. Although the cylinder-air results suggest there is considerable work yet to be done, it has been demonstrated that this level of agreement is attainable.

Results from three WMO-endorsed cylinder-air round-robin intercomparisons (1991/1993, 1995/1997, and 1998/2000) suggest that the Meteorological Service of Canada (MSC) has maintained traceability of its internal calibration scale to the WMO CO_2 mole fraction scale to within 0.03 μmol mol^{-1}. However, it cannot be concluded, based on these results alone, that atmospheric measurements made by MSC and NOAA (which maintains the WMO CO_2 scale) are comparable to this same level of agreement. Additional errors may be introduced into measurements of atmospheric air when ambient samples are collected, dried, stored, extracted, and analyzed. Cylinder-air comparisons are expressly designed to exclude these potential sources of error. To complement the periodic cylinder-air comparisons, laboratories are establishing ongoing flask-air intercomparison (ICP) experiments whereby laboratories can more directly compare atmospheric measurements. CCGG has ongoing ICP activities with the Commonwealth Scientific and Industrial Research Organization (CSIRO, Australia); MSC (Canada); National Institute for Water and Atmospheric Research (NIWA, New Zealand); and CMDL Halocarbons and other Atmospheric Trace Species group (HATS).

The effectiveness of a flask-air ICP experiment depends on several essential features. First, participants must view the ICP activity as an additional level of quality control whereby measurements are routinely scrutinized. Potential problems identified by a collaborating laboratory should not be viewed as an embarrassment but as proof that the ICP is working effectively. Second, the ICP activity is an ongoing long-term program of routine (at least weekly) comparisons of atmospheric samples. Third, the ICP experiment must include supporting measurements (e.g., control samples) that can be used to narrow possible causes when differences are observed. Fourth, the ICP activity should have minimal impact on daily operations. This is accomplished only if participating laboratories have advanced data management tools in place. Analysis of ICP samples and processing and data exchange between laboratories must be automatic and routine. Finally, ICP results must be summarized automatically and made readily available to participants. Timely feedback improves the likelihood that potential problems are detected early (Figure 2.24).

At this time, only the ICP experiments with CSIRO and MSC include the essential features described above and are proving to be valuable tools to monitor measurement quality and assess comparability. The MSC-NOAA flask-air ICP experiment, begun in late 1999, is modeled after the long-time CSIRO-NOAA experiment [*Masarie et al.*, 2001] whereby both laboratories routinely analyze the same atmospheric air sample. MSC and NOAA independently collect samples of air weekly at Alert, Nunavut, Canada, using their respective flasks and sample collection strategies. Station personnel collect at approximately the same time one pair of MSC flasks and two pairs of NOAA flasks. All flasks are shipped to MSC in Downsview, Ontario, where one of the two NOAA flask pairs is first analyzed by the Carbon Cycle Research Laboratory (CCRL) at MSC for CO_2, CH_4, CO, N_2O, and SF_6 before being shipped to Boulder and analyzed a second time by CCGG for the same suite of trace gases.

Figure 2.25 shows CO_2 measurement differences (MSC minus NOAA) from analysis of the same air in flask
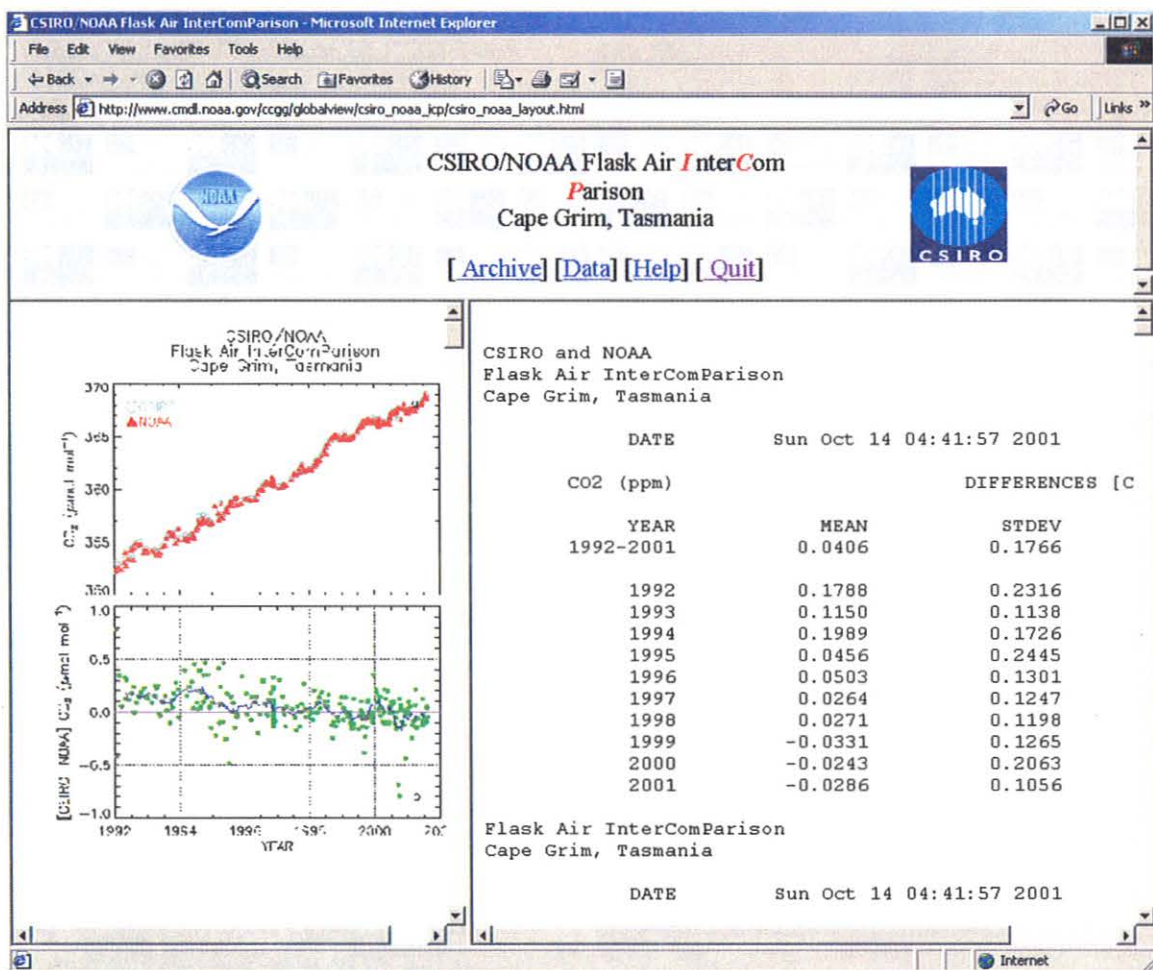

Fig. 2.24. Up-to-date flask-air intercomparison results available to participating laboratories with restricted WWW page access.
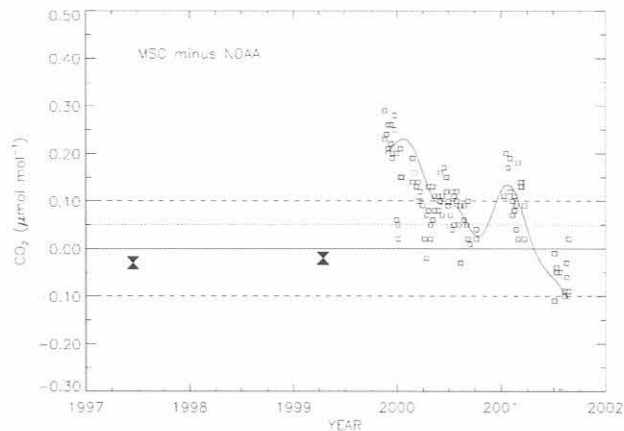
Fig. 2.25. Differences (MSC minus NOAA) between independent measurements of the same air in flask samples collected at Alert, Nunavut, Canada (open squares). Also plotted is a smooth curve fitted to the differences between individual measurements. The mean differences (MSC minus NOAA) determined from multiple intercomparisons of air in high-pressure cylinders are shown as solid hourglass symbols. The dotted and dashed lines about the zero difference line identify ±0.05 and ±0.1 μmol mol^{-1} target levels.

samples collected at Alert. The average difference is 0.10 ± 0.14 μmol mol^{-1} (n = 104). High-frequency (4-6 wk) noise in the differences is small and enables us to better pinpoint when systematic changes in the distribution occur than in the CSIRO-CMDL comparison. This information is used by MSC and NOAA to re-examine experimental changes that may have inadvertently introduced errors, i.e., errors that went undetected by conventional internal quality assurance procedures (see section 2.2.2). Results from the cylinder-air round-robin experiments are also shown in Figure 2.25 and clearly demonstrate that the maintenance of direct traceability to the WMO CO_2 mole fraction scale does not guarantee comparability among atmospheric observations. Note that, without first establishing traceability, exclusion of calibration as a possible cause for the observed differences in flask measurements would not be possible. Both components of quality control are essential. The probable causes of the observed differences between MSC and NOAA may be narrowed to errors introduced during sample collection, storage, extraction, and analysis at either or both laboratories. MSC and NOAA are currently working together to understand the causes of these differences.

2.8. INVERSE MODELING

Predicting the response of the climate system to anthropogenic emissions of radiatively active atmospheric trace species, such as CO_2 and CH_4, is complicated by important contributions to the budgets of these species from terrestrial biospheric and oceanic processes. In the case of the terrestrial biosphere, interannual variability in parameters such as temperature and precipitation may lead to significant interannual variability in sources of these

gases [e.g., *Bousquet et al.*, 2000; *Dlugokencky et al.*, 2001]. Future attempts to manage carbon reservoirs depend critically on the ability to understand and quantify the behavior of terrestrial and oceanic carbon sources and sinks. Two approaches currently being used toward this end are prognostic models of oceanic and terrestrial processes, and inverse models. The latter technique, long used for geophysical problems such as seismology, acoustic tomography, and satellite data retrievals, is an attempt to reconcile predictions from a prognostic model with observations of the trace species in a global network. Early attempts were designed to obtain the interhemispheric gradient of CO_2 fluxes [*Tans et al.*, 1990; *Enting and Mansbridge*, 1991; *Ciais et al.*, 1995a,b; *Bousquet et al.*, 1996; *Law and Simmonds*, 1996]; however, with the expansion of the CO_2 observational network, attempts have been made over recent years to obtain flux distributions over continental scales [e.g., *Fan et al.*, 1998; *Bousquet et al.*, 2000]. Results of the recent TRANSCOM III model intercomparison suggest that the network is currently still too sparse to allow accurate resolution of continental-scale fluxes. The addition of more observation sites, especially over continental and tropical regions, would improve the accuracy of current flux estimates. In addition, it appears that the current generation of transport models needs improvement so that subgrid-scale processes, such as boundary layer transport and convective transport, are accurately represented and do not introduce biases.

Ongoing work by CCGG is focused on development of an operational inverse calculation for flux retrievals at continental scales. The mass balance technique used for these calculations is described in detail by *Bruhwiler et al.* [2000]. A modification to the technique allows the propagation of spatial flux patterns (basis, or response functions, used to quantify the effect of each source region at any particular location) for an arbitrary number of months, resulting in potentially more accurate and stable solutions. In practice, it has been found that response functions need not be calculated for more than about 6 months, and sufficient accuracy may be achieved with only 4 months. This modified version of the mass balance technique may be run using constraints such as semi-empirical ocean flux estimates [*Takahashi et al.*, 1999] and/or terrestrial flux estimates inferred from satellite observations of greenness, e.g., the Carnegie-Ames-Stanford Approach (CASA) model [*Randerson et al.*, 1997]; however, the flux estimates described here were calculated without the use of such prior constraints. The latter strategy allows for the evaluation of flux estimates against the semi-empirical ocean fluxes and satellite-derived estimates of terrestrial fluxes.

Estimates of carbon fluxes were calculated for 11 terrestrial and 11 oceanic regions, corresponding to those used in the TRANSCOM III model intercomparison. The transport model used is Tracer Model Version 3 [TM3, *Heimann*, 1995] with nine vertical levels and a horizontal resolution of 8° latitude by 10° longitude. The model's transport is driven by European Centre for Medium-Range Weather Forecasting (ECMWF) re-analysis wind fields for the years from 1979 through 1993. Inversions for the years after 1993 are typically run using wind fields of all 15 years

to define a range of flux estimates. Flux estimates are calculated at monthly intervals so that seasonal cycles may be resolved.

The CO_2 observations used to constrain the inversions are a subset of the GLOBALVIEW-CO_2 data set, consisting of both actual and extended records at 114 network sites distributed globally. The majority of the stations used reflect the behavior of CO_2 in the marine boundary layer. The unresolved variability, or model-data mismatch, is assumed to be 0.5 ppm for oceanic sites and 2.0 ppm for continental sites. The larger error for continental sites is intended to reflect the greater difficulty of modeling continental boundary layer processes.

Carbon flux estimates calculated for the period from 1979 to 1999 show considerable interannual variability in both summertime uptake and spring/autumn respiration. The average uptake over North America for this period is about 0.8 Gt C yr^{-1}, and the net global uptake is partitioned unequally between the land and oceanic regions, with more uptake over land regions. The average uptake by oceans is estimated to be 1.0 Gt C yr^{-1} compared with a net uptake of 2.0 Gt C yr^{-1} found by *Takahashi et al.* [1999]. It is interesting to note that the estimated terrestrial uptake in boreal continental regions is smaller than that suggested by CASA and larger in temperate regions. Whether this bias exists in the CASA model or in the inverse calculations is currently under investigation. Because of the relative sparseness of the observational network in tropical continental and oceanic regions, flux estimates tend be extremely noisy in the tropics and average to zero. This is a reflection of the lack of constraints in these regions. There is a clear need for more observations in these regions.

Figure 2.26 shows estimated terrestrial carbon flux anomalies for 1981 through 1999. For each year, fluxes were estimated using all 15 years of ECMWF windfields. Although this approach was taken because wind fields are not available past 1993, use of multiple years of meteorology for the same flux estimates provides a means to estimate the importance of interannual variability in transport processes. This issue is of special importance, considering that it has been fairly common practice in inverse calculations to use only 1 year of meteorology cyclically. In order to calculate the anomalous carbon fluxes, an average seasonal cycle was subtracted from the time series of total land flux estimates. The upper and lower limits on 12-mo running means of the flux anomalies reflect annual average behavior of the anomalies. Although the running mean anomalies are sensitive to transport differences at a level of about 1 Gt C yr^{-1}, the monthly anomalies may range by as much as about 3 Gt C yr^{-1}. It is therefore highly desirable to use wind fields for the appropriate year when doing these sorts of calculations.

The smoothed flux anomalies in Figure 2.26 show extended periods of positive anomaly (net emission from the terrestrial biosphere) as well as periods of net uptake. Significant positive anomalies occur after the El Niño of 1982-1983 as well as after the 1987-1988 El Niño. The late 1980s are a period of extended net emission from the terrestrial biosphere, while the early 1990s are a period of uptake. A large positive anomaly occurs in 1998 both for the terrestrial biosphere and the oceans (not shown).
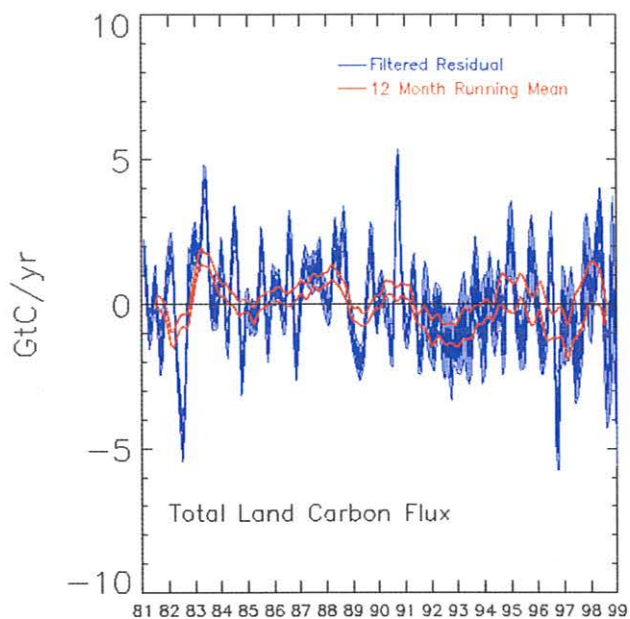

Fig. 2.26. Estimated terrestrial carbon flux anomalies for 1981 through 1999. For each year, fluxes were estimated using all 15 years of ECMWF wind fields. The shaded purple region shows upper and lower limits on the anomalous carbon flux for each month of the inversion calculated by subtraction of an average seasonal cycle. The red lines show upper and lower limits on 12-mo running means of the flux anomalies and reflect annual average behavior of the anomalies.

Comparison to global temperature and precipitation fields (not shown) suggests that the anomalies track trends in these variables.

Plans to improve the current generation of inversions include the use of the NCAR Model of Atmospheric Transport and Chemistry (MATCH), which may be run at higher resolution with more current wind fields from the National Centers for Environmental Prediction (NCEP) re-analysis data set; use of a modified Kalman filter to allow for error propagation; and use of additional observational constraints such as isotopic measurements. In the future, more measurements may become available, which will result in significant improvements in flux estimates.

2.9. REFERENCES

Andres, R.J., G. Marland, and S. Bischof, Global and latitudinal estimates of ^{13}C from fossil-fuel consumption and cement manufacture, *Publ. 4541*, Oak Ridge Natl. Lab., Environ. Sci. Div., Oak Ridge, TN (available at http://cdiac.esd.ornl.gov/ftp/db1013/db1013.txt), 1996.

Bakwin, P.S., P.P. Tans, D.F. Hurst, and C. Zhao, Measurements of carbon dioxide on very tall towers: Results of the NOAA/CMDL program, *Tellus, 50B*, 401-415, 1998a.

Bakwin, P.S., P.P. Tans, J.W.C. White, and R.J. Andres, Determination of the isotopic ($^{13}C/^{12}C$) discrimination by terrestrial biology from a global network of observatories, *Global Biogeochem. Cycles, 12*, 555-562, 1998b.

Bekki, S., K.S. Law, and J.A. Pyle, Effect of ozone depletion on CH_4 and CO concentrations, *Nature, 371*, 595-597, 1994.

Berger, B.W., K.J. Davis, P.S. Bakwin, C. Yi, and C. Zhao, Long-term carbon dioxide fluxes from a very tall tower in a northern forest: Flux measurement methodology, *J. Oceanic Atmos. Technol., 18*, 529-542, 2001.

Bousquet, P., P. Ciais, P. Monfray, Y. Balkanski, M. Ramonet, and P.P. Tans, Influence of two different atmospheric transport models on inferring sources and sinks of atmospheric CO_2, *Tellus, 48B*, 568-582, 1996.

Bousquet, P., P. Peylin, P. Ciais, C. Le Quere, P. Friedlingstein, and P.P. Tans, Regional changes in carbon dioxide fluxes of land and oceans since 1980, *Science, 290*, 1342-1346, 2000.

Bruhwiler, L., P. Tans, and M. Ramonet, A time-dependent assimilation and source retrieval technique for atmospheric tracers, in *Inverse Methods in Global Biogeochemical Cycles*, edited by P. Kasibheta et al., *Geophys. Monogr. 114*, pp. 265-277, Am. Geophys. Union, Washington, DC, 2000.

Ciais, P., P.P. Tans, J.W.C. White, M. Trolier, R.J. Francey, J.A. Berry, D.R. Randall, P.J. Sellers, J.G. Collatz, and D.S. Schimel, Partitioning of ocean and land uptake of CO_2 as inferred by $\delta^{13}C$ measurements from the NOAA Climate Monitoring and Diagnostics Laboratory Global Air Sampling Network, *J. Geophys. Res., 100*, 5051-5070, 1995a.

Ciais, P., P.P. Tans, M. Trolier, J.W.C. White, and R.J. Francey, A large northern hemisphere terrestrial CO_2 sink indicated by the $^{13}C/^{12}C$ ratio of atmospheric CO_2, *Science, 269*, 1098-1102, 1995b.

Dedikov, J.V., G.S. Akopova, N.G., Gladkaja, A.S. Piotrovskij, V.A. Markellov, S.S. Salichov, H. Kaesler, A. Ramm, A.M. von Blumencron, and J. Lelieveld, Estimating methane releases from natural gas production and transmission in Russia, *Atmos. Environ., 33*, 3291-3299, 1999.

Denning, A.S., I.Y. Fung, and D. Randall, Latitudinal gradient of atmospheric CO_2 due to seasonal exchange with land biota, *Nature, 376*, 240-243, 1995.

Denning, A.S., T. Takahashi, and P. Friedlingstein, Can a strong atmospheric CO_2 rectifier effect be reconciled with a "reasonable" carbon budget?, *Tellus, 51B*, 249-253, 1999.

Dlugokencky, E.J., L.P. Steele, P.M. Lang, and K.A. Masarie, The growth rate and distribution of atmospheric methane, *J. Geophys. Res., 99*, 17,021-17,043, 1994a.

Dlugokencky, E.J., K.A. Masarie, P.M. Lang, P.P. Tans, L.P. Steele, and E.G. Nisbet, A dramatic decrease in the growth rate of atmospheric methane in the northern hemisphere during 1992, *Geophys. Res. Lett., 21*, 45-48, 1994b.

Dlugokencky, E.J., L.P. Steele, P.M. Lang, and K.A. Masarie, Atmospheric methane at Mauna Loa and Barrow observatories: Presentation and analysis of in situ measurements, *J. Geophys. Res., 100*, 23,103-23,113, 1995.

Dlugokencky, E.J., E.G. Dutton, P.C. Novelli, P.P. Tans, K.A. Masarie, K.O. Lantz, and S. Madronich, Changes in CH_4 and CO growth rates after the eruption of Mt. Pinatubo and their link with changes in tropical tropospheric UV flux, *Geophys. Res. Lett., 23*, 2761-2764, 1996.

Dlugokencky, E.J., K.A. Masarie, P.M. Lang, and P.P. Tans, Continuing decline in the growth rate of atmospheric methane, *Nature, 393*, 447-450, 1998.

Dlugokencky, E.J., B.P. Walter, K.A. Masarie, P.M. Lang, and K.S. Kasischke, Measurements of an anomalous global methane increase during 1998, *Geophys. Res. Lett., 28*, 499-502, 2001.

Enting, I.G., and J.V. Mansbridge, Latitudinal distribution of sources and sinks of CO_2: Results of an inversion study, *Tellus, 43B*, 156-170, 1991.

Fan, S.-M., M. Gloor, J. Mahlman, S. Pacala, J. Sarmiento, T. Takahashi, and P. Tans, A large terrestrial carbon sink in North America implied by atmospheric and ocean CO_2 data and models, *Science, 282*, 442-446, 1998.

Fung, I., C.B. Field, J.A. Berry, M.V. Thompson, J.T. Randerson, C.M. Malmström, P.M. Vitousek, G.J. Collatz, P.J. Sellers, D.A.

Randall, A.S. Denning, F. Badeck, and J. John, Carbon 13 exchanges between the atmosphere and the biosphere, *Global Biogeochem. Cycles, 11*, 507-533, 1997.

Gemery, P.A., M. Trolier, and J.W.C. White, Oxygen isotope exchange between carbon dioxide and water following atmospheric sampling using glass flasks, *J. Geophys. Res., 101*, 14,415-14,420, 1996.

GLOBALVIEW-CH_4: Cooperative Atmospheric Data Integration Project—Methane [CD-ROM], NOAA Clim. Monit. and Diagnostics Lab., Boulder, CO (also available on Internet via anonymous FTP to ftp.cmdl.noaa.gov, Path: ccg/ch4/ GLOBALVIEW), 2001.

GLOBALVIEW-CO_2: Cooperative Atmospheric Data Integration Project—Carbon Dioxide [CD-ROM], NOAA Clim. Monit. and Diag. Lab., Boulder, CO (also available on Internet via anonymous FTP to ftp.cmdl.noaa.gov, Path: ccg/co2/ GLOBALVIEW), 2001.

Heimann, M., The global atmospheric tracer model TM2, edited by D. Klimarechenzentrum, *Tech. Rep. No. 10*, 53 pp., Max Planck Institut fur Meteorologie, Germany, 1995.

Karlsdóttir, S., and I.S.A. Isaksen, Changing methane lifetime: Possible cause for reduced growth, *Geophys. Res. Lett., 27*, 93-96, 2000.

Kitzis, D., and C. Zhao, CMDL/Carbon Cycle Gases Group standards preparation and stability, *NOAA TM ERL CMDL-14*, 14 pp., NOAA Environ. Res. Labs., Boulder, CO, 1999.

Krol, M., P.J. van Leeuwen, and J. Lelieveld, Global OH trend inferred from methylchloroform measurements, *J. Geophys. Res., 103*, 10,697-10,711, 1998.

Law, R.M., and I. Simmonds, The sensitivity of deduced CO_2 sources and sinks to variations in transport and imposed surface concentrations, *Tellus, 48B*, 613-625, 1996.

Lloyd, J., and G.D. Farquhar, ^{13}C discrimination during CO_2 assimilation by the terrestrial biosphere, *Oecologia, 99*, 201-215, 1994.

Masarie, K.A., L.P. Steele, and P.M. Lang, A rule-based expert system for evaluating the quality of long-term, in situ gas chromatographic measurements of atmospheric methane, *NOAA Tech. Memo. ERL CMDL-3*, 37 pp., NOAA Environ. Res. Labs., Boulder, CO, 1991.

Masarie, K.A., R.L. Langenfelds, C.E. Allison, T.J. Conway, E.J. Dlugokencky, R.J. Francey, P.C. Novelli, L.P. Steele, P.P. Tans, B. Vaughn, and J.W.C. White, The NOAA/CSIRO Flask-Air Intercomparison Program: A strategy for directly assessing consistency among atmospheric measurements derived from independent laboratories, *J. Geophys. Res., 106*, 20,445-20,464, 2001.

Miller, J.B., D. Yakir, J.W.C. White, and P.P. Tans, Measurement of $^{18}O/^{16}O$ in the soil-atmosphere CO_2 flux, *Global Biogeochem. Cycles, 13*, 761-774, 1999.

Miller, J.B., K.A. Mack, R.W. Dissly, J.W. White, and P.P. Tans, Development of analytical methods and measurements of $^{13}C/^{12}C$ in atmospheric CH_4 from the NOAA CMDL global air sampling network, *J. Geophys. Res.*, in press, 2002.

Montzka, S.A., C.M. Spivakovsky, J.H. Butler, J.W. Elkins, L.T. Lock, and D.J. Mondeel, New observational constraints for atmospheric hydroxyl on global and hemispheric scales, *Science, 288*, 500-503, 2000.

Novelli, P.C., J.W. Elkins, and L.P. Steele, The development and evaluation of a gravimetric reference scale for measurements of atmospheric carbon monoxide, *J. Geophys. Res., 96*, 20,731-20,750, 1991.

Novelli, P.C., J.E. Collins, R.C. Myers, G.W. Sachse, and H.E. Scheel, Reevaluation of the NOAA/CMDL carbon monoxide reference scale and comparisons with reference scales at NASA-Langley and at the Fraunhofer Institute, *J. Geophys. Res., 99*, 12,833-12,839, 1994.

Novelli, P.C., K.A. Masarie, and P.M. Lang, Distributions and recent changes of carbon monoxide in the lower troposphere, *J. Geophys. Res., 103*, 19,015-19,033, 1998a.

Novelli, P.C., V.S. Connors, H.G. Reichle, Jr., B.E. Anderson, C.A.M. Brenninkmeijer, E.G. Brunke, B.G. Doddridge, V.W.J.H. Kirchhoff, K.S. Lam, K.A. Masarie, T. Matsuo, D.D. Parrish, H.E. Scheel, and L.P. Steele, An internally consistent set of globally distributed atmospheric mixing ratios developed using results from an intercomparison of measurements, *J. Geophys. Res., 103*, 19,285-19,293, 1998b.

Peterson, J., P. Tans, and D. Kitzis, CO_2 round-robin reference gas intercomparison, in *Report of the Ninth WMO Meeting of Experts on Carbon Dioxide Concentration and Related Tracer Measurement Techniques*, Aspendale, Victoria, Australia, Sept. 1-4, 1997, edited by R. Francey, pp. 30-33, World Meteorol. Org., Geneva, 1999.

Peylin, P., P. Ciais, A.S. Denning, P.P. Tans, J.A. Berry, and J.W.C. White, A 3-dimensional study of $\delta^{18}O$ in atmospheric CO_2: Contribution of different land ecosystems, *Tellus, 51B*, 642-667, 1999.

Prinn, R.G., J. Huang, R.F. Weiss, D.M. Cunnold, P.J. Fraser, P.G. Simmonds, A. McCulloch, C. Harth, P. Salameh, S. O'Doherty, R.H.J. Wang, L. Porter, and B.R. Miller, Evidence for substantial variations of atmospheric hydroxyl radicals in the past two decades, *Science, 292*, 1882-1888, 2001.

Randerson, J.T., M.V. Thompson, T.J. Conway, I.Y. Fung, and C.B. Field, The contribution of terrestrial sources and sinks to trends in the seasonal cycle of atmospheric carbon dioxide, *Global Biogeochem. Cycles, 11*, 535-560, 1997.

Reshetnikov, A.I., N.N. Paramonova, and A.A. Shashkov, An evaluation of historical methane emissions from the Soviet gas industry, *J. Geophys. Res., 105*, 3517-3529, 2000.

Schnell, R.C., D.B. King, and R.M. Rosson (Eds.), *Climate Monitoring and Diagnostics Laboratory Summary Report No. 25 1998-1999*, 154 pp., NOAA Oceanic and Atmos. Res., Boulder, CO, 2001.

Takahashi, T., R.H. Wanninkhof, R.A. Feely, R.F. Weiss, D.W. Chipman, N. Bates, J. Olafsson, C. Sabine, and S.C. Sutherland, Net sea-air CO_2 flux over the global oceans: An improved estimate based on the sea-air pCO_2 difference, in *Proc. of the 2nd Int. Symp. on CO_2 in the Oceans*, edited by N. Nojiri, pp. 9-15, Center for Global Environ. Res., NIEST, Tsukuba, Japan, 1999.

Tans, P.P., T.J. Conway, and T. Nakazawa, Latitudinal distribution of the sources and sinks of atmospheric carbon dioxide derived from surface observations and an atmospheric transport model, *J. Geophys. Res., 94*, 5151-5172, 1989.

Tans, P.P., I.Y. Fung, and T. Takahashi, Observational constraints on the global atmospheric CO_2 budget, *Science, 247*, 1431-1438, 1990.

Tans, P.P., J.A. Berry, and R.F. Keeling, Oceanic $^{13}C/^{12}C$ observations: A new window on ocean CO_2 uptake, *Global Biogeochem. Cycles, 7*, 353-368, 1993.

Tans, P.P., P.S. Bakwin, L. Bruhwiler, T.J. Conway, E.J. Dlugokencky, D.W. Guenther, D.R. Kitzis, P.M. Lang, K.A. Masarie, J.B. Miller, P.C. Novelli, K.W. Thoning, M. Trudeau, B.H. Vaughn, J.W.C. White, and C. Zhao, Carbon cycle, in, *Climate Monitoring and Diagnostics Laboratory Summary Report No. 25 1998-1999*, edited by R.C. Schnell, D.B. King, and R.M. Rosson, pp. 24-46, NOAA Oceanic and Atmos. Res., Boulder, CO, 2001.

Thoning, K.W., P.P. Tans, and W.D. Komhyr, Atmospheric carbon dioxide at Mauna Loa Observatory, 2, Analysis of the NOAA GMCC data, 1974-1985, *J. Geophys. Res., 94*, 8549-8565, 1989.

Townsend, A.R., G.P. Asner, P.P. Tans, and J.W.C. White, Tropical land use effects on atmospheric ^{13}C imply a sizable terrestrial carbon sink in equatorial latitudes, *Geophys. Res. Lett.*, in press, 2002.

Walter, B.P., Development of a process-based model to derive methane emissions from natural wetlands for climate studies, Ph.D. dissertation, Examensarbeit 60, Max-Planck-Inst. für Meteorol., Hamburg, Germany, 1998.

Walter, B.P., and M. Heimann, A process-based, climate sensitive model to derive methane emissions from natural wetlands: Applications to five wetland sites, sensitivity to model parameters and climate, *Global Biogeochem. Cycles, 14*, 745-765, 2000.

WMO (World Meteorological Organization), Scientific requirements, in *Report of the WMO/UNEP/ICSU Meeting on Instruments, Standardization and Measurement Techniques for Atmospheric CO_2*, Geneva, Sept. 8-11, 14 pp., 1981.

Wotawa, G., P.C. Novelli, M. Trainer, and C. Granier, Interannual variability of summertime CO concentrations in the Northern Hemisphere explained by boreal forest fire in North America and Russia, *Geophys. Res. Lett.*, in press, 2002.

Yakir, D., J.A. Berry, C.B. Osmond, and L. Giles, Isotopic heterogeneity of water in transpiring leaves: Identification of the component that controls the $\delta^{18}O$ of atmospheric O_2 and CO_2, *Plant Cell Environ., 17*, 73-80, 1994.

Yi, C., K.J. Davis, B.W. Berger, and P.S. Bakwin, Long-term observations of the dynamics of the continental planetary boundary layer, *J. Atmos. Sci., 10*, 1288-1299, 2001.

Zhao, C., P. Tans, and K. Thoning, A high precision manometric system for absolute calibrations of CO_2 in dry air, *J. Geophys. Res., 102*, 5885-5894, 1997.

3. Aerosols and Radiation

3.1. AEROSOL MONITORING

E. ANDREWS (EDITOR), D. DELENE, D. JACKSON, A. JEFFERSON,
J. OGREN, P. SHERIDAN, AND J. WENDELL

3.1.1. SCIENTIFIC BACKGROUND

Aerosol particles affect the radiative balance of Earth both directly, by scattering and absorbing solar and terrestrial radiation, and indirectly, through their action as cloud condensation nuclei (CCN) with subsequent effects on the microphysical and optical properties of clouds. Evaluation of climate forcing by aerosols, defined here as the perturbation of the Earth's radiation budget induced by the presence of airborne particles, requires knowledge of the spatial distribution of the particles and their optical and cloud-nucleating properties, and suitable models of radiative transfer and cloud physics. Obtaining a predictive relationship between the aerosol forcing and the physical and chemical sources of the particles additionally requires knowledge of regional- and global-scale chemical processes, physical transformation, and transport models for calculation of the spatial distributions of the major chemical species that control the optical and cloud-nucleating properties of the particles. Developing and validating these various models requires a diverse suite of in situ and remote observations of the aerosol particles on a wide range of spatial and temporal scales.

Aerosol measurements began at the CMDL baseline observatories in the mid-1970s as part of the Geophysical Monitoring for Climatic Change (GMCC) program. The objective of these baseline measurements was to detect a response, or lack of response, of atmospheric aerosols to changing conditions on a global scale. Since the inception of the program, scientific understanding of the behavior of atmospheric aerosols has improved considerably. One lesson learned is that residence times of tropospheric aerosols are generally less than 1 week, and that human activities primarily influence aerosols on regional/ continental scales rather than global scales. In response to this increased understanding, and to more recent findings that anthropogenic aerosols create a significant perturbation in the Earth's radiative balance on regional scales [*Charlson et al.,* 1992; *NRC,* 1996], CMDL expanded its aerosol research program to include regional aerosol monitoring stations. The goals of this regional-scale monitoring program are to (1) characterize means, variabilities, and trends of climate-forcing properties of different types of aerosols, and (2) understand the factors that control these properties.

No single approach to observing the atmospheric aerosol can provide the necessary data for monitoring all the relevant dimensions and spatial/temporal scales required to evaluate climate forcing by anthropogenic aerosols. In situ observations from fixed surface sites, ships, balloons, and aircraft can provide very detailed characterizations of the atmospheric aerosol, but on limited spatial scales. Remote sensing methods from satellites, aircraft, or the surface can determine a limited set of aerosol properties from local to global spatial scales, but they cannot provide the chemical information needed for linkage with global chemical models. Fixed ground stations are suitable for continuous observations over extended time periods, but lack vertical resolution. Aircraft and balloons can provide the vertical dimension, but not continuously. Only when systematically combined can these various types of observations produce a data set where point measurements can be extrapolated with models to large geographical scales, where satellite measurements can be compared with the results of large-scale models, and where process studies have a context for drawing general conclusions from experiments conducted under specific conditions.

Measurements of atmospheric aerosols are used in three fundamentally different ways for aerosol/climate research: algorithm development for models and remote-sensing retrievals, parameter characterization, and model validation. Laboratory and field process studies guide the development of parameterization schemes and the choice of parameter values for chemical transport models that describe the relationship between emissions and concentration fields of aerosol species. Systematic surveys and monitoring programs provide characteristic values of aerosol properties that are used in radiative transfer models to calculate the radiative effects of the aerosols, and to retrieve aerosol properties from satellites and other remote sensing platforms. And finally, monitoring programs provide spatial and temporal distributions of aerosol properties that are compared with model results to validate the models. Each of these three modes of interaction between applications and measurements requires different types of data and entails different measurement strategies. *Ogren* [1995] applied the thermodynamic concept of "intensive" and "extensive" properties of a system to emphasize the relationship between measurement approach and applications of aerosol observations.

Intensive properties do not depend on the amount of aerosol present and are used as parameters in chemical transport and radiative transfer models (e.g., atmospheric residence time and single-scattering albedo). Extensive properties vary strongly in response to mixing and removal processes and are most commonly used for model validation (e.g., mass concentration and optical depth). Intensive properties are more difficult and expensive to measure than extensive properties because they generally are defined as the ratio of two extensive properties. As a result, different measurement strategies are needed to meet the data needs of the various applications. Measurements of a few carefully chosen extensive properties, of which aerosol optical depth and species mass concentrations are prime candidates, are needed in many locations to test the ability of the models to predict spatial and temporal variations on regional to global scales and to detect changes in aerosol concentrations resulting from changes in aerosol sources. The higher cost of determining intensive properties suggests a strategy of using a limited number of highly instrumented sites to characterize means and variabilities of intensive properties for different regions or aerosol types, supplemented with surveys by aircraft and ships to characterize the spatial

variability of these parameters. CMDL's regional aerosol monitoring program is primarily focused on the characterization of intensive properties.

CMDL's measurements provide ground truth for satellite observations and global models, as well as key aerosol parameters for global-scale models (e.g., scattering efficiency of sulfate particles and hemispheric back-scattering fraction). An important aspect of this strategy is that the chemical measurements are linked to the physical measurements through simultaneous, size-selective sampling that allows the observed aerosol properties to be connected to the atmospheric cycles of specific chemical species [e.g., *Quinn et al.*, 2002].

3.1.2. EXPERIMENTAL METHODS

Extensive aerosol properties monitored by CMDL include condensation nucleus (CN) concentration, aerosol optical depth (δ), and components of the aerosol extinction coefficient at one or more wavelengths, i.e., total scattering (σ_{sp}), backward hemispheric scattering (σ_{bsp}), and absorption (σ_{ap}). At the regional sites, size-resolved impactor and filter samples (submicrometer and supermicrometer size fractions) are obtained for gravimetric and chemical (ion chromatograph) analyses. All size-selective sampling, as well as the measurements of the components of the aerosol extinction coefficient at the regional stations, is performed at a low, controlled relative humidity (<40%) to eliminate confounding effects due to changes in ambient relative humidity. Data from the continuous sensors are screened to eliminate contamination from local pollution sources. At the regional stations, the screening algorithms use measured wind speed, direction, and total particle number concentration in real time to prevent contamination of the chemical samples. At the baseline stations, algorithms use measured wind speed and direction to exclude data that are likely to have been locally contaminated.

Prior to 1995, data from the baseline stations were manually edited to remove spikes from local contamination. Since 1995, an automatic editing algorithm has been applied to the baseline data in addition to manual editing of local contamination spikes. For the baseline stations, Barrow, Alaska (BRW), Mauna Loa, Hawaii (MLO), American Samoa (SMO), and South Pole, Antarctica (SPO), as well as for Sable Island (WSA), data are automatically removed when the wind direction is from local sources of pollution (such as generators and buildings) as well as when the wind speed is less than a threshold value (0.5-1 m s^{-1}). In addition, at MLO data for upslope conditions (1800-1000 UTC) are excluded because the airmasses do not represent "background" free tropospheric air for this case. A summary of the data-editing criteria for each station is presented in Table 3.1.

Integrating nephelometers are used to determine the light scattering coefficient of the aerosol. These instruments illuminate a fixed sample volume from the side and observe the amount of light that is scattered by particles and gas molecules in the direction of a photomultiplier tube. The instrument integrates over scattering angles of 7°-170°. Depending on the station, measurements are performed

TABLE 3.1. Data-Editing Summary for NOAA Baseline and Regional Stations

Station	Editing	Clean Sector
South Pole	a, b, c	0° < WD < 110°, 330° < WD < 360°
Samoa	a, b, c	0° < WD < 165°, 285° < WD < 360°
Mauna Loa	a, b, c, d	90° < WD < 270°
Barrow	a, b, c	0° < WD < 130°
Sable Island	a, b, c	0° < WD < 35°, 85° < WD < 360°
Southern Great Plains	a	
Bondville	a	

a: Manual removal of local contamination spikes.
b: Automatic removal of data not in clean sector.
c: Automatic removal of data for low wind speeds.
d: Removal of data for upslope wind conditions.
WD: Wind direction.

at three or four wavelengths in the visible and near-infrared. Newer instruments allow determination of the hemispheric backscattering coefficient by use of a shutter to prevent illumination of the portion of the instrument that yields scattering angles less than 90°. A particle filter is inserted periodically into the sample stream to measure the light scattered by gas molecules, which is subtracted from the total scattered signal to determine the contribution from the particles alone. To calibrate the instruments the sample volume is filled with CO_2 gas, which has a known scattering coefficient.

The aerosol light absorption coefficient is determined with a continuous light absorption photometer. This instrument continuously measures the amount of light transmitted through a quartz filter while particles are deposited on the filter. The rate of decrease of trans-missivity, divided by the sample flow rate, is directly proportional to the light absorption coefficient of the particles. Newer instruments (particle soot absorption photometers (PSAPs), Radiance Research, Seattle, Washington) are calibrated in terms of the difference of light extinction and scattering in a long-path extinction cell, for laboratory test aerosols. Older instruments at the baseline stations (aethalometers, Magee Scientific, Berkeley, California) were calibrated by the manufacturer in terms of the equivalent amount of black carbon (BC) from which the light absorption coefficient is calculated, assuming a mass absorption efficiency of the calibration aerosols of 10 m^2 g^{-1}.

Particle number concentration is determined with a CN counter that exposes the particles to a high supersaturation of butanol vapor. This causes the particles to grow to a size where they can be optically detected and counted. The instruments in use have lower particle-size detection limits of 10-20 nm diameter.

Summaries of the extensive measurements obtained at each site are given in Tables 3.2 and 3.3. Table 3.4 lists the intensive aerosol properties that can be determined from the directly measured extensive properties. These properties are used in chemical transport models to determine the radiative effects of the aerosol concentrations calculated by the models. Inversely, these properties are used in

TABLE 3.2. CMDL Baseline Aerosol Monitoring Stations (Status as of December 2001)

Category	Baseline Arctic	Baseline Free Troposphere	Baseline Marine	Baseline Antarctic
Location	Point Barrow	Mauna Loa	American Samoa	South Pole
Designator	BRW	MLO	SMO	SPO
Latitude	71.323°N	19.539°N	14.232°S	89.997°S
Longitude	156.609°W	155.578°W	170.563°W	102.0°E
Elevation (m)	8	3397	77	2838
Responsible institute	CMDL	CMDL	CMDL	CMDL
Status	Operational, 1976; major upgrade, 1997	Operational, 1974; major upgrade, 2000	Operational, 1977	Operational, 1974
Sample RH	RH < 40%	RH < 40%	Uncontrolled	Uncontrolled
Sample size fractions	D < 1 μm, D < 10 μm	D < 1 μm, D < 10 μm	Uncontrolled	Uncontrolled
Optical measurements	$\sigma_{sp}(3\lambda)$, $\sigma_{bsp}(3\lambda)$, $\sigma_{ap}(1\lambda)$	$\sigma_{sp}(3\lambda)$, $\sigma_{bsp}(3\lambda)$, $\sigma_{ap}(1\lambda)$, $\delta(6\lambda)$	None	$\sigma_{sp}(4\lambda)$
Microphysical measurements	CN concentration	CN concentration	CN concentration	CN concentration
Chemical measurements	Major ions, mass	None	None	None

TABLE 3.3. CMDL Regional Aerosol Monitoring Sites (Status as of December 2001)

Category	Perturbed Marine	Perturbed Continental	Perturbed Continental
Location	Sable Island, Nova Scotia, Canada	Bondville, Illinois	Lamont, Oklahoma
Designator	WSA	BND	SGP
Latitude	43.933°N	40.053°N	36.605°N
Longitude	60.007°W	88.372°W	97.489°W
Elevation (m)	5	230	315
Responsible institute	CMDL	CMDL	CMDL
Collaborating institute(s)	AES Canada, NOAA/PMEL	University of Illinois, Illinois State Water Survey	DOE/ARM
Status	Operational, August 1992; inactive, April 2000	Operational, July 1994	Operational, July 1996; chemistry added, February 2000
Sample RH	RH < 40%	RH < 40%	RH < 40%
Sample size fractions	D < 1 μm, D < 10 μm	D < 1 μm, D < 10 μm	D < 1 μm, D < 10 μm
Optical measurements	$\sigma_{sp}(3\lambda)$, $\sigma_{bsp}(3\lambda)$, $\sigma_{ap}(1\lambda)$	$\sigma_{sp}(3\lambda)$, $\sigma_{bsp}(3\lambda)$, $\sigma_{ap}(1\lambda)$	$\sigma_{sp}(3\lambda)$, $\sigma_{bsp}(3\lambda)$, $\sigma_{ap}(1\lambda)$, $\delta(7\lambda)$
Microphysical measurements	CN concentration	CN concentration	CN, $n(D)$ concentration
Chemical measurements	Major ions, mass	Major ions, mass	Major ions, mass

AES, Atmospheric Environment Service; PMEL, Pacific Marine Environment Laboratory; DOE/ARM, Department of Energy/Atmospheric Radiation Measurement.

TABLE 3.4. Intensive Aerosol Properties Derived from the CMDL Network

Properties	Description
$\mathring{a}$	The Ångström exponent, defined by the power-law $\sigma_{sp} \propto \lambda^{-\mathring{a}}$, describes the wavelength-dependence of scattered light. In the figures, $\mathring{a}$ is calculated from measurements at 550- and 700-nm wavelengths. Situations where the scattering is dominated by submicrometer particles typically have values around 2, whereas when the scattering is dominated by particles larger than a few micrometers in diameter, values are close to 0.
ω_0	The aerosol single-scattering albedo, defined as $\sigma_{sp}/(\sigma_{ap} + \sigma_{sp})$, describes the relative contributions of scattering and absorption to the total light extinction. Purely scattering aerosols (e.g., sulfuric acid) have values of 1, whereas very strong absorbers (e.g., elemental carbon) have values around 0.3.
g, b	Radiative transfer models commonly require one of two integral properties of the angular distribution of scattered light (phase function): the asymmetry factor g or the hemispheric backscatter fraction b. The asymmetry factor is the cosine-weighted average of the phase function, ranging from a value of -1 for entirely backscattered light to $+1$ for entirely forward-scattered light. The hemispheric backscatter fraction b is defined as σ_{bsp}/σ_{sp}.
$f(RH)$	The hygroscopic growth factor, defined as $\sigma_{sp}(RH = 85)/\sigma_{sp}(RH = 40)$, describes the humidity dependence of scattering on relative humidity (RH).
α_i	The mass scattering efficiency for species i, defined as the slope of the linear regression line relating σ_{sp} and the mass concentration of the chemical species. It is used in chemical transport models to evaluate the radiative effects of each chemical species predicted by the model. This parameter has typical units of $m^2\ g^{-1}$.

algorithms to interpret satellite remote-sensing data to determine aerosol amounts based on measurements of the radiative effects of the aerosol.

3.1.3. ANNUAL CYCLES

The annual cycles of aerosol optical properties for the four baseline and three regional stations are illustrated in Figures 3.1 and 3.2, respectively. The data are presented in the form of box and whisker plots that summarize the distribution of values. Each box ranges from the lower to upper quartiles with a central bar at the median value, while the whiskers extend to the 5th and 95th percentiles. The statistics are based on hourly averages of each parameter for each month of the year; also shown are the annual statistics for the entire period of record. The horizontal line across each plot represents the annual median, so measurements above and below the median can easily be discerned. The annual cycles for the baseline stations are based on data through the end of 2001, except at SMO, where scattering measurements were made only from 1977 to 1991 and CN from 1977 to 1997. In general, changes in long-range transport patterns dominate the annual cycles of the baseline stations.

Figure 3.1 shows that, for BRW, the high values of CN, σ_{sp}, and σ_{ap} are observed during the Arctic haze period when anti-cyclonic activity transports pollution from the lower latitudes of Central Europe and Russia. A more stable polar front characterizes the summertime meteorology. High cloud coverage and precipitation scavenging of accumulation-mode (0.1- to 1.0-μm diameter) aerosols account for the annual minima in σ_{sp} and σ_{ap} from June to September. In contrast, CN values have a secondary maximum in the summer, which is thought to be the result of sulfate aerosol production from gas-to-particle conversion of dimethyl sulfide (DMS) oxidation products from local oceanic emissions [*Radke et al.*, 1990]. The aerosol single-scattering albedo displays little annual variability and is indicative of highly scattering sulfate and seasalt aerosol. A September minimum is observed in Ångström exponent ($\mathring{a}$) when σ_{sp} and accumulation-mode aerosols are also low but when primary production of coarse-mode seasalt aerosols from open water is high [*Quinn et al.*, 2002; *Delene and Ogren*, 2002]. *Quinn et al.* [2002] have also shown, based on their chemical analysis of the submicrometer aerosol particles at BRW, that seasalt has a dominant role in controlling scattering in the winter; non-seasalt sulfate is the dominant scatterer in the spring; and both components contribute to scattering in the summer.

For MLO, the highest σ_{sp} and σ_{ap} values occur in the springtime and result from the long-range transport of pollution and mineral dust from Asia. However, little seasonality is seen in CN concentrations at MLO, indicating that the smallest particles (<0.1-μm diameter), which usually dominate CN concentration, are not enriched during these long-range transport events. At SPO, both the aerosol σ_{sp} and $\mathring{a}$ display seasonal cycles, with a σ_{sp} maximum and an $\mathring{a}$ minimum in austral winter associated with the transport of coarse-mode seasalt from the Antarctic coast to the interior of the continent. The summertime

peaks in CN and $\mathring{a}$ are associated with fine-mode sulfate aerosol and correlate with a seasonal sulfate peak found in the ice core, presumably from coastal biogenic sources [*Bergin et al.*, 1998]. At SMO, aerosol extensive properties display no distinct seasonal variation. At BRW and MLO, albedo values above 1.0 are due to instrument noise at low aerosol concentration. These high albedo values are not present in daily averaged data. Furthermore, these high albedo values are not present if data are excluded where σ_{sp} is below 1 Mm^{-1}. Hence, the high albedo values result from an instrument detection limitation problem.

Based on only 4-7 years of measurements, the annual cycles for the regional stations (Figure 3.2) are less certain than those of the baseline stations. The proximity of the regional sites to North American pollution sources is apparent in the results, with monthly median values of σ_{sp} that are up to 2 orders of magnitude higher than values from the baseline stations. The Bondville, Illinois, site (BND), situated in a rural agricultural region, displays an autumn high in σ_{ap} and a low in ω_0 that coincide with anthropogenic and dust aerosols emitted during the harvest [*Delene and Ogren*, 2002]. As evident in the lower σ_{sp} and σ_{ap} values, the Southern Great Plains site (SGP), Lamont, Oklahoma, is more remote than BND. SGP has a similar but less pronounced annual cycle with late-summer highs in σ_{sp} and σ_{ap}, and a corresponding minimum in ω_0 [*Delene and Ogren*, 2002; *Sheridan et al.*, 2001]. Little seasonal variability is observed in aerosol properties at Sable Island, Nova Scotia (WSA). Values of $\mathring{a}$ tend to be higher in the summer and very likely result from transport of fine-mode sulfate aerosol from the continent and lower coarse-mode production of particles with lower summer wind speeds [*Delene and Ogren*, 2002].

3.1.4. LONG-TERM TRENDS

Figure 3.3 shows long-term trends in CN concentration and σ_{sp} for the baseline observatories, and Figure 3.4 shows long-term trends in $\mathring{a}$ for the baseline observatories and σ_{ap} and ω_0 for BRW and MLO. The monthly means are plotted along with a linear trend line fitted to the data. At BRW, the aerosol properties exhibit an annual decrease in σ_{sp} of about 2% yr^{-1} since 1980. This reduction in aerosol scattering has been attributed to decreased anthropogenic emissions from Europe and Russia [*Bodhaine*, 1989] and is most apparent during March when the Arctic haze effect is largest. The corresponding decrease in the Ångström exponent over the same time period points to a shift in the aerosol size distribution to a larger fraction of coarse-mode seasalt aerosol. *Stone* [1997] noted a long-term increase in both surface temperatures and cloud coverage at BRW for 1965-1995 that derives from changing circulation patterns and may account for the reduction in σ_{sp} by enhanced scavenging of accumulation-mode aerosols.

In contrast to the reduction in σ_{sp} at BRW, CN concentrations, which are most sensitive to particles with diameters <0.1 μm, have increased since 1976. There is an offset in CN concentration starting in 1998 that corresponds
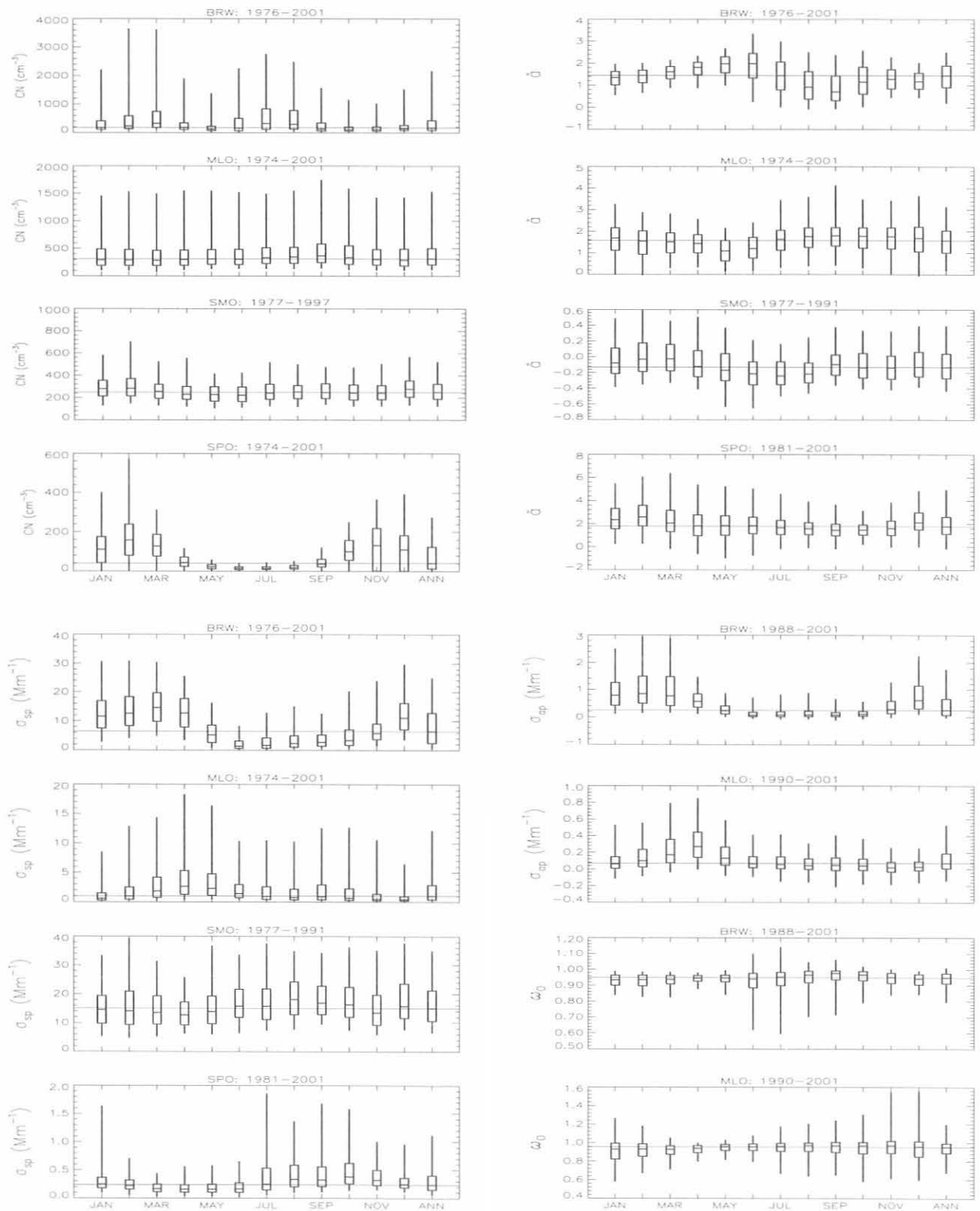
Fig. 3.1. Box and whisker plots of annual cycles showing statistics for condensation nuclei (CN) concentration, Ångström exponent (å), and total scattering coefficient (σ_{sp}) at baseline stations BRW, MLO, SMO, and SPO; and for absorption coefficient (σ_{ap}) and single scattering albedo (ω_o) at BRW and MLO. Statistics representing the entire period are given in the last column (ANN). Each box ranges from the 25th to 75th quartiles, and the horizontal line represents the median value. The whiskers extend to the 5th and 95th quartiles.

55
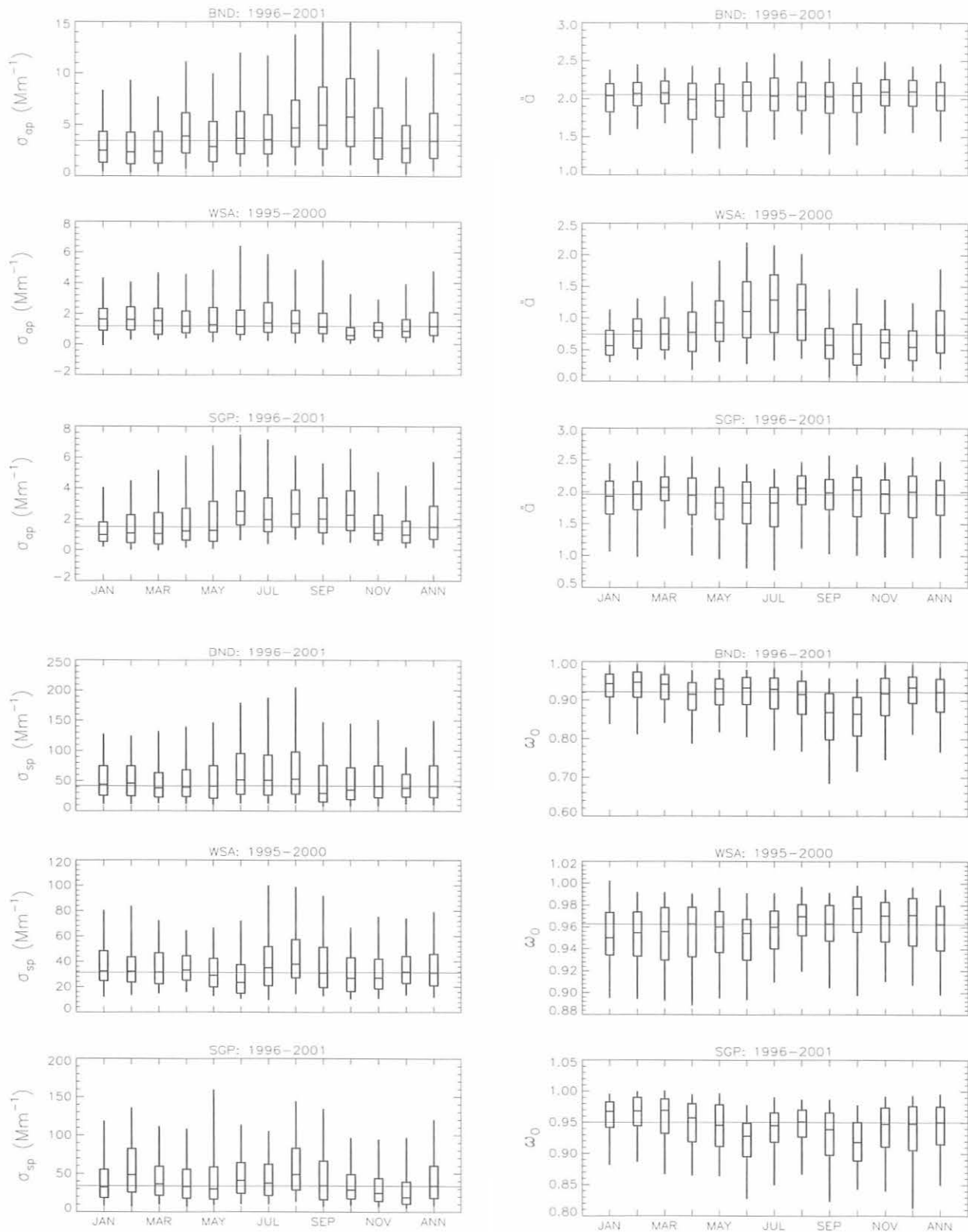
Fig. 3.2. Box and whisker plots of annual cycles for regional stations at BND, WSA, and SGP showing statistics for absorption coefficient (σ_{ap}), Ångström exponent ($\mathring{a}$), total scattering coefficient (σ_{sp}), and single-scattering albedo (ω_0). Statistics representing the entire period are given in the last column (ANN). The boxes and whiskers are as in Figure 3.1.
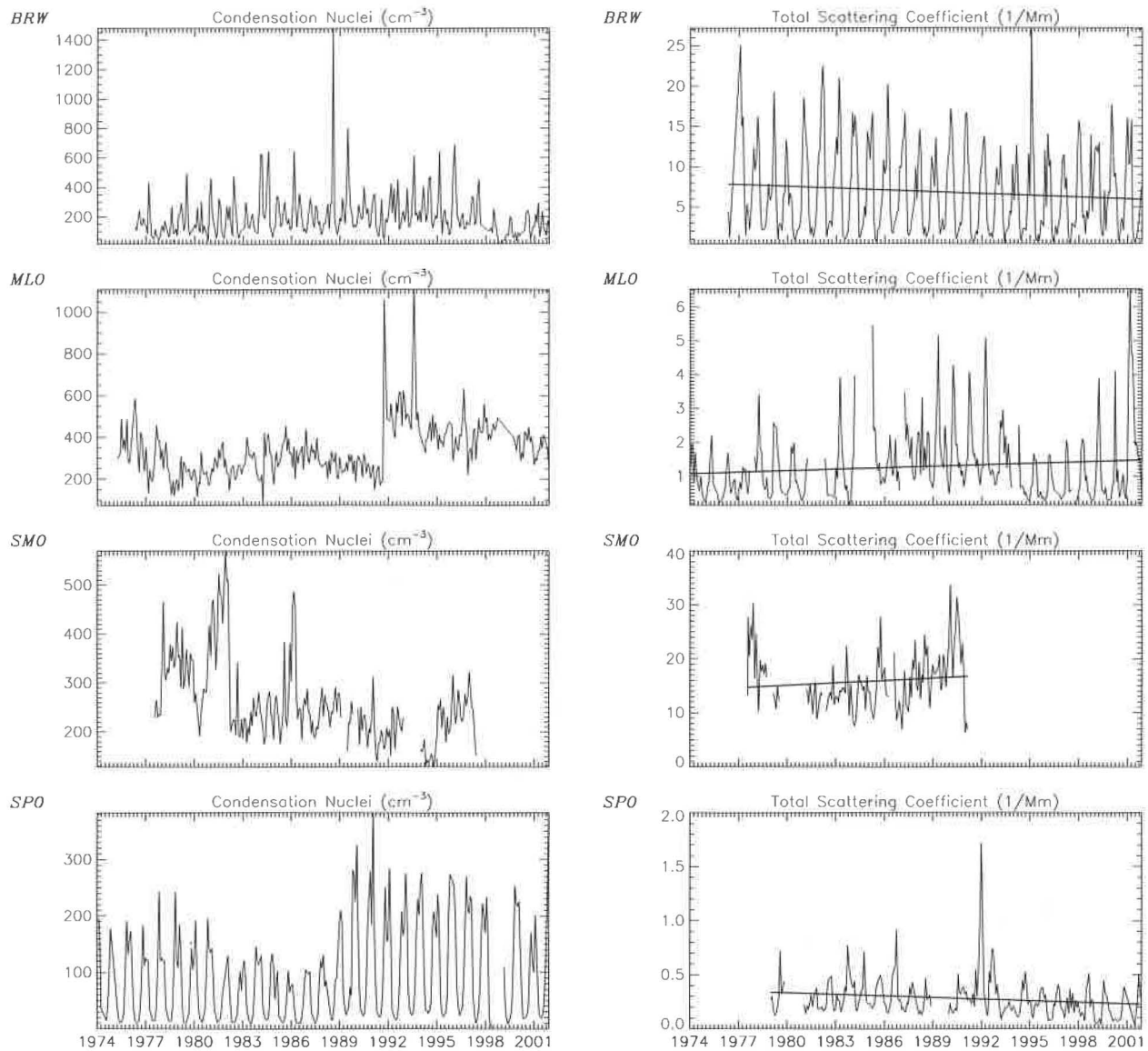
Fig. 3.3. Long-term trends for baseline stations of monthly averaged condensation nuclei concentration (left panels) and total scattering coefficient at 550 nm (right panels). A simple linear fit is given for the scattering coefficient but is omitted for the condensation nuclei because instrument changes make a trend line inappropriate.

to a change to a new CN sampling inlet. Similarly, the step increases in CN concentration in late 1991 at MLO and 1989 at SPO are due to replacement of the CN counter with a butanol-based instrument with a lower size detection limit. The reason for the decrease in CN and increase in *å* at SMO is not readily apparent, but it could stem from changes in long-term circulation patterns.

Previous reports describe the aerosol data sets: for BRW, *Bodhaine* [1989, 1995]; *Quakenbush and Bodhaine* [1986]; *Bodhaine and Dutton* [1993]; *Barrie* [1996]; *Delene and Ogren* [2002]; for MLO, *Bodhaine* [1995]; *Delene and Ogren* [2002]; for SGP, *Delene and Ogren* [2002]; *Sheridan*

et al. [2001]; *Bergin et al.* [2000]; for SMO, *Bodhaine and DeLuisi* [1985]; for SPO, *Bodhaine et al.* [1986, 1987, 1992]; *Bergin et al.* [1998]; and for WSA, *McInnes et al.* [1998]; *Delene and Ogren* [2002].

3.1.5. SPECIAL STUDIES

Comparison of Aerosol Light Scattering and Absorption Measurements at Mauna Loa, Hawaii

CMDL has measured both aerosol light scattering (since 1974) and aerosol light absorption (since 1990) at MLO. In spring 2000 new light scattering and absorption instruments
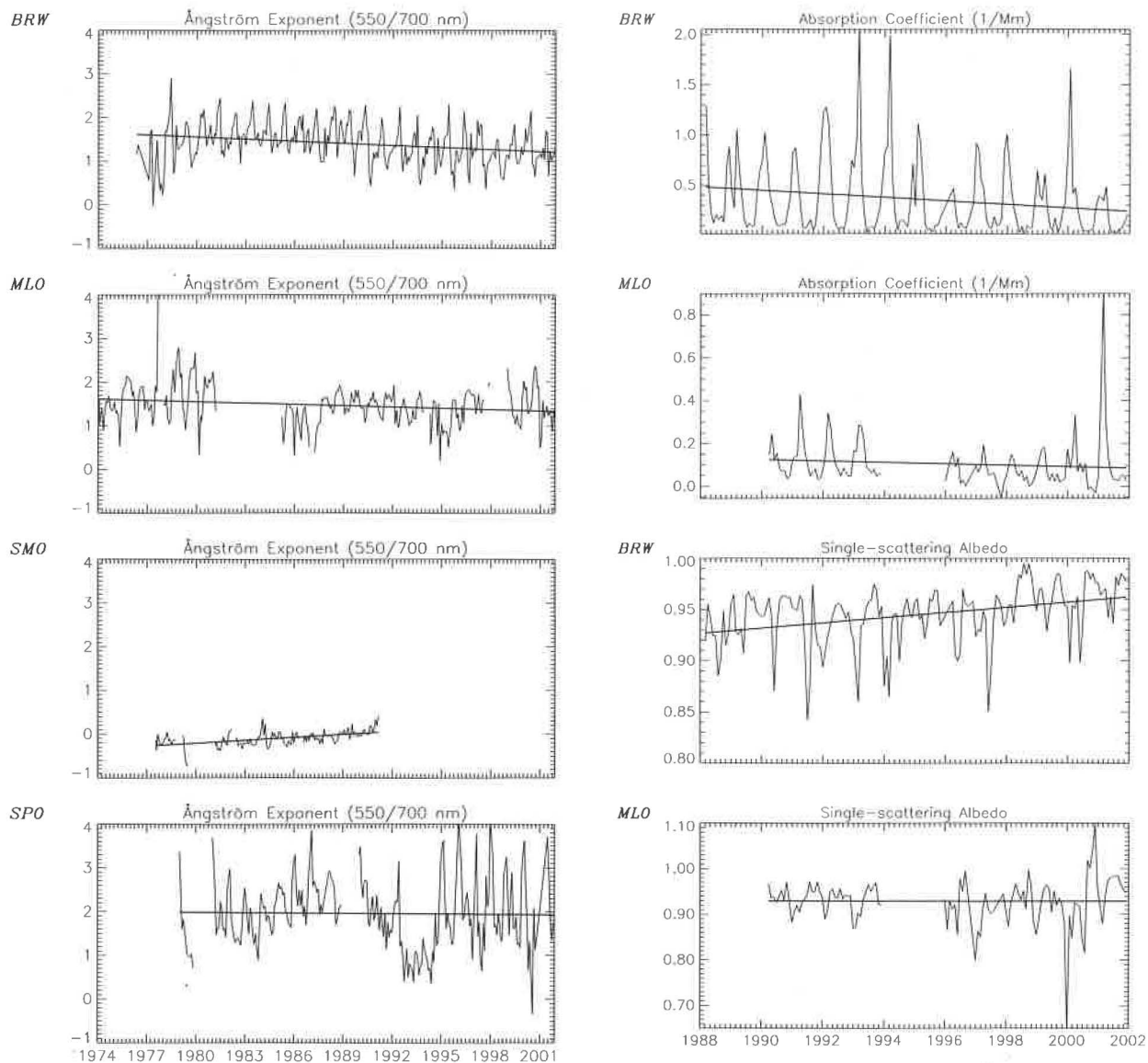
Fig. 3.4. Long-term trends for baseline stations of monthly averaged Ångström exponent (550/700 nm) (left panels); and absorption coefficient and single scattering albedo at BRW and MLO (right panels). Simple linear fits to the data are shown.

were installed at Mauna Loa (within 2 m of the old instruments). Prior to the upgrade, light scattering was measured with a three-wavelength nephelometer (MS Electron, Seattle, Washington), and light absorption was measured with an aethalometer (Magee Scientific, Berkeley, California). This original sampling system did not include size or relative humidity control of the aerosol sample. The new instruments are designated MLN (Mauna Loa New) to distinguish them from the collocated MLO instruments. The new system obtains measurements at two size cuts by using a valve to switch between a 10-μm and 1-μm impactor.

Relative humidity is maintained at no more than 40% by heating the air sample as necessary. Table 3.5 lists the instruments and their period of operation at Mauna Loa.

It is important to assess how measurements from these instruments compare in order to maintain data consistency for the entire measurement period. The MLO and MLN systems were operated simultaneously for approximately 1 year (spring 2000–spring 2001). One year of simultaneous light scattering and 3 months of light absorption (the aethalometer broke in August 2000) measurements from the collocated instruments are compared here.

TABLE 3.5. Instrument Inventory at Mauna Loa Observatory

Instrument	Period of Operation	Station	Comments
MRI nephelometer	1974-spring 2000	MLO	Four wavelengths, no size cut
MRI nephelometer (operating at one wavelength because of instrument problems)	Summer 1982-spring 1984	MLO	One wavelength (550 nm), no size cut
MS Electron nephelometer	Spring 1994-spring 2001	MLO	Three wavelengths, no size cut
Magee Scientific aethalometer	1990-present	MLO	Broadband, no size cut; specific absorption of 10 m^2 g^{-1} used to convert [BC] to σ_{ap}
TSI nephelometer (model number 3563)	Spring 2000-present	MLN	Three wavelengths, total and back scatter, 1- and 10-μm size cuts
Radiance Research particle soot absorption photometer (PSAP)	Spring 2000-present	MLN	565-nm wavelength, 1- and 10-μm size cuts

MRI, Meteorology Research Inc.

The comparison procedure was as follows:

- Select data for the overlap period, May 2000 through April 2001.
- Estimate the absorption coefficient for the aethalometer using $\sigma_{ap} = 10$ m^2 g^{-1} × [BC].
- Apply quality-control edit corrections to data sets (e.g., remove spikes and contaminated data).
- For the MLN data set, use only 10-μm size cut data.
- Correct the MLN PSAP data for (a) scattering by particles within the filter and (b) spot size. Also, remove low transmittance data (e.g., transmittance <0.5, per *Bond et al.* [1999]).
- Calculate hourly averages of scattering and absorption coefficients.
- Determine the least-squares linear fit and correlation coefficient for the data sets. Perform the regression for both a calculated and forced-to-zero y-intercept.

Figure 3.5 shows that, on an hourly basis, there is excellent correlation between the nephelometer measurements ($R^2 = 0.94$), and the instruments agree fairly well (the slope is 1.1). This agreement is also seen when the data are separated for upslope (polluted) and downslope (cleaner) conditions. Because the two instruments appear to be in good agreement, the old nephelometer was removed during annual maintenance in May 2001.

The comparison between the PSAP and the aethalometer (Figure 3.6) was over a much shorter time period: May 2000-early August 2000. In early August the aethalometer feed sprocket was replaced, and after the replacement, measurements from the two instruments became completely uncorrelated ($R^2 = 0.02$). Prior to the feed sprocket replacement, the absorption measurements show that the PSAP measured absorption coefficients ~3 times higher than the aethalometer although the instruments were fairly well correlated ($R^2 \approx 0.6$). The difference between the two instruments suggests that the assumed BC absorption efficiency of 10 m^2 g^{-1} may not be appropriate for Mauna Loa. Additional comparisons between the PSAP and aethalometer are planned to resolve this discrepancy.

Determination of the Light Absorption Efficiency of Graphitic Carbon in Indian Ocean Aerosols

Carbonaceous particles in the atmosphere are generally thought to contain up to two major classes of carbon:
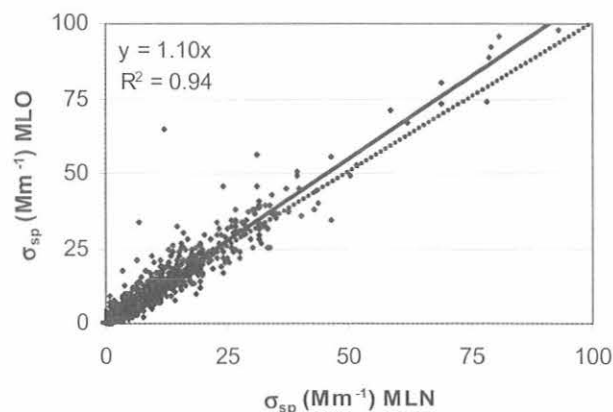

Fig. 3.5. Comparison of scattering measured by the new nephelometer (σ_{sp} MLN) with scattering measured by the old nephelometer (σ_{sp} MLO) for 550-nm wavelength, spring 2000-spring 2001. The solid black line shows the fit when the y-intercept is forced through the origin; the dashed line is the 1:1 line.
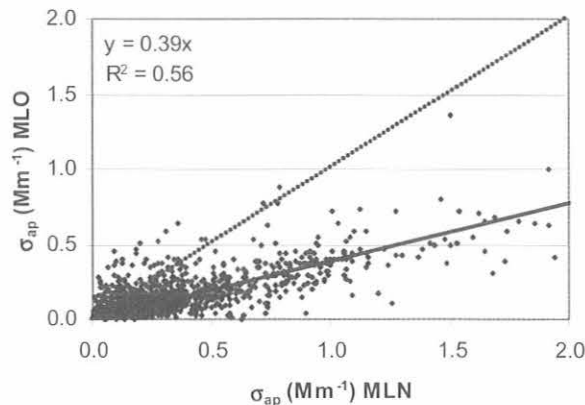

Fig. 3.6. Comparison of absorption measured by the PSAP (σ_{ap} MLN) with absorption measured by the aethalometer (σ_{ap} MLO), May 2000-August 2000. The solid black line shows the fit when the y-intercept is forced through the origin; the dashed line is the 1:1 line.

organic carbon (OC) and black carbon (BC, also called elemental carbon, EC). Visible light absorption by atmospheric aerosols is typically dominated by particles containing BC. The mass measurement of BC in atmospheric aerosol samples has most often been performed by thermal evolved gas analysis [e.g., *Cachier et al.*, 1989] or thermal optical reflectance (TOR) methods [e.g., *Chow et al.*, 1993]. The light absorption coefficient (σ_{ap}) of aerosol samples has been determined with optical (usually filter-based) instruments, such as the aethalometer [e.g., *Bodhaine*, 1995], the PSAP [e.g., *Bond et al.*, 1999], or photoacoustic techniques [e.g., *Arnott et al.*, 1999]. All of these measurement techniques depend directly on the amount of aerosol sampled for the analysis, and all have associated measurement uncertainties, artifacts, interferences, and other problems that must be taken into account.

A measure of the efficiency with which atmospheric aerosols absorb visible radiation is desirable for model inputs and other applications. The aerosol light absorption efficiency, α, is defined as

$$\alpha = \sigma_{ap}/m_c , \qquad (1)$$

where σ_{ap} is total absorption (in Mm^{-1}), and m_c is the mass concentration of absorbing carbon (in μg m^{-3}). The parameter α has also been called the specific attenuation cross section, the specific absorption coefficient, and the BC mass absorption coefficient in previous studies. Over the past two decades, reported values of α have ranged from ~1 to 25 m^2 g^{-1}. Most of the variability in α has been attributed to differences in aerosol composition, shape, size, mixing state (i.e., internal vs. external), and amount of scattering material present. The challenge for researchers is to determine what portion of the variability in α is caused by instrument uncertainty or differences in measurement methods and what portion is due to real differences in the studied aerosols.

A new method of determining the α of graphitic carbon (GC), a specific and dominant component of BC, is reported here. The PSAP instrument was used to obtain the σ_{ap} of aerosol samples collected during the Indian Ocean Experiment (INDOEX) in early 1999. The PSAP is a filter-based instrument in which aerosol particles are continuously deposited onto a filter. A transmittance measurement is made through the particle deposit and simultaneously compared with an identical measurement through a second, particle-free filter. Through careful calibration of the raw transmittance signals against derived absorption from an extinction cell/nephelometer system [*Bond et al.*, 1999], a measurement of suspended-state aerosol absorption is obtained.

For the analysis of GC mass, CMDL collaborated with colleagues at the Institute for Tropospheric Research (IFT) in Leipzig, Germany. The Raman instrument used in this study to quantify GC mass was a Bruker IFS 55 spectrometer equipped with a FRA-106 Raman module in a backscatter configuration. Calibration of the Raman spectrometer for GC mass on the PSAP filters was performed as documented in *Mertes et al.* [2002] using a commercially available carbon black standard (Monarch 71,

Cabot Corporation, Boston, Massachusetts). The atmospheric concentration of GC can then be calculated from the GC filter mass, using the volume of air sampled through the PSAP filters.

This investigation has two advantages over previous studies. First, the GC responsible for light absorption and not the thermographic EC is used. Thus, a quantifiable, dominant component of light absorbing carbon is obtained. Second, the correlation between σ_{ap} and m_c is analyzed from identical aerosol samples (i.e., the same particles), so any variability between samples does not come from examining different populations of particles in the two analyses.

The INDOEX Intensive Field Phase (IFP) was conducted during February and March 1999. The site for CMDL surface measurements was the Kaashidhoo Climate Observatory (KCO), on the island of Kaashidhoo in the Republic of Maldives. During this period of the winter monsoon, dry winds from the northeast sweep over the area. These winds bring very polluted air from India and Southeast Asia over the Maldives. The INDOEX aerosols have been found to contain significant fractions of BC [*Ramanathan et al.*, 2001]; probable sources of these aerosols include biomass and biofuel burning, vehicle exhaust, industrial releases, and other anthropogenic emissions.

Figure 3.7 shows a time series of σ_{ap} plotted alongside GC concentration. Overall, there was good agreement between the two parameters over the course of the IFP. The initial portion of the experiment (through DOY 70) was a period of higher aerosol concentrations at KCO punctuated by two rainfall events that removed aerosols from the atmosphere. From DOY 71 through nearly the end of the IFP, light absorption coefficients were relatively lower, but still several times larger than at typical rural, midcontinental sites in the United States [*Delene and Ogren*, 2002]. In Figure 3.7, each symbol represents the analysis of one PSAP filter. When high concentrations of aerosols were present, filters were changed up to five times per day to prevent the PSAP filter transmittance measurement from dropping below 0.5. During cleaner periods (e.g., the rainfall events), filters were changed as infrequently as once per day.
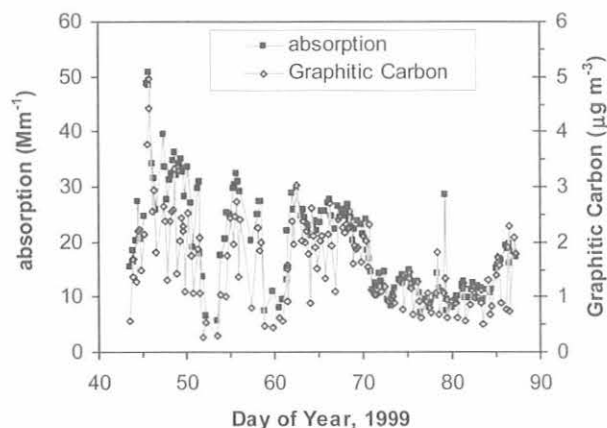

Fig. 3.7. Time series of absorption and graphitic carbon measured at KCO during February-March 1999.

Figure 3.8 shows σ_{ap} plotted against GC. In this analysis, the PSAP filters were grouped according to their filter loading, and one obvious outlier was removed from the "Medium Loading" category. The PSAP manufacturer's manual states that absorption measurements should be reliable as long as the filter transmittance (Tr, or I/I_0) remains above 0.5. The calibrations recommended by *Bond et al.* [1999], however, were performed using PSAPs with Tr values maintained above 0.7, so this grouping of lightly loaded filters is the only one in which the *Bond et al.* [1999] PSAP calibration corrections can be applied reliably. The slope of the linear least squares regression line through the lightly loaded filters equates to an α of 9.7 m^2 g^{-1}, with a very small offset and an R^2 value of 0.86. The filters with higher GC loadings show regression slopes between roughly 9.0 and 10.4, but with significant y-intercepts. These zero offsets may be due to uncertainties in the nonlinear filter loading corrections used in the PSAP instrument. While GC currently is thought to be the major aerosol absorber of visible radiation, other forms of carbonaceous material (e.g., amorphous C, organic C) need to be studied in a similar manner to quantify their contributions to visible light absorption by aerosols.

In Situ Aerosol Profile Measurements over the Southern Great Plains Cloud and Radiation Testbed (CART) Site

The objective of this project is to obtain a statistically significant data set of in situ measurements of the vertical distribution of aerosol properties (e.g., light scattering and absorption). The measurements will be used to answer the following scientific questions:

- How do aerosol properties vary throughout the year?
- Under what conditions can surface-based measurements of these properties be used to calculate the direct aerosol radiative forcing from a measured aerosol optical depth (and what conditions inhibit such calculations)?
- How do local and regional perturbations (e.g., fires) influence the vertical profile characteristics?
- How do data from these flights compare with other measurements of atmospheric characteristics, e.g., aerosol optical depth (AOD)?

The data are obtained on an instrumented light aircraft (Cessna C-172N) over the Southern Great Plains (SGP) CART site in Lamont, Oklahoma. The aerosol instrument package on the aircraft is similar to the one operating at the surface SGP site. The aircraft flew 225 profile flights between March 2000 and December 2001. For each profile flight, the Cessna flew nine level legs over (or near) the SGP site. The legs were flown at altitudes of 467, 610, 915, 1220, 1525, 1830, 2440, 3050, and 3660 m above sea level, and flights were made several times each week. Aerosol data were collected at 1 Hz and averaged over the duration of each level flight segment (~10-min averages for the four highest levels, ~5-min averages for the five lowest levels). Aerosol optical properties obtained for each level leg include σ_{sp}, σ_{bsp}, and σ_{ap} coefficients. From these extensive properties the following intensive aerosol optical properties were derived: ω_0, b, and $\mathring{a}$. All measurements on the aircraft were made at low humidity (RH $\leq$ 40%).
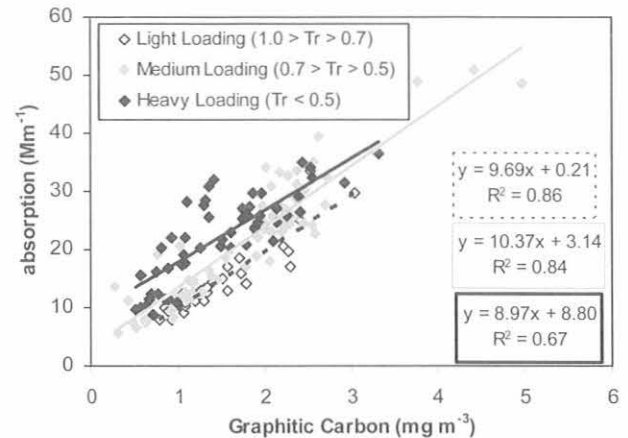

Fig. 3.8. Comparison of GC and absorption coefficient measured at KCO during February-March 1999. The solid dark line is the fit to the heavy loading data; the gray line is the fit to the medium loading data; and the dashed black line is the fit to the light loading data. One outlier has been removed from the "Medium Loading" data set.

There is good agreement ($R^2 = 0.82$) between lowest level leg and surface extinction ($\sigma_{ext} = \sigma_{ap} + \sigma_{sp}$) values, indicating submicrometer aerosol (predominantly scattering aerosol) in the 150 m above the surface is well-mixed. Much of the variability in the parameters measured at the surface site appears to be captured by the weekly profiling flights. The comparison is not as good ($R^2 = 0.49$) for single-scattering albedo and is due to measured differences in absorption between the surface and the lowest flight level. These observed differences appear to be real because side-by-side tests of the two PSAPs show good agreement (within 8%). Comparison of other derived properties at the lowest flight level with surface properties are excellent for backscatter fraction and green-blue Ångström exponent, but less so for the green-red Ångström exponent.

Figure 3.9 shows the medians and ranges (as indicated by percentiles) of a representative extensive aerosol optical property (extinction) and a representative intensive aerosol optical property (single-scattering albedo) at STP, low RH, and $D < 1$ µm, obtained at the surface and during vertical profiling flights. The line in the center of the box represents the median, while the edges of the box give the 25th and 75th percentiles, and the whiskers extend to the 5th and 95th percentiles. In general, the values for extensive properties (extinction, absorption, and scattering coefficients) vary by up to a factor of 3, while the medians for intensive aerosol properties (single scattering albedo, backscatter fraction, and Ångström exponent) are much less variable (less than 10% variation). Figure 3.9 suggests that the median values of the extensive properties tend to decrease with altitude from the surface upward. Such behavior is expected as distance from the ground-based sources of aerosol particles increases. The median values of the intensive properties do not display a strong dependence with altitude.
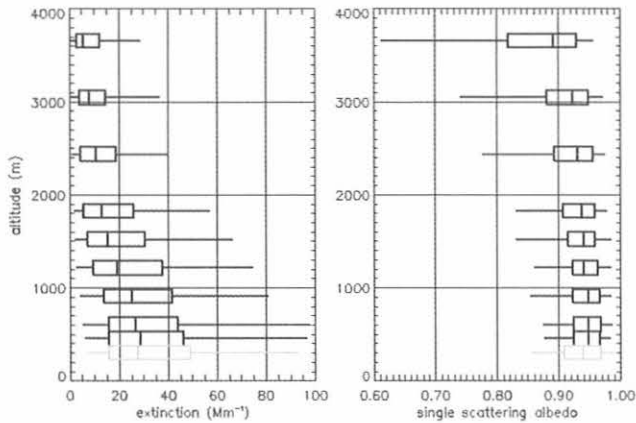
Fig. 3.9. Statistical box and whisker plots of vertical profiles of extinction (left) and albedo (right) over the SGP site, March 2000-March 2001. Black plots are from aircraft flights; gray plots are surface measurements. The boxes and whiskers are as in Figure 3.1.

More indicative of the overall variability of the aerosol are the ranges of the parameters, as indicated by the percentiles in Figure 3.9. Extensive properties can differ by up to 2 orders of magnitude between flights and even between individual levels of the same flight. The intensive properties, while still displaying a range of values, vary at most by an order of magnitude (i.e., green-red Ångström exponent, level 3660 m) but more commonly by less than a factor of 2. The parameter ranges display different tendencies with height. Extensive properties become less variable at higher altitudes, due to consistently low concentrations of aerosol particles. Conversely, intensive properties become more variable with altitude for a similar reason: low concentrations of aerosol particles result in more noise when calculating the values of these parameters.

The surface measurements are representative of the frequency distributions aloft, particularly for intensive properties such as albedo (Figure 3.9). However, the correlations (not shown) between column average and surface values are lower (e.g., extinction $R^2 = 0.65$; albedo $R^2 = 0.30$) than correlations between lowest flight level and surface values. Thus, while surface aerosol measurements are statistically representative of the air aloft, they may not be representative of day-to-day variations in the column.

Measurements from the profile flights can also be compared with measurements by remote sensing instruments located at SGP, i.e., the Cimel sun/sky radiometer and the multi-filter rotating shadowband radiometer (MFRSR). After incorporation of corrections for supermicrometer, upper tropospheric, and stratospheric aerosol particles, comparison in Figure 3.10 of aerosol optical depth (AOD) calculated from aircraft measurements with AOD obtained from the remote sensing instruments shows fair correlation ($R^2 \approx 0.5$, Cimel; $R^2 \approx 0.8$, MFRSR), although the aircraft AODs are lower than those derived from the radiation instruments, with an offset in the range of -0.03 or -0.04.

Long-term surface measurements can represent a statistical distribution of aerosol properties aloft. However, day-to-day variability between the surface and aloft may not always be captured and causes a poor relationship between surface and column average quantities. Comparison of the in situ and remote sensing instruments shows fair correlation for AOD although the aircraft AOD is consistently lower than that of the remote sensing instruments.

Measurements of Aerosol Optical Properties from a Surface Site in Korea (ACE-Asia)

An intensive field campaign known as the Asian Pacific Regional Aerosol Characterization Experiment (ACE-Asia) took place in April 2001 in eastern Asia. The goal of ACE-Asia was to gather data for regional climate models as well
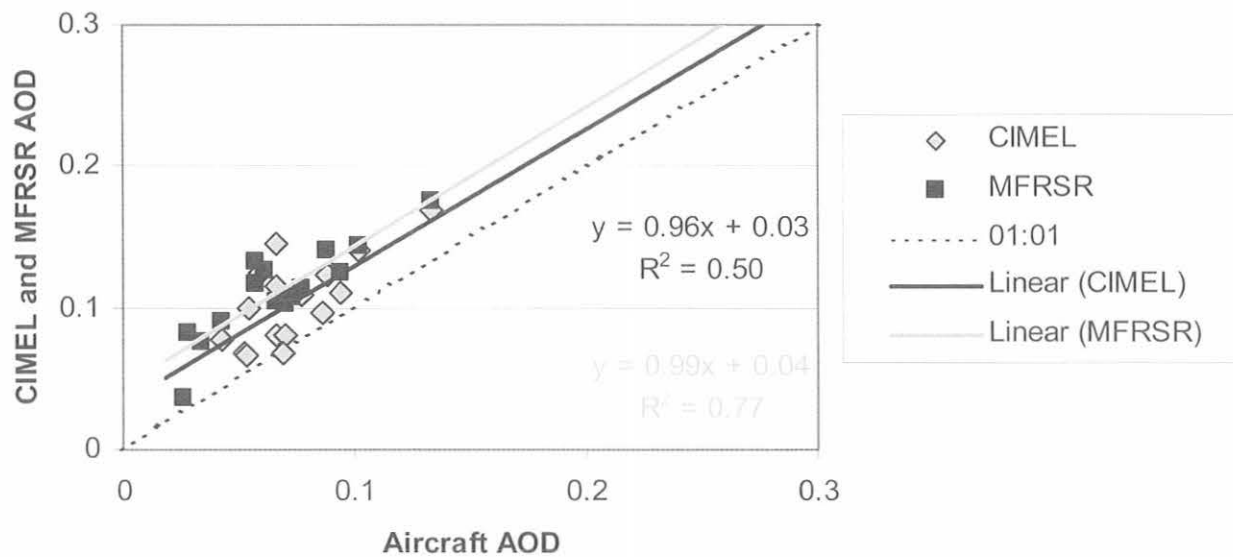

Fig. 3.10. Comparison of aerosol optical depth (AOD) measured on aircraft with AOD derived from Cimel and MFRSR remote sensing instruments at the SGP site, for March 2000-March 2001.

as to understand better the interactions between aerosols and radiation, gas phase species, transport, and clouds.

This large field study was a multi-platform, international effort with scientific measurements being recorded from land-based sites, ships, aircraft, and satellites. Scientists from Korea, United States, Great Britain, China, Japan, and Australia worked together to characterize aerosol radiative, chemical, and size properties. These aerosol properties, as well as their covariance, strongly influence the Earth's radiative balance. The primary surface site was located at the Upper Air Meteorological Observation Facility near the small town of Kosan on Cheju Island, South Korea. The site is strategically located between several major aerosol source regions. Depending on wind conditions, the scientists observed anthropogenic aerosol from Japan, Korea, and China; large dust outbreaks from northern China; relatively clean marine air; or even local crop burning.

As part of this effort, CMDL conducted in situ measurements of the aerosol optical properties as well as full column measurements of solar radiation at Kosan. The ground-based measurements included aerosol scattering coefficient as a function of particle size, wavelength, and relative humidity, and the aerosol absorption coefficient as a function of size. These observations provide a direct measure of the surface aerosol extinction of visible radiation. For full column measurements of the atmosphere, radiometers from CMDL measured the total, direct, and diffuse (scattered light by aerosol) solar radiation. These observations can be used to derive the AOD, or amount of solar radiation attenuated by aerosols, and the aerosol forcing efficiency.

The aerosol scattering coefficient was highly variable during the campaign, ranging between 20 and 250 Mm^{-1}. Spring in Korea is known as the dust season when southeasterly winds bring dust to the region from the Gobi Desert. Several such events, note particularly day of year (DOY) 101-104 and DOY 110, are apparent from the data (Figure 3.11). On these days over 60% of the aerosol scattering was in the total size mode, as indicated by the
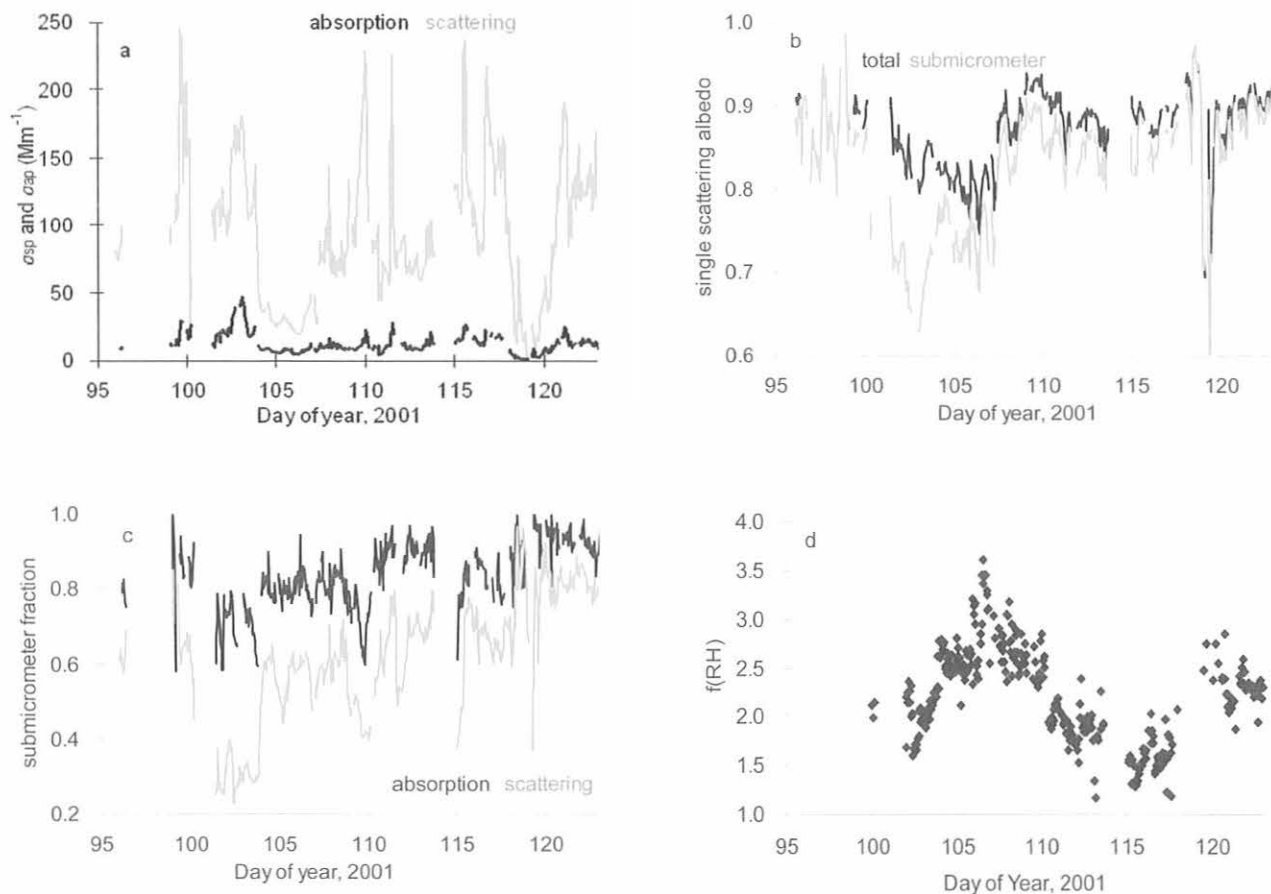

Fig. 3.11. Time series of aerosol measurements from Kosan during ACE-Asia in 2001: (a) total absorption and scattering coefficients, (b) total and submicrometer single-scattering albedo, (c) submicrometer fraction of aerosol absorption and scattering, and (d) total aerosol hygroscopic growth factor. All values are reported for a wavelength of 550 nm.

low values of the ratio of the submicrometer to total aerosol scattering coefficients (Figure 3.11c). The aerosol single-scattering albedo during the dust events declined slightly to ~0.80 for total aerosol and as low as 0.63 for submicrometer aerosol (Figure 3.11b). Most of the aerosol absorption during the campaign was in the submicrometer particles. The aerosol hygroscopic growth factor, $f(RH) = \sigma_{sp}(RH=85)/\sigma_{sp}(RH=40)$, a measure of the increase in scattering due to aerosol water uptake, was relatively high during the dust events, ranging from 1.5 to 2.5 (Figure 3.11d). The low single-scattering albedo and high hygroscopic growth factor indicate the aerosol at the site was composed of not only dust but also very likely of absorbing elemental and hygroscopic species such as sulfate, oxidized organics, and seasalt.

Mean aerosol optical properties from Kosan as well as from two other anthropogenically perturbed sites are given in Table 3.6. Although all three sites receive anthropogenic aerosol, there are significant differences in the aerosol optical properties between the sites, demonstrating the importance of long-term, regional measurements at a variety of locations. Kosan, South Korea, and Kaashidhoo, Republic of Maldives, are anthropogenically perturbed marine sites, and Bondville, Illinois, is an anthropogenically perturbed continental site. The aerosol scattering coefficient from Kosan is higher than from either the Kaashidhoo or the Bondville site, indicating a high aerosol loading in eastern Asia during the spring. Kosan and Kaashidhoo have higher light absorption coefficients than Bondville, consistent with a larger contribution of combustion aerosol (e.g., from biomass burning or limited pollution control on vehicles and industries). Consistent with the higher absorption coefficients at Kosan and Kaashidhoo, those sites have lower single-scattering albedo values than Bondville, with Kaashidhoo being significantly lower than Kosan. The $f(RH)$ value at Kosan was significantly higher than at Kaashidhoo or Bondville. The $f(RH)$ at Kosan did not correlate well with seasalt aerosol, but was probably high due to extensive mixing with polluted air masses containing sulfates and nitrates from both China and Korea as well as cloud processing. At Kaashidhoo the aerosol was more reflective of the source

emissions, which were high in black carbon and, periodically, dust and had undergone little cloud processing. The strong inversion layer present during the INDOEX sampling at Kaashidhoo prevented significant processing of the aerosol in the boundary layer, whereas the frontal systems present during ACE-Asia promoted strong vertical mixing between the boundary layer and lower free troposphere and hence faster aerosol cloud processing. The similarity of the $f(RH)$ values at KCO and BND is most likely coincidental and not from a similar aerosol composition. Finally, at all three sites, the absorbing aerosol was concentrated in the submicrometer aerosol, as suggested by the high values of the submicrometer fraction of absorbing aerosol (Table 3.6). However, Kosan and Kaashidhoo had lower values of the submicrometer fraction of scattering aerosol than Bondville, most likely due to the presence of seasalt and/or dust at those two sites.

The sunphotometers give a measure of the direct solar irradiance in seven narrowband wavelength channels. Preliminary data from these instruments (screened for clouds) give a measure of the AOD. On days with the highest pollution, the AOD for 500-nm radiation was as high as 0.7, and on days with clean marine air the value dropped to a low of 0.1. During the major dust event from DOY 101 to 104 the AOD was 0.45 to 0.7, indicating relatively low sunlight levels from a heavy loading of aerosol. Figure 3.12 shows both the AOD at 500 nm and the aerosol Ångström exponent, a measure of the aerosol size, for a 3-mo period from March 31 to July 9, 2001, at Kosan.

Systematic Variation of Aerosol Optical Properties

Aerosol optical properties measured over several years at BND, SGP, WSA, and BRW have been analyzed to determine the importance of the variability in aerosol optical properties to direct aerosol radiative forcing calculations and to investigate whether systematic relationships exist between various aerosol optical properties, i.e., σ_{ap}, ω_o, b, $\mathring{a}$, and aerosol radiative forcing ($\Delta F/\delta$), and the amount of aerosol present (measured as σ_{sp}). Systematic relationships among aerosol properties can be used to check for consistency among measured and modeled

TABLE 3.6. Means and Standard Deviations of Aerosol Optical Properties of Anthropogenically Influenced Aerosols at 550 nm

Aerosol Property	Kosan (KOS)	Kaashidhoo (KCO)	Bondville (BND)
σ_{sp}*	92 (53)	73 (28)	54 (43)
σ_{ap}*	12 (8)	16 (9)	4 (3)
ω_o	0.87 (0.05)	0.82 (0.03)	0.92 (0.06)
$f(RH)$	2.2 (0.5)	1.7 (0.1)	1.7 (0.4)†
$F\sigma_{sp}$‡	0.61 (0.16)	0.67 (0.08)	0.86 (0.09)
$F\sigma_{ap}$‡	0.83 (0.09)	0.84 (0.06)	0.92 (0.38)

KOS data for April 2001; KCO data for mid-February-March 1999; BND data for all of 2000.

*Values are for total ($D < 10$ μm) aerosol.

†*Rood,* personal communication, 2002.

‡$F\sigma_{sp}$ and $F\sigma_{ap}$ are the submicrometer fractions of aerosol scattering and absorption, respectively.
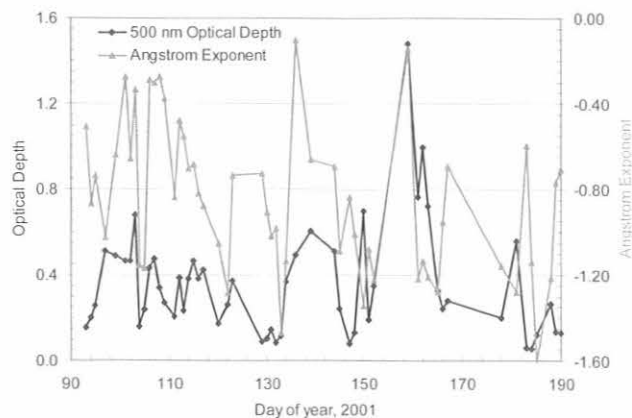

Fig. 3.12. Aerosol optical depth measured at 500 nm and aerosol Ångström exponent from the 412/862-nm wavelength pair, March 31-July 9, 2001, at Kosan.

climatologies. Also, systematic relationships can be used in model parameterization to reduce uncertainties resulting from insufficient knowledge of aerosol properties. The performance of different models can be evaluated with measurements, and if models predict the parameters that are observed, the measurements can be used to validate the models.

Knowledge concerning systematic relationships among aerosol properties can be useful in reducing uncertainties in remotely sensed data because they can be used to make better assumptions about unknown aerosol properties. *Remer and Kaufman* [1998] illustrated the importance of using a dynamic model where aerosol properties vary with aerosol load for the inversion of remote sensing data. The reason to use a dynamic aerosol model is to represent systematic changes in one aerosol property as another property changes. Because of their importance and usefulness, systematic relationships among aerosol optical properties were investigated at the four surface sites. Figure 3.13 shows systematic relationships among low
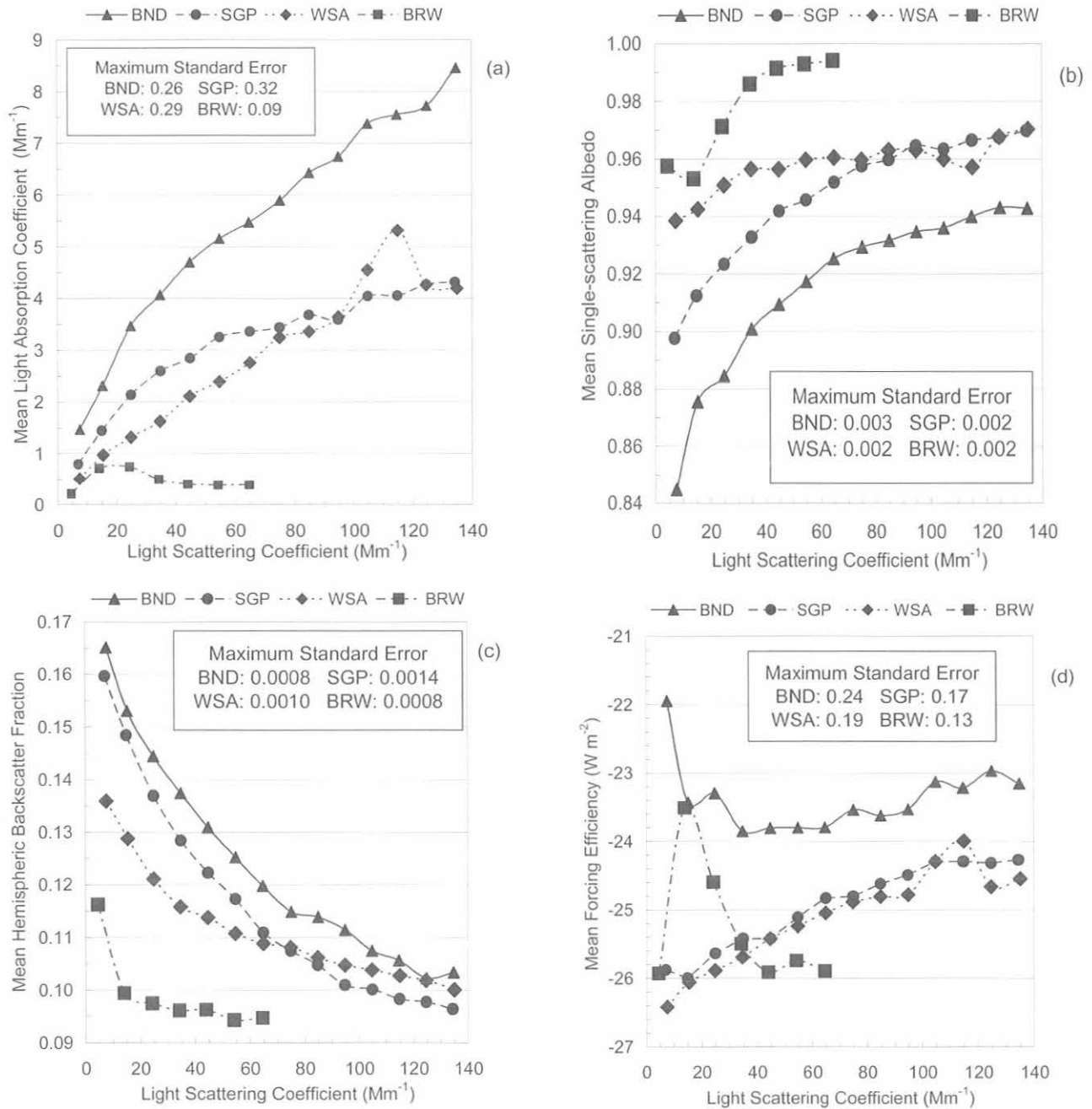
Fig. 3.13. (a) Mean aerosol light absorption coefficient (σ_{ap}), (b) mean single-scattering albedo (ω_o), (c) mean hemispheric backscatter fraction (b), and (d) mean forcing efficiency ($\Delta F/\delta$), all versus the aerosol light scattering coefficient (σ_{sp}), for BND, SGP, WSA, and BRW. Plots are based on all valid hourly averaged aerosol measurements (>50% 1-min data within the hour) for systems with TSI 3563 nephelometers. The mean values were calculated over 10-Mm^{-1} σ_{sp} bins. The maximum standard error (sample standard deviation /square root of the number of points) at each station is given in the text boxes.

relative humidity (<40%), aerosol optical properties (σ_{ap}, ω_o, b, and $\Delta F/\delta$), and the aerosol load (measured as σ_{sp} at 550-nm wavelength). The mean aerosol optical properties were calculated over σ_{sp} intervals of 10 Mm^{-1}, and the corresponding maximum standard error for each station is given in the graph. The standard errors are considerably smaller than the changes over 10-Mm^{-1} bins, which implies a high level of significance to the relationships. The σ_{ap} does not increase as rapidly as the σ_{sp}, resulting in a systematic increase in ω_o as σ_{sp} increases at all four stations. All four stations also show a systematic decrease in b as σ_{sp} increases. In terms of $\Delta F/\delta$, the relationship between b and σ_{sp} acts to offset the relationship between ω_o and σ_{sp}. The b-σ_{sp} relationship results in a decrease in the magnitude of the $\Delta F/\delta$ as σ_{sp} increases, while the ω_o-σ_{sp} relationship results in an increase in the magnitude of the $\Delta F/\delta$ as σ_{sp} increases. For SGP and WSA, the b-σ_{sp} relationship is more important and results in a decrease in the magnitude of $\Delta F/\delta$ as σ_{sp} increases. For BND, the ω_o-σ_{sp} relationship is more important for σ_{sp} less than 40 Mm^{-1} and results in an increase in the magnitude of $\Delta F/\delta$ as σ_{sp} increases; however above 40 Mm^{-1}, the b-σ_{sp} relationship is more important and results in a decrease in the magnitude of $\Delta F/\delta$ as σ_{sp} increases. Similarly at BRW, the relative importance of one relationship compared with the other determines how $\Delta F/\delta$ changes as σ_{sp} increases.

Figure 3.14 illustrates two systematic relationships, one between $\mathring{a}$ and σ_{sp} and the other between submicrometer scattering fraction R_{sp} and $\mathring{a}$. The strong relationship between R_{sp} and $\mathring{a}$ indicates that $\mathring{a}$ is sensitive to changes in the relative amount of submicrometer scattering aerosol. At BND and SGP $\mathring{a}$ decreases as σ_{sp} drops below 30 Mm^{-1}, whereas at WSA and BRW $\mathring{a}$ increases as σ_{sp} drops below 30 Mm^{-1} (Figure 3.14a). Above 30 Mm^{-1} all four stations show a fairly constant $\mathring{a}$ with increasing σ_{sp}. This systematic relationship suggests that during low aerosol concentration events, the continental sites (BND and SGP) have more relatively larger particles present, while the marine sites (WSA and BRW) have more relatively smaller particles present. The $\mathring{a}$-σ_{sp} relationship at BND and SGP is consistent with the relationship between the Ångström exponent and aerosol optical thickness (derived from Sun/sky scanning spectral radiometer measurements) for the mid-Atlantic region of the eastern United States [*Remer and Kaufman*, 1998]. It is interesting to note that while the $\mathring{a}$-σ_{sp} relationship is different between SGP and WSA, the $\Delta F/\delta$-σ_{sp} relationship is very similar. This suggests that the $\Delta F/\delta$-σ_{sp} relationship is not influenced by changes in the submicrometer to total aerosol fraction but rather by changes in the submicrometer aerosol size distribution (b-σ_{sp} relationship) and the aerosol composition (ω_o-σ_{sp} relationship).

Systematic relationships exist between various aerosol properties (σ_{ap}, ω_o, b, $\Delta F/\delta$, and $\mathring{a}$) and σ_{sp} and also between $\mathring{a}$ and submicrometer scattering fraction R_{sp} (Figure 3.14b). These systematic relationships are qualitatively similar among the four stations; however, the quantitative relationships are different at each station, which is indicative of the occurrence of different aerosol types and size distributions at each station. Systematic relationships
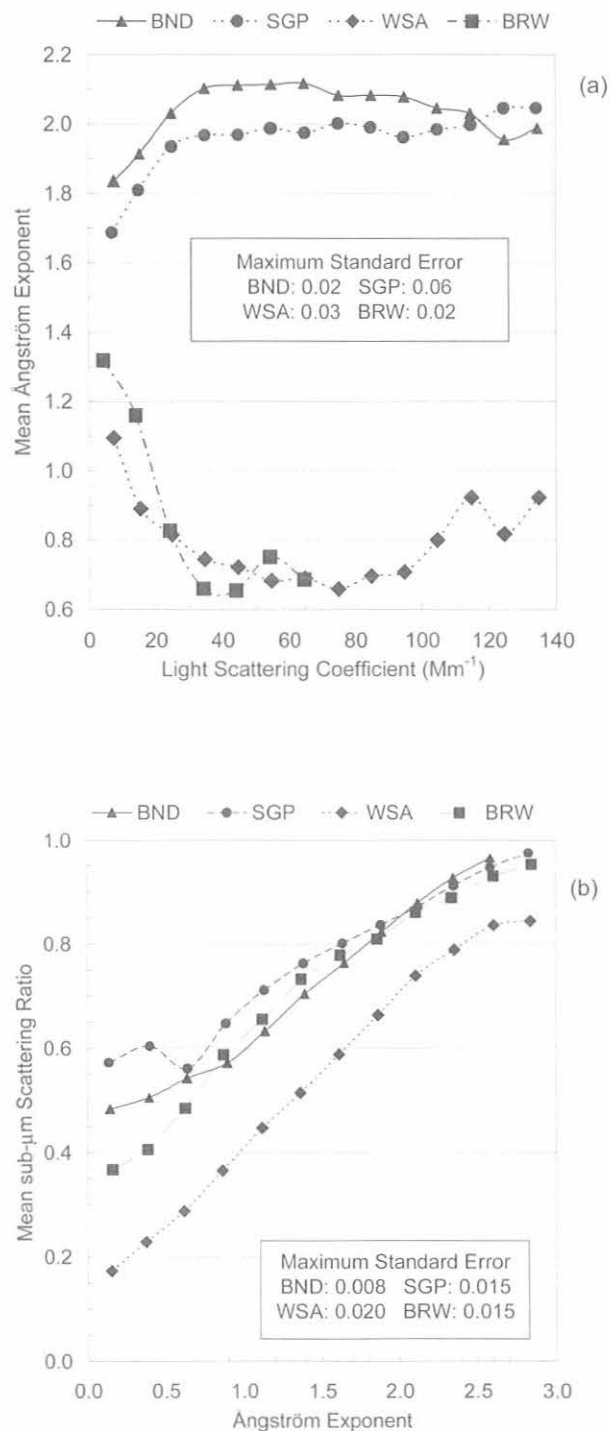

Fig. 3.14. (a) Mean Ångström exponent ($\mathring{a}$) versus aerosol light scattering coefficient (σ_{sp}) and (b) submicrometer scattering fraction (R_{sp}) versus Ångström exponent, for BND, SGP, WSA, and BRW. Plots are based on all valid hourly averaged aerosol measurements (>50% 1-min data within the hour) for systems with TSI 3563 nephelometers. The $\mathring{a}$ values were calculated over 10-Mm^{-1} σ_{sp} bins, and the mean R_{sp} was calculated from 0.25-Å exponent bins. The maximum standard error (sample standard deviation /square root of the number of points) at each station is given in the text boxes.

and the regional, yearly, weekly, and daily variations in optical properties can be used to check for consistency between climatologies based either on observations or models. The existence of systematic changes in aerosol optical properties with changes in aerosol concentration indicate that care should be taken when using average values in algorithms to retrieve aerosol properties, such as optical depth, from satellite data. An algorithm that uses a static representation for aerosol optical properties will have a systematic bias in derived values.

3.2. SOLAR AND THERMAL ATMOSPHERIC RADIATION

B. BODHAINE (EDITOR), G. ANDERSON, G. CARBAUGH, E. DUTTON, B. HALTER, D. JACKSON, D. LONGENECKER, D. NELSON, R. STONE, R. TATUSKO, AND N. WOOD

3.2.1. RADIATION MEASUREMENTS

Introduction

The CMDL Solar and Thermal Atmospheric Radiation (STAR) project provides supporting information for baseline climate monitoring activities and investigates trends and variations in the observed surface radiation budget. Energy associated with the Earth's radiation budget is not only responsible for maintaining the thermal state of the planet but also causes atmospheric and oceanic motions. Expected trends in surface radiation quantities at globally remote sites caused by anthropogenic activities are near or below the level of detectability, on the decadal time scale. However, there are gaps in the knowledge of basic climatological variability in the global surface radiation budget such that STAR measurements can contribute to a fundamental understanding of atmospheric and climato- logical processes. These contributions include definition of diurnal and annual cycles and effects of cloudiness, actual variation on daily to decadal time scales, major volcanic eruptions, unexpectedly high concentrations of anthropogenic pollution in the Arctic, constituent variations on narrowband irradiance (e.g., ozone and ultraviolet (UV) changes), and possible anthropogenic modification to cloudiness. The STAR group also makes remote sensing measurements of various atmospheric constituents that are potentially responsible for variations in surface radiation quantities, particularly aerosol optical depth. In addition to the research conducted by CMDL and the locally maintained data archives, STAR measurements contribute to several global databases. Databases that are global in extent are needed to evaluate radiation and energy budgets in diagnoses of the climate. STAR observations also contribute to satellite-based projects by helping verify point estimates and thereby allowing intervening features of the atmosphere to be deduced.

A major goal of the monitoring program is to obtain a record of surface radiation parameters that is as long and complete as possible and that can be examined for all scales of natural and modified variability. Of particular interest is the determination of the magnitude, representativeness, and possible consequences of any observed changes. To this end, the STAR group maintains continuous surface radiation budget observations at several globally diverse sites, along with various ancillary observations. The following describes those projects and changes since the previous *CMDL Summary Report* [*Schnell et al.*, 2001].

Baseline Monitoring Sites

Surface radiation measurements have been made at the four principal CMDL baseline observatories (BRW, MLO, SMO, and SPO) since the mid-1970s, with some measurement series going back to 1957. The different environments and observing conditions at the sites resulted in somewhat different measurement programs evolving at each site. The basic measurements made at all sites include the downward components of solar radiation: global, diffuse, and direct. Broadband thermal infrared (IR) irradiance measurements were added over the past 15 years. Upward solar and thermal IR are measured at sites where the surrounding terrain is representative of a larger regional area, such as at SPO and BRW, for at least part of the year. The records acquired at these sites constitute some of the longest known series available by the United States for solar radiation research. The raw data are routinely transmitted from the field sites over telephone lines or the Internet to the central data processing facility in Boulder, where data editing, final calibrations, graphical inspection, and archiving are performed, as discussed in section 3.2.9.

Other Measurement Sites

Boulder Atmospheric Observatory (BAO Tower). Obser- vations of upwelling and downwelling solar and thermal irradiances began in 1985 at the top of a 300-m-tall tower, known as the Boulder Atmospheric Observatory (BAO), which is located near Erie, Colorado. Nearly continuous observations of these quantities were made with hourly resolution until 1992, 3-min resolution until 1998, and 1- min resolution thereafter. The upwelling data provide a unique view of surrounding agricultural land, making the data more representative than typical surface-based solar radiation budget observations. This site has contributed data to the World Climate Research Program (WCRP) Baseline Surface Radiation Network (BSRN). Applications of data from this site were described in the 1998-1999, and earlier, *CMDL Summary Report*s [e.g., *Schnell et al.*, 2001]. Since 1990, observations of direct solar and downwelling solar irradiances have also been made near the base of the tower. Measurements of aerosol optical depth were added in the past 2 years, as were observations of the direct solar beam with an all-weather absolute cavity radiometer.

Kwajalein. Observations of direct solar and downwelling solar and thermal IR irradiance began on Kwajalein in 1989. Kwajalein is a small, <4-km^2, island in the tropical western Pacific. Data obtained at this location are virtually free of any effects of the island and therefore are often taken as representative of the open ocean in that region. Data from Kwajalein have been used as oceanic representative by *Dutton* [1993], *Whitlock et al.* [1995], and *Bishop et al.* [1997], and are currently being used by the Cloud and Earth's Radiant Energy System (CERES) and the European Centre for Medium-Range Weather Forecasts (ECMWF) global circulation model (GCM). Substantial upgrades to the Kwajalein radiation measurements were carried out

in the past 2 years because a corrosive marine environment requires that much attention be given to the instrumentation. The Kwajalein site is a participant in the BSRN program and receives much of its funding from the National Aeronautics and Space Administration (NASA), which has a large interest in CMDL's radiation mea-surement activities in general.

The installation of a new permanent stairway to the Kwajalein measurement platform was completed, new tables for sensors and the solar tracker were constructed, and all equipment was relocated during August 2000.

Bermuda. Observations of downwelling solar and thermal IR began at the NASA Tracking Station at the east end of Bermuda in 1990. The rather small size and low relief of this island, located in the lower midlatitude westerlies, has minimal influence on the irradiance mea-surements, although some clouds of orographic origin are known to exist there in the summer months under certain synoptic meteorological conditions. Data from Bermuda have been submitted to the BSRN data archive and were used by *Whitlock et al.* [1995] and *Bishop et al.* [1997], and currently by the CERES program in satellite comparison and validation studies and by ECMWF and Geophysical Fluid Dynamics Laboratory (GFDL) in their GCM testing. The monitoring site was moved in 1998 from the NASA Tracking Station (32.2670°N, 64.6670°W) near the east end of the island to the top of Prospect Hill near the center of the island (32.3009°N, 64.7659°W). The site is ably tended by the Bermuda Biological Station for Research and is also funded largely by NASA.

Basic Measurements

Broadband irradiance. The basic broadband measure-ments currently conducted at each of the four baseline observatories for the past 26 years include normal direct and downward broadband solar irradiance and downward solar irradiance in the 0.28-μm to 2.8-μm band. Downward broadband thermal irradiance measurements were added

at all sites in more recent years as well as upwelling irradiance measurements at SPO and BRW. The current suite of measurements at all sites is shown in Table 3.7. Data are sampled at 1 Hz with 1-min averages recorded on computer media. Preliminary data from all CMDL radiation sites are generally available, graphically, within a couple of days of acquisition in the Radiation section of the CMDL web site, and subsequently as described in section 3.2.9. The *CMDL Summary Report* for 1998-1999 [*Schnell et al.*, 2001; page 59] shows different example summaries of the 24-yr record of total solar irradiance collected at SMO using the single pyranometer technique.

Filter wheel NIP. The wideband spectral direct solar irradiance measurements are made with a filter wheel normal incidence pyrheliometer (FWNIP). One of the applications of these data is to compare them with a high-spectral-resolution radiative transfer model [*Bird and Riordan*, 1986] that is based on Beer's law and is intended for use at the surface only. The aerosol optical depth and precipitable water are adjusted within the model to obtain the best match with the FWNIP observations. This provides a low-precision but relatively stable estimate of mean visible aerosol optical depth and water vapor at the four baseline observatories. The accuracy of the method for obtaining aerosol optical depth and water vapor is limited by the dependence on the absolute values of the extra-terrestrial solar spectrum and instrument calibration, unlike other typical applications in sunphotometry. The updated data records from these observations are shown in Figure 3.15 through near the end of 2001. The accuracy of the data is on the order of 0.03 optical depth units, or about 2 to 3 times poorer than sunphotometer-derived values and should only be used when sunphotometer-derived data are not available.

MLO apparent transmission. The transmission for direct broadband solar irradiance through the atmosphere above MLO is monitored as a quantity known as the apparent transmission. This quantity is computed as the average

TABLE 3.7. Measurement Types Made at Each Station, 2000-2001

	BRW	Bermuda	BAO	MLO	Kwajalein	SMO	SPO
Broadband Irradiance (until otherwise noted)							
Direct solar beam	X	X	X	X	X	X	X
Diffuse solar	X	X	X	X	X	X	X
Total downward solar	X	X	X	X	X	X	X
Reflected solar	X		X				X
Downward IR	X	X	X	X	X	X	X
Upward IR	X		X				X
Other Measurements							
Spectral optical depth	X	X	X	X	X		X
All-sky digital imagery	X		X				
UV-B	X	X	X	X	X		
High-resolution spectral UV			X*		X		
Wideband direct solar irradiance (FWNIP)	X			X		X	X

BRW, Barrow, Alaska; BAO, Boulder Atmospheric Observatory (Erie, Colorado); MLO, Mauna Loa, Hawaii; SMO, American Samoa; SPO, South Pole, Antarctica.
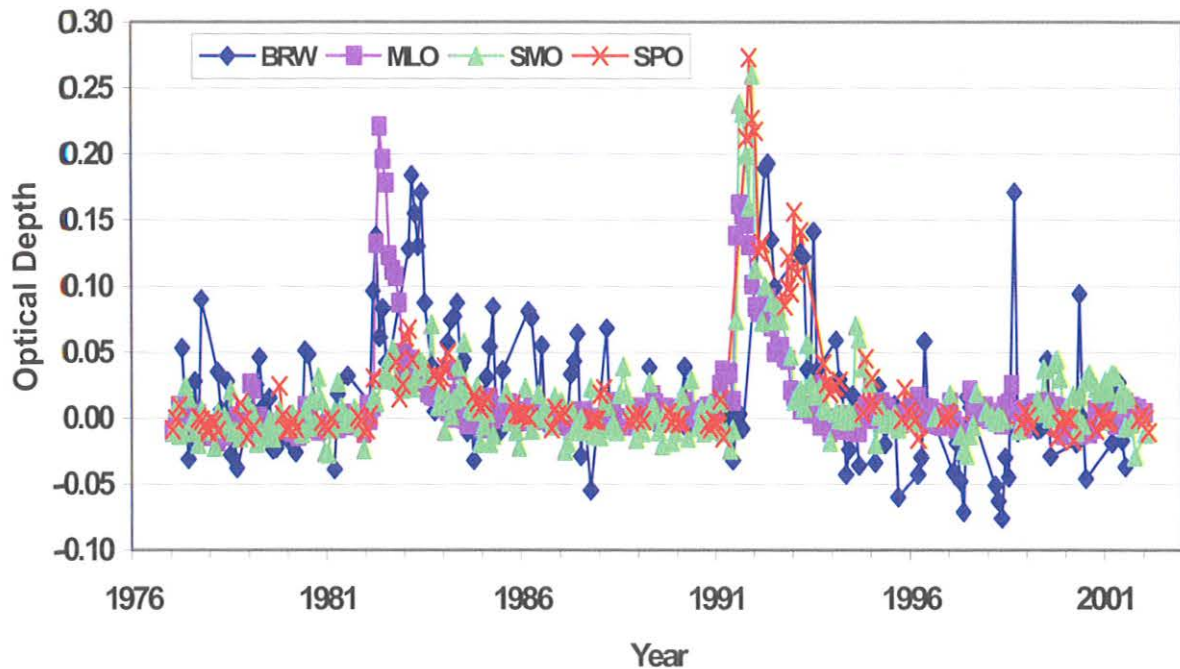*Instrument located in Boulder about 16 km west of BAO.

Fig. 3.15. Aerosol optical depth anomalies, monthly averages from wideband filter wheel NIP estimates.

of three successive ratios of direct solar irradiance, where each ratio is the quotient of the irradiance at an integer airmass divided by the irradiance at the next smaller integer airmass, as first defined by *Ellis and Pueschel* [1971]. The apparent transmission measurement is inherently stable over time because it is independent of a radiometer calibration value and is therefore also quite sensitive to small changes in transmission that can be due to aerosols, ozone, or water vapor.

Studies by *Bodhaine et al.* [1981] and *Dutton et al.* [1985] have shown that aerosols tend to dominate observed changes in the monthly averages of apparent transmission such that the major observed excursions in the record, shown in Figure 3.16, are due to aerosols. The major observable features in Figure 3.16 are the effects of several volcanoes, particularly Agung in 1963, El Chichón in 1982, and Pinatubo in 1991, and an annual oscillation caused primarily by the springtime transport of Asian dust aerosol over the site [*Bodhaine et al.*, 1981]. Figure 3.16 is complete through 2001 and shows that the recovery from the eruption of Mt. Pinatubo required several years. The fact that the Mauna Loa apparent transmission record took several years to recover from Pinatubo is evidence of the sensitivity of the measurement, because it is known from other measurements by CMDL and others that the optical depth of Pinatubo in 1995 was already very low, on the order of 0.005 at 500 nm. *Dutton and Bodhaine* [2001] have used the MLO transmission record to deduce the maximum possible change in certain solar radiation budget quantities that could have occurred over the length of the record. The long-term atmospheric transmission was con-
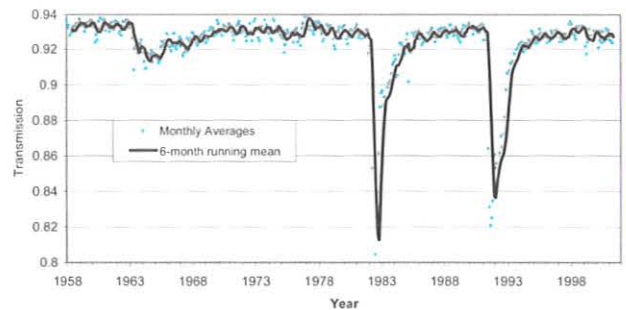
Fig. 3.16. Apparent solar transmission observed at Mauna Loa.

verted to net solar irradiance at MLO by comparison to more recent accurate measurements of surface irradiance, and assumptions about the constancy of underlying reflectivity and extraterrestrial solar irradiance. The 42-year time series of the deduced net solar irradiance at the level of MLO is shown in Figure 3.17 [*Dutton and Bodhaine*, 2001]. The maximum sustained solar radiative forcing from varying atmospheric transmission over Mauna Loa, determined from deduced net solar irradiance changes at 3.4 km above sea level (ASL), was less than -0.3 W m^{-2} over the last 40 years. In other words, the only linear trend that could have existed in net solar irradiance at the level of Mauna Loa but not have been detected would be between 0 W m^{-2} and -0.075 W m^{-2} per decade, thereby also eliminating the possibility of any positive trend. This work
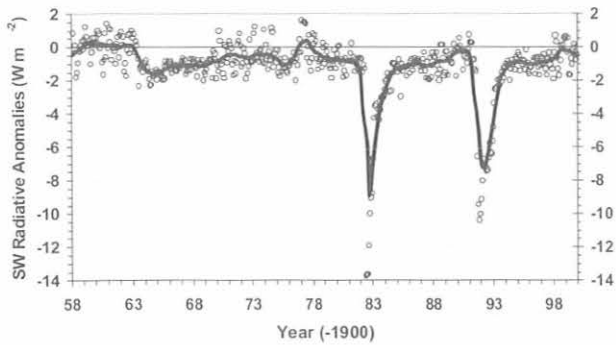
Fig. 3.17. Net solar irradiance variations at the height of Mauna Loa because of changes in atmospheric transmission over Mauna Loa.

provides a longer history and more accurate determination of actual observed variations in radiative forcing as related to potential climate change than any other known directly observed radiation record.

Improvements in Diffuse Solar Irradiance Measurements

Total downwelling solar irradiance is the primary input component of the Earth's energy budget. One step in the improvement of the instantaneous surface-based solar irradiance measurements was the BSRN recommendation for using the combination of the separately measured direct and diffuse irradiance, which incorporates the highly accurate direct beam measurement capabilities developed over the past four decades and greatly reduces the cosine response error inherent in the single-instrument flat-plate receiver of the pyranometer. This method of measuring total solar irradiance led to improvements discussed by *Ohmura et al.* [1998], *Bush et al.* [1999], and *Michalsky et al.* [1999]. This recommendation has placed new require-ments on the necessary documented accuracy of diffuse measurements. Although accuracy specifications for direct solar irradiance are rather easily determined, there are difficulties for the diffuse component because no reference standards exist. This has resulted in some recent modifications in the way in which STAR is making diffuse irradiance measurements, both in the type of instruments used and the adjustments for thermal offsets induced in certain diffuse pyranometers. The specifics of new diffuse solar measurements and adjustments to older data are given by *Dutton et al.* [2001]. With these changes, it is estimated that diffuse irradiance is currently measured to within about 5 W m^{-2}. This results in accuracies to within about 8 W m^{-2} for total solar irradiance when determined from the combined diffuse and direct measurements. STAR is involved in ongoing national and international efforts to promote the development of international reference standards and further improve the absolute accuracy of solar diffuse measurements.

Each CMDL BSRN site was also equipped to monitor diffuse sky radiation with a tracking-disk-shaded black and white pyranometer to augment the diffuse sky measurements made with single-black-detector-type pyranometers. The addition of pyranometers with black and white detectors enables more thorough monitoring of zero-offset effects. Solar trackers at each site were modified to enable installation of the additional shaded black and white detector pyranometers.

Thermal IR Irradiance Measurement Improvements

Although there have been substantial reductions in the uncertainty of thermal IR measurements in the past 10 years, from nearly ±30 W m^{-2} in the late 1980s to about ±5 W m^{-2} now (based on experiences in CMDL and elsewhere), there still appears to be room for further improvements and the potential for the establishment of a measurement reference standard. Over the past 2 years, STAR has become involved in the efforts of BSRN and the World Radiation Center (WRC) in Davos, Switzerland, to work toward these potential improvements. This work is through the establishment of new radiance measurement capabilities that rely on absolute, self-calibrating, sky-scanning instruments that could eventually determine a world reference group similar to that used to establish the World Radiometric Reference (WRR) for solar direct beam observations. CMDL, working with BSRN, helped organize and participated in the International Pyrgeometer and Absolute Sky-scanning Radiometer Comparisons (IPASRC-I and II), in the central United States during September 1998 and in the Arctic at Barrow during March 2001, respectively, where this process to establish such capabilities and reference standards began [*Philipona et al.*, 1998]. The results of the first of these comparisons and the operation of the sky scanner suggest that an absolute longwave irradiance measurement made routinely in the field can achieve the accuracy of close to ±1-2 W m^{-2} [*Philipona et al.*, 2001].

3.2.2. BASELINE SURFACE RADIATION NETWORK

The STAR group has the primary management role in BSRN and has carried out the duties of International Project Manager for the past 7 years. BSRN is intended not only to supply the international climate research community with the best possible surface irradiance data from a globally and climatologically diverse long-term network, but also to keep advancing the state of the art in improvements of those measurements so that research uses of the data can continue to be expanded. Support of the U.S. BSRN program comes from several agencies, NOAA/National Weather Service (NWS), NOAA/Oceanic and Atmospheric Research (OAR), NASA, and the U.S. Department of Energy/Atmospheric Radiation Measurement (DOE/ARM), and is funded internationally by more than 15 participating countries that operate surface BSRN stations and contribute technical experts to the group's efforts. The BSRN data are being utilized in major satellite and GCM research programs mentioned earlier. The program was conceived in 1988, began operations in 1992, and is intended to operate indefinitely until there are no further extensive research needs for such data. Activities of BSRN are further summarized by *Ohmura et al.* [1998]. The BSRN program is part of WCRP and the Global Energy and Water Cycle Experiment (GEWEX).

3.2.3. Solar Radiation Calibration Facility

SRF Radiometric Standards Activity

Self-calibrating cavity radiometers (referred to as cavities) are the basic references for all CMDL broadband solar radiation measurements. Long-term performance of these sensors is checked and documented through regular comparisons with peer cavities from other private and public sector groups and agencies as well as other countries. Also, the CMDL reference cavities are periodically compared with the World Standard Group (WSG) radiometers that are kept at the World Radiation Center in Davos, Switzerland. NOAA has participated in these periodic comparisons since they began more than 30 years ago. These International Pyrheliometer Comparisons (IPCs) are sponsored by the World Meteorological Organization (WMO). The most recent intercomparison, IPC IX, was conducted at the World Radiation Center in Davos from September 25 to October 13, 2000. CMDL, as a WMO Region IV radiation center, participated in the comparison with three NOAA Solar Radiation Facility (SRF) cavities, TMI67502, AHF28553, and AWX32448. The SRF reference cavities were compared with the WSG radiometers, and ratios of measurements from these cavity radiometers to the World Radiation Reference (WRR) were established. The ratios for the three SRF references that participated in IPC IX are listed in Table 3.8. Results of recent annual comparisons of CMDL reference cavities with peer cavities at the National Renewable Energy Laboratory (NREL) in Golden, Colorado, are also listed. The NREL pyrheliometer comparisons (NPCs) provide an annual check of the NOAA references with NREL references.

SRF Special Projects

A self-calibrating cavity radiometer equipped with a calcium fluoride window was deployed at the CMDL BAO BSRN site in August 2000 and has operated continuously since installation. Additional installations at other CMDL BSRN sites are planned. Other special projects during the 2000-2001 period included a comparison of a CMDL reference radiometer with reference radiometers of the Australian Bureau of Meteorology during May 2000. The comparison was conducted at Alice Springs, Australia, after CMDL participation in the Biennial BSRN Meeting held in Melbourne, Australia, in early May 2000. SRF also completed specification and procurement of solar radiation monitoring hardware and sensors for a number of inter-

TABLE 3.8. Ratios of Measurements from Three SRF Reference Cavity Radiometers to Measurements from WSG and Peer Radiometers, Obtained During Pyrheliometer Comparisons

Pyrheliometer Comparison	TMI 67502	AHF 28553	AWX 32448
IPC VIII (1995)	0.99869	0.99756	
NPC 1998		0.99783	
NPC 1999		0.99741	1.00086
IPC IX (2000)	0.99966	0.99733	1.00038
NPC 2001		0.99704	1.00073

national projects during 2000-2001. These projects included ACE-Asia, BSRN sites (Algeria, South Africa, and Russia), and Global Atmospheric Watch (GAW) baseline sites (Algeria, Argentina, Brazil, and Indonesia). Support for various CMDL/STAR group field campaigns (albedo measurement, sunphotometry, ACE-Asia, and ARM) was also provided. A report of the SRF historical maintenance of radiometric references, characterization, and calibration of sensors used at CMDL monitoring sites was published in March 2000 [*Nelson*, 2000]. Collaboration was undertaken with other authors on publications investigating pyrano-meter zero-offset effects and utilization of broadband pyranometer data to model UV irradiances [e.g., *Dutton et al.*, 2001].

3.2.4. Monitoring Aerosol Optical Depth

BRW and SPO

Background. Atmospheric aerosols affect the Earth's radiation budget directly through interactions with solar and terrestrial radiation and indirectly as cloud condensation and ice nuclei. While the impact of aerosols is probably most pronounced downwind of midlatitude industrial complexes [e.g., *Charlson et al.*, 1992], high-latitude regions are also sensitive to variations in atmospheric turbidity. This is especially true in the Arctic when airborne pollutants and dust from Eurasia are transported poleward, and whereas aerosols tend to have a cooling effect at low and middle latitudes, their radiative effects are less certain at high latitudes. The effects of high surface albedo in conjunction with low solar angles may cause a warming instead [*Cacciari et al.*, 2000]. The focus of the CMDL aerosol program is to characterize the means, variability, and trends of aerosols regionally. A further goal is to understand the factors that control the distribution of aerosols and their radiative properties.

Need for monitoring. In 1998 the Scientific Committee on Antarctic Research (SCAR) recognized the importance of polar aerosol characterization and recommended the establishment of an international network of solar spectrophotometers to monitor aerosol optical depth (AOD) at high southern latitudes. Such a network now exists, and some participating countries also maintain sites in the Arctic, thus providing a polar perspective. CMDL has monitored aerosol properties at two polar sites (BRW and SPO), since the mid-1970s. An overview of these activities is given by *Stone* [2000] and references therein. Histori-cally, ground-based in situ properties of aerosols were derived with nephelometer measurements [e.g., *Bodhaine*, 1992, 1996]. In recent years a strategy was adopted to relate chemical and physical properties by means of simultaneous size-selective sampling, allowing observed aerosol properties to be correlated with atmospheric cycles of specific chemical species [*Ogren*, 1995]. In addition, CMDL has monitored effective visible (500-nm) aerosol optical depth at BRW and SPO. The derivation utilizes data from pyrheliometers fitted with moderately wideband filters [*Dutton and Christy*, 1992]. While not a precise measure, the long time series have been valuable for the definition of seasonal cycles and for the documentation of episodic perturbations caused by the presence of volcanic aerosols.

Figure 3.18 highlights the extreme increases in visible extinction at polar latitudes, which were caused by the eruptions of El Chichón and Pinatubo in 1983 and 1991, respectively. After major eruptions, volcanic aerosols are dispersed globally by stratospheric winds and then decay exponentially. Over polar regions, however, decay times tend to be longer [*Stone et al.*, 1993, 1994]. The prolonged lifetime of volcanic aerosols at high latitudes may result from unusual processes that occur within the polar vortex. Aerosols may persist if dynamical processes favor vaporization at high altitudes and regeneration of particles at lower altitudes [*Hofmann and Rosen*, 1987]. Also, natural elimination processes may be suppressed because mixing within the polar vortex is minimal. A limited number of spectral observations of aerosol extinction at BRW were used to derive some understanding of composition and size distributions of volcanic aerosols [*Dutton et al.*, 1984; *Stone et al.*, 1993]; however, quantifying the direct or indirect radiative forcing by volcanic aerosols is not yet possible because continuous observational records are lacking.

On an annual basis, Arctic haze [*Dutton et al.*, 1989] and Asian dust, and occasionally smoke from forest fires, influence the BRW record [*Stone*, 2002]. In recent decades, significant variability in the concentration of haze during spring at BRW has been observed. *Bodhaine and Dutton* [1993] documented a downward trend of Arctic haze during the 1980s when emissions of haze-forming pollutants in Eurasia may have decreased. However, a definitive explanation for the trend has not been given. While emission rates are certain to influence the distribution of haze, changes in atmospheric transport may also be a factor. Atmospheric circulation in this region has undergone
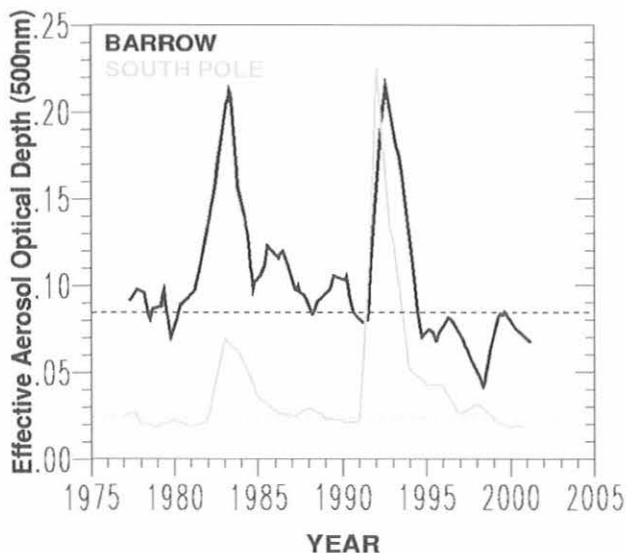
significant shifts in recent decades [*Stone*, 1997; *Stone et al.*, 2002]. In the future, closer attention will be given to the role of transport as it affects the evolution of specific aerosol types (i.e., haze, dust, smoke, or volcanic).

At SPO, intrusions of seasalt aerosols are observed when storms reach the high plateau from surrounding oceanic regions [*Bergin et al.*, 1998; *Bodhaine*, 1992]. Although the direct radiative impact of such aerosols can be studied theoretically [e.g., *Cacciari et al.*, 2000], verification of results will require more continuous monitoring of aerosols in conjunction with measurements of the surface radiation budget. The indirect effects of aerosols (i.e., their role in influencing cloud morphology) has yet to be investigated and will also require correlative studies using highly resolved data sets.

New projects. To address the aforementioned needs, CMDL has enhanced its monitoring programs at BRW and SPO to include continuous measurements of spectral AOD during sunlit periods using photometers fitted with narrowband (10-nm) 1-in-diameter interference filters. Because background values of Arctic and Antarctic optical depths are small (see Figure 3.18), the determination of spectral AOD at BRW and SPO requires extraordinary care to produce high-quality data sets. The main features of these new programs include the following:

- Deployment of four-channel, sun-tracking photometers to measure extinction at nominal wavelengths centered at 412, 500, 675, and 862 nm (368, 412, 500, and 865 nm prior to July 2000).
- One-minute acquisition of raw voltages.
- Acquisition of ancillary data to assure data quality.
- Merging of photometric data with station pressure and temperature to account for Rayleigh scattering using the method of *Bodhaine et al.* [1999], and to correct airmass for refraction at low solar angles.
- Thermally controlling instruments to within ±1°C of established set points to assure filter stability and longevity.
- Merging of daily ozone and NO_2 data to account for absorption by these constituents.
- Performing pre- and post-season calibrations at MLO, with the Langley method, to document and correct for any filter degradation.
- Careful screening of data with an interactive, graphical editor to eliminate cloud contamination, and by reference to independent radiation data.

Preliminary results. Preliminary processing of data from SPO beginning January 2000 and from BRW beginning March 2000 indicates significant contrasts in aerosol concentration as well as in spectral signature. Time series of 1-min-resolved AOD are now being generated for detailed investigations of the direct and indirect radiative forcing of aerosols. In addition, it is possible to characterize varying types of particles, thus providing a basis to parameterize aerosols in climate models. Figure 3.19 shows a time series of spectral AODs and derived Ångström exponents (å) during March-April 2000. Values of å are defined by a power law, where $AOD \propto \lambda^{-å}$. In this case, Ångström exponents were derived for the channel pairs labeled in the lower panel. Generally, Ångström exponents are inversely proportional to mean particle size.

Fig. 3.18. Time series of effective visible aerosol optical depth (AOD) derived from filtered pyrheliometric measurements made at BRW and SPO. Two-year smoothed values are shown to highlight the periods of increased AOD following the eruptions of El Chichón and Pinatubo. The dashed lines represent the long-term average background conditions at each site.
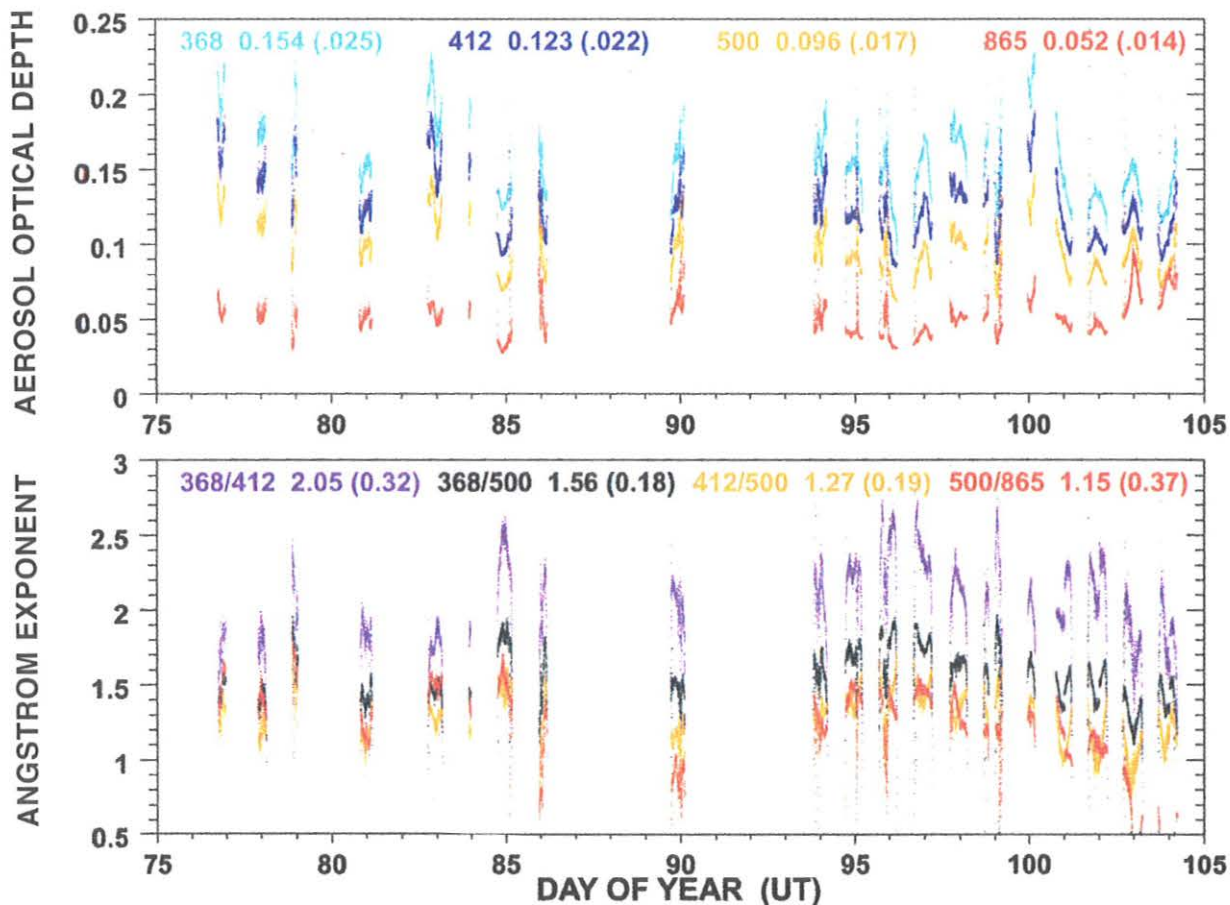
Fig. 3.19. (a) Time series of 1-min spectral aerosol optical depth derived from measurements made with the CMDL SP01-A four-ch annel sunphotometer at Barrow, Alaska, during March-April 2000, and (b) Ångström exponents, calculated for the channel pairs indicate d in the legend. Means and (standard deviations) for the period are also given in the respective legends.

Similar time series from SPO (not shown) reveal less variability. The 500-nm optical depths at SPO are in the range 0.015-0.025, and Ångström exponents are significantly larger than at BRW, indicating the dominance of small particles at SPO.

Previously, the main features of the annual aerosol cycle at the surface at SPO were established with the combination of nephelometer data and derived values of Ångström exponent to infer particle size spectra. Clear signatures distinguish modes of coarse (sodium) and small (sulfur) particles, where peak sodium concentrations are associated with the rapid, poleward transport of seasalt from oceanic regions, principally the Weddell and Ross Seas. *Bergin et al.* [1998] showed how in situ aerosol measurements from South Pole could be correlated with records of chemical species captured in firn samples to study past climate. In the future, correlating surface and columnar properties of aerosols will lead to better interpretation of the firn data in terms of past climate forcing. According to *Bergin et al.* [1998], the possibility exists to resolve, on a seasonal basis, a record of aerosol properties dating from 1000 years ago.

Moreover, the natural (e.g., seasalt, biogenic, or volcanic) signatures should be distinguishable from anthropogenic ones.

Goals. The large spatial and temporal differences observed in polar records of aerosols highlight the importance of assimilating similar data from other sites to better characterize polar aerosols spatially and temporally. Initially, efforts should focus on establishment of "background" values of AOD in both polar regions, from which future perturbations, whether from volcanic activity, anthropogenic factors, or other factors, can be referenced. As evidenced in Figure 3.18, the high latitudes are currently experiencing a period of volcanic quiescence; no major eruptions have occurred in recent years, and AOD values are below historical minima (dashed lines indicate the long-term background). Therefore, the opportunity to establish baseline values of spectral AOD and derived properties, such as size spectra [e.g., *King et al.*, 1978], now exists. Once natural seasonal variations are understood over broad spatial scales, climate forcing by polar aerosols can be assessed with greater confidence. Only through inter-

national cooperation can adequate information be provided to modelers challenged to improve aerosol parameterizations as called for by the Intergovernmental Panel on Climate Change (IPCC) [*Houghton et al.*, 2001]. Also, the remote sensing community will benefit from these efforts because valid retrievals of surface and atmospheric properties require that accurate corrections be made to account for extinction by aerosol particles in the atmosphere.

Steps have been taken by researchers from several countries to coordinate their polar activities in this regard. Participating countries include Italy, Australia, Germany, Japan, United States, Russia, England, and France. Although a variety of photometers have been used and the data records are of variable length and continuity, there is agreement that an archive of polar AOD data will provide the basis for better characterization of polar aerosols spatially and temporally. Once these data are assimilated, analyses in conjunction with model studies should provide the means to more accurately quantify the peculiar radiative effects of aerosols at high latitudes. The immediate objective of this group is to convene a workshop to set goals for future collaborations and to establish such an archive that may be modeled after the Baseline Surface Radiation Network protocols [*Ohmura et al.*, 1998].

Bermuda, BAO, Boulder, and Kwajalein

Routine monitoring of aerosol optical depth continued at Bermuda, BAO, Boulder, and Kwajalein with multi-filter rotating shadowband radiometers (MFRSRs) and tracking sunphotometers. MFRSRs were first installed at Bermuda in February 1996, BAO in August 1996, Boulder David Skaggs Research Center (DSRC) laboratory in July 1999, and Kwajalein in April 1996. Data are downloaded by telephone and stored in the STAR data archive. With the intent of eventually replacing all MFRSRs with tracking sunphotometers, the MFRSRs at BAO and Kwajalein were removed in August 2000. Optical depth data analysis for all stations is performed routinely by first finding mornings and afternoons that produce acceptable Langley plots so that a time series of V_o values (instrument calibration constant) may be formed. This V_o time series is then smoothed, and a new V_o is calculated from the smoothed time series for every 1-min data point in the data set. These new V_o values along with the 1-min direct-beam irradiance data are used to calculate new total optical depth values. Finally, aerosol optical depth is calculated by subtracting other components of optical depth, such as that due to Rayleigh scattering, ozone absorption, and absorption by other gases.

3.2.5. MLO AND BOULDER UV SPECTRORADIOMETERS

Solar radiation measured at the Earth's surface depends on the absorption and scattering of the atmosphere, the Earth-Sun distance, and the irradiance of the Sun. The UV portion of the spectrum is controlled primarily by Rayleigh scattering by air molecules, scattering by clouds, and absorption by ozone. Under clear-sky conditions, at a given site and for a given solar zenith angle (SZA), variations in UV are strongly correlated (inversely) with variations in total ozone. As part of the Network for the Detection of Stratospheric Change (NDSC) a UV spectroradiometer

(labeled UVL) was installed at MLO (19.533°N, 155.578°W, 3.4 km) in July 1995. This instrument operated until June 1997, and a new instrument (UV3) was installed in November 1997 and continues in operation at MLO to the present.

To provide an additional site for these studies, a UV spectroradiometer (UVL, the same instrument initially installed at MLO) was installed at the Boulder laboratory (39.991°N, 105.261°W, 1.62 km) in June 1998. This instrument was replaced with a new instrument (UV4) in September 1999. Finally, the UV4 instrument was replaced with another new instrument (UV5) in August 2001. Of note is the fact that UV5 participated in an instrument comparison at the Table Mountain, Colorado, research site during June-July 2001, immediately before it was installed in Boulder. This instrument has continued in operation at Boulder to the present. All of these instruments (UVL, UV3, UV4, UV5) were constructed by the National Institute of Water and Atmosphere (NIWA) group at Lauder, New Zealand, under a cooperative program agreement with CMDL. The various spectroradiometers used at MLO and Boulder are summarized in Table 3.9. The goal of this program is to study the relationship between UV and ozone and to determine long-term trends, if any, in UV. MLO and Boulder are both excellent sites for this study because of the prevalence of clear skies and the collocation of Dobson ozone spectrophotometers.

Data analysis is accomplished through the use of software provided by the NIWA-Lauder research group. This software runs on IBM PC-type machines and is designed to read the raw monthly data files, apply calibrations, and calculate a UV spectrum for each observation. The program asks for instrument name (such as UVL), year, month, and block number as input while running, and therefore it is necessary to know which instrument was located at a particular location and time in order to process the data. The program automatically calculates certain integrated spectra such as UVB, UVA, and erythema, and has the capability of calculating any special action spectrum, such as deoxyribonucleic acid (DNA) or vitamin D. The erythema spectrum [*McKinlay and Diffey*, 1987] is important because it represents the response function of human skin to UV radiation, and it is used in studies of sunburning. The vitamin D spectrum [*MacLaughlin et al.*, 1982] is important because exposure to sunlight causes the photosynthesis of vitamin D in human skin. In this report

TABLE 3.9. UV Spectroradiometers at MLO and Boulder

Instrument	Date
MLO	
UVL	July 1995–June 1997
UV3	November 1997–present
Boulder	
UVL	June 1998–September 1999
UV4	September 1999–August 2001
UV5	August 2001–present

results are presented only for erythema because at the time of this writing there is no general agreement among researchers on the correct vitamin D spectrum for use in these calculations.

UV data from MLO were presented by *Bodhaine et al.* [1996, 1997], *McKenzie et al.* [2001], and briefly in *CMDL Summary Reports No. 23, 24, and 25* [*Hofmann et al.*, 1996, 1998; *Schnell et al.*, 2001]. The UV irradiances measured at MLO are much larger than at low-altitude midlatitude locations, primarily because of less Rayleigh scattering, but also because of lower column ozone in the subtropics. Boulder can be considered a midaltitude site, since it lies about half-way between MLO and sea level. Here the complete data set is presented, selected for clear mornings at MLO, and clear mornings and afternoons at Boulder. Clear mornings occur at MLO approximately 60% of the time, providing an excellent site for solar radiation measurements. Clear skies occur less often, and UV data tend to be noisier, at Boulder. Clear afternoons are accepted in addition to clear mornings at Boulder in order to increase the number of data points. All processed spectral data are available from the solar radiation division of the CMDL program.

Instrumentation

The UVL spectroradiometer was described by *McKenzie et al.* [1992] and *Bodhaine et al.* [1997]. Briefly, a diffuser designed to minimize cosine error and machined from Teflon is mounted as a horizontal incidence receptor to view the whole sky. For UVL, stepper-motor-driven gratings cover the spectral range of 290-450 nm in a single scan with a bandpass of about 1 nm. The newer instruments (UV3, UV4, and UV5) cover the range 285-450 nm with a bandpass of about 0.8 nm, and use fiber optic cables to transmit the light from the sensor to the spectrometer. A complete forward scan for UVL requires about 3 min. The UV3, UV4, and UV5 instruments do a backward scan and then a forward scan centered at the desired SZA, and therefore require about 6 min for a complete measurement. All instruments are programmed to perform scans every 5° of SZA during daytime hours, starting at 95° SZA in the morning and ending at 95° SZA in the afternoon. During midday for 2.5 hours the sampling interval is changed to once every 15 min because the SZA changes slowly during that time.

Absolute calibrations of the spectroradiometers are performed at approximately 6-mo intervals with 1000-W FEL lamps traceable to NIST standards. A dedicated calibration bench is set up at MLO for these calibrations. The Boulder instrument is calibrated by NOAA's Surface Radiation Research Branch (SRRB) with a portable 1000-W lamp calibrator. Weekly stability calibrations are performed at both sites with mercury lamps for wavelength calibration and 45-W standard lamps for long-term stability checks. The long-term accuracy of the spectroradiometer systems is expected to be better than ±5%.

Data Analysis

For the following analyses, UV spectroradiometer data for 45° and 65° SZA were chosen for clear mornings at MLO during the July 1995-October 2001 time period. This gives approximately 6.5 years of data, and includes ozone values in the range of about 200-350 Dobson units (DU).

For Boulder data, 65° SZA and the period July 1998-October 2001 were used, covering an ozone range of about 220-400 DU. Note that 45° and 65° are the smallest SZAs attained year round at the MLO and Boulder sites, respectively. The 65° SZA data are used for comparisons between MLO and Boulder. Clear mornings at MLO and Boulder were determined in the same manner as in previous studies; that is, a day was accepted as a clear day at MLO if the sky was cloudless from dawn through the time of the desired scan, and if Dobson ozone data were available for that morning. At Boulder, generally, the sky had to be clear at the time of the scan, Dobson ozone data had to be available, and clear afternoons were also accepted. The Dobson ozone observation closest to the time of the UV scan was used. Figures 3.20 and 3.21 show MLO ozone and UV erythema data for July 1995-October 2001 for 45° and 65° SZAs, respectively. Figure 3.22 shows similar data for Boulder for June 1998-October 2001 for 65° SZA. Erythemal radiation data were obtained from the spectroradiometer data for both sites by applying the erythemal weighting function of *McKinlay and Diffey* [1987] and integrating over wavelength for each scan, as discussed by *Bodhaine et al.* [1997]. The inverse relationship of UV erythema and ozone at both sites is apparent.
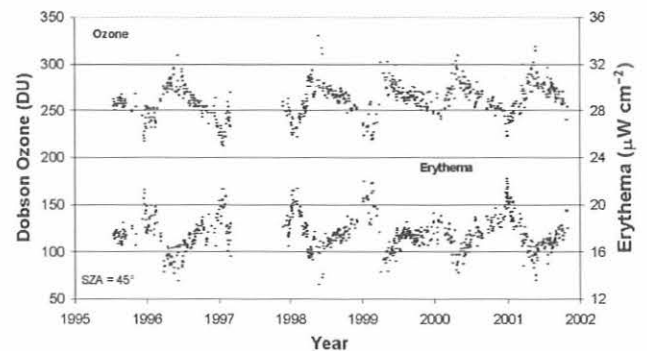

Fig. 3.20. Erythemal irradiance at 45° SZA (bottom) and total ozone (top) for clear-sky mornings at MLO over the time period July 1995-October 2001.
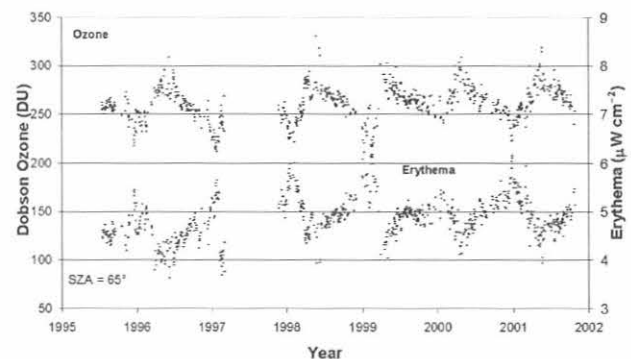

Fig. 3.21. Erythemal irradiance at 65° SZA (bottom) and total ozone (top) for clear-sky mornings at MLO over the time period July 1995-October 2001.
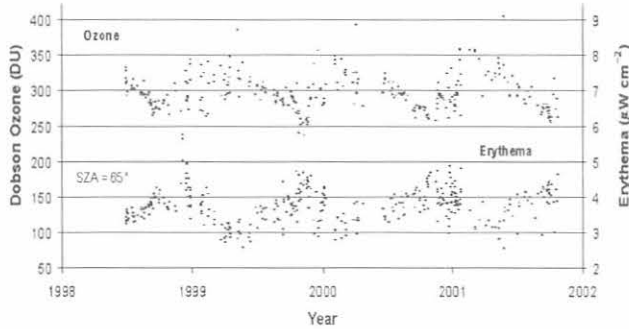
Fig. 3.22. Erythemal irradiance at 65° SZA (bottom) and total ozone (top) for clear-sky mornings and afternoons at Boulder over the time period June 1998-October 2001.
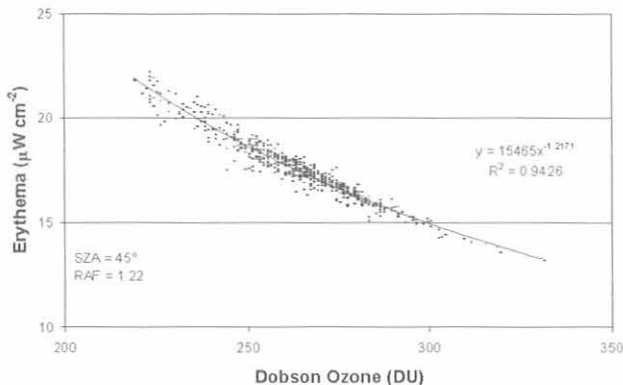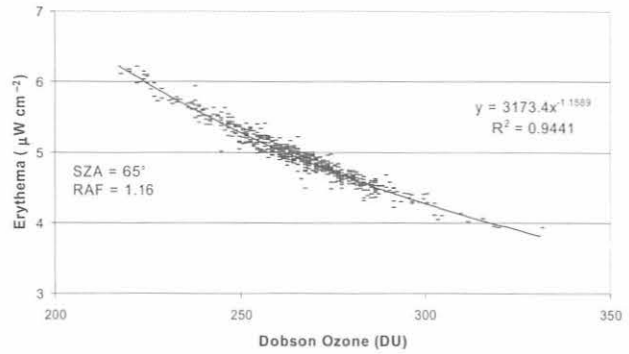

Fig. 3.24. Power law regression between erythemal irradiance at 65° SZA and Dobson total ozone at MLO over the time period November 1997-October 2001. The graph is plotted on a linear scale to facilitate reading the units. The exponent of the power law function (1.16) gives the RAF.
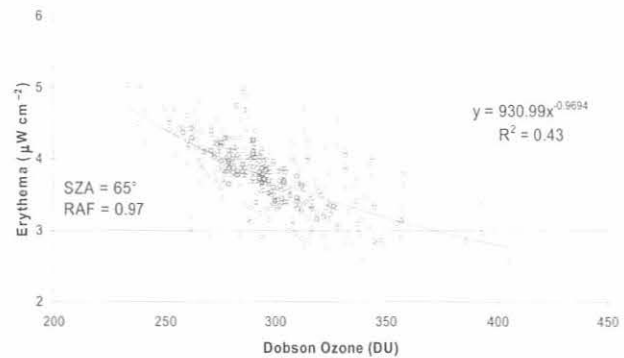
Figures 3.23 and 3.24 show the relationships between UV erythema and ozone at MLO for November 1997-October 2001 for 45° and 65° SZAs, respectively, corresponding to the most recent instrument configuration. Figure 3.25 shows the relationship between UV erythema and ozone at Boulder for the time period June 1998-October 2001 for 65° SZA. The radiative amplification factor (RAF), defined as the percent change of UV (erythemal) irradiance divided by the percent change of total ozone, was calculated for both sites, using the power-law formulation of *Madronich* [1993]: RAF = $-\Delta\ln(I)/\Delta\ln(O_3)$, where I is UV irradiance. The RAF is simply the slope of a straight-line fit on a log-log plot. The data for Boulder are subject to more scatter because of more variable sky conditions than at MLO. The scatter in the Boulder data can be reduced significantly by plotting the ratio of erythemal to 340-nm irradiance against ozone. Since ozone effects are essentially absent at 340 nm, this reduces the effects of aerosols, clouds, and other atmospheric variations.

Fig. 3.25. Power law regression between erythemal irradiance at 65° SZA and Dobson total ozone at Boulder over the time period June 1998-October 2001. The graph is plotted on a linear scale to facilitate reading the units. The exponent of the power law function (0.97) gives the RAF.

Fig. 3.23. Power law regression between erythemal irradiance at 45° SZA and Dobson total ozone at MLO over the time period November 1997-October 2001. The graph is plotted on a linear scale to facilitate reading the units. The exponent of the power law function (1.22) gives the RAF.

Figure 3.26 shows the RAF at MLO as a function of wavelength for SZAs of 45° and 65°. In general the RAF decreases with increasing wavelength, and the ozone dependence is negligible for 340 nm. It is clear from the figure that the RAF is consistently larger for larger SZAs. Figure 3.27 shows the RAF at MLO as a function of SZA for SZAs in the range 15°-85°. The apparent break in the slope of the data for SZAs <35° is most likely caused by the fact that smaller numbers of data points are available for SZAs of 15°-35° because these smaller SZAs are not reached during winter months, which means that somewhat different ranges of ozone data are used for those data points.

Conclusions

- Erythemal irradiance calculated from UV spectra at MLO and Boulder is inversely correlated with Dobson total ozone.
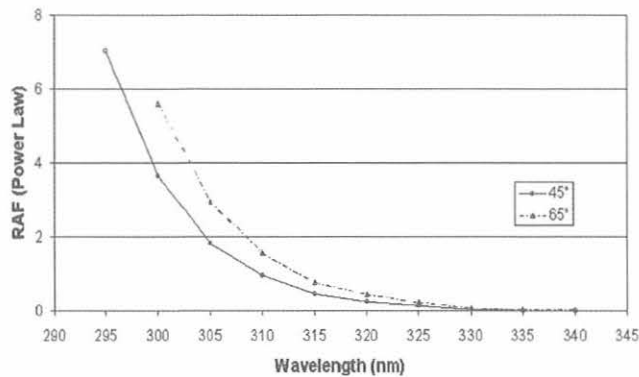- No significant trend in UV irradiance may be inferred because of the limited time period.

Fig. 3.26. Erythema RAF as a function of wavelength at MLO for 45° and 65° SZAs for November 1997-October 2001.
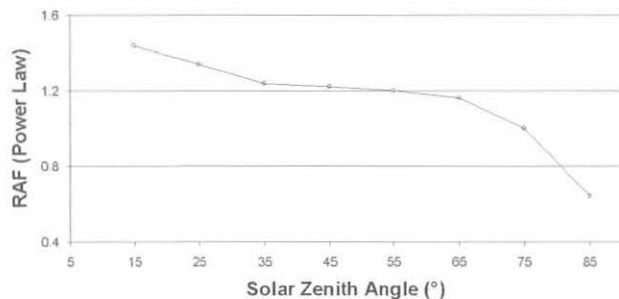

Fig. 3.27. Erythema RAF as a function of SZA at MLO for November 1997-October 2001.

3.2.6. BROADBAND UV

As part of the various programs being operated by the CMDL STAR group, broadband UV instruments (Yankee UVB-1) have been in use at MLO, BRW, BAO, Bermuda, Kwajalein, and Boulder. These instruments have been compared at various times with the MLO UV spectroradiometer that was installed at MLO in July 1995 [*Bodhaine et al.*, 1998]. The calibration of the broadband instrument, reporting in erythemal units, is strongly dependent on total ozone because the erythemal response defined for human skin is significantly different from the spectral response of the broadband instrument [*Bodhaine et al.*, 1998]. When a broadband instrument is placed in the field, it is necessary to know the calibration as a function of ozone to determine accurate erythemal irradiance. However, the manufacturers of broadband instruments do not generally provide information on the ozone dependence of the calibration. Because of these uncertainties the broadband measurement program was suspended on December 31, 2000, and the only instruments remaining in operation are those at MLO and Boulder, the locations of UV spectroradiometers.

3.2.7. RADIATIVE EFFECTS OF AN EARLIER SPRING SNOWMELT IN NORTHERN ALASKA

Regional climate models fail to adequately simulate the complicated feedbacks that are peculiar to the Arctic. Empirical analyses of data from BRW and other Alaska North Slope sites provide a better physical understanding of climate change in this region. In particular, data from BRW reveal important factors that determine the annual cycle of snow cover there and the radiative perturbations caused by variations in surface albedo. What modelers refer to as a "temperature-albedo feedback" is evaluated in response to an advance in the date when the snow melts in spring on the North Slope. The timing of snowmelt is found to have a significant influence on the net surface radiation budget (NSRB) and temperature regime there.

Trend analyses of climate records from several northern Alaskan sites show variations on seasonal to decadal time scales. Time series have been correlated with synoptic-scale atmospheric circulation patterns to understand the interaction of dynamical and radiative processes. *Dutton and Endres* [1991] and *CMDL Summary Report No. 25* [*Schnell et al.*, 2001; pp. 65-67] give a historical overview of CMDL's monitoring of snowmelt at BRW. The detection and attribution of climate change in the vicinity of BRW are discussed in several published papers [e.g., *Stone*, 1997, 2001; *Lawrimore et al.*, 2001; *Stone et al.*, 2001, 2002]. Only the main results are summarized here.

A trend toward an earlier disappearance of snow in spring (i.e., melt date) in northern Alaska has been documented. Correlated variations in the timing of snowmelt are revealed in several independent records. Since the mid-1960s the spring melt has advanced by about 8.0 (±4.0) days over a significant region of northern Alaska, as shown in Figure 3.28. Earlier spring snowmelt is, in part, the consequence of decreased snowfall in winter, followed by warmer, cloudier spring conditions [e.g., *Stone et al.*, 2002].

In turn, changes in snowfall, temperature, and cloudiness are attributed to variations, or shifts, in regional circulation patterns, as is illustrated in Figure 3.29. Back-trajectories [*Harris and Kahl*, 1994] were used in the analyses. For example, snowfall, measured in units of water equivalent precipitation (WEPC), is reduced when the advection of relatively warm, moist air from the north Pacific Ocean is blocked by a high-pressure system centered northwest of BRW during winter (Figure 3.29b versus 3.29a). Warm spring conditions prevail if there is more frequent flow from the south, as indicated in Figures 3.29d and 3.29f versus 3.29c and 3.29e. The combination would result in an earlier melting of the snow pack during May-June.

One consequence of an earlier melt is the increase in the NSRB that tends to warm the near-surface air through an albedo feedback. Table 3.10 contrasts the NSRB and temperatures for 3 early versus 3 late years of snowmelt at BRW. An early melt enhances the gain of radiant energy at the surface, warming the air in turn. In this case, a 2-wk advance in the melt date in June increases the NSRB by 25%, with an associated rise in temperature of about 1°. After an early melt, slight warming persists through August on average.
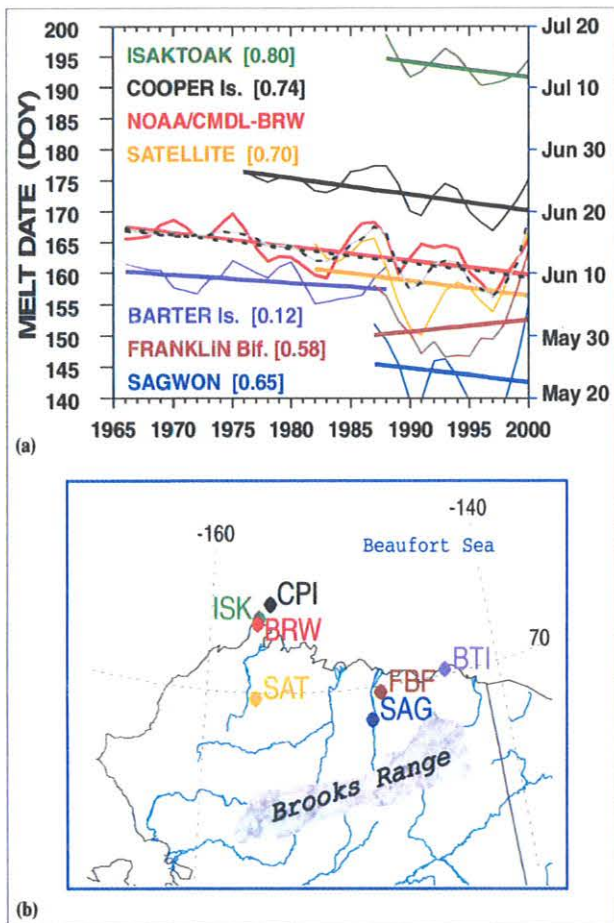
Fig. 3.28. (a) Analyses of six independent time series of measured or proxy melt dates (day of year) compared with the 1966-2000 CMDL BRW record (in red). Five-year smoothed time series and linear fits are shown. Each is cross correlated with the BRW record with coefficients indicated in brackets for individual sites that are labeled and color-coded. The dashed analysis (unlabeled) is for an ensemble average of the 142 station-years, normalized to the BRW timeframe. (b) Map of Alaska's North Slope showing the location of sites making up the ensemble [from *Stone et al.*, 2002].

This last result supports theoretical predictions of a positive feedback due to diminished snow and ice cover in the Arctic as a result of global warming. This temperature-albedo feedback is expected to enhance warming over the northern high latitudes [e.g., *Serreze et al.*, 2000]. The CMDL BRW observations are found to be representative of northern Alaska and establish baseline conditions for evaluating future climate change in this sensitive region of the Arctic. Also, the time series will be useful for verifying regional climate model simulations and for validating remote sensing algorithms being developed to monitor surface temperature and albedo needed to estimate the surface radiation balance [*Key et al.*, 1997]. Continued monitoring of the snow cycle at BRW and the factors that determine it is essential. The timing of the spring melt on a pan-Arctic scale will influence not only the regional energy budget (temperature regime) but also biogeochemical cycles that affect the sources and sinks of methane and carbon dioxide, imposing other potential climate effects [e.g., *Oechel et al.*, 1995; *Myneni et al.*, 1997]. Already, the changing Arctic climate is affecting indigenous people who depend on fishing and hunting grounds that are being modified [*Morrison et al.*, 2001].

3.2.8. UV VARIABILITY IN THE ALASKAN ARCTIC

Objectives

With support from the Arctic Research Initiative (ARI) in 1997 and 1998, a network of three UV meters was installed in Alaska, at BRW and at the NWS offices at Nome and St. Paul Island. The objective of this network is to provide information on the geographical distribution and temporal trends of UV radiation at climatically diverse sites in the Arctic.

Methods and Results

This network was maintained with support from ARI in FY 2000 and 2001, and included annual calibrations at the manufacturer. In addition, LI-COR sensors and data acquisition systems were installed at Nome and St. Paul Island to measure both downwelling and upwelling photosynthetically active radiation (PAR). The data from the upward and downward sensors can be used to provide information on changes in albedo to aid in the assessment of UV variability. Further information about the instruments, site descriptions, or requests for data access can be obtained from CMDL's website (http://www.cmdl.noaa.gov/star/index.html).

Table 3.11 provides an overview of the monitoring periods for 1998-2001 at the three sites. The table also provides information on the number of days with good and bad data, calibration dates at Biospherical Instruments Inc. (BSI), and comments. With the exception of Barrow and Nome for 2000, there has been less than a 10% loss in data during the monitoring period each year. In 2000, the losses of data at BRW and Nome were due to a PC malfunction and not to instrument failure. Unfortunately, since data are downloaded onto a PC, there is no way to retrieve lost data.

Of all three UV meters, the BRW instrument has exhibited the best stability, with a ±4% drift or less on four of the channels (305, 320, 340, and 380 nm). The stability of any one channel is evaluated by comparison of calibration factors, which are provided after the instruments undergo an absolute calibration each winter by the manufacturer. Unfortunately, there is a significant drift in the 313-nm channel for all three instruments, where the calibration factors have changed by as much as 40% from one year to the next. Therefore, until the problem is resolved and data are corrected, any interpretation about dose rates at 313 nm is not possible. As noted in Table 3.11, a channel was changed in the UV instrument at St. Paul for 1999 and 2000. The replacement of any channel makes an evaluation of stability problematic. In addition, when the St. Paul instrument was returned to the manufacturer in December 1999 for calibration, the diffuser was found to have leaked. This would affect all channels within the instrument's housing and therefore invalidate a comparison of calibration factors from the previous year. Although Nome had only

Late Melt Date at BRW
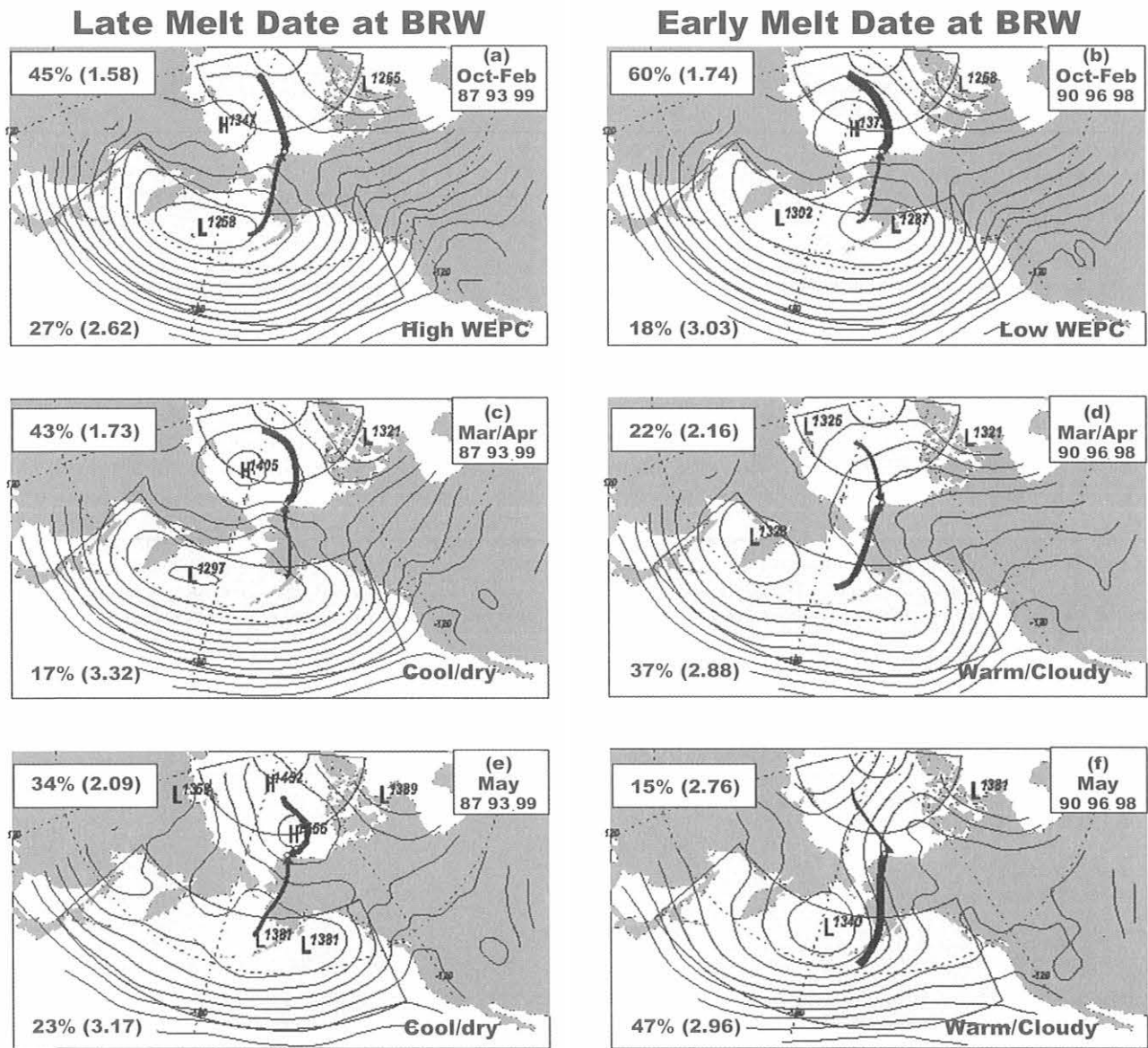
Early Melt Date at BRW

Fig. 3.29. Averaged, 1500-m back trajectories relative to BRW and corresponding 850-hPa geopotential height fields for (a) October-February 1987, 1993, and 1999, (b) October-February 1990, 1996, and 1998, (c) March-April 1987, 1993, and 1999, (d) March-April 1990, 1996, and 1998, (e) May 1987, 1993, and 1999, and (f) May 1990, 1996, and 1998, showing the multiyear, seasonal average, 5-day air flow from source regions indicated as lightly shaded areas. The percent frequency of transport and average transit time from each source region (in days) are indicated in the legends. In each panel the upper left legend relates to flow from the Arctic source region, and the lower left legend relates to flow from the North Pacific source region. The thickness of trajectories is proportional to their frequency and their lengths inversely proportional to average speed along track. These average trajectories represent the mean flow of all individual trajectories from the respective regions over each period indicated in the upper right-hand legend. The late melt dates at BRW were due to higher October-February snowfall (measured as water equivalent precipitation (WEPC)), followed by cool/dry spring weather conditions, compared with early melt date years. A more detailed explanation is given by *Stone et al.* [2002].

the 320-nm channel replaced in December 1998, an analysis of the calibration factors shows a significant drift in the 305-nm channel (up to 18%) from one year to the next. Detailed information about the replacements of channels can be obtained from CMDL.

Despite the calibration issues, the data can be used to obtain a preliminary overview of the variability in UV at different latitudes in Alaska. Figure 3.30 provides a summary of the monthly average daily total energy (J m^{-2} nm^{-1}) for all three sites. Data for the 313-nm channel are not included because of the large changes of the calibration factors for that channel. In addition, for the Nome and St. Paul instruments, the 340-nm channel was substituted with a PAR channel, which is an integrated measurement across the 400-700 nm spectrum.

TABLE 3.10. Comparison of Net Surface Radiation Budget
and 2-m Air Temperatures for Late Versus
Early Years of Snowmelt at BRW

Years Sampled	Late Melt Date (1992, 1999, 2000)	Early Melt Date (1990, 1996, 1998)
Melt date (DOY)	164 (0.8)	150 (0.8)
NSRB (MJ m^{-2})		
June	306 (2)	385 (7)
May–August	860 (17)	970 (43)
T$_{2m}$ (°C)		
June	0.9 (0.59)	1.8 (0.36)
July–August	3.3 (0.62)	3.6 (0.87)

DOY, day of year; NSRB, net surface radiation budget (in units of total radiative energy); T$_{2m}$, air temperature at 2 m above ground level. Standard deviations are given in parentheses.

Therefore, there is no 340-nm channel for either Nome or St. Paul. Monthly averages were computed if there were 18 days or more per month with good data.

An annual variability in UV levels is clearly evident for all three sites, with maximum values for all wavelengths in May or June (Figure 3.30). Nome has the highest UV levels at 305 and 320 nm for all three years compared with BRW and St. Paul. Barrow is at the highest latitude of the three sites, and therefore would receive much less solar radiation over the course of the year, even when the Sun is above the horizon for 24 hours per day. St. Paul is usually under the influence of low-level stratus clouds, which would block more incoming UV radiation. Nome has many days that are spectacularly clear. The anomalously low UV levels at 305 nm at St. Paul in the year 2000 are most likely due to a reduced sensitivity in that channel over the monitoring period, which necessitated its replacement in December (see Table 3.11).

In 2000, two LI-COR PAR sensors were installed at both St. Paul and Nome. A PAR sensor measures in the 400-700 nm solar spectrum. At both sites, one sensor faces upward (to measure downwelling or incident PAR) and the other sensor faces downward (to measure upwelling or reflected PAR). Table 3.12 summarizes the monitoring periods for the LI-COR sensors at St. Paul and Nome. Of the 338 days of data for St. Paul for 2000-2001, 212 were found to be good. The remaining 126 days had a downwelling PAR offset of 5 W m^{-2} or greater, which will be corrected later using a linear regression technique. This will enable all the data to be evaluated for 2000. At Nome, data were obtained for 232 days during 2000-2001; 225 of these were considered good days. The remaining 7 bad days were due to missing data. To investigate whether the LI-COR downwelling PAR is equivalent to the measurements obtained by the BSI PAR at

TABLE 3.11. Site Summary of UV Monitoring at Barrow, Nome, and St. Paul, for 1998-2001

	1998	1999	2000	2001
Barrow				
Start of monitoring	May 15	Feb. 3	Feb. 8	March 29
End of Monitoring	Oct. 27	Nov. 1	Oct. 16	Oct. 31
Good days	158	244	213	
Bad days (% loss)	4 (2.5%)	5 (2.1%)	24 (10.1%)	
Calibrations at BSI	April 30, 1998; Dec. 17, 1998	Dec. 9, 1999	Dec. 12, 2000	
Comments	Diffuser replaced in March 1998 and recalibrated April 1998		PC malfunction	
Nome				
Start of monitoring	June 11	Feb. 24	Feb. 9	Feb. 9
End of monitoring	Oct. 24	Oct. 28	Nov. 6	Nov. 9
Good days	134	226	237	
Bad days (% loss)	5 (3.6%)	10 (4.2%)	30 (11.2%)	
Calibrations at BSI	April 28, 1998	Feb. 16, 1999; Dec. 1999	Dec. 12, 2000	
Comments	320-nm channel replaced in Dec. 1998		22 days lost because of PC malfunction	
St. Paul				
Start of monitoring	June 6	March 1	March 7	Feb. 27
End of monitoring	Oct. 25	Oct. 14	Nov. 3	Nov. 7
Good days	135	211	231	
Bad days (% loss)	7 (5%)	16 (7%)	7 (2.9%)	
Calibrations at BSI	April 30, 1998	Feb. 16, 1999	Jan. 25, 2000; Dec. 12, 2000	
Comments	320-nm channel replaced in Dec. 1998	380-nm channel bad from March 1 to June 10, 1999	305-nm channel replaced prior to Dec. 2000 calibration	

Barrow

320 nm
340 nm
380 nm
305 nm

May-98 Sep-98 Jan-99 May-99 Sep-99 Jan-00 May-00 Sep-00

Nome

320 nm
380 nm
305 nm

May-98 Sep-98 Jan-99 May-99 Sep-99 Jan-00 May-00 Sep-00

St. Paul

320 nm
380 nm
305 nm

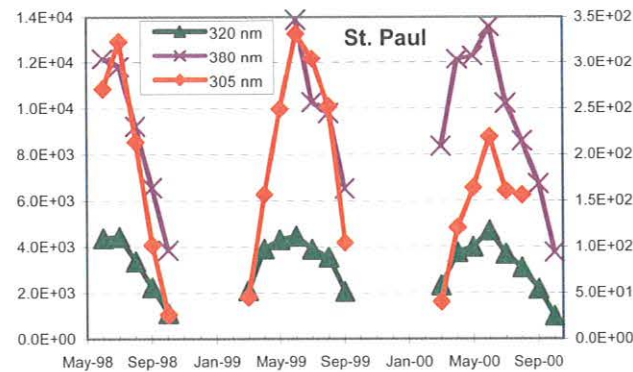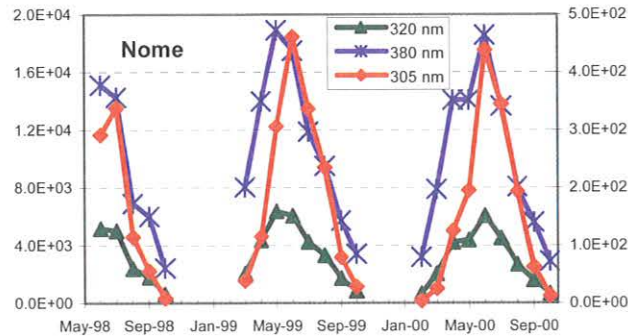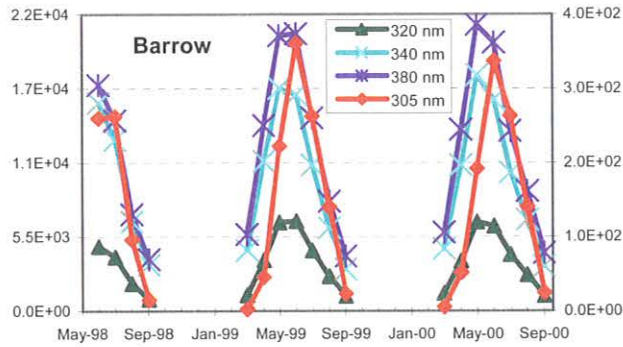May-98 Sep-98 Jan-99 May-99 Sep-99 Jan-00 May-00 Sep-00

Fig. 3.30. Monthly average of daily total energy (J m^{-2} nm^{-1}) for 1998-2000 for Barrow, Nome, and St. Paul. The 305-nm channel is plotted on the right scale.

TABLE 3.12. Summary of LI-COR PAR
Sensors at Nome and St. Paul

	2000	2001
	St. Paul	
Start of monitoring	March 29	March 19
End of monitoring	Nov. 20	Nov. 15
Good days	108	104
Bad days (% loss)	126 (54%)	0 (0%)
Comments	From Nov. 20, 2000, to March 19, 2001, the downwelling PAR was turned off and sensor returned for repair	
	Nome	
Start of monitoring	April 11	April 22
End of monitoring	Aug. 29	Dec. 31
Good days	147	78
Bad days (% loss)	7 (5%)	0 (0%)
Comments	From Aug. 29, 2000, to March 29, 2001, the upwelling PAR was turned off and sensor returned for repair	Although the upwelling PAR sensor was re-deployed on March 29, 2001, it was incorrectly installed until April 22

Nome and St. Paul, a linear regression was applied with the 1-min solar noon values obtained from each instrument. At St. Paul, both the LI-COR sensor and BSI PAR compare very well, with an average difference between the two instruments of only about 4% (comparing only the 2000 data). However, at Nome, the LI-COR PAR measurements are 65% below those obtained by the BSI PAR during 2000, and the sensitivity of the LI-COR sensor appeared to be decreasing in 2001. Fortunately, the LI-COR downwelling PAR at Nome and St. Paul track the BSI PAR (r^2 = 0.99 at both sites), so the Nome LI-COR downwelling data were easily corrected using the equation obtained from the linear regression analysis.

When a ratio of the reflected flux density to the incident flux density is taken, one can obtain the albedo of the surface. In the Arctic the surface albedo can vary from less than 0.05 to more than 0.9. Figure 3.31 provides a preliminary analysis of albedo for Nome and St. Paul for 2000 and up to the last day of processing in 2001 (July 8). The albedos were calculated with data from sunrise to sunset (or for solar zenith angles between 0° and 85°). Days showing an offset were not included in the analysis for this report. In 2000 the range of albedos at Nome was 0.03 to 0.52; at St. Paul, the range was 0.03 to 0.95. St. Paul shows much lower albedos for the March-April period in 2001. At first, this was thought to be due to an instrument malfunction. However, upon examination of the meteorological observations for St. Paul, the albedos in Figure 3.31 are representative of both snow depth and snowfall amounts that were reported in both years. St. Paul had snow depths of more than 0.6 m (2 ft) throughout March and into mid-April in 2000. Only on May 1 did the snow depths decrease from 10.2 cm (4 in) to a trace, thus the dramatic decrease seen in the albedo for St. Paul in early May 2000. In contrast, 2001 was a very dry year for St. Paul, with little to no snow accumulation from January through April. This is reflected in the low albedo values, with the exception of a peak on March 27, which is most likely due to the fact that St. Paul received 1.5 cm (0.6 in) of snow that day. The next few days had trace amounts of snowfall, and albedo was seen to decrease. Even a small
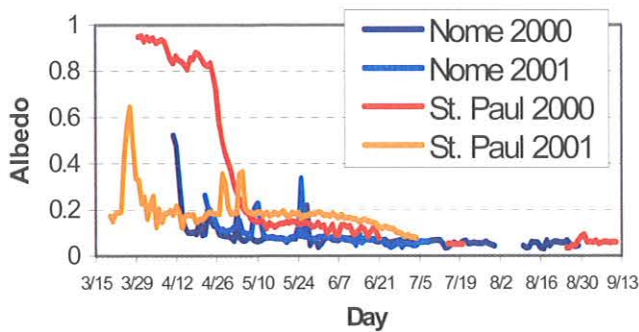
Fig. 3.31. Daily average albedo for Nome and St. Paul for 2000 and 2001, calculated with data from sunrise to sunset.

snowfall of 1.5 cm was enough for the albedo to increase threefold. At Nome the instrument did not operate correctly when it was installed in the early part of 2000. If it had, it is quite likely that measured albedos would have been as high as those seen for St. Paul because snow depths were greater than 0.6 m (2 ft) prior to April 4, but then plummeted to 12.7 cm (5 in) in less than 2 weeks, with little to no additional measurable precipitation after April 22, when the albedo reached its minimum levels. The large amount of missing data for the beginning of 2001 at Nome is due to bad weather that made it impossible for the site operator to install the repaired sensor, and when the sensor was installed in late March, it was erroneously inverted until April 22. Had the sensor been installed sooner and the inversion discovered earlier, more than likely the measured albedos would have been as high as St. Paul in 2000 because Nome received substantial snowfall that spring. The two peaks, on May 9 and again on May 25, are the result of two snowfall events, with more than 5.1 cm (2 in) measured each time.

Figure 3.32 shows the annual variability of daily total column ozone (Dobson units) obtained from the Total Ozone Mapping Spectrometer (TOMS) for the three sites for 1998–2000. Not shown on this plot is the ozone obtained from the Dobson spectrophotometer, which is located at BRW. A linear regression analysis between the Barrow TOMS and Dobson ozone indicates that for all 3 years both data sets are highly correlated, with $r^2 = 0.98$. However, TOMS consistently overestimates total column ozone by an average of 3.4% (averaged over all 3 years) and as high as 10%. As can be seen in Figure 3.32, for all three sites, the maximum levels of ozone occur in February or March and then decrease over the course of the summer, with minimum levels of ozone occurring in August, September, or October. Note the lower maximum ozone levels at all three sites in February and March 2000 as compared with 1998 and 1999. Low levels of ozone were also found during the SAGE III (Stratospheric Aerosol and Gas Experiment) Ozone Loss and Validation Experiment (SOLVE) in early March 2000, when scientists from the United States, Canada, Russia, and Japan measured ozone losses as high as 55% across much of Scandinavia and north central Siberia.

In conclusion, these three sites can be used to evaluate long-term trends in UV and ozone, and the data can be used by researchers doing impact-related analyses as well as by the satellite community to improve algorithms used to estimate UV. This is important because of expected ozone losses over the next 20 years or more due to a cooling stratosphere in the Arctic region, with potential impacts on human health and on the marine and terrestrial ecosystems.

3.2.9. DATA PROCESSING

Solar radiation data are currently being monitored by STAR at 11 sites: the four CMDL baseline observatories (BRW, MLO, SMO and SPO); three BSRN sites (BAO,
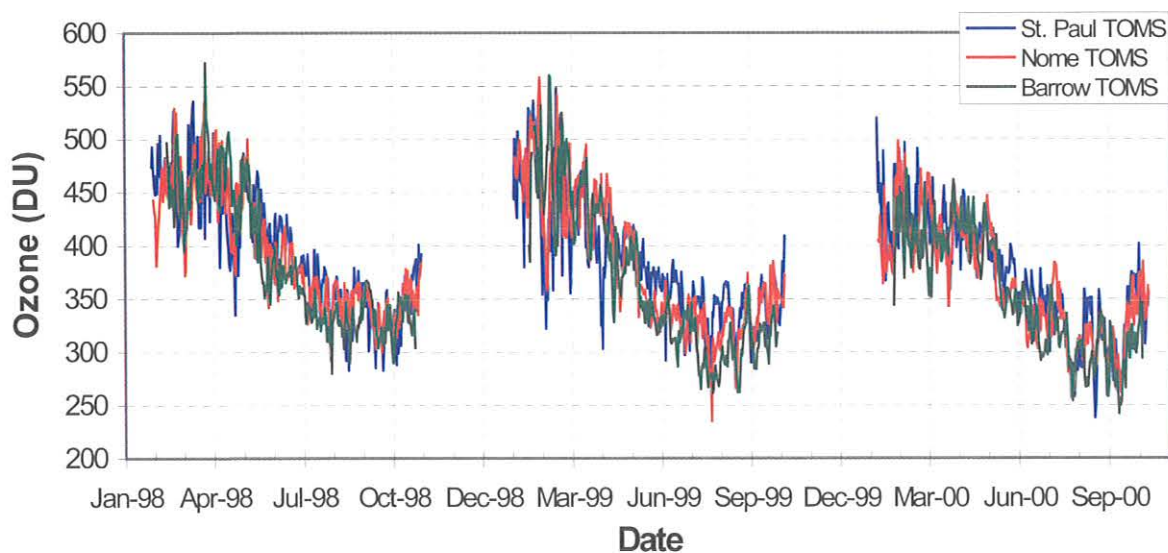

Fig. 3.32. Daily total column ozone from the Earth Probe Total Ozone Mapping Spectrometer (TOMS) for St. Paul, Nome, and Barrow, 1998–2000.

Bermuda, and Kwajalein); two UV monitoring sites (Nome and St. Paul, both in Alaska); Kosan, Korea; and CMDL's headquarters at the DSRC in Boulder. Thermal (IR) radiation is also monitored at all these sites with the exception of St. Paul and Nome.

Five meteorological data streams (wind speed, wind direction, pressure, temperature, and relative humidity) are monitored by the STAR group at the BSRN sites. Pressure, temperature, and relative humidity are monitored at Kosan. Temperature measurements are made at BRW to be used in conjunction with a new IR sensor, and pressure is measured for use with sunphotometer data at SPO.

Sunphotometers have been installed at BRW, MLO, SPO, BAO, Kwajalein, Boulder, and Kosan. Data from the sunphotometers, as well as the meteorological and radiation data, are collected by Campbell Scientific data loggers. Windowed, cavity radiometers are operating at two sites (BAO and Boulder). Data from these instruments are collected by custom programs and stored locally on a PC. Multi-filter rotating shadowband radiometers (MFRSRs) continue to operate at Bermuda, Kosan, and at Boulder. MFRSR data are collected and stored locally on a PC. UV data are monitored at BRW, in addition to Nome and St. Paul. BSI instruments are used to collect the UV data and store the data onsite on a PC.

The MLO Automated Solar Dome data are collected by a custom program on a PC running at that site. Also at MLO, data are monitored on a precision filter radiometer (PFR), which is a tracking sunphotometer used for optical depth measurements. The PFR data are collected by a Campbell Scientific data logger. All-sky images are made with Yankee Environmental Systems (YES) Total Sky Imagers at three sites (BAO, BRW, and Boulder). These data are collected and processed by YES proprietary software. All data that are collected on the Campbell data loggers are transferred to CMDL over telephone lines, with the exception of data from SPO. Calls to the data loggers are made at regular intervals varying from 2 to 12 hours depending on the site being called. All other data are retrieved via the Internet. Some of the Internet connections are, however, made over telephone lines.

Each morning all data from all sites are permanently stored on one of the CMDL servers in Boulder. The data are then loaded into archive files. All archive files for all projects have exactly the same format. Uniformity among the archive files has simplified data access. Plots and lists of the data are available to CMDL scientists from the archive files. Modifications can be made at field sites after data review.

Currently the solar and thermal radiation, meteorology, and sunphotometer data are being edited using qualitative and quantitative methods. CMDL is a contributing member of the BSRN network. The radiation and meteorology data are sent to the BSRN database in Zurich, Switzerland. Access to the data for people outside CMDL is available from BSRN, or from CMDL directly upon request.

3.3. REFERENCES

Arnott, W.P., H. Moosmüller, C.F. Rogers, T. Jin, and R. Bruch, Photoacoustic spectrometer for measuring light absorption by aerosol: Instrument description, *Atmos. Environ., 33*, 2845-2852, 1999.

Barrie, L.A., Occurrence and trends of pollution in the Arctic troposphere, in *Chemical Exchange Between the Atmosphere and Polar Snow*, edited by E.W. Wolff and R.C. Bales, *NATO ASI Series I, 43*, pp. 93-129, Springer-Verlag, Berlin, 1996.

Bergin, M.H., E.A. Meyerson, J.E. Dibb, and P.A. Mayewski, Relationship between continuous aerosol measurements and firn core chemistry over a 10-year period at the South Pole, *Geophys. Res. Lett., 25*, 1189-1192, 1998.

Bergin, M.H., R.S. Halthorne, S.E. Schwartz, J.A. Ogren, and S. Nemesure, Comparison of aerosol column properties based on nephelometer and radiometer measurements at the SGP ARM site, *J. Geophys. Res., 105*, 6807-6818, 2000.

Bird, R.E., and C. Riordan, Simple solar spectral model for direct and diffuse irradiance on horizontal and tilted planes at the Earth's surface for cloudless atmospheres, *J. Appl. Meteorol., 25*, 87-97, 1986.

Bishop, J.K, W.B. Rossow, and E.G. Dutton, Surface solar irradiance from the International Satellite Cloud Climatology Project 1983-1991, *J. Geophys. Res., 102*, 6883-6910, 1997.

Bodhaine, B.A., Barrow surface aerosol: 1976-1987, *Atmos. Environ., 23*, 2357-2369, 1989.

Bodhaine, B.A., The U. S. aerosol monitoring program in Antarctica, Proc. *4th Workshop Italian Research on Antarctic Atmosphere*, Porano, Italy, Oct. 21-23, 1991, edited by M. Colacino, G. Giovanelli, and L. Stefanutti, pp. 15-25, Ital. Phys. Soc., Bologna, Italy, 1992.

Bodhaine, B.A., Aerosol absorption measurements at Barrow, Mauna Loa, and South Pole, *J. Geophys. Res., 100*, 8967-8975, 1995.

Bodhaine, B.A., Central Antarctica: Atmospheric chemical composition and atmospheric transport, in *Chemical Exchange Between the Atmosphere and Polar Snow*, edited by E.W. Wolff and R.C. Bales, *NATO ASI Series I, 43*, pp. 145-172, Springer-Verlag, Berlin, 1996.

Bodhaine, B.A., and J.J. DeLuisi, An aerosol climatology of Samoa, *J. Atmos. Chem., 3*, 107-122, 1985.

Bodhaine, B.A., and E.G. Dutton, A long-term decrease in Arctic haze at Barrow, Alaska, *Geophys. Res. Lett., 20*, 947-950, 1993.

Bodhaine, B.A., B.G. Mendonca, J.M. Harris, and J.M. Miller, Seasonal variation in aerosols and atmospheric transmission at Mauna Loa Observatory, *J. Geophys. Res., 88*, 6769-6772, 1981.

Bodhaine, B.A., J.J. DeLuisi, J.M. Harris, P. Houmere, and S. Bauman, Aerosol measurements at the South Pole, *Tellus, 38B*, 223-235, 1986.

Bodhaine, B.A., J.J. DeLuisi, J.M. Harris, P. Houmere, and S. Bauman, PIXE analysis of South Pole aerosol, in *Nuclear Instruments and Methods in Physics Research, B22*, pp. 241-247, Elsevier, Holland, 1987.

Bodhaine, B.A., J.M. Harris, and J.A. Ogren, Aerosol optical properties at Mauna Loa Observatory: Long-range transport from Kuwait?, *Geophys. Res. Lett., 19*, 581-584, 1992.

Bodhaine, B.A., R.L. McKenzie, P.V. Johnston, D.J. Hofmann, E.G. Dutton, R.C. Schnell, J.E. Barnes, S.C. Ryan, and M. Kotkamp, New ultraviolet spectroradiometer measurements at Mauna Loa Observatory, *Geophys. Res. Lett., 23*, 2121-2124, 1996.

Bodhaine, B.A., E.G. Dutton, D.J. Hofmann, R.L. McKenzie, and P.V. Johnston, UV measurements at Mauna Loa: July 1995 to July 1996, *J. Geophys. Res., 102*, 19,265-19,273, 1997.

Bodhaine, B.A., E.G. Dutton, R.L. McKenzie, and P.V. Johnston, Calibrating broadband UV instruments: Ozone and solar zenith angle dependence, *J. Atmos. Oceanic Technol., 15*, 916-926, 1998.

Bodhaine, B.A., N.B. Wood, E.G. Dutton, and J.R. Slusser, On Rayleigh optical depth calculations, *J. Atmos. Oceanic Technol., 16*, 1854-1861, 1999.

Bond, T.C., T.L. Anderson, and D. Campbell, Calibration and intercomparison of filter-based measurements of visible light absorption by aerosol, *Aerosol Sci. Technol., 30*, 582-600, 1999.

Bush, B.C., F.P.J. Valero, A.S. Simpson, and L. Bignone, Characterization of thermal effects in pyranometers: A data correction algorithm for improved measurement of surface insolation, *J. Atmos. Oceanic Technol., 17*, 165-175, 1999.

Cacciari, A., A. Lupi, C. Tomasi, V. Viatale, and S. Marani, Calculation of the radiative forcing caused by aerosol particles in Antarctic regions (Terra Nova Bay), *Proc. 8ᵗʰ Workshop Italian Research on Antarctic Atmosphere*, Bologna, Italy, Oct. 20-22, 1999, edited by M. Colacino and G. Giovanelli, pp. 455-467, Ital. Phys. Soc., Bologna, Italy, 2000.

Cachier, H., M.P. Brémond, and P. Buat-Ménard, Determination of atmospheric soot carbon with a simple thermal method, *Tellus, 41B*, 379-390, 1989.

Charlson, R.J., S.E. Schwartz, J.M. Hales, R.D. Cess, J.A. Coakley, J.E., Hansen, and D.J. Hofmann, Climate forcing by anthropogenic aerosols, *Science, 255*, 423-420, 1992.

Chow, J.C., J.G. Watson, L.C. Pritchett, W.R. Pierson, C.A. Frazier, and R.G. Purcell, The DRI thermal/optical reflectance carbon analysis system: Description, evaluation and applications in US air quality studies, *Atmos. Environ., 17A*, 1185-1201, 1993.

Delene, D.J., and J.A. Ogren, Variability of aerosol optical properties at four North American surface monitoring sites, *J. Atmos. Sci., 59*, 1135-1150, 2002.

Dutton, E.G., An extended comparison between Lowtran7-computed and observed broadband thermal irradiances: Global extreme and intermediate surface conditions, *J. Atmos. Oceanic Technol., 10*, 326-336, 1993.

Dutton, E.G., and B.A. Bodhaine, Solar irradiance anomalies caused by clear-sky transmission variations above Mauna Loa: 1958-99, *J. Clim., 14*, 3255-3262, 2001.

Dutton, E.G., and J.R. Christy, Solar radiative forcing at selected locations and evidence for global lower tropospheric cooling following the eruptions of El Chichón and Pinatubo, *Geophys. Res. Lett., 19*, 2313-2316, 1992.

Dutton, E.G., and D.J. Endres, Date of snow melt at Barrow, Alaska, USA, *Arctic Alpine Res., 23*, 115-119, 1991.

Dutton, E.G., J.J. DeLuisi, and B. Bodhaine, Features of aerosol optical depth observed at Barrow, March 10-20, 1983, *Geophys, Res. Lett., 11*, 385-388, 1984.

Dutton, E.G., J.J. DeLuisi, and A.P. Austring, Interpretation of Mauna Loa atmospheric transmission relative to aerosols, using photometric precipitable water amounts, *J. Atmos. Chem., 3*, 53-68, 1985.

Dutton, E.G., J.J. DeLuisi, and G.A. Herbert, Shortwave aerosol optical depth of Arctic haze measured on board the NOAA WP-3D during AGASP-II, April 1986, *J. Atmos. Chem., 9*, 71-79, 1989.

Dutton, E.G., J.J. Michalsky, T. Stoffel, B.W. Forgan, J. Hickey, D. W. Nelson, T.L. Alberta, and I. Reda, Measurement of broadband diffuse solar irradiance using current commercial instrumentation with a correction for thermal offset errors, *J. Atmos. Oceanic Technol., 18*, 297-314, 2001.

Ellis, H.T., and R.F. Pueschel, Solar radiation: Absence of air pollution trends at Mauna Loa, *Science, 172*, 845-846, 1971.

Harris, J.M., and J.D.W. Kahl, Analysis of 10-day isentropic flow patterns for Barrow, Alaska: 1985-1992, *J. Geophys. Res., 99*, 25,845-25,855, 1994.

Hofmann, D.J., and J.M. Rosen, On the prolonged lifetime of the El Chichón sulfuric acid aerosol cloud, *J. Geophys. Res., 92*, 9825-9830, 1987.

Hofmann, D.J., J.T. Peterson, and R.M. Rosson (Eds.), *Climate Monitoring and Diagnostics Laboratory No. 23 Summary Report 1994-1995*, 161 pp., NOAA Environ. Res. Labs., Boulder, CO, 1996.

Hofmann, D.J., J.T. Peterson, and R.M. Rosson (Eds.), *Climate Monitoring and Diagnostics Laboratory Summary Report No. 24 1996-1997*, 166 pp., NOAA Environ. Res. Labs., Boulder, CO, 1998.

Houghton, J.T., Y. Ding, D.J. Griggs, M. Noguer, P.I. van der Linden, and D. Xiaosu (Eds.), *Climate Change 2001: The Scientific Basis: Contribution of Working Group 1 to the Intergovernmental Panel on Climate Change (IPCC)*, 944 pp., Cambridge Univ. Press, New York, 2001.

Key, J.R., A.J. Schweiger, and R.S. Stone, Expected uncertainty in satellite-derived estimates of surface radiation budget at high latitudes, *J. Geophys. Res., 102*, 15,837-15,847, 1997.

King, M.D., D.M. Byrne, B.M. Herman, and J.A. Reagan, Aerosol size distributions obtained by inversion of spectral optical depth measurements, *J. Atmos. Sci., 35*, 2153-2167, 1978.

Lawrimore, J.H., M.S. Halpert, G.D. Bell, M.J. Menne, B. Lyon, R.C. Schnell, K.L. Gleason. D.R. Easterling, W. Thiaw, W.J. Wright, R.R. Heim Jr., D.A. Robinson, and L. Alexander, Climate Assessment for 2000, *Bull. Am. Meteorol. Soc., 82(6)*, S1-S55, 2001.

MacLaughlin, J.A., R.R. Anderson, and M.F. Holick, Spectral character of sunlight modulates photosynthesis of previtamin D₃ and its photoisomers in human skin, *Science, 216*, 1001-1003, 1982.

Madronich, S., The atmosphere and UV-B radiation at ground level, in *Environmental UV Photobiology*, edited by A.R. Young, L.O. Bjorn, J. Moan, and W. Nultsch, pp. 1-39, Plenum Press, New York, 1993.

McInnes, L.M., M.H. Bergin, J.A. Ogren, and S.E. Schwartz, Differences in hygroscopic growth between marine and anthropogenic aerosol, *Geophys. Res. Lett., 25*, 513-516, 1998.

McKenzie, R.L., P.V. Johnston, M. Kotkamp, A. Bittar, and J.D. Hamlin, Solar ultraviolet spectroradiometry in New Zealand: Instrumentation and sample results from 1990, *Appl. Opt., 31*, 6501-6509, 1992.

McKenzie, R.L., P.V. Johnston, D. Smale, B.A. Bodhaine, and S. Madronich, Altitude effects on UV spectral irradiance deduced from measurements at Lauder, New Zealand, and at Mauna Loa Observatory, Hawaii, *J. Geophys. Res., 106*, 22,845-22,860, 2001.

McKinlay, A.F., and B.L. Diffey, A reference action spectrum for ultraviolet induced erythema in human skin, *J. Int. Comm. Illum., 6*, 17-22, 1987.

Mertes, S., B. Dippel, and A. Schwarzenböck, Comparison of the Particle Soot Absorption Photometer (PSAP) absorption measurement to graphitic carbon quantification on the PSAP internal filters, *Aerosol Sci. Technol.*, in press, 2002.

Michalsky, J., E.G. Dutton, M. Rubes, D. Nelson, T. Stoffel, M. Wesley, M. Splitt, and J. Deluisi, Optimal measurement of surface shortwave irradiance using current instrumentation, *J. Atmos. Oceanic Technol., 16*, 55-69, 1999.

Morrison, J., et al., Study of Environmental Arctic Change (SEARCH) Science Plan, 2001 (available at http://psc.apl.washington.edu/search), 2001.

Myneni, R.B., C.D. Keeling, C.J. Tucker, G. Asrar, and R.R. Nemani, Increased plant growth in the northern high latitudes from 1981 to 1991, *Nature, 386*, 698-702, 1997.

Nelson, D.W., The NOAA Climate Monitoring and Diagnostics Laboratory Solar Radiation Facility, *NOAA TM OAR CMDL-15*, 36 pp., NOAA Clim. Monit. and Diag. Lab., Boulder, CO, 2000.

NRC (National Research Council), *Aerosol Radiative Forcing and Climatic Change*, 161 pp., National Academy Press, Washington, DC, 1996.

Oechel, W.C., G.L. Vourlitis, S.J. Hastings, and S.A. Bochkrez, Effects of Arctic CO_2 flux over two decades: Effects of climate change at Barrow, Alaska, *Ecol. Appl., 5*, 846-855, 1995.

Ogren, J.A., A systematic approach to in situ observations of aerosol properties, in *Aerosol Forcing of Climate*, edited by R.J. Charlson and J. Heintzenberg, pp. 215-226, Wiley, New York, 1995.

Ohmura, A., H. Gilgen, H. Hegner, G. Müller, M. Wild, E.G. Dutton, B. Forgan, C. Fröhlich, R. Philipona, A. Heimo, G. Konig-Langlo, B. McArthur, R. Pinker, C.H. Whitlock, and K. Dehne, Baseline Surface Radiation Network (BSRN)/WCRP: New precision radiometry for climate research, *Bull. Am. Meteorol. Soc., 79*, 2115-2136, 1998.

Philipona, R., C. Fröhlich, K. Dehne, J. DeLuisi, J. Augustine, E. Dutton, D. Nelson, B. Forgan, P. Novotny, J. Hickey, S.P. Love, S. Bender, B. McArthur, A. Ohmura, J.H. Seymour, J.S. Foot, M. Shiobara, F.P.J. Valero, and A.W. Strawa, The BSRN pyrgeometer round-robin calibration experiment, *J. Atmos. Oceanic Technol., 15*, 687-696, 1998.

Philipona, R.C., E.G. Dutton, T. Stoffel, J. Michalsky, I. Reda, A. Stifter, P. Wendling, N. Wood, S.A. Clough, E.J. Mlawer, G. Anderson, H.E. Revercomb, and T.R. Shippert, Atmospheric longwave irradiance uncertainty: Pyrgeometers compared to an absolute sky-scanning radiometer, AERI, and radiative transfer model calculations, *J. Geophys. Res.*, *106*, 28,129-28,141, 2001.

Quakenbush, T.K., and B.A. Bodhaine, Surface aerosols at the Barrow GMCC observatory: Data from 1976 through 1985, *NOAA Data Rep. ERL ARL-10*, 230 pp., NOAA Air Resources Lab., Silver Spring, MD, 1986.

Quinn, P.K., T.L. Miller, T.S. Bates, J.A. Ogren, E. Andrews, and G.E. Shaw, A three-year record of simultaneously measured aerosol chemical and optical properties at Barrow, Alaska, *J. Geophys. Res.*, in press, 2002.

Radke, L.F., C.A. Brock, R.J. Ferek, and D.J. Coffman, Summertime Arctic hazes, *Eos Trans. AGU*, *71*(43), 1264, 1990.

Ramanathan, V., et al., Indian Ocean Experiment: An integrated analysis of the climate forcing and effects of the great Indo-Asian haze, *J. Geophys. Res.*, *106*, 28,371-28,398, 2001.

Remer, L.A., and Y.J. Kaufman, Dynamic aerosol model: Urban/industrial aerosol, *J. Geophys. Res.*, *103*, 13,859-13,871, 1998.

Schnell, R.C., D.B. King, and R.M. Rosson, (Eds.), *Climate Monitoring and Diagnostics Laboratory Summary Report No. 25 1998-1999*, 154 pp., NOAA Environ. Res. Labs., Boulder, CO, 2001.

Serreze, M.C., J.E. Walsh, F.S. Chapin III, T. Osterkamp, M. Dyurgerov, V. Romanovsky, W.C. Oechel, J. Morrison, T. Zhang, and R.G. Barry, Observational evidence of recent change in the northern high-latitude environment, *Clim. Change, 46*, 159-207, 2000.

Sheridan, P.J., D.J. Delene, and J.A. Ogren, Four years of continuous surface aerosol measurements from the DOE/ARM Southern Great Plains CART site, *J. Geophys. Res., 106*, 20,735-20,747, 2001.

Stone, R.S., Variations in Western Arctic temperatures in response to cloud radiative and synoptic-scale influences, *J. Geophys. Res., 102*, 21,769-21,776, 1997.

Stone, R.S., Climate monitoring at Barrow, Alaska, and South Pole: An overview of U.S. studies of polar surface radiation balance and aerosols, *Proc. 8th Workshop Italian Research on Antarctic Atmosphere*, Bologna, Italy, Oct. 20-22, 1999, edited by M. Colacino and G. Giovanelli, pp. 83-98, Ital. Phys. Soc., Bologna, Italy, 2000.

Stone, R.S., Factors that determine when the seasonal snowmelt occurs in Northern Alaska, *Proc. 2nd Wadati Conf. on Global Change and the Polar Climate*, Tsukuba, Japan, March 7-9, 2001, pp. 87-90, 2001.

Stone, R.S., Monitoring aerosol optical depth at Barrow, Alaska, and South Pole: Historical overview, recent results, and future goals, *Proc. 9th Workshop Italian Research on Antarctic Atmosphere*, Rome, Italy, Oct. 22-24, 2001, Ital. Phys. Soc., Bologna, Italy, in press, 2002.

Stone, R.S., J. Key, and E. Dutton, Properties and decay of stratospheric aerosols in the Arctic following the 1991 eruptions of Mount Pinatubo, *Geophys. Res. Lett., 20*, 2359-2362, 1993.

Stone, R.S., E.G. Dutton, and J.R. Key, Properties and decay of Pinatubo aerosols in polar regions compared with tropical observations, *Proc. 8th Conf. on Atmospheric Radiation*, Nashville, TN, Jan. 23-28, 1994, pp. 432-434, Am. Meteorol. Soc., Boston, 1994.

Stone, R.S., E.G. Dutton, J.M. Harris, and D. Longenecker, The advancing date of spring snowmelt in the Alaskan Arctic, *Proc. 11th ARM Science Team Meeting*, Atlanta, GA, March 19-23, 2001 (available at http://www.arm.gov/docs/documents/technical/conf_0103/stone-rs.pdf), 2001.

Stone, R.S, E.G. Dutton, J.M. Harris, and D. Longenecker, Earlier spring snowmelt in northern Alaska as an indicator of climate change, *J. Geophys. Res.*, in press, 2002.

Whitlock, C.H., T.P. Charlock, W.F. Staylor, R.T. Pinker, I. Laszlo, A. Ohmura, H. Gilgen, T. Konzelman, R.C. DePasquale, C.D. Moast, S.R. LeCroy, and N.A. Ritchey, First global WCRP shortwave surface radiation budget dataset, *Bull. Am. Meteorol. Soc., 76*, 905-922, 1995.

4. Ozone and Water Vapor

J. Harris (Editor), G. Carbaugh, D. Chao, M. Clark, R. Evans, B. Johnson,
M. O'Neill, S. Oltmans, D. Quincy, D. Sherman, B. Vasel, H. Vomel, and B. Walsh

4.1. Continuing Programs

4.1.1. Total Ozone Observations

Total ozone observations continued throughout 2000 and 2001 at the 16 stations that constitute the U.S. Dobson spectrophotometer network (Table 4.1). Of the 16 stations, CMDL personnel operated five, the National Weather Service (NWS) operated five, two are university stations, and four are foreign cooperative stations. All station instruments are either fully automated or semiautomated, except for the one at the Peruvian site. In addition, a Brewer spectrophotometer was operated on a nearly continuous basis at Boulder.

The automated system at Haute Provence, France, was finally made operational in August 2000, but was not fully reliable until December of that year. Observations at Tallahassee are continuing at Florida State University until the new NWS office is completed in January 2002, but due to personnel problems, observations are not made consistently, and the data record is not very useful. Several months of data were lost from the University of Alaska, Fairbanks, because of a failure in the 20-year-old controller unit. The replacement parts were very difficult to obtain. The dome at the Nashville (Old Hickory) site was reinsulated by a local contractor.

New computers and programs were installed at all the sites, and a new protocol was established for data transfer.

Many sites transmit observational data daily, allowing preliminary ozone values to be available in near-real time.

Provisional daily total ozone amounts applicable to local apparent noon for the stations listed in Table 4.1 were archived at the World Ozone and Ultraviolet Data Centre (WOUDC), Canada, in *Ozone Data for the World*. Table 4.2 lists the monthly mean total ozone amounts measured at the stations in the network for 2000 and 2001.

Observations of total column ozone with the Dobson spectrophotometer at South Pole Observatory (SPO) with the Sun as a light source are limited to less than half of the year. Moon observations are infrequent due to adverse winter weather conditions and limited observing periods. Optical measurements with the Dobson spectrophotometer cannot be made at all during twilight periods. To better define the year-round column ozone measurements, integrated column ozone amounts from the ozonesondes are used to supplement the Dobson data during the dark and twilight months (Figure 4.1). This new data set has been analyzed with a recently developed technique [*Harris et al.*, 2001] for describing long-term column ozone changes. The decline in ozone (expressed as residuals) at SPO began in the 1970s (Figure 4.2) and has persisted through most of the record since then. Growth rates were mostly negative (Figure 4.3) throughout this period, with the largest declines in the 1970s and mid-1980s. The overall growth rate (decline) was $-8.1 \pm 0.5\%$ decade^{-1}. Even though human-produced, ozone-destroying halogen compounds have begun

TABLE 4.1. U.S. Dobson Ozone Spectrophotometer Station Network for 2000-2001

Station	Period of Record	Instrument No.	Agency
Bismarck, North Dakota	Jan. 1, 1963-present	33	NOAA
Caribou, Maine	Jan. 1, 1963-present	34	NOAA
Wallops Is., Virginia	July 1, 1967-present	38	NOAA, NASA
SMO	Dec. 19, 1975-present	42	NOAA
Tallahassee, Florida	May 2, 1964-Nov. 30, 1989; Nov. 1, 1992-present	58	NOAA, Florida State University
Boulder, Colorado	Sept. 1, 1966-present	61	NOAA
Fairbanks, Alaska	March 6, 1984-present	63	NOAA, University of Alaska
Lauder, New Zealand	Jan. 29, 1987-present	72	NOAA, National Institute of Water and Atmospheric Research
MLO	Jan. 2, 1964-present	76	NOAA
Nashville, Tennessee	Jan. 2, 1963-present	79	NOAA
Perth, Australia	July 30, 1984-present	81	NOAA, Australian Bureau Meteorology
SPO	Nov. 17, 1961-present	82	NOAA
Haute Provence, France	Sept. 2, 1983-present	85	NOAA, Centre National de la Recherche Scientifique, University of Riems
Marcapomacocha, Peru	Feb 26, 2001-present	87	NOAA, Servicio Nacional de Meteorologia e Hidrologia
BRW	June 6, 1986-present	91	NOAA
Fresno, California/ Hanford, California	June 22, 1983-March 13, 1995; March 15, 1995-present	94	NOAA

TABLE 4.2. Provisional 2000 and 2001 Monthly Mean Total Ozone Amounts (DU)

Station	Jan.	Feb.	March	April	May	June	July	Aug.	Sept.	Oct.	Nov.	Dec.
					2000							
Bismarck, North Dakota	314	353	348	341	336	327	300	293	287	287	312	332
Caribou, Maine	–	369	356	387	359	341	335	318	304	292	280	334
Wallops Is., Virginia	328	318	339	[327]	336	[311]	[312]	302	286	279	278	303
SMO	[244]	247	246	249	252	252	257	256	260	259	259	247
Tallahassee, Florida	#	#	#	#	#	#	#	#	#	#	#	#
Boulder, Colorado	304	320	337	311	301	310	302	298	274	273	282	302
Fairbanks, Alaska	–	–	391	393	389	336	326	296	290	339	[339]	–
Lauder, New Zealand	272	259	253	272	279	303	319	332	362	364	329	285
MLO	258	267	273	288	278	271	265	264	254	254	251	238
Nashville, Tennessee	308	309	305	318	313	298	301	294	281	264	264	293
Perth, Australia	276	250	266	269	282	294	311	314	320	294	274	276
SPO	270	267	[246]	[248]	[237]	–	[231]	[226]	–	186	287	322
Haute Provence, France	322	–	–	–	–	–	–	–	[295]	292	285	295
Marcapomacocha, Peru	–	[262]	254	[249]	247	245	243	259	262	258	254	254
BRW	–	–	[403]	396	390	335	[314]	287	290	[285]	–	–
Hanford, California	290	322	318	299	305	306	303	298	282	280	273	276
					2001							
Bismarck, North Dakota	329	381	371	380	–	[296]	299	292	282	294	282	318
Caribou, Maine	[342]	[365]	[394]	[402]	[346]	[325]	348	[307]	–	–	–	–
Wallops Is., Virginia	323	297	348	342	344	317	315	308	285	[293]	275	267
SMO	246	248	242	244	243	239	238	245	253	259	267	–
Tallahassee, Florida	#	#	#	#	#	#	#	#	#	#	#	–
Boulder, Colorado	305	335	330	330	328	314	297	290	270	279	276	296
Fairbanks, Alaska	–	[410]	417	390	–	–	–	309	311	330	[321]	–
Lauder, New Zealand	279	261	260	271	297	338	325	354	346	357	328	301
MLO	248	252	267	283	287	279	270	271	263	251	239	232
Nashville, Tennessee	298	289	319	[282]	–	338	316	311	291	291	273	269
Perth, Australia	268	258	265	267	278	272	293	301	327	331	–	[289]
SPO	265	233	–	–	214	223	249	–	–	139	168	238
Haute Provence, France	332	325	331	365	342	333	322	[298]	315	278	286	286
Marcapomacocha, Peru	249	[250]	[246]	252	[246]	–	–	–	–	–	–	–
BRW	–	[358]	423	407	403	340	316	292	–	–	–	–
Hanford, California	305	326	314	343	315	304	304	293	278	271	264	287

Monthly mean ozone values in square brackets are derived from observations made on fewer than 10 days per month.

–, no data; #, data are too sparse for meaningful monthly averages.

to decline very slowly in the stratosphere, ozone amounts have not shown any sign of recovery to their pre-1970s levels. This is expected because at the South Pole there is more than enough chlorine and bromine in the stratosphere to destroy most of the ozone in the 14- to 22-km altitude range during the spring (see section 4.1.5).

4.1.2. UMKEHR OBSERVATIONS

Umkehr observations made with the Automated Dobson Network instruments continued in 2000 and 2001 at Boulder, Colorado; Haute Provence, France; Lauder, New Zealand; Mauna Loa Observatory (MLO), Hawaii; Perth, Western Australia; and the Geophysical Institute, University of Alaska. Data processing has been completed for Boulder, Haute Provence, Lauder, and the Geophysical Institute through September 2001, and the vertical profiles are available from WOUDC. Processing has also been completed through June 2001 for MLO. Problems at Perth have yet to be resolved.

4.1.3. CALIBRATION OF DOBSON SPECTROPHOTOMETERS

Seven Dobson ozone spectrophotometers in the CMDL network, as well as eight others, were calibrated during 2000 and 2001. Table 4.3 lists all the instruments calibrated and the resulting calibration difference expressed as a percent ozone difference. This percent difference is between the ozone calculated from the test and from the
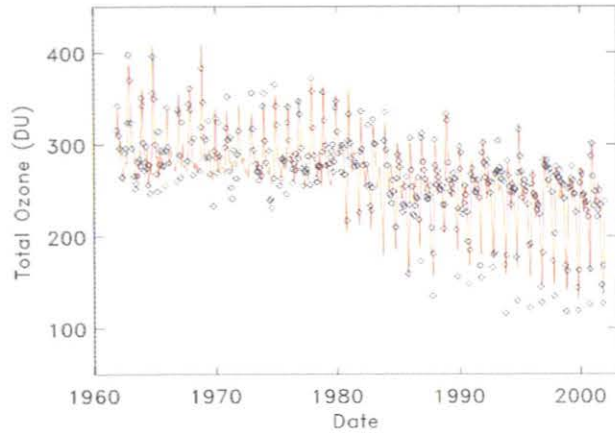
Fig. 4.1. Monthly mean (◇) and model (solid line) total ozone at SPO. The model accounts for the seasonal, quasi-biennial, solar, and detrended temperature dependencies in the data.
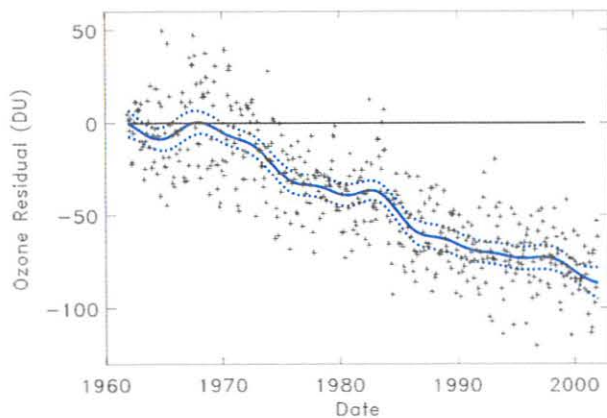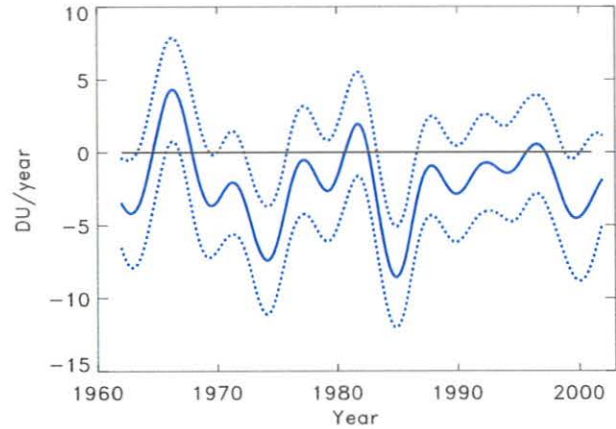

Fig. 4.3. Instantaneous growth rate of total column ozone (solid curve) at SPO, found by differentiation of the tendency curve shown in Figure 4.2. The dashed curves show the 95% confidence limits estimated with a bootstrap method.

Fig. 4.2. Ozone residuals (+) at SPO after removal of known variations, and the tendency curve (solid curve) found from the filtering of the residuals. The dashed curves show the 95% confidence limits about each point on the curve.

standard instrument, using the measurements based on the most common observation type (ADDSGQP). The value is then averaged over μ (optical path length through the atmosphere, calculated from solar zenith angle) values of 1, 2, and 3, and normalized to a total ozone value of 300 Dobson units (DU). This number represents the instrument measurement status before any repair or calibration adjustment is made. The table also lists the location of the calibration and the standard instrument used. The Boulder station instrument is normally compared with the standard whenever intercomparisons are made. The MLO station instrument is compared with the Primary Standard (D083) each summer. The Primary and Secondary Standards are

compared twice yearly. These instruments are maintained to within ±1% of the Primary Standard.

CMDL participated in international Dobson spectro-photometer calibrations at the South African Weather Bureau in Pretoria, South Africa, in 2000 and at Lauder, New Zealand, in 2001 as part of its role as the World Center for Dobson Calibrations. The Japanese regional standard Dobson instrument was calibrated at MLO during August-September 2001.

4.1.4. SURFACE OZONE

Observations of surface ozone were continued at each of the four baseline observatories, Barrow Observatory (BRW), MLO, Samoa Observatory (SMO), and SPO, as well as at Niwot Ridge, Colorado; Westman Islands, Iceland; and Arrival Heights, Antarctica. In June 2000 a TEI Model 49C ozone analyzer was installed at Summit Station, Greenland. Data from BRW, MLO, SMO, and SPO have been processed through 2001. The monthly mean data for the four sites are given in Table 4.4 for 2000 and 2001. Revised data for 1998 and 1999 for BRW and data for 1999 at MLO are also included. For MLO the average is based on downslope (1000-1800 UTC) data. The data system at SMO experienced a number of outages after the measurements were restarted in 1997 after about a 15-mo gap that included all of 1996 and the first 3 months of 1997. Most of the data for 1997 and 1998 have, however, been recovered from a backup paper chart record.

Trends have been computed for each of the long-term data sets (Figure 4.4), by the methods described in *Harris et al.* [2001], modified to remove effects of the seasonal cycle, surface temperature, and autocorrelation before the trend is fitted. As an example, Figure 4.5 shows the monthly surface ozone data and the model fit for MLO.

The numerical trends are summarized in Table 4.5. The standard errors are determined by a Monte Carlo technique. At BRW surface ozone amounts were generally increasing

TABLE 4.3. Dobson Ozone Spectrophotometers Calibrated in 2000-2001

Station	Instrument Number	Original Calibration Date	Calibration Correction (%)	Standard Number	Place
		2000			
Tamanrasset, Algeria	11	July 22, 1993	+2.4	65	Pretoria, South Africa
Maun, Botswana (proposed)	15	N/A	N/A	65	Pretoria, South Africa
University of Nairobi, Kenya	18	March 7, 1995	-0.2	65	Pretoria, South Africa
Seychelles	57	1988	+2.0	65	Pretoria, South Africa
Irene, South Africa	89	February 12, 1997	-0.8	65	Pretoria, South Africa
Springbok, South Africa	132	February 11, 1995	Calibration broken	65	Pretoria, South Africa
Lagos, Nigeria	5703	July 22, 1993	+4.4	65	Pretoria, South Africa
Admunsen-Scott, Antarctica	82	N/A	N/A	83	Boulder, Colorado
		2001			
Bismarck, North Dakota	33	April 27, 1995	+0.7	83	Boulder, Colorado
Caribou, Maine	34	October 5, 1995	+0.3	65	Boulder, Colorado
Nashville, Tennessee	79	October 3, 1995	+1.0	83	Boulder, Colorado
Samoa	42	February 1997	-1.1	83	Lauder, New Zealand
Lauder, New Zealand	72	February 1997	+0.2	83	Lauder, New Zealand
Perth, Australia	81	February 1997	+0.9	83	Lauder, New Zealand
Melbourne, Australia (regional standard)	105	February 1997	0.0	83	Lauder, New Zealand

TABLE 4.4. Monthly Mean Surface Ozone Mixing Ratios (ppbv)

Year	Jan.	Feb.	March	April	May	June	July	Aug.	Sept.	Oct.	Nov.	Dec.
						Barrow						
1998*	33.3	29.2	23.5	26.7	22.6	16.3	24.4	21.7	24.9	30.0	33.4	30.7
1999*	29.5	28.3	13.0	9.4	23.3	22.4	18.7	19.2	22.3	31.1	29.9	30.6
2000	27.4	27.2	19.3	10.0	11.3	24.4	17.9	19.1	23.6	30.9	35.2	30.8
2001	30.0	31.3	—	17.3	16.9	23.3	20.4	21.4	25.4	34.9	34.8	33.7
					Mauna Loa (1000-1800 UTC)							
1999	43.1	48.5	48.4	54.9	44.1	41.6	48.3	35.9	46.2	39.4	38.5	36.0
2000	40.8	43.1	46.9	53.8	41.0	45.5	36.2	37.2	—	33.1	33.6	41.3
2001	39.8	40.1	49.4	51.6	46.7	37.2	34.9	39.0	33.8	48.3	37.0	41.7
						South Pole						
2000	26.5	19.8	19.8	24.3	28.7	31.4	32.3	31.8	32.0	27.5	29.1	32.0
2001	27.3	21.6	20.5	23.7	28.0	31.1	34.5	33.6	33.0	28.2	30.2	28.5
						Samoa						
1995	8.4	7.5	5.9	12.0	—	—	18.1	19.7	—	17.7	12.7	13.1
1996	—	—	—	—	—	—	—	—	—	—	—	—
1997	—	—	—	8.2	15.3	23.7	16.5	15.7	14.5	11.8	11.1	10.6
1998	6.8	6.7	7.7	13.5	15.3	16.3	21.8	17.5	15.0	13.6	10.2	10.6
1999	9.1	7.3	7.3	—	17.6	13.9	16.9	—	16.2	15.1	13.8	8.2
2000	5.0	8.4	4.9	6.6	7.5	15.7	16.7	15.2	14.3	15.4	11.7	9.6
2001	7.8	8.3	5.9	9.3	17.6	13.3	15.2	18.9	19.1	16.8	15.5	10.9
					Summit, Greenland							
2000	—	—	—	—	—	54.8	—	42.8	44.8	44.4	41.3	43.0
2001	42.1	42.2	45.1	45.7	49.9	49.3	42.8	46.2	41.9	46.6	41.9	41.6

—, no data.
*Data for 1998 and 1999 are revised.
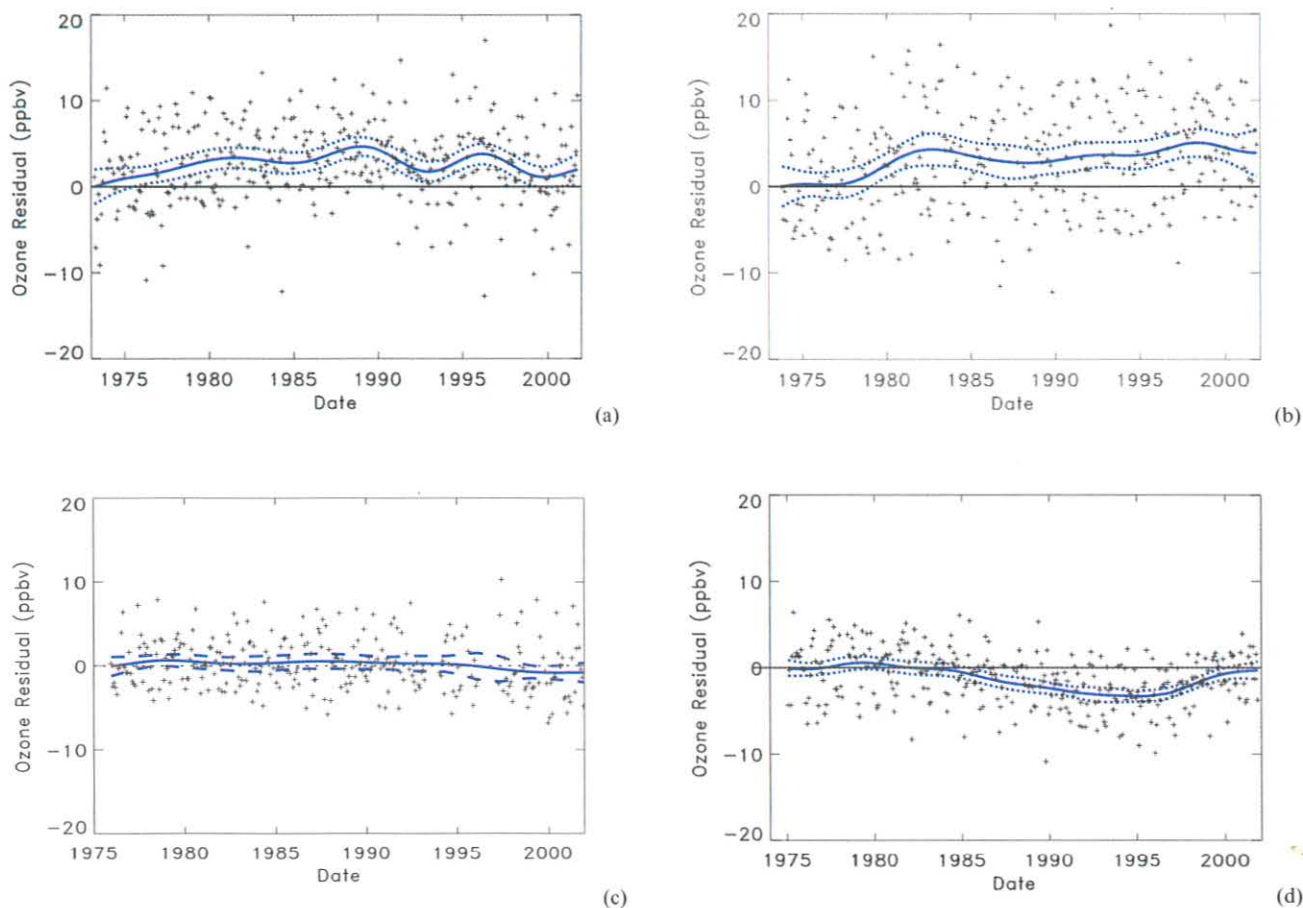
Fig. 4.4. Residual (+) and tendency curve (solid curve) of surface ozone mixing ratios at (a) BRW, (b) MLO, (c) SMO, and (d) SPO. The solid curve is a smooth fit to the filtered residuals. The dashed curves give the 95% confidence interval for the fit at each point.
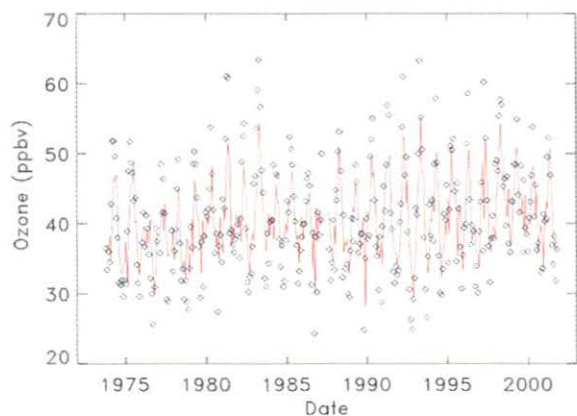
Fig. 4.5. Monthly mean surface ozone (◇) and the modeled result (solid line) for MLO.

TABLE 4.5. Average Growth Rate and Standard Error in Surface Ozone Mixing Ratio (ppbv yr^{-1}) at Four CMDL Sites

	BRW	MLO	SMO	SPO
Trend	0.07	0.15	-0.02	-0.01
Standard error*	0.04	0.06	0.04	0.03

*Determined by a Monte Carlo technique.

in the 1980s and early 1990s but have declined somewhat in recent years. At MLO there has been an overall increase, but after relatively higher ozone amounts in the late 1990s, the past 2 years have had lower values. At SMO ozone mixing ratios have remained relatively unchanged. The significant decline at SPO through the 1980s and early 1990s has nearly recovered in recent years with little overall change now evident. A recent study [Crawford et al., 2001]

shows that at SPO during the summer there is vigorous photochemical production of ozone involving the release of nitrogen oxides from the deposit of nitrogen-bearing compounds on the snow surface. This quite likely has minimal impact on the overall tropospheric ozone burden at SPO (or over Antarctica) but does play a role in the reduction of the amplitude of the surface ozone seasonal cycle.

4.1.5. OZONESONDES

Table 4.6 lists the CMDL ozonesonde sites for 2000-2001. Weekly ozonesondes were launched at eight sites, and daily ozonesondes were launched during three intensive campaigns, the Texas Air Quality Study (TexAQS), Total Ozone Measurements by Satellites, Sondes, and Spectrophotometers at Fairbanks (TOMS³F), and Southern Great Plains/Cloud and Radiation Testbed (SGP/CART). SMO and Fiji missed several weeks due to supply shortages. A critical task of the ozonesonde project is the testing of ozonesonde performance at CMDL and in field and laboratory intercomparison projects. The Jülich Ozonesonde Intercomparison Experiment (JOSIE-2000) held at the Research Center in Jülich, Germany, in September 2000 provided the venue for one such intercomparison. Results are described in section 4.2.1.

All the sites and campaigns used electrochemical concentration cell (ECC) ozonesondes purchased from EN-SCI Corporation and Science Pump Corporation. The ozonesondes used a 2% potassium iodide sensing solution. CMDL average pump efficiencies were used to process the data [*Johnson et al.*, 2002]. Pump efficiencies are determined in CMDL's environmental chamber by measuring ozonesonde flow rates at ambient pressures between 100 and 5 hPa with an oil bubble flowmeter. About 10-12 new ozonesondes per year are selected randomly for calibration in the environmental chamber to ensure that the average pump efficiency remains consistent.

Ozonesondes are sometimes found by hikers, farmers, etc., after the flight and returned to CMDL where they are cleaned and reconditioned, and the pump efficiency is measured. The sondes are then checked for accuracy against a UV calibrator at surface pressure before they are flown again. The Boulder site is the only location routinely using reconditioned ozonesondes. Despite the additional testing, the reconditioned ozonesondes show a relatively high failure rate above 20 km, where the measurements appear to be too low. In 2000 nearly 20% of the reconditioned ozonesonde flights showed this problem above 20 km. For comparison a typical failure rate at a site with new ozonesondes is about 3-10%.

In 2001 the failure rate for the reconditioned ozonesondes at Boulder was reduced to 13%. The decrease may be related to an additional cleaning procedure, started on May 1, 2001, that involves pressure flushing of the ion bridge between the cathode and anode cells of the ECC ozonesonde sensor with distilled water (1-m column head pressure). Prior to use of the flushing procedure, the sensor cells were only soaked for several days, filling up both the anode and cathode chamber with 5 mL of distilled water.

Overall, the successful Boulder ozonesonde flights compare very well with the Boulder Dobson spectro-photometer, measuring within $1.7 \pm 4.4\%$ when the constant mixing ratio extrapolation method is used to compute the residual ozone above the burst altitude of the balloon, and $-1.6 \pm 3.6\%$ when the solar backscatter ultraviolet (SBUV) residual tables from *McPeters et al.* [1997] are used.

Since 1986 the ozonesondes flown at SPO have provided a detailed look at the yearly ozone hole development. Balloonborne ozonesondes are launched once per week throughout the year, but the frequency is increased to two or more per week once the first signs of ozone depletion appear in late August, and then to every other day as the ozone hole minimum approaches. Figure 4.6 shows the typical pre-ozone-hole profiles during the winter compared with the minimum total column ozone observed in late September. The main ozone depletion layer at 14-21 km continues to show near-complete ozone destruction each

TABLE 4.6. Summary of 2000-2001 Ozonesonde Sites, Projects, and Total Number of Sondes

Ozonesonde Sites	2000		2001		Project
	Totals	Dates	Totals	Dates	
Station (weekly)					
Boulder, Colorado	60	Full year	51	Full year	NOAA long term
MLO	46	Full year	61	Full year	NOAA long term
SPO	68	Full year	71	Full year	NOAA long term
Fiji	34	Full year	36	Full year	PEM Tropics/SHADOZ
SMO	43	Full year	35	Full year	PEM Tropics/SHADOZ
Trinidad Head, California	47	Full year	44	Full year	NOAA "Health of the Atmosphere"
Huntsville, Alabama	52	Full year	47	Full year	NOAA "Health of the Atmosphere"
Galapagos	50	Full year	50	Full year	SOWER/SHADOZ
Intensives (~daily)					
Houston, Texas	27	Aug. 18-Sept. 14			TexAQS 2000
Fairbanks, Alaska			30	March 20-April 25	TOMS³F
Lamont, Oklahoma			7	Aug. 27-Sept. 1	SGP/CART

PEM Tropics, Pacific Exploratory Mission in the Tropics; SHADOZ, Southern Hemisphere Additional Ozonesondes; SOWER, Soundings of Ozone and Water in the Equatorial Region.
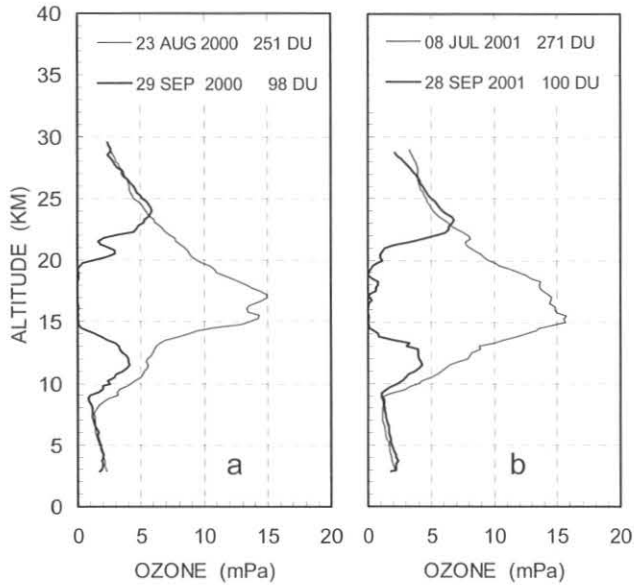
Fig. 4.6. SPO ozonesonde profiles measured in (a) 2000 and (b) 2001 showing the pre-ozone-hole profiles in austral winter and the minimum total column ozone profiles in late September. Total column ozone values (DU) are given for the dates shown.

year. Years 2000 (Figure 4.6a) and 2001 (Figure 4.6b) were similar in total column ozone minimums: 98 ± 4 DU on September 29 and 100 ± 4 DU on September 28, respectively. These minimums were about 7-10 days earlier than the average minimum date observed at SPO. The recovery, however, occurred much sooner in 2000 than in 2001 because in 2000 the polar vortex deteriorated and shifted away from South Pole. Total column ozone was already at 259 DU on November 3, 2000, but did not exceed 220 DU until December 8, 2001 (Figure 4.7).

Twenty-seven ozonesondes were flown at Houston, Texas, from August 18 to September 14, 2000, during the TexAQS 2000 field program. The project included several groups measuring gaseous and particulate air pollutants from ground instruments and aircraft platforms. The ozonesondes were launched every afternoon at 1500 local time during the campaign. Figure 4.8 shows the average ozonesonde profiles (and 1 standard deviation bars) measured during the late-summer project in Houston. The highest surface ozone mixing ratio measured by the ozonesondes during the 4-wk period was 113 ppbv on August 31, 2000. Total ozone averaged 291 ± 12 DU, which differed by −1.0 ± 3% from the NASA Total Ozone Mapping Spectrometer (TOMS) total ozone measurements.

Seven ozonesondes were launched from the U.S. SGP/CART site near Lamont, Oklahoma, during an intensive measurement campaign from August 27 to September 1, 2001. Total ozone remained very steady during the week at 302 ± 4 DU measured by the ozonesondes. For comparison, TOMS measured 297 ± 6 DU.

4.1.6. ATMOSPHERIC WATER VAPOR

Water vapor measurements with balloonborne frost-point hygrometers continued at Boulder, Colorado. In addition water vapor soundings were made at Kiruna, Sweden, during January and March 2000 as part of the SAGE III (Stratospheric Aerosol and Gas Experiment) Ozone Loss and Validation

Fig. 4.7. SPO total column ozone (DU) measured by ozonesondes during the development and recovery time period of the Antarctic ozone hole. The 1967-1971 measurements were made prior to the existence of the yearly ozone hole.
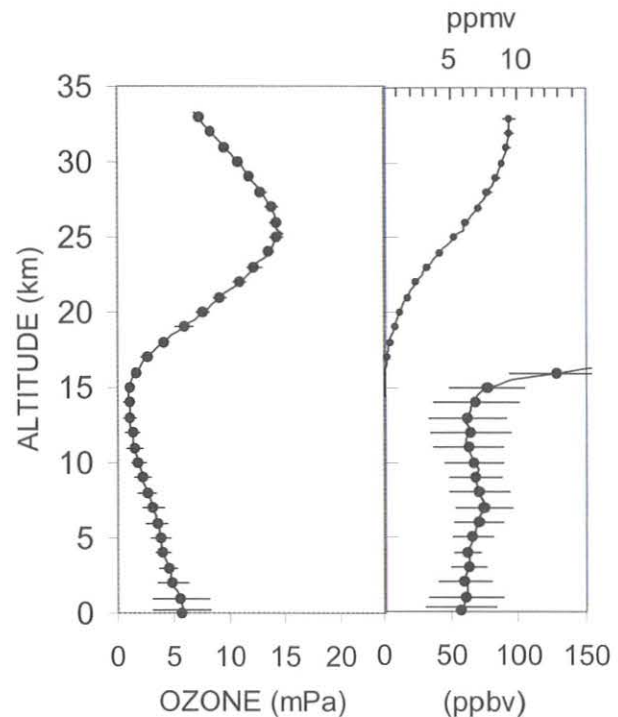
Fig. 4.8. Average of 27 ozone partial pressure (left panel) and ozone mixing ratio (right panel) profiles measured during the Houston (TexAQS-2000) campaign. The error bars represent 1 standard deviation.

Experiment (SOLVE) campaign. The long-term record of stratospheric water vapor measurements at Boulder [*Oltmans et al.*, 2000] through 2001 has been analyzed with the technique described by *Harris et al.* [2001]. The technique is also briefly described in section 4.2.3. The autoregressive model was modified for water vapor to include only the seasonal cycle as an explanatory variable. The residuals from the model with the long-term variation added back (Figure 4.9) have been fitted after the data were filtered in the frequency domain to produce a tendency curve. The changes in this tendency curve, found by differentiation, give the instantaneous growth rate curve (Figure 4.10). The growth rate shows relatively large year-to-year variations, including periods of significant negative growth, but the average growth rate has been positive. The deviations of approximately ±0.5 ppmv are around an average water vapor mixing ratio of about 4 ppmv. The largest positive excursions in the growth rate (1982, 1987, 1992, and 1997) occur several months prior to warm-phase El Niño/Southern Oscillation (ENSO) events. The average growth rate over the 20-yr observational record has been 0.04 ± 0.01 ppmv yr^{-1} or about 0.9% yr^{-1}. The increase in stratospheric water vapor at Boulder is confirmed by a number of other data sets including those from the Halogen Occultation Experiment (HALOE) instrument on the Upper Atmosphere Research Satellite (UARS) [*Rosenlof et al.*, 2001]. Several data sets predating the Boulder record also suggest that water vapor may have been increasing in the stratosphere for several decades [*Rosenlof et al.*, 2001].

During the winter of 1999-2000 the Third European Stratospheric Experiment on Ozone in 2000 (THESEO 2000) SOLVE campaign launched several water vapor soundings from Kiruna, Sweden. During two of the soundings (January and March 2000) multiple water-vapor-measuring instruments were flown in proximity in both space and time. On the flight of January 27, 2000, the Lyman-α hygrometer of the Forschungszentrum-Jülich and the cryogenic, chilled-mirror hygrometer of CMDL were flown within 2 hours of
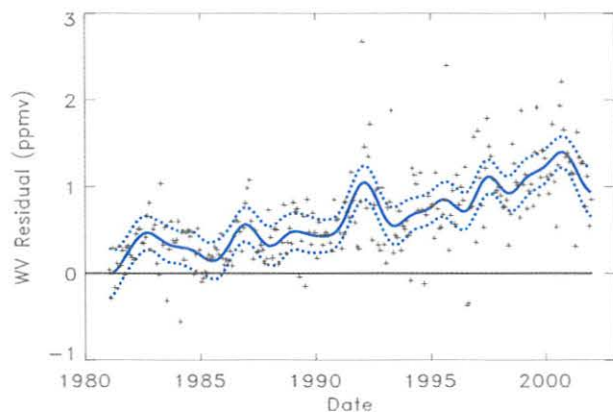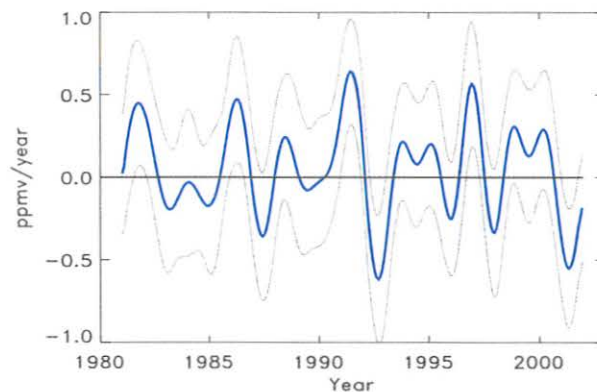
Fig. 4.10. The instantaneous (monthly) growth rate of water vapor (solid curve) in the 16-24 km layer over Boulder, Colorado. The dashed curves give the 95% confidence interval of the growth rate.

each other. The results agreed very closely in both absolute amount (differences <5%) and replication of small structural features in the profile [*Schiller et al.*, 2002].

4.1.7. ATMOSPHERIC TRANSPORT

The CMDL isentropic trajectory model is used to understand better the role of transport in the distribution of trace species measured at the baseline observatories, as well as those measured on ships, on aircraft, and at other experimental sites. The standard gridded meteorological data used as input to the CMDL trajectory model come from the European Centre for Medium-Range Weather Forecasts (ECMWF) through the National Center for Atmospheric Research (NCAR). These data usually become available about 1 month after collection. Sixteen years of meteorological data (1986-2001) are now available on a CMDL server. The trajectory program is automated so that obtaining large volumes of trajectories (e.g., for a site climatology) is straightforward.

The trajectory input data are fairly coarse because of storage and processing constraints. The data have a horizontal resolution of 2.5° latitude × 2.5° longitude, a vertical resolution of 14 levels (from surface to 10 hPa), and a temporal resolution of 12 hours. Trajectories produced with these data are not suitable for diagnosis of mesoscale transport, but rather they track large-scale regional airflow. The gridded winds are interpolated kinematically to isentropic surfaces with the specification of arrival height, arrival pressure, or potential temperature. A description of the isentropic model is on the web (http://www.cmdl.noaa.gov/ozwv/traj/trajinfo.html). The method of wind interpolation to the isentropic surface is detailed in section 3.13.4 of *Summary Report No. 11* [*Harris and Bodhaine*, 1983].

Trajectories for various sites of interest are provided in real time on CMDL's trajectory website (http://www.cmdl.noaa.gov/ozwv/traj). CMDL scientists and collaborators are encouraged to contact the project leader to request a new site be added to this group. These trajectories are made with meteorological data downloaded twice daily

Fig. 4.9. Water vapor mixing ratio residuals (+) for the 16-24 km layer over Boulder, Colorado. The solid curve is a fit to the filtered monthly residuals. The dashed curves represent the 95% confidence interval based on the application of a Monte Carlo technique.

from the National Centers for Environmental Prediction (NCEP). The differences between the ECMWF and NCEP data sets are usually slight, but to avoid confusion, it is recommended that the real-time trajectories be used only as a first look. Trajectories for publication should be based on the ECMWF data.

A new feature on the website is the capability to plot trajectories from the observatory archives (http://www. cmdl.noaa.gov/ozwv/traj/siteplot.html). The archives contain ECMWF trajectories arriving at the observatories for 1986 through the last date of available data (1 or 2 months prior to the present). Several arrival altitudes are provided. The user may obtain Postscript files and print the trajectories. Another new website (http://www.cmdl.noaa. gov/ozwv/traj/tchentry.html) allows a scientist to format the input parameters for a set of trajectory calculations and mail this information to the project leader.

Trajectories have been used to investigate the relationships of trace gas and aerosol measurements to their sources and sinks. Some studies utilizing trajectories at the CMDL observatories are cited in section 4.1.7 of *CMDL Summary Report No. 24* [*Hofmann et al.*, 1998]. More recently, *Harris et al.* [2000] analyzed trace gas correlations during winter dark periods at BRW with the use of trajectories. These papers are also listed on the web (http://www.cmdl.noaa.gov/ozwv/traj/papers.html).

4.1.8. STRATOSPHERIC AEROSOLS

The MLO lidar measurements of aerosol backscatter and stratospheric/mesospheric temperature continued during 2000 and 2001. The frequency of measurements was about 42 per year, similar to previous years. The record of MLO total stratospheric integrated aerosol backscatter since 1999 is shown in Figure 4.11, along with the record from the Boulder lidar. The same background levels and annual cycle continued and were summarized by *Barnes and Hofmann* [2001]. No aerosol increases from volcanic eruptions were identified.
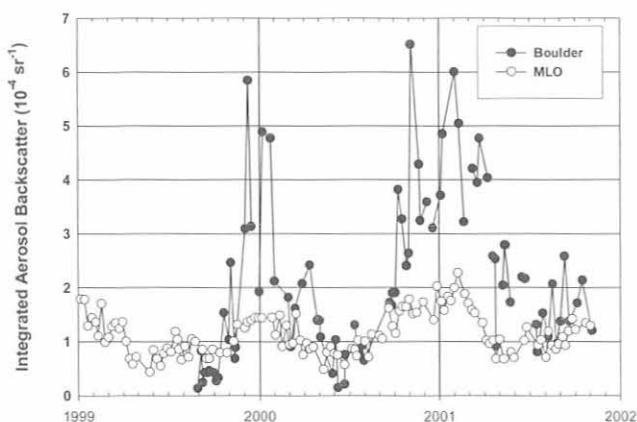
The Boulder lidar was installed in 1999 and operated with a single detector channel for all altitudes. Because of the high-altitude variability of the tropopause, measuring the stratosphere proved to be a problem for the single channel, and a second detector was added and optimized for the troposphere in April 2000. Several Asian dust episodes were measured with this channel in spring 2001. The Boulder data show much more variability than the MLO data. The annual cycle of stratospheric aerosol above Boulder is in phase with that of MLO, peaking in the winter, but has a much larger amplitude. Much of the winter increase in the stratospheric aerosol layer above Boulder is due to the lowering of the tropopause height (from 15 km in summer to 10 km in winter). A stratospheric layer is much harder to identify above Boulder where there are often larger aerosol concentrations in the upper troposphere than in the stratosphere. The tropopause height at MLO (16 km in summer and 17.5 km in winter) varies much less than that of Boulder, and the MLO stratospheric layer is always clearly defined because the upper troposphere generally has very small aerosol concentrations. The variability of the peak scattering ratio is larger at Boulder than at MLO (Figure 4.12). The peak ratio is usually several kilometers above the tropopause and may be a better quantity than the integrated aerosol backscatter (IABS) for comparison of MLO and Boulder data.

Work for a NOAA grant to make the ruby lidar stratospheric aerosol record available to researchers was completed in 2001. The entire record since 1974 was standardized and error estimates were included in the data files. The observations are now available by anonymous ftp to the public (mloftp.mlo.noaa.gov). Part of the work was completed by a local high school science teacher and high school student.

One new measurement added to the MLO lidar was water vapor. The Raman-shifted wavelength due to water molecules was measured to obtain profiles from the station altitude to approximately 14 km. The lidar is able to reach

Fig. 4.11. Lidar measurements of integrated aerosol backscatter (IABS) for the stratosphere. At MLO the altitude range is 15.8 to 33 km; in Boulder the range is tropopause to 30 km.
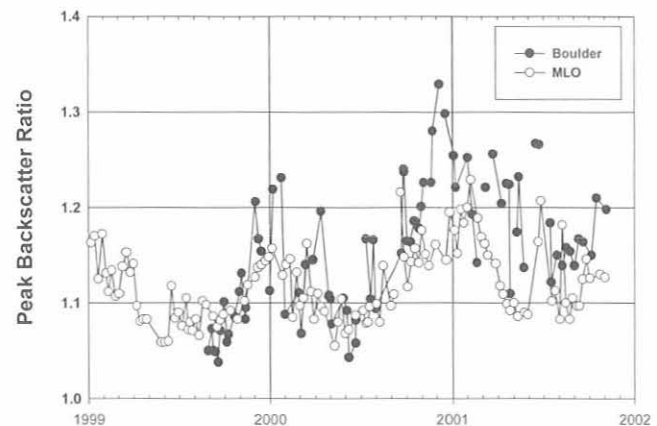
Fig. 4.12. Lidar measurements of peak aerosol backscatter ratio for the stratosphere. The backscatter ratio is the total scattering (molecular + aerosol) divided by the molecular scattering. A ratio of 1.0 is pure molecular scattering.

altitudes above that of radiosondes, and also measure aerosols simultaneously, which is useful for cirrus cloud studies. A National Aeronautics and Space Administration (NASA)-funded program will use the lidar and sondes to validate water vapor, temperature, and ozone for the Atmospheric Infrared Sounder (AIRS) satellite instrument to be launched in 2002. The measurement of water vapor profiles by lidar is limited by the weak signal in the cold, dry upper troposphere. New red-sensitive detectors and a new 74-cm-diameter mirror were installed to increase the water vapor signal. The optical support structure was extended to accommodate the long focal length of the new mirror. The old ruby telescope was remounted at the same time to test new components.

4.2. SPECIAL PROJECTS

4.2.1. JOSIE-2000

JOSIE-2000 was held at the Research Center, Jülich, Germany, in September 2000, during two 9-day periods. The project, sponsored by the World Meteorological Organization (WMO), provided an excellent opportunity to compare ozone profile measurements from various ozonesonde groups, using slightly different ozonesonde preparation procedures, sensing solutions, or instruments.

During JOSIE-2000, ozonesondes were tested in seven separate simulated flight conditions in an environmental chamber, with an ultraviolet (UV)-photometer as an ozone reference. The chamber accommodated four ozonesondes during each simulation. Eight different groups participated; seven used ECC ozonesondes and one Japanese group used the KC79 ozonesonde. The testing procedure was similar to the JOSIE-1996 campaign [Smit et al., 1998], where all participants brought their own ozonesondes and preparation equipment.

Among the JOSIE participants, three different cathode sensor solution recipes were used, three pump-efficiency algorithm curves were used for data processing, and ozonesondes were from EN-SCI Corporation and Science Pump Corporation. CMDL used both Science Pump and EN-SCI ozonesondes. The only major difference for CMDL during JOSIE-2000 compared with JOSIE-1996 was the switch from the standard buffered 1% KI sensor solution, used by all ECC ozonesonde groups in JOSIE-1996, to unbuffered 2% KI sensor solutions. CMDL's measured pump efficiencies were nearly the same in both JOSIE campaigns. A comparison of the CMDL results at JOSIE in 1996 and 2000 showed that the unbuffered 2% KI sensor solution improved the stratospheric measurements, averaging about 6% greater than the UV-reference compared with 15% greater with the 1% KI. The agreement was not as good near the surface where the 2% KI ozonesondes were about 8% too low. However, several calibrations in CMDL (in the laboratory and outside) comparing ozonesonde measurements to measurements made with surface instruments with UV techniques were consistently within ±2%.

Figure 4.13 shows one of the JOSIE-2000 simulations with both a model 2Z EN-SCI and Science Pump 6A ozonesonde. The profile simulation, run in a sinusoidal
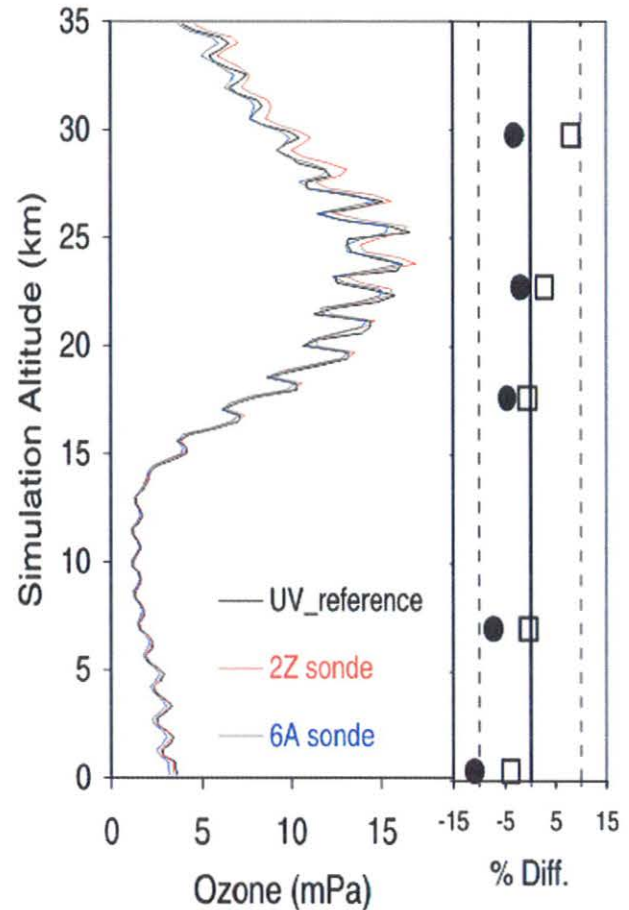
Fig. 4.13. Comparison of models 6A and 2Z ECC ozonesondes during JOSIE-2000 simulation experiments. Both ozonesondes used unbuffered 2% KI cathode-sensing solution. The chart on the right shows the percent differences (UV minus sonde) between the UV-reference and both the 6A ozonesonde (black circles) and the 2Z ozonesonde (squares).

wave pattern, illustrates the general difference observed between the two manufacturers of ECC ozonesondes. On average, the 6A model was about 4% lower than the 2Z model near the surface and nearly 10% lower near the top of the profile. The UV-reference was approximately in between both ozonesonde profiles.

4.2.2. DOBSON AND OZONESONDE MEASUREMENTS AT FAIRBANKS DURING TOMS[3]F

TOMS[3]F was a campaign to investigate the differences in total ozone measurements produced by ground-based and space-based instruments. The experiment was prompted by differences as high as 4% between values reported by Dobson or Brewer stations and the space-based TOMS, TOMS being higher. The difference is dependent on both total ozone and latitude. The campaign period of March and April 2001 coincides with high total ozone and low

Sun, which appear to cause the differences. The experiment was funded primarily by NASA, and included CMDL, NASA, Meteorological Service of Canada (MSC), and University of Alaska, Fairbanks (UAF) instruments and personnel.

Dobson Measurements

The Dobson instrument and the method of operation are well documented [*Dobson*, 1931]. Briefly, the instrument measures the intensity differences of selected wavelength pairs (called A, C, and D) in the UV by attenuating the more intense wavelength to match the intensity of the other. If the atmospheric ozone absorption coefficients for those wavelengths and the instrument extraterrestrial constant are known, the total ozone amount can be calculated from the difference in the intensity between the two wavelengths of a pair either on direct sunlight or light from the zenith sky. Normally, measurements on two pairs are made to reduce the effects of other atmospheric constituents. Measurements using the A and D pairs on direct sunlight are considered the most accurate, and the results of other measurement types are normalized to the AD-pair type. Measurements using the C and D pairs on direct sunlight are used when the Sun is lower in the sky, i.e., higher solar zenith angles (SZAs). Measurements can also be made on the light scattered from the zenith sky, and ozone estimated from the results. If a series of measurements is made on the zenith sky as the Sun rises or sets (SZA changes from greater than 90° to 60°, or the reverse), the resultant time series of readings versus zenith angle has a characteristic shape that is related to the ozone distribution with height. This curve is called the Umkehr effect [*Götz*, 1931].

During the TOMS[3]F campaign, measurements were made with both the normal Fairbanks station instrument, D063 (an automated instrument), and the World Standard Dobson instrument, D083. D083 made measurements in the period March 20-April 3, 2001; D063 made measurements throughout the campaign. This analysis concentrates on the period when both instruments were operational in Fairbanks, and stratospheric temperature data were available from the extensive balloon ozonesonde campaign. D083 made 453 observations, 139 of which were AD-pair type, 138 were CD-pair type, and the rest were various zenith measurements. D063 made 656 observations over a longer period, 161 of which were AD-pair type, 131 were CD-pair type, and the rest were various zenith observations. Figure 4.14 shows an overview of the total ozone measurements during the intensive measurement period. Eight measurements of the Umkehr effect were made with both instruments operating coincident with ozonesonde flights.

The measurements were reduced using the published instrument characteristics and ozone absorption information, and both the normal algorithm, which uses ozone coefficients based on a standard midlatitude ozone profile assuming a −46.3°C stratosphere, and an algorithm from the actual stratospheric conditions measured by the balloon flights. The first discovery was a difference in the ozone calculated by the two instruments (AD-pair-type measurement), with D063 approximately 1-2% lower than D083 (Figure 4.15). An investigation of quasi-simultaneous measurements showed a calibration difference between the
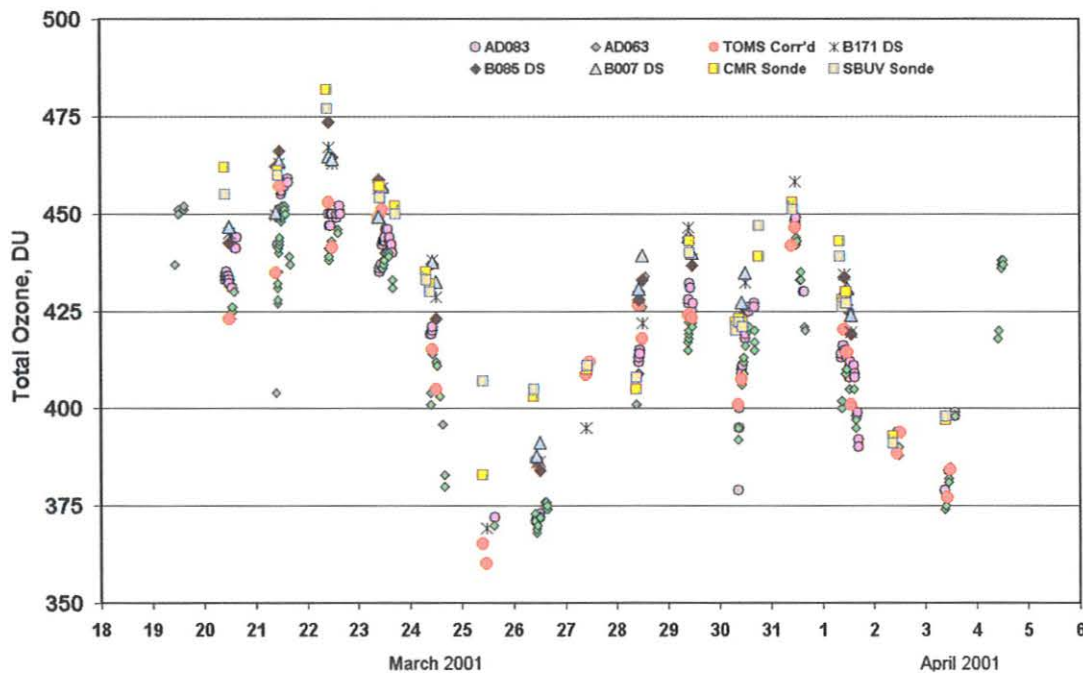
Fig. 4.14. Total ozone measurements at Fairbanks, Alaska, during the primary period of TOMS[3]F. AD represents direct-Sun Dobson spectrophotometer observations from instruments D083 and D063; B are direct-Sun Brewer measurements; TOMS is the Total Ozone Mapping Spectrometer; and the ozonesonde totals are computed by the constant mixing ratio (CMR) residual method and by climatological averages based on solar backscatter ultraviolet (SBUV) satellite data.
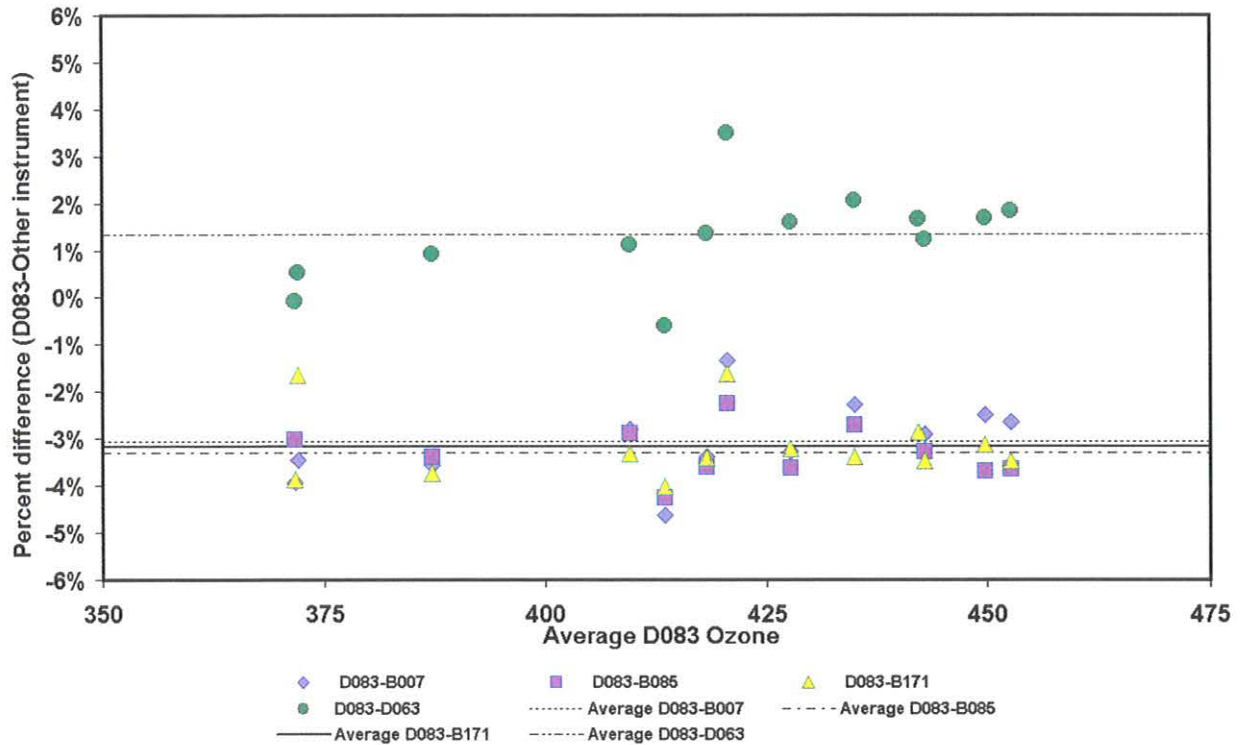
Fig. 4.15. Average percent difference between D083 (uncorrected for stratospheric temperature), and D063 (uncorrected) and the Brewer instruments, based on daily averages of direct-Sun observations, μ < 3.2.

two instruments that accounts for the difference at lower SZAs but not at higher SZAs. The unexplained difference is related to μX, where μ is the optical path length of the direct solar beam through the most UV-light-absorbing part of the atmosphere, and is calculated from SZA. μ is dimensionless and varies from 1 at SZA = 0° to approximately 12 at SZA = 90°. X is the total column ozone amount in Dobson units. Both factors control the UV light intensity as seen by the instruments at the time of the measurement. Investigations by scientists at UAF showed that this μX dependence could be explained by scattered, off-band light within the instrument. (The instrument is a double prismatic monochromator. Multiple surfaces allow for multiple reflections, which produce both spurious spectra and scattered white light in the optical path.) Because the D083 instrument, as well as the D063 instrument, appeared to have some μX dependence, a double-grating monochromator Brewer 171 that has had the internal stray light measured independently was used as a reference. This Brewer instrument's measured stray light was found to be very low. Because an apparent lack of μX dependence of the CD-pair-type measurement in Figure 4.16 was noted as opposed to the μX dependence of the AD-pair in Figure 4.17, a model was derived to evaluate internally scattered light using only the relationship between the CD- and AD-pair-type observations (Figure 4.18). The physical alignment of several optical components during C-wavelength-pair measurements results in less scattered light in the optical path.

Considering the difference between the instruments (μ range: 3.2 or less), the average is approximately 3% between the Brewer B171 results and Dobson D083 AD-pair results,
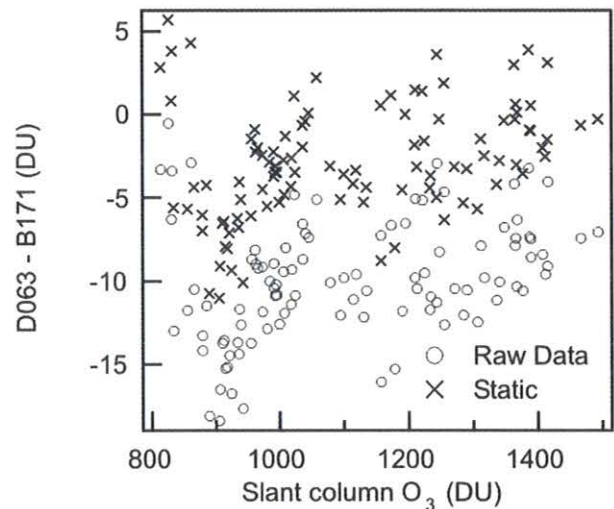
Fig. 4.16. The difference between D063 CD-pair direct-Sun ground quartz plate observations and B171 observations versus the slant column of ozone (μX). The open circles are the raw (reprocessed) Dobson data, and the crosses are the Dobson data corrected for the mean stratospheric temperature, known as the static correction.
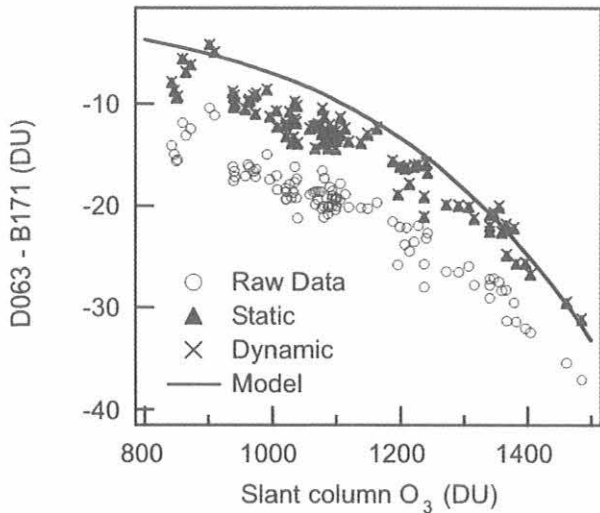
Fig. 4.17. The difference between D063 AD-pair direct-Sun ground quartz plate observations and the B171 observations versus the slant column of ozone (μX). The open circles are the raw (reprocessed) Dobson data, the filled triangles are the Dobson data corrected for mean stratospheric temperature, and the crosses are the Dobson data corrected for both stratospheric temperature and known absorption nonlinearity arising from finite slit widths. The solid curve is from a model that assumes 0.09% of the Dobson A-long light intensity is scattered into the Dobson A-short measured intensity.

Fig. 4.18. The ratio between D063 CD-pair and AD-pair near-coincident observations plotted versus the slant column of ozone (μX). The open circles are the ratios for the raw (reprocessed) Dobson data, and the curve is from a model assuming 0.09% stray light on the Dobson A-pair observation, and no stray light on the C- or D-pair observations.

with Brewer measurements higher (Figure 4.15) using the normal analysis method for Dobson measurements. After the analysis including the effect of the colder stratospheric temperature on the ozone absorption coefficients at the wavelengths used by the Dobson instrument, there remains an approximate 2% difference. The wavelengths used by the Brewer instrument have been shown to be independent of stratospheric temperature, and Dobson-Brewer intercomparisons at smaller μX (<900 DU) values and lower latitude sites with warmer stratospheric temperatures agree well. The difference at higher μX can be attributed to the effect of forward-scattered light in the atmosphere in the Dobson instruments' field of view, scattered light within the Dobson instruments, or a combination of the two.

Another conclusion of this campaign is that when selecting data, the μX factor would be a better criterion than the μ value. Making such a change in the selection process could have an effect on trend analysis at high latitudes, so the entire long-term data sets would have to be re-selected.

The Umkehr measurements with the C-wavelength pair produced very similar ozone profiles from both instruments, though the profiles differed from the balloon profiles. The differences can be attributed to the time difference between the measurements, the information content of the Umkehr measurement, and weaknesses in the reduction algorithm.

Ozonesonde Measurements

Thirty electrochemical concentration cell (ECC) ozonesonde instruments were flown during the TOMS[3]F campaign between March 20 and April 25, 2001. The ozonesondes provided vertical profiles of ozone con-

centration and an additional total column ozone measurement for comparison with the ground-based and satellite observations. The balloonborne instruments were launched from the University of Alaska, Fairbanks, every day, with several days of two to three balloon flights. Figure 4.14 shows that the ozonesondes measured slightly higher total ozone than the other methods, approximately 4.1% higher than Dobson instrument D083 and 2% higher than TOMS measurements. Figure 4.19 shows the average ozone partial pressure and mixing ratio measured during the campaign. The most variability in the profiles was observed near the ozone peak, as indicated by the standard deviation bars. The ozonesondes showed very good precision up to an altitude of 34 km.

The TOMS[3]F campaign was the first field project that used the EN-SCI Global Positioning System (GPS) interface board with ozonesondes. The ozonesondes used Vaisala RS80-N radiosondes to measure pressure, temperature, and relative humidity, while the GPS board collected latitude, longitude, and altitude data approximately every 5 seconds. The GPS altitude provided the location of the sonde, and thus winds, during the entire flight. The GPS altitude proved to be very beneficial in the correction of the calculated geopotential height from the Vaisala pressure and temperature data. Below 25 km the two altitudes compared very well, but above 25 km the difference (Vaisala geopotential – GPS altitude) was in the range from −200 m to +1000 m.

4.2.3. LONG-TERM TOTAL OZONE TRENDS

A new method was developed to investigate total ozone variations that are in the range of about 3.5 years to decades [Harris et al., 2001]. The goal of the study was to create a
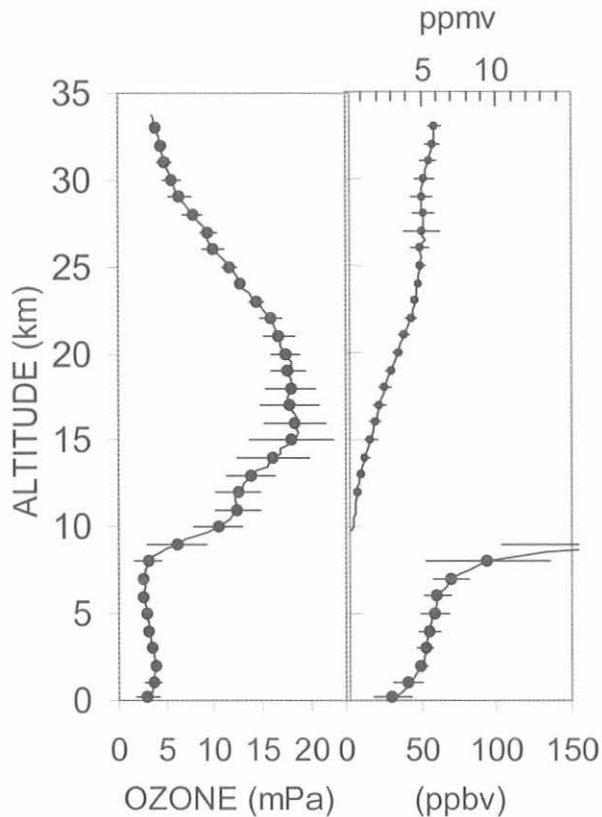
Fig. 4.19. Average ozonesonde partial pressure (left panel) and mixing ratio (right panel) profiles measured during the TOMS³F campaign at Fairbanks, Alaska. The error bars represent 1 standard deviation.
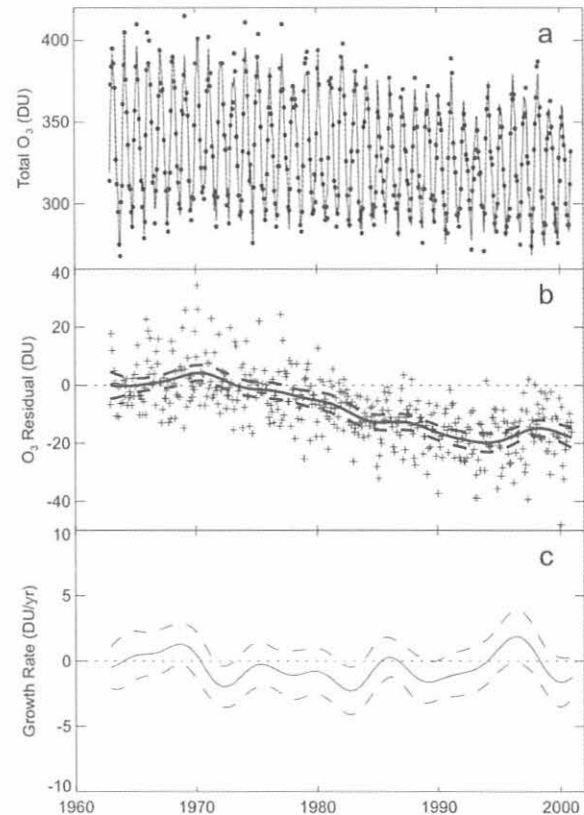

Fig. 4.20. Bismarck, North Dakota, total ozone data. (a) Ozone monthly means (filled circles) and the AR fit (solid line). (b) Total ozone tendency curve (solid curve) with 95% confidence limits (dashed curves). Residuals combined with the cubic function from the AR fit are shown as plus signs. The points and the tendency curve have been adjusted so that the tendency curve starts at zero. (c) The growth rate curve and 95% confidence limits.

trend line that is somewhat flexible so that the recent decreases as well as the (probable) recovery can be tracked. The method combines traditional total ozone trend-finding, i.e., autoregressive modeling (AR), techniques with trend analysis methods developed in CMDL by the Carbon Cycle Greenhouse Gases group. The intent was to first remove explained variations in the ozone. This step regresses total ozone to seasonal harmonics, the solar cycle, quasi-biennial oscillation (QBO) in equatorial stratospheric winds, detrended temperature at 100 and 500 hPa, and a cubic polynomial. The residuals of this fit are added back to the cubic function prior to the next step. Then a smooth curve is fitted to the resulting data according to methods of *Thoning et al.* [1989], with a filter chosen to remove periods in the data of fewer than about 3.5 years. The derivative of this smooth ozone "tendency curve" is the ozone growth rate curve. Integration of the growth rate curve gives the average growth rate. Uncertainties of the curves and the growth rate average are determined by bootstrap techniques.

First the method was applied to individual station data from the Dobson total ozone network. These data are archived at WOUDC in Downsview, Ontario, Canada. Figure 4.20a shows total ozone monthly means and the AR fit of explained variation for Bismarck, North Dakota. Figure 4.20b shows the total ozone tendency curve with

95% confidence limits for Bismarck. Residuals combined with the cubic function from the AR fit are also shown. Figure 4.20c shows the growth rate curve for Bismarck and the 95% confidence limits. Averaging the monthly values along this curve gives an overall growth rate of –1.4% decade⁻¹ for the period December 1962 through December 2000. Bootstrap methods were used to determine a standard error (S.E.) of 0.2% decade⁻¹. For the individual stations examined, total ozone decreases ranged from 1 to 2% decade⁻¹ since the 1960s and from 2 to 4% decade⁻¹ over the period 1979-1997.

Figure 4.21a depicts the total ozone tendency curves for six midlatitude Dobson sites. The long-term total ozone decrease is clearly evident, with the ozone decline beginning in the early 1970s. Some of the stations share common features (peaks and dips). The common features in the ozone tendency curves are accentuated in the growth rate curves for the four similar midlatitude records (Caribou, Bismarck, Wallops Island, and Arosa) shown in Figure 4.21b. While keeping in mind that the exact locations of maxima and minima are somewhat uncertain
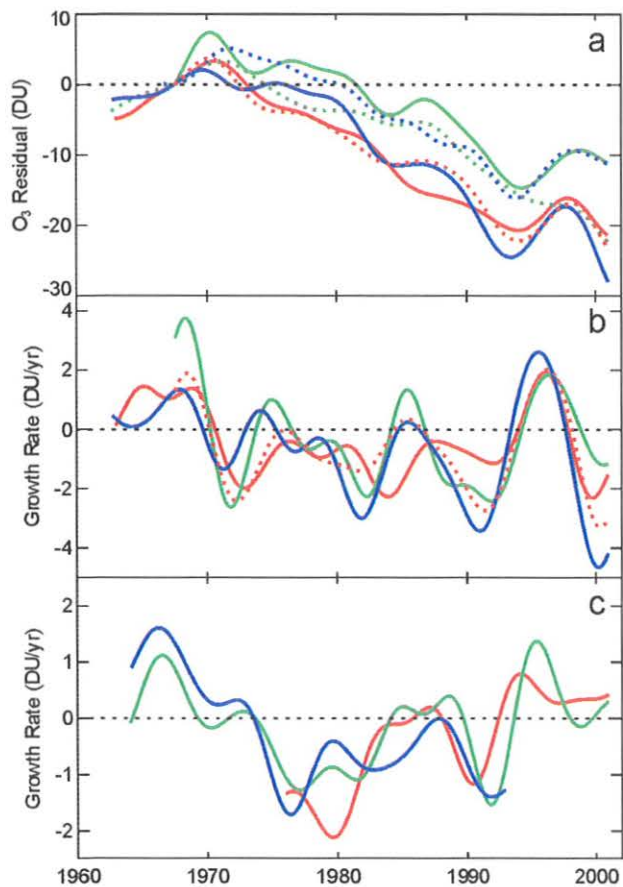
Fig. 4.21. Comparisons of total ozone tendency and growth rate curves. (a) Midlatitude tendency curves for Bismarck, North Dakota (solid red), Nashville, Tennessee (dotted green), Wallops Island, Virginia (solid green), Boulder, Colorado (dotted blue), Caribou, Maine (solid blue), and Arosa, Switzerland (dotted red). Tendency curves have been set to zero on July 1967 (the beginning of the shortest record) to aid the comparison. (b) Growth rate curves for four coherent midlatitude sites with the same colors as in (a). (c) Growth rate curves for the tropical sites, Samoa (red), Mauna Loa (green), and Huancayo (blue).

To further explore the total ozone growth rate coherence seen among the Dobson sites, CMDL obtained the TOMS/solar backscatter UV (SBUV) merged total ozone monthly data set (http://code916.gsfc.nasa.gov/Data_services/merged/). These data cover all longitudes, and latitudes from 60°N to 60°S. Data are gridded 5° of latitude by 10° of longitude and are available with few data gaps from November 1978 through December 2000. In the data set there are 24 × 36 grid cells, each of which can be thought of as a separate site with a time series consisting of 266 months of data. Each of the 864 time series was processed in the same way that the Dobson station data were processed earlier.

The results are compiled in Figure 4.22, which depicts the average growth rate in percent per decade over the entire grid. In this figure the cooler colors (green, blue, purple) denote relatively larger ozone decreases compared with the hotter colors (yellow, orange, red). In the area near the tropics that is cross-hatched in white, the total ozone growth rate is not statistically different from zero. The greatest ozone loss rate (or negative growth rate) in the southern hemisphere (SH) is centered at 0°E and 50-60°S (>8% decade^{-1}). This may be a result of some asymmetry of the Antarctic continent and the preferred pattern of vortex breakup after the ozone hole forms in the spring. The greatest loss rates in the northern hemisphere (NH) occur over Western Europe, Great Britain, Siberia, and the North Pacific (>3% decade^{-1}).

The next step was to look at the total ozone time series averaged over 5°-latitude zones. Figure 4.23 shows the total ozone deviation since 1978. This plot is analogous to the total ozone tendency curves for the six sites shown in Figure 4.21a. Again hot colors signify relatively more ozone. This plot shows a steady decrease in the high latitudes of the SH. More than 35 DU of total ozone has been lost since November 1978 at 60°S compared with more than 15 DU at 60°N. The NH high midlatitudes have seen a slight recovery since the low point in 1995. The areal coverage of the region representing more than a 10-DU loss has increased from about 40° and poleward in 1988 to about 23° and poleward at the end of 2000.

Figure 4.24 shows the instantaneous zonal growth rate for 60°N-60°S. Seen in this plot are the growth rate evolution in time and the patterns of growth rate coherence. The instantaneous growth rate is not statistically distinguishable from zero over most of the warm colors (−2 to 2% decade^{-1}). Outside of this area, the largest loss rates (greatest negative growth rates) occurred in 1982, 1991, and 1999 in both hemispheres. The largest loss rates of the time series (>9% decade^{-1}) occurred in 1982-1983 in the most southerly latitudes. Events that may have contributed to this decrease are the El Chichón volcanic eruption, the declining phase of the solar cycle, and a very large El Niño event (peaking in early 1983). Loss rates in 1991-1992 were very likely influenced by the eruption of Mt. Pinatubo and possibly by the decline in the solar cycle. These reasons are not present during the high loss rates of 1999. It is interesting to note that the NH losses during 1982 and 1999 peaked at 30°N rather than at higher latitudes. Finally, during 1995-2000 there was a positive growth rate for ozone (>2% decade^{-1}) in the high northern latitudes. Warm temperatures in the stratosphere and boreal fires may have contributed to this effect.

because of the filtering process, it is noted that the coherence among these sites is maintained over their entire records. The growth rate curves for three tropical sites shown in Figure 4.21c also have coherence, although the pattern is different from that of the midlatitude curves. It is interesting to note that SMO's pattern leads that of MLO by more than 1 year. The two sites are separated by only 15° of longitude but lie on opposite sides of the equator. The causes for growth rate coherence are not known, though widespread meteorological and dynamical patterns are possibilities [*Zerefos et al.*, 1994; *Ziemke et al.*, 1997]. Some consecutive cycles of the midlatitude growth rate curves match the solar cycle. This could be fortuitous or a hint at a possible secondary effect not accounted for by the fit to the solar index.
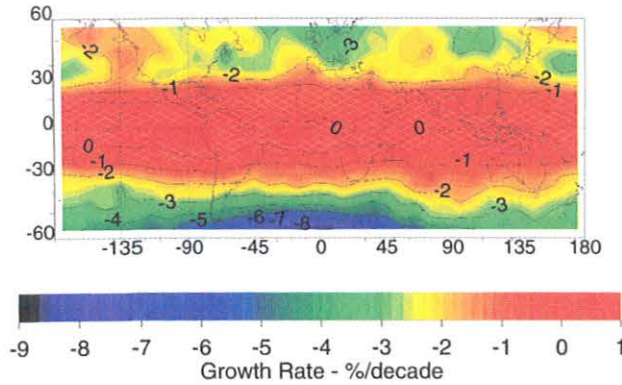
100

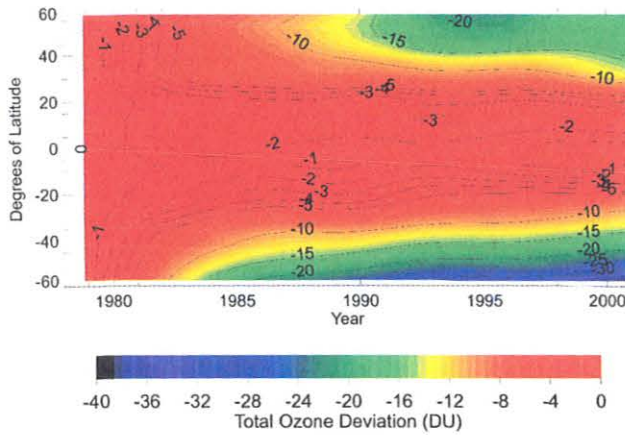Fig. 4.22. The average total ozone growth rate in percent per decade for November 1978-December 2000.

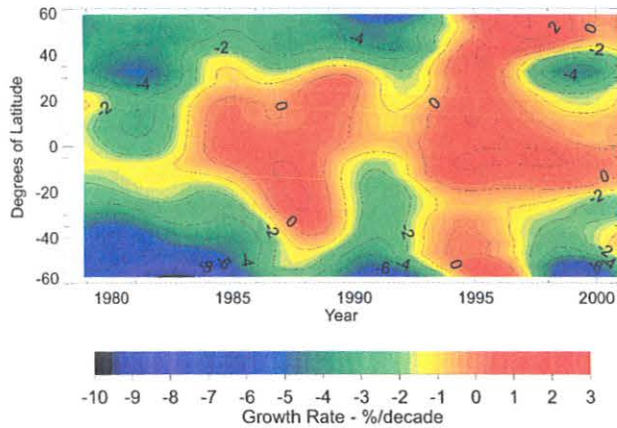Fig. 4.23. The total ozone zonal deviation in percent per decade since November 1978.

Fig. 4.24. The instantaneous zonal total ozone growth rate in percent per decade.

4.2.4. LONGITUDINAL AND TEMPORAL DISTRIBUTION OF DEHYDRATION IN THE TROPICAL TROPOPAUSE REGION

Balloonborne observations of frost-point temperature and ozone at several equatorial locations provide an accurate data set of water vapor and ozone with high vertical resolution around the tropical tropopause. Observations are analyzed here for San Cristóbal, Galápagos, Ecuador, in the eastern Pacific; Juazeiro do Norte in northeastern Brazil; along a ship cruise in the western equatorial Pacific; and Christmas Island in the central equatorial Pacific. At San Cristóbal, observations began in 1998 on a campaign basis and are ongoing as part of Soundings of Ozone and Water in the Equatorial Region (SOWER) [Hasebe et al., 1999], with the most recent campaign in November-December 2001. The observations are limited to ozone and water vapor. There is no direct evidence for the presence of ice particles; however, supersaturation observed in most spring profiles combined with large temperature variations during the observation period strongly suggest the presence of ice particles. High relative humidities well above ice saturation can force ice particle formation through homogeneous nucleation, and the subsequent sedimentation of these particles would lead to the removal of water substance. Thus, the observations of supersaturation with respect to ice imply dehydration, allowing a study of some of the characteristic processes at the tropical tropopause and of the regions that control the amount of water vapor entering the stratosphere. These processes are shown as a schematic in Figure 4.25.
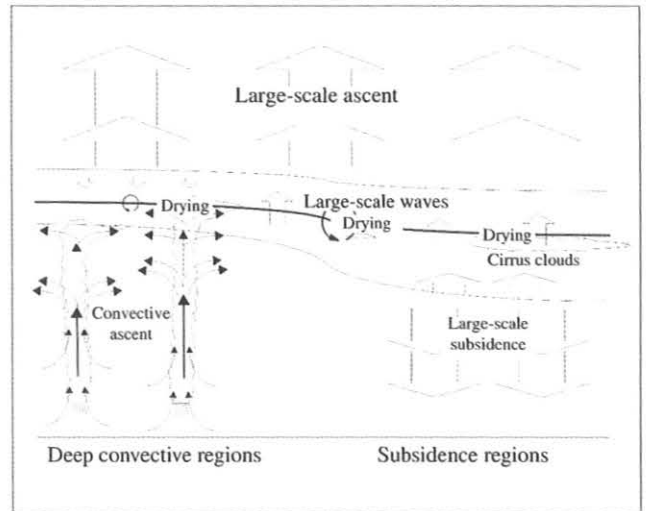
Fig. 4.25. Schematic of the transport and dehydration processes across the tropical tropopause. The tropopause is indicated by the solid thick line; the tropopause transition region is indicated by thin lines above and below. Drying occurs at the temperature minimum close to the lapse-rate tropopause, induced by convection, large-scale waves, and slow ascent. Breaking of large-scale waves is one of the sources of ozone in the tropopause transition region below the tropopause. The impact of the different deep convective regions on the transition region depends on the altitude reached by typical convection within each region.

Deep convection in the western Pacific transports lower tropospheric air to the tropopause, dehydrating the air to very low mixing ratios, while maintaining high relative humidities and low ozone concentrations [*Vömel et al.,* 1995]. Downward motion in the lower stratosphere above regions of deep convection [*Gage et al.,* 1991; *Sherwood,* 2000] may be responsible for the extremely steep gradients of water vapor and ozone observed directly at the tropopause. Away from regions of deep convection, subsidence lowers the relative humidity in the middle troposphere; however, the upper troposphere remains at high relative humidities and low ozone values indicative of the recent convective origin of the air. In regions where deep convection does not reach the tropical tropopause or where subsidence prevails, saturation and subsequent dehydration within the transition layer may still occur, driven only by slow, large-scale ascent [*Vömel et al.,* 2002]. Kelvin waves and other large-scale waves may contribute to the dehydration process in these regions [*Fujiwara et al.,* 2001]. Not all equatorial regions show saturation, and some regions may not participate at all in the dehydration of rising air. There is a strong seasonal cycle in the dehydration process at the tropical tropopause. At San Cristóbal, nonconvective dehydration was observed during the March campaigns, but not during the September campaigns.

A transition region around the tropopause can be identified by the increase in relative humidity with altitude up to the tropopause [*Vömel et al.,* 2002], in addition to the increase in ozone [*Folkins et al.,* 1999]. While wave breaking across the tropical tropopause and midlatitude intrusions are sources for ozone in this transition region [*Fujiwara et al.,* 1998], the general upward motion in the transition region driven by the stratospheric extratropical pump [*Holton et al.,* 1995, and references therein] maintains a high relative humidity within this layer. The seasonal cycle of relative humidity within the transition region is driven by the seasonal cycle of the stratospheric extratropical pump. In addition, the relative importance of different regions for the dehydration process changes with season. Based on CMDL measurements from several equatorial sites, it appears that the zonal average of the tropopause relative humidity shows a seasonal cycle as well. Furthermore, the seasonal cycle of the tropopause temperature shows a rapid cooling between September and December. The water vapor mixing ratio of 6 ppmv, when air passed the tropical tropopause in September, is not found later at higher altitudes when the new seasonal minimum at the tropopause is established (Figure 4.26), indicating a secondary or continuing dehydration of this air through December [*Vömel et al.,* 2002]. Since average vertical velocities in the lower stratosphere are significantly larger during the northern winter, it appears that the northern winter months play a stronger role than the northern summer months in the dehydration of air entering the stratosphere.

Considering that the tropopause temperature in the equatorial eastern Pacific during September is too warm to allow saturation and the presence of cirrus clouds, reports of subvisible cirrus in this region may indicate that these clouds are not ice clouds but rather a mixture of nitric acid
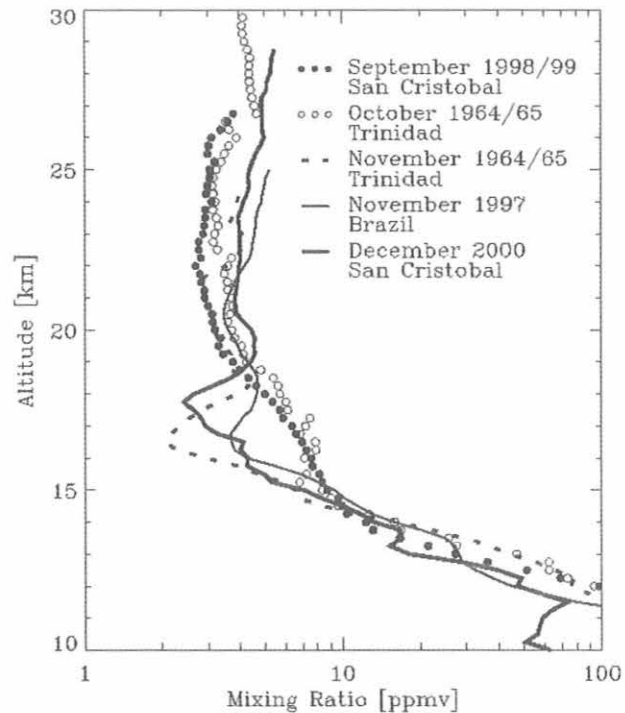
Fig. 4.26. Development of the dehydration between September and December. The profiles at San Cristóbal and Trinidad are the average for all profiles of the month(s); the profile at Juazeiro, Brazil, is a single profile.

and water similar to some types of stratospheric clouds found in the winter polar stratosphere.

CMDL's analysis identified three different dehydration processes that can occur at the tropical tropopause. It also showed that not all regions participate in dehydration of air in the tropopause transition region. Air entering the stratosphere will most likely have experienced a mixed history of the various dehydration and mixing processes, making quantitative modeling very difficult. There is a regional preference as well as a seasonal preference for dehydration, and the transport of water vapor into the stratosphere does not occur in a temporally and spatially uniform manner. This is contrary to the analysis by *Dessler* [1998], who suggested that theories including spatial and temporal preference "are no longer necessary." *Newell and Gould-Stewart* [1981] suggested that air enters the stratosphere predominantly over the western Pacific during the northern hemisphere winter and early spring, as well as over the Indian Ocean during the monsoon season; they called this phenomenon the "stratospheric fountain." However, the sharp gradients of water vapor and ozone at the tropopause in deep convective regions, as well as the offset between regions of deep convection and regions of coldest tropopause temperatures [*Nishida et al.,* 2000], indicate that the regions of deep convection are not necessarily where air enters the stratosphere. The regional and seasonal preference for the dehydration process still needs to be quantified in detail.

Deep convective regions play an important role as a source of air in the transition region below the tropopause. This air may be transported horizontally away from the area of deep convection before entering the stratosphere [*Holton and Gettleman*, 2001]. Furthermore, overshooting deep convection may directly inject air into the lowermost stratosphere. If the tropopause temperature is cold enough, air in the transition region may be dehydrated further in nonconvective regions. The extratropical stratospheric pump provides a zonally averaged view, but there is no reason to assume that the vertical ascent in the lower tropical stratosphere is zonally symmetric. CMDL's analysis has not addressed this issue, but studies showing descending motion above the deep convective regions in the maritime continent already indicate that there are important zonal asymmetries in the vertical ascent in the lower tropical stratosphere. It is plausible that cold tropopause temperatures also correlate with regions of stronger vertical ascent, which would not only imply a regional preference for the dehydration of air entering the stratosphere, but also a regional preference for the entry point. It is also important to point out that there has been a significant increase in stratospheric water vapor [*Oltmans et al.*, 2000] and, at the same time, a decrease in the tropical tropopause temperature [*Zhou et al.*, 2001]. These two trends are not easily reconcilable. They also show that the atmosphere that led to the formulation of the stratospheric fountain hypothesis has changed and that the conclusions that are derived now will necessarily be different without refuting the stratospheric fountain hypothesis.

As a last point, the classifications "stratospheric" and "tropospheric" for air that is respectively above and below the lapse-rate tropopause need to be questioned. Air in the transition region has stratospheric signatures, like higher ozone concentrations and higher vertical stability than air in the middle troposphere. At the same time, this air has higher values of relative humidity and typical tropospheric tracers as well as the potential for cloud formation. In this region there is a mixture of both stratospheric and tropospheric air, and the question of whether convection overshoots the tropopause or not should be replaced by questions of how deep convection penetrates into the transition layer and how much nonconvective and wave-driven processes contribute to the makeup of the air in this region.

4.2.5. Tropical Tropospheric Ozone

Ozone vertical profile measurements obtained during 1995-1999 from ozonesondes flown at Fiji, Samoa, Tahiti, and the Galápagos provide a picture of ozone in the troposphere over the tropical south Pacific Ocean [*Oltmans et al.*, 2001]. The seasonal variation at each of these sites is significant. The seasonal behavior at the western Pacific sites is similar, with the Tahiti pattern typical (Figure 4.27). At sites in both the eastern Pacific (i.e., Galápagos; Figure 4.28) and the western Pacific, ozone mixing ratios are greatest at almost all levels in the troposphere during September-November and smallest during March-May. The vertical profile has a relative
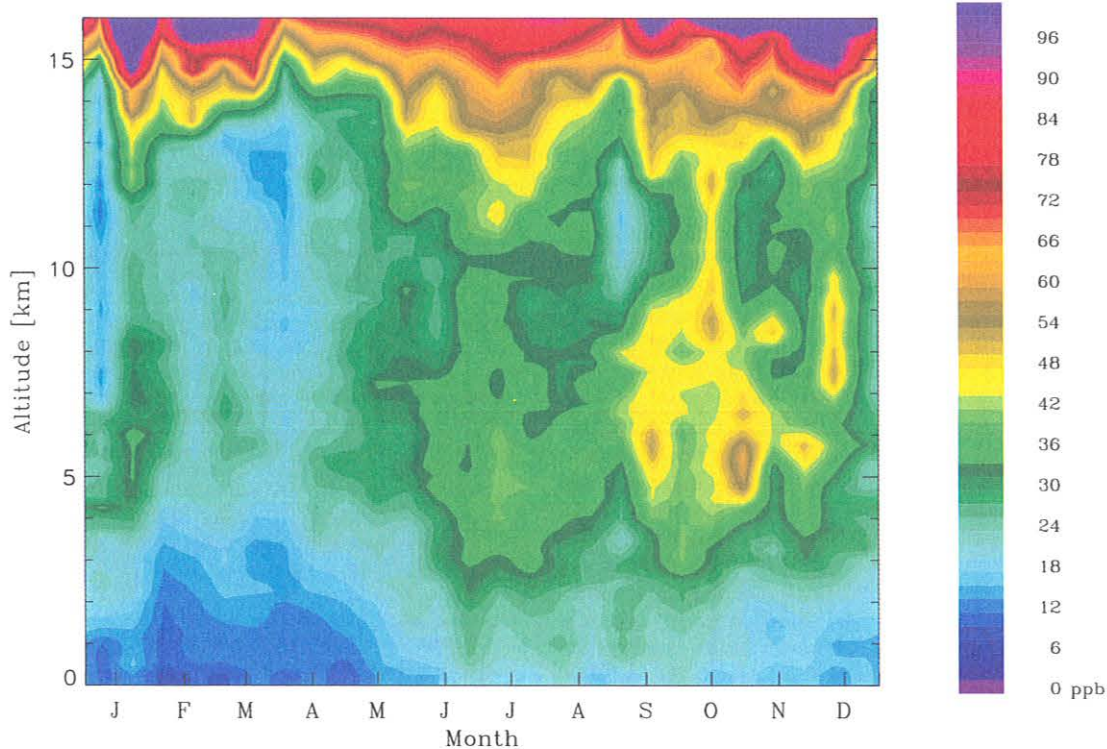
Fig. 4.27. Cross section of average ozone mixing ratios in the troposphere at Tahiti for 1995-1999.
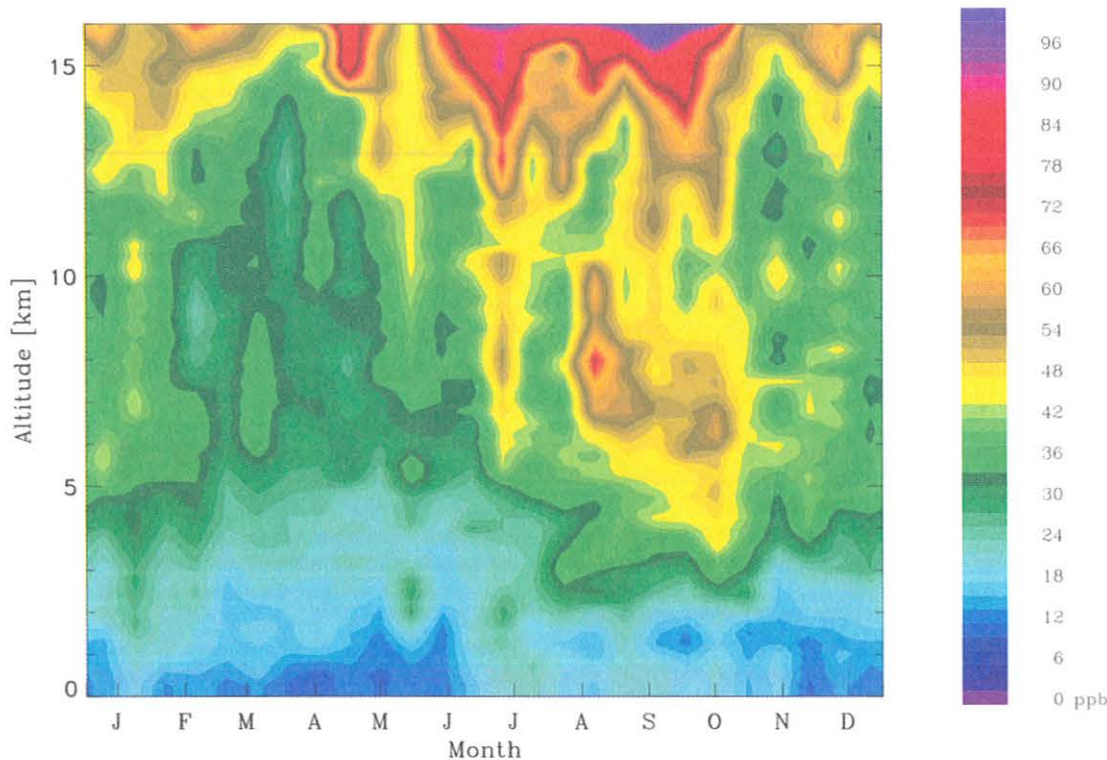
Fig. 4.28. Cross section of average ozone mixing ratios in the troposphere at Galápagos for 1998-1999.

maximum at all the sites in the troposphere throughout the year; the largest mixing ratios are usually found near the tropopause. This maximum is particularly pronounced during September-November. On average, throughout the troposphere, the Galápagos site has larger ozone mixing ratios than the western Pacific sites. The enhanced ozone in the midtroposphere during September-November is associated with transport from the continents. In the western Pacific this transport is usually from southern Africa (although 10-day back trajectories do not always reach the continent) but also may come from Australia and Indonesia. In the Galápagos the ozone peak in the midtroposphere is associated with transport from the South American continent, and particularly from northern Brazil. High ozone concentrations within potential source regions and transport characteristics associated with the ozone mixing ratio peaks in both the western and eastern Pacific suggest that these enhanced ozone mixing ratios result from biomass burning. In the case of the western Pacific sites, low ozone mixing ratios in the upper troposphere are associated with transport that originates in the convective western Pacific. In the Galápagos the lower ozone mixing ratios in the upper troposphere may be associated both with transport from the upper tropical troposphere in the western Pacific and also with convection in northern South America and Central America.

4.3. REFERENCES

Barnes, J.E., and D.J. Hofmann, Variability of the stratospheric background aerosol over Mauna Loa Observatory, *Geophys. Res. Lett.*, *28*, 2895-2898, 2001.

Crawford, J.H., D.D. Davis, G. Chen, M. Buhr, S. Oltmans, R. Weller, L. Mauldin, F. Eisele, R. Shetter, B. Lefer, R. Arimoto, and A. Hogan, Evidence for photochemical production of ozone at the South Pole surface, *Geophys. Res. Lett.*, *28*, 3641-3644, 2001.

Dessler, A.E., A reexamination of the "stratospheric fountain" hypothesis, *Geophys. Res. Lett.*, *25*, 4165-4168, 1998.

Dobson, G.M.B., A photoelectric spectrophotometer for measuring the amount of atmospheric ozone, *Proc. Roy. Soc.*, *43*, 324-337, 1931.

Folkins, I., M. Loewenstein, J. Podolske, S.J. Oltmans, and M. Proffitt, A barrier to vertical mixing at 14 km in the tropics: Evidence from ozonesondes and aircraft measurements, *J. Geophys. Res.*, *104*, 22,095-22,102, 1999.

Fujiwara, M., K. Kita, and T. Ogawa, Stratosphere-troposphere exchange of ozone associated with the equatorial Kelvin wave as observed with ozonesondes and rawinsondes, *J. Geophys. Res.*, *103*, 19,173-19,182, 1998.

Fujiwara, M., F. Hasebe, M. Shiotani, N. Nishi, H. Vömel, and S. Oltmans, Water vapor control at the tropopause by the equatorial Kelvin wave observed over Galápagos, *Geophys. Res. Lett.*, *28*, 3143-3146, 2001.

Gage, K.S., J.R. McAfee, D.A. Carter, A.C. Riddle, G.C. Reid, and B.B. Balsley, Direct measurement of long-term mean vertical motions over the tropical Pacific using wind-profiling Doppler radar, *Science*, *254*, 1771-1773, 1991.

Götz, F.W.P., Zum Strahlungsklima des Spitzbergen Sommers, *Gerlands Beit. Geophys., 31,* 119-154, 1931.

Harris, J.M., and B.A. Bodhaine (Eds.), *Geophysical Monitoring for Climatic Change No. 11 Summary Report 1982,* 160 pp., NOAA Environ. Res. Labs., Boulder, CO, 1983.

Harris, J.M., E.J. Dlugokencky, S.J. Oltmans, P.P. Tans, T.J. Conway, P.C. Novelli, K.W. Thoning, and J.D.W. Kahl, An interpretation of trace gas correlations during Barrow, Alaska, winter dark periods, 1986-1997, *J. Geophys. Res., 105,* 17,267-17,278, 2000.

Harris, J.M., S.J. Oltmans, P.P. Tans, R.D. Evans, and D.L. Quincy, A new method for describing long-term changes in total ozone, *Geophys. Res. Lett., 28,* 4535-4538, 2001.

Hasebe, F., H. Vömel, M. Shiotani, N. Nishi, S. Oltmans, T. Ogawa, and K. Gage, First results from SOWER/Pacific, *SPARC Newslett., 12,* 22-23, 1999.

Hofmann, D.J., J.T. Peterson, and R.M. Rosson (Eds.), *Climate Monitoring and Diagnostics Laboratory No. 24 Summary Report 1996-1997,* 166 pp., NOAA Environ. Res. Labs., Boulder, CO, 1998.

Holton, J.R., and A. Gettelman, Horizontal transport and the dehydration of the stratosphere, *Geophys. Res. Lett., 28,* 2799-2802, 2001.

Holton, J.R., P.H. Haynes, M.E. McIntyre, A.R. Douglass, R.B. Brood, and L. Pfister, Stratosphere-troposphere exchange, *Rev. Geophys., 33,* 403-439, 1995.

Johnson, B.J., S.J. Oltmans, H. Vömel, H.G.J. Smit, T. Deshler, and C. Kröger, ECC ozonesonde pump efficiency measurements and tests on the sensitivity to ozone of buffered and unbuffered ECC sensor cathode solutions, *J. Geophys. Res.,* in press, 2002.

McPeters, R.D., G.J. Labow, and B.J. Johnson, A satellite-derived ozone climatology for balloonsonde estimation of total column ozone, *J. Geophys. Res., 102,* 8875-8885, 1997.

Newell, R.E., and S. Gould-Stewart, A stratospheric fountain?, *J. Atmos. Sci., 38,* 2789-2796, 1981.

Nishida, M., A. Shimizu, T. Tsuda, C. Rocken, and R.H. Ware, Seasonal and longitudinal variations in the tropical tropopause observed with the GPS occultation technique (GPS/MET), *J. Meteorol. Soc. Japan, 78,* 691-700, 2000.

Oltmans, S.J., H. Vömel, D.J. Hofmann, K.H. Rosenlof, and D. Kley, The increase in stratospheric water vapor from balloonborne, frostpoint hygrometer measurements at Washington, D.C., and Boulder, Colorado, *Geophys. Res. Lett., 27,* 3453-3456, 2000.

Oltmans, S.J., B.J. Johnson, J.M. Harris, H. Vömel, A.M. Thompson, K. Koshy, P. Simon, R.J. Bendura, J.A. Logan, F. Hasebe, M. Shiotani, V.W.J.H. Kirchhoff, M. Maata, G. Sami, A. Samad, J. Tabuadravu, H.

Enriquez, M. Agama, J. Cornejo, and F. Paredes, Ozone in the Pacific tropical troposphere from ozonesonde observations, *J. Geophys. Res., 106,* 32,503-32,525, 2001.

Rosenlof, K.H., S.J. Oltmans, D. Kley, J.M. Russell III, E.-W. Chiou, W.P. Chu, D.G. Johnson, K.K. Kelly, H.A. Michelsen, G.E. Nedoluha, E.E. Remsberg, G.C. Toon, and M.P. McCormick, Stratospheric water vapor increases of the past half-century, *Geophys. Res. Lett., 28,* 1195-1198, 2001.

Schiller, C., R. Bauer, F. Cairo, T. Deshler, A. Dörnbrack, J. Elkins, A. Engel, H. Flentje, N. Larsen, I. Levin, M. Müller, S. Oltmans, H. Ovarlez, J. Ovarlez, C. Poss, J. Schreiner, F. Stroh, C. Voigt, and H. Vömel, Dehydration in the Arctic stratosphere during the THESEO2000/SOLVE campaigns, *J. Geophys. Res.,* in press, 2002.

Sherwood, S.C., A "stratospheric drain" over the maritime continent, *Geophys. Res. Lett., 27,* 677-680, 2000.

Smit, H.G.J., W. Sträter, M. Helten, D. Kley, D. Ciupa, H.J. Claude, U. Köhler, B. Hoegger, G. Levrat, B.J. Johnson, S.J. Oltmans, J.B. Kerr, D.W. Tarasick, J. Davies, M. Shitamichi, S.K. Srivastav, and C. Vialle, JOSIE: The 1996 WMO international intercomparison of ozonesondes under quasi flight conditions in the environmental simulation chamber at Jülich, *Proc. of the XVIII Quadrennial Ozone Symposium,* L'Aquila, Italy, Sept. 12-21, 1996, edited by R. Bojkov and G. Visconti, 971-974, 1998.

Thoning, K.W., P.P. Tans, and W.D. Komhyr, Atmospheric carbon dioxide at Mauna Loa Observatory, 2, Analysis of the NOAA GMCC data, 1974-1985, *J. Geophys. Res., 94,* 8549-8565, 1989.

Vömel, H., S.J. Oltmans, D. Kley, and P.J. Crutzen, New evidence for the stratospheric dehydration mechanism in the equatorial Pacific, *Geophys. Res. Lett., 22,* 3235-3238, 1995.

Vömel, H., S.J. Oltmans, B.J. Johnson, F. Hasebe, M. Shiotani, M. Fujiwara, N. Nishi, M. Agama, J. Cornejo, F. Paredes, and H. Enriquez, Balloon-borne observations of water vapor and ozone in the tropical upper troposphere and lower stratosphere, *J. Geophys. Res.,* in press, 2002.

Zerefos, C.S., K. Tourpali, and A.F. Bais, Further studies on possible volcanic signal to the ozone layer, *J. Geophys. Res., 99,* 25,741-25,746, 1994.

Zhou, X.-L., M.A. Geller, and M. Zhang, Cooling trend of the tropical cold point tropopause temperatures and its implications, *J. Geophys. Res., 106,* 1511-1522, 2001.

Ziemke, J.R., S. Chandra, R.D. McPeters, and P.A. Newman, Dynamical proxies of column ozone with application to global trend models, *J. Geophys. Res., 102,* 6117-6129, 1997.

5. Halocarbons and other Atmospheric Trace Species

B.D. Hall (Editor), J.H. Butler, A.D. Clarke, G.S. Dutton, J.W. Elkins, D.F. Hurst,
D.B. King, E.S. Kline, J. Lind, L.T. Lock, D. Mondeel, S.A. Montzka, F.L. Moore,
J.D. Nance, E.A. Ray, P.A. Romashkin, and T.M. Thompson

5.1. Overview

The mission of the Halocarbons and other Atmospheric Trace Species (HATS) group is to study halocarbons and other trace gases that cause chemical and radiative change in the atmosphere. The goal of HATS is to measure and interpret the distributions and trends of these species in the troposphere, stratosphere, and ocean with the best analytical instrumentation available. The species measured include nitrous oxide (N_2O); many halogenated species, such as halocarbons, fluorocarbons, perfluorocarbons (PFCs), and sulfur hexafluoride (SF_6); organic nitrates, such as peroxyacetyl nitrate (PAN); organic sulfur gases, such as carbonyl sulfide (COS); and hydrocarbons (HCs). The halocarbons include the chlorofluorocarbons (CFCs); chlorocarbons (CCs), such as CCl_4, CH_3CCl_3, $CHCl_3$, CH_2Cl_2, and C_2Cl_4; hydrochlorofluorocarbons (HCFCs); hydrofluoro-carbons (HFCs); methyl halides (CH_3Br, CH_3Cl, and CH_3I); bromocarbons (CH_2Br_2 and $CHBr_3$); and halons.

Three primary research areas involving these trace gases are stratospheric ozone depletion, climate change, and air quality. For example, the CFCs and N_2O are major ozone-depleting and greenhouse gases. The trace gas SF_6 is a greenhouse gas with a large global warming potential, but its net warming is small because of its low concentration in the atmosphere. Short-lived halocarbons, PAN, and the HCs play an important role in global and regional pollution. PAN is a major precursor of tropospheric ozone in the remote marine atmosphere. Tropospheric COS is a relatively stable sulfur molecule that contributes to the stratospheric aerosol layer.

Research conducted by HATS in 2000 and 2001 included (1) weekly flask sampling and analysis of air from remote and continental-influenced sites, (2) operation of instrumentation for hourly, in situ measurements of trace gases at the four CMDL baseline observatories, Barrow Observatory (BRW), Mauna Loa Observatory (MLO), Samoa Observatory (SMO), and South Pole Observatory (SPO), and at four continental-influenced sites, (3) preparation and maintenance of trace gas standards, (4) participation on airborne campaigns with in situ gas chromatographs (GCs) on aircraft and balloon payloads, (5) investigation of oceanic processes that influence trace gas composition of the atmosphere, and (6) measurement of many trace gases in firn air from South Pole.

Continuing programs within HATS are based upon in situ and flask measurements of the atmosphere from the 4 CMDL baseline observatories and 10 cooperative stations (Figure 5.1). Table 5.1 lists the geographic locations and other useful information for all the sites. There are currently 14 flask sites and 8 in situ sampling sites in the HATS atmospheric sampling network.

One of the highlights of this report is that the total equivalent chlorine (Cl + Br) in the troposphere continues to decrease at about 1% yr[-1] as a result of the Montreal Protocol [*UNEP*, 1987]. Total equivalent chlorine in the stratosphere appears to have leveled off or peaked at most altitudes. The main reason for the decline in the troposphere is that methyl chloroform (CH_3CCl_3) concentrations continued to decline to less than half of the peak levels present in 1992. However, atmospheric concentrations of the halons and CFC-12 are still increasing because of permitted production in the developing countries and the large bank of chemicals that exists in the developed countries. As a result of the halon increase, the total bromine in the troposphere and stratosphere is still increasing. Once atmospheric CH_3CCl_3 is depleted, the trend in total equivalent chlorine may significantly change, requiring further observation.

Other significant results include the global increases in atmospheric N_2O and SF_6 observed from both flask and in situ monitoring, the continued growth of the CFC replacements (HCFCs and HFCs), and the decline in the northern hemispheric concentrations of $CHCl_3$ and C_2Cl_4 as a result of the U.S. Clean Air Act. Carbonyl sulfide distributions from both in situ and flask measurements are described for the first time and show a strong seasonal cycle. A new flask station was added in 2001 at Trinidad Head, California. Airborne measurements were conducted in the upper troposphere and lower stratosphere in the northern polar region during the 1999 and 2000 Stratospheric Aerosol and Gas Experiment III (SAGE III) Ozone Loss and Validation Experiment (SOLVE) conducted from Kiruna, Sweden. The rapid-sampling airborne gas chromatograph was also used to measured CFCs, halons, and chlorinated solvents in Russia along the trans-Siberian railway during June-July 2001 in a collaboration with Russian and German scientists. The construction of the next-generation airborne GC with electron capture and mass spectrometric detection was funded by the National Aeronautics and Space Administration (NASA) Instrument Incubation Program to measure trace gases, including hydrocarbons and organic nitrates, that influence atmospheric chemistry in the upper troposphere. An in situ GC system, equipped with one mass selective detector and two electron capture detectors, is being built for the new U.S. West Coast sampling site (Trinidad Head, California, or elsewhere on the U.S. West Coast) to monitor pollution originating in Asia and transported over the Pacific Ocean.

5.2. Continuing Programs

5.2.1. Flask Samples

Overview

Arrangements were made in 2001 to add two new stations to the sampling network. One of these is an additional remote site in the far southern hemisphere, located at
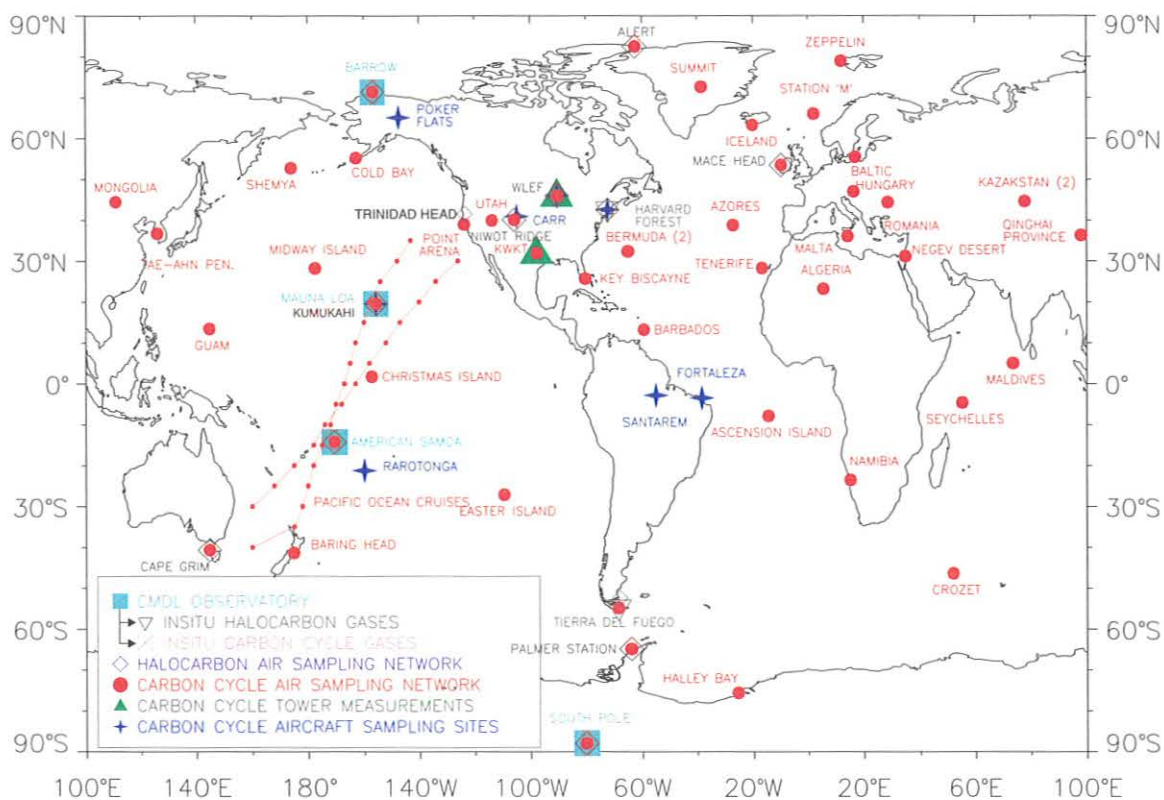
Fig. 5.1. Geographic locations of stations in the CMDL/HATS flask and in situ networks, along with CMDL/Carbon Cycle Greenhouse Gases (CCGG) stations (N_2O and SF_6 collected in glass flasks) and tower sites (triangles, future in situ halocarbon measurement).

TABLE 5.1. Geographic and Network Information for HATS Network Sites

Code	Station	Latitude	Longitude	Elevation (m)	LST − GMT (h)	Type
ALT	Alert, Northwest Territories, Canada*	82.45°N	62.52°W	210	-4	F
BRW	Point Barrow, Alaska	71.32°N	136.60°W	11	-9	F, I
MHD	Mace Head, Ireland (University College)	53.33°N	9.90°W	42	0	F
LEF	WLEF tower, Wisconsin (CMDL/CCGG)	45.95°N	90.28°W	470	-6	F, I
HFM	Harvard Forest, Massachusetts (Harvard University)	42.54°N	72.18°W	340	-5	F, I
THD	Trinidad Head, California (Humbolt State University)	41.05°N	124.15°W	109	-8	F
NWR	Niwot Ridge, Colorado (University of Colorado)	40.04°N	105.54°W	3013	-7	F, I
ITN	WITN tower, North Carolina (CMDL/CCGG)†	35.37°N	77.39°W	9	-5	F, I
MLO	Mauna Loa, Hawaii	19.54°N	155.58°W	3397	-10	F, I
KUM	Cape Kumukahi, Hawaii	19.52°N	154.82°W	3	-10	F
SMO	Tuluila, American Samoa	14.23°S	170.56°W	77	-11	F, I
CGO	Cape Grim, Tasmania, Australia‡	40.41°S	144.64°E	94	+10	F
TDF	Ushuaia, Argentina (WMO GAW station)§	54.82°S	68.32°W	10	-3	F, I
PSA	Palmer Station, Antarctica¶	64.92°S	64.00°W	10	+12	F
SPO	South Pole, Antarctica	89.98°S	102.00°E	2841	+12	F, I

F, flasks; I, in situ.
*Cooperative site with Environment Canada.
†Site's flask and in situ GC instrument closed down on June 12, 1999.
‡Cooperative site with Commonwealth Scientific and Industrial Research Organization (CSIRO) and Bureau of Meteorology, Australia.
§Began collecting data in November 2001.
¶Only glass flasks used.

Ushuaia, near Tierra del Fuego (TDF), Argentina (Figure 5.1, Table 5.1). This is a cooperative site with the Argentine government and is a Global Atmospheric Watch (GAW) station sponsored by the World Meteorological Organization (WMO). The second site, located at Trinidad Head, California (THD), is considered a regional sampling site and has been established for evaluating regional-scale air quality. It is anticipated that Trinidad Head will receive a mix of air from over the remote ocean and from nearby forests and small towns. It also may be useful for detecting air masses transported from Asia. Sampling at Mace Head, Ireland (MHD), was suspended for almost a year, as flasks began disappearing in transit. Biweekly sampling at MHD was reinitiated near the end of 2001. Efforts to improve sampling frequency and precision at all sites have continued throughout 2000-2001.

Flasks brought into the laboratory are analyzed on two to four instruments, depending upon the species being examined and the size of the individual sampling flask (Table 5.2). Analyses are performed by a gas chromatograph with electron capture detection (GC-ECD) and/or a gas chromatograph with mass spectrometric (GC-MS) detection. Although all 300-ml flasks have been retired, there still remain some 850-ml flasks, which contain a marginal amount of air for all of these low-level analyses. Most flask analyses are of samples from the network, although many are from research cruises, firn air sampling, and other special projects. One hundred new electro-polished, stainless-steel flasks were recently purchased from Lab Commerce (formerly known as Meritor Corporation, San Jose, California) to supply the new sites, to upgrade flask quality and quantity at old sites, and to use for special projects.

In 1996, 269 flasks from the network were filled and delivered to the Boulder laboratory for analysis. This number has increased each year, reaching a total of 415 in 2000 (Figure 5.2). This increase is the result of added sites and more efficient turnover of flasks between Boulder and the field sites. This was accomplished through improved record keeping of flasks coming to Boulder and by addition of flasks to the network. Sampling success has steadily improved from that for 1996 at all sites (Table 5.3). This was mainly the result of small leak repairs and valve replacements on flasks, where necessary. These repairs greatly improved the agreement in flask pressure between simultaneously sampled pairs (Figure 5.3).

GC-ECD Results

CFC-12 continues to increase in the atmosphere; however, it may have leveled off in the northern hemisphere (Figure 5.4). Mixing ratios of CFC-11 continue to drop steadily (Figure 5.5). The CFC-11 growth rate (-1.75 ± 0.11 (95% C.L.) ppt yr^{-1}, 0.7% yr^{-1}) for 2000 through mid-2001 does not differ from the rate determined for 1997-
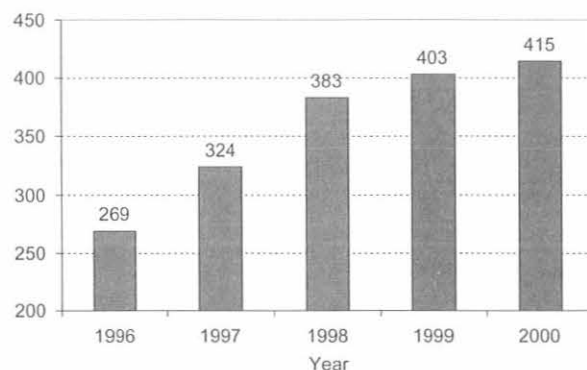
Fig. 5.2. Number of flask pairs filled and returned to Boulder each year from the HATS station network.

TABLE 5.2. Instrumentation for HATS Flask Analysis

Instrument	Type	Gases	Frequency of Network Data
OTTO	GC-ECD (three-channel, isothermal)	N_2O, CFCs (3), CCs (2), SF_6	Weekly
LEAPS	GC-ECD (one-channel, temperature–programmed)	Halons (2), CH_3Cl, CH_3Br, $CHCl_3$	Semimonthly to monthly
HCFC-MS	GC-MSD (one-channel temperature-programmed)	HCFCs (3), HFCs (1), CFCs (3), halons (1), CCs (6), BrCs (3), COS	Semimonthly
HFC-MS	GC-MSD (one-channel, temperature-programmed)	HCFCs (5), HFCs (2), CFCs (2), halons (2), CCs (6), BrCs (3), BrCCs (3)	Semimonthly to monthly

OTTO, not an acronym; LEAPS, Low Electron Attachment Potential Species; BrCs, bromocarbons; BrCCs, bromochlorocarbons.

TABLE 5.3. Percentage Sampling Success at CMDL Observatories and Cooperative Sampling Sites

Sampling Station	1996	1997	1998	1999	2000
Barrow, AK	69%	94%	88%	87%	90%
Mauna Loa, HI	69%	83%	90%	96%	94%
American Samoa	54%	67%	73%	88%	88%
South Pole	77%	69%	77%	88%	81%
Alert, Canada	52%	46%	67%	67%	65%
Niwot Ridge, CO	63%	92%	87%	77%	88%
Cape Grim, Australia	60%	69%	85%	87%	85%
WLEF tower, WI	12%	35%	69%	92%	100%
Harvard Forest, MA	46%	62%	69%	69%	88%
Kumukahi, HI	50%	54%	67%	69%	83%
Palmer, Antarctica	—	8%	65%	81%	96%
Mace Head, Ireland*	—	—	8%	15%	—
WITN tower, NC†	65%	62%	62%	38%	—

Sampling success is defined as the fraction of flasks analyzed relative to the number expected (i.e., one pair per week).

*Sampling was discontinued temporarily in 2000 because of loss of flasks in shipments.
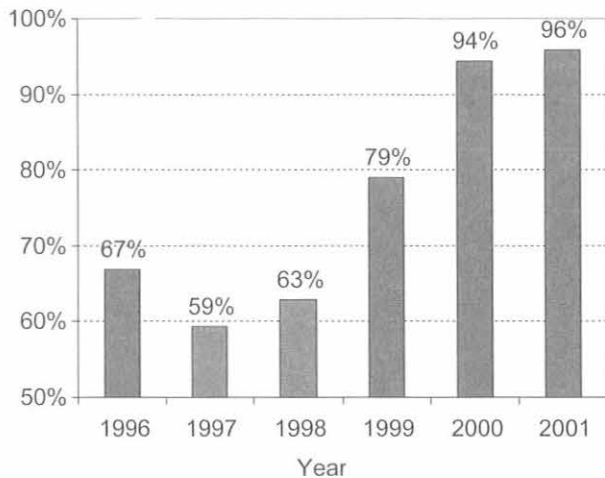
†Site was discontinued indefinitely in 1999.

Fig. 5.3. Percentage of flask pairs agreeing within 1 psi in total pressure upon arrival in Boulder.
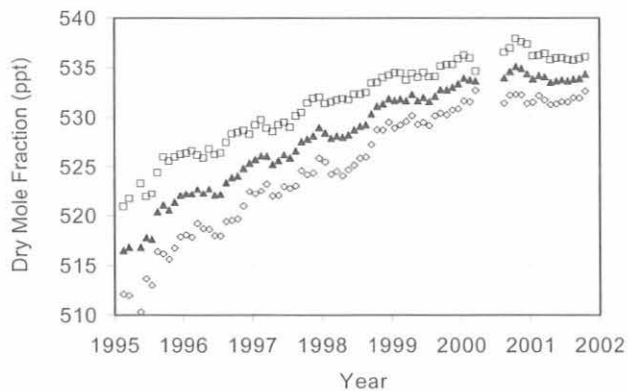
2001 (-1.73 ± 0.03 ppt yr^{-1}). CFC-113 and CCl$_4$ are also both decreasing, at about 1% yr^{-1}. The global growth rate of N$_2$O (Figure 5.6) during 1978-2000 was 0.74 ± 0.01 ppb yr^{-1}, which amounts to a mean of about 0.25% yr^{-1}. During 1999 through mid-2001, the global growth rate was 0.73 ± 0.06 ppb yr^{-1}, which does not differ from the 23-yr average. Sulfur hexafluoride (Figure 5.7) still appears to be increasing linearly in the atmosphere, with a growth rate of about 0.22 ± 0.01 ppt yr^{-1} since 1996.

The mixing ratios of halons are still increasing slowly in the atmosphere, in spite of a ban on their production in developed countries as of 1994. The global growth rate of halon-1301 (Figure 5.8) from 1999 through 2000 (0.06 ± 0.07 ppt yr^{-1}) does not differ significantly at the 95% confidence level from the 1995-2000 average of 0.06 ± 0.01 ppt yr^{-1}, nor from the1995-1996 average of 0.044 ± 0.011 ppt yr^{-1} reported in *Butler et al.* [1998]. The growth rate of halon-1211 (Figure 5.9) seems to be slowing, having dropped from a steady rate of 0.16 ± 0.02 ppt yr^{-1} in the late 1980s and early 1990s to 0.094 ± 0.04 ppt yr^{-1} for 1999 through mid-2001.

Fig. 5.4. Recent measurements of CFC-12 in the atmosphere. Measurements are monthly averages of GC-ECD data: northern hemisphere means (squares), global means (triangles), and southern hemisphere means (diamonds).
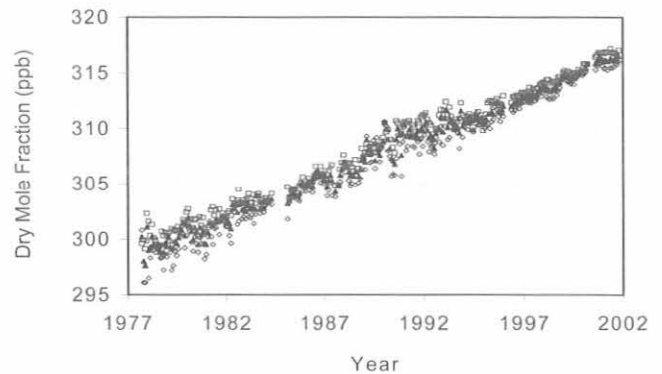
Fig. 5.6. Atmospheric history of N$_2$O since 1977 (GC-ECD monthly means; symbols as in Figure 5.4). A new GC-ECD instrument has been used since 1994.

Fig. 5.5. Recent measurements of CFC-11 in the atmosphere showing a steady loss rate since 1997 (GC-ECD monthly means; symbols as in Figure 5.4).
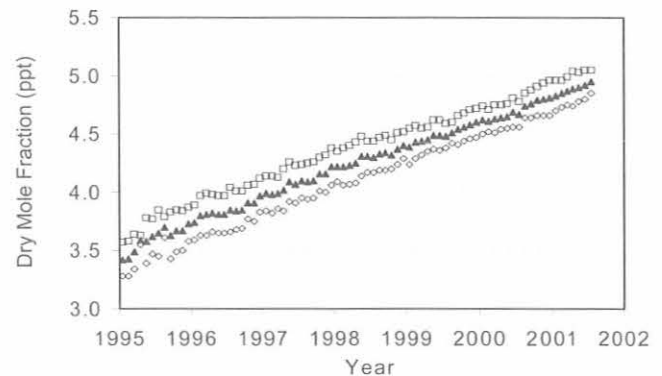
Fig. 5.7. Recent history of atmospheric SF$_6$ from CMDL flask measurements (GC-ECD monthly means; symbols as in Figure 5.4).
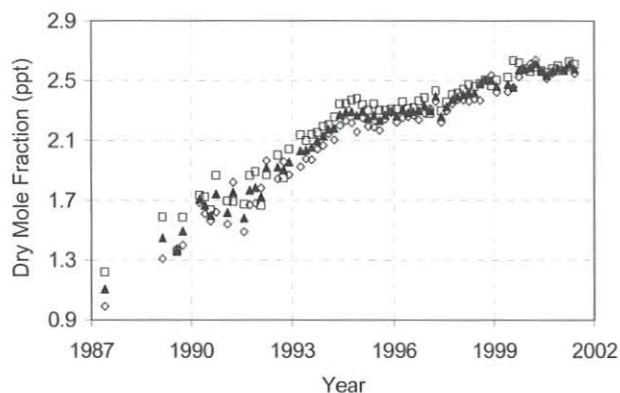
Fig. 5.8. Atmospheric history of halon-1301 (GC-ECD bimonthly averages; symbols as in Figure 5.4).
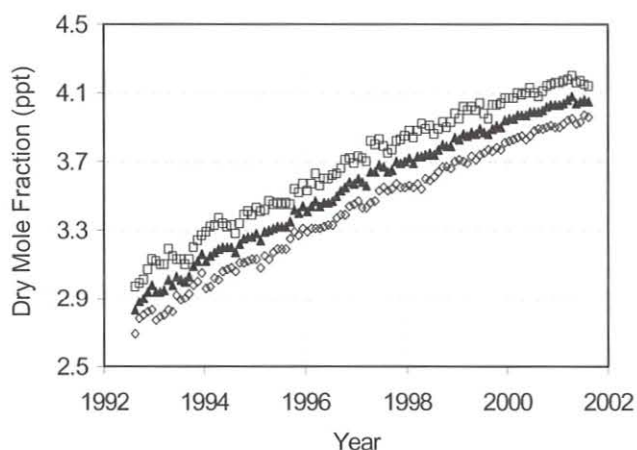
Fig. 5.9. Recent atmospheric history of halon-1211 (GC-MSD monthly means; symbols as in Figure 5.4).

GC-MS Results

Chlorofluorocarbons alternatives measurement program. Measurements of CFC alternatives and other trace gases were continued during 2000-2001 from flasks collected at 12 locations. In both years, three samples per month, on average, were filled and analyzed on GC-MSD instrumentation at 11 of the 12 sites. Fewer samples from MHD were collected and analyzed owing to difficulties associated with shipping.

Tropospheric mixing ratios of HCFCs and HFCs continued to increase during 2000-2001 (Figure 5.10, Table 5.4). Fairly linear rates of increase have been observed for HCFC-22, HCFC-141b, HCFC-142b, and HFC-134a since 1998. By mid-2001, chlorine in the three most abundant HCFCs amounted to nearly 190 ppt, or almost 7% of all chlorine carried by long-lived, purely anthropogenic halocarbons. Total chlorine from the HCFCs increased at between 8 and 9 ppt yr^{-1} over this period. Despite rapid
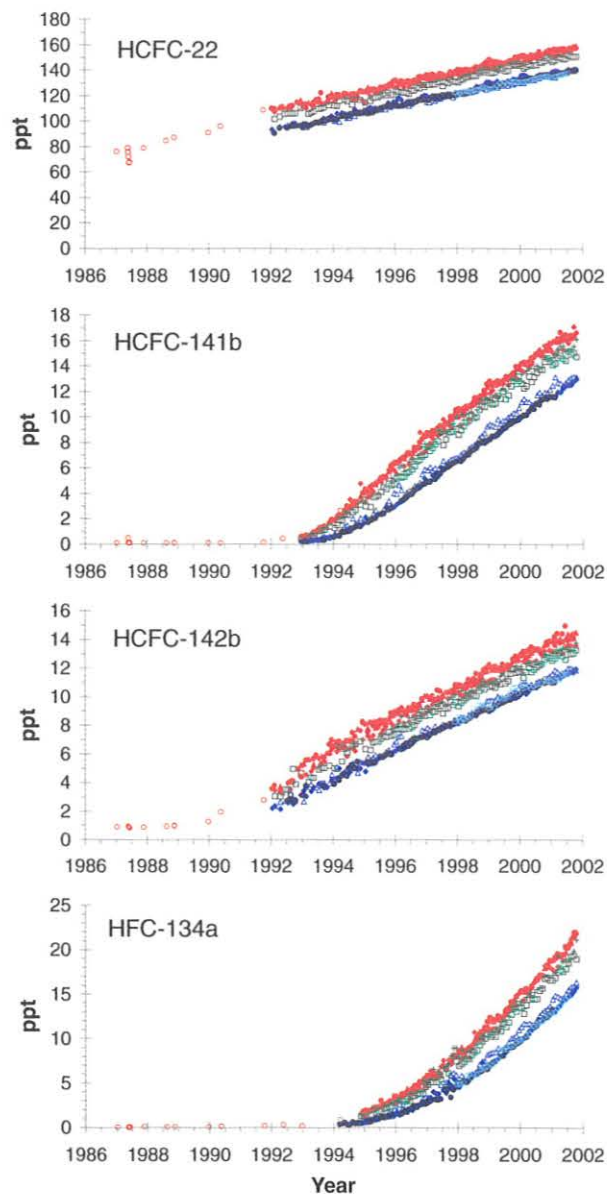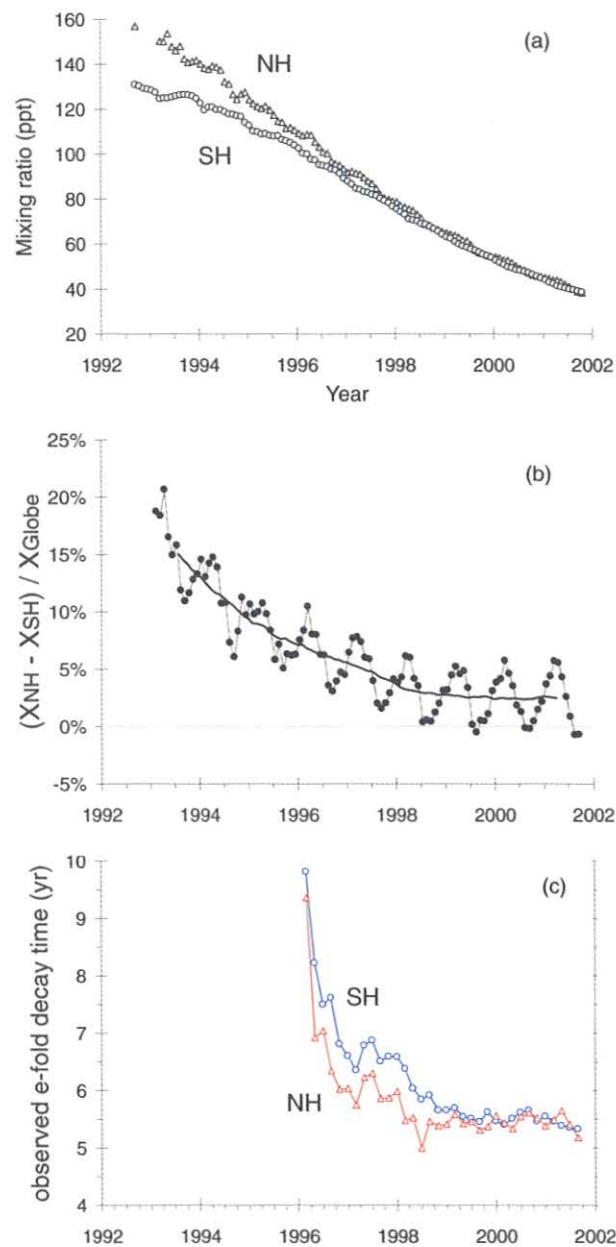

Fig. 5.10. Atmospheric dry mole fractions (ppt) of selected HCFCs and HFC-134a measured by GC-MSD in the CMDL flask program. Each point represents monthly means at one of eight or nine stations: ALT, BRW, NWR, red; KUM, MLO, green; SMO, CGO, PSA, SPO, blue. Also plotted are results from analysis of archived air samples (open red circles) filled at NWR and in past cruises from both hemispheres.

relative growth observed for HFC-134a during the mid-1990s, a fairly constant rate of increase of 3.2 ppt yr^{-1} has been observed since 1998 (Table 5.4).

Atmospheric methyl chloroform. Atmospheric mixing ratios of methyl chloroform (1,1,1-trichloroethane, CH_3CCl_3) continue to decline exponentially (Figure 5.11).

110

TABLE 5.4. Global Burden (Mixing Ratio) and Rate of
Change of HCFCs and HFC-134a

Compound	Mean 2000 (ppt)	Mean 2001 (ppt)	Growth Rate (ppt yr^{-1})
HCFC-22	141.6	146.3	5.0 (1992-2001)
HCFC-141b	12.7	14.0	1.7 (1998-2001)*
HCFC-142b	11.7	12.5	1.0 (1998-2001)*
HFC-134a	13.8	17.2	3.2 (1998-2001)

Quantities are estimated from latitudinally weighted measurements at
seven remote stations: SPO, CGO, SMO, MLO, NWR, BRW, and ALT.
    * Slower growth is indicated in 2000-2001 (0.1-0.2 ppt yr^{-1} less than
shown).

During 2000 through mid-2001, the growth rate of CH_3CCl_3
declined at about 18% yr^{-1}. The exponential decay time
constant has been consistent at 5.5 ± 0.1 yr since the
beginning of 1998, and continues to provide an upper limit
to the global lifetime of CH_3CCl_3 in the atmosphere
[*Montzka et al.*, 2000]. If it is presumed those emissions of
CH_3CCl_3 have not changed substantially from that estimated
for 1998-1999 [*Montzka et al.*, 2000; *Prinn et al.*, 2001],
then these results continue to suggest a global lifetime for
CH_3CCl_3 of 5.2 years (for the years 1998-2001). In contrast
to estimates of CH_3CCl_3 lifetime for the years before 1995,
this lifetime estimate is very insensitive to calibration
uncertainties. It is still sensitive, however, to the magnitude
of present-day emissions.

Slightly shorter estimates of methyl chloroform lifetime
have been reported by *Prinn et al.* [2001] for the period
1978-2000. They suggest, however, that the methyl
chloroform lifetime has changed over time. They also
estimate a lifetime longer than 5.0 years in the later 1990s,
which is reasonably consistent with 5.2 years in 1998-2001.
The outstanding question with regard to this issue is
understanding this apparent change in lifetime. Does it
stem from inaccurate estimates of emissions, decreases in
OH in recent years, or a change in the true lifetime of
methyl chloroform that is unrelated to OH?

The hemispheric difference has not changed substantially
since 1998; for the years 1998-2001, the hemispheric
difference is estimated to be 2.8 (±0.4)%. This difference is
similar at all sampling stations at comparable latitudes in
the two hemispheres: 2-3% in the tropics deduced from
SMO, MLO, and KUM data; 2-3% in midlatitudes deduced
from CGO, NWR, and LEF data; and 2-4% in polar regions
deduced from PSA, SPO, BRW, and ALT data (see Table
5.1 for station definitions and locations). The constancy in
both the decay time constant and the hemispheric difference
suggests that the influence of emissions on estimates of
global lifetime and hemispheric lifetimes has either been
small or relatively constant since 1998.

Overall trends in ozone-depleting gases. Ground-based
measurements provide an indication of the burden and trend
of individual ozone-depleting gases. The sum of chlorine
and bromine atoms in long-lived trace gases provides an
estimate of equivalent tropospheric chlorine (ETCl) after

Fig. 5.11. (a) Atmospheric dry mole fractions (ppt) of CH_3CCl_3
measured by GC-MSD in the CMDL flask program. Each point
represents a monthly hemispheric surface mean as determined by a
latitudinal weighting of results from individual sampling stations
(northern hemisphere = triangles, southern hemisphere = circles). (b) The
hemispheric mixing ratio difference for CH_3CCl_3 at the Earth's surface
in recent years. The difference was inferred from weighted, monthly
mean mixing ratios at three to six sampling stations in each hemisphere.
Monthly differences (solid circles) are connected with a thin line; the
heavy curve represents a 12-mo running mean difference. (c) The
observed e-fold decay time for monthly hemispheric surface means of
CH_3CCl_3 shown in (a). A fairly constant exponential decay in surface
mixing ratios of CH_3CCl_3 has been observed since the beginning of
1998; the exponential time constant for this decay is 5.5 years.

the enhanced efficiency of bromine to destroy ozone compared with chlorine is included (a factor of 50 is used here; *Solomon et al.* [1995]). ETCl provides an indication of the upper limit to ozone-depleting chlorine and bromine in the future stratosphere. Better approximations of trends in inorganic halogen in the lower stratosphere can be derived from ETCl after accounting for the different rates at which halocarbons photo-oxidize in the stratosphere. These rates have been estimated empirically or with models and are applied as weighting factors to mixing ratios of individual gases in the calculation of effective equivalent chlorine (EECl) and effective equivalent stratospheric chlorine (EESC) [*Daniel et al.*, 1995; *Montzka et al.*, 1996]. The only difference between EECl and EESC is that EESC explicitly includes a 3-yr time lag (dates associated with EECl correspond to the time when the surface measurement was made).

The net sum of ozone-depleting halogen from purely anthropogenic gases continued to decrease during 2000-2001 (Figure 5.12). The rates of decline for EECl and ETCl in 2001 were about 1% yr^{-1} and 0.5% yr^{-1}, respectively. Amounts of EECl during mid-2001 were about 5.5% below the peak observed near the beginning of 1994. The rate of decline in both EECl and ETCl has slowed by about one-third compared with peak values as the influence of methyl chloroform has diminished.

The two scenarios for EECl and ETCl shown in Figure 5.12 provide some insight into causes of past changes and the future evolution of net halogen in the atmosphere. The measured trends in EECl and ETCl since 1998 have remained fairly close to scenario A, in which constant emissions were presumed [*Montzka et al.*, 1999]. Although substantial reductions in emissions were realized during the 1990s, these results suggest that these emission reductions have slowed in recent years, perhaps owing to enhanced CFC production in developing countries.

The updated projections for scenario B (Figure 5.12, solid lines) are somewhat different from the ones made previously (see references noted in Figure 5.12). The main difference arises from consideration of halons in the future. In the present calculation it has been assumed halon emissions will decrease in future years in reasonable accord with reported halon production [*Fraser et al.*, 1999] and a small allotment for additional future production.

Shorter-lived gases. Measurements of other chlorinated and brominated trace gases were continued during 2000-2001 (Figure 5.13). The results suggest further decreases in mixing ratios of CH_2Cl_2 and C_2Cl_4. Interannual variability is observed for the methyl halides and will be discussed in future publications.

Non-stainless-steel flasks circulated to sampling stations. Although most samples are routinely collected in stainless-steel flasks in the HATS program, glass flasks have also been used recently. Glass flasks are particularly useful when known artifacts affect sampling in steel flasks. Glass flasks sampled during the South Pole 2000 winter allowed for additional measurements of compounds that undergo substantial degradation in stainless-steel flasks during the long period between sampling and analysis (Figure 5.14). Glass flasks are also useful to determine if results for more reactive gases are independent of flask type. Preliminary
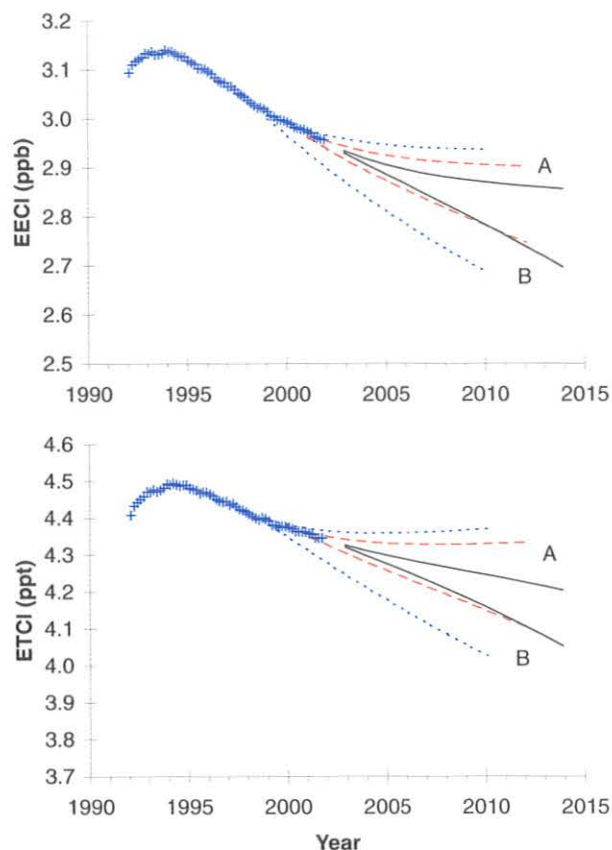
Fig. 5.12. The measured and potential future burden of ozone-depleting halogen in the lower atmosphere. Ozone-depleting halogen is estimated from tropospheric measurements of anthropogenic halocarbons by appropriate weighting factors to calculate effective equivalent chlorine (EECl) for midlatitudes (top) and equivalent tropospheric chlorine (ETCl) as an upper limit for polar latitudes (bottom) [*Daniel et al.*, 1995; *Montzka et al.*, 1996, 1999]. A constant offset was added to account for CH_3Cl and CH_3Br. Projections are based on two limiting scenarios: A, emissions of all long-lived halogenated gases (CFCs, HCFCs, CH_3CCl_3, CCl_4, and halons) remain constant at 2001 levels, and B, scenario A with the exception that emissions of CFCs, CH_3CCl_3, halons, and CCl_4 continue decreasing at 5 to 8% yr^{-1}. Future scenarios have been formulated in previous *CMDL Summary Reports* and other publications with ambient air measurements through 1997 (short-dashed lines [*Montzka et al.*, 1999]) and through 1999 (long-dashed lines [*Hall et al.*, 2001]). Updates to current emission rates and their rates of change based on measurements through 2001 were used to update projections for both scenarios (solid lines).

results of glass flasks filled at CGO and SPO show good consistency for HCFC-22, HCFC-142b, and HFC-134a. Glass flasks are not without problems for some compounds, however. Poor consistency is observed for HCFC-141b and C_2Cl_4 in glass flasks; this contamination probably is associated with the Teflon seals in these flasks and does not suggest trouble in results reported from stainless-steel flasks for these gases.

Carbonyl sulfide. Measurements of carbonyl sulfide (COS) were begun from flasks during 2000-2001. COS is
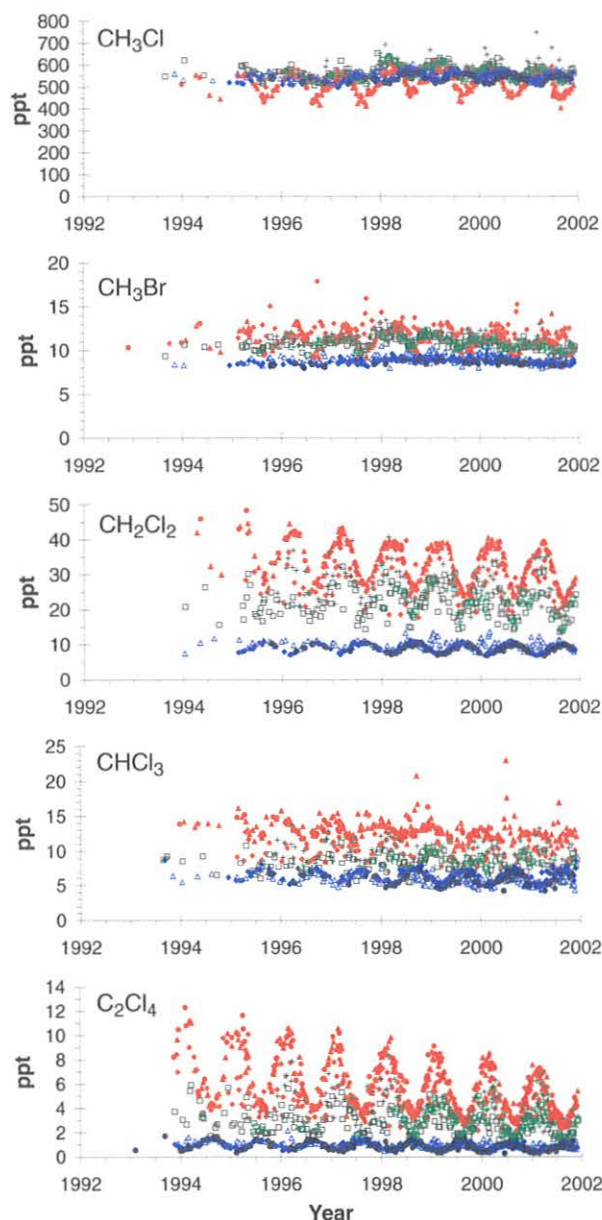
Fig. 5.13. Atmospheric dry-air mole fractions (ppt) determined for selected chlorinated trace gases and CH₃Br by GC-MSD in the CMDL flask program. Each point represents the mean of two simultaneously filled flasks from one of eight or nine stations (symbols same as in Figure 5.10). Results shown for all compounds except C₂Cl₄ are from 2.4-L stainless-steel flasks only.

Fig. 5.14. Mixing ratios determined from different sites and different types of flasks. Results for CH₃Br and CCl₄ from Cape Grim, Tasmania (40°S), from stainless-steel flasks (red pluses) are compared with data obtained from South Pole from stainless-steel flasks (open blue diamonds) and glass flasks (solid black circles).

an abundant sulfur-containing gas that is believed to contribute significantly to the sulfur found in the stratosphere. More recent model calculations, however, have suggested a lesser role for COS in maintaining the stratospheric aerosol than was previously thought [*Kjellström*, 1998].

The results from flasks show a small hemispheric difference biased slightly toward higher levels in the southern hemisphere, strong seasonal variations at all sites except SMO, and seasonality in the two hemispheres that is not 180 days out of phase (Figure 5.15). These features are also evident in data from Chromatograph for Atmospheric Trace Species (CATS) GC-ECD instrumentation located at selected sites. Many conflicting reports regarding hemispheric distributions and seasonality can be found in the current literature for COS. These observations will add substantially to the understanding of the global budget of this gas.

5.2.2. IN SITU GAS CHROMATOGRAPH MEASUREMENTS

Radiatively Important Trace Species

The Radiatively Important Trace Species (RITS) project has ended. Table 5.5 outlines, for each station and data channel, the shutoff dates for the RITS equipment. Channel A measured N₂O, CFC-12 (CCl₂F₂), and CFC-11 (CCl₃F); channel B measured CFC-11, CH₃CCl₃, and CCl₄; and channel C measured N₂O. The RITS instruments continued to collect data until data from the replacement CATS instruments showed similar trends and equal or better precision. The precision for a particular chemical was
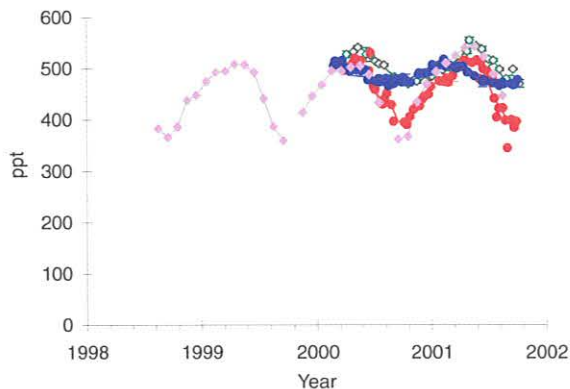
Fig. 5.15. Mixing ratios for COS determined from sampling and analysis of stainless-steel flasks at BRW (red), KUM (green), and CGO (blue). Also shown are monthly means at BRW from the on-site CATS GC-ECD (purple diamonds). For clarity, SMO data are not shown.

TABLE 5.6. CATS Project Startup and Overlap Schedule with RITS

Station	Installation Date	Overlap with RITS (months)
BRW	June 16, 1998	8
NWR	Oct. 13, 2000	10
MLO	Sept. 29, 1998	18 [26]*
SMO	Dec. 4, 1998	17 [22]*
SPO	Jan. 30, 1998	34

*Months in brackets are for the one channel that continued to be operated after the others were turned off.

determined as the standard deviation of the ratio of the responses of two calibration gases over an extended period of time (usually more than 1 month). Calibration gases are normally very stable for the species of interest.

Instruments associated with the CATS project, developed to replace the aging RITS instruments and add new measurement capabilities, continue to operate at the CMDL field sites. A CATS system was installed at NWR in October 2000. Table 5.6 shows the installation dates for the CATS instruments and the duration of the RITS-CATS comparisons.

A two-channel Hewlett-Packard 5890 GC-ECD used in the RITS project was refurbished for installation at Ushuaia, Tierra del Fuego, Argentina (TDF), as part of a cooperative venture with the Servicio Meteorologico Nacional de Argentina, sponsored by WMO. The TDF site is part of the WMO GAW program. This GC measures N_2O and SF_6 on the first channel and CFC-12, CFC-11, CFC-113, CH_3CCl_3, and CCl_4 on the second channel. A significant difference between this system and the previous RITS system is that nitrogen carrier gas with a CO_2 dopant is used on the N_2O-SF_6 channel as opposed to 5% CH_4 in argon (P-5). The use of CO_2-doped N_2 should (a) eliminate any CO_2 interference

on the N_2O signal and (b) improve carrier gas quality (high-quality P-5 is difficult to obtain, particularly at remote sites).

The TDF GC system was installed on October 26, 2001, providing the first in situ CFC measurements in South America. Scientists from Argentina are interested in measuring CFCs because stratospheric chlorine from CFCs contributes to the formation of the Antarctic ozone hole. During vortex breakup, low-ozone events can occur over southern South America. Furthermore, while the total atmospheric chlorine burden is dropping [Montzka et al., 1999; Elkins, 2000], CFC-12 is slowly increasing. Under the Montreal Protocol on Substances that Deplete the Ozone Layer [UNEP, 1987] and its amendments, developing countries can produce CFCs until 2010.

Mixing Ratio Calculation Methods

Over the past 3 years the RITS three-channel GC instruments at the CMDL baseline observatories have been replaced by four-channel GC instruments (CATS). In addition to the five trace gases measured by RITS instruments (N_2O, CFC-11, CFC-12, CH_3CCl_3, and CCl_4), CATS instruments measure SF_6, CFC-113, $CHCl_3$, COS, halon-1301, halon-1211, CH_3Cl, CH_3Br, HCFC-142b, and HCFC-22.

Both RITS and CATS instruments are calibrated using two calibration tanks that are sampled alternately along with ambient air. One calibration standard (C1) consists of a mixture of 90% ambient air and 10% synthetic ultrapure air. The other standard (C2) is 100% ambient air. The sequence of sample injections is C1, A1, C2, A2, where A1 and A2 are ambient air samples obtained at two different heights on the sampling tower. Each sample chromatograph is 30 minutes in length; thus the full sequence takes 2 hours. Both RITS and CATS in situ measurement programs have utilized several different methods to compute the trace gas concentrations in air samples bracketed by two calibration samples. This section focuses on the difficulties involved in these calculations. A new algorithm, designed to minimize problems associated with calibration tank changes and uncertainties in the assignment of calibration tank mixing ratios (see section 5.2.3), is presented here.

One-point method. The simplest method of calculating mixing ratios is to use only one calibration tank as a reference measurement:

TABLE 5.5. RITS Project Shutdown Schedule

Station	Channel*	Date and Time (GMT)
BRW	A, B, C	Feb. 17, 1999 (2100)
NWR	A, B, C	Aug. 7, 2001 (1900)
MLO	A, C	April 10, 2000 (2130)
	B	Dec. 18, 2000 (2030)
SMO	A, B	April 22, 2000 (0530)
	C	Sept. 30, 2000 (0000)
SPO	A, B	Nov. 30, 2000 (0200)

* See text for channel definitions.

$$\chi_a = \frac{R_a}{R_c} \chi_c \quad . \tag{1}$$

where R_a is the ECD response of the air sample, R_c is the ECD response of the calibration sample, χ_c is the known mixing ratio of the calibration sample, and χ_a is the mixing ratio of the air sample. The one-point method can be plagued by nonlinearities in chromatography and detector response (Figure 5.16). Compounding problems occur when the calibration tank is replaced with a new tank with different assigned concentrations. Because the one-point method approximates the actual ECD response with a straight line with a zero intercept, a change in the mixing ratio of the calibration tank (χ_c and R_c) results in a different slope used to approximate the ECD response (Figure 5.16a). This can lead to discontinuities in the atmospheric record when the true ECD response is nonlinear. Small errors can occur even when two calibration tanks are used (i.e., mixing ratio is determined as the mean of two one-point calculations).

Two-point method. The results of both calibration tanks together can be used to calculate mixing ratios by approximation of the ECD response with a straight line with a nonzero intercept (Figure 5.17):

$$\chi_a = \frac{\left(R_a - R_{c1}\right)(\chi_{c1} - \chi_{c2})}{R_{c1} - R_{c2}} + \chi_{c1} \quad , \tag{2}$$

where R_a is the ECD response of the air sample, R_{c1} is the ECD response of C1, R_{c2} is the ECD response of C2, χ_{c1} is the known mixing ratio of C1, and χ_{c2} is the known mixing ratio of C2. Improvements in accuracy, compared with the one-point method, can sometimes be obscured by precision problems associated with the two-point method. Random noise in both measured quantities R_{c1} and R_{c2} can affect the slope and intercept. Averaging calibration tank responses over short time periods can improve precision. Changing calibration tanks can also lead to discontinuities in the atmospheric record when the two-point method is used, because different segments of the nonlinear response curve are encountered as calibration tanks with different mixing ratios are used. This is particularly true for trace gases with strong tropospheric trends (such as CH_3CCl_3).

In addition to difficulties associated with nonlinear ECD response, the accuracies of both the one-point and two-point methods are dependent on the accuracies of the mixing ratios assigned to the calibration gases (χ_{c1} and χ_{c2}). To address these issues, a new method that utilizes the thousands of routine measurements made of each calibration tank during normal operation was developed. The method can be used to adjust assigned calibration tank concentrations (within specified uncertainties) to provide a self-consistent set of calibration standards and minimize discontinuities in the atmospheric time series.

Statistical ratio method. The CATS GCs make continuous measurements of each calibration tank every day, about 12 injections per day. Over the lifetime of the calibration tank (usually 9 to 12 months) nearly 4000 separate measurements of each calibration tank can be
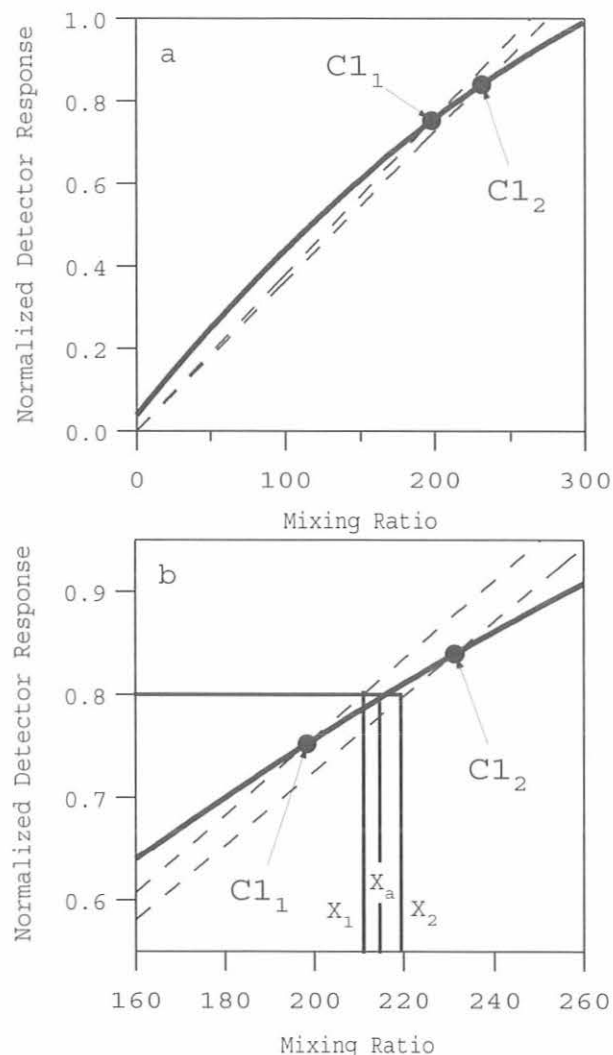
Fig. 5.16. Estimates of mixing ratio by the one-point method. Plot (a) is full scale and (b) is expanded. Both plots demonstrate the potential problems that can occur with only a single calibration measurement. The nonlinear response curve (solid) is the normalized response to a known quantity of a particular molecule (in arbitrary units). The one-point method uses a single measurement of an assigned mixing ratio ($C1_1$) and assumes a linear response (dotted lines). For an ECD with a nonlinear response, a calibration error will occur if the air sample and calibration gas have significantly different responses. The solid vertical lines (X_1, X_2) correspond to the mixing ratios calculated for a response of 0.8 using two different calibration standards ($C1_1$ and $C1_2$). The middle vertical line (X_a) is the actual mixing ratio if the response curve is known.

made. Several comparisons of one calibration tank to another (Figure 5.18) can be used to adjust the assigned mixing ratios such that the effects of calibration tank changes are minimized.

A two-step procedure is used to establish a self-consistent set of calibration tank mixing ratios. The first step takes advantage of the fact that the mean response ratio of calibration tanks is functionally related to the assigned calibration tank values:
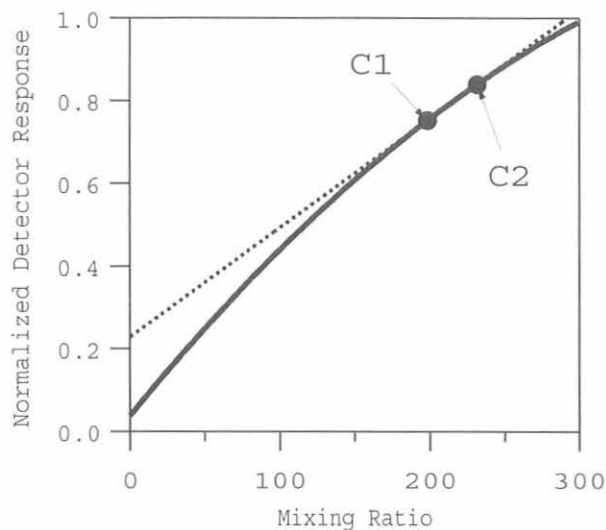
Fig. 5.17. Estimates of mixing ratio by the two-point method. This method utilizes two calibration tank measurements (Cl and C2) to approximate the response curve (solid) with a straight line (dashed).
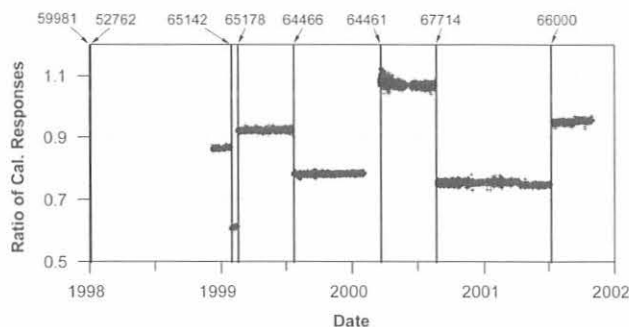

Fig. 5.18. Response ratio (C1/C2) for CH_3CCl_3 at SMO for different pairs of calibration standards. Calibration tank changes are shown as vertical lines identified by cylinder number along the top of the figure.

Fig. 5.19. (a) Mean response ratio for CH_3CCl_3 at SMO plotted against the ratio of assigned CH_3CCl_3 concentration for each calibration tank pair. A linear least-squares fit through the calibration tank ratios (solid line) is used to compute an average effective response curve. Residual differences are plotted at the top of the graph and demonstrate the magnitude of errors associated with a calibration tank change. (b) Mean response ratio as in (a) except that calibration tank concentrations have been adjusted to minimize the residuals.

$$B_{ij} = f(\chi_{c1,i}, \chi_{c2,j}) \approx m\left(\frac{\chi_{c1,i}}{\chi_{c2,j}}\right) + b \quad , \tag{3}$$

where B_{ij} is the response ratio of the ith C1 tank to the jth C2 tank, $\chi_{c1,i}$ is the assigned concentration for the ith C1 tank, and $\chi_{c2,j}$ is the assigned concentration for the jth C2 tank. The ratio B_{ij} can vary between 0.5 and 1.1 depending on the growth rate of the compound analyzed and when the calibration tanks were prepared. Plotting the measured mean calibration tank ratios (B_{ij}) versus assigned concentration ratios creates an effective ECD response curve (Figure 5.19a) that can be fitted with a least-squares regression line. The line represents a long-term average ECD response for a particular molecule. If the

chromatography is stable over the period of all B_{ij} measurements, the linear fit can be used to calculate air concentrations and estimate errors. The functional relationship is nearly linear for all compounds measured by the CATS instruments. Problems arise in the linear representation when there are chromatographic problems, such as co-eluting compounds and ECD response curves that show relatively large nonzero intercepts. For current tropospheric mixing ratios of all species measured by CATS instruments, equation (3) seems to provide a good estimate for the effective response curve.

Once the slope and intercept of the effective response curve are known, uncertainties in the assigned calibration tank mixing ratios can be incorporated:

$$B_{ij} = m\left(\frac{\chi_{c1,i} + \sigma_{c1,i}}{\chi_{c2,j} + \sigma_{c2,j}}\right) + b \quad , \qquad (4)$$

where $\sigma_{c1,i}$ is the possible uncertainty associated with the ith C1 and $\sigma_{c2,j}$ is the possible uncertainty associated with the jth C2. A numerical algorithm is used to iteratively adjust all $\sigma_{c1,i}$ and $\sigma_{c2,j}$ to minimize the residual difference (Figure 5.19b). The adjustments to the calibration tank values are constrained by the estimated uncertainties on the assigned values (section 5.2.3). For most compounds the adjustments are less than 0.5% of the ambient mixing ratio.

Equation (4) can be rewritten in terms of χ_a to yield two equations to compute atmospheric mixing ratio using the optimal values of $\sigma_{c1,i}$ and $\sigma_{c2,j}$:

$$\chi_a = (\chi_{c1,i} + \sigma_{c1,i})\, m\left(\frac{R_{c1,i}}{R_a} - b\right)^{-1} \quad , \qquad (5)$$

$$\chi_a = (\chi_{c2,j} + \sigma_{c2,j})\frac{1}{m}\left(\frac{R_a}{R_{c2,j}} - b\right) \quad . \qquad (6)$$

If both calibration tanks are in operation, the average of equations (5) and (6) is used. Atmospheric mixing ratios calculated with the statistical ratio method tend to be more precise than with the two-point method and are more accurate than the one-point method. The gain in precision comes from use of the average response curve rather than estimation of a response curve from each sequence of measurements, as in the case of the two-point method.

Figures 5.20 and 5.21 illustrate the differences between results from the two-point method and from the statistical ratio method. Figure 5.20a shows discontinuities in the mixing ratio for CH_3CCl_3 at SMO calculated with the two-point method. These discontinuities are the result of rapidly changing atmospheric CH_3CCl_3 mixing ratios, and calibration tanks that have widely varying CH_3CCl_3 relative to the atmosphere. The CH_3CCl_3 data shown in Figure 5.20b were calculated with the statistical ratio method. These data clearly represent a continuous time series. The missing data seen prior to the 64461 calibration tank change correspond to a period in which the C2 tank (65178) was emptied before the arrival of its replacement. Even though the ratio of calibration tanks cannot be used for this period, the statistical relationship used to derive equations (5) and (6) is still valid. In this case the atmospheric mixing ratio can be calculated with equation (5) without having to rely on the one-point calculation method. The CFC-11 data from BRW shown in Figure 5.21 do not show large discontinuities associated with calibration tank changes. However, application of the statistical ratio method reveals a possible downward trend in CFC-11 concentration (Figure 5.21b) that is not apparent in data computed with the two-point method (Figure 5.21a).

The application of the statistical ratio method is new to the HATS in situ program and may undergo further enhancements. For example, the two-point method may be preferred during periods when chromatography is
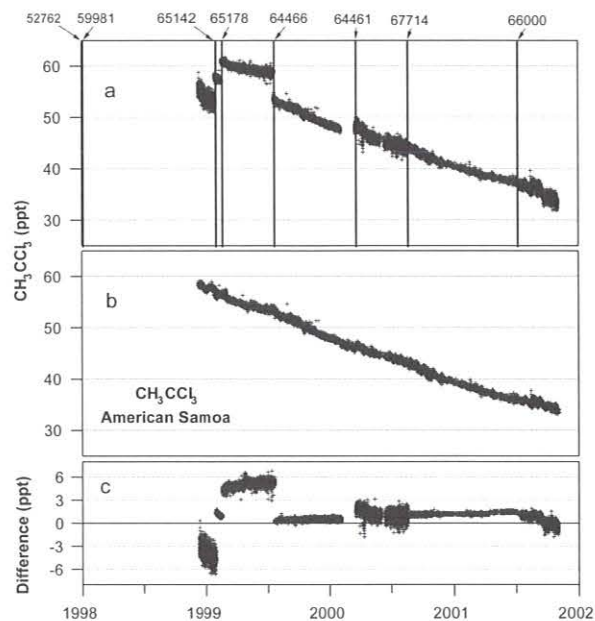

Fig. 5.20. CH_3CCl_3 data from SMO computed with two different methods: (a) the two-point method and (b) the statistical ratio method. The difference between methods (a) and (b) is shown in (c). Note that many of the discontinuities in (a) are absent in (b). Calibration tank changes are shown as vertical lines identified by cylinder number along the top of (a).
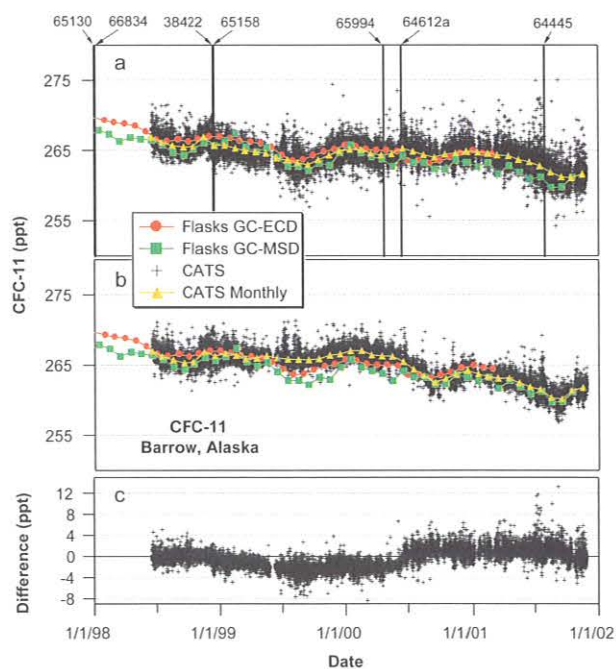

Fig. 5.21. CFC-11 data from BRW, as in Figure 5.20. Also included are data from flasks analyzed on GC-ECD (red) and GC-MSD (green) instruments, and monthly mean values from the CATS instrument (yellow). Although discontinuities are not apparent in (a), the statistical ratio method (b) dramatically improves precision.

noticeably different from the statistics upon which the method is based. However, with each additional working standard, the entire data record could change significantly when the statistical ratio method is applied. A future improvement might be to use equation (2) in conjunction with the estimated $\sigma_{c1,i}$ and $\sigma_{c2,j}$ for these periods.

5.2.3. GRAVIMETRIC STANDARDS

Calibration Scales

Numerous standards were prepared in 2000-2001. In total, 62 gravimetric standards were prepared and 89 working standards were filled at NWR during this period.

The calibration scales of N_2O, SF_6, CFC-12, CFC-11, CH_3CCl_3, CCl_4, and halon-1211 were examined with the aim of incorporating all HATS measurements, as well as CCGG N_2O and SF_6 flask measurements, on common scales. This involved analysis of numerous working standards used by the flask programs, airborne programs, and in situ programs. This work will continue into the near future and will include additional molecules.

A key element of this work involved the preparation of additional gravimetric standards for N_2O and SF_6 (Figures 5.22 and 5.23). Previous scales for these molecules had been defined by a limited number (four to six) of gravimetric

Fig. 5.23. (a) Second-order calibration curve and (b) residual, resulting from analysis of gravimetric standards that define the 2000 SF_6 scale. Standards prepared from similar primary standards are shown as similar symbols.

Fig. 5.22. (a) Second-order calibration curve and (b) residual, resulting from analysis of gravimetric standards that define the 2000 N_2O scale. Standards prepared from similar primary standards are shown as similar symbols.

standards. While these standards were useful for defining a scale over a wide concentration range, the lack of multiple standards with near-ambient concentrations presented difficulties in establishing the long-term stability of these scales. New primary standards were prepared from the same reagents used to establish the original scales. Secondary/tertiary standards were prepared from the new primary standards as well as from existing primary standards. The 2000 N_2O scale is about 1 ppb lower than the 1993 scale, and it is 0.5 ppb higher than that predicted using 300 and 330 ppb National Institute of Standards and Technology (NIST) Standard Reference Materials (SRMs). The 2000 SF_6 scale differs from the 1994 scale [Geller et al., 1997] by less than 0.1 ppt, which is within the uncertainty associated with the 1994 scale.

A scale based on a large number of standards makes it easier to identify outliers (standards that, for whatever reason, do not agree with the majority) (Figure 5.23). These new N_2O-SF_6 standards have also helped to improve the long-term stability of the N_2O and SF_6 scales (e.g., the loss or drift of a single standard does not affect the scale as much as it would if the scale were defined by only a few standards). More information on gravimetric standards used to define HATS scales,

including a list of the standards used to define the new 2000 N_2O and 2000 SF_6 scales, is available on the CMDL/HATS website (http://www.cmdl.noaa.gov/hats/standard/scales.htm).

A second element of this work involved the analysis of reagent-grade materials used to prepare primary standards. The reagents used to prepare primary CH_3CCl_3, CCl_4, and CFC-12 standards were sent to NIST (Gaithersburg, Maryland) for purity analysis. No significant volatile impurities were found in CFC-12 or CCl_4 reagents. However, the CH_3CCl_3 reagent used to establish the 1996 CH_3CCl_3 scale [see *Hall et al.*, 2001] was found to contain impurities amounting to approximately 6.4% (by mole). New high-purity reagent-grade CH_3CCl_3 was purchased from a different vendor (Sigma-Aldrich, St. Louis, Missouri.). The purity of this new reagent is approximately 99.8% based on the NIST analysis (99.9% according to the manufacturer's assay). New primary standards were prepared from this reagent. These new standards show a molar response that is roughly 5% higher than those prepared from the old reagent, which is consistent with the results of the reagent analysis. Development of a new CH_3CCl_3 scale is under way. It is expected that this new scale will be about 5% lower than the 1996 scale used in the publications of *Hurst et al.* [1997], *Volk et al.* [1997], *Butler et al.* [1999], *Montzka et al.* [1999, 2000], and *Romashkin et al.* [1999].

Gravimetric standards for carbonyl sulfide (COS) were prepared from newly purchased COS reagent. Several ppt-level standards were prepared in 29-L Aculife-treated aluminum cylinders. The stability of these standards is being evaluated. Two of five ppt-level standards are already showing signs of COS loss. Although many of the working standards used in the in situ program do not show COS loss, the viability of aluminum cylinders for COS at the ppt level is still being evaluated.

New gravimetric standards for CO were prepared in 1999-2000. These new standards helped to confirm that secondary standards prepared in 1989 had drifted and that a scale update was needed [*Tans et al.*, 2001]. The scale will be maintained by preparation of new gravimetric standards every 2 years and by comparison of ppb-level standards to ppm-level NIST SRMs.

Calibration of Working Standards

Working standards continue to be calibrated using a four-channel gas chromatograph similar to those used for in situ measurements (CATS). The initial calibration of this instrument was established in 1999 by comparison of a working standard (natural air at ambient concentration) to gravimetric standards, as well as to previous working standards. Routine calibration is maintained by comparison of the working standard to five additional working standards (mixtures of natural and ultrapure air at concentrations ranging from 40% to 100% of ambient). These comparisons are performed every 1-2 months or after a significant change in GC operating parameters. Frequent analysis of these working standards enables detection of small changes in GC performance or response characteristics without depletion of gravimetric standards. Each set of gravimetric standards used to define a particular scale is analyzed yearly.

The routine analysis of the working standards also provides information on the day-to-day variability of the GC. This information can be used to provide an estimate of the uncertainties associated with the calibration of working standards using this instrument. Knowledge of the day-to-day variability is crucial if small changes (drift) are to be detected. Table 5.7 shows the precision over a single day and uncertainties over multiday periods, associated with the calibration of a working standard. The information in Table 5.7 is related only to the performance of the CATS instrument and does not describe the accuracy of the calibration scales. It is useful to assess how well two identical standards can be calibrated, or the degree to which two calibrations of the same standard, performed months or years apart, can be expected to agree (assuming that the standard is stable over this period). Instrument precision on a given day (Table 5.7) is often very good, 0.4 ppb for N_2O, for example. However, differences in the mean concentration determined on different days can occur because of the imprecise nature of the calibration method and small changes in response characteristics associated with changes in carrier gas purity, column condition, etc. For these reasons, standards are typically analyzed on 2-3 different days. Uncertainties associated with multiday calibrations are larger than the daily precision and decrease with additional analysis, as expected. Although it is impractical to analyze working standards over 10 days, these data provide an estimate of the best overall uncertainty achievable with the CATS calibration system.

New High-Pressure Cylinders

Aluminum cylinders are not ideal for the long-term storage of methyl halides. Air stored in Aculife-treated aluminum cylinders, particularly those purchased since 1998, tend to show decreases of CH_3Br and increases in CH_3Cl over time. The rate of change of these compounds is highly variable and cylinder specific. A small number of these cylinders seem to be relatively stable, but an alternative is clearly needed.

TABLE 5.7. Precision and Uncertainties Associated with the Calibration of Working Standards

	Precision*	Uncertainty (3 days)†	Uncertainty (10 days)†
N_2O (ppb)	0.4	0.8	0.5
CFC-12 (ppt)	0.8	1.3	0.8
CFC-11 (ppt)	0.6	1.0	0.6
CFC-113 (ppt)	0.2	0.5	0.3
CH_3CCl_3 (ppt)	0.2	0.6	0.3
CCl_4 (ppt)	0.2	0.7	0.4
SF_6 (ppt)	0.03	0.04	0.02
Halon-1211 (ppt)	0.02	0.03	0.02

*Typical daily precision (expressed as $2\sigma/N^{0.5}$) associated with 8-10 comparisons of an unknown to a reference standard at ambient concentration. These data are similar to those of *Hall et al.* [2001].

†Uncertainties associated with a multiday calibration (95% confidence level). The uncertainties associated with the 3-day calibration are typical for the calibration of working standards used in the flask and in situ programs.

In an attempt to obtain gas cylinders that will be superior to aluminum cylinders for the long-term storage of methyl halides, several electropolished, stainless-steel cylinders were purchased. These cylinders are approved by the Department of Transportation for transport at pressures of 6200 kPa (900 psi). Preliminary stability testing involved filling cylinders with moist ultrapure air and moist natural air. No significant changes were observed in the ultrapure air samples (i.e., outgassing of compounds normally detected with CATS instruments was not observed).

5.3. AIRBORNE PROJECTS

The Airborne Chromatograph for Atmospheric Trace Species (ACATS-IV) [*Romashkin et al.*, 2001] and Lightweight Airborne Chromatograph Experiment (LACE) [*Moore et al.*, 2002] are GC instruments designed to measure CFCs, N_2O, SF_6, and other trace gases aboard aircraft (ACATS-IV and LACE) and balloon (LACE) platforms. Measurements of these trace gases in the lower stratosphere can provide insight into the chemistry and transport of that region. This section describes some of the science results deduced from measurements made during the Stratospheric Aerosol and Gas Experiment III (SAGE III) Ozone Loss and Validation Experiment (SOLVE) (with ACATS-IV and LACE) and the Atmospheric Chemistry and Combustion Effects Near the Tropopause II (ACCENT-II) campaign (with LACE).

SOLVE was an investigation of wintertime stratospheric ozone losses in the Arctic vortex using in situ and remotely sensed measurements made from aircraft and balloon platforms. The primary goal of SOLVE was to increase knowledge of the processes that influence northern polar ozone from late autumn through late winter. A second objective, validation of SAGE III ozone measurements, was not achieved because the satellite was not deployed prior to the campaign. SOLVE was conducted simultaneously with the Third European Stratospheric Experiment on Ozone 2000 (THESEO 2000), which included independent measurements from aircraft and balloons.

ACATS-IV was part of the NASA high-altitude ER-2 aircraft payload during the 2000 SOLVE campaign. The ER-2 aircraft flew 11 science flights from Kiruna, Sweden (67.9°N, 21.1°E), and 5 transit flight segments between Kiruna and NASA Dryden, Edwards, California, between January 9 and March 18, 2000. Science flights included deep vortex penetrations to 90°N, vortex edge and extra-vortex surveys, and multiple-level flights for vertical profiling. ACATS-IV produced science-quality data for each of these flights. As discussed by *Romashkin et al.* [2001], ACATS-IV was modified for SOLVE by decreasing the interval between measurements of N_2O, SF_6, CFC-12, and halon-1211 to 70 seconds, while CFC-11, CFC-113, $CHCl_3$, CH_3CCl_3, CCl_4, H_2, and CH_4 were measured every 140 seconds. *Romashkin et al.* [2001] also provided detailed information about the operation and calibration of ACATS-IV, the processing of data, and the precision and errors of measurements.

LACE was flown on two NASA-sponsored flights of the Observations of the Middle Stratosphere (OMS) balloon. The first flight, November 19, 1999, occurred just after the vortex edge had formed. The second flight, March 5, 2000, occurred just prior to vortex breakup.

Several significant alterations were made to the ER-2 payload for SOLVE. One important change was the replacement of the NASA Airborne Tunable Laser Absorption Spectrometer (ATLAS), a long-standing source of high-quality, 1-Hz N_2O data, with a new, compact, lightweight tunable diode laser spectrometer (Argus) designed to provide high-quality, 1-Hz N_2O data as well as high-precision measurements of CH_4 every 3 seconds. A comparison of coincident N_2O data from ACATS-IV, ATLAS, and the NASA Jet Propulsion Laboratory (JPL) Aircraft Laser Infrared Absorption Spectrometer (ALIAS) during two previous ER-2 campaigns [*Hurst et al.*, 2000] showed typical agreement of 1.9% between ACATS-IV and ATLAS, 2.7% between ACATS-IV and ALIAS, and 2.8% between ALIAS and ATLAS. A similar comparison of SOLVE N_2O data revealed typical agreement of 3.8% between ACATS-IV and Argus, 2.6% between ACATS-IV and ALIAS, and 4.0% between ALIAS and Argus [*Hurst et al.*, 2002]. The poorer agreement between N_2O instruments during SOLVE spawned the idea to construct a self-consistent, high-resolution N_2O data set from the data of the three in situ N_2O instruments. An objective statistical method was developed to reduce biases between the instruments, then combine their measurements into a "unified" N_2O data set with 3-s temporal resolution [*Hurst et al.*, 2002]. The quality of unified N_2O data was evaluated by integration of the data over the canister-filling periods of the National Center for Atmospheric Research (NCAR) Whole Air Sampler (WAS) during SOLVE ER-2 flights. The N_2O data from the canisters agree with the integrated unified N_2O data within about 1.5%, which is better than the agreement between any pair of N_2O instruments.

Record ozone losses for the Arctic stratosphere have been reported for winter 1999/2000 [*Richard et al.*, 2001; *Salawitch et al.*, 2002]. These losses are predominantly attributed to chemical O_3 destruction driven by the most widespread presence of polar stratospheric clouds (PSCs) in the Arctic since the 1970s [*Rex et al.*, 2002] and near-peak levels of total halogen (Cl + Br) in the lower stratosphere [*Elkins*, 2000]. Measurements of chlorinated and brominated source gases in the lower stratosphere, combined with CMDL surface measurements of these gases, attest to the high availability of inorganic halogen in the older air masses of the Arctic vortex. Figure 5.24 illustrates that organic chlorine (CCl_y) and organic bromine (CBr_y) are more than 50% converted to inorganic chlorine (Cl_y) and inorganic bromine (Br_y) in air masses with mean ages greater than 4.5 and 3.0 years, respectively. In addition, severe denitrification [*Popp et al.*, 2001] (Figure 5.25) greatly inhibited chlorine and bromine deactivation reactions that moderate O_3 destruction rates [*Gao et al.*, 2001]. *Fahey et al.* [2001] described the first in situ measurements of the large HNO_3-containing particles whose gravitational sedimentation resulted in the observed severe denitrification. In contrast, significantly dehydrated air masses (>10% H_2O loss) were rarely encountered between 17 and 21 km, indicating that temperatures in this altitude range were often below the temperature at which nitric acid trihydrate (NAT) forms, but seldom below the ice frost point. However, *Herman et al.* [2002] reported a slight decrease in total hydrogen with altitude that resulted from the widespread sedimentation of PSC particles during the winter.

Cumulative O_3 loss and O_3 loss rates in the Arctic vortex during SOLVE have been calculated from measurements made by instruments aboard the ER-2 aircraft and balloons. *Richard et al.* [2001] analyzed in situ data to determine a cumulative O_3 loss of 58 ± 4% at 19-km altitude between February 3 and March 12, 2000. Their calculations are based on the wintertime evolution of the vortex O_3:N_2O relationship (Figure 5.26a). Ozone loss rates at 19 km were as high as 51 ± 3 ppb d^{-1} during late winter (Figure 5.26b) [*Richard et al.*, 2001]. *Rex et al.* [2002] examined data from 770 O_3 sondes launched from 29 northern stations to sample distinct air masses twice over several day intervals as they circumnavigated the pole and reported 70% cumulative O_3 loss near 18-km altitude and a cumulative

Fig. 5.25. Coincident in situ measurements of NO_y with the NOAA Aeronomy Laboratory total reactive nitrogen instrument [*Fahey et al.*, 1989] and N_2O with ACATS-IV on board the ER-2 aircraft during SOLVE (black circles). These data document severe and extensive denitrification in the Arctic vortex. The reference curve, a quadratic fit to NO_y and N_2O measured by the balloonborne MkIV interferometer on December 3, 1999 (open diamonds), represents the early-vortex NO_y:N_2O relationship before the onset of denitrification. Points below the reference curve indicate that air masses between 17 and 21 km altitude were denitrified by up to 75%. Nitrification at lower altitudes (14-16 km) is shown by points above the reference curve. (Figure adapted from *Popp et al.* [2001].)

Fig. 5.24. Top: Total chlorine (solid curve), organic chlorine (CCl$_y$, gray squares), and inorganic chlorine (Cl$_y$, black circles) as a function of mean age for air masses sampled by ACATS-IV during SOLVE. The fraction of organic chlorine converted to inorganic chlorine reservoirs was approximated by the black circles using the right axis scale. Bottom: Same as the top graph, but for bromine. CCl$_y$ and CBr$_y$ are the sums of chlorinated and brominated source gases measured in the lower stratosphere by ACATS and the NCAR whole air sampler. Total chlorine and total bromine were determined from CMDL global surface trends of source gases with appropriate age spectral weightings. Cl$_y$ and Br$_y$ were calculated as the difference between total Cl (Br) and CCl$_y$ (CBr$_y$). Mean ages were calculated from ACATS measurements of SF$_6$ in the lower stratosphere and the SF$_6$ global surface trend [*Geller et al.*, 1997].

column reduction of 117 ± 14 Dobson units (DUs) by late March 2000. *Salawitch et al.* [2002] studied the evolution of O_3:N_2O relationships to conclude that chemical O_3 loss between 14 and 22 km caused a 61-DU reduction of column O_3 between late November 1999 and March 5, 2000. The ozone loss and loss rates deduced in these three studies are in good agreement.

Grooss et al. [2002] used data from ACATS-IV and other instruments to initialize a stratospheric chemistry and transport model, the Chemical Lagrangian Model of the Stratosphere (CLaMS), that simulated Arctic ozone loss during SOLVE. Model simulations agreed well with the observed ozone loss at 450 K (about 19-km altitude) but tended to underestimate O_3 losses at higher altitudes, probably because of the limited amount of data used to initialize the model at higher altitudes and the absence of diabatic descent in the model.

Accurate differentiation between wintertime changes in vortex O_3 caused by chemistry and those caused by transport relies strongly on determinations of how much extra-vortex air mixes into the vortex. The vortex edge is a barrier to the exchange of midlatitude and vortex air. Previous work implied that differences between vortex and extra-vortex tracer-tracer relationships were due to large-scale, homogeneous descent in the vortex and significant in-mixing of extra-vortex air [*Plumb et al.*, 2000]. Descent can be roughly estimated by tracking the motion of air parcels with an inert tracer, as shown for N_2O in Figure 5.27. Most of the molecules measured by ACATS-IV and LACE are inert in the vortex, lacking local sources and
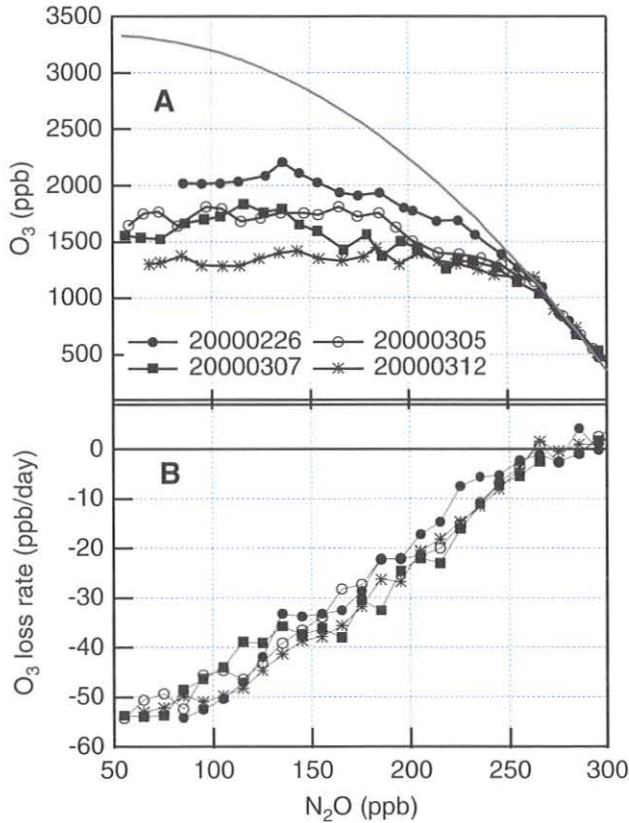
Fig. 5.26. (a) Coincident in situ measurements of O_3 with the NOAA Aeronomy Laboratory dual-beam ultraviolet photometer [*Proffitt and McLaughlin*, 1983] and N_2O with ACATS-IV on board the ER-2 aircraft during SOLVE. These data show the wintertime losses of O_3 in the Arctic vortex. The gray reference curve, a quadratic fit to O_3 and N_2O measured during four ER-2 and balloon flights between December 3, 1999, and February 3, 2000, represents the early-vortex O_3:N_2O relationship prior to ozone losses. Data from subsequent ER-2 flights demonstrate cumulative O_3 losses of up to 60% from early February to mid-March 2000. (b) Ozone loss rates calculated from differences between O_3:N_2O relationships in the early vortex and for the four ER-2 flights shown in (a). (Figure adapted from *Richard et al.* [2001].)
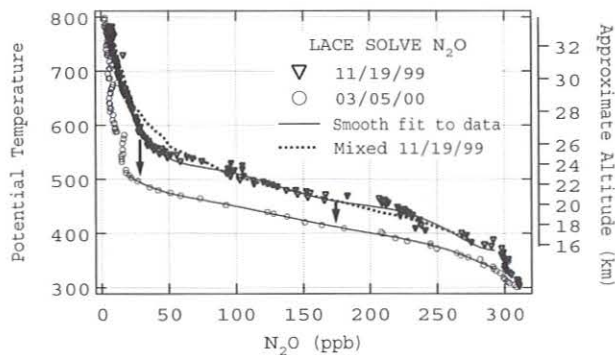
Fig. 5.27. Profiles of N_2O as a function of potential temperature (K) from LACE for the two OMS balloon flights during the SOLVE mission. Solid curves through the data are fits used in the calculation of descent in the vortex between the flights. Also included is a representation of a well-mixed early-vortex profile (dashed curve) from the differential descent mixing calculation.

sinks on the time scales of transport. Because these molecules have different vertical mixing ratio profiles, each molecule allows for an independent measurement of descent and other transport characteristics. This calculation of descent is only valid if mixing between air parcels of differing tracer concentration does not occur on similar time scales. In the absence of chemistry, this type of mixing can be seen as a shift in the curved tracer-tracer correlation plots (Figure 5.28).

Ray et al. [2002] were unable to produce the vortex tracer-tracer relationships observed by LACE and ACATS-IV during SOLVE by modeling homogeneous descent and in-mixing of extra-vortex air. They showed, instead, that differential descent and isentropic mixing within the vortex could produce the observed vortex relationships. These processes were folded into the descent calculations (dotted line in Figure 5.27) to give the final descent rates shown in Figure 5.29a. Note the good agreement across all tracers. The differential descent needed to reproduce the changes in tracer-tracer correlations is shown in Figure 5.29b. The lack of significant in-mixing of extra-vortex air during winter 1999/2000 is an important finding because it identifies chemistry, not transport, as the predominant cause of the large ozone losses observed during SOLVE. Analyses
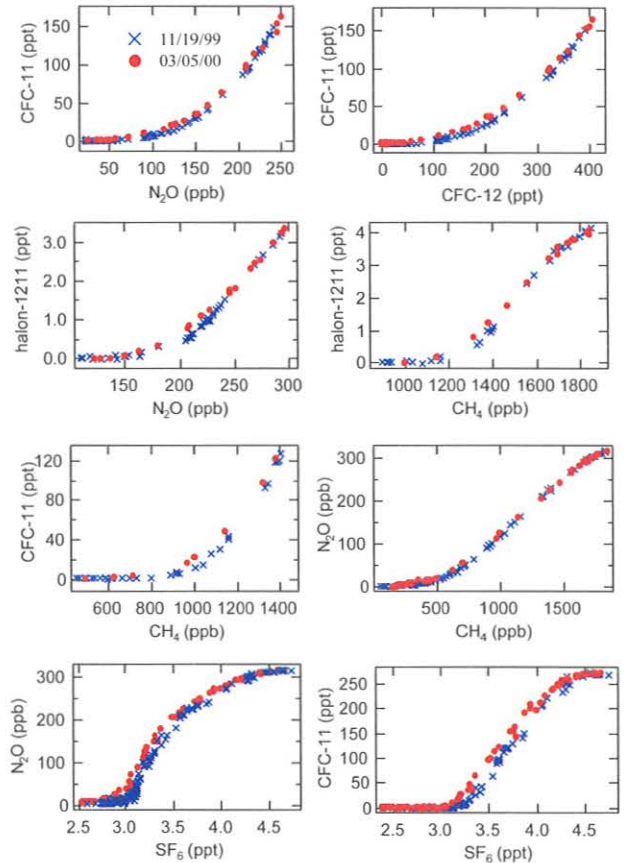

Fig. 5.28. Tracer-tracer correlation curves from the two LACE SOLVE flights. Data from the second flight are significantly shifted from the first flight toward the concave side of the curves, which suggests mixing of some type occurred.
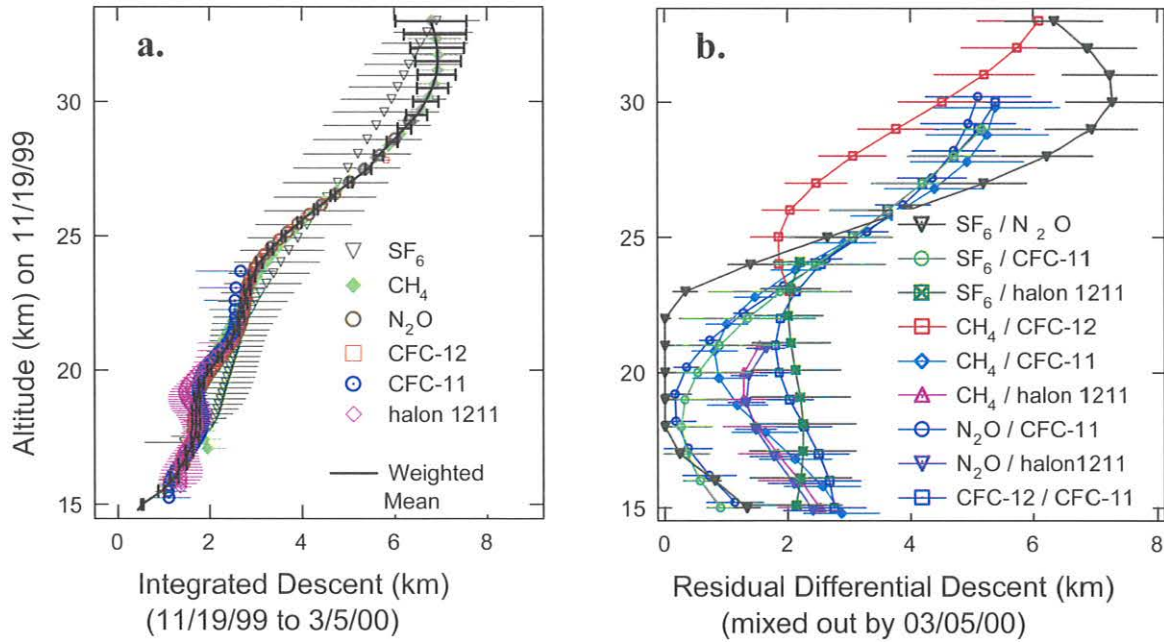
Fig. 5.29. (a) Integrated and (b) differential descent deduced from measurements associated with two LACE flights within the core of the Arctic vortex during SOLVE. Error bars represent the calculated statistical uncertainty.

by *Greenblatt et al.* [2002] and *Morgenstern et al.* [2002] using unified N_2O and ACATS-IV tracer data also conclude that the 1999/2000 Arctic vortex was strongly isolated and experienced little in-mixing.

The importance of accurate determinations of mean age distributions in the stratosphere has been stressed by *Andrews et al.* [2001]. Compared with mean ages calculated from in situ measurements of age tracers like SF_6 and CO_2, mean ages from many stratospheric transport models are underestimated by as much as a factor of 2. If general circulation rates in the models are decreased to increase mean ages, model tracer distributions fail to match observed distributions. Hence, model evaluations of important environmental issues related to trace gases, such as the impacts of exhaust from a proposed fleet of stratospheric aircraft and ozone layer recovery time scales, may be of limited accuracy until these discrepancies between models and observations are reduced. Using long-lived tracer data from ACATS, LACE, and other instruments, *Andrews et al.* [2002] have constructed accurate distributions of mean age in the stratosphere that will help improve the transport in models.

SF_6 is a strong greenhouse gas with a long lifetime. Estimating its atmospheric lifetime is important in terms of its contribution to the Earth's radiative budget as well as its use as a tracer of atmospheric motion. The stratospheric lifetime of SF_6 is dominated by loss that occurs in the mesosphere. Evidence of this loss is measurable in mesospheric air that descends into the polar vortices. Moore et al. [Measured SF_6 loss and its influence on age-of-air calculations, in preparation, 2002] calculated the stratospheric lifetime of SF_6 from OMS data assuming that

(a) the age of air calculated with CO_2 data [*Andrews et al.*, 2002] is correct, and differences between CO_2 and SF_6 age-of-air estimates from vortex data (Figure 5.30) are due to SF_6 loss, and (b) the loss of SF_6 occurs over 6 months, and the mesospheric air descends only into the northern vortex (6 months later the process repeats into the southern
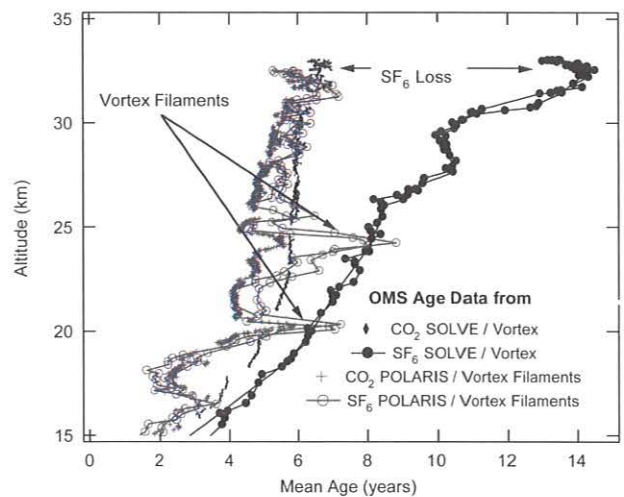

Fig. 5.30. Age-of-air estimates from both CO_2 and SF_6 data, assuming all stratospheric sources or sinks are taken into account. The difference between these two age estimates, seen both in the vortex filaments and the vortex core data, is then assumed to be due to SF_6 loss in the mesosphere.

vortex). The net loss within the northern vortex was multiplied by two to estimate the yearly loss rate. Their new estimate for the stratospheric lifetime of SF_6 is 600 (+200, −100) years, which is better constrained than the previously reported range of 600-3200 years [*Morris et al.*, 1995]. The upper bound in the new estimate is less certain than the lower bound because of an uncertainty in SF_6 loss above 32 km within the vortex.

Significant global O_3 destruction will continue well into the 21st century because of the high halogen burden of the stratosphere [*Prinn et al.*, 1999]. Accurate predictions of future O_3 levels require accurate determinations of halogen budgets and their trends. Stratospheric chlorine [*Woodbridge et al.*, 1995] and bromine [*Wamsley et al.*, 1998] budgets are periodically calculated from ACATS, LACE, and WAS measurements of halogenated source gases, allowing the determination of trends. The calculation methods have been revised over time to reflect significant changes in the tropospheric trends of some halocarbons. An important, recent refinement in these calculations is the weighting of tropospheric trends with age spectra [*Hall and Plumb*, 1994; *Andrews et al.*, 2001] instead of mean age, to determine trends in total chlorine (Cl_{tot}) and total bromine (Br_{tot}) entering the stratosphere [*Elkins*, 2000]. These revisions improve calculations of total inorganic chlorine (Cl_y) and total inorganic bromine (Br_y) as the difference between total chlorine (bromine) and the sum of chlorinated (brominated) source gases CCl_y (CBr_y).

Schauffler et al. [2002] have recently revised the stratospheric chlorine budget based on WAS and ACATS-IV measurements made during SOLVE. A comparison of ACATS-IV and WAS CCl_y for SOLVE reveals differences of 0.015-0.190 ppb (Figure 5.31), with WAS values always larger because the ACATS-IV method does not account for chlorine from CFC-114, CFC-114a, CFC-115, CH_2Cl_2, C_2Cl_4, HCFC-142b, and HCFC-141b. These omissions account for 0.023-0.130 ppb of the CCl_y differences. The rest of the discrepancy results from calibration-scale differences and disparity in the HCFC-22 and CH_3Cl mixing ratios calculated by ACATS-IV but measured by WAS. The two independent data sets are complementary in that ACATS reports CCl_y more frequently (every 140 seconds) than WAS, but the WAS CCl_y data are inherently more accurate.

Trends in Cl_y determined from ACATS and LACE measurements near 19-, 20.5-, and 27.5-km altitude over the period 1992-2000 imply that Cl_y either peaked or leveled off by the year 2000 (Figure 5.32a). The sum of chlorinated source gases (CCl_y, or ETCl) measured at the surface by CMDL (Figure 5.32a) illustrates the decreasing trend in Cl_{tot} [*Montzka et al.*, 1999], largely because of the rapid decline in CH_3CCl_3. These surface CCl_y data represent an upper limit for Cl_y and are closely matched by Halogen Occultation Experiment (HALOE) Cl_y (HCl) data at 55-km altitude, where near-complete conversion of CCl_y to Cl_y has occurred (Figure 5.32a). Upward trends in Br_y, apparent at all three altitudes (Figure 5.32b), are driven predominantly by continued emissions of halons. The increasing sum of brominated source gases (CBr_y) measured at the surface by CMDL provides an upper limit for Br_y.

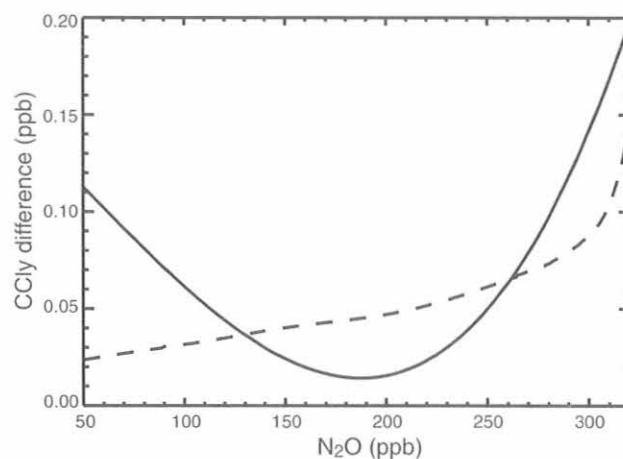Of pivotal importance to stratospheric ozone are the combined influences of chlorine and bromine trends. The

Fig. 5.31. Differences between WAS and ACATS-IV determinations of CCl_y as a function of N_2O (solid curve). Values range from 0.015 to 0.190 ppb. Partial differences in CCl_y that result from the ACATS omission of CFC-114, CFC-114a, CFC-115, CH_2Cl_2, C_2Cl_4, HCFC-142b, and HCFC-141b (dashed curve) range from 0.023 to 0.130 ppb. The remaining differences between WAS and ACATS-IV CCl_y result from calibration scale differences and the fact that CH_3Cl and HCFC-22 are calculated by ACATS-IV and measured by WAS. (Figure adapted from *Schauffler et al.* [2002].)

weighted sum of inorganic chlorine and bromine, namely equivalent inorganic chlorine ($ECl_y = Cl_y + 45 \times Br_y$), reflects the fact that Br_y is on average 45 times more efficient than Cl_y at the destruction of O_3 [*Daniel et al.*, 1999]. Trends in ECl_y (Figure 5.32c) mimic the decline or leveling off of Cl_y (Figure 5.32a), because Cl_y is 100-150 times more abundant than Br_y and the upward Br_y trend does little to offset the decreasing trend in Cl_y. Future trends in ECl_y, and hence O_3, are strongly dependent on this interplay between increasing bromine and decreasing chlorine abundance. Continued halon accumulation in the atmosphere may eventually overshadow reduced chlorine burdens, especially as the rate of CH_3CCl_3 decline approaches zero.

Up to this point, HATS airborne GCs were specifically designed to make measurements in the upper troposphere and lower stratosphere. Tropospheric issues such as air quality and the accumulation of greenhouse gases are expected to take a higher priority in this century. Funding was provided by the NASA Instrument Incubator Program to develop the PAN and other Trace Hydrohalocarbons Experiment (PANTHER) next-generation airborne GC. A mass selective detector will be combined with two or more ECD channels to focus on more reactive and shorter-lived species. The first test flight of PANTHER is scheduled for spring 2002 on the NASA ER-2 aircraft. Key molecules measured on this test flight will include peroxyacetyl nitrate (PAN), acetone ($CH_3C(O)CH_3$), and HCFCs. PAN comprises the largest fraction of oxides of nitrogen (NO_y) under natural conditions in the troposphere and is a precursor of O_3. Acetone is a precursor of PAN and an important source of hydroxyl radical in the upper troposphere.
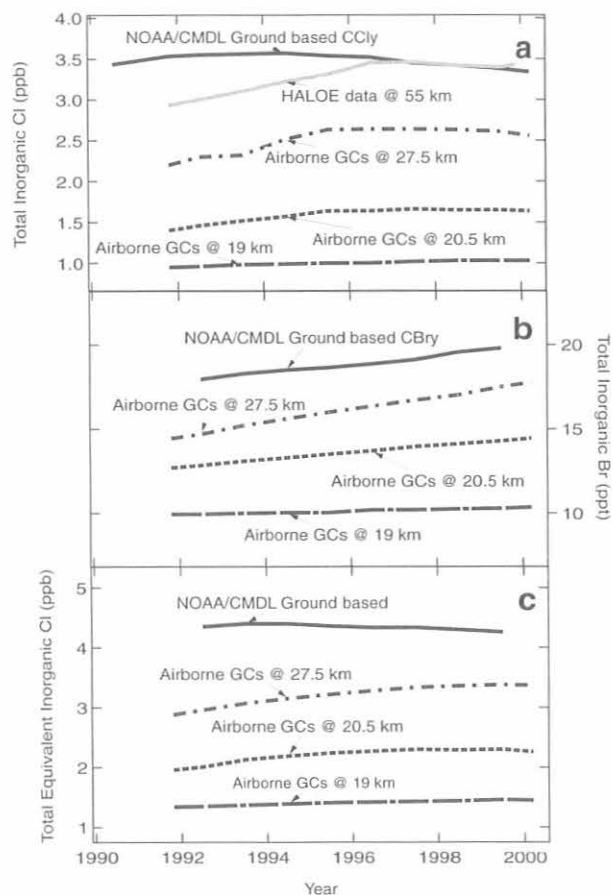
Fig. 5.32. Estimates of total inorganic halogen from airborne GCs (including ACATS and LACE): (a) total inorganic chlorine (ppb), (b) total inorganic bromine (ppt), and (c) total equivalent inorganic chlorine (ppb), at equivalent altitudes of 19, 20.5, and 27.5 km. HALOE inorganic chlorine data at 55 km are plotted in (a) (updated by *Anderson et al.* [2000]). CMDL ground-based data are plotted in (a)-(c).

5.4. OCEAN PROJECTS

5.4.1. DATA ANALYSIS

Natural halocarbons are important contributors to the destruction of stratospheric ozone. For example, methyl bromide (CH_3Br) and methyl chloride (CH_3Cl) together are the source of about one-quarter of the equivalent chlorine in the troposphere [*Butler*, 2000], where equivalent chlorine is one way to evaluate the ozone-depleting capacity of the atmosphere [*Daniel et al.*, 1995]. Other brominated compounds, such as dibromomethane (CH_2Br_2) and bromoform ($CHBr_3$), also might be significant sources of bromine to the upper atmosphere [e.g., *Schauffler et al.*, 1999; *Sturges et al.*, 2000]. An understanding of the sources and sinks of these compounds would enable the prediction of changes in the cycling of these compounds associated with climate change. Because the oceans are both a source and a sink of most natural halocarbons,

oceanic measurements have constituted one component of the HATS group research effort.

Data obtained from previous field missions were analyzed during 2000-2001. The variability in sea surface temperature (SST) has been shown to account for one-half to two-thirds of the variability in methyl bromide oceanic saturations, according to *King et al.* [2000]. In that study, data from six cruises were fitted with two quadratic equations. While global extrapolations with this relationship appear reasonable, this relationship does not accurately reproduce observations on a regional basis. However, reexamination of the data, along with inclusion of data from a 1999 expedition to the Pacific Ocean, has significantly improved the ability to reproduce field observations.

Data from seven research cruises (five conducted by CMDL and two by Dalhousie University) were divided seasonally into two data sets: spring-summer and fall-winter. These data include measurements from the Atlantic [*Lobert et al.*, 1996; *Groszko and Moore*, 1998; *King et al.*, 2000], the Pacific [*Lobert et al.*, 1995; *Groszko and Moore*, 1998; *King et al.*, 2000; unpublished CMDL data], and the Southern Ocean [*Lobert et al.*, 1997]. Measurements made between March 20 and September 21 were considered spring-summer if north of the equator and fall-winter if south of the equator. Data collected during the remainder of the year were assigned to fall-winter if north of the equator and spring-summer if south of the equator. Each seasonal data set was fitted with two quadratic equations, describing data above and below 16°C (Figure 5.33).

The new equations represent a significant improvement over the existing equations, particularly in temperate regions. For example, the previous equations could account for only about 15% of the seasonal difference (summertime supersaturations and fall undersaturations) in CH_3Br saturation anomaly observed in the North Atlantic temperate waters [*King et al.*, 2000]. However, the new equations can reasonably reproduce the observed seasonal difference for CH_3Br in these waters. The seasonal SST relationships also improve the ability to estimate the mean saturation anomaly for a given data set. For the two most recent cruises, Gas Exchange Experiment (Gas Ex 98) [*King et al.*, 2000] and Bromine Air-sea Cruise Pacific (BACPAC 99) [*Schnell et al.*, 2001], the mean CH_3Br saturation anomalies estimated with the new equations are about 90% of the measured values. In contrast, the mean saturation anomalies as determined with the old equations [*King et al.*, 2000] are only about 60% of the measured values.

Methyl bromide saturation anomaly maps have been generated with the seasonal SST relationships and a global map of SSTs (Figure 5.34). The SST data set consists of 1° × 1° monthly means from the National Oceanographic Data Center (NODC) [*Levitus*, 1982]. Each grid point represents a 3-mo average value. In this model CH_3Br undersaturations are predicted in both the tropics and polar regions throughout the year. The temperate waters, however, show a strong seasonal cycle in both hemispheres. With the data used to create these maps, the global, annually averaged CH_3Br saturation anomaly is calculated

Spring/Summer

$R^2 = 0.66$ $R^2 = 0.51$
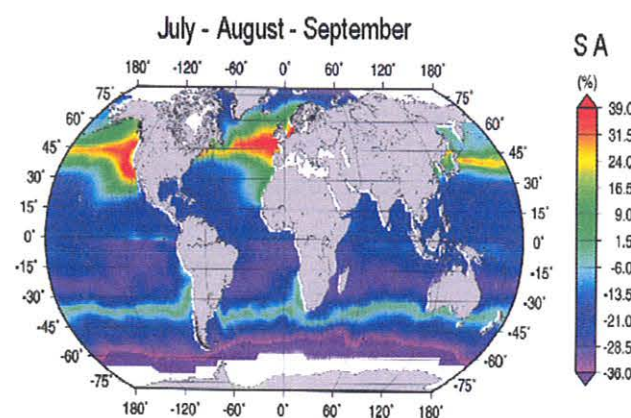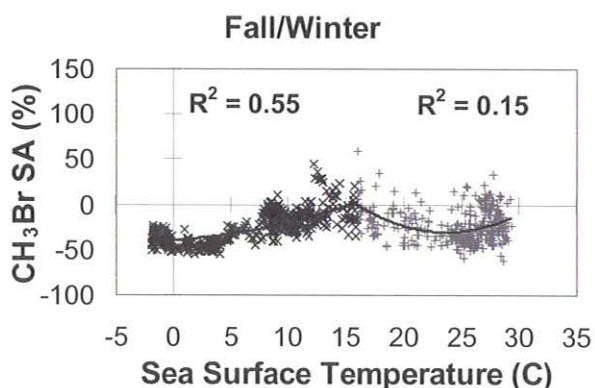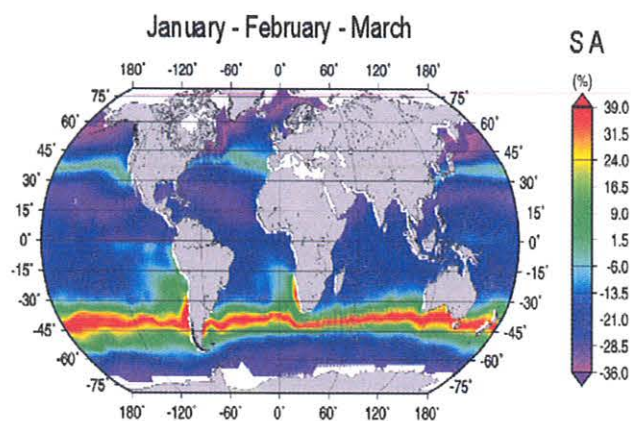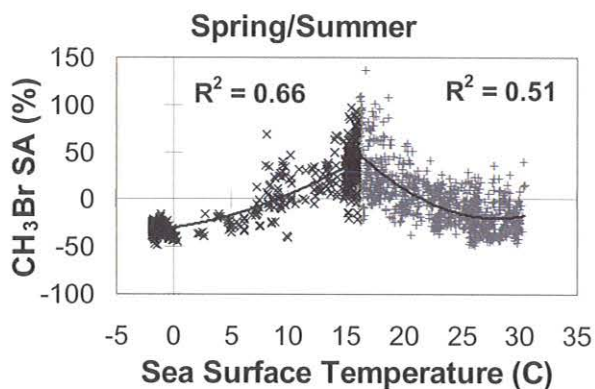

Fall/Winter

$R^2 = 0.55$ $R^2 = 0.15$

Fig. 5.33. Methyl bromide saturation anomaly data from five CMDL cruises and two Dalhousie University cruises between 1994 and 1999, plotted as a function of sea surface temperature. The data are divided seasonally, with local spring and summer data in the upper plot and local fall and winter data in the lower plot. Quadratic fits are used to describe data above and below 16°C for each seasonal data set.

January - February - March SA

July - August - September SA

Fig. 5.34. Methyl bromide saturation anomalies plotted as 3-mo averages on 1° by 1° grid size. These maps were generated with relationships between saturation anomaly and sea surface temperature (shown in Figure 5.33). White spaces represent regions with insufficient sea surface temperature data to calculate a value for the CH₃Br saturation anomaly.

to be −15.5%. The calculated global, annually averaged CH₃Br flux is −19.9 Gg yr^{-1}. Both of these values agree with other published estimates [e.g., *Lobert et al.*, 1997; *King et al.*, 2000].

5.4.2. 2001 OCEAN CRUISE

During fall 2001 the HATS group participated on a research cruise in the Southern Ocean. The Australian ship *Aurora Australis* departed Hobart, Tasmania, on October 29 and returned to Hobart on December 13. The vessel headed south toward the Antarctic coast before returning to Australia, retracing a previous Climate Variability and Predictability (CLIVAR) cruise track (Figure 5.35). The HATS group measured over 20 halogenated compounds in the surface seawater and overlying atmosphere. The results will be coordinated with those obtained by research groups from NOAA Atlantic Oceanographic and Meteorological Laboratory (AOML) (halocarbon depth profiles) and the University of California at Irvine (methyl bromide and methyl chloride degradation rates).
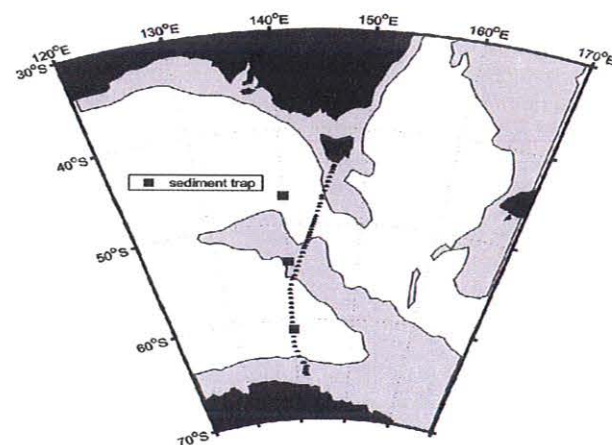

Fig. 5.35. The cruise track for the fall 2001 cruise on which the HATS group participated. The *Aurora Australis* departed Hobart, Tasmania, and returned to Hobart after approaching the Antarctic coast.

5.5. SPECIAL PROJECTS

5.5.1. METHYL HALIDE EMISSIONS FROM TOMATO PLANTS

Fieldwork

The atmospheric budgets of most natural halocarbons are poorly defined. For both methyl bromide (CH_3Br) and methyl chloride (CH_3Cl), best estimates of the known sinks outweigh best estimates of the known sources by 30-50% [*Kurylo et al.*, 1999]. Although plant production of natural halocarbons has not been studied extensively, there is considerable new evidence that plants are involved in the cycling of these compounds. Previous studies have primarily involved the use of a flux chamber, which does not isolate the plant from the soil and potentially stresses the plant [e.g., *Gan et al.*, 1998; *Redeker et al.*, 2000; *Rhew et al.*, 2000, 2001]. Soils are potentially problematic because they have been observed to remove CH_3Br from the atmosphere [e.g., *Varner et al.*, 1999].

The HATS group conducted an experiment in a hydroponic greenhouse in Northern California (McKinleyville) over a 2-wk period in July 2001. The greenhouse was covered with double-layered polyethylene and housed about 400 tomato plants (*Lycopersicon esculentum*). The plants were grown in bags of inert support material (Pearlite) without soil and were flushed with an aqueous nutrient mixture at frequent intervals throughout the day. During each experiment, the greenhouse was sealed, and halocarbon concentrations were measured in the greenhouse atmosphere with a GC-MSD located at the site. Sampling lines were placed in the center and at one end of the greenhouse. Fans were used to keep the greenhouse atmosphere well mixed. No concentration differences were observed between the two sampling locations. Experiments were started in the late afternoon/early evening and were run until the air temperature in the greenhouse exceeded about 35°C, usually about noon the following day. Eight experiments were run in total, and each experiment lasted 16-20 hours. The standard nutrient mixture was used first for two control experiments (C-1 and C-2). This nutrient mixture contained no significant halide concentrations. A solution containing about 5 ppm Br⁻, Cl⁻, and I⁻ was added in line with the nutrient mixture during the third, fourth, and fifth experiments (H5-1, H5-2, and H5-3). During the final three experiments (H20-1, H20-2, and H20-3), a solution of about 20 ppm Br⁻, Cl⁻, and I⁻ was added in line with the nutrient mixture. These halide solutions were added continuously over the course of several days, not just during the experiments themselves.

Results and Discussion

During C-1 and C-2, no production of CH_3Br (Figure 5.36a) or CH_3Cl was observed, but methyl iodide (CH_3I) (Figure 5.36b) increased by a factor of about 5 by the end of the experiments. Production was also observed for several other halogenated compounds, including bromochloromethane (CH_2BrCl), dibromomethane (CH_2Br_2), dibromochloromethane ($CHBr_2Cl$), and bromoform ($CHBr_3$) (Figure 5.36c). In general, anthropogenic compounds, such as CFC-11 (Figure
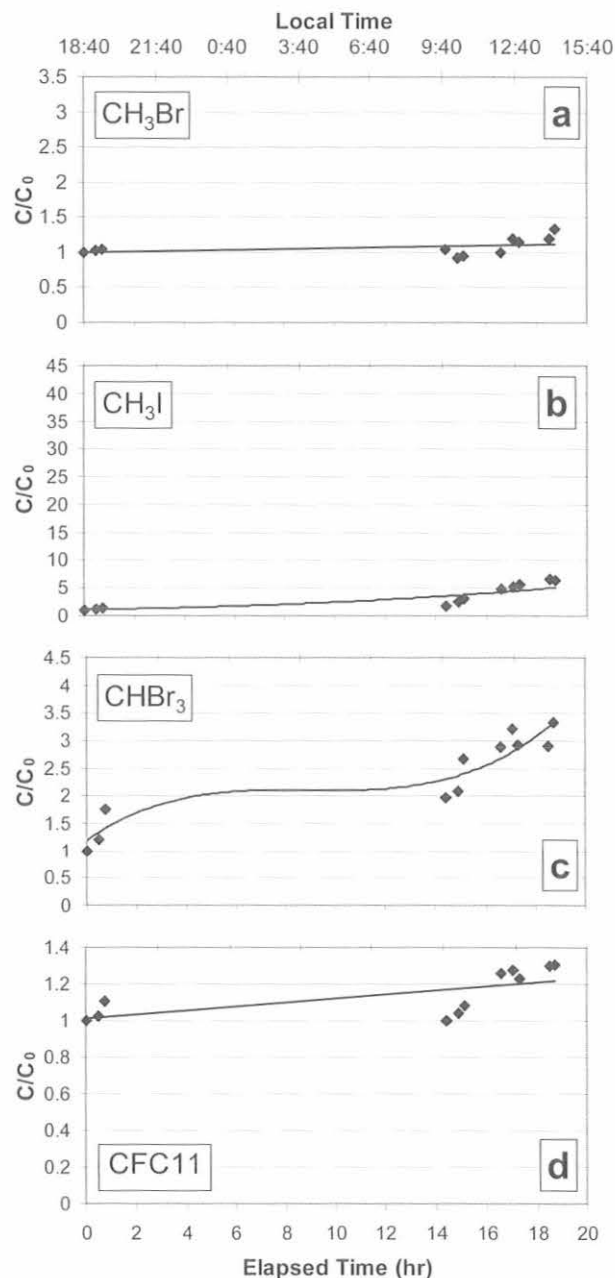

Fig. 5.36. Concentration changes of (a) CH_3Br, (b) CH_3I, (c) $CHBr_3$, and (d) CFC-11, during a greenhouse experiment, plotted as a function of time. All concentrations were normalized to the corresponding initial concentration (C/C_0). During this experiment, no halide ions were added to the nutrient mixture.

5.36d), CFC-113, and halon-1211, remained relatively constant over the course of the study, suggesting that large-scale contamination from materials in the greenhouse or from the greenhouse itself was unlikely.

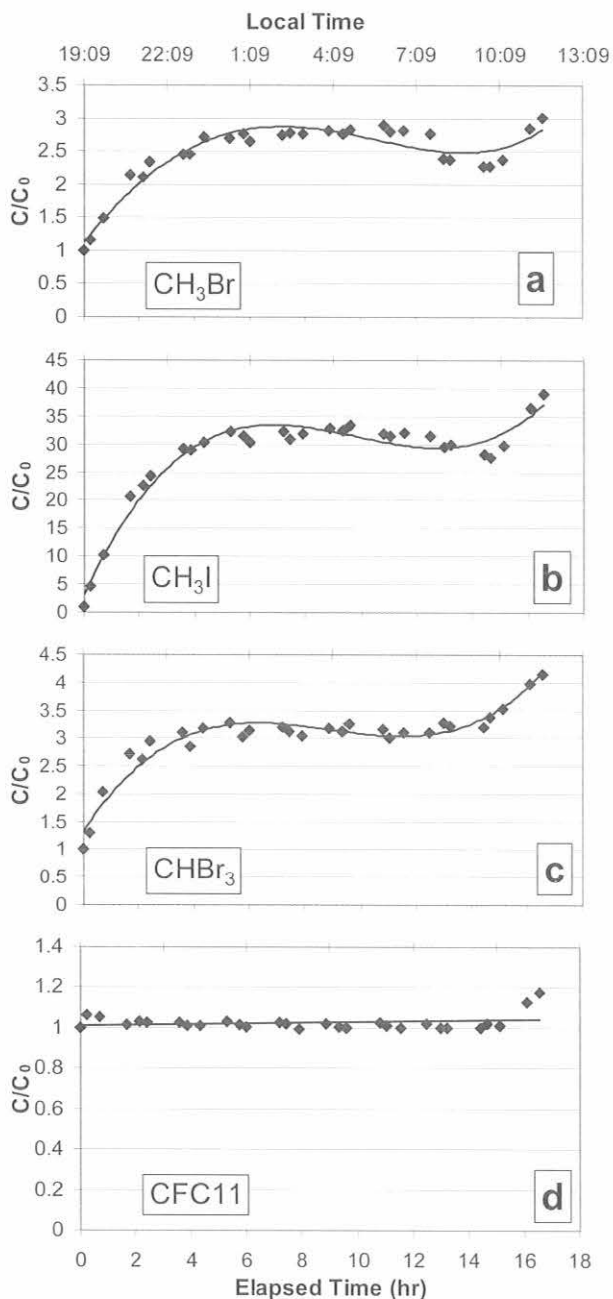The addition of the halide solution affected the production rates of only CH_3Br and CH_3I (Figure 5.37a,b).

Fig. 5.37. Concentration changes of (a) CH_3Br, (b) CH_3I, (c) $CHBr_3$, and (d) CFC-11, during a greenhouse experiment, plotted as a function of time. All concentrations were normalized to the corresponding initial concentration (C/C_0). During this experiment, a solution containing about 20 ppm Br^-, Cl^-, and I^- flushed the plants with the nutrient mixture.

During experiments H20-1, H20-2, and H20-3, CH_3Br increased by nearly a factor of 3. Production of CH_3I increased by a factor of about 35 during these experiments, almost an order of magnitude more than with the standard nutrient mixture alone. Production for other halogenated compounds, such as $CHBr_3$ (Figure 5.37c) and $CHBr_2Cl$,

did not change noticeably between experiments run with and without the halide solution.

Similar results were observed for the H5 experiments. Only CH_3Br and CH_3I production differed from the other experiments. The production for those two compounds increased with each experiment. Production during H5-3 approached the values that were observed during the H20 experiments. This suggests that production of CH_3Br and CH_3I by tomato plants is a function of halide concentration. More studies are necessary to determine if these observations are reproducible for these and other plants.

Although tomato plants were chosen for little other reason than opportunity, this study suggests that many plants could emit significant amounts of organic halogens to the atmosphere. It also supports propositions from other investigators that there is a relationship between halide concentration in the soil and organic halogen production by plants [e.g., *Redeker et al.*, 2000; *Rhew et al.*, 2000]. This preliminary study has raised many questions. One question concerns the production of polybrominated compounds when no halides were added, whereas CH_3Br concentrations remained constant. It is also unknown why the production of CH_3Br and CH_3I increased with the addition of the halide solution while that of other halocarbons did not. The potential variability of production rates as a function of plant growth stage was also not addressed in this study. Further studies of these and other plants will be necessary before these questions can be adequately addressed.

5.5.2. TRANS-SIBERIAN OBSERVATIONS INTO THE CHEMISTRY OF THE ATMOSPHERE (TROICA)

From June 27 to July 10, 2001, about 11,000 in situ measurements of CFC-12, halon-1211, N_2O, and SF_6, and nearly 5000 measurements of CFC-11, CFC-113, $CHCl_3$, CH_3CCl_3, CCl_4, CH_4, and H_2 were made along 17,000 km of the fully electrified trans-Siberian railway between Moscow and Khabarovsk, Russia (Figure 5.38), with the ACATS-IV gas chromatograph (GC). These measurements were part of the seventh Trans-Siberian Observations into the Chemistry of the Atmosphere (TROICA-7) scientific expedition, a collaboration between CMDL, the Coooperative Institute for Research in Environmental Sciences (CIRES), NASA, the Max Planck Institute for Chemistry (Mainz, Germany), and the Russian Institute of Atmospheric Physics (Moscow). TROICA expeditions were inaugurated by German and Russian scientists in 1995 and have taken place annually during different seasons [*Crutzen et al.*, 1998; *Oberlander et al.*, 2002]. The primary CMDL objective for TROICA-7 was to make frequent (every 70 or 140 seconds) measurements of halocarbon and greenhouse gases along the trans-Siberian railway, creating a database to which future TROICA measurements of these gases can be compared. CMDL participation in TROICA-7 produced the first extensive set of halocarbon measurements in Russia by American scientists.

As during past TROICA expeditions, German and Russian scientists operated in situ analyzers for CO, CO_2, O_3, CH_4, NO_x, ^{222}Rn, H_2O, aerosols, solar radiation, temperature, pressure, and relative humidity [*Crutzen et al.*, 1998]. A global positioning system receiver tracked
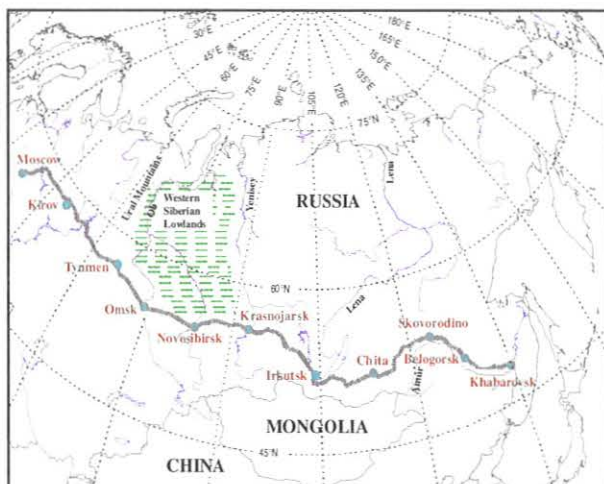
Fig. 5.38. Route of the TROICA-7 science expedition along the trans-Siberian railway. Each of the transects, Moscow-Khabarovsk and Khabarovsk-Moscow, was approximately 8500 km in length and took 6.25 days. Major cities along the railway are indicated by filled circles.

electric locomotive. Air intakes for instruments were attached to a frame structure on top of the science car. ACATS-IV sampled air at approximately 4 L min^{-1} through 5 m of 6.4-mm-outside-diameter Dekabon tubing with a Teflon diaphragm pump (model UN05, KNF Neuberger Inc., Princeton, New Jersey). A 2-mm-pore glass fiber filter was used to keep large particles out of the intake tubing. The sample stream was dried with $Mg(ClO_4)_2$.

The train traveled at a mean and maximum speed of 57 and 129 km h^{-1}. Numerous stops were made during the 6.25 days required to travel each direction. There were 216 scheduled stops at stations with durations of 2-90 minutes. Track maintenance and stop signals accounted for 43 unscheduled, non-station stops with durations of 1-69 minutes. In general, population density decreased with distance from Moscow, though large, industrialized cities were encountered almost daily along the length of the railway. East of the Ural Mountains, the population density is greatest in southern Siberia, near the railway. Rural areas were typically birch and larch forest (taiga) or rolling grasslands with some large lowland areas. The Moscow-Khabarovsk segment of the railway spans latitudes of 48.6° to 58.6°N and altitudes of 0 to 998 m above sea level. Temperature ranged from 3° to 33°C, with three daytime highs >30°C and three nighttime lows <10°C. Rain, heavy at times, was encountered on 12 of the 14 travel days.

movements of the train, and visual observations along the route were recorded in detail. A microwave temperature profiler was also part of the payload. All instruments were housed in a special rail car (Research Institute of Railroad Transport of Russia) situated immediately behind the

Large fluctuations in the mixing ratios of some gases were observed during the expedition, as illustrated by the time series for the refrigerant CFC-12 and fire extinguishing agent halon-1211 (Figure 5.39). The variability (1 standard
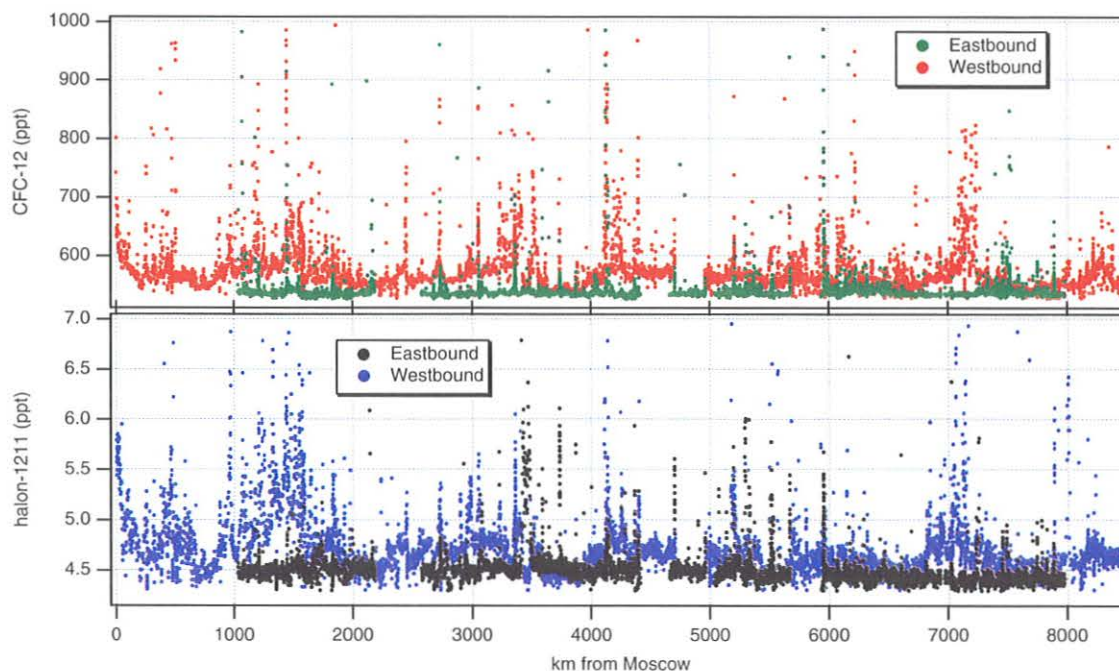

Fig. 5.39. Time series of CFC-12 (top) and halon-1211 (bottom) mixing ratios during TROICA-7 as a function of distance from Moscow. For CFC-12, there were 34 and 83 measurements >1000 ppt during the eastbound and westbound transects, respectively, that are off-scale in this figure. There were 2 eastbound and 41 westbound halon-1211 measurements >7 ppt that are off-scale. Of interest for these two gases are their high variability along the railway and their generally higher mixing ratios during the westbound transect.

deviation) of every gas measured along the railway was at least 50% greater than its measurement precision (Table 5.8). Variability relative to the mean mixing ratio was very high (>70%) for $CHCl_3$ and CO; 11-32% for CFC-12, halon-1211, H_2, and CO_2; 6-9% for CFC-113 and CH_4; and <3% for N_2O, SF_6, CFC-11, CH_3CCl_3, and CCl_4. Fluctuations in mixing ratio observed along the railway were also much greater than at Point Barrow, Alaska (BRW), during June-July 2001 (Table 5.8) except for CH_3CCl_3, which showed about the same low variability at both locations. Ratios of TROICA-7 to BRW variability for gases other than CH_3CCl_3 ranged from 1.7 for SF_6 to 59 for CFC-12.

For gases that exhibited concentrations higher than the northern hemispheric background, a major concern is the possibility of air sample contamination due to train-based sources forward and/or aft of the sampling inlets. No known sources of the measured gases were located forward of the sample inlets, but >100 m aft there were small coal-fired water heaters in passenger carriages and a working air conditioner in the restaurant car. There was also an inoperative air conditioning unit in the science carriage with no discernible pressure of CFC-12. Intuitively, a forward source would frequently contaminate the air stream sampled by instruments, especially at high train speeds. An aft source could have contaminated samples when the train was moving slowly or stopped.

To explore the possibility of contamination by train-based sources, data for four highly variable gases (CFC-12, halon-1211, CO, and CO_2) were separated by train speed: high, low, and stopped. Forward contamination of samples was investigated by comparison of data at high train speeds with CMDL data at remote, high-latitude northern hemisphere sites during June-July 2001. For these gases, 30-60% of the data taken at high train speeds were representative of well-mixed, background air masses,

indicating that samples were not consistently contaminated by forward sources. This is supported by the fact that elevated mixing ratios (>80th percentile) were detected less frequently at high train speeds than when the train was stopped. However, this evidence, along with significantly lower fractions of background CFC-12 and CO mixing ratios at stops compared with high train speeds, suggests that aft sources on the train many have contaminated samples when the train was stopped. Of course, these biases may simply reflect the fact that the train stopped primarily at stations in populated areas where sources were present. To explore train contamination from aft sources during stops, CFC-12, halon-1211, CO, and CO_2 measurements made at scheduled station stops were separated from those made at unscheduled, non-station stops. For these four gases, fractions of background data at non-station stops (57-80%) were 1.4 to 2.3 times greater than at station stops (24-47%). Fractions of elevated mixing ratios at station stops were also factors of 1.3 to 3.5 higher than at non-station stops. Though these statistics for station and non-station stops do not preclude the possibility of sample contamination by the train during stops, they strongly imply that sources proximate to train stations in populated areas were responsible for the elevated mixing ratios measured during stops.

CFC-12 and halon-1211 concentrations were quite variable during both the eastbound and westbound transects of TROICA-7 (Figure 5.39), but were generally higher throughout the westbound return to Moscow because of large, sustained concentration increases observed on some nights. These increases, also seen in CO_2, ^{222}Rn, and $CHCl_3$ data (Figures 5.40 and 5.41), occurred beneath nocturnal temperature inversions that were much stronger and prolonged during the westbound transect (Figures 5.40a and 5.41a). Increases in ^{222}Rn and CO_2 beneath the nighttime inversions were generally broad and well-correlated because

TABLE 5.8. Summary Statistics of Gas Measurements During TROICA-7 and at Barrow, Alaska

						TROICA-7		
Gas	N	Mean	Median	Precision*	Variability†	$75^{th} - 25^{th}$ Percentile	$95^{th} - 5^{th}$ Percentile	BRW Variability‡
N_2O (ppt)	10815	316.7	316.4	0.6	1.9	1.1	3.7	0.8
SF_6 (ppt)	11086	5.00	4.99	0.05	0.15	0.07	0.19	0.09
CFC-12 (ppt)	11132	573	551	4	118	36	123	2
Halon-1211 (ppt)	11125	4.66	4.55	0.04	0.52	0.25	0.94	0.04
CFC-11 (ppt)	4629	263.0	262.0	0.5	5.3	1.3	6.3	1.2
CFC-113 (ppt)	4573	82.3	81.9	0.3	7.2	0.9	2.3	0.7
$CHCl_3$ (ppt)	4929	16.3	14.1	0.2	12.6	4.2	15.3	1.7
CH_3CCl_3 (ppt)	4700	38.9	38.8	0.5	0.8	1.1	2.1	0.8
CCl_4 (ppt)	4690	102.7	102.5	0.4	2.5	0.6	2.3	0.4
H_2 (ppb)	4634	549	507	14	177	66	350	15
CO (ppb)	8241	146	126	10	102	59	218	5
CH_4 (ppb)	4459	1882	1852	16	109	83	212	21
CO_2 (ppm)	10706	379.3	365.3	1	41.8	24.9	127.8	1.4

*Precision is expressed as the standard deviation of residuals of ACATS-IV calibration measurements made during the expedition, where residuals are deviations of raw calibration data from smoothed, drift-corrected calibration data.

†TROICA-7 variability is expressed as 1 standard deviation.

‡ BRW variability is expressed as the standard deviation of residuals of hourly averages of in situ observations made at Point Barrow, Alaska (72° N), during June-July 2001. Residuals are deviations from smooth curve fits to the data that account for seasonal cycles and longer-term trends.
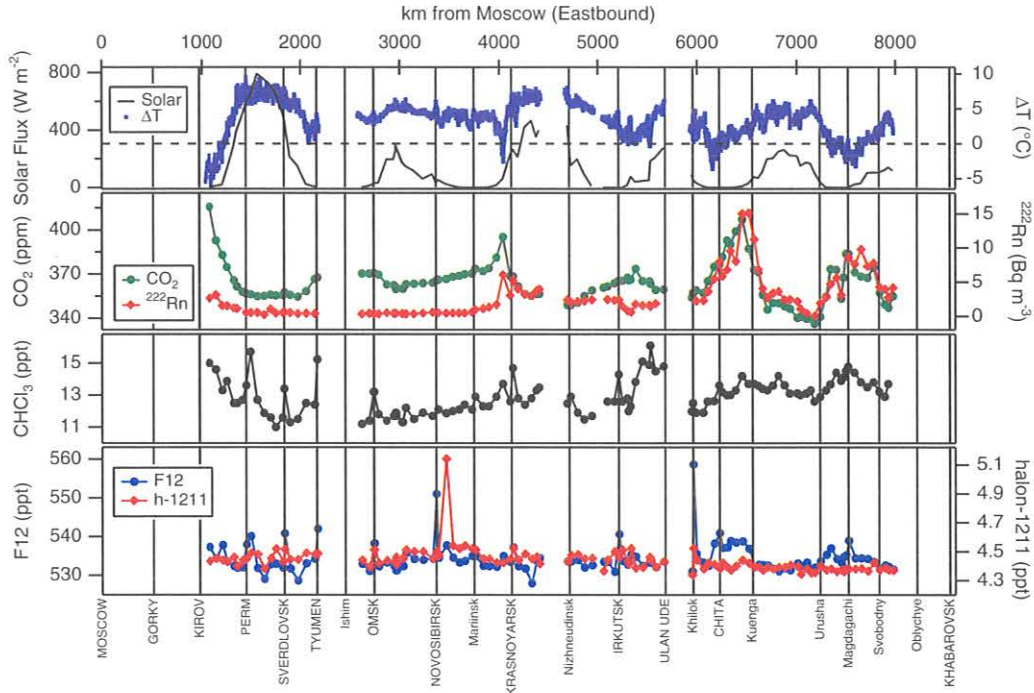
Fig. 5.40. Solar flux, temperature difference, and mixing ratios for CO_2, ^{222}Rn, CFC-12, halon-1211, and $CHCl_3$ during the eastbound transect of TROICA-7. The mixing ratios of these gases increased broadly beneath relatively weak temperature inversions during several nights of the transect. CFC-12, halon-1211, and $CHCl_3$ mixing ratios also sharply increased near several cities. Data for these gases are the 20th percentiles in 1-h windows. Solar fluxes identify daytime and nighttime periods. ΔT is the difference in temperature at 0 and 600 m above the science car roof such that $\Delta T < 0$ indicates a temperature inversion. Major cities along the railway are listed along the bottom axis.
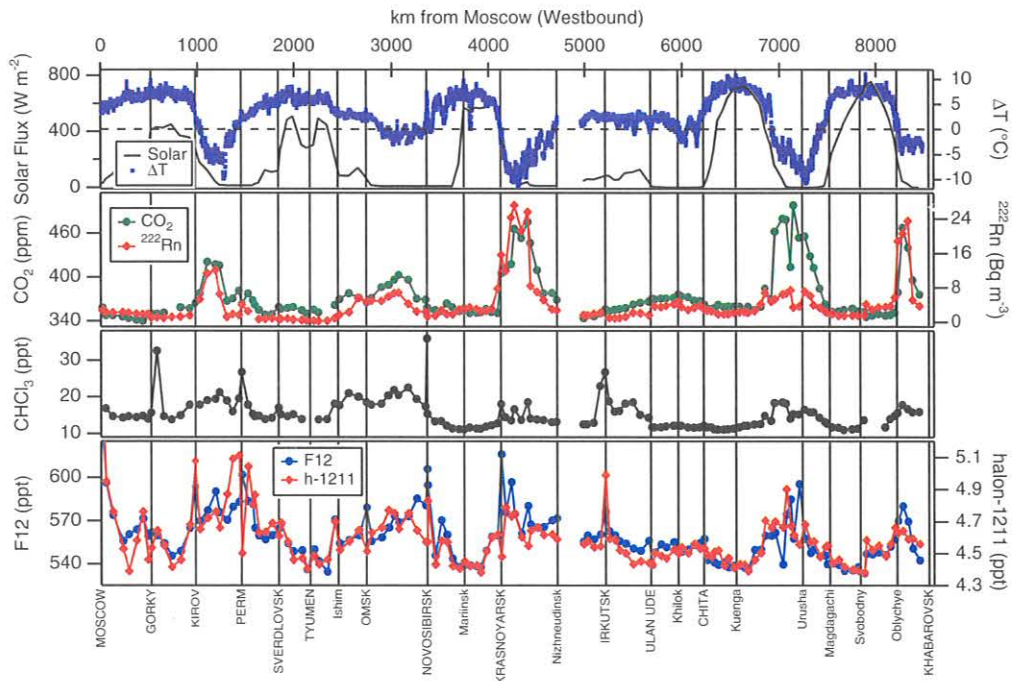

Fig. 5.41. Same as Figure 5.40, except for the westbound transect of TROICA-7. Time series should be viewed from right to left (east to west) as the train returned to Moscow. Several strong nighttime temperature inversions caused large, broad increases in gas concentrations. Note the greatly expanded concentration ranges compared with those in Figure 5.40, the result of stronger temperature inversions and perhaps greater emissions from upwind sources.

both gases are widely emitted by soils. Similar nighttime increases in ^{222}Rn, CO_2, and other gases have been observed during previous TROICA expeditions [Bergamaschi et al., 1998; Crutzen et al., 1998; Oberlander et al., 2002]. $CHCl_3$, CFC-12, and halon-1211 mixing ratios increased broadly beneath several nighttime inversions and sharply near some cities. Nighttime increases in these halocarbons were typically coincident with increased ^{222}Rn and CO_2, but their magnitudes were not generally consistent with ^{222}Rn and CO_2 increases, possibly because of geographical variations in the strengths of halocarbon sources.

Analyses of the TROICA-7 data continue in an effort to characterize the source emissions, transport, and boundary layer dynamics responsible for the observed trace gas variability. Under the *Montreal Protocol on Substances that Deplete the Ozone Layer* [*UNEP*, 1987], non-Article 5 (developed) countries like Russia and the United States were required to cease production of halons and CFCs by January 1994 and 1996, respectively. Economic difficulties prevented Russia from meeting these target dates. Only with substantial financial incentives did Russia finally cease CFC and halon production in December 2000. Inspectors have since verified that Russia is no longer producing CFCs and halons. It is of great interest now to determine whether the detected emissions of CFC-12 and halon-1211 along the trans-Siberian railway are related to stockpile leaks, discharges from in-use structures and equipment, or seepage from abandoned structures and discarded equipment. CMDL scientists intend to be part of the next TROICA expedition proposed for winter 2002/2003.

5.5.3. FIRN AIR SAMPLING, 2001

In January 2001, CMDL scientists joined investigators from Bowdoin University, Princeton University, and the University of Wisconsin to collect an archive of 20th century air from the firn (snowpack) at South Pole (Figure 5.42). Samples were collected into separate pairs of 3-L glass flasks for measurements of O_2/N_2 (by Bowdoin and Princeton) and carbon cycle gases (by CMDL/CCGG); individual 3-L stainless-steel and glass flasks for measurements of halocarbons, N_2O, SF_6, and COS; large (33-L) stainless-steel canisters to maintain an archive of air for future analyses; and a few canisters each for measurement of $^{14}CH_4$ (by NIWA and CSIRO) and very low-level analyses of SF_6 (by Scripps Institution of Oceonograpy, SIO) (Table 5.9). All samples were analyzed during 2001, including initial analyses of the archive canisters. Although it was hoped to obtain air dating back to the turn of the century, the analyses suggest that the earliest date was 1921 for CO_2 and just after 1900 for gases that diffuse more slowly, such as methyl bromide and methyl chloride.

CMDL scientists have been participating in the collection and analysis of firn air from Antarctica and Greenland since 1995. Samples have been analyzed from Vostok, Taylor Dome, South Pole, and Siple Dome in Antarctica and from Tunu in Greenland. The data have been used to estimate the atmospheric histories of these gases where real-time measurements were not available [*Battle et al.*, 1996; *Butler et al.*, 1999], extending the earliest records of many trace

Fig. 5.42. Bladder being sent down into one of the two holes at South Pole for subsequent sampling of firn air. The 10-m-long bladder was pressurized to inhibit airflow from above while firn air was sampled through a 15-cm-high, stainless-steel-lined open chamber situated between the bottom of the bladder and the bottom of the hole. Each of two holes, extending ultimately to the snow-ice transition at 122-m depth, was drilled and sampled at 2- to 10-m increments. The drill lies on the snow to the left.

gases from the late 1970s back to the end of the 19th century. They also have been used to evaluate seasonal biasing of the mean gas mixing ratios [*Severinghaus et al.*, 2001]. The 2001 sampling at South Pole was the second deep sampling conducted at that site; the first was in 1995. Samples from this most recent collection provide a unique opportunity to examine the diffusion of trace gases in the firn (Figures 5.43 and 5.44), which should reduce error in the estimation of the age of the firn air. Also, the oldest firn air ever collected comes from South Pole, which makes the archived samples particularly valuable for future analyses of gases not yet reported.

Preliminary evaluation of the data from the 2001 campaign shows that diffusion rates of gases in the firn are very close to molecular rates, calculated by extrapolation of measurements made at very high temperatures to the temperature of the firn, ~ −50 °C. Although often used in models of firn air movement, such extrapolated values are always suspect. Determination of the actual diffusion rates in the firn will remove this uncertainty and allow for the direct calculation of gas diffusion at these temperatures and, subsequently, the mean age of the air at each depth.

TABLE 5.9. Gases Measured in South Pole Firn Air, 2001

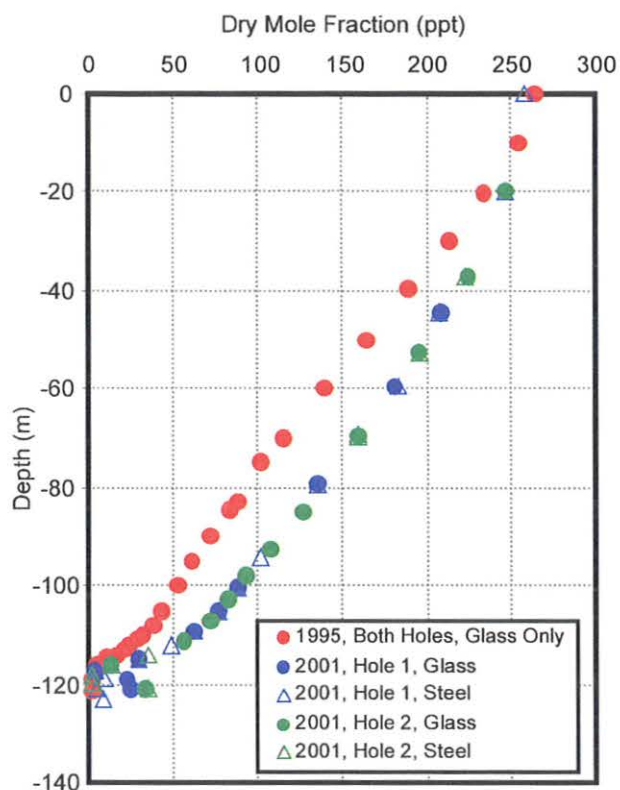| Institution	Gas
CMDL or Univ. of Colorado	CO_2, CO, CH_4, N_2O, H_2, SF_6, CFCs, HCFCs, HFC-134a, CH_3Br, CH_3Cl, CH_3I, COS, halons, $^{13}CO_2$
Princeton Univ. or SIO	$^{15}N_2O$, $N_2^{18}O$, $^{15}N_2$, $^{18}O_2$, $^{17}O_2$, $^{14}CO_2$, Ar, Kr, Xe, Ne, Ar/N_2, O_2/N_2, SF_6
NIWA or CSIRO	$^{14}CH_4$

Fig. 5.43. CFC-11 in South Pole firn air in 1995 and 2001. Samples in 1995 were collected from two separate holes, but only into glass flasks. Samples in 2001 also were collected from two separate holes, but both glass and electropolished stainless-steel flasks were used. Note the lower value at the surface in 2001, reflecting the decreased atmospheric burden between 1995 and 2001. Also note the 20-m penetration at mid-depth, where the gradient is steepest and vertical restriction still low.
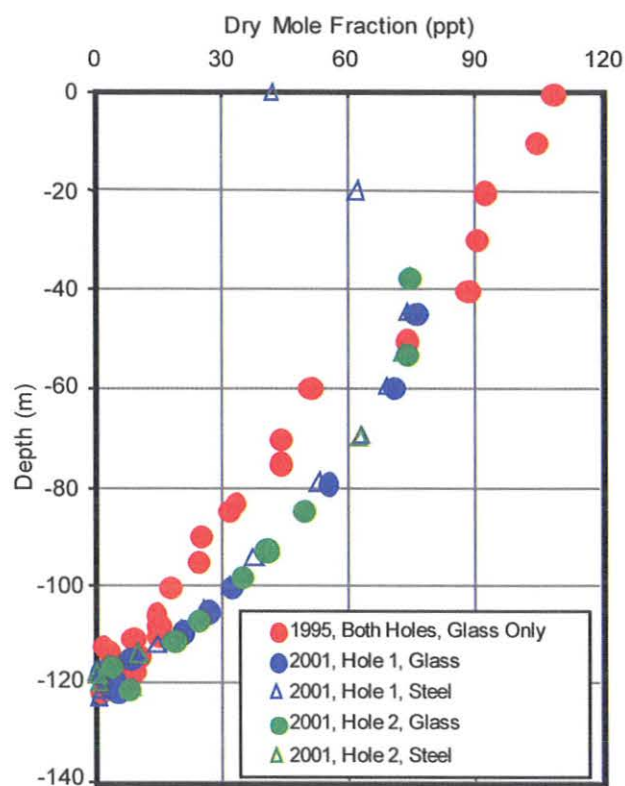

Fig. 5.44. CH_3CCl_3 in South Pole firn air in 1995 and 2001. The 1995 sampling suffered from contamination in the glass flasks, which compromises the interpretation of some of the data points. The 2001 sampling was apparently free of contamination. Note not only the penetration that is similar to that of CFC-11 (Figure 5.43), but also the evidence for the stark turnaround in the CH_3CCl_3 trend in the atmosphere. The turnover occurred in about 1994 in the southern hemisphere, which was an insufficient time lag for this signal to be recorded in the firn in 1995. (The northern hemispheric turnover, in about 1993, was recorded in Greenland firn as early as 1996 [*Butler et. al.*, 1999].) By 2001, the peak of CH_3CCl_3 had penetrated to 45-m depth.

Data are being analyzed and evaluated with the objectives to (1) improve estimates of trace gas diffusion at low temperatures and the corresponding effect on mean-age estimates for firn air samples and (2) report 20th century histories of gases, such as COS, previously not analyzed throughout the century. Other laboratories are currently analyzing the archive of air in 33-L canisters in an attempt to obtain reliable records of additional gases. It is anticipated that sufficient air will be available for analysis of even more gases and isotopes as new analytical techniques become available.

5.6. REFERENCES

Anderson, J., J.M. Russell III, S. Solomon, and L.E. Deaver, Halogen Occultation Experiment confirmation of stratospheric chlorine decreases in accordance with the Montreal Protocol, *J. Geophys. Res., 105*, 4483-4490, 2000.

Andrews, A.E., K.A. Boering, S.C. Wofsy, B.C. Daube, D.B. Jones, S. Alex, M. Loewenstein, J.R. Podolske, and S.E. Strahan, Empirical age spectra for the midlatitude lower stratosphere from in situ observations of CO_2: Quantitative evidence for a subtropical "barrier" to horizontal transport, *J. Geophys. Res., 106*, 10,257-10,274, 2001.

Andrews, A.E., K.A. Boering, B.C. Daube, S.C. Wofsy, M. Loewenstein, H. Jost, J.R. Podolske, R.L. Herman, R.D. May, E.J. Moyer, J.W. Elkins, G.S. Dutton, D.F. Hurst, F.L. Moore, E.A. Ray, P.A. Romashkin, P.R. Wamsley, and S.E. Strahan, Mean ages of stratospheric air derived from in situ observations of CO_2, CH_4, and N_2O, *J. Geophys. Res.*, in press, 2002.

Battle, M., M. Bender, T. Sowers, P.P. Tans, J.H. Butler, J.W. Elkins, J.T. Ellis, T. Conway, N. Zhang, P. Lang, and A.D. Clarke, Atmospheric gas concentrations over the past century measured in air from firn at the South Pole, *Nature, 383*, 231-235, 1996.

Bergamaschi, P., C.A.M. Brenninkmeijer, M. Hahn, T. Röckmann, D.H. Scharffe, P.J. Crutzen, N.F. Elansky, I.B. Belikov, N.B.A. Trivett, and D.E.J. Worthy, Isotope analysis based source identification for atmospheric CH_4 and CO sampled across

Russia using the trans-Siberian railroad, *J. Geophys. Res., 103*, 8227-8235, 1998.

Butler, J.H., Better budgets for methyl halides?, *Nature, 403*, 260-261, 2000.

Butler, J.H., S.A. Montzka, A.D. Clarke, J.M. Lobert, and J.W. Elkins, Growth and distribution of halons in the atmosphere, *J. Geophys. Res., 103*, 1503-1511, 1998.

Butler, J.H., M. Battle, M. Bender, S.A. Montzka, A.D. Clarke, E.S. Saltzman, C. Sucher, J. Severinghaus, and J.W. Elkins, A twentieth century record of atmospheric halocarbons in polar firn air, *Nature, 399*, 749-765, 1999.

Crutzen, P.J., N.F. Elansky, M. Hahn, G.S. Golitsyn, C.A.M. Brenninkmeijer, D.H. Scharffe, I.B. Belikov, M. Maiss, P. Bergamaschi, T. Röckmann, A.M. Grisenko, and V.M. Sevostyanov, Trace gas measurements between Moscow and Vladivostok using the trans-Siberian railroad, *J. Atmos. Chem., 29*, 179-194, 1998.

Daniel, J.S., S. Solomon, and D.L. Albritton, On the evaluation of halocarbon radiative forcing and global warming potentials, *J. Geophys. Res., 100*, 1271-1285, 1995.

Daniel, J.S., S. Solomon, R.W. Portmann, and R.R. Garcia, Stratospheric ozone destruction: The importance of bromine relative to chlorine, *J. Geophys. Res., 104*, 23,871-23,880, 1999.

Elkins, J.W., Trends of trace gases, total chlorine, and total bromine in the lower stratosphere from 1991 through 2000, *Eos Trans. AGU, 81*, F88, 2000.

Fahey, D.W., K.K. Kelly, G.V. Ferry, L.R. Poole, J.C. Wilson, D.M. Murphy, M. Loewenstein, and K.R. Chan, In situ measurements of total reactive nitrogen, total water, and aerosol in a polar stratospheric cloud in the Antarctic, *J. Geophys. Res., 94*, 11,299-11,315, 1989.

Fahey, D.W., R.S. Gao, K.S. Carslaw, J. Kettleborough, P.J. Popp, M.J. Northway, J.C. Holecek, S.C. Ciciora, R.J. McLaughlin, T.L. Thompson, R.H. Winkler, D.G. Baumgardner, B. Gandrud, P.O. Wennberg, S. Dhaniyala, K. McKinney, T. Peter, R.J. Salawitch, T.P. Bui, J.W. Elkins, C.R. Webster, E.L. Atlas, H. Jost, J.C. Wilson, R.L. Herman, A. Kleinböhl, and M. von König, The detection of large HNO₃-containing particles in the winter Arctic stratosphere, *Science, 291*, 1026-1031, 2001.

Fraser, P.J., D.E. Oram, C.E. Reeves, S.A. Penkett, and A. McCulloch, Southern hemispheric halon trends (1978-1998) and global halon emissions, *J. Geophys. Res., 104*, 15,985-15,999, 1999.

Gan, J., S.R. Yates, H.D. Ohr, and J.J. Sims, Production of methyl bromide by terrestrial higher plants, *Geophys. Res. Lett., 25*, 3595-3598, 1998.

Gao, R.S., E.C. Richard, P.J. Popp, G.C. Toon, D.F. Hurst, P.A. Newman, J.C. Holecek, M.J. Northway, D.W. Fahey, M.Y. Danilin, B. Sen, K. Aikin, P.A. Romashkin, J.W. Elkins, C.R. Webster, S.M. Schauffler, J.B. Greenblatt, C.T. McElroy, L.R. Lait, T.P. Bui, and D. Baumgardener, Observational evidence for the role of denitrification in Arctic stratospheric ozone loss, *Geophys. Res. Lett., 28*, 2879-2882, 2001.

Geller, L.S., J.W. Elkins, J.M. Lobert, A.D. Clarke, D.F. Hurst, J.H. Butler, and R.C. Myers, Tropospheric SF₆: Observed latitudinal distribution and trends, derived emissions, and interhemispheric exchange time, *Geophys. Res. Lett., 24*, 675-678, 1997.

Greenblatt, J.B., H. Jost, M. Loewenstein, J.R. Podolske, T.P. Bui, D.F. Hurst, J.W. Elkins, R.L. Herman, C.R. Webster, S.M. Schauffler, E.A. Atlas, P.A. Newman, L.R. Lait, M. Müller, A. Engel, and U. Schmidt, Definining the polar vortex edge from an N₂O:potential temperature correlation, *J. Geophys. Res.*, in press, 2002.

Grooss, J.-U., G. Günther, P. Konopka, R. Müller, D.S. McKenna, F. Stroh, B. Vogel, A. Engel, M. Müller, K. Hoppel, R. Bevilacqua, E. Richard, R.M. Stimpfle, C.R. Webster, J.W. Elkins, D.F. Hurst, and P.A. Romashkin, Simulation of ozone depletion in spring 2000 with the Chemical Lagrangian Model of the Stratosphere (CLaMS), *J. Geophys. Res.*, in press, 2002.

Groszko, W., and R.M. Moore, Ocean-atmosphere exchange of methyl bromide: NW Atlantic and Pacific Ocean studies, *J. Geophys. Res., 103*, 16,737-16,741, 1998.

Hall, B.D., J.W. Elkins, J.H. Butler, S.A. Montzka, T.M. Thompson, L. Del Negro, G.S. Dutton, D.F. Hurst, D.B. King, E.S. Kline, L. Lock,

D. MacTaggart, D. Mondeel, F.L. Moore, J.D. Nance, E.A. Ray, and P.A. Romashkin, Halocarbons and other atmospheric trace species, in *Climate Monitoring and Diagnostics Laboratory Summary Report No. 25 1998-1999*, edited by R.C. Schnell, D.B. King, and R.M. Rosson, pp. 91-113, NOAA Oceanic and Atmos. Res., Boulder, CO, 2001.

Hall, T.M., and R.A. Plumb, Age as a diagnostic of stratospheric transport, *J. Geophys. Res., 99*, 1059-1070, 1994.

Herman, R.L., K. Drdla, J.R. Spackman, D.F. Hurst, C.R. Webster, J.W. Elkins, E.M. Weinstock, J.G. Anderson, B.W. Ganrud, G.C. Toon, M.R. Schoeberl, A.E. Andrews, S.C. Wofsy, H. Jost, E.L. Atlas, D.W. Fahey, and T.P. Bui, Hydration, dehydration, and the total hydrogen budget of the 1999-2000 winter Arctic stratosphere, *J. Geophys. Res.*, in press, 2002.

Hurst, D.F., P.S. Bakwin, R.C. Meyers, and J.W. Elkins, Behavior of trace gas mixing ratios on a very tall tower in North Carolina, *J. Geophys. Res., 102*, 8825-8835, 1997.

Hurst, D.F., G.S. Dutton, P.A. Romashkin, J.W. Elkins, R.L. Herman, E.J. Moyer, D.C. Scott, R.D. May, C.R. Webster, J. Grecu, M. Loewenstein, and J.R. Podolske, Comparison of in situ N₂O and CH₄ measurements in the upper troposphere and lower stratosphere during STRAT and POLARIS, *J. Geophys. Res., 105*, 19,811-19,822, 2000.

Hurst, D.F., S.M. Schauffler, J.B. Greenblatt, H. Jost, R.L. Herman, J.W. Elkins, P.A. Romashkin, E.L. Atlas, S.G. Donnelly, J.R. Podolske, M. Loewenstein, C.R. Webster, G.J. Flesch, and D.C. Scott, The construction of a unified, high-resolution nitrous oxide data set for ER-2 flights during SOLVE, *J. Geophys. Res.*, in press, 2002.

King, D.B., J.H. Butler, S.A. Montzka, S.A. Yvon-Lewis, and J.W. Elkins, Implications of methyl bromide supersaturations in the temperate North Atlantic Ocean, *J. Geophys. Res., 105*, 19,763-19,769, 2000.

Kjellström. E., A three-dimensional global model study of carbonyl sulfide in the troposphere and the lower stratosphere, *J. Atmos. Chem., 29*, 151-177, 1998.

Kurylo, M.J., J.M. Rodriguez, M.O. Andreae, E.L. Atlas, D.R. Blake, J.H. Butler, S. Lal, D.J. Lary, P.M. Midgley, S.A. Montzka, P.C. Novelli, C.E. Reeves, P.G. Simmonds, L.P. Steele, W.T. Sturges, R.F. Weiss, and Y. Yokouchi, Short-lived ozone-related compounds, in *Scientific Assessment of Ozone Depletion: 1998, Global Ozone Res. and Monit. Proj. Rep. 44*, pp. 2.1-2.56, World Meteorol. Org., Geneva, 1999.

Levitus, S., Climatological atlas of the world ocean, *NOAA Prof. Pap., 13*, U.S. Govt. Print. Off., Washington, DC, 1982.

Lobert, J.M., J.H. Butler, S.A. Montzka, L.S. Geller, R.C. Myers, and J.W. Elkins, A net sink for atmospheric CH₃Br in the East Pacific Ocean, *Science, 267*, 1002-1005, 1995.

Lobert, J.M., J.H. Butler, L.S. Geller, S.A. Yvon, S.A. Montzka, R.C. Myers, A.D. Clarke, and J.W. Elkins, BLAST94: Bromine Latitudinal Air/Sea Transect 1994: Report on oceanic measurements of methyl bromide and other compounds, *NOAA Tech. Memo. ERL CMDL-10*, 39 pp., NOAA Oceanic and Atmos. Res., Boulder, CO, 1996.

Lobert, J.M., S.A. Yvon-Lewis, J.H. Butler, S.A. Montzka, and R.C. Myers, Undersaturation of CH₃Br in the Southern Ocean, *Geophys. Res. Lett., 24*, 171-172, 1997.

Montzka, S.A., J.H. Butler, R.C. Myers, T.M. Thompson, T.H. Swanson, A.D. Clarke, L.T. Lock, and J.W. Elkins, Decline in the tropospheric abundance of halogen from halocarbons: Implications for stratospheric ozone depletion, *Science, 272*, 1318-1322, 1996.

Montzka, S.A., J.H. Butler, J.W. Elkins, T.M. Thompson, A.D. Clarke, and L.T. Lock, Present and future trends in the atmospheric burden of ozone-depleting halogens, *Nature, 398*, 690-694, 1999.

Montzka, S.A., C.M. Spivakovsky, J.H. Butler, J.W. Elkins, L.T. Lock, and D.J. Mondeel, New observational constraints for atmospheric hydroxyl on global and hemispheric scales, *Science, 288*, 500-503, 2000.

Moore, F.L., J.W. Elkins, E.A. Ray, G.S. Dutton, R.E. Dunn, D.W. Fahey, R.J. McLaughlin, T.L. Thompson, P.A. Romashkin, D.F. Hurst, and P.R. Wamsley, Balloonborne in situ gas chromatograph for measurements in the troposphere and stratosphere, *J. Geophys. Res.*, in press, 2002.

Morgenstern, O., J.A. Pyle, A. Iwi, W.A. Norton, J.W. Elkins, D.F. Hurst, and P.A. Romashkin, On the diagnosis of mixing from tracer-tracer correlations, 2, Comparison of model and measurements, *J. Geophys. Res.*, in press, 2002.

Morris, R.A., T.M. Miller, A.A. Viggiano, J.F. Paulson, S. Solomon, and G. Reid, Effects of electron and ion reactions on atmospheric lifetimes of fully fluorinated compounds, *J. Geophys. Res., 100,* 1287-1294, 1995.

Oberlander, E.A., C.A.M. Brenninkmeijer, P.J. Crutzen, N.F. Elansky, G.S. Golitsyn, I.G. Granberg, D.H. Scharffe, R. Hofmann, I.B. Belikov, H.G. Paretzke, and P.F.J. van Velthoven, Trace gas measurements along the trans-Siberian railroad: The TROICA 5 expedition, *J. Geophys. Res.*, in press, 2002.

Plumb, R.A., D.W. Waugh, and M.P. Chipperfield, The effects of mixing on tracer relationships in the polar vortices, *J. Geophys. Res., 105,* 10,047-10,062, 2000.

Popp, P.J., M.J. Northway, J.C. Holecek, R.S. Gao, D.W. Fahey, J.W. Elkins, D.F. Hurst, P.A. Romashkin, G.C. Toon, B. Sen, S.M. Schauffler, R.J. Salawitch, C.R. Webster, R.L. Herman, H. Jost, T.P. Bui, P.A. Newman, and L.R. Lait, Severe and extensive denitrification in the 1999-2000 Arctic winter stratosphere, *Geophys. Res. Lett., 28,* 2875-2878, 2001.

Prinn, R.G., R. Zander, D.M. Cunnold, J.W. Elkins, A. Engel, P.J. Fraser, M.R. Gunson, M.K.W. Ko, E. Mahieu, P.M. Midgley, J.M. Russell III, C.M. Volk, and R.F. Weiss, Long-lived ozone-related compounds, in *Scientific Measurement of Ozone Depletion: 1998, Global Ozone Res. and Monit. Proj. Rep. 44,* pp. 1.1-1.54, World Meteorol. Org., Geneva, 1999.

Prinn, R.G., J. Huang, R.F. Weiss, D.M. Cunnold, P.J. Fraser, P.G. Simmonds, A. McCulloch, C. Harth, P. Salameh, S. O'Doherty, R.H.J. Wang, L. Porter, and B.R. Miller, Evidence for substantial variations of atmospheric hydroxyl radicals in the past two decades, *Science, 292,* 1882-1888, 2001.

Proffitt, M.H., and R.C. McLaughlin, Fast-response dual-beam UV-absorption ozone photometer suitable for use in stratospheric balloons, *Rev. Sci. Instrum., 54,* 1719-1728, 1983.

Ray, E.A., F.L. Moore, J.W. Elkins, D.F. Hurst, P.A. Romashkin, G.S. Dutton, and D.W. Fahey, Descent and mixing in the northern polar vortex from in situ tracer measurements, *J. Geophys. Res.*, in press, 2002.

Redeker, K.R., N.-Y. Wang, J.C. Low, A. McMillan, S.C. Tyler, and R.J. Cicerone, Emissions of methyl halides and methane from rice paddies, *Science, 290,* 966-969, 2000.

Rex, M., et al., Chemical depletion of Arctic ozone in winter 1999/2000, *J. Geophys. Res.*, in press, 2002.

Rhew, R.C., B.R. Miller, and R.F. Weiss, Natural methyl bromide and methyl chloride emissions from coastal salt marshes, *Nature, 403,* 292-295, 2000.

Rhew, R.C., B.R. Miller, M.K. Vollmer, and R.F. Weiss, Shrubland fluxes of methyl bromide and methyl chloride, *J. Geophys. Res., 106,* 20,875-20,882, 2001.

Richard, E.C., K. Aikin, A. Andrews, B.C. Daube, C. Gerbig, S.C. Wofsy, P.A. Romashkin, D.F. Hurst, J.W. Elkins, E.A. Ray, F.L. Moore, T. Deschler, and G.C. Toon, Severe chemical ozone loss inside the Arctic polar vortex during winter 1999-2000 inferred from in situ airborne measurements, *Geophys. Res. Lett., 28,* 2197-2200, 2001.

Romashkin, P.A., D.F. Hurst, J.W. Elkins, G.S. Dutton, and P.R. Wamsley, Effect of the tropospheric trend on the stratospheric tracer-tracer correlations: Methyl chloroform, *J. Geophys. Res., 104,* 26,643-26,652, 1999.

Romashkin, P.A., D.F. Hurst, J.W. Elkins, G.S. Dutton, D.W. Fahey, R.E. Dunn, F.L. Moore, R.C. Myers, and B.D. Hall, In situ measurements of long-lived trace gases in the lower stratosphere by

gas chromatography, *J. Atmos. Oceanic Technol., 18,* 1195-1204, 2001.

Salawitch, R.J., J.J. Margitan, B. Sen, G.C. Toon, G.B. Osterman, M. Rex, J.W. Elkins, E.A. Ray, F.L. Moore, D.F. Hurst, P.A. Romashkin, R.M. Bevilacqua, K. Hoppel, E.C. Richard, and T.P. Bui, Chemical loss of ozone during the Arctic winter of 1999-2000: An analysis based on balloon-borne observations, *J. Geophys. Res.*, in press, 2002.

Schauffler, S.M., E.L. Atlas, D.R. Blake, F. Flocke, R.A. Lueb, J.M. Lee-Taylor, V. Stroud, and W. Travnicek, Distributions of brominated organic compounds in the troposphere and lower stratosphere, *J. Geophys. Res., 104,* 21,513-21,535, 1999.

Schauffler, S.M., E.L. Atlas, S.G. Donnelly, A.E. Andrews, S.A. Montzka, J.W. Elkins, D.F. Hurst, P.A. Romashkin, and V. Stroud, Chlorine budget and partitioning during SOLVE, *J. Geophys. Res.*, in press, 2002.

Schnell, R.C., D.B. King, and R.M. Rosson (Eds.), *Climate Monitoring and Diagnostics Laboratory Summary Report No. 25 1998-1999,* 154 pp., NOAA Oceanic and Atmos. Res., Boulder, CO, 2001.

Severinghaus, J.P., A. Grachev, and M. Battle, Thermal fractionation of air in polar firn by seasonal temperature gradients, *Geochem. Geophys. Geosyst., 2,* paper number 2000GC000146 (electronic journal), 2001.

Solomon, S., D. Wuebbles, I. Isaksen, J. Kiehl, M. Lal, P. Simon, and N.-D. Sze, Ozone depletion potentials, global warming potentials, and future chlorine/bromine loading, in *Scientific Assessment of Ozone Depletion: 1994, Global Ozone Res. and Monit. Proj. Rep. 37,* pp. 13.1-13.36, World Meteorol. Org., Geneva, 1995.

Sturges, W.T., D.E. Oram, L.J. Carpenter, S.A. Penkett, and A. Engel, Bromoform as a source of stratospheric bromine, *Geophys. Res. Lett., 27,* 2081-2084, 2000.

Tans, P.P., P.S. Bakwin, L. Bruhwiler, T.J. Conway, E.J. Dlugokencky, D.W. Guenther, D.R. Kitzis, P.M. Lang, K.A. Masarie, J.B. Miller, P.C. Novelli, K.W. Thoning, M. Trudeau, B.H. Vaughn, J.W.C. White, and C. Zhao, Carbon cycle, in *Climate Monitoring and Diagnostics Laboratory Summary Report No. 25 1998-1999,* edited by R.C. Schnell, D.B. King, and R.M. Rosson, pp. 24-46, NOAA Oceanic and Atmos. Res., Boulder, CO, 2001.

UNEP (United Nations Environmental Programme), *Montreal Protocol on Substances that Deplete the Ozone Layer: Final Act,* 15 pp., New York, 1987.

Varner, R.K., P.M. Crill, and R.W. Talbot, An estimate of the uptake of atmospheric methyl bromide by agricultural soils, *Geophys. Res. Lett., 26,* 727-730, 1999.

Volk, C.M., J.W. Elkins, D.W. Fahey, G.S. Dutton, J.M. Gilligan, M. Loewenstein, J.R. Podolske, K.R. Chan, and M.R. Gunson, Evaluation of source gas lifetimes from stratospheric observations, *J. Geophys. Res., 102,* 25,543-25,564, 1997.

Wamsley, P.R., J.W. Elkins, D.W. Fahey, G.S. Dutton, C.M. Volk, R.C. Myers, S.A. Montzka, J.H. Butler, A.D. Clarke, P.J. Fraser, L.P. Steele, M.P. Lucarelli, E.L. Atlas, S.M. Schauffler, D.R. Blake, F.S. Rowland, W.T. Sturges, J.M. Lee, S.A. Penkett, A. Engel, R.M. Stimpfle, K.R. Chan, D.K. Weisenstein, M.K.W. Ko, and R.J. Salawitch, Distribution of halon-1211 in the upper troposphere and lower stratosphere and the 1994 total bromine budget, *J. Geophys. Res., 103,* 1513-1526, 1998.

Woodbridge, E.L., J.W. Elkins, D.W. Fahey, L.E. Heidt, S. Solomon, T.J. Baring, T.M. Gilpin, W.H. Pollock, S.M. Schauffler, E.L. Atlas, M. Loewenstein, J.R. Podolske, C.R. Webster, R.D. May, J.M. Gilligan, S.A. Montzka, K.A. Boering, and R.J. Salawitch, Estimates of total organic and inorganic chlorine in the lower stratosphere from in situ and flask measurements, *J. Geophys. Res., 100,* 3057-3064, 1995.

6. Cooperative Programs

UV Spectroradiometer Monitoring Program: Calculation of Total Column Ozone from Spectra of Global Irradiance Measured at South Pole and Barrow and Comparison with CMDL/Dobson and NASA/TOMS Ozone Data

G. Bernhard, C.R. Booth, and J.C. Ehramjian
Biospherical Instruments Inc., 5340 Riley St., San Diego, California 92110-2621

Introduction

The U.S. National Science Foundation's Office of Polar Programs (NSF/OPP) Ultraviolet Spectroradiometer Monitoring Network was established in 1988 to collect data on the consequences of ozone depletion. The network currently consists of several sites with automated, high-resolution spectroradiometers (Table 1). Three are in Antarctica, including the CMDL site at South Pole Station. Another instrument is deployed at the CMDL facility in Barrow, Alaska. Now in its fourteenth year of operation, the network continues to make measurements of ultraviolet (UV) spectral irradiance and provides a variety of data products to quantify biologically relevant UV exposures. Biospherical Instruments Inc. is responsible for operation and maintenance of the network, and distribution of data to the scientific community.

The network is equipped with Biospherical Instruments Inc. model SUV-100 spectroradiometers. Each instrument contains a double monochromator with holographic gratings and a photomultiplier tube detector. Spectra are sampled automatically every 15 min between 280 and 600 nm with a spectral bandwidth of 1.0 nm full width at half maximum (FWHM). Tungsten-halogen and mercury vapor calibration lamps are used for daily automatic internal calibrations of both responsivity and wavelength registration. All instrument functions, calibration activities, and solar data acquisition are computer controlled. Further details on the spectroradiometers are described by *Booth et al.* [1994, 2000]. Data from the network, network operations reports, and an extensive list of references can be accessed via the website www.biospherical.com.

UV Radiation Climate at SPO and BRW

This report focuses on data from the South Pole Observatory (SPO) and the Barrow Observatory (BRW) CMDL facilities. The SPO site is a unique place for atmospheric studies because of the stable meteorological conditions, negligible aerosol influence, frequent cloudless days, constant and well-defined high surface albedo, and virtually constant solar zenith angle (SZA) during one day. The conditions at BRW are quite different from SPO. Cloud cover is highly variable, and significant changes in surface albedo occur due to the springtime snowmelt and changes in sea ice coverage. Also, Barrow undergoes significant changes in incident irradiance due to Arctic storms.

Figures 1 and 2 contrast the radiation patterns of both sites. Time series of integrated spectral irradiance at local solar noon are depicted for two wavelength bands covering the period 1991-2001. One spectral band (Figure 1) represents spectral irradiance in the visible, integrated between 400 and 600 nm. From Figure 1 it is evident that visible radiation at SPO shows little variation from one day to the next, or between consecutive years. In contrast, irradiances in the 400-600 nm band at BRW are highly variable during fall due to day-to-day changes in cloud cover. Because of the difference in latitude, radiation levels in the visible are usually lower at SPO than at BRW.

Figure 2 shows deoxyribonucleic acid (DNA)-weighted irradiance, which has been calculated from measured solar spectra and the action spectrum for DNA damage suggested by *Setlow* [1974]. DNA-weighted irradiance has a high contribution from wavelengths in the UVB and is therefore

TABLE 1. Installation Sites of the Ultraviolet Spectroradiometer Monitoring Network

Site	Latitude	Longitude	Established	Location
South Pole	90°00'S	-	February 1988	ARO*
McMurdo Station	77°51'S	166°40'E	March 1988	Arrival heights
Palmer Station	64°46'S	64°03'W	May 1988	T-5 building
Ushuaia, Argentina	54°49'S	68°19'W	November 1988	CADIC†
Barrow, Alaska	71°18'N	156°47'W	December 1990	UIC-NARL‡
San Diego, California	32°45'N	117°11'W	October 1992	Biospherical Instruments Inc.

*ARO, Atmospheric Research Observatory; system relocated to this new, joint NSF-CMDL facility in January 1997.

† CADIC, Centro Austral de Investigaciones Cientificas, Argentina.

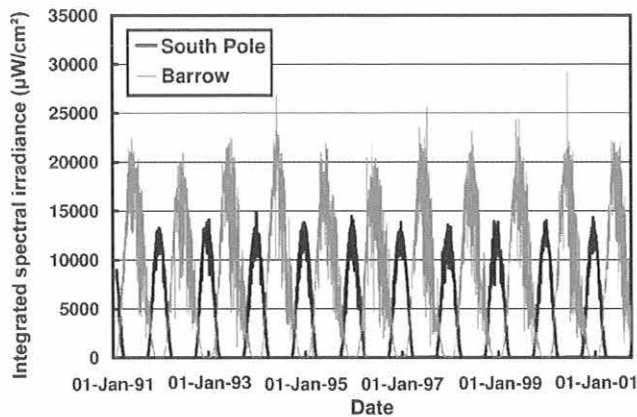‡ UIC-NARL, Ukpeagvik Inupiat Corporation-Naval Arctic Research Laboratory.

Fig. 1. Visible spectral irradiance (400-600 nm integral) at local solar noon at South Pole and Barrow for the period 1991-2001.
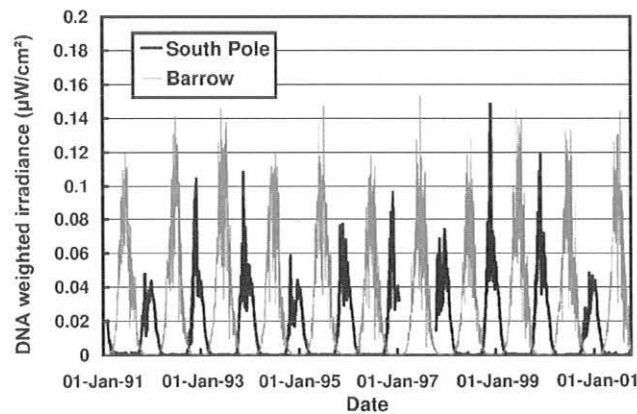

Fig. 2. DNA-weighted irradiance at local solar noon at South Pole and Barrow for the period 1991-2001.

very sensitive to changes in atmospheric ozone concentrations. In contrast to visible radiation, DNA-weighted irradiance at SPO shows high day-to-day fluctuations because of the ozone influence. For example, the peak in DNA-weighted irradiance observed at SPO in late November 1998 is due to extraordinarily low total column ozone values and the comparatively high solar elevations prevailing during this part of the year. UV levels in the austral spring of 2000 were affected by the unusual behavior of the ozone hole of that year, which was exceptionally large until early October 2000 before it exhibited an unprecedented rate of decrease in size and depth. Between mid-October and mid-December 2000, levels of DNA-weighted irradiance at SPO were low compared with typical values from other years.

CALCULATION OF TOTAL COLUMN OZONE FROM SPECTRA OF GLOBAL IRRADIANCE

A new method was developed in 2001 to retrieve total column ozone from measurements of spectral global irradiance of the SUV-100 network instruments. In brief, the method is based on the comparison of measured spectra with results of the radiative transfer model UVSPEC/libRadtran, available at www.libradtran.org. For every measured spectrum, several model runs with different values of the model input parameter "ozone column" are performed. The ozone value retrieved by the method is the model ozone value that gives the best agreement between measurement and model. More details on the algorithm are given by *Bernhard et al.* [2002].

The assessment of the method revealed that its accuracy is affected by the atmospheric ozone profile when SZAs are larger than 75°. This fact is particularly important for SPO and BRW, where large SZAs are prevailing. Ozone values were therefore retrieved both with standard profiles and profiles measured by CMDL with balloon ozonesondes [*Bernhard et al.,* 2002].

COMPARISON OF OZONE VALUES

Values of total column ozone retrieved from the SUV-100 measurements with the algorithm introduced above were compared with Dobson ozone measurements performed by CMDL at SPO and BRW, and with satellite ozone observations by the National Aeronautics and Space Administration (NASA) Earth Probe Total Ozone Mapping Spectrometer (TOMS). Figure 3 shows the ratios of ozone values from the SUV-100 and TOMS to the Dobson values at SPO for the period October-December 2000, referenced to the CMDL Dobson measurements. SUV-100 ozone values were determined with CMDL balloonsonde ozone and temperature profiles in the retrieval algorithm. Figure 3 shows that SUV-100 and Dobson measurements agree to within ±1.5% for SZAs as high as 80°. TOMS observations are generally 5-10% higher than Dobson ozone
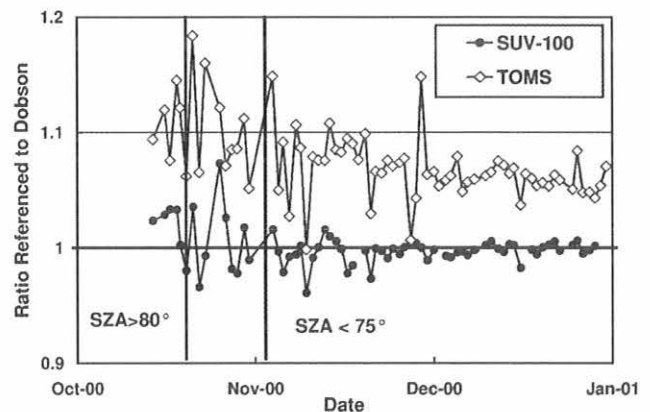

Fig. 3. Comparison of SUV-100 and TOMS total column ozone measurements at South Pole with CMDL Dobson ozone observations during austral spring 2000.

measurements. This deviation of TOMS and ground-based ozone observations at high latitudes of the southern hemisphere has been noticed before [e.g., *Piacentini et al.*, 2000]. Because SUV-100 measurements represent an independent data set, they can be used to validate ozone measurements from other instruments, elucidating the observed discrepancies.

SUV-100 ozone values at BRW were calculated for March-April 2001 during the period of the Total Ozone Measurements by Satellites, Sondes, and Spectrometers at Fairbanks (TOMS[3]F) campaign. Preliminary results show that Dobson observations during April 2001 were on average 2% lower than SUV-100 measurements; TOMS and SUV-100 data agreed to within ±0.5%. Despite the good agreement, uncertainties in the SUV-100 data are larger at BRW than at SPO, because no ozone and temperature profile observations are available from Barrow. Profiles were therefore taken from CMDL balloonsonde flights at Fairbanks. Because Barrow and Fairbanks are separated by more than 6° latitude, the definition of the profile is less accurate than it is for South Pole. As of this writing, the data are still under evaluation. One further objective is to quantify the recently observed drift of TOMS ozone data due to deterioration of the instrument's scan mirror, by comparing different versions of TOMS data with SUV-100 ozone retrievals.

REFERENCES

Bernhard, G., C.R. Booth, and J.C. Ehramjian, Comparison of measured and modeled spectral ultraviolet irradiance at Antarctic stations used to determine biases in total ozone data from various sources, in *Ultraviolet Ground- and Space-Based Measurements, Models, and Effects*, edited by J.R. Slusser, J.R. Hermon, and W. Gao, *Proc. SPIE, 4482*, in press, 2002.

Booth, C.R., T.B. Lucas, J.H. Morrow, C.S. Weiler, and P.A. Penhale, The United States National Science Foundation's polar network for monitoring ultraviolet radiation, in *Ultraviolet Radiation in Antarctica: Measurement and Biological Effects*, edited by C.S. Weiler and P.A. Penhale, *Antarct. Res. Ser., 62*, pp. 17-37, Am. Geophys. Union, Washington, DC, 1994.

Booth, C.R., G. Bernhard, J.C. Ehramjian, L.W. Cabasug, V.V. Quang, and S.A. Lynch, NSF Polar Programs UV Spectroradiometer Network 1999-2000 Operations Report, Biospherical Instruments Inc., San Diego, CA, 2000.

Piacentini, R.D., E. Crino, F. Sirur, and M. Ginzburg, Inter-comparison between TOMS/EP and Southern Cone Ozone Project (SCO3P)/WMO ground based ozone data, poster presented at the 2nd SPARC General Assembly, Mar del Plata, Argentina, (www.aero.jussieu.fr/~sparc/SPARC2000_new/index2.html), Nov. 6-10, 2000.

Setlow, R.B., The wavelength in sunlight effective in producing skin cancer: A theoretical analysis, *Proc. Natl. Acad. Sci. U.S.A., 71*, 3363-3366, 1974.

Size-Resolved Trace Elemental and Organic Aerosols at Mauna Loa Observatory, Spring 2000

Thomas A. Cahill, Steven S. Cliff, Michael Jimenez-Cruz,
Sarah G. Riddle, Peter B. Kelly, and Kevin D. Perry
DELTA Group, University of California, Davis 95616

The size distribution of aerosols is of key importance in their climatic impact. To better establish this parameter, and in anticipation of the large Aerosol Characterization Experiment (ACE)-Asia project of spring 2001, our new 8-stage slotted Davis Rotating-drum Unit for Monitoring (DRUM) sampler was deployed at Mauna Loa Observatory (MLO) to collect aerosols during the Asian transport period each spring. While we had earlier worked with data from simple fine filters (< 2.5-μm diameter, 1989-present) and a 3-stage sampler (spring 1996), the present sampler was designed to map the optically important region below 1 μm with five submicron size classifications: 1.15 to 0.75, 0.75 to 0.56, 0.56 to 0.34, 0.34 to 0.23, and 0.23 to 0.07 μm

aerodynamic diameter. Regretfully, the samples were integrated over 6 weeks because of a failure of the drum rotation system, a problem that was corrected for the studies at MLO in spring and summer 2001. The samples were scanned for elemental content, sodium through uranium, by the new synchrotron-x-ray fluorescence (S-XRF) aerosol and climate microprobe at the Advanced Light Source, Lawrence Berkeley National Laboratory, and for organic matter with the Laser Desorption/Ionization Time-of-Flight Mass Spectrometer (LDI TOFMS) at Davis.

The data for aerosol elements in Figure 1 show that chlorine (and sodium, not shown) as a tracer of sea salt aerosols is essentially absent below 1 μm, while iron (a

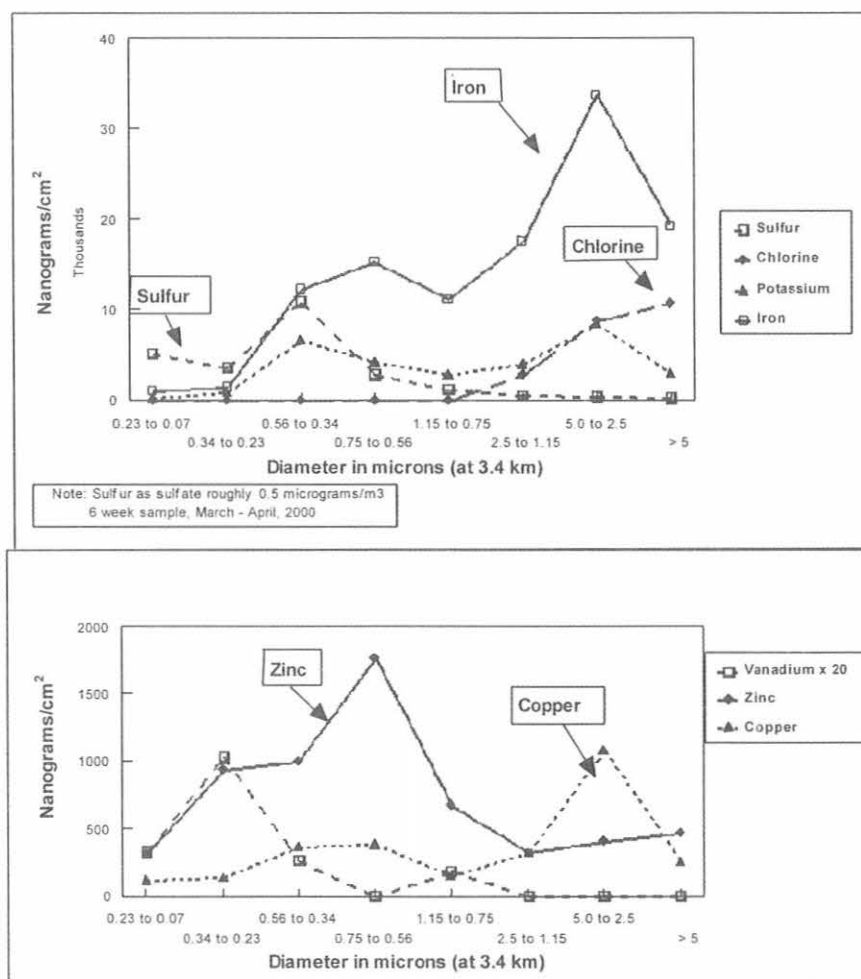Fig. 1. Six-week composite sample of size-resolved aerosols measured at Mauna Loa Observatory, March-April 2000.
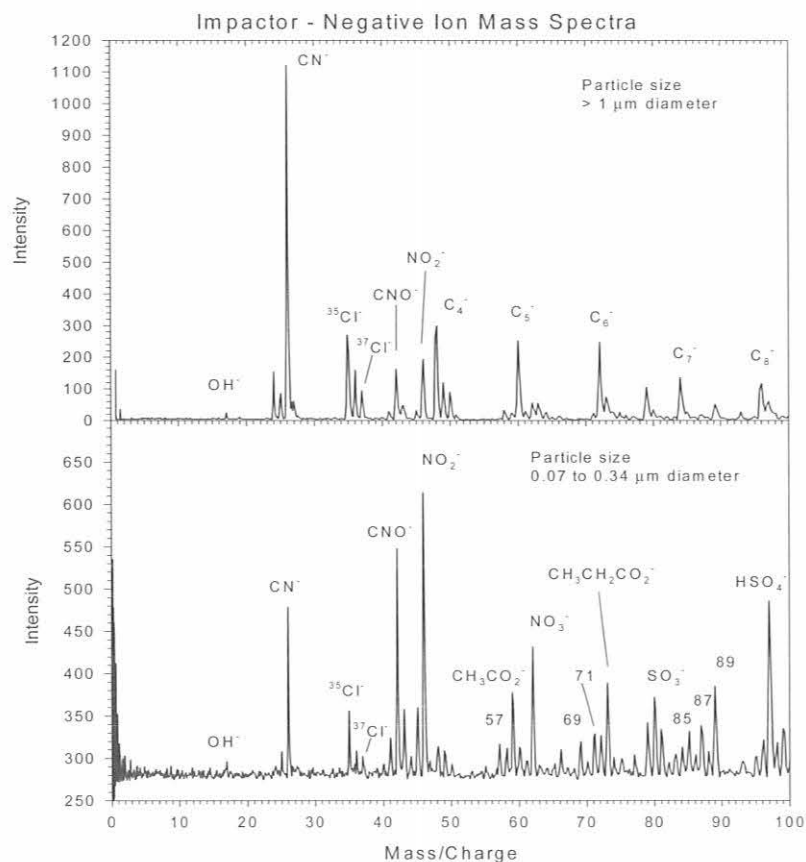
Impactor - Negative Ion Mass Spectra

Fig. 2. Sample mass spectra of organic matter at Mauna Loa Observatory, March-April 2000.

soil tracer) has two separate peaks, one submicron (0.66 ± 0.3 µm) and one supermicron (approximately 4 µm, with the uncertainty associated with the inlet capture). All the soil, which includes fine soil on upslope winds, appears consistent with Asian sources. Except for a small amount of sulfur associated with the sea salt, sulfur was fine, peaking at 0.45 ± 0.3 µm. The very fine/ultrafine sulfur is not the tail of the larger peak, but represents a third mode that we hypothesize is primarily industrial, based on recent data in the United States and Asia. This association is strengthened by the trace element data, which have a complex size profile indicative of diverse sources and processes and an important ultrafine component. The resolution of these hypotheses must await the availability of time-resolved data.

The samples were also analyzed by LDI TOFMS for organic speciation. Some of the results are shown in Figure

2 and exhibit dramatic differences as a function of size. The HSO_4^- peak is not seen in the supermicron fraction, but is prominent in the ultrafine aerosols. Normally, this is associated with a sulfuric acid aerosol. Again, much work needs to be done to understand these complex results.

In summary, a great deal was learned during these tests, both about sampling and analysis in the very clean conditions at MLO and in the complex suite of compositional techniques that can now be employed on such samples. The soils are even finer than estimated in our earlier work, and thus more important per unit mass in terms of optical impact. The organics possess complicated patterns in size and bear little resemblance to existing source profiles such as biomass burning, and diesel and automotive smoke.

Migration Rates and Flight Behavior of Migrating Eiders Near Towers at Barrow, Alaska

ROBERT H. DAY AND JOHN R. ROSE

ABR, Inc., Environmental Research and Services, P.O. Box 80410, Fairbanks, Alaska 99708-0410

BRIAN A. COOPER AND RICHARD J. BLAHA

ABR, Inc., Environmental Research and Services, P.O. Box 249, Forest Grove, Oregon 97116-0249

During spring and fall migration, Common (*Somateria mollissima*) and King (*S. spectabilis*) eiders pass Point Barrow, Alaska, in large numbers [*Thompson and Person,* 1963; *Timson,* 1975; *Day et al.,* 1998; *Suydam et al.,* 1997, 2000]. Spectacled (*S. fischeri*) and Steller's (*Polysticta stelleri*) eiders also pass Point Barrow, although in small numbers. Common and King eider populations are declining dramatically, and populations of these two species are so low that they are protected under the Endangered Species Act. Because populations of all four species are in trouble, conservation of existing populations becomes increasingly important.

We studied movements and behavior of eiders migrating past the Atmospheric Radiation Measurement (ARM) tower at the CMDL Barrow Observatory (BRW) and the GEOCORONA tower at the U.S. Air Force Point Barrow Long Range Radar Site near Barrow, Alaska, under various levels of visibility in August–September 2000. The objectives of this study were to (1) determine flight tracklines of eiders migrating in the vicinity of the ARM tower (primary interest) and the GEOCORONA tower (secondary interest); (2) measure movement rates, behavior, and flight altitudes of migrating eiders in this area; (3) determine whether any of these attributes varied by visibility category, especially near these towers; and (4) assess the probability of collision of migrating eiders with these towers. Both ornithological radar and visual methods were used for sampling.

During radar sampling, 13,434 eiders were recorded in 133 identified radar echoes. Another 442 "eiderlike" radar targets that were unidentified to species, possibly representing an additional ~45,000 eiders, based on mean flock size, were recorded. During visual sampling, 19,023 eiders (6,090 of them not detected by radar) were recorded in 187 flocks (56 of them not detected by radar). Hence, data were collected on at least 19,524 eiders (not counting possibly ~45,000 eiders represented by unidentified eiderlike radar targets) over the 21 days of sampling.

Mean daily movement rates of "eiders" (i.e., unidentified eiders + unidentified ducks + unidentified waterfowl + unidentified targets that were eiderlike in flight characteristics) on radar ranged between 0 and 12.8 radar targets per hour. "Eiders" were recorded migrating on all days except one, indicating pulsed, but fairly continuous, migration during this period.

Mean movement rates of "eiders" were significantly higher during the night than during the day, during nights without precipitation, and during nights with good visibility. Frequent tailwinds at night may have increased nocturnal

movement rates; however, all of the increase could not be explained by wind direction, suggesting that movement rates actually are higher at night.

"Eiders" passed the ARM tower at a significantly greater distance from the tower during the day than at night and at a greater distance during daytime without precipitation than during all other light conditions. Visibility did not affect the distance at which they passed the tower.

"Eiders" exhibited little variation in flightlines by time of day, light condition, or session visibility. Essentially all movement was to the north of the site, around or over Brant Point, and, eventually, over Duck Camp and/or North Salt Lagoon. Only 14 (2.4%) of 590 "eider" radar targets passed south of the ARM tower, and only 9 (1.5%) passed ≤500 m from this tower, indicating that a very low percentage of all birds crossed inland near this tower.

Straight-line flight was, by far, the dominant flight behavior, occurring >99% of the time on radar and >95% of the time during visual sampling. Frequencies of straight-line flight and non-straight-line flight did not differ significantly by time of day, light condition, or session visibility. "Eider" echoes occurring ≤500 m from the tower exhibited only straight-line flight, regardless of visibility category.

During visual sampling, "eiders" exhibited substantial variation in minimal flight altitude, ranging from 0 m above ground level (agl; i.e., landing) to 70 m agl, with the overall mean flight altitude being ~12 m agl. "Eiders" observed on radar and visually exhibited no discernible response to the tower as they passed the ARM tower, regardless of visibility category and distance from this tower. The overall distance from this tower at which birds passed was large, however, in that only 5 (2.7%) of 186 flocks seen visually passed ≤500 m from the tower.

"Eider" movements discussed here were similar to those seen previously near Barrow, although the amount of nocturnal migration was not previously known to be this large. Several observed aspects of the flight behavior of "eiders" suggest that, although these birds are extremely vulnerable to collisions with human-made objects, the preferred route of movement by migrating "eiders" in this area is over the base of Barrow Spit, near Duck Camp, with few flying inland near the towers. That "eiders" flew significantly farther from the tower during the daytime than they did at night, mostly passing around Brant Point, suggests that these birds are strongly relying on visual cues to orient themselves and fly around Brant Point, rather than that they are avoiding the ARM tower.

We conclude that the probability of collision of migrating "eiders" with the existing structures at Barrow is low. However, it is recommend that (1) no new tall structures (such as towers) be built closer to the coast than these existing structures already are, and (2) any tall structures (such as towers) that are built in this area should be visible to "eiders" at a distance to give them a greater distance in which to react and avoid collisions.

REFERENCES

Day, R.H., J.R. Rose, and B.A. Cooper, Evaluation of ornithological radar for monitoring eider migration at Point Barrow, Alaska, unpublished report prepared for U.S. Fish and Wildlife Service, Fairbanks, AK, and North Slope Borough, Barrow, AK, 42 pp., ABR, Inc., Fairbanks, AK, and Forest Grove, OR, 1998.

Suydam, R., L. Quakenbush, M. Johnson, J.C. George, and J. Young, Migration of King and Common eiders past Point Barrow, Alaska, in spring 1987, spring 1994, and fall 1994, in *King and Common Eiders of the Western Canadian Arctic*, edited by D.L. Dickson, *Occasional Paper No. 94*, pp. 21-28, Canadian Wildlife Service, Ottawa, 1997.

Suydam, R.S., D.L. Dickson, J.B. Fadely, and L.T. Quakenbush, Population declines of King and Common eiders of the Beaufort Sea, *Condor, 102*, 219–222, 2000.

Thompson, D.Q., and R.A. Person, The eider pass at Point Barrow, Alaska, *J. Wildlife Manage., 27*, 348–356, 1963.

Timson, R.S, Late summer migration at Barrow, Alaska, unpublished report, 25 pp., U.S. Fish and Wildlife Service, Anchorage, AK, 1975.

Occurrence Probability of Pc1 Micro Pulsations Observed at Barrow During the Solar Quiet Period

KANJI HAYASHI

Department of Earth and Planetary Science, The University of Tokyo, Bunkyo, Tokyo, Japan 133-0033

Observation of short-period magnetic pulsations at the CMDL Barrow Observatory (BRW) continued uninterrupted since 1995 using an induction magnetometer with a digital data logger. All the acquired daily data produced at a 5.2-mb rate at Barrow has been compiled into an archive of the Solar-Terrestrial Energy Program (STEP) Polar Network. Quick-look plots of Fourier dynamic spectra including 9 days on a page have been produced and are publicly accessible at http://hpep3.eps.s.u-tokyo.ac.jp. We show in the data set synoptic characteristics of Pc1-type magnetic pulsations deduced from features of the dynamic spectra during the solar quiet period of 1995-1997.

Pc1-type spectra were searched on every spectral chart, and their occurrence was examined in bins of 0.1-0.5 Hz, 0.5-1.0 Hz and above 1.0 Hz for every 2 hours of universal time (UT). Table 1 shows occurrence probabilities of Pc1 pulsations involved in the bins of the three frequency bands for every 2 hours. Statistics were developed on four ensembles: the whole period, the equinox seasons, the summer seasons, and the winter seasons. Occurrence probability in the low-frequency band is found to be high around local Barrow noon (UT − 12 hours, approximately) to afternoon and is highest in the summer season. Small enhancements of Pc1 occurrence in high and middle frequency bands are found from midnight to early morning both in winter and equinox seasons, but are suppressed in summer seasons. Taking into account the geomagnetic latitude (69.9°) of Barrow and past reports of similar observations, the above results can be considered reasonable. It will be interesting to see how the previously noted tendencies will be modified by the recent solar active period. These effects will be determined as the final data become available. These results will also be derived from simultaneous data from identical instruments operated at more than 20 locations at various latitudes. Toward this end, a special algorithm to pick up Pc1 events automatically is being developed because such an algorithm is essential to the efficient processing of such a large amount of data and to produce frequency statistics efficiently.

TABLE 1. Time Dependency of Occurrence Probabilities of Pc1 Micro Pulsations During the Solar Quiet Period, 1995-1997, Observed at Barrow, Alaska.

Time (UT)	Occurrence Probability					
	0.1-0.5 Hz	0.5-1.0 Hz	1.0-2.0 Hz	0.1-0.5 Hz	0.5-1.0 Hz	1.0-2.0 Hz
	Whole period (809 days)			*Equinox seasons (358 days)*		
0-2	41.53	25.59	1.61	48.32	31.01	1.40
2-4	35.97	10.51	1.24	39.66	13.13	1.12
4-6	9.02	2.22	0.49	10.89	3.07	0.56
6-8	1.48	1.73	0.37	2.23	2.51	0.56
8-10	0.25	1.85	0.62	0.28	2.51	0.56
10-12	0.12	2.72	0.87	0.28	3.35	1.68
12-14	0.00	4.45	1.36	0.00	4.75	1.96
14-16	0.74	6.67	2.10	0.56	6.98	3.07
16-18	3.09	7.29	1.98	3.35	7.54	2.51
18-20	5.32	6.92	1.61	4.75	6.70	1.68
20-22	11.99	7.91	1.36	11.73	10.34	1.68
22-24	21.14	14.71	0.87	22.07	16.48	1.68
	Summer seasons (197 days)			*Winter seasons (254 days)*		
0-2	56.85	22.34	2.03	22.83	22.05	1.57
2-4	59.90	7.61	0.51	14.96	9.45	1.97
4-6	19.80	2.03	1.02	1.18	1.18	0.00
6-8	3.05	2.03	0.51	0.00	0.39	0.00
8-10	0.51	3.05	1.52	0.00	0.00	0.00
10-12	0.00	3.55	0.51	0.00	1.18	0.00
12-14	0.00	2.54	0.51	0.00	5.51	1.18
14-16	1.52	2.54	1.52	0.39	9.45	1.18
16-18	4.57	2.03	1.02	1.57	11.02	1.97
18-20	7.11	3.55	0.51	5.12	10.24	2.36
20-22	16.75	6.60	1.02	9.45	5.91	1.18
22-24	29.44	13.20	1.02	14.17	13.78	0.39

NIWA's NDSC UV/Visible Measurements at the Mauna Loa Observatory

P.V. JOHNSTON

National Institute of Water and Atmospheric Research, Lauder, New Zealand 9182

The National Institute of Water and Atmospheric Research (NIWA) started Network for the Detection of Stratospheric Change (NDSC)-certified ultraviolet (UV)/ visible spectroscopic measurements of stratospheric nitrogen dioxide (NO_2) in July 1996 at the CMDL Mauna Loa Observatory (MLO). In December 1999 a new UV/visible spectrometer was installed to measure stratospheric bromine monoxide (BrO), an important species, in current attempts to model future nonpolar ozone trends. In addition to this instrument, a second NO_2- measuring spectrometer was installed in the NDSC building. The BrO instrument makes what is expected to be defined as NDSC standard measurements; however, full certification cannot be completed until a community BrO instrument intercomparison is undertaken. This is planned for March 2003.

Measurements of NO_2 and BrO have been successfully made on most days over the reported period. Although one of the two NO_2 instruments failed in December 2000 and could not be repaired until August 2001, the backup NO_2 spectrometer maintained data continuity. The data were presented at the 2001 NDSC Symposium [*Kreher et al.*, 2001].

NO_2 data measured at MLO in the NDSC database have been archived to the end of 2000.

REFERENCE

Kreher, K., P.V. Johnston, G.E. Bodeker, J.A. Burrowes, J.B. Liley, and M.P. Chipperfield, Time series of NO_2 data at low, middle and high latitudes: Observations and comparison with model results, paper presented at Network for the Detection of Stratospheric Change (NDSC) 2001 Symposium "Celebrating 10 Years of Atmospheric Research," NDSC, Palais des Congrès "Le Palatium," Arcachon, France, September 24-27, 2001.

Quasi-Biennial Oscillation Signatures in Ozone and Temperature Profiles Measured by the JPL Lidar at Mauna Loa

T. LeBlanc and I.S. McDermid

Table Mountain Facility, Jet Propulsion Laboratory, California Institute of Technology, Wrightwood, California 92397

INTRODUCTION

The stratospheric quasi-biennial oscillation (QBO) is most easily identified as an alternation of descending westerly and easterly wind regimes in the equatorial lower stratosphere [e.g., *Reed et al.*, 1961] with a period varying from 22 to 34 months. To attempt to elucidate the exact mechanisms of the equatorial and extratropical QBO, and because the QBO has a major impact on the interannual variability of the stratosphere and in turn on major issues such as ozone depletion and climate change, it is critical to maintain low-, mid-, and high-latitude continuous long-term measurements of the key atmospheric parameters. As part of the Network for the Detection of Stratospheric Change (NDSC), a Jet Propulsion Laboratory (JPL) lidar has been taking long-term measurements of middle atmospheric temperature and ozone at Mauna Loa Observatory, Hawaii (MLO, 19.5°N, 155.5°W), since 1993 [*McDermid et al.*, 1995]. The first simultaneous observations of the vertical structure (20-50 km) of the temperature and ozone QBO at a subtropical station are presented here.

LIDAR DATA SET

The data presented here extend from June 1, 1994, to September 30, 2000. The corresponding ~800 individual ozone and temperature profiles were computed into monthly means between June 1994 and September 2000. Then the climatological means were calculated for the period October 1994-September 2000 for each month of the year, thus covering three full QBO cycles. These climatological monthly means were subtracted from the individual monthly means to obtain what is hereafter called the "deseasonalized" ozone and temperature profiles. The seasonal (mainly annual and semiannual) components were removed, leaving the possible signatures of the QBO, solar cycle, long-term trend, and any other interannual variations. Because of the relatively short measurement period, no attempt was made to isolate each of these interannual components.

QBO WINDS

A comparison of the NOAA/National Weather Service (NWS)-Hilo monthly mean zonal winds near 30-km altitude with the near-equatorial monthly mean zonal winds at 10 hPa (~30-31 km) shows a clear in-phase correlation, indicating that Hawaii is under the influence of the equatorial QBO winds. The 2D time-height section of the zonal winds at Hilo is shown in Figure 1 (bottom panel). In this panel the altitude range extends from 15 to 35 km, but the scale of the vertical axis has been chosen to match that of the ozone and temperature plots displayed above it. The contours range

from –10 (violet) to +10 m s^{-1} (red) with a 1 m s^{-1} interval. The QBO structure is well identified and is therefore used as the QBO wind reference to investigate the phases of the temperature and ozone QBO signatures in the next sections.

QBO SIGNATURES IN THE TEMPERATURE PROFILES

The 2D time-height section of the deseasonalized stratospheric temperatures is shown in Figure 1 (top panel). No QBO signature was identified above 60 km. The contours range from –3 (violet) to +3% (red) with a 0.5% interval. The most striking feature observed here is a clear seasonally synchronized QBO anomaly near 35-36 km in winter with an amplitude exceeding 3% (6-7 K). The warm phase coincides with the maximum westerlies at 30 km, i.e., with an expected easterly shear above 30 km. The cold phase coincides with the maximum easterlies at 30 km, i.e., with an expected westerly shear above 30 km.

QBO SIGNATURES IN THE OZONE PROFILES

The center panel of Figure 1 shows the 2D time-height section of the deseasonalized ozone profiles. The plot is divided into two parts. The lower part (between 20 and 30 km) shows the deseasonalized ozone number density (in %), with contours ranging from –12 (violet) to +12% (red) with a 2% interval. The upper part (above 30 km) shows the deseasonalized ozone mixing ratio, with contours ranging from –0.5 (violet) to +0.5 ppmv (red) with a 0.1 ppmv interval. Although the lidar measures ozone number density, the mixing ratio is preferred for display above 30 km to avoid excessive percentage values in the upper regions where the ozone number density is very low. No ozone number density contour is displayed below 20 km because of the large relative variability in the lower stratosphere (±100%). Note that since relative quantities are considered, the contours of the ozone mixing ratios and number densities above and below 30 km should, and do, exhibit very consistent structures. As was the case for temperature, a strong seasonally synchronized QBO signature can be observed in winter-spring with an amplitude exceeding 0.5 ppmv (10%) near 31 km.

DISCUSSION

This first investigation of simultaneous temperature and ozone QBO signatures at Mauna Loa, Hawaii, has revealed a remarkably consistent pattern, typical of the expected extratropical asymmetrical effect of the stratospheric QBO. Although less organized and weaker (10-15 m s^{-1}), the observed QBO winds from NOAA/NWS in Hilo, Hawaii, are in phase with the equatorial QBO winds. The temperature and ozone results obtained by the JPL ozone lidar show a clear
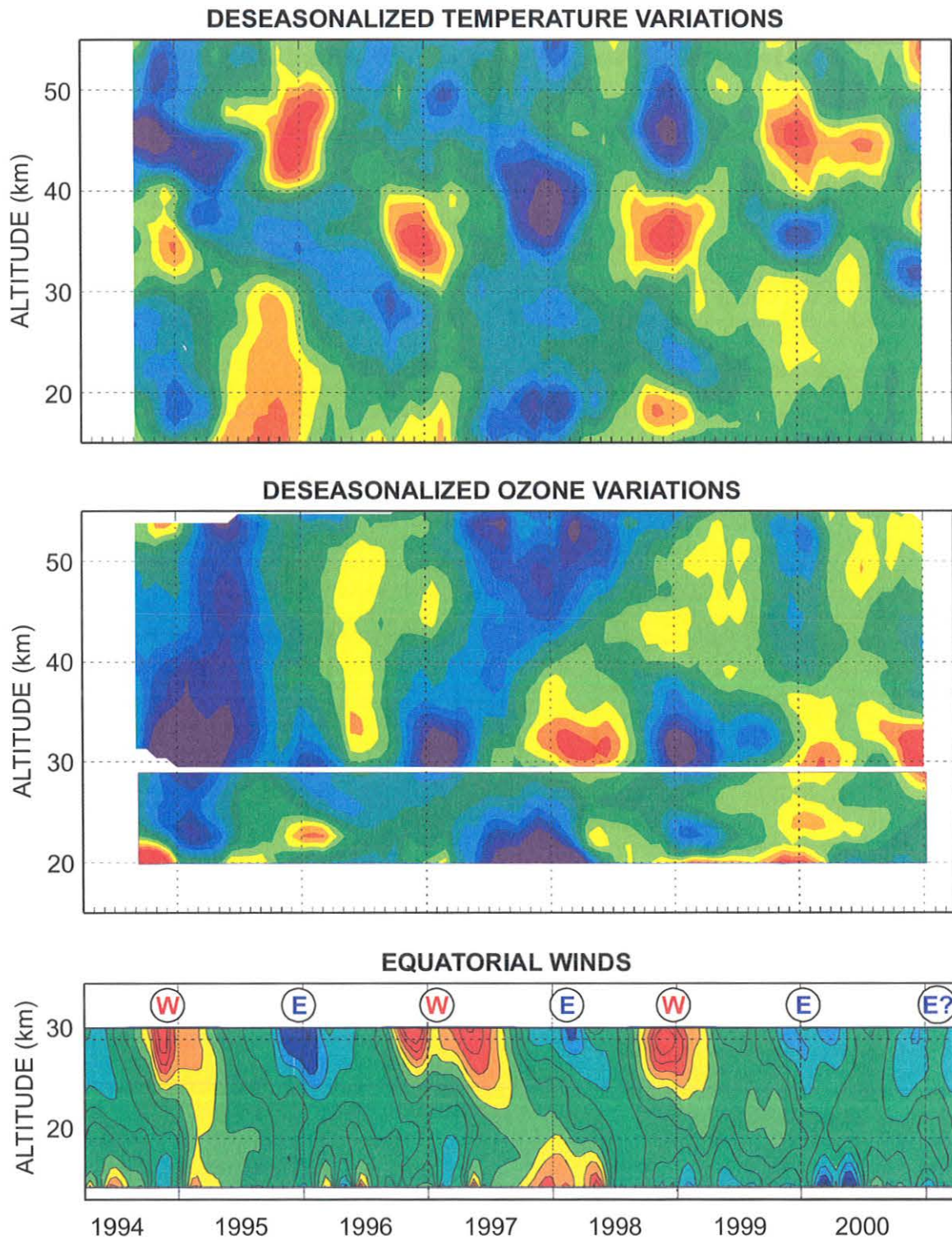
Fig. 1. Two-dimensional time-height sections of the deseasonalized temperature (top), ozone (center), and winds (bottom). Top: The temperature contours range from –3 (violet) to +3% (red) with a 0.5% interval. Center: For ozone, the lower part (between 20 and 30 km) shows the ozone number density (in %), with contours ranging from –12 (violet) to +12% (red) with a 2% interval; the upper part (above 30 km) shows the ozone mixing ratio with contours ranging from –0.5 (violet) to +0.5 ppmv (red) with a 0.1 ppmv interval. Bottom: For the monthly mean winds at Hilo, Hawaii, contours range from –10 (violet) to +10 m s⁻¹ (red) with a 1 m s⁻¹ interval.

146

QBO signature at several altitudes and times of year, highly consistent with previous observations [e.g., *Randel and Wu*, 1996] and with the mechanisms suggested by modelers.

Both the prevalent temperature and ozone QBO anomalies are seasonally synchronized (northern hemisphere winter) and out of phase with the expected equatorial anomalies, indicating that Hawaii is located in the subtropical branch of the asymmetrical QBO-induced meridional circulation. The QBO-related temperature perturbations observed at Hawaii are clearly out of phase with those expected from thermal-wind balance at the equator, i.e., positive (hot) at 47 and 24 km, and negative (cold) at 35 km for easterly winds maximizing at 30 km. The QBO-related ozone perturbations appear to match remarkably well with those observed, for example, by the Stratospheric Aerosol and Gas Experiment (SAGE II) [*Randel and Cobb*, 1994; *Randel and Wu*, 1996], and simulated by *Jones et al.* [1998]: positive slightly above and below the altitude of easterlies (31 and 23 km, respectively, for easterlies maximizing just below 30 km) and a negative perturbation well above (>45 km). A weak signal has also been observed at 24 km in summer that appears to match the model results of *Jones et al.* [1998], but this signal is not consistent enough from year to year to be certain of its actual existence.

These results suggest that the mechanisms for production of the ozone QBO are more complex than that for temperature. Above the ozone concentration peak, the ozone QBO is both chemically and dynamically produced through the combined effect of the QBO nonlinear horizontal and vertical advection of NO_y, and the horizontal advection of ozone. Below the ozone concentration peak, the ozone QBO is dynamically produced by nonlinear advection of ozone out of and into the neighboring latitudes. For temperature, the thermal wind balance causes the QBO signature in the subtropics to be out of phase with that at the equator. The warm phase in Hawaii coincides with the maximum easterly shear at the equator. The cold phase in Hawaii coincides with the maximum westerly shear at the equator.

A strong El Niño event in 1997-1998 considerably disturbed the QBO signature in both ozone and temperature. Its main effect was to reduce the lower stratospheric ozone amount, and to cool down the lower stratosphere up to 25-27 km. Both El Niño/Southern Oscillation (ENSO) signatures in ozone and temperature are consistent with previous observations [*Shiotani*, 1992; *Randel and Cobb*, 1994; *Randel et al.*, 2000]. Despite this disruptive event, and even though the ozone/temperature lidar data set covers only three full QBO cycles, the results presented here have shown several significant QBO signatures and remain promising for a more detailed investigation of the temperature and ozone interannual variability at this latitude.

REFERENCES

Jones, D.B.A., H.R. Schneider, and M.B. McElroy, Effects of the quasi-biennial oscillation on the zonally averaged transport of tracers, *J. Geophys. Res.*, *103*, 11,235-11,249, 1998.

McDermid, I.S., T.D. Walsh, A. Deslis, and M. White, Optical systems design for a stratospheric lidar system, *Appl. Opt.*, *34*, 6201-6210, 1995.

Randel, W.J., and J.B. Cobb, Coherent variations of monthly mean total ozone and lower stratosphere temperatures, *J. Geophys. Res.*, *99*, 5433-5474, 1994.

Randel, W.J., and F. Wu, Isolation of the ozone QBO in SAGE II data by singular-value decomposition, *J. Atmos. Sci.*, *53*, 2546-2559, 1996.

Randel, W.J., F. Wu, and D.J. Gaffen, Interannual variability of the tropical tropopause derived from radiosonde data and NCEP reanalyses, *J. Geophys. Res.*, *105*, 15,509-15,523, 2000.

Reed, R.J., W.J. Campbell, L.A. Rasmussen, and R.G. Rogers, Evidence of a downward propagating annual wind reversal in the equatorial stratosphere, *J. Geophys. Res.*, *66*, 813-818, 1961.

Shiotani, M., Annual, quasi-biennial, and El Niño-Southern Oscillation (ENSO) time-scale variations in equatorial total ozone, *J. Geophys. Res.*, *97*, 7625-7633, 1992.

Investigation of Chemical Transfer Processes between Atmosphere and Snow at South Pole

JOSEPH R. MCCONNELL

Division of Hydrologic Sciences, Desert Research Institute, Reno, Nevada 89512

ROGER C. BALES

Department of Hydrology and Water Resources, University of Arizona, Tucson 85721

Oxidation by OH is the primary atmospheric sink for many environmentally important gases, including methane (CH_4), carbon monoxide (CO), and halogenated hydrocarbons. Because of its very short lifetime, OH is not preserved in snow and ice. Hydrogen peroxide (H_2O_2) is a sink for OH, and, because it is preserved in snow and ice, concentrations of H_2O_2 preserved in ice sheets offer the potential to reconstruct past atmospheric concentrations of H_2O_2 and, hence, OH. However, to make use of the chemical archive, a quantitative understanding of the processes that control atmosphere-to-snow transfer and preservation of H_2O_2 in polar environments is required. Through a cooperative agreement with CMDL at South Pole, we have been making year-round measurements of H_2O_2 concentration in the surface and near-surface snow since November 1994. These year-round measurements in the surface snow complement more intensive, summertime measurements in the atmosphere and in snow pits and shallow cores. The summer sampling and all sample analyses at South Pole are conducted under NSF-funded grants.

Results of the nearly continuous, year-round surface-snow sampling (November 1994 through January 2001) are shown in Figure 1. Replicate samples are collected at each sampling period and error bars show the variability (1 σ) of the H_2O_2 concentration between replicates. There is a distinct annual cycle in H_2O_2 concentration in the surface

snow that results from a combination of very strong changes in atmospheric concentration of H_2O_2 throughout the year [*Stewart and McConnell*, 1999], a strong annual temperature cycle at South Pole, and a highly nonlinear partitioning of the H_2O_2 between air and snow as a function of temperature [*Conklin et al.*, 1993; *McConnell et al.*, 1997]. Because deposition of H_2O_2 is reversible, preservation is strongly dependent on depositional parameters such as temperature and snow accumulation rate and timing [*McConnell*, 1997; *McConnell et al.*, 1998, *Hutterli et al.*, 2001]. By reversible we mean that some fraction of the deposited mass cycles between the snow and air until the snow is cut off from the atmosphere by burial. The net result is that while we have measured a strong decrease in H_2O_2 concentration in firn cores from South Pole representing snow deposited over the past ~30 years, much of the observed decrease is likely the result of a slow release of H_2O_2 from supersaturated layers near the surface. The decrease with depth is pronounced at South Pole because the relatively cold temperatures slow diffusion-controlled release of H_2O_2 from the snow pack and because the low snow accumulation rates allow exchange with the atmosphere for many years after the snow is deposited.

Formaldehyde (HCHO) concentrations also provide information on the atmospheric oxidation capacity, and HCHO studies in the air and snow at South Pole are integral to our overall research effort. Results of recent snow pit and shallow core studies at South Pole, in agreement with similar studies in Greenland and other Antarctic locations, show that HCHO deposition is also reversible and that exchange with the atmosphere is much greater than for H_2O_2 (M. Hutterli et al., HCHO in Antarctic snow: Preservation in ice cores and air-snow exchange, submitted to *Geophysical Research Letters*, 2002). HCHO concentrations in snow samples are time-sensitive, thereby precluding year-round surface snow sampling by onsite CMDL personnel.

Year-round surface snow studies at South Pole have recently been expanded to include sampling for trifluoroacetate (TFA). TFA is the primary atmospheric degradation product of the CFC replacement HFC-134a, and there is concern about the environmental consequences of a build up of this strongly hydrophilic compound in natural waters. South Pole is a particularly appropriate location to carry out such sampling because atmospheric measurements of the primary precursor, HFC-134a, and other related compounds have been made by CMDL since ~1994 [*Montzka et al.*, 1996]. Moreover, measurements of HFC-134a in the firn air at South Pole have recently been reported [*Butler et al.*, 1999]. As with the H_2O_2 studies, the

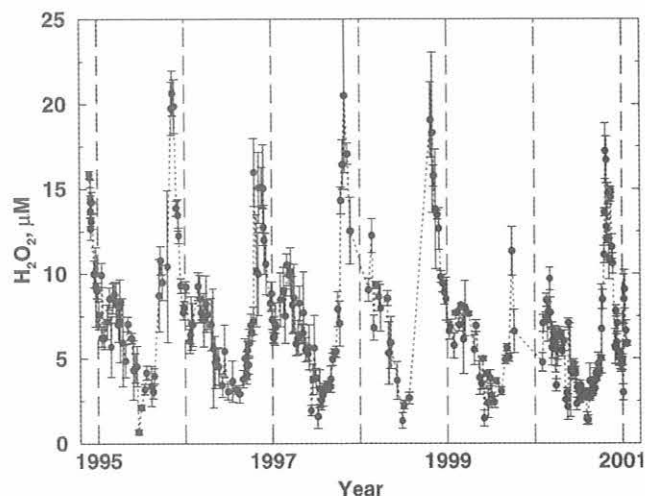Fig. 1. Hydrogen peroxide in surface snow at South Pole. Error bars show 1 standard deviation in replicate measurements.

year-round sampling by onsite CMDL personnel complements more intensive summer snow pit sampling conducted under NSF funding. The TFA project has only started recently; therefore, no results are available at this time.

The year-round South Pole data, made possible through the cooperative agreement with CMDL, are also important for the interpretation of similar H_2O_2, HCHO, and TFA data from snow pits and shallow cores collected in summertime in West Antarctica as part of the International Trans-Antarctic Scientific Expedition (ITASE) [Frey et al., 2001].

REFERENCES

Butler, J.H., M. Battle, M.L. Bender, S.A. Montzka, A.D. Clarke, E.S. Saltzman, C.M. Sucher, J.P. Severinghaus, and J.W. Elkins, A record of atmospheric halocarbons during the twentieth century from polar firn air, Nature, 399, 749-755, 1999.

Conklin, M.H., A. Sigg, A. Neftel, and R.C. Bales, Atmosphere-snow transfer function for H_2O_2: Microphysical considerations, J. Geophys. Res., 98, 18,367-18,376, 1993.

Frey, M., J. McConnell, R. Bales, and M. Hutterli, Peroxides and formaldehyde in West Antarctica: Atmospheric and snow chemistry measurements along the ITASE traverse, Eos Trans. AGU, 82, S234, 2001.

Hutterli, M.A., J.R. McConnell, R.W. Stewart, H.-W. Jacobi, and R.C. Bales, Impact of temperature-driven cycling of hydrogen peroxide (H_2O_2) between air and snow on the planetary boundary layer, J. Geophys. Res., 106, 15,395-15,404, 2001.

McConnell, J.R., Investigation of the atmosphere-snow transfer process for hydrogen peroxide, Ph.D. dissertation, Department of Hydrology and Water Resources, University of Arizona, 1997.

McConnell, J.R., J.R. Winterle, R.C. Bales, A.M. Thompson, and R.W. Stewart, Physically based inversion of surface snow concentrations of hydrogen peroxide to atmospheric concentrations at South Pole, Geophys. Res. Lett., 24, 441-444, 1997.

McConnell, J.R., R.C. Bales, R.W. Stewart, A.M. Thompson, M.R. Albert, and R. Ramos, Physically based modeling of atmosphere-to-snow-to-firn transfer of hydrogen peroxide at South Pole, J. Geophys. Res., 103, 10,561-10,570, 1998.

Montzka, S.A., J.H. Butler, R.C. Myers, T.M. Thompson, T.H. Swanson, A.D. Clarke, L.T. Lock, and J.W. Elkins, Decline in the tropospheric abundance of halogen from halocarbons: Implications for stratospheric ozone depletion, Science, 272, 1318-1322, 1996.

Stewart, R., and J. McConnell, Antarctic photochemistry: Uncertainty analysis, Eos Trans. AGU, 80, F197-F198, 1999.

Microwave Measurements of Middle Atmospheric Water Vapor From Mauna Loa, 1996-2001

Gerald E. Nedoluha, Richard M. Bevilacqua, R. Michael Gomez, and Brian C. Hicks

Naval Research Laboratory, Code 7227, Washington, D.C. 20375-5320

James M. Russell III

Hampton University, Hampton, Virginia 23668

Introduction

The Naval Research Laboratory Water Vapor Millimeter-wave Spectrometer (WVMS) system has been making nearly continuous middle-atmospheric water vapor profile measurements at Mauna Loa, Hawaii (19.5°N, 204.4°E), since March 1996. The measurements are made at 22 GHz, an emission line that is sufficiently optically thin to allow ground-based measurements of the middle atmosphere through the troposphere. The Mauna Loa site is ideal for these measurements both because of its high altitude, which minimizes the tropospheric signal, and because of its relatively low latitude, which minimizes the seasonal variations in the middle atmosphere and thus simplifies the monitoring of long-term changes in middle-atmospheric water vapor.

Measurements of water vapor provide important information on several processes in the middle atmosphere. Water vapor is an ideal transport tracer and has been used in numerous studies of atmospheric transport in the middle atmosphere [e.g., *Bevilacqua et al., 1990; Nedoluha et al., 1996; Summers et al., 1997*]. Water vapor is also the reservoir of odd hydrogen in the middle atmosphere, and, although the studies of short-term variations in Halogen Occultation Experiment (HALOE) data (D.E. Siskind et al., A search for an anticorrelation between H_2O and O_3 in the lower mesosphere, submitted to *Journal of Geophysical Research*, 2002) suggest that the effect of water vapor on ozone is not yet well described by standard photochemical models, it is important to ozone chemistry. Changes in middle-atmospheric water vapor may also impact stratospheric temperatures and thus indirectly affect ozone depletion [*Kirk-Davidoff et al., 1999*].

WVMS Measurements

The WVMS3 instrument at Mauna Loa is the third such instrument to be deployed. It is essentially identical to the WVMS2 instrument that operated at the Network for the Detection of Stratospheric Change (NDSC) site at Table Mountain, California (34.4°N, 242.3°E), from August 1993 to November 1997. These instruments are both very similar to the WVMS1 instrument that is taking measurements at the NDSC site at Lauder, New Zealand (45.0°S, 169.7°E).

The retrieval of a vertical water vapor profile with ground-based microwave measurements relies upon the change in pressure as a function of altitude. The line width of the spectrum decreases monotonically with altitude due to the dependence on pressure broadening. Thus the resultant signal, which is the sum of the emission from all altitudes, can be deconvolved to retrieve a vertical profile. Details of the measurement technique and instrumentation are given by *Nedoluha et al.* [1995, 1996].

The mixing ratios retrieved from 40 to 80 km using 500 scan (~1 wk) integrations are shown in Figure 1. There is a summer peak in the upper mesospheric mixing ratio consistent with the upward motion of the atmosphere in the summer hemisphere. The large positive trend in water vapor that was observed by the WVMS instruments at Table Mountain and Lauder and by HALOE in the early 1990s [*Nedoluha et al., 1998*] is not apparent in the data from Mauna Loa since 1996. Nevertheless, interesting variations are captured by both HALOE and the ground-based instruments.

A comparison of WVMS and HALOE data at several altitudes is shown in Figure 2. There is an offset between the average values of the HALOE and WVMS measurements at 50 km and 60 km, but the annual and interannual variations at Mauna Loa are very similar. Note in particular the interannual variation in the December/January minima at and above 60 km. Similar variations from WVMS measurements at Table Mountain and from
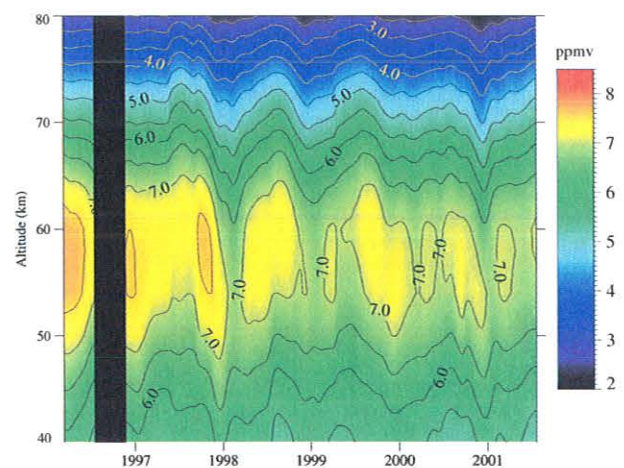

Fig. 1. Water vapor mixing ratios retrieved from WVMS3 measurements at Mauna Loa, Hawaii (19.5°N, 204.4°E). The data are smoothed using a Gaussian filter with a (1/e) width of 25 days.
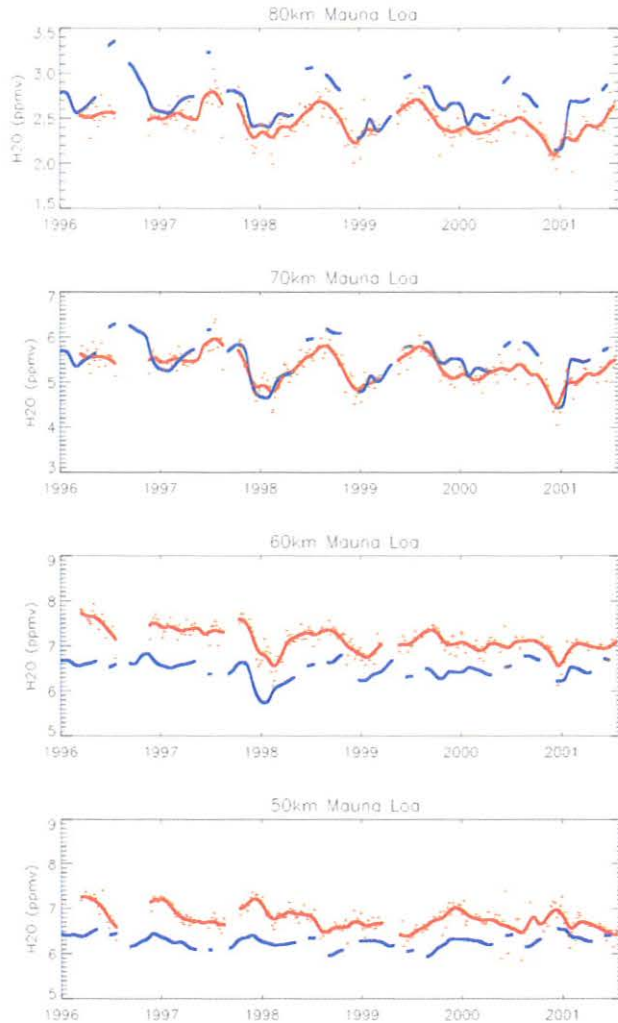
150

Fig. 2. Lines: WVMS (red) and HALOE (blue) data at several altitudes smoothed as in the contour plots. Measurement gaps of >50 days are left blank. Points: WVMS retrievals from approximately weekly averaged integrations. The HALOE data are all taken from within ±5° latitude of the WVMS measurements, and have been convolved with the WVMS averaging kernels to present data with similar sensitivity and resolution.

earlier HALOE data suggest that these variations may be related to the quasi-biennial oscillation (QBO) [*Nedoluha et al.*, 2000]. Preliminary comparisons with interannual variations in High Resolution Doppler Imager (HRDI) zonal winds and with interannual variations in HALOE temperatures suggest that there may be a correlation between strong zonal wind gradients, high temperatures, and low water vapor mixing ratios in the upper mesosphere.

REFERENCES

Bevilacqua, R.M., D.F. Strobel, M.E. Summers, J.J. Olivero, and M. Allen, The seasonal variation of water vapor and ozone in the upper mesosphere: Implications for vertical transport and ozone photochemistry, *J. Geophys. Res., 95*, 883-893, 1990.

Kirk-Davidoff, D.B., E.J. Hinsta, J.G. Anderson, and D.W. Keith, The effect of climate change on ozone depletion through changes in stratospheric water vapour, *Nature, 402*, 399-401, 1999.

Nedoluha, G.E., R.M. Bevilacqua, R.M. Gomez, D.L. Thacker, W.B. Waltman, and T.A. Pauls, Ground-based measurements of water vapor in the middle atmosphere, *J. Geophys. Res., 100*, 2927-2939, 1995.

Nedoluha, G.E., R.M. Bevilacqua, R.M. Gomez, W.B. Waltman, B.C. Hicks, D.L. Thacker, and W.A. Matthews, Measurements of water vapor in the middle atmosphere and implications for mesospheric transport, *J. Geophys. Res., 101*, 21,183-21,193, 1996.

Nedoluha, G.E., R.M. Bevilacqua, R.M. Gomez, D.E. Siskind, B.C. Hicks, J.M. Russell III, and B.J. Connor, Increases in middle atmospheric water vapor as observed by the Halogen Occultation Experiment and the ground-based Water Vapor Millimeter-wave Spectrometer from 1991 to 1997, *J. Geophys. Res., 103*, 3531-3543. 1998.

Nedoluha, G.E., R.M. Bevilacqua, R.M. Gomez, B.C. Hicks, J.M. Russell III, and B.J. Connor, Ground-based microwave observations of middle atmospheric water vapor in the 1990s, in *Atmospheric Science Across the Stratopause*, edited by D.E. Siskind, S.D. Eckerman, and M.E. Summers, *Geophysical Monograph, 123*, pp. 257-270, Am. Geophys. Union, Washington, DC, 2000.

Summers, M.E., D.E. Siskind, J.T. Bacmeister, R.R. Conway, S.E. Zasadil, and D.F. Strobel, Seasonal variations of middle atmospheric CH₄ and H₂O with a new chemical-dynamical model, *J. Geophys. Res., 102*, 3503-3526, 1997.

Aerosol Chemical Species and Volatile Organic Compounds at Barrow

SACHIO OHTA, NAOTO MURAO, AND TATSUYA FUKASAWA

Graduate School of Engineering, Hokkaido University, Sapporo 060-8628, Japan

INTRODUCTION

In winter and spring, a dense haze occurs in the Arctic. This "Arctic haze" contains large amounts of particulate pollutants, such as soot, sulfate, organics, and heavy metals, and gaseous pollutants, such as sulfur dioxide, nitric acid, and volatile organic compounds (VOCs) [*Shaw, 1995*]. The soot particles strongly absorb solar radiation, which changes the thermal structure of the Arctic atmosphere. Deposited soot reduces snow surface albedo, which perturbs the radiation budget in the Arctic [*Blanchet, 1989; Aoki et al., 1998*]. In addition, heavy metals, such as lead, vanadium, and arsenic, and VOCs, such as benzene, trichloroethylene, and tetrachloroethylene, in the haze attract concern with respect to their possible human health impacts because they are known carcinogenic compounds.

In this study results are reported from the measurement of the concentrations of chemical species in fine particles (aerosols less than 2 μm in diameter) and VOCs collected at the CMDL Barrow Observatory in 1999-2001. The measurement results serve as basic data with which to evaluate possible effects of pollutants on climate, human health, and ecosystems in the Alaskan Arctic.

MATERIALS AND METHODS

Atmospheric fine particles were collected on Teflon filters (Sumitomo Electric Industry Inc., FP-1000, 47 mm) and quartz fiber filters (Pallflex 2500 QAT-UP, 47 mm) simultaneously by drawing outdoor air through a cyclone separator with a 50% cut point of 2-μm diameter at a flow rate of 20 L min^{-1}. Each sample was integrated over a 2-wk period from August 1999 through June 2001. Ionic components of aerosols collected on the Teflon filter were extracted ultrasonically with distilled-deionized water and analyzed with an ion chromatograph (IC, Yokogawa Analytical Systems) for anions (model IC 7000, column Excelpack ICS0-A23) and for cations (model ICS-C25). Metal components of aerosols on the Teflon filter were extracted with a mixed solution of nitric acid and hydrofluoric acid and analyzed with an inductively coupled plasma mass spectrometer (ICP-MS, Yokogawa Analytical Systems, HP 4500). The carbonaceous components of aerosols (elemental and organic carbon) on the quartz fiber filters were determined by sample combustion in a condensation nuclei (CN) coder at 850°C coupled with a flame ionization detector (FID) with a nickel catalyst methanizer [*Ohta and Okita, 1984*].

VOCs were sampled once a month from March 2000 through August 2001. Air was drawn into a collection tube (Carbotrap 317, SUPELCO) at a flow rate of 100 mL min^{-1} for 2 hours. The collected VOCs were thermally desorbed and injected into a mass spectrometer using a Thermal Deposition Cold Trap (TCT) injector.

RESULTS AND DISCUSSION

Two-week average concentrations of chemical species in fine particles in the atmosphere collected at CMDL, Barrow, from August 1999 through June 2001 are presented in Figure 1. The concentrations of species ranged as follows: elemental carbon (EC), 0.001-0.32 μg C m^{-3}; organic carbon (OC), 0.20-0.69 μg C m^{-3}; sulfate (SO$_4^{-2}$), 0.09-1.7 μg m^{-3}; nitrate (NO$_3^-$), 0.00-0.15 μg m^{-3}; chloride (Cl$^-$), 0.001-1.81 μg m^{-3}; ammonium (NH$_4^+$), 0.00-0.14 μg m^{-3}; seasalt cations (S.S.C.), 0.007-1.8 μg m^{-3}; and soil particles (Soil), 0.003-0.25 μg m^{-3}. The concentrations of S.S.C. and Soil were calculated respectively as follows:

$$[\text{S.S.C.}] = 1.194 \times [\text{Na}^+] \text{ and } [\text{Soil}] = 12.35 \times [\text{Al}] \ .$$

The total amount of the chemical species increased in winter and spring (November-April) and decreased in summer and autumn (May-October). In particular, concentrations of EC and SO$_4^{-2}$ increased in winter and spring, in concert with the occurrence of Arctic haze [*Shaw, 1995*].

In preparation for the OC measurements, the quartz fiber filters were pretreated by heating at 850°C in air for 1 hour to remove organic contaminants. But, due to the heating, the clean surfaces of the quartz fiber filters easily absorbed gaseous organics in the sampling air. Thus the OC concentration reported herein may be overestimated.

Figure 2 shows 2-wk average concentrations of metal components of fine particles in the atmosphere at Barrow. The concentrations (ng m^{-3}) of species ranged as follows: vanadium (V), 0.02-0.82; manganese (Mn), 0.00-1.73; copper (Cu), 0.00-0.83; zinc (Zn), 0.00-6.48; arsenic (As), 0.00-1.97; and lead (Pb), 0.06-6.68. These concentrations increased in winter and spring (November-April) and decreased in summer and autumn (May-October), similar to concentrations of EC and SO$_4^{-2}$, again due to Arctic haze. Concentrations of Zn and Pb, increased in January and February 2000 and January to May 2001. Zn and Pb are emitted mainly from solid waste incineration and automobile exhausts, respectively.

Table 1 shows atmospheric concentrations of VOCs from March 2000 through August 2001 at Barrow. The concentrations (ppbv) ranged as follows: chloroform (0.005-0.014); 1, 2-dichloroethane (0.00-0.012); carbon tetrachloride (0.00-0.11); ethylbenzene (0.008-0.11); m, p-xylene (0.01-0.15); styrene (0.006-0.092); o-xylene (0.007-0.096); 1-ethyl-3-methyl-benzene (0.002-0.04); 1, 3, 5-trimethylbenzene (0.002-0.11); 1, 2, 4-trimethylbenzene (0.008-0.50); and 1, 4-dichlorobenzene (0.001-0.057). Except for chloroform, 1, 2-dichloroethane, and carbon tetrachloride, concentrations of the other compounds had seasonal variations with spring maxima. Data from five of the compounds listed in Table 1 are plotted in Figure 3.
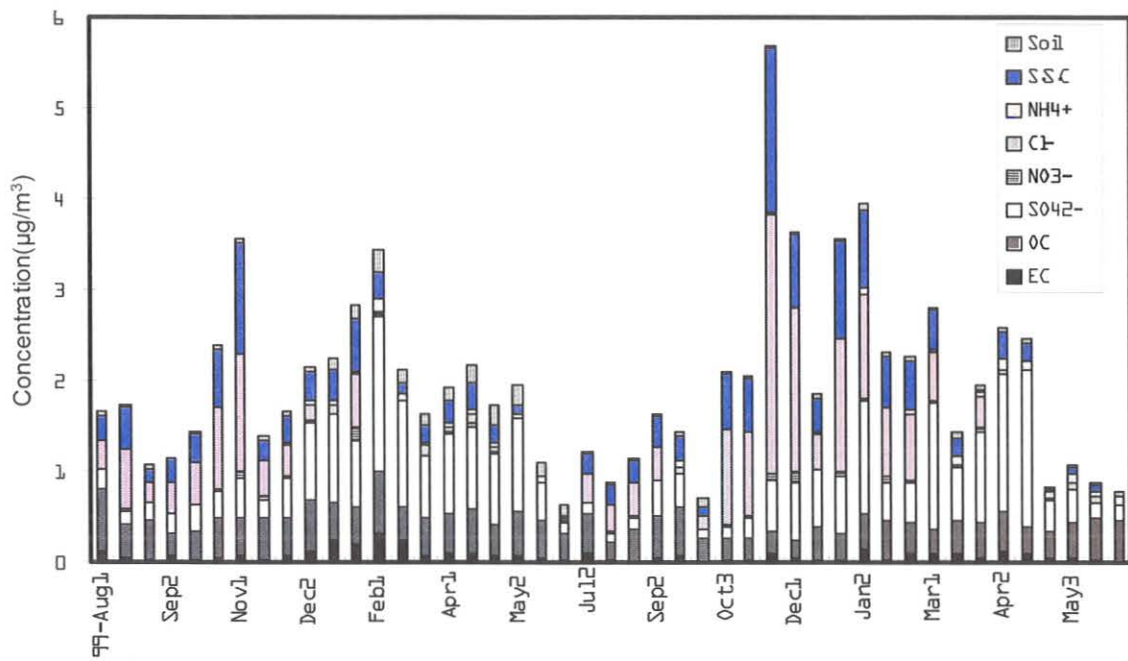
Fig. 1. Two-week average concentrations of chemical species in fine particles in the atmosphere at Barrow.
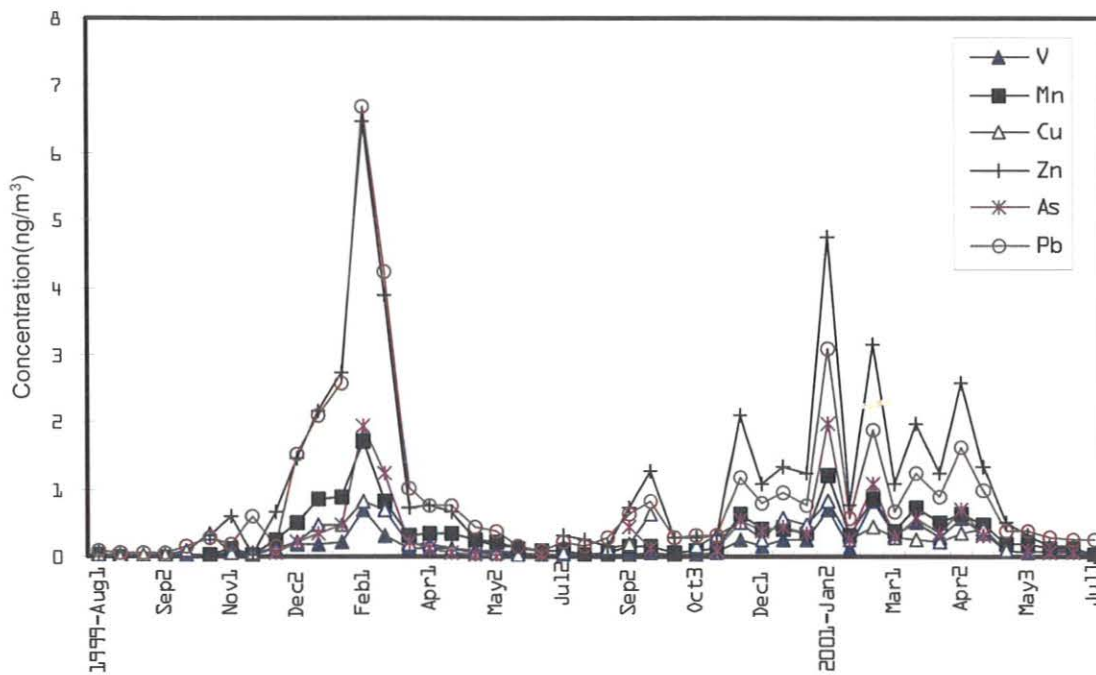

Fig. 2. Two-week average concentrations of metal components of fine particles in the atmosphere at Barrow.

153

TABLE 1. Concentrations of Volatile Organic Compounds (VOCs) in the Atmosphere at Barrow

| Compound	Concentration (ppbv)								
	March-December 2000								
	March 9	*March 30*	*April 27*	*May 26*	*June 26*	*July 26*	*Oct. 26*	*Nov. 15*	*Dec. 21*
Chloroform	0.012	0.012	0.013	0.011	0.013	0.013	0.011	0.014	0.010
Ethane, 1,2-dichloro	0.007	0.007	0.009	0.006	0.004	0.006	0.005	0.005	0.007
Carbon tetrachloride	0.060	0.064	0.083	0.075	0.051	0.088	0.073	0.065	0.092
Ethylbenzene	0.064	0.068	0.049	0.052	0.008	0.009	0.027	0.024	0.062
m,p-Xylene	0.120	0.126	0.084	0.094	0.012	0.011	0.043	0.036	0.091
Styrene	0.044	0.075	0.081	0.073	0.006	0.009	0.029	0.028	0.048
o-Xylene	0.090	0.096	0.054	0.059	0.009	0.007	0.026	0.021	0.064
Benzene, 1-ethyl-3-methyl-	0.018	0.021	0.010	0.010	0.002	0.003	0.005	0.003	0.012
Benzene, 1,3,5-trimethyl-	0.023	0.026	0.015	0.015	0.002	0.003	0.007	0.004	0.016
Benzene, 1,2,4-trimethyl-	0.098	0.110	0.058	0.060	0.008	0.011	0.027	0.017	0.061
Benzene, 1,4-dichloro-	0.002	0.007	0.035	0.011	0.001	0.008	0.005	0.002	0.023
	January-August 2001								
	Jan. 18	*Feb. 26*	*March 30*	*April 25*	*May 18*	*June 15*	*July 18*	*Aug. 25*	
Chloroform	0.011	0.013	0.011	0.008	0.008	0.005	0.008	0.008	
Ethane, 1,2-dichloro-	0.012	0.012	0.011	0.008		0.005			
Carbon tetrachloride	0.106	0.101	0.103	0.100	0.099		0.084	0.099	
Ethylbenzene	0.067	0.111	0.082	0.083	0.049	0.013	0.053	0.049	
m,p-Xylene	0.093	0.148	0.093	0.103	0.060	0.014	0.048	0.060	
Styrene	0.068	0.092	0.054	0.049	0.039	0.013	0.019	0.039	
o-Xylene	0.066	0.089	0.057	0.077	0.038	0.011	0.028	0.038	
Benzene, 1-ethyl-3-methyl-	0.040	0.023	0.010	0.022	0.010	0.004	0.005	0.010	
Benzene, 1,3,5-trimethyl-	0.111	0.034	0.015	0.046	0.015	0.006	0.006	0.015	
Benzene, 1,2,4-trimethyl-	0.498	0.127	0.058	0.210	0.058	0.025	0.023	0.058	
Benzene, 1,4-dichloro-	0.038	0.057	0.006	0.007	0.007	0.008	0.011	0.007	
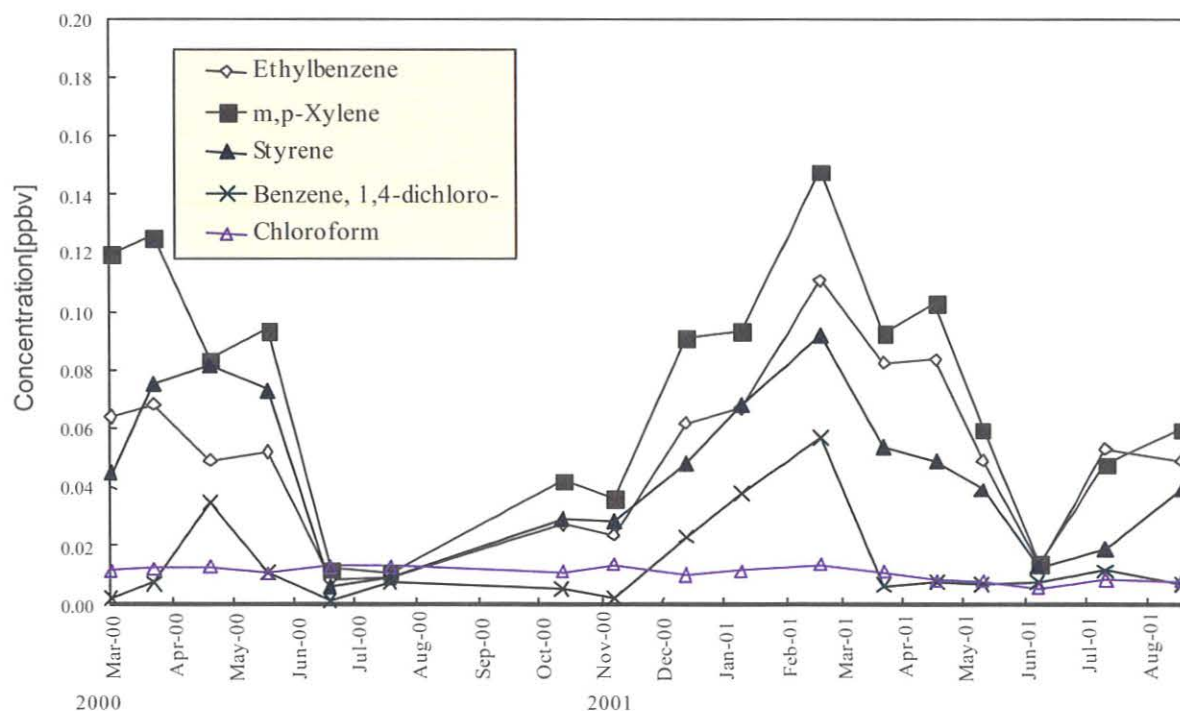
Fig. 3. Concentrations of VOCs in the atmosphere at Barrow.

Ethylbenzene is used as a solvent, and xylene, styrene, and other benzenes are emitted from automobile exhaust, reinforcing that these gases have been transported at least 6,000 miles from Eurasia. Since the VOCs were sampled only for 2 hours each sample day, the measured VOC concentrations inevitably depend on weather conditions and transport history. Thus wind direction, wind speed, and atmospheric stability must be checked on the days the VOCs were sampled, as well as the back trajectories for the sampling times, in order to better interpret the data.

REFERENCES

Aoki, T., T. Aoki, M. Fukabori, and Y. Zaizen, Spectral albedo observation on the snow field at Barrow, Alaska, *Climate Monitoring and Diagnostics Laboratory Summary Report No. 24 1996-1997*, edited by D.J. Hofmann, J.T. Peterson, and R.M. Rosson, pp. 122-123, NOAA Environ. Res. Labs., Boulder, CO, 1998.

Blanchet, J.-P., Toward estimation of climatic effects due to Arctic aerosols, *Atmos. Environ., 23*, 2609-2625, 1989.

Ohta, S., and T. Okita, Measurements of particulate carbon in urban and marine air in Japanese areas, *Atmos. Environ., 11*, 2439-2445, 1984.

Shaw, G.E., The Arctic haze phenomenon, *Bull. Am. Meteorol. Soc., 76*, 2403-2413, 1995.

Advanced Global Atmospheric Gases Experiment (AGAGE)

R.G. Prinn

Massachusetts Institute of Technology, Cambridge, Massachusetts 02139

R.F. Weiss

Scripps Institution of Oceanography, University of California, La Jolla, California 92093

D.M. Cunnold

Georgia Institute of Technology, Atlanta, Georgia 30332

P.J. Fraser

CSIRO, Division of Atmospheric Research, Victoria, Australia 3195

P.G. Simmonds

University of Bristol, School of Chemistry, Bristol, United Kingdom BS8 1TS

Introduction

The Advanced Global Atmospheric Gases Experiment (AGAGE) and its predecessors provide continuous high-frequency gas chromatographic measurements of biogenic and anthropogenic gases that are carried out at globally distributed sites in order to quantitatively determine the source and sink strengths and circulation of a large number of chemically and radiatively important long-lived gases. The program that started in 1978 is conveniently divided into three parts associated with three changes in instrumentation: the Atmospheric Lifetime Experiment (ALE), the Global Atmospheric Gases Experiment (GAGE), and AGAGE. Beginning in 1978, these three successive automated, high-frequency, in situ experiments have documented the long-term behavior of the measured concentrations of these important gases over the past 23 years and show both the evolution of latitudinal gradients and the high-frequency variability due to sources and circulation.

AGAGE began over the 1993-1996 time period and continues to the present. It has two instrument components. First, a highly improved gas chromatographic system measures five biogenic/anthropogenic gases (CH_4, N_2O, $CHCl_3$, CO, and H_2) and five anthropogenic gases (CCl_3F, CCl_2F_2, CH_3CCl_3, CCl_2FCClF_2, and CCl_4). Each species is measured 36 times per day with an electron capture detector (ECD), flame ionization detector (FID), and mercuric oxide reduction detector (MRD; this detector is for CO and H_2 and is currently present at only two of the stations, Mace Head, Ireland, and Cape Grim, Tasmania). Second, a gas chromatograph-mass spectrometer (GC-MS) system measures a wide range of hydrochlorofluorocarbons and hydrofluorocarbons: CH_2FCF_3 (HFC-134a), CH_3CCl_2F (HCFC-141b), CH_3CClF_2 (HCFC-142b), etc. These are now serving as interim or permanent alternatives to the chlorofluorocarbons and other long-lived halocarbons regulated by the Montreal Protocol [*UNEP*, 1996]. Also measured with the GC-MS system are the methyl halides (CH_3Cl, CH_3Br, and CH_3I) and the halons ($CBrF_3$ and $CBrClF_2$). AGAGE also includes development and use of new, much more accurate absolute calibrations for most of the measured gases.

The ALE, GAGE, and AGAGE stations have been located in five globally distributed localities: (1) Ireland, first at Adrigole, 52°N, 10°W (1978-1983), then at Mace Head, 53°N, 10°W (1987-present); (2) U.S. West Coast, first at Cape Meares, Oregon, 45°N, 124°W (1979-1989), then at Trinidad Head, California, 41°N, 124°W (1995-present); (3) Ragged Point, Barbados, 13°N, 59°W (1978-present); (4) Cape Matatula, American Samoa, 14°S, 171°W (1978-present); (5) Cape Grim, Tasmania, 41°S, 145°E (1978-present).

Of special significance is the AGAGE operation at Samoa. It enables a direct intercomparison with similar real-time measurements (and also with flask measurements) by the CMDL group. This intercomparison has already aided us in determining the net effect of calibration and instrument differences on the measurements by each group so that the data from both the AGAGE and CMDL networks can be utilized in combination by theoreticians to investigate chemical and meteorological phenomena.

Recent Progress

The instrumentation and calibrations used in the ALE, GAGE, and AGAGE experiments and a history of the majority of the anthropogenic ozone-depleting and climate-forcing gases in air based on these experiments have been described in detail [*Prinn et al.*, 2000]. We provide estimates of the long-term trends in total chlorine contained in long-lived halocarbons involved in ozone depletion. We summarize interpretations of these measurements using inverse methods to determine trace gas lifetimes and emissions. Finally, we provide a combined observational and modeled reconstruction of the evolution of chlorocarbons by latitude in the atmosphere over the past 60 years, which can be used as boundary conditions for interpreting trapped air in glaciers and oceanic measurements of chlorocarbon tracers of the deep oceanic circulation [*Prinn et al.*, 2000; see also *Walker et al.*, 2000].

A recent analysis of the entire 1978-2000 ALE-GAGE-AGAGE CH_3CCl_3 data set indicates that OH levels in the southern hemisphere are higher than in the northern hemisphere and that OH levels rose between 1978 and 1988,

and then subsequently decreased in 2000 to levels below 1978 values [*Prinn et al.*, 2001]. The 1994-1998 AGAGE CHCl$_3$ measurements have been analyzed, showing that this gas has a pronounced seasonal cycle (driven largely by OH), a global average baseline mole fraction of 8.9 ppt with no significant trend, and a global lifetime of 6.3 months. Inverse methods indicate emissions are predominantly in the 30°N-90°N region [*O'Doherty et al.*, 2001]. *Miller* [1998] established the abundance and trends of CHClF$_2$ and CH$_3$Br. *Huang* [1999] produced new estimates of OH using CH$_3$CCl$_3$, CHClF$_2$, CH$_2$FCF$_3$, CH$_3$CCl$_2$F, and CH$_3$CClF$_2$, simultaneously. An analysis of the GAGE-AGAGE measurements of CH$_4$ for 1985-1999 indicates a decreasing trend, in agreement with previous independent analyses, and has yielded estimates of CH$_4$ emissions in each semi-hemisphere [*Cunnold et al.*, 2002]. Measurements of CH$_3$Br from AGAGE and other investigators have been modeled with the 3D Model of Atmospheric Transport and Chemistry (MATCH) [*Jensen*, 1999]. A comprehensive discussion of the use of Kalman filters in trace gas inverse problems has been published [*Prinn*, 2000]. A critical analysis of polynomial-based approaches to the CH$_3$CCl$_3$ inverse problem has also been published [*Prinn and Huang*, 2001].

AGAGE GC-MRD measurements of hydrogen at Cape Grim have been reported and interpreted [*Simmonds et al.*, 2000]. GAGE/AGAGE measurements of CCl$_3$F indicate its global concentrations reached a maximum in 1993 and decayed slightly after that, while CCl$_2$F$_2$ levels continued to increase, but only slowly since 1993 [*Cunnold et al.*, 1997; *Prinn et al.*, 2000]. Several AGAGE scientists were lead authors or co-authors in the 1998 ozone assessment [*Kurylo et al.*, 1999; *Prinn et al.*, 1999]. Analysis of regional pollution events in Ireland suggest that industry estimates of the rate of decline in European emissions are too small [*Derwent et al.*, 1998a]. Measurements of CCl$_4$ from July 1978 to June 1995 show a maximum in its global concentration in 1990, followed by a small decrease since then [*Simmonds et al.*, 1998a]. GC-MS measurements of CH$_2$FCF$_3$, CH$_3$CCl$_2$F, and CH$_3$CClF$_2$ at Mace Head indicate rapid increases in the levels of these CFC replacements, and that industry estimates of HCFC-141b and particularly HCFC-142b emissions appear far too small to explain the observations [*Simmonds et al.*, 1998b]. Measurements of CHClF$_2$ (HCFC-22) in the Cape Grim archive and at La Jolla have been used to estimate OH concentrations, and this yields values larger than those determined from CH$_3$CCl$_3$ (but because of the larger uncertainty in the HCFC-22-based estimate, the difference is not statistically significant) [*Miller et al.*, 1998].

A Lagrangian dispersion model has been used to analyze 1996 Mace Head observations showing that North American sources occasionally produce pollution events at this station, which are about 10% of those due to the European sources [*Ryall et al.*, 1998]. Mace Head data for CH$_4$, N$_2$O, and CO$_2$ have been analyzed to elucidate European and northern-hemispheric sources [*Derwent et al.*, 1998b]. *Wamsley et al.* [1998] reported measurements of the halon CBrClF$_2$. *Fraser et al.* [1999] discussed halon trends and emissions over the past 20 years. *Fraser and Prather* [1999] reviewed the current prognosis for recovery of the ozone layer. D.S. Cohan, et al. (Methyl iodide observations at Cape Grim, Tasmania, using the AGAGE GC-MS instrument, submitted

to *Journal of Atmospheric Chemistry*, 2002) reported AGAGE CH$_3$I measurements at Cape Grim and interpreted them using trajectory analysis. *Dunse et al.* [2001] reported the results of modeling studies of Cape Grim pollution episodes recorded in AGAGE measurements.

The ALE/GAGE/AGAGE data are available through the Department of Energy-Carbon Dioxide Information Analysis Center (DOE-CDIAC) World Data Center (e-mail to cpd@ornl.gov, Dataset No. DB-1001).

REFERENCES

Cunnold, D.M., R.F. Weiss, R.G. Prinn, D.E. Hartley, P.G. Simmonds, P.J. Fraser, B.R. Miller, F.N. Alyea, and L. Porter, GAGE/AGAGE measurements indicating reductions in global emissions of CCl$_3$F and CCl$_2$F$_2$ in 1992-1994, *J. Geophys. Res.*, *102*, 1259-1269, 1997.

Cunnold, D.M., et al., GAGE/AGAGE measurements of methane at five sites from 1985-1999 and source inferences there from, *J. Geophys. Res.*, in press, 2002.

Derwent, R., P.G. Simmonds, S. O'Doherty, and D. Ryall, The impact of the Montreal Protocol on halocarbon concentrations in northern hemisphere baseline and European air masses at Mace Head, Ireland, from 1987-1996, *Atmos. Environ.*, *32*, 3689-3702, 1998a.

Derwent, R., P.G. Simmonds, S. O'Doherty, P. Ciais, and D. Ryall, European source strengths and Northern Hemisphere baseline concentrations of radiatively active trace gases at Mace Head, Ireland, *Atmos. Environ*, *32*, 3703-3715, 1998b.

Dunse, B.L., L.P. Steele, P.J. Fraser, and S.R. Wilson, An analysis of Melbourne pollution episodes observed at Cape Grim from 1995-1998, in *Baseline 97-98*, pp. 34-42, CSIRO-DAR and Bureau Meteorology, Aspendale, Australia, 2001.

Fraser, P.J., and M.J. Prather, An uncertain road: The science of atmospheric recovery, *Nature*, *398*, 663-664, 1999.

Fraser, P.J., D. Oran, C. Reeves, S. Penkett, and A. McCulloch, Southern hemispheric halon trends (1978-1998) and global halon emissions, *J. Geophys. Res.*, *104*, 15,985-15,999, 1999.

Huang, J., Optimal determination of global tropospheric OH concentrations using multiple trace gases, Ph.D. dissertation, 163 pp., Mass. Inst. of Technol., Cambridge, 1999.

Jensen, C., Terrestrial sources and sinks of atmospheric methyl bromide: Three-dimensional modeling of tropospheric abundance and sensitivities, M.S. dissertation, *MIT Center for Global Change Science Report 62*, 41 pp., Mass. Inst. of Technol., Cambridge, 1999.

Kurylo, M.J., et al., Short-lived ozone-related compounds, in *Scientific Assessment of Ozone Depletion: 1998, Global Ozone Res. and Monit. Proj. Rep. 44*, pp. 2.1-2.56, World Meteorol. Org., Geneva, 1999.

Miller, B.R., Abundances and trends of atmospheric chloro-difluoromethane and bromomethane, Ph.D. dissertation, 149 pp., Univ. of Calif., San Diego, 1998.

Miller, B.R., J. Huang, R.F. Weiss, R.G. Prinn, and P.J. Fraser, Atmospheric trend and lifetime of chlorodifluoromethane (HCFC-22) and the global tropospheric OH concentration, *J. Geophys. Res., 103*, 13,237-13,248, 1998.

O'Doherty, S., et al., In situ chloroform measurements at AGAGE atmospheric research stations from 1994-1998, *J. Geophys. Res., 106*, 20,429-20,444, 2001.

Prinn, R.G., Measurement equation for trace chemicals in fluids and solution of its inverse, in *Inverse Methods in Global Biogeo-chemical Cycles*, edited by P. Kasibhatla et al., pp. 3-18, *Geophysical Monograph, No. 114*, Am. Geophys. Union, Washington, DC, 2000.

Prinn, R.G., and J. Huang, Comment on "Global OH trend inferred from methylchloroform measurements" by M. Krol et al., *J. Geophys. Res., 106*, 23,151-23,158, 2001.

Prinn, R.G., R. Zander, D.M. Cunnold, J.W. Elkins, A. Engel, P.J. Fraser, M.R. Gunson, M.K.W. Ko, E. Mahieu, P.M. Midgley, J.M. Russell III, C.M. Volk, and R.F. Weiss, Long-lived ozone-related compounds, in *Scientific Assessment of Ozone Depletion: 1998, Global Ozone Res. and Monit. Proj. Rep. 44*, pp. 1.1-1.54, World Meteorol. Org., Geneva, 1999.

Prinn, R.G., R.F. Weiss, P.J. Fraser, P.G. Simmonds, D.M. Cunnold, F.N. Alyea, S. O'Doherty, P. Salameh, B.R. Miller, J. Huang, R.H.J. Wang, D.E. Hartley, C. Harth, L.P. Steele, G. Sturrock, P.M. Midgley, and A. McCulloch, A history of chemically and radiatively important gases in air deduced from ALE/GAGE/AGAGE, *J. Geophys. Res., 115*, 17,751-17,792, 2000.

Prinn, R.G., J. Huang, R. Weiss, D. Cunnold, P. Fraser, P. Simmonds, A. McCulloch, P. Salameh, S. O'Doherty, R. Wang, C. Harth, L. Porter, and B. Miller, Evidence for significant variations in atmospheric hydroxyl radicals over the last two decades, *Science, 293*, 1048-1054, 2001.

Ryall, D., R. Maryon, R. Derwent, and P.G. Simmonds, Modeling long-range transport of CFCs to Mace Head, Ireland, *Q. J. R. Meteorol. Soc., 124*, 417-446, 1998.

Simmonds, P.G., D.M. Cunnold, R.F. Weiss, R.G. Prinn, P.J. Fraser, and A. McCulloch, Global trends and emission estimates of carbon tetrachloride (CCl_4) from in situ background observations from July 1978 to June 1995, *J. Geophys. Res., 103*, 16,017-16,027, 1998a.

Simmonds, P.G., J. Huang, R. Prinn, S. O'Doherty, R. Derwent, D. Ryall, G. Nickless, and D. Cunnold, Calculated trends and atmospheric abundance of 1,1,1,2-tetrafluoroethane, 1,1-dichloro-1-fluoroethane, and 1-chloro-1,1-fluoroethane using automated in situ gas chromatography-mass spectrometry measurements recorded at Mace Head, Ireland, from October 1994 to March 1997, *J. Geophys. Res., 103*, 16,029-16,037, 1998b.

Simmonds, P.G., R.G. Derwent, S. O'Doherty, D.B. Ryall, L.P. Steele, R.J. Langenfelds, P. Salameh, H.J. Wang, C.H. Dimmer, and L.E. Hudson, Continuous high frequency observations of hydrogen at the Mace Head baseline atmospheric monitoring station over the 1994-1998 period, *J. Geophys. Res., 105*, 12,105-12,121, 2000.

UNEP (United Nations Environmental Programme), *Handbook for the International Treaties for the Protection of the Ozone Layer*, 4th ed., Nairobi, Kenya, 1996.

Walker, S.J., R.F. Weiss, and P.K. Salameh, Reconstructed histories of the annual mean atmospheric mole fractions for the halocarbons CFC-11, CFC-12, CFC-113, and carbon tetrachloride, *J. Geophys. Res., 105*, 14,285-14,296, 2000.

Wamsley, P., et al., Distribution of halon-1211 ($CBrClF_2$) in the upper troposphere and lower stratosphere and the 1994 bromine budget, *J. Geophys. Res., 103*, 1513-1526, 1998.

USDA UVB Monitoring and Research Network Langley Calibrations at Mauna Loa Observatory

JAMES SLUSSER

USDA UVB Monitoring and Research Network, Natural Resource Ecology Laboratory,
Colorado State University, Fort Collins 80523-1499

INTRODUCTION

The U.S. Department of Agriculture (USDA) ultraviolet B (UVB) Monitoring and Research Network [*Bigelow et al.,* 1998] set up a climatological site as well as an experimental research site at Mauna Loa Observatory, Hawaii (MLO), in November 1997 in order to investigate its new instrumentation's performance and ability to self-calibrate using the Sun as a source. The USDA Network makes measurements at 28 U.S. and 2 Canadian sites with the Yankee Environmental Systems (Turners Falls, MA) UV multi-filter rotating shadowband radiometer (UV-MFRSR). The measurements are made every 20 seconds and combined to 3-min averages. The UV-MFRSR [*Bigelow et al.,* 1998] is a seven-channel ultraviolet version of the visible multi-filter rotating shadowband radiometer described by *Harrison et al.* [1994]. This UV instrument contains separate solid-state detectors, each with nominal 2-nm full-width half-maximum (FWHM) ion-assisted-deposition interference filters at 300-, 305-, 311-, 318-, 325-, 332-, and 368-nm nominal-center wavelengths. The 368-nm wavelength is a standard WMO wavelength, and the others, except 300 nm, are close to Dobson wavelengths. The 300-nm channel was chosen as the shortest wavelength where sufficient signal-to-noise ratio was achievable. Each detector shares a common diffuser, thereby allowing total horizontal (no blocking) and diffuse horizontal (direct beam blocked by the shadowband) irradiance to be measured simultaneously at each passband. Direct normal irradiance is derived in near-real time by firmware included within the data-logging component of the instrument.

LANGLEY CALIBRATIONS

The Langley method of calibrating the UV-MFRSR was explored by *Slusser et al.* [2000] under the exceptionally clear skies at MLO. The objective of the study was to compare Langley calibration factors with those from standard lamps. This method has several advantages over the traditional standard lamp calibrations: the Sun is a free, universally available, and very constant source, and nearly continual automated field calibrations can be made. Although 20 or so Langley events are required for an accurate calibration, the radiometer remains in the field during calibration. Difficulties arise as a result of changing ozone optical depth during the Langley event and the breakdown of the Beer-Lambert law over the finite filter bandpass, since optical depth changes rapidly with wavelength. The Langley calibration of the radiometers depends critically upon the spectral characterization of each channel and on the wavelength and absolute calibration of the extraterrestrial spectrum used. Results of Langley calibrations for two UV-MFRSRs at Mauna Loa were compared with calibrations using two National Institute of Standards and Technology (NIST) traceable lamps. The two radiometers were run simultaneously: one on a Sun-tracker using a collimating tube and the other in the conventional shadowband configuration. Both radiometers were calibrated with two secondary 1000-W lamps, and later the spectral response functions of the channels were measured.

The range of air mass factors at a given wavelength suitable for Langley plots is governed by the sum of the products of the optical depths and the individual air mass factors. Extinction of the direct beam is much larger in the UV than in the visible region of the spectrum. This is the result of both the strong absorption due to ozone and the molecular Rayleigh scattering, which increases approximately as λ^{-4}, resulting in a combined optical depth exceeding 3.0 at 300 nm. Current state-of-the-art solid-state detectors are limited to not more than four decades of dynamic range. Therefore the range of air masses appropriate for UV Langley plots is more restricted than for the visible, where at 415 nm the total optical depth is typically less than 0.5. After a number of ranges were tried, an air mass range of 1.2 to 2.2 [solar zenith angle (SZA) 33.6° to 63.0°] was determined to be suitable for the UV, instead of the range of 2 to 6 (SZA 60.0° to 80.4°) commonly used in the visible part of the spectrum [*Harrison and Michalsky,* 1994].

Extrapolations to zero air mass voltage in the UV, central to the Langley calibrations, are more variable than those in the visible region as a consequence of the diurnal variations in the ozone and to a smaller extent aerosol optical depth. Large changes in ozone optical depth in the Hartley-Huggins band below 320 nm over the finite 2.0-nm passband of the UV-MFRSR result in the failure of the Beer-Lambert law, adding to the uncertainty of the Langley-derived calibrations [*Wilson and Forgan,* 1995]. Since shorter wavelengths are attenuated more strongly than the longer as the SZA or column ozone increases, the effective center wavelength of the passband shifts to the red. Further complications result from the larger fraction of diffuse light in the field of view around the Sun's disc due to molecular scattering at these shorter UV wavelengths [*Tüg and Bauman,* 1994; *McKenzie and Johnston,* 1995]. Corrections for these problems were performed as discussed in *Slusser et al.* [2000].

The ratio of Langley to lamp calibration factors for the two radiometers after 213 days in 1998 for the seven channels from 300 nm to 368 nm, using the shadowband configuration, ranged from 0.988 to 1.070. The estimated uncertainty in accuracy of the Langley calibrations ranged

from ±3.8% at 300 nm to ±2.1% at 368 nm. For all channels calibrated with Central UV Calibration Facility (CUCF) lamps the estimated uncertainty was ±2.5%. The Langley and lamp calibration factors from two lamps agreed to within their combined uncertainties for all channels of the first radiometer and for all but one channel of the second radiometer. These are the first successful Langley cali-brations of filter radiometers at 300 nm and 305 nm. The Langley calibration factors with the radiometer in the shadowband mode for all the channels agreed with those derived from lamps, from 0% difference to at worst 7% higher at 300 nm. The uncertainty due to the radiometer signal-to-noise ratio is smaller using the Langley method than during lamp calibrations, which constitutes a major advantage of UV Langley calibrations for these radiometers.

There were no significant differences in Langley calibration factors when the radiometer was in the shadow-band configuration compared with when it was on the Sun-tracker. This suggests that in the UV the shadowband is equally as capable as the Sun-tracker in isolating the direct beam. This study shows that using Langley-method shadow-band UV radiometers at a high-altitude site is an effective method to obtain calibrations that approach the accuracy of those from lamps. Advantages over lamp calibrations include superior signal-to-noise ratio, automated operation, no loss of instrument operation, and reference to an absolute, nearly unchanging standard that is universally available. Used together with lamp calibrations, the Langley method provides continual checks of radiometer and lamp stability. The advantage of a shadow-band over a Sun-tracker radio-meter is that in addition to the direct beam the shadowband radiometer retrieves global and diffuse irradiances.

REFERENCES

Bigelow, D.S., J.R. Slusser, A.F. Beaubien, and J.H. Gibson, The USDA Ultraviolet Radiation Monitoring Program, *Bull. Am. Meteorol. Soc., 79*, 601-615, 1998.

Harrison, L., and J. Michalsky, Objective algorithms for the retrieval of optical depths from ground-based measurements, *Appl. Opt., 33,* 5126-5132, 1994.

Harrison, L., J. Michalsky, and J. Berndt, Automated multi-filter rotating shadowband radiometer: An instrument for optical depth and radiation measurements, *Appl. Opt., 33,* 5118-5125, 1994.

McKenzie, R.L., and P.V. Johnston, Comment on "Problems of UV-B radiation measurements in biological research: Critical remarks on current techniques and suggestions for improvements" by H. Tüg and M.E.M. Baumann, *Geophys. Res. Lett., 22,* 1157-1158, 1995.

Slusser, J.R., J.H. Gibson, D. Kolinski, P. Disterhoft, K. Lantz, and A.F. Beaubien, Langley method of calibrating UV filter radiometers, *J. Geophys. Res., 105,* 4841-4849, 2000.

Tüg, H., and M. Baumann, Problems of UV-B radiation measurements in biological research: Critical remarks on currents techniques and suggestions for improvements, *Geophys. Res. Lett., 21,* 689-692, 1994.

Wilson, S.R., and B.W. Forgan, In situ calibration technique for UV spectral radiometers, *Appl. Opt., 34,* 5475-5484, 1995.

Long-Term Trends of Trace Gases over Mauna Loa

R. VAN ALLEN, F.J. MURCRAY, T.M. STEPHEN, AND R.D. BLATHERWICK

Department of Physics and Astronomy, University of Denver, Denver, Colorado 80208-0202

INTRODUCTION

Since November 1991, the University of Denver (DU) has operated a very high resolution (~0.0035 cm^{-1}) Fourier transform spectrometer (FTS) from the Network for the Detection of Stratospheric Change (NDSC) site at Mauna Loa Observatory to obtain atmospheric transmission spectra in the infrared region of the solar electromagnetic spectrum. Initially, a Bomem DA3.002 FTS was employed. This instrument required considerable operator attention and was consequently only operated routinely once a week at sunrise, and more frequently when DU personnel were on site for maintenance or for special campaigns. The spectral regions routinely covered were 750-1250 cm^{-1} and 2400-3050 cm^{-1}, and vertical column densities of N_2O, O_3, HNO_3, HCl, and $CHClF_2$ were retrieved from the data. In August 1995, this system was replaced with a Bruker 120HR system. The new system includes a weather station and control software designed and fabricated at DU. It is almost completely automated, requiring an operator only to fill the detector dewars with liquid nitrogen, and runs twice daily when weather permits. With the installation of this instrument, additional spectral intervals were added, permitting the retrieval of column densities for additional molecules. In this study the trends for 12 molecules are presented, and O_3 values measured with the FTS are compared with Dobson measurements for the 10-yr period of 1991-2000.

RESULTS AND DISCUSSION

Shown here are the cumulative results of the observations: a 10-yr record for O_3, HNO_3, N_2O, HCl, and $CHClF_2$ (HCFC-22), and a 6-yr record for CH_4, C_2H_6, HCN, NO, NO_2, HF, and CO.

The analysis was performed using the computer code SFIT [*Rinsland et al.*, 1984], which minimized the root mean square residual between a simulated spectrum and the observed spectrum by multiplying an assumed vertical volume mixing ratio profile by a scaling factor. The present analysis employed the HITRAN 96 spectral-line-parameter data base [*Rothman et al.*, 1998] and the pressure-temperature profiles from the daily National Weather Service radiosondes launched from Hilo, Hawaii.

A comparison was conducted between O_3 measured with a Dobson [*Dobson and Harrison*, 1926; *Dobson*, 1957] and FTS measurements (Figure 1) (R. Van Allen et al., unpublished manuscript, 2002). For this comparison points that were as close in time as possible were chosen, but always within 24 hours. For the 1991-1994 data, measured with a Bomem spectrometer, a systematic offset between FTS measurements and the Dobson was found. The Dobson data were taken from the World Ozone and Ultraviolet Data Centre (WOUDC). The ratio average (Dobson/FTS) for 1991-1992 is 1.03, with a standard deviation (SD) of 0.04, and for 1993-1994 the average ratio is 1.03, with a SD of
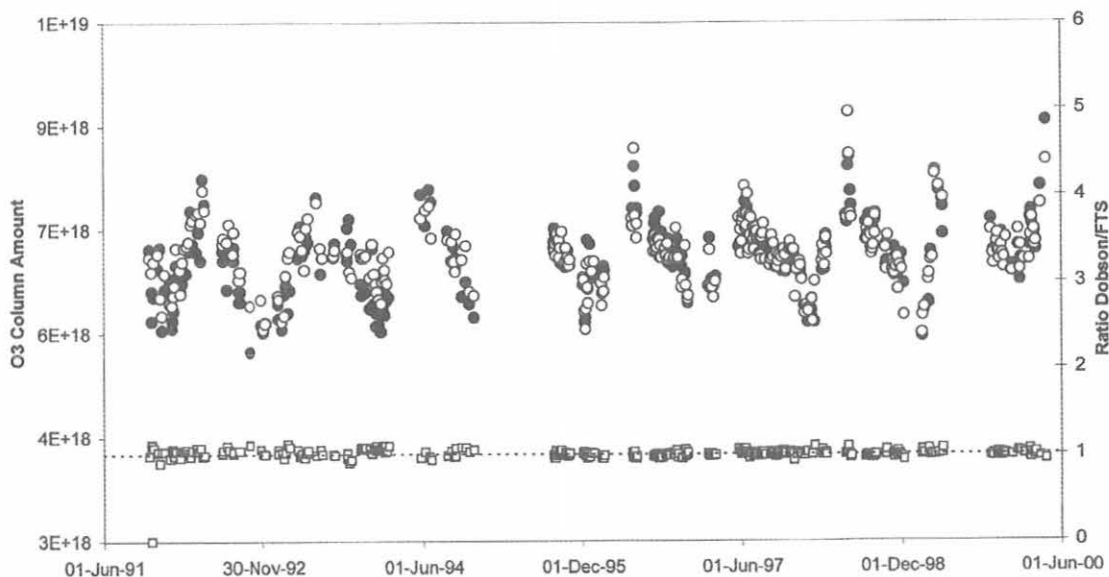
Fig. 1. Comparison between O_3 retrieved with a Dobson (white circles) and with a FTS (black circles), at MLO. The ratio Dobson/FTS (open square) is also shown.

0.05. This comparison of the 1991-1992 data agrees well with previous studies [*David et al.*, 1993]. The small difference in the systematic offset between the current and the previous analysis is due to the fact that points were matched in the current comparison, while the previous study used averages. The agreement between Dobson and FTS values is much improved for the Bruker data. The average ratio for 1995-2000 is 1.00, with a SD of 0.025.

The seasonal cycles of O_3 and HNO_3 are shown in Figure 2. Ozone amounts showed no obvious trend from 1991 to 2000. The recovery of HNO_3 from Pinatubo-induced high levels is apparent from 1991 to 1996, with an overall
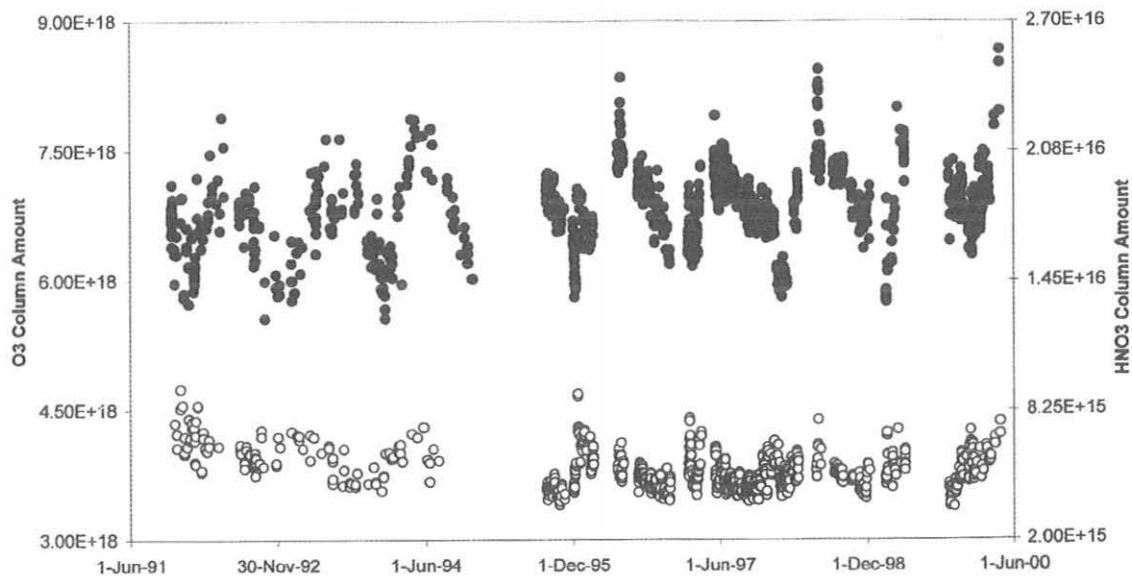
Fig. 2. Total column amounts of O_3 (black circles) and HNO_3, (white circles), at MLO.
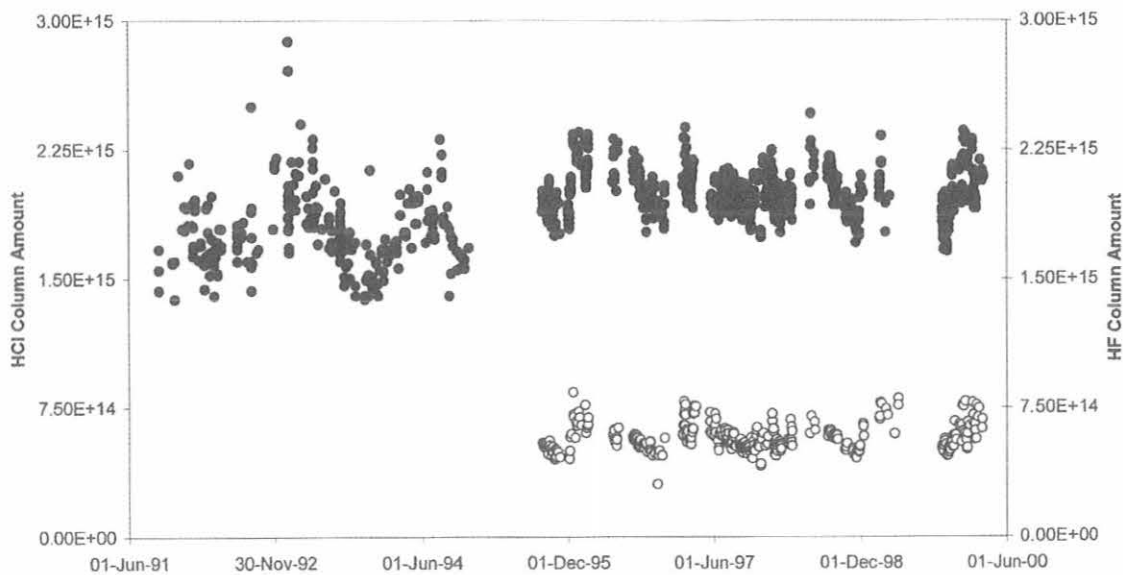
Fig. 3. Total column amounts of HCl (black circles) and HF (white circles), at MLO.

decrease of about 30%. During 1997-2001 there is no apparent trend in HNO_3.

The quasi-seasonal trend in HCl and HF is shown in Figure 3. The increase in HF is approximately 12% from 1995 to 2001. The increase in HCl for the same time period is about 6%.

Figure 4 shows the high variability of CO, and the overall increase in HCFC-22 of about 50% between 1991 and 1998, where the trend levels off.

Figure 5 shows C_2H_6 and HCN. The high values of C_2H_6, HCN, and CO at the end of 1997 and in 1998 correlate with
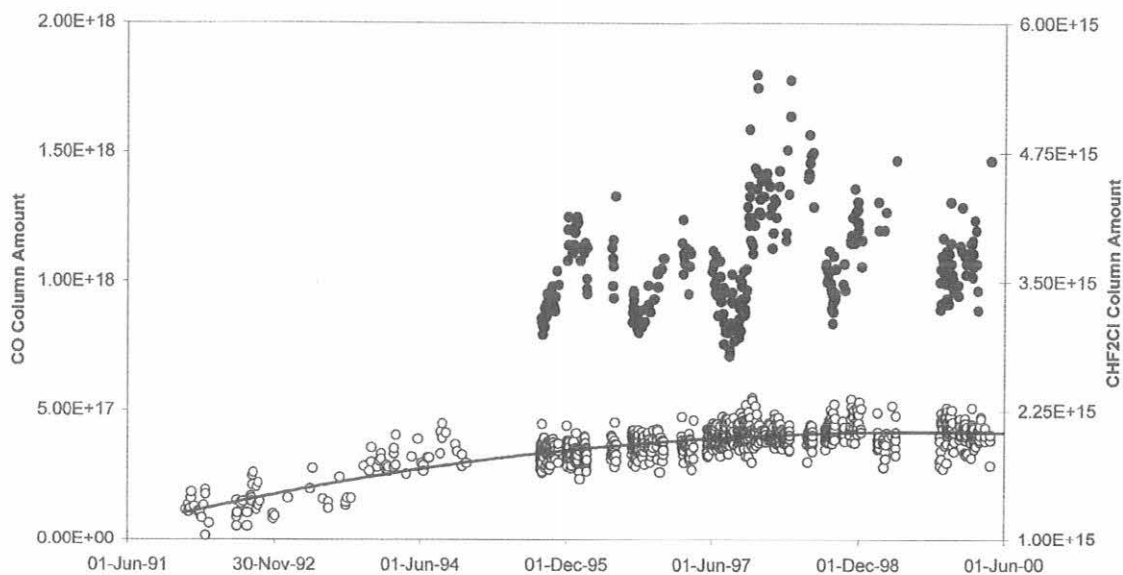
Fig. 4. Total column amounts of HCFC-22 (white circles) and CO (black circles), at MLO. The polynomial fit (second order) shows that HCFC-22 amounts level off in 1998.
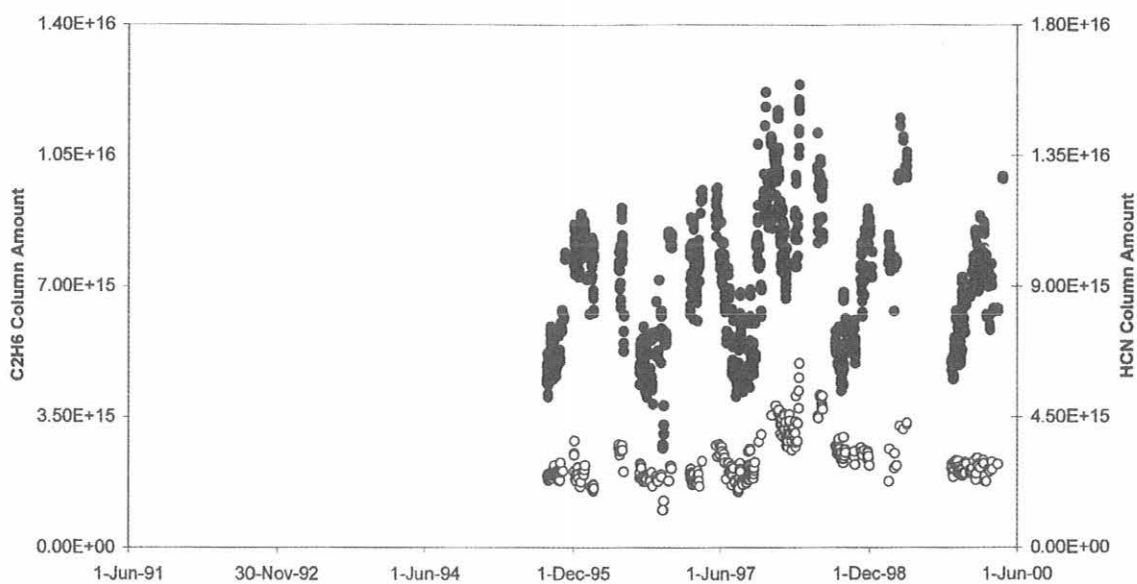
Fig. 5. Total column amounts of C_2H_6 (black circles) and HCN (white circles), at MLO.

Asian tropical fires [*Rinsland et al.*, 1999]. Figure 6 shows NO and NO_2. Photochemistry is evident in AM-PM differences.

Figure 7 shows CH_4 and N_2O. No significant trends are observed, and the retrieval of these molecules can be used to study the achievable precision.
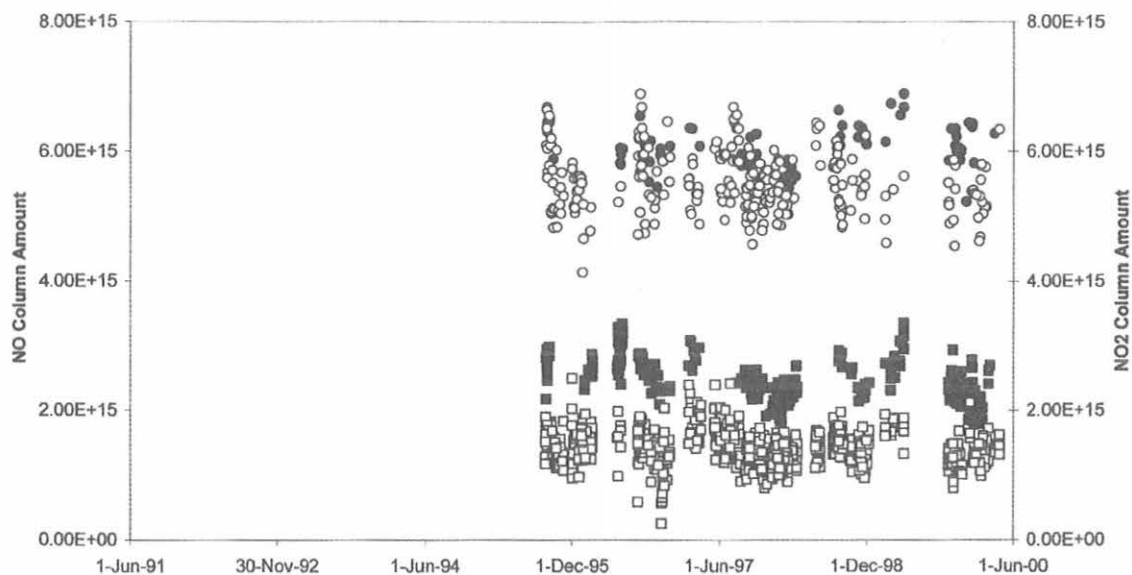
Fig. 6. Total column amounts of NO-sunset (black circles), NO-sunrise (white circles), NO_2-sunset (black squares), and NO_2-sunrise (white squares), at MLO.
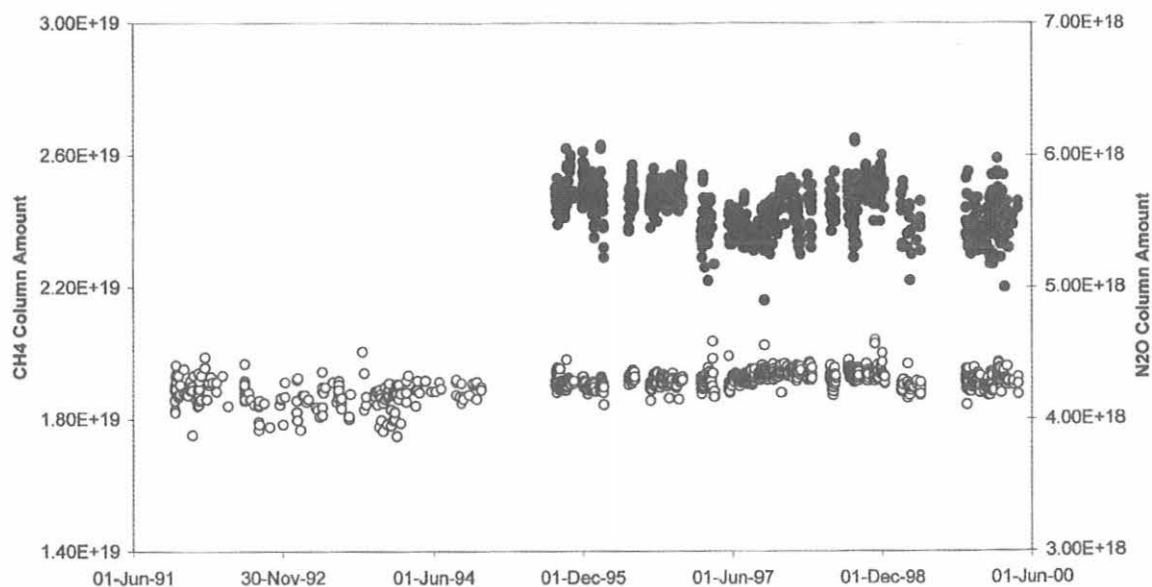
Fig. 7. Total column amounts of CH_4 (black circles) and N_2O (white circles), at MLO.

REFERENCES

David, S.J., S.A. Beaton, M.H. Anderberg, and F.J. Murcray, Determination of total ozone over Mauna Loa using very high resolution infrared solar spectra, *Geophys. Res. Lett.*, *20*, 2055-2058, 1993.

Dobson, G.M.B., Observer's handbook for the ozone spectro-photometer, *Ann. Int. Geophys. Year*, *5*, 90, 1957.

Dobson, G.M.B., and D.N. Harrison, Measurements of the amount of ozone in the Earth's atmosphere and its relation to other geophysical conditions, *Proc. Roy. Soc., A110*, 660-693, 1926.

Rinsland, C.P., R.E. Boughner, J.C. Larsen, G.M. Stokes, and J.W. Broult, Diurnal variations of atmospheric nitric oxide: Ground based infrared spectroscopic measurements and their interpretation with time-dependent photochemical model calculations, *J. Geophys. Res.*, *89*, 9613-9622, 1984.

Rinsland, C.P., et al., Infrared spectroscopic measurements of free tropospheric CO, C_2H_6, and HCN above Mauna Loa, Hawaii: Seasonal variations and evidences for enhanced emissions from the Southeast Asian tropical fires of 1997-1998, *J. Geophys. Res., 104*, 18,667-18,680, 1999.

Rothman, L.S., et al., The HITRAN molecular spectroscopic database and HAWKS (HITRAN Atmospheric Work Station): 1996 edition, *J. Quant. Spectrosc. Radiat. Transfer, 60*, 665-710, 1998.

Geomagnetic Field Monitoring at Barrow, Alaska

E.W. WORTHINGTON

U.S. Geological Survey, College Magnetic Observatory, Fairbanks, Alaska 99775

J.J. LOVE

U.S. Geological Survey, Box 25046 MS 966, Denver, Colorado 80225

Temporal variations in the Earth's magnetic field occur over an astonishingly wide spectrum, with periods ranging over 20 orders of magnitude: sub-milliseconds to tens of millions of years [*Parkinson*, 1983; *Courtillot and LeMouel*, 1988]. These variations have a variety of causes and effects, some of which are understood and others of which remain rather more mysterious. Magnetic field variations with periods less than a few decades can be monitored and studied with magnetic observatories, such as that operated by the U.S. Geological Survey (USGS) in Barrow, Alaska.

The most rapid geomagnetic field variations are of external origin, coming from the ionosphere and magnetosphere. The magnetic field is particularly time dependent during so-called "magnetic storms," which, at the surface of the Earth, are prominent manifestations of the variable conditions in the near-Earth space environment, or "space-weather." The most energetic magnetic storms occur during peaks in solar activity and when the interplanetary magnetic field (IMF) becomes intimately connected with that of the Earth (Figure 1) [*Russell*, 1991; *Gonzales et al,.* 1994; *Cowley*, 1995; *Burch*, 2001].

Data from ground-based magnetic observatories play an important role in the diagnosis of space weather conditions, which influence the performance and reliability of technological systems that are critical to modern civilization [*Dooling*, 1995; *Scott*, 1997; *Nordwall*, 1999]. During stormy conditions both high- and low-frequency radio technological systems that are critical to modern civilization communication can be difficult if not impossible, Global Positioning Systems (GPSs) can be degraded, satellite electronics can be damaged, satellite drag can be enhanced, and astronaut and high-altitude pilots can be subjected to enhanced levels of radiation [*Maynard*, 1995; *Shea and Smart*, 1998; *Feynman and Gabriel*, 2000].

Toward the other end of the temporal scale, geomagnetic variations with periods longer than a few decades, including the occasional reversal of the magnetic field, are of internal origin, caused by fluid motion in the Earth's liquid iron outer core [*Busse*, 1983; *Bloxham and Gubbins*, 1989; *Love*, 1999]. It is well known that the compass does not usually point toward true north. In fact, the deviation from north, or declination, differs depending on the observer's geographic location. Furthermore, over historical times, declination and the entire magnetic vector change noticeably with time. These complexities, while scientifically interesting, have long been a nuisance for navigators [*Jackson et al.*, 1997] and helped to motivate some of the original research in geomagnetism.

THE GEOMAGNETIC OBSERVATORY

The Barrow Geomagnetic Observatory is the northern-most of 14 USGS digital magnetic observatories. Established in 1949 by what was then the U.S. Coast and Geodetic Survey, responsibility for observatory operation was passed on to NOAA in 1970 and then ultimately to the USGS in 1973. Its location puts it near the boundary of the auroral zone and polar cap, two distinctly different regions of the Earth's magnetic field. As such it is an important site in the global network of geomagnetic observatories, which, in combination, allows for global monitoring of geomagnetic field variations. Ground-based stations, such as the Barrow Geomagnetic Observatory, serve as controls for internal and external field modeling, as reference stations for satellite measurements made within or above the ionosphere, and as absolute calibration locations for field surveys.

Over its lifetime Barrow Observatory (Figure 2) has been extensively upgraded, with new buildings, magnetometers, and data transmission equipment installed to meet modern demands for precision and timeliness [*Townshend*, 2001]. Building insulation and heaters provide a thermally stable environment for the magnetometers even though the outside temperature can reach –50°C. All buildings and exterior structures must be capable of handling wind speeds in excess of 113 km (70 mi) per hour.
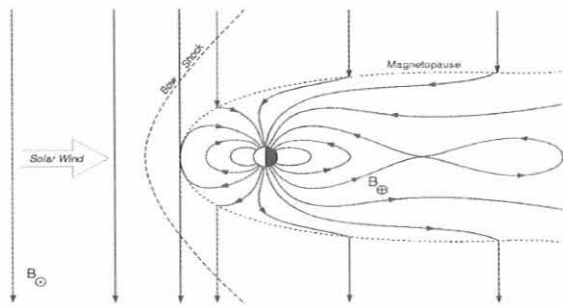
Fig. 1. Southward orientation of the interplanetary magnetic field, being swept toward the Earth by the solar wind, results in severe geomagnetic storms. At the front of the magnetosphere, this geometry is unstable and field reconnection occurs with the geomagnetic field. As the interplanetary magnetic field is blown past the Earth, the geomagnetic field is peeled back, causing acceleration of charged particles in the magnetosphere. A related effect occurs in the tail of the magnetosphere, where neighboring but oppositely directed field lines can reconnect, with a resulting recoil and acceleration of charged particles. The time-dependent particle accelerations amount to induced electric currents that sustain their own magnetic fields and contribute to the magnetic variations detectable at the Earth's surface.

Fig. 2. Top: The variation building that houses the fluxgate magnetometer. Bottom: The main building that contains data collection electronics.

Fig. 3. The magnetic field components. The Cartesian components (X, Y, Z) define north, east, down; the spherical components (F, I, D) define intensity, inclination, declination; H is the horizontal component of intensity.

Magnetic measurements at Barrow are made consistent with standards set by Intermagnet, an international consortium that oversees the operation of about 80 magnetic observatories throughout the world. Being a vector, the Earth's magnetic field has both direction and intensity; field components are defined in Figure 3. To measure the various parts of the magnetic vector, the observatory is equipped with a tri-axial fluxgate magnetometer and a total field proton magnetometer, both of which are controlled by a digital data acquisition system. The fluxgate, shown in Figure 4, continuously records variations in the Earth's magnetic field, specifically, the horizontal field (H), the deviation from geographic north, or declination (D), and the vertical field component (Z). To account for a slow drift in calibration, the intensity (F) is measured absolutely by the proton magnetometer, and direction is measured absolutely by hand with a declination-inclination magnetometer, consisting of a single-axis fluxgate magnetometer mounted to a theodolite (Figure 5).

Piers within the site buildings (Figure 6) provide stable platforms to make the vectorial magnetic measurements, but the active permafrost layer makes pier construction difficult. At most observatories large non-magnetic concrete piers are set straight into the ground. However, at

Barrow a pier can shift because concrete acts as a heat conductor, warming the permafrost, and thereby causing a seasonal freezing and thawing. To avoid this, a hole is
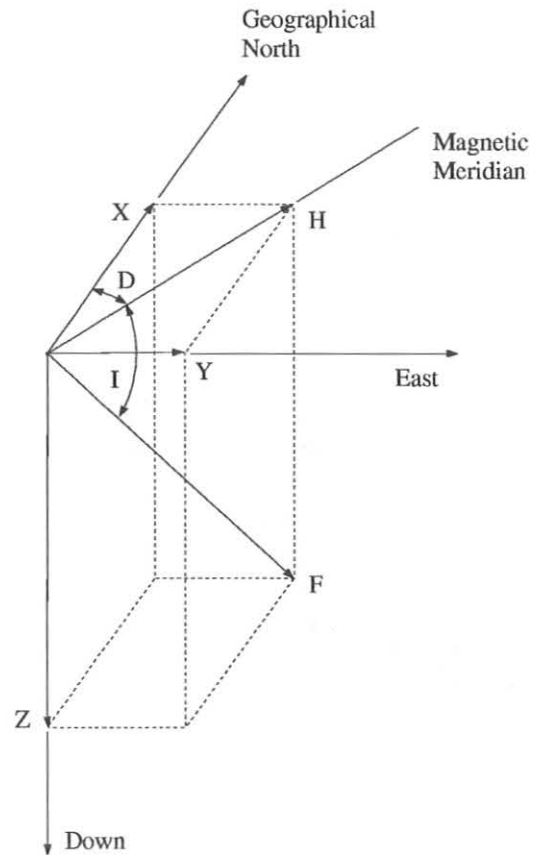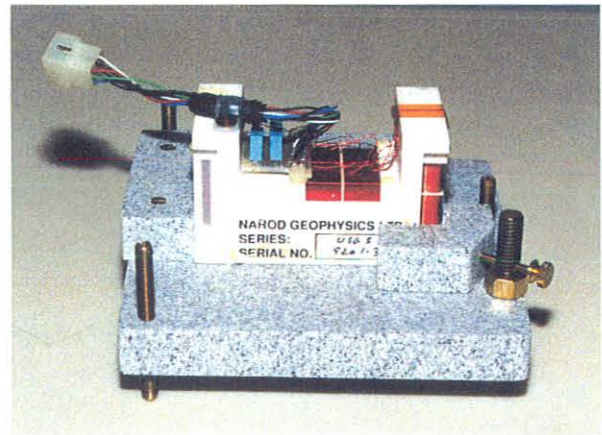

Fig. 4. A tri-axial fluxgate sensor of the type used to measure magnetic field variations at Barrow.
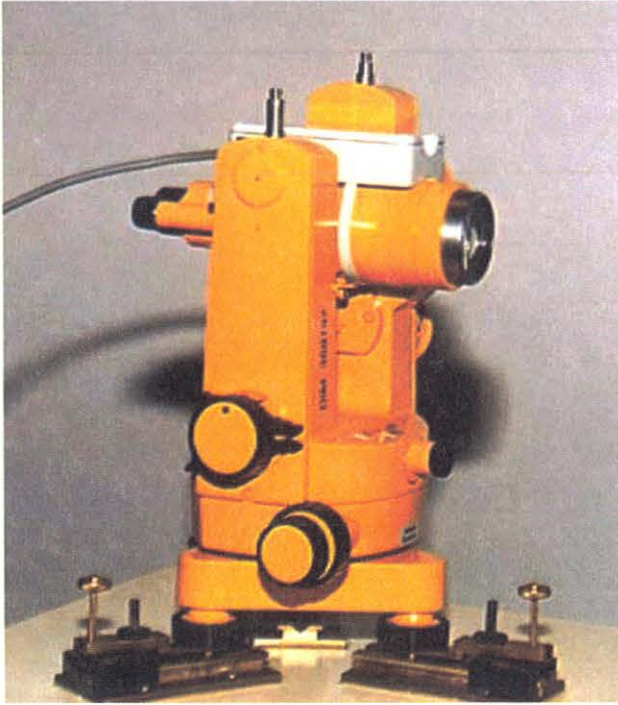
167

Fig. 5. A declination-inclination magnetometer of the type used to measure the absolute magnetic field direction.

drilled to a depth below the active permafrost layer, and a long wooden post is then frozen into place during the wintertime. The post is packed around with insulating Styrofoam. The top part of the post is encased in a concrete jacket, which uses Styrofoam pellets and vermiculite as the aggregate. This concrete is a thermal insulator but retains enough strength to achieve stability. The surface around the pier is covered with rigid foam insulation to insulate the ground from the building.
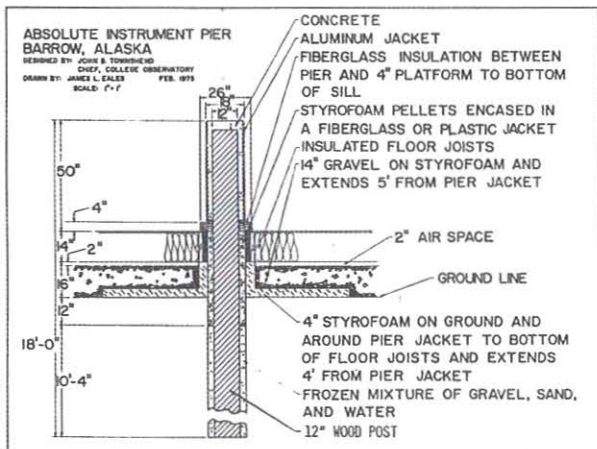

Fig. 6. The design of the absolute pier used at Barrow.

MAGNETIC DATA: EXAMPLES AND USES

Data from Barrow are transmitted via a combination of satellite and ground links to the USGS Geomagnetism Group, which is part of the Central Region Geologic Hazards Team headquartered in Golden, Colorado. Near-real-time data from Barrow, together with similar data from the group's other observatories, are forwarded by the USGS to the NOAA Space Environment Center (SEC) and to the U.S. Air Force for use to forecast space-weather phenomena. Final processed data from Barrow, and the other 13 USGS observatories, are sent to NOAA to be archived, and they are also distributed on Intermagnet CDs.

During magnetic storms, data recorded at Barrow display a high level of activity compared with data from observatories at lower latitudes. As an example, data recorded during the so-called "great" magnetic storm of March 1989 are shown in Figure 7. This storm induced currents in power grids, thereby causing system-wide power blackouts in Quebec, power equipment problems in the northeastern United States, radio communication blackouts, and increased satellite drag that actually altered the orbits of a number of satellites [*Joselyn*, 1989]. The sharp, sudden onset of magnetic field variation in the beginning of March 13 is the result of a large mass ejected 2 days earlier from the surface of the Sun (Figure 7).

The higher level of activity seen at Barrow is caused by magnetic fields sustained by the auroral electrojet (AE). As illustrated in Figure 1, with an enhancement of the solar wind caused by ejection of charged particles from the Sun's surface and a coupling of the solar and geomagnetic fields, energy stored in the magnetosphere is released as an electric current. This current flows into the ionosphere near the geomagnetic poles and drives the auroral electrojet, a symptom of which are the bright auroras seen during magnetic storms. Barrow is one of 12 high-latitude magnetic observatories that provide magnetic data to compute the AE index, a simple measure of the auroral electrojet intensity [*Parkinson*, 1983; *McPherron*, 1995]. Near-real-time and historical values of AE can be obtained from the World Data Center at Kyushu University, Japan.

Long-term averages of the magnetic data can be used to study the dynamic processes operating in the Earth's liquid iron outer core, which is the site of the dynamo that sustains the main part of the geomagnetic field. With annual means of magnetic data it is possible to observe the slow drift in the field that results from fluid motion in the core. Figure 8 shows the change in the declination, inclination, and intensity at Barrow since the observatory was opened in 1949. Ultimately, the data from Barrow and other observatories are used to generate maps and models of the Earth's magnetic field, such as the International Geomagnetic Reference Field [*Macmillan and Quinn*, 2000].

CONCLUSION

The USGS Geomagnetism Group is working to upgrade the facilities at Barrow so that measurements are made with better precision and finer temporal resolution. Data transmission capabilities are being upgraded so that the data can be distributed in real time with improved reliability. All
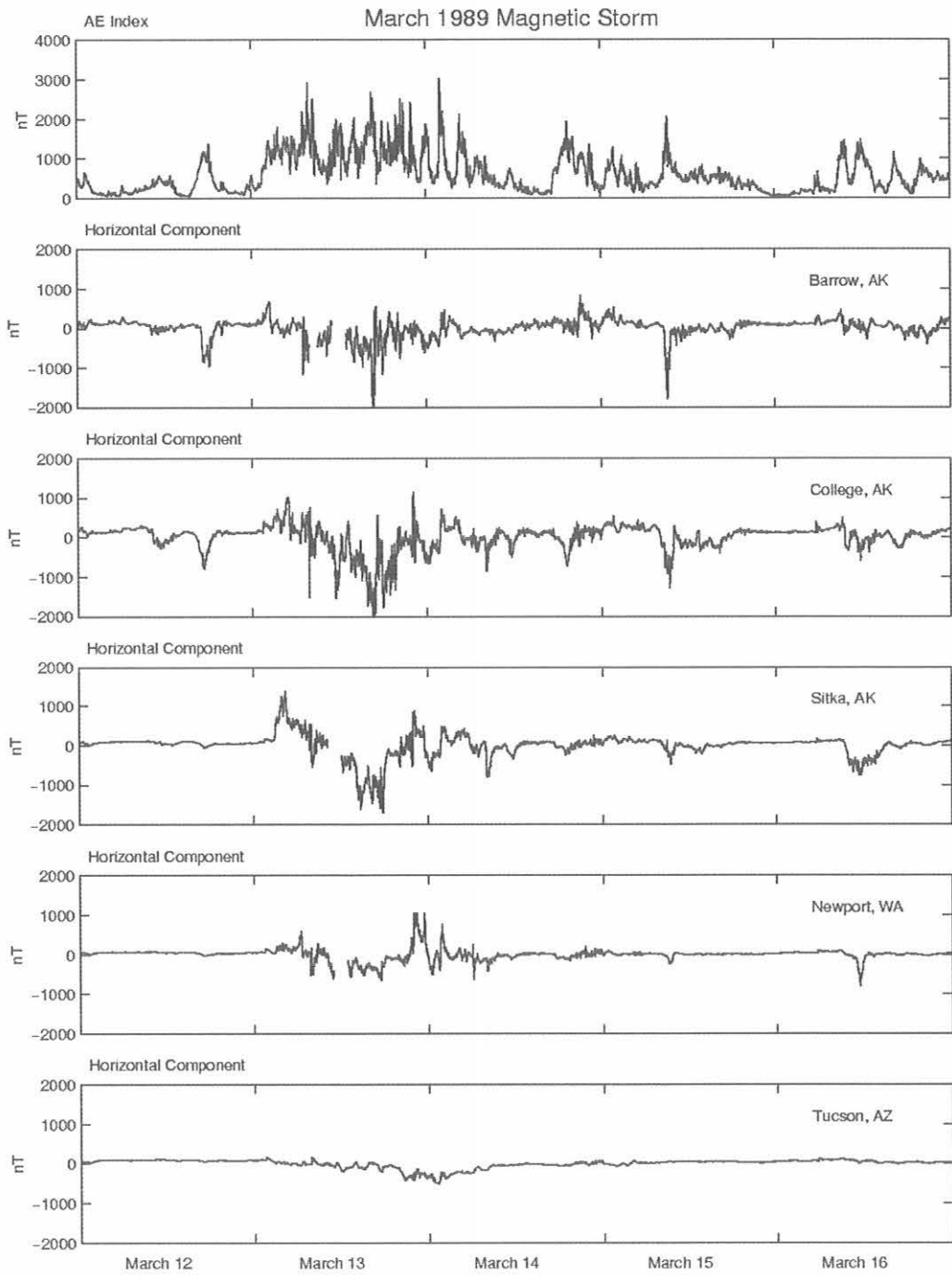
Fig. 7. Measurements made during the "great storm" of March 1989. The top panel is the AE index, which measures auroral electrojet current; below are the horizontal magnetic fields as measured at five different USGS magnetic observatories.
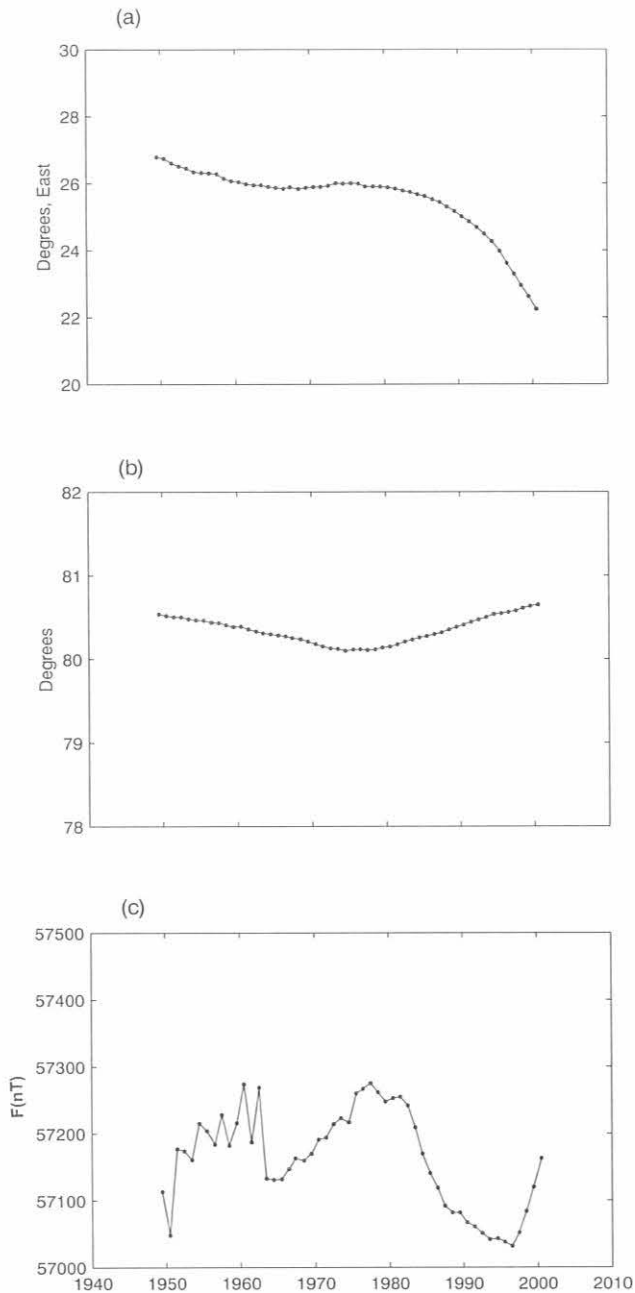
Fig. 8. Field components at Barrow from 1949 to present: (a) declination angle, (b) inclination angle, and (c) intensity as measured in nanoTeslas (nT). Reduction in the scatter seen in the field intensity after 1962 reflects an instrument upgrade.

these efforts will enhance the scientific and societal relevance of the USGS Barrow Geomagnetic Observatory.

REFERENCES

Bloxham, J., and D. Gubbins, The evolution of the Earth's magnetic field, *Sci. Am., 260,* 68-75, 1989.

Burch, J.L., The fury of space storms, *Sci. Am., 284,* 86-94, 2001.

Busse, F.H., Magnetohydrodynamics of the Earth's core, *Ann. Rev. Earth Planet. Sci., 11,* 241-268, 1983.

Courtillot, V., and J.L. LeMouel, Time variations of the Earth's magnetic field: From daily to secular, *Ann. Rev. Earth Planet. Sci., 16,* 389-476, 1988.

Cowley, T.G., The Earth's magnetosphere: A brief beginner's guide, *Eos, Trans. AGU, 76,* 525-529, 1995.

Dooling, D., Stormy weather in space, *IEEE Spectrum, 32,* 64-72, 1995.

Feynman, J., and S.B. Gabriel, On space weather consequences and predictions, *J. Geophys. Res., 105,* 10,543-10,564, 2000.

Gonzales, W.D., J.A. Joselyn, Y. Kamide, H.W. Kroehl, G. Rostoker, B.T. Tsurutani, and V.M. Vasyliunas, What is a geomagnetic storm?, *J. Geophys. Res., 99,* 5771-5792, 1994.

Jackson, A., A.R.T. Jonkers, and A. Murray, Past attractions, *Astron. Geophys., 38,* 10-16, 1997.

Joselyn, J., Case study of the great geomagnetic storm of 13 March 1989, paper AAS 89-418 presented at AAS/AIAA Astrodynamics Specialist Conf., Stowe, VT, August 1989.

Love, J.J., Reversals and excursions of the geodynamo, *Astron. Geophys., 40,* 6.14-6.19, 1999.

Macmillan, S., and J.M. Quinn, The 2000 revision of the joint UK/US geomagnetic field models and an IGRF 2000 candidate model, *Earth Planets Space, 52,* 1149-1162, 2000.

Maynard, N.C., Space weather prediction, *Rev. Geophys., Part 1 Suppl. 33,* 547-557, 1995.

McPherron, R.L., Magnetospheric dynamics, in *Introduction to Space Physics,* edited by M.G. Kivelson and C.T. Russell, pp. 400-458, Cambridge University Press, Cambridge, UK, 1995.

Nordwall, B.D., Natural hazards threaten milsats, *Aviat. Week Space Technol., 150,* 59-60, 1999.

Parkinson, W.D., *Introduction to Geomagnetism,* 433 pp., Scottish Academic Press, Edinburgh, 1983.

Russell, C.T., The magnetosphere, *Ann. Rev. Earth Planet. Sci., 19,* 169-182, 1991.

Scott, W.B., Operators place high value on space weather forecasting, *Aviat. Week Space Technol., 147,* 54-55, 1997.

Shea, M.A., and D.F. Smart, Space weather: The effects on operations in space, *Adv. Space Res., 22,* 29-38, 1998.

Townshend, J.B., Fifty years of monitoring geophysical data at Barrow, Alaska, in *Fifty More Years Below Zero,* edited by D.W. Norton, pp. 61-64, Univ. of Alaska, Fairbanks, 2001.

UAF-Frontier Snowfall/Blowing Snow Observations at CMDL, Barrow: Preliminary Result for 2001

DAQING YANG
Water and Environmental Research Center, University of Alaska, Fairbanks 99775

KONOSUKE SUGIURA
Frontier Observational Research System for Global Change, Tokyo 105-0013, Japan

TETSUO OHATA
Institute of Low Temperature Science, Hokkaido University, Sapporo, Japan

BACKGROUND

Systematic errors caused by wind-induced undercatch, wetting, and evaporation losses in precipitation measurement have long been recognized as affecting all types of precipitation gauges. The need to correct these biases, especially for solid precipitation measurement, has now been more widely acknowledged, as the magnitude of the errors and their variation among gauges have become known and their potential effects on regional, national, and global climatological, hydrological, and climate change studies have been recognized.

To assess the national methods of measuring solid precipitation, the World Meteorological Organization (WMO) initiated the Solid Precipitation Measurement Intercomparison Project in 1985. Thirteen countries participated in this project, and the experiments were conducted at 20 selected sites in these countries from 1986 to 1993. Methods of bias correction have been developed for many national precipitation gauges commonly used in the northern hemisphere [*Yang et al.,* 1995, 1998a, 1999, 2000; *Goodison et al.,* 1998]. Test implementations of the WMO correction procedures have been made to the archived precipitation data in some regions/countries [*Metcalfe and Goodison,* 1993; *Førland et al.,* 1996; *Yang et al.,* 1998b]. The bias corrections have increased the winter and annual precipitation amounts by up to 50-100% in the high-latitude regions. These results clearly show that precipitation amounts in these regions are much higher than previously reported. This points to a need to review our understanding of freshwater balance and the assessment of atmospheric model performance in the Arctic regions.

The Arctic climate is characterized by low temperature, generally low precipitation, and high winds. Arctic precipitation events generally produce small amounts, but they occur frequently and often with blowing snow. Because of the special conditions in the Arctic, the systematic errors of gauge-measured precipitation and factors such as wind-induced undercatch, evaporation, and wetting losses, underestimates caused by not accounting for trace amounts of precipitation and over/under measurement because of blowing snow are enhanced and need special attention. This issue has been a consideration in World Climate Research Program (WCRP) projects. For instance, the WCRP/Arctic Climate System Study (ACSYS) program concludes that correction of gauge precipitation observations is a major issue with respect to solid precipitation in the polar regions and that this issue is particularly relevant to studies of the freshwater cycle in the Arctic region being undertaken in ACSYS and Global Energy and Water Cycle Experiment (GEWEX) projects, such as the GEWEX Asian Monsoon Experiment (GAME)-Siberia [*Yang and Ohata,* 2001] and the Mackenzie Basin GEWEX Study (MAGS).

The review of the WMO Intercomparison results by the WCRP/ACSYS project concluded that although the results of the WMO Solid Precipitation Measurement Intercomparison have not been fully tested in Arctic conditions, the general principles and the results from the WMO project can serve as a guide for developing correction procedures for Arctic precipitation data. It is recommended that an intercomparison experiment be conducted to further test the national precipitation gauges commonly used in Arctic regions and to evaluate the existing bias correction procedures.

Recognizing the importance of the precipitation data quality to cold-region hydrological and climatic investigations, the Japan Frontier Research System for Global Change and the Water and Environmental Research Center (WERC), University of Alaska, Fairbanks (UAF), have collaboratively undertaken a gauge intercomparison experiment and blowing/drifting snow observation study at the Barrow, Alaska, CMDL research laboratory. The goals of this research are to (1) review the existing bias-correction procedures that have been developed in gauge intercomparison experiments and that may be suitable for high latitude regions; and (2) test and evaluate the applicability of the WMO bias-correction methods in polar regions of high winds with blowing/drifting snow conditions.

SITE AND INSTRUMENTATION

This study was carried out at the CMDL Barrow site. In February and September 2001, several precipitation gauges were installed for intercomparison. These include reference gauges and various national standard gauges commonly used in the Arctic regions:

- Double fence intercomparison reference (DFIR) at 2.5 m; WMO reference (Figure 1).
- Wyoming snow fence system at 2.5 m; U.S. reference gauge for snowfall observations (Figure 2).
- NOAA-ETI gauge at 1 m.
- Hellmann gauge at 2 m; standard gauge for Greenland, Denmark, and Germany.

Fig. 1. WMO double fence intercomparison reference (DFIR).

Fi.g. 2. U.S. Wyoming snow fence.

- Russian Tretyakov gauge at 2 m; Russian standard gauge, also used in Mongolia and other countries.
- U.S. National Weather Service (NWS) 8-in (20-cm) nonrecording gauge at 2 m; U.S. standard gauge, widely used in other countries.

An automatic weather station for blowing/drifting snow observations in winter months was set up to investigate blowing snow mass fluxes as functions of wind speed, air temperature, and height, and to evaluate their impact on gauge snowfall observations.

DATA ANALYSIS AND PRELIMINARY RESULTS

Data analysis follows the guidelines established in the WMO Solid Precipitation Measurement Intercomparison Project, with a focus on defining mean catch ratio of gauges and the relation of gauge catch as a function of wind speed and air temperature.

Up to December 2001, 31 precipitation events, i.e., 3 rainfall cases and 28 snowfall cases, have been collected. The event total precipitation amounts measured range from trace (when the gauges registered zero amount of precipitation) up to 40 mm. These event data sometimes were the total accumulation of several precipitation events, because the gauges were emptied irregularly. The data also include a few cases of blowing-snow events during high wind conditions.

Preliminary analysis of collected data shows that the mean catches of the gauges relative to the DFIR for snowfall observations were about 90% for the Wyoming snow fence, 59% for the Tretyakov gauge, 24% for the U.S. 8-in gauge, and 27% for the Hellmann gauge (Figure 3). These mean catches are close to the results for similar testing environments of the WMO gauge intercomparison experiments. For instance, the catch ratios of the Wyoming fence to the DFIR were 89% and 87% at Regina and Valdai, respectively. The mean catch of snowfall for the U.S. 8-in gauge at Valdai was 44% [*Yang et al.*, 1998a]. For the Tretyakov and Hellmann gauges, the mean catch of snowfall was reported to be 63-65% and 43-50%, respectively, at the northern test sites of the WMO experiment [*Yang et al.*, 1995, 1999].

FUTURE WORK

Continued intercomparison data need to be collected at Barrow in the next few winter seasons. A comprehensive data set will enable us to carry out (1) compatible analysis with the WMO intercomparison data sets, (2) analysis of the catch ratio versus wind speed/temperature, and (3) assessment of the applicability of the WMO methods and results in the Arctic regions. In addition, the impact of blowing/drifting snow on gauge catch is another issue that needs research attention. We will develop procedures to quantify the flux of blowing snow into a snow gauge and evaluate the impact of blowing/drifting snow to bias correction of gauge-measured snowfall data in the polar regions. This work will also generate bias-corrected precipitation data sets and climatology for Barrow and northern Alaska, including seasonal/annual regional precipitation maps.
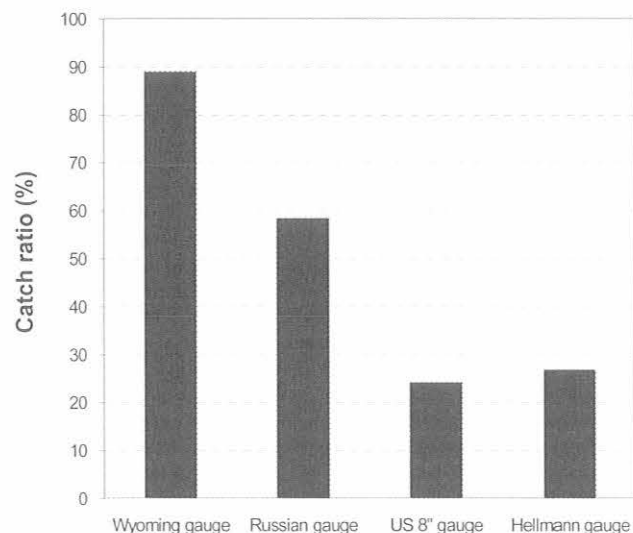
Fig. 3. Mean catch ratio of four gauges versus the DFIR, Barrow.

REFERENCES

Førland, E.J., P. Allerup, B. Dahlström, E. Elomaa, T. Jónsson, H. Madsen, J. Perälä, P. Rissanen, H. Vedin, and F. Vejen, Manual for operational correction of Nordic precipitation data, *DNMI-klima Rep. 24/96*, 66 pp., Norwegian Meteorol. Inst., Oslo, 1996.

Goodison, B.E., P.Y.T. Louie, and D. Yang, WMO solid precipitation measurement intercomparison, final report, *WMO/TD-No.872*, 212 pp., World Meteorol. Org., Geneva, 1998.

Metcalfe, J.R., and B.E. Goodison, Correction of Canadian winter precipitation data, in *Proc. Eighth Symp. On Meteorol. Observ. and Instrum.*, Anaheim, CA, Jan. 17-22, pp. 338-343, Am. Meteorol. Soc., Boston, MA, 1993.

Yang, D., and T. Ohata, A bias corrected Siberian regional precipitation climatology, *J. Hydrometeorol.*, *2*, 122-139, 2001.

Yang, D., B.E. Goodison, J.R. Metcalfe, V.S. Golubev, E. Elomaa, T. Gunther, R. Bates, T. Pangburn, C. Hanson, D. Emerson, V. Copaciu, and J. Milkovic, Accuracy of Tretyakov precipitation gauge: Result of WMO Intercomparison, *Hydrol. Proc.*, *9*, 877-895, 1995.

Yang, D., B.E. Goodison, C.S. Benson, and S. Ishida, Adjustment of daily precipitation at 10 climate stations in Alaska: Application of WMO Intercomparison results, *Water Resour. Res.*, *34*, 241-256, 1998a.

Yang, D., B.E. Goodison, J.R. Metcalfe, V.S. Golubev, R. Bates, T. Pangburn, and C.L. Hanson, Accuracy of NWS 8" standard non-recording precipitation gauge: Result and application of WMO Intercomparison, *J. Atmos. Ocean. Technol.*, *15*, 54-68, 1998b.

Yang, D., E. Elomaa, T. Gunther, V. Golubev, B.E. Goodison, B. Sevruk, H. Madsen, and J. Milkovic, Wind-induced precipitation undercatch of the Hellmann gauges, *Nordic Hydrol.*, *30*, 57-80, 1999.

Yang, D., D.L. Kane, L.D. Hinzman, B.E. Goodison, J.R. Metcalfe, P.Y.T. Louie, G.H. Leavesley, D.G. Emerson, and C.L. Hanson, An evaluation of the Wyoming gauge system for snowfall measurement, *Water Resour. Res.*, *36*, 2665-2677, 2000.

The ANSTO-CMDL Radon Program at MLO

W. Zahorowski and S. Chambers

Australian Nuclear Science and Technology Organisation, Menai, NSW 2234, Australia

Paul Fukumura-Sawada

NOAA Mauna Loa Observatory, Hilo, Hawaii 96720

The ability to predict the impact of rapid development in the Asian Pacific region on climate is dependent upon an improved scientific understanding of the radiative forcing of aerosols and trace gases, as well as the efficient implementation of these processes in regional and global climate models. Finding suitable tools to evaluate the performance of transport, mixing, and chemical processes within such models is challenging.

The well-defined source and sink pathways of radon-222 make it an ideal tracer of atmospheric dynamics. Its origins are almost exclusively terrestrial, and because it is a noble gas that does not react chemically with other species, its predominant sink is by radioactive decay. The half-life of radon (3.81 days) is comparable with the lifetimes of short-lived atmospheric pollutants (e.g., NO_x, SO_2, CO, and O_3) and residence times of water and aerosols. This time scale is also comparable with many important aspects of atmospheric dynamics, making radon a useful tracer at local, regional, or global scales. This predictable behavior means measurements of radon concentration are sufficient to indicate whether an air mass has been in contact with land in the past several weeks. Consequently, the simulation of radon transport is currently one of the best evaluation tools for transport schemes in regional and global circulation models. Subgrid mixing processes also cause significant changes in radon concentrations. Thus comparisons between observed and modeled radon concentrations can be used to improve local mixing schemes. Changes in radon concentration can be measured with high precision and temporal resolution at permanent stations and on board ships with automated detectors.

The last decade witnessed the first serious attempts to model radon concentrations on global and regional scales and to compare the modeled results with observations. The purpose of radon simulations varied; some were aimed at the development or validation of subgrid mixing schemes and indication of regions associated with largest uncertainties [e.g., *Jacob and Prather*, 1990; *Stockwell et al.*, 1998], others at the intercomparison of models [e.g., *Genthon and Armengaud*, 1995] or the comparison of different meteorological input data sets [e.g., *Mahowald et al.*, 1997]. In general, a better understanding of the key atmospheric features that control transport, mixing, and distribution of radon has been sought by detailed comparisons of modeled radon time series and vertical profiles with the best radon data sets available [e.g., *Mahowald et al.*, 1997; *Stockwell et al.*, 1998; *Dentener et al.*, 1999]. *Dentener et al.* [1999] contrasted the modeled data for MLO with those from other surface baseline stations including Cape Grim, Tasmania, and Kerguelen, Crozet, and Amsterdam Islands, all in the Indian Ocean.

A first comprehensive evaluation and intercomparison of global atmospheric transport models using radon time series was published in 1997 [*Jacob et al.*, 1997]. The intercomparison, sponsored by the World Climate Research Program (WCRP), evaluated and compared convective and synoptic processes in 20 models. Results were compared with the observed mean radon concentrations.

Consequently, at MLO the focus remains on two uses for radon data: (1) as one of the selection criteria of baseline air samples, because it provides a quantitative, continuous measure of the influence of the Asian continent on air samples at MLO, and (2) as a tracer to test the accuracy of global-scale atmospheric transport models.

The present detection system was first launched in 1994 and has been improved in recent years. The fundamental characteristics of the instrumentation are included in *Summary Report No. 23* [*Hofmann et al.*, 1996]. A thorough discussion of the principle of operation of the radon detector can be found in *Whittlestone and Zahorowski* [1998]. It is pertinent to note that the lower limit of detection for the radon detector currently deployed at MLO (20 mBq m^{-3}) matches the lowest radon concentration reported for oceanic air.

The only instrument problem for this period (1989-present) is an apparent reduction in air sampling rate from late October 2000 until April 2001. Evidence from other equipment indicates that this was simply due to a faulty flow meter. The problem was subsequently rectified by installation of a new flow meter.

Most recently the MLO data recorded during the first Asian Pacific Regional Aerosol Characterization Experiment (ACE-Asia) Intensive Operation Period (IOP) (April–May 2001) were combined with corresponding time-series data from observations at two ACE-Asia surface stations: Kosan (Cheju Island, South Korea) and Hok Tsui (Hong Kong). The combined set is intended to be used in a model intercomparison exercise of two global chemical transport models in support of the IOP.

Data for the reported period may be obtained by contacting Wlodek Zahorowski (wlodek.zahorowski @ansto.gov.au).

References

Dentener, F., J. Feichter, and A. Jeuken, Simulation of the transport of Rn[222] using on-line and off-line global models at different horizontal resolutions: A detailed comparison with measurements, *Tellus, 51B*, 573-602, 1999.

Genthon, C., and A. Armengaud, Radon 222 as a comparative tracer of transport and mixing in two general circulation models of the atmosphere, *J. Geophys. Res., 100*, 2849-2866, 1995.

Hofmann, D.J., J.T. Peterson, and R.M. Rosson (Eds.), *Climate Monitoring and Diagnostics Laboratory No. 23 Summary Report 1994-1995*, 161 pp., NOAA Environ. Res. Labs., Boulder, CO, 1996.

Jacob, D., and M. Prather, Radon-222 as a test of convective transport in a general circulation model, *Tellus, 42B*, 118-134, 1990.

Jacob, D.J., et al., Evaluation of intercomparison of global atmospheric transport models using ^{222}Rn and other short-lived tracers, *J. Geophys. Res., 102*, 5953-5970, 1997.

Mahowald, N.M., P.J. Rasch, B.E. Eaton, S. Whittlestone, and R.G. Prinn, Transport of ^{222}radon to the remote troposphere using the Model of Atmospheric Transport and Chemistry and assimilated winds from ECMWF and the National Center for Environmental Prediction/NCAR, *J. Geophys. Res., 102*, 28,139-28,151, 1997.

Stockwell, D.Z., M.A. Kritz, M.P. Chippperfield, and J.A. Pyle, Validation of an off-line three-dimensional chemical transport model using observed radon profiles, 2, Model results, *J. Geophys. Res., 103*, 8433-8445, 1998.

Whittlestone, S., and W. Zahorowski, Baseline radon detectors for shipboard use: Development and deployment in the First Aerosol Characterization Experiment (ACE 1), *J. Geophys. Res., 103*, 16,743-16,751, 1998.

7. Publications by CMDL Staff, 2000-2001

Bakwin, P.S., Carbon cycle, in *Plant Sciences*, vol. 1, edited by R. Robinson, pp. 122-126, Macmillan Reference USA, NY, 2001.

Barnes, J.E., and D.J. Hofmann, Variability in the stratospheric background aerosol over Mauna Loa Observatory, *Geophys. Res. Lett., 28(15),* 2895-2898, 2001.

Battle, M., M.L. Bender, P.P. Tans, J.W.C. White, J.T. Ellis, T. Conway, and R.J. Francey, Global carbon sinks and their variability inferred from atmospheric O_2 and $\delta^{13}C$, *Science, 287,* 2467-2470, 2000.

Bell, G.D., M.S. Halpert, R.C. Schnell, R.W. Higgins, J. Lawrimore, V.E. Kousky, R. Tinker, W. Thiaw, M. Chelliah, and A. Artusa, Climate Assessment for 1999, *Bull. Am. Meteorol. Soc., 81(6),* pp. S1- S50, 2000.

Berger, B.W., K.J. Davis, C. Yi, P.S. Bakwin, and C.L. Zhao, Long-term carbon dioxide fluxes from a very tall tower in a northern forest: Flux measurement methodology, *J. Atmos. Oceanic Technol., 18,* 529-542, 2001.

Bergin, M.H., S.E. Schwartz, R.N. Halthore, J.A. Ogren, and D.L. Hlavka, Comparison of aerosol optical depth inferred from surface measurements with that determined by sun photometry for cloud-free conditions at a continental U.S. site, *J. Geophys. Res., 105,* 6807-6816, 2000.

Bousquet, P., P. Peylin, P. Ciais, C. LeQuéré, P. Friedlingstein, and P. Tans, Regional changes in carbon dioxide fluxes of land and oceans since 1980, *Science, 290,* 1342-1346, 2000.

Bowling, D.R., P.P. Tans, and R.K. Monson, Partitioning net ecosystem carbon exchange with isotopic fluxes of CO_2, *Global Change Biol., 7,* 127-145, 2001.

Bruhwiler, L.P., P. Tans, and M. Ramonet, A time-dependent assimilation and source retrieval technique for atmospheric tracers, in *Inverse Methods in Global Biogeochemical Cycles,* edited by P. Kasibhatla, M. Heimann, P. Rayner, N. Mahowald, R.G. Prinn, and D.E. Hartley, *Geophys. Monogr. 114,* pp. 265-277, Am. Geophys. Union, Washington, DC, 2000.

Butler, J.H., Methyl bromide: An introduction to its use, its impacts, and its future, *IGAC Activities Newsl., 19,* p. 8, Int. Global Atmos. Chem. Proj., Cambridge, MA, 2000.

Carrico, C.M., M.J. Rood, J.A. Ogren, C. Neusub, A. Wiedensohler, and J. Heintzenberg, Aerosol optical properties at Sagres, Portugal, during ACE-2, *Tellus, 52B,* 694-715, 2000.

Chan, L.Y., C.Y. Chan, H.Y. Liu, S. Christopher, S.J. Oltmans, and J.M. Harris, A case study on the biomass burning in Southeast Asia and enhancement of tropospheric ozone over Hong Kong, *Geophys. Res. Lett., 27(10),* 1479-1482, 2000.

Chan, C.Y., L.Y. Chan, Y.G. Zheng, J.M. Harris, S.J. Oltmans, and S. Christopher, Effects of 1997 Indonesian forest fires on tropospheric ozone enhancement, radiative forcing, and temperature change over the Hong Kong region, *J. Geophys. Res., 106(D14),* 14,875-14,885, 2001.

Chung, Y.S., and P.P. Tans, Monitoring greenhouse gases at Tae-Ahn Peninsula, Korea, *J. Korean Meteorol. Soc., 36,* 25-34, 2000.

Cohen, R.C., K.K. Perkins, L.C. Koch, R.M. Stimpfle, P.O. Wennberg, T.F. Hanisco, E.J. Lanzendorf, G.P. Bonne, P.B Voss, R.J. Salawitch, L.A. Del Negro, J.C. Wilson, C.T. McElroy, and T.P. Bui, Quantitative constraints on the atmospheric chemistry of nitrogen oxides: An analysis along chemical coordinates, *J. Geophys. Res., 105(D19),* 24,283-24,304, 2000.

Cooper, O.R., J.L. Moody, D.D. Parrish, M. Trainer, T.B Ryerson, J.S. Holloway, G. Hübler, F.C. Fehsenfeld, S.J. Oltmans, and M.J. Evans, Trace gas signatures of the airstreams within North Atlantic cyclones: Case studies from the North Atlantic Regional Experiment (NARE '97) aircraft intensive, *J. Geophys. Res., 106(D6),* 5437-5456, 2001.

Crawford, J.H., D.D. Davis, G. Chen, M. Buhr, S. Oltmans, R. Weller, L. Mauldin, F. Eisele, R. Shetter, B. Lefer, R. Arimoto, and A. Hogan, Evidence for photochemical production of ozone at the South Pole surface, *Geophys. Res. Lett., 28(19),* 3641-3644, 2001.

Delene, D.J., and T. Deshler, Calibration of a photometric cloud condensation nucleus counter designed for deployment on a balloon package, *J. Atmos. Oceanic Technol., 17,* 459-467, 2000.

Dlugokencky, E.J., B.P. Walter, K.A. Masarie, P.M. Lang, and E.S. Kasischke, Measurements of an anomalous global methane increase during 1998, *J. Geophys. Res., 28(3),* 499-502, 2001.

Dutton, E.G., and B.A. Bodhaine, Solar irradiance anomalies caused by clear-sky transmission variations above Mauna Loa: 1958-99, *J. Clim., 14,* 3255-3265, 2001.

Dutton, E.G., J.J. Michalsky, T. Stoffel, B.W. Forgan, J. Hickey, D.W. Nelson, T.L. Alberta, and I. Reda, Measurement of broadband diffuse solar irradiance using current commercial instrumentation with a correction for thermal offset errors, *J. Atmos. Oceanic Technol., 18,* 297-314, 2001.

Elkins, J.W., F.L. Moore, and E.S. Kline, Next generation airborne gas chromatograph for NASA airborne platforms, *Proc., Earth Science Technol. Conf. 2001,* College Park, MD, August 28-30, 2001 [*CD ROM NP-2001-8-338-GSFC*], pp. 356-363, NASA Earth Sci. Technol. Off., 2001.

Eluszkiewicz, J., R.S. Hemler, J.D. Mahlman, L. Bruhwiler, and L.L. Takacs, Sensitivity of age-of-air calculations to the choice of advection scheme, *J. Atmos. Sci., 57(19),* 3185-3201, 2000.

Fahey, D.W., R.S. Gao, K.S. Carslaw, J. Kettleborough, P.J. Popp, M.J. Northway, J.C. Holecek, S.C. Ciciora, R.J. McLaughlin, T.L. Thompson, R.H. Winker, D.B. Baumgardner, B. Gandrud, P.O. Wennberg, S. Dhaniyala, K. McKinney, T. Peter, R.J. Salawitch, T.P. Bui, J.W. Elkins, C.R. Webster, E.L. Atlas, H. Jost, J.C. Wilson, R.L. Herman, A. Kleinböhl, and M. von König, The detection of large HNO_3-containing particles in the winter Arctic stratosphere, *Science, 291,* 1026-1031, 2001.

Folkins, I., S.J. Oltmans, and A.M. Thompson, Tropical convective outflow and near surface equivalent potential temperatures, *Geophys. Res. Lett., 27(16),* 2549-2552, 2000.

Fujiwara, M., F. Hasebe, M. Shiotani, N. Nishi, H. Vömel, and S.J. Oltmans, Water vapor control at the tropopause by equatorial Kelvin waves observed over the Galápagos, *Geophys. Res. Lett., 28(16),* 3143-3146, 2001.

Gao, R.S., E.C. Richard, P.J. Popp, G.C. Toon, D.F. Hurst, P.A. Newman, J.C. Holecek, M.J. Northway, D.W. Fahey, M.Y.

Danilin, B. Sen, K. Aikin, P.A. Romashkin, J.W. Elkins, C.R. Webster, S.M. Schauffler, J.B. Greenblatt, C.T. McElroy, L.R. Lait, T.P. Bui, and D. Baumgardner, Observational evidence for the role of denitrification in Arctic stratospheric ozone loss, *Geophys. Res. Lett.*, *28(15)*, 2879-2882, 2001.

Gloor, M., P. Bakwin, D. Hurst, L. Lock, R. Draxler, and P. Tans, What is the concentration footprint of a tall tower?, *J. Geophys. Res.*, *106(D16)*, 17,831-17,840, 2001.

Harris, J.M., E.J. Dlugokencky, S.J. Oltmans, P.P. Tans, T.J. Conway, P.C. Novelli, K.W. Thoning, and J.D.W. Kahl, An interpretation of trace gas correlations during Barrow, Alaska, winter dark periods, 1986-1997, *J. Geophys. Res.*, *105(D13)*, 17,267-17,278, 2000.

Harris, J.M., S.J. Oltmans, P.P. Tans, R.D. Evans, and D.L. Quincy, A new method for describing long-term changes in total ozone, *Geophys. Res. Lett.*, *28(24)*, 4535-4538, 2001.

Haszpra, L., Z. Barcza, P.S. Bakwin, B.W. Berger, K.J. Davis, and T. Weidinger, Measuring system for the long-term monitoring of biosphere/atmosphere exchange of carbon dioxide, *J. Geophys. Res.*, *106(D3)*, 3057-3069, 2001.

Houweling, S., F. Dentener, J. Lelieveld, B. Walter, and E. Dlugokencky, The modeling of tropospheric methane: How well can point measurements be reproduced by a global model?, *J. Geophys. Res.*, *105(D7)*, 8981-9002, 2000.

Hurst, D.F., G.S. Dutton, P.A. Romashkin, J.W. Elkins, R.L. Herman, E.J. Moyer, D.C. Scott, R.D. May, C.R. Webster, J. Grecu, M. Loewenstein, and J.R. Podolske, Comparison of in situ N_2O and CH_4 measurements in the upper troposphere and lower stratosphere during STRAT and POLARIS, *J. Geophys. Res.*, *105(D15)*, 19,811-19,822, 2000.

Kim, J., S.-N. Oh, H.-M. Cho, M.-K. Park, K.-R. Kim, and J.W. Elkins, Background monitoring and long-range transport of atmospheric CFC-11 and CFC-12 at Kosan, Korea, *Environ. Monitor. Assess.*, *70*, 47-56, 2001.

King, D.B., J.H. Butler, S.A. Montzka, S.A. Yvon-Lewis, and J.W. Elkins, Implications of methyl bromide supersaturations in the temperate North Atlantic Ocean, *J. Geophys. Res.*, *105(D15)*, 19,763-19,769, 2000.

Koloutsou-Vakakis, S., C.M. Carrico, P. Kus, M.J. Rood, Z. Li, R. Shrestha, J.A. Ogren, J.C. Chow, and J.G. Watson, Aerosol properties at a midlatitude Northern Hemisphere continental site, *J. Geophys. Res.*, *106(D3)*, 3019-3032, 2001.

Kuck, L.R., T. Smith Jr., B.B. Balsley, D. Helmig, T.J. Conway, P.P. Tans, K. Davis, M.L. Jensen, J.A. Bognar, R.V. Arrieta, R. Rodriques, and J.W. Birks, Measurements of landscape-scale fluxes of carbon dioxide in the Peruvian Amazon by vertical profiling through the atmospheric boundary layer, *J. Geophys. Res. 105*, 22,137-22,146, 2000.

Lawrimore, J., M.S. Halpert, G.D. Bell, M.J. Menne, B. Lyon, R.C. Schnell, K.L. Gleason, D.R. Easterling, W. Thiaw, W.J. Wright, R.R. Heim Jr., D.A. Robinson, and L. Alexander, Climate Assessment for 2000, *Bull. Am. Meteorol. Soc.*, *82(6)*, S1-S55, 2001.

Lee, A.M., H.K. Roscoe, and S. Oltmans, Model and measurements show Antarctic ozone loss follows edge of polar night, *Geophys. Res. Lett.*, *27(22)*, 3845-3848, 2000.

Lefohn, A.S., S.J. Oltmans, T. Dann, and H.B. Singh, Present-day variability of background ozone in the lower troposphere, *J. Geophys. Res.*, *106(D9)*, 9945-9958, 2001.

Lelieveld, J., P.J. Crutzen, V. Ramanathan, M.O. Andreae, C.A.M. Brenninkmeijer, T. Campos, G.R. Cass, R.R. Dickerson, H. Fischer, J.A. de Gouw, A. Hansel, A. Jefferson, D. Kley, A.T.J. de Laat, S. Lal, M.G. Lawrence, J.M. Lobert, O.L. Mayol-Bracero, A.P. Mitra, T. Novakov, S.J. Oltmans, K.A. Prather, T. Reiner, H. Rodhe, H.A. Scheeren, D. Sikka, and J. Williams, The Indian Ocean Experiment: Widespread air pollution from South and Southeast Asia, *Science, 291*, 1031-1036, 2001.

Masarie, K.A., R.L. Langenfelds, C.E. Allison, T.J. Conway, E.J. Dlugokencky, R.J. Francey, P.C. Novelli, L.P. Steele, P.P. Tans, B. Vaughn, and J.W.C. White, NOAA/CSIRO flask air intercomparison experiment: A strategy for directly assessing consistency among atmospheric measurements made by independent laboratories, *J. Geophys. Res.*, *106(D17)*, 20,445-20,464, 2001.

McKenzie, R.L., P.V. Johnston, D. Smale, B.A. Bodhaine, and S. Madronich, Altitude effects on UV spectral irradiance deduced from measurements at Lauder, New Zealand, and at Mauna Loa Observatory, Hawaii, *J. Geophys. Res.*, *106*, 22,845-22,860, 2001.

Miloshevich, L.M., H. Vömel, A. Paukkunen, A.J. Heymsfield, and S.J. Oltmans, Characterization and correction of relative humidity measurements from Vaisala RS80-A radiosondes at cold temperatures, *J. Atmos. Oceanic Technol.*, *18*, 135-156, 2001.

Montzka, S.A., C.M. Spivakovsky, J.H. Butler, J.W. Elkins, L.T. Lock, and D.J. Mondeel, New observational constraints for atmospheric hydroxyl on global and hemispheric scales, *Science, 288*, 500-503, 2000.

Nagurnyi, A.P., N.A. Zaitseva, G.V. Alekseev, E.Y. Medvedchenko, A. Shumbera, J.D. Kahl, and R. Schnell, Archive of radiosonde data obtained at the ice drifting station North Pole (in Russian), *Meteorol. Hydrol.*, *6*, 55-62, 2001.

Nelson, D.W., The NOAA Climate Monitoring and Diagnostics Laboratory Solar Radiation Facility, *NOAA Tech. Memo. OAR CMDL-15*, 36 pp., NOAA Clim. Monit. and Diag. Lab., Boulder, CO, 2000.

Neuman, J.A., R.S. Gao, D.W. Fahey, J.C. Holecek, B.A Ridley, J.G. Walega, F.E. Grahek, E.C. Richard, C.T. McElroy, T.L. Thompson, J.W. Elkins, F.L. Moore, and E.A. Ray, In situ measurements of HNO_3, No_y, NO, and O_3 in the lower stratosphere and upper troposphere, *Atmos. Environ.*, *35*, 5789-5797, 2001.

Newchurch, M.J., L. Bishop, D. Cunnold, L.E. Flynn, S. Godin, S.H. Frith, L. Hood, A.J. Miller, S. Oltmans, W. Randel, G. Reinsel, R. Stolarski, R. Wang, E.-S. Yang, and J.M. Zawodny, Upper-stratospheric ozone trends 1979-1998, *J. Geophys. Res.*, *105(D11)*, 14,625-14,636, 2000.

Newman, P.A., J.C. Wilson, M.N. Ross, C.A. Brock, P.J. Sheridan, M.R. Schoeberl, L.R. Lait, T.P. Bui, M. Loewenstein, and J.R. Podolske, Chance encounter with a stratospheric kerosene rocket plume from Russia over California, *Geophys. Res. Lett.*, *28(6)*, 959-962, 2001.

Oltmans, S.J., H. Vömel, D.J. Hofmann, K.H. Rosenlof, and D. Kley, The increase in stratospheric water vapor from balloonborne, frostpoint hygrometer measurements at Washington, D.C., and Boulder, Colorado, *Geophys. Res. Lett.*, *27(21)*, 3453-3456, 2000.

Oltmans, S.J., B.J. Johnson, J.M. Harris, H. Vömel, A.M. Thompson, K. Koshy, P. Simon, R.J. Bendura, J.A. Logan, F. Hasebe, M. Shiotani, V.W.J.H. Kirchhoff, M. Maata, G. Sami, A. Samad, J. Tabuadravu, H. Enriques, M. Agama, J. Cornejo, and F. Paredes, Ozone in the Pacific tropical troposphere from

ozonesonde observations, *J. Geophys. Res., 106(D23)*, 32,503-32,525, 2001.

Peppler, R.A., C.P. Bahrmann, J.C. Barnard, J.R. Campbell, M.-D. Cheng, R.A. Ferrare, R.N. Halthore, L.A. Heilman, D.L. Hlavka, N.S. Laulainen, C.-J. Lin, J.A. Ogren, M.R. Poellot, L.A. Remer, K. Sassen, J.D. Spinhirne, M.E. Splitt, and D.D. Turner, ARM Southern Great Plains site observations of the smoke pall associated with the 1998 Central American fires, *Bull. Am. Meteorol. Soc., 18(11)*, 2563-2591, 2000.

Philipona, R., E.G. Dutton, T. Stoffel, J. Michalsky, I. Reda, A. Stifter, P. Wendling, N. Wood, S.A. Clough, E.J. Mlawer, G. Anderson, H.E. Revercomb, and T.R. Shippert, Atmospheric longwave irradiance uncertainty: Pyrgeometers compared to an absolute sky-scanning radiometer, atmospheric emitted radiance interferometer, and radiative transfer model calculations, *J. Geophys. Res., 106(D22)*, 28,129-28,141, 2001.

Polissar, A.V., P.K. Hopke, and J.M. Harris, Source regions for atmospheric aerosol measured at Barrow, Alaska, *Environ. Sci. Technol., 36(21)*, 4214-4226, 2001.

Popp, P.J., M.J. Northway, J.C. Holecek, R.S. Gao, D.W. Fahey, J.W. Elkins, D.F. Hurst, P.A. Romashkin, G.C. Toon, B. Sen, S.M. Schauffler, R.J. Salawitch, C.R. Webster, R.L. Herman, H. Jost, T.P. Bui, P.A. Newman, and L.R. Lait, Severe and extensive denitrification in the 1999-2000 Arctic winter stratosphere, *Geophys. Res. Lett., 28(15)*, 2875-2878, 2001.

Portman, R.W., S. Solomon, R.W. Sanders, J.S. Daniel, and E.G. Dutton, Cloud modulation of zenith-sky oxygen photon path lengths over Boulder, Colorado: Measurements versus model, *J. Geophys. Res., 106*, 1139-1155, 2001.

Quinn, P.K., T.S. Bates, T.L. Miller, D.J. Coffman, J.E. Johnson, J.M. Harris, J.A. Ogren, G. Forbes, T.L. Anderson, D.S. Covert, and M.J. Rood, Surface submicron aerosol chemical composition: What fraction is not sulfate?, *J. Geophys. Res., 105(D5)*, 6785-6805, 2000.

Ramanathan, V., P.J. Crutzen, J. Lelieveld, A.P. Mitra, D. Althausen, J. Anderson, M.O. Andreae, W. Cantrell, G.R. Cass, C.E. Chung, A.D. Clarke, J.A. Coakley, W.D. Collins, W.C. Conant, F. Dulac, J. Heintzenberg, A.J. Heymsfield, B. Holben, S. Howell, J. Hudson, A. Jayaraman, J.T. Kiehl, T.N. Krishnamurti, D. Lubin, G. McFarquhar, T. Novakov, J.A. Ogren, I.A. Podgorny, K. Prather, K. Priestly, J.M. Prospero, P.K. Quinn, K. Rajeev, P. Rasch, S. Rupert, R. Sadourney, S.K. Satheesh, G.E. Shaw, P. Sheridan, and F.P.J. Valero, Indian Ocean Experiment: An integrated analysis of the climate forcing and effects of the great Indo-Asian haze, *J. Geophy. Res., 106(D22)*, 28,371-28,398, 2001.

Randel, W.J., F. Wu, A. Gettelman, J.M. Russell III, J.M. Zawodny, and S.J. Oltmans, Seasonal variation of water vapor in the lower stratosphere observed in Halogen Occultation Experiment data, *J. Geophys. Res., 106(D13)*, 14,313-14,325, 2001.

Richard, E.C., K.C. Aikin, A.E. Andrews, B.C. Daube Jr., C. Gerbig, S.C. Wofsy, P.A. Romashkin, D.F. Hurst, E.A. Ray, F.L. Moore, J.W. Elkins, T. Deshler, and G.C. Toon, Severe chemical ozone loss inside the Antarctic polar vortex during winter 1999-2000 inferred from in situ airborne measurements, *Geophys. Res. Lett., 28(11)*, 2197-2200, 2001.

Romashkin, P.A., D.F. Hurst, J.W. Elkins, G.S. Dutton, D.W. Fahey, R.E. Dunn, F.L. Moore, R.C. Myers, and B.D. Hall, In situ measurements of long-lived trace gases in the lower

stratosphere by gas chromatography, *J. Atmos. Oceanic Technol., 18*, 1195-1204, 2001.

Rosenlof, K.H., S.J. Oltmans, D. Kley, J.M. Russell III, E.-W. Chiou, W.P. Chu, D.G. Johnson, K.K. Kelly, H.A. Michelsen, G.E. Nedoluha, E.E. Remsberg, G.C. Toon, and M.P. McCormick, Stratospheric water vapor increases over the past half-century, *Geophys. Res. Lett., 28(7)*, 1195-1198, 2001.

Ryan, S., Estimating volcanic CO_2 emission rates from atmospheric measurements on the slope of Mauna Loa, *Chem. Geol., 177*, 201-211, 2001.

Ryan, S.C., A.L. Dick, and L.P. Steele, Ecosystem CO_2 exchange near Cape Grim Tasmania, in *Baseline Atmospheric Program Australia 1997-98*, edited by N.W. Tindale, N. Derek, and R.J. Francey, pp. 8-19, Bureau of Meteorol. and CSIRO Atmos. Res., Melbourne, Australia, 2001.

Schnell, R.C., Global atmospheric environment change monitoring in the 21st century, *Proc. Conf. on Direction for Atmospheric Environmental Research Toward the 21st Century*, Seoul, Korea, June 2000, pp. 85-95, Natl. Inst. of Environ. Res., Incheon, Korea, 2000.

Schnell, R.C., D.B. King, and R.M. Rosson (Eds.), *Climate Monitoring and Diagnostics Laboratory Summary Report No. 25 1998-1999*, 154 pp., NOAA Oceanic and Atmos. Res., Boulder, CO, 2001.

Sheridan, P.J., D.J. Delene, and J.A. Ogren, Four years of continuous surface aerosol measurements from the Department of Energy's Atmospheric Radiation Measurement Program Southern Great Plains Cloud and Radiation Testbed site, *J. Geophys. Res., 106(D18)*, 20,735-20,747, 2001.

Spivakovsky, C.M., J.A. Logan, S.A. Montzka, Y.J. Balkanski, M. Foreman-Fowler, D.B.A. Jones, L.W. Horowitz, A.C. Fusco, C.A.M. Brenninkmeijer, M.J. Prather, S.C. Wofsy, and M.B. McElroy, Three-dimensional climatological distribution of tropospheric OH: Update and evaluation, *J. Geophys. Res., 105(D7)*, 8931-8980, 2000.

Stephens, B.B., S.C. Wofsy, R.F. Keeling, P.P. Tans, and M.J. Potosnak, The CO_2 budget and rectification airborne study: Strategies for measuring rectifiers and regional fluxes, in *Inverse Methods in Global Biogeochemical Cycles*, edited by P. Kasibhatla, M. Heimann, P. Rayner, N. Mahowald, R.G. Prinn, and D.E. Hartley, *Geophys. Monogr. 114*, pp. 311-324, Am. Geophys. Union, Washington, DC, 2000.

Stone, R.S., Climate monitoring at Barrow, Alaska, and South Pole: An overview of U.S. studies of polar surface radiation balance and aerosols, *Proc. 8th Workshop Italian Research on Antarctic Atmosphere*, Bologna, Italy, Oct. 20-22, 1999, edited by M. Colacino and G. Giovanelli, pp. 83-98, Italian Phys. Soc., Bologna, Italy, 2000.

Stone, R.S., Factors that determine when the seasonal snowmelt occurs in Northern Alaska, *Proc. Second Wadati Conference on Global Change and the Polar Climate*, Tsukuba, Japan, March 7-9, 2001, pp. 87-90, 2001.

Sukhorukov, F.V., V.M. Gavshin, I.N. Malikova, S.I. Kovalev, Y.I. Malikov, and P.A. Romashkin, Cesium-137 in the environment of the Altay Region (Russia), *Water Air Soil Pollut., 118*, 395-406, 2000.

Thompson, A.M., B.G. Doddridge, J.C. Witte, R.D. Hudson, W.T. Luke, J.E. Johnson, B.J. Johnson, S.J. Oltmans, and R. Weller, A tropical Atlantic paradox: Shipboard and satellite views of a tropospheric ozone maximum and wave-one in

January-February 1999, *Geophys. Res. Lett., 27(20)*, 3317-3320, 2000.

Vömel, H., D. Toohey, T. Deshler, and C. Kröger, Sunset observations of ClO in the Arctic polar vortex and implications for ozone loss, *Geophys. Res. Lett., 28*, 4183-4186, 2001.

Voss, P.B., R.M. Stimpfle, R.C. Cohen, T.F. Hanisco, G.P. Bonne, K.K. Perkins, E.J. Lanzendorf, J.G. Anderson, R.J. Salawitch, C.R. Webster, D.C. Scott, R.D. May, P.O. Wennberg, P.A. Newman, L.R. Lait, J.W. Elkins, and T.P. Bui, Inorganic chlorine partitioning in the summer lower stratosphere, modeled and measured [ClONO$_2$]/[HCl] during POLARIS, *J. Geophys. Res., 106*, 1713-1732, 2001.

Weatherhead, E.C., G.C. Reinsel, G.C. Tiao, C.H. Jackman, L. Bishop, S.M. Hollandsworth-Frith, J. DeLuisi, T. Keller, S.J. Oltmans, E.L. Fleming, D.J. Wuebbles, J.B. Kerr, A.J. Miller, J. Herman, R. McPeters, R.M. Nagatani, and J.E. Frederick, Detecting the recovery of total column ozone, *J. Geophys. Res., 105(D17)*, 22,201-22,210, 2000.

Wisthaler, A., A. Hansel, M. Schwartzmann, C. Scheiring, W. Lindinger, and E.E. Ferguson, Relaxation of vibrationally excited HCN$^+$ and DCN$^+$ ions in collisions with He, *J. Chem. Phys., 112*, 731-735, 2000.

Yi, C., K.J. Davis, P.S. Bakwin, B.W. Berger, and L.C. Marr, Influence of advection on measurements of the net ecosystem-atmosphere exchange of CO$_2$ from a very tall tower, *J. Geophys. Res., 105(D8)*, 9991-9999, 2000.

8. Specialized Abbreviations and Acronyms

ABL   atmospheric boundary layer
ACATS   Airborne Chromatograph for Atmospheric Trace Species
ACCENT   Atmospheric Chemistry and Combustion Effects Near the Tropopause
ACD   Atmospheric Chemistry Division (NCAR)
ACE   Aerosol Characterization Experiment
ACE-Asia   Asian Pacific Regional Aerosol Characterization Experiment
ACSYS   Arctic Climate System Study
AE   auroral electrojet
AERONET   Aerosol Robotics Network (NASA)
AES   Atmospheric Environment Service (Canada)
AGAGE   Advanced Global Atmospheric Gases Experiment
AIRKIT   Air Kitzis sampler
AIRS   Atmospheric Infrared Sounder
ALE   Atmospheric Lifetime Experiment
ALIAS   Aircraft Laser Infrared Absorption Spectrometer
ALT   Alert, Canada, sampling site
ANSTO   Australian Nuclear Science and Technology Organization
AOD   aerosol optical depth
AOML   Atlantic Oceanographic and Meteorological Laboratory (NOAA)
ARL   Air Resources Laboratory (NOAA)
ARM   Atmospheric Radiation Measurement (DOE)
ARO   Arctic Research Office (NOAA)
ARO   Atmospheric Research Observatory (South Pole, Antarctica)
ASA   Antarctic Support Associates
ASL   above sea level
ATLAS   Airborne Tunable Laser Absorption Spectrometer
ATMOS   Atmospheric Trace Molecule Spectroscopy
AVHRR   Advanced Very High Resolution Radiometer
BACPAC   Bromine Air-sea Cruise Pacific
BAO   Boulder Atmospheric Observatory
BASC   Barrow Arctic Science Consortium
BC   black carbon
BIF   Balloon Inflation Facility
BND   Bondville, Illinois
BRW   Barrow Observatory, Barrow, Alaska (CMDL)
BSI   Biospherical Instruments Inc., San Diego, California
BSRN   Baseline Surface Radiation Network
CADIC   Centro Austral de Investigaciones Cientificas, Argentina
CAF   Clean Air Facility (South Pole, Antarctica)
CALTECH   California Institute of Technology
CART   Cloud and Radiation Testbed
CAS   Clean Air Sector
CASA   Carnegie-Ames-Stanford Approach
CATS   Chromatograph for Atmospheric Trace Species
CCGG   Carbon Cycle Greenhouse Gases group (CMDL)
CCN   cloud condensation nuclei
CCRL   Carbon Cycle Research Laboratory
CDIAC   Carbon Dioxide Information Analysis Center
CERES   Clouds and Earth's Radiant Energy System
CFC   chlorofluorocarbon
CGO   Cape Grim Observatory, Tasmania, Australia
CIRES   Cooperative Institute for Research in Environmental Sciences (University of Colorado)
CLaMS   Chemical Lagrangian Model of the Stratosphere
CLIVAR   Climate Variability and Predictability Programme
CMDL   Climate Monitoring and Diagnostics Laboratory (NOAA)
CN   condensation nuclei
CNC   condensation nuclei counter
CRN   Climate Reference Network (NOAA)

CSIRO	Commonwealth Scientific and Industrial Research Organization (Australia)
CUCF	Central UV Calibration Facility
DEW	Distant Early Warning
DFIR	double fence intercomparison reference
DMS	dimethyl sulfide
DNA	deoxyribonucleic acid
DOE	U.S. Department of Energy
DOY	day of year
DRUM	Davis Rotating-drum Unit for Monitoring
DSRC	David Skaggs Research Center (Boulder, Colorado)
DU	Dobson unit
DU	University of Denver
EC	elemental carbon
ECC	electrochemical concentration cell
ECD	electron capture detector
ECl	equivalent chlorine
ECMWF	European Centre for Medium-Range Weather Forecasts
EECl	effective equivalent chlorine
EESC	effective equivalent stratospheric chlorine
EML	Environmental Measurements Laboratory (DOE)
ENSO	El Niño/Southern Oscillation
EOS	Earth Observing System
EPA	Environmental Protection Agency
ETCl	equivalent tropospheric chlorine
FID	flame ionization detector
FSU	Florida State University
FSU	Former Soviet Union
FT	free troposphere
FTIR	Fourier transform infrared (spectrometer)
FTP	File Transfer Protocol
FTS	Fourier transform spectrometer
FWHM	full width at half maximum
FWNIP	filter wheel normal incidence pyrheliometer
GAGE	Global Atmospheric Gases Experiment
GAME	GEWEX Asian Monsoon Experiment
GAW	Global Atmospheric Watch
GC	gas chromatograph
GC	graphitic carbon
GCM	global circulation model
GC-MS	gas chromatograph-mass spectrometer
GEOSECS	Geochemical Ocean Sections
GEWEX	Global Energy and Water Cycle Experiment
GFDL	Geophysical Fluid Dynamics Laboratory (NOAA)
GMCC	Geophysical Monitoring for Climatic Change (now CMDL) (NOAA)
GPS	Global Positioning System
HALOE	Halogen Occultation Experiment
HAO	High Altitude Observatory
HATS	Halocarbons and other Atmospheric Trace Species group (CMDL)
HC	hydrocarbon
HCFC	hydrochlorofluorocarbon
HFC	hydrofluorocarbon
HP	Hewlett-Packard
HPA	Hawaii Preparatory Academy
HRDI	High Resolution Doppler Imager
HST	Hawaii Standard Time
HVO	Hawaii Volcano Observatory
IAC	Institute of Atmospheric Chemistry (China)
IAEA	International Atomic Energy Agency
IC	ion chromatograph
ICP	inductively coupled plasma
ICP	intercomparison
IFP	Intensive Field Phase

IFT	Institute for Tropospheric Research
IMF	interplanetary magnetic field
INDOEX	Indian Ocean Experiment
INSTAAR	Institute for Arctic and Alpine Research (University of Colorado)
IPASRC-I	International Pyrgeometer and Absolute Sky-scanning Radiometer Comparison
IPC	International Pyrheliometer Comparison
IPCC	Intergovernmental Panel on Climate Change
IR	infrared
ISCAT	Investigation of Sulfur Chemistry in the Antarctic Troposphere
ITCZ	Intertropical Convergence Zone
ITN	Grifton, North Carolina, sampling site
JMA	Japan Meteorological Agency
JOSIE	Jülich Ozonesonde Intercomparison Experiment
JPL	Jet Propulsion Laboratory
KCO	Kaashidhoo Climate Observatory
KUM	Cape Kumukahi, Hawaii, sampling site
LACE	Lightweight Airborne Chromatograph Experiment
LAN	Local Area Network
LDI TOFMS	Laser Desorption Ionization Time-of-Flight Mass Spectrometer
LEAPS	Low Electron Attachment Potential Species
MAGICC	Measurements of Atmospheric Gases Influencing Climate Change
MAKS	Martin and Kitzis Sampler
MATCH	Model of Atmospheric Transport and Chemistry
MBL	marine boundary layer
MFRSR	multi-filter rotating shadowband radiometer
MHD	Mace Head, Ireland, sampling site
MLN	Mauna Loa New
MLO	Mauna Loa Observatory, Hawaii (CMDL)
MOPITT	Measurement of Pollution in the Troposphere
MRD	mercuric oxide reduction detector
MRI	Meteorological Research Institute, Japan
MRI	Meteorology Research, Inc.
MSC	Meteorological Service of Canada
MSD	mass selective detector
NARL	Naval Arctic Research Laboratory
NASA	National Aeronautics and Space Administration
NAT	nitric acid trihydrate
NAVSWC	Naval Surface Weapons Center
NCAR	National Center for Atmospheric Research
NCDC	National Climatic Data Center
NCEP	National Centers for Environmental Prediction (NOAA)
NDIR	non-dispersive infrared analyzer
NDSC	Network for the Detection of Stratospheric Change
NERL	National Exposure Research Laboratory
NH	northern hemisphere
NILU	Norwegian Institute for Air Research
NIP	normal incidence pyrheliometer
NIST	National Institute of Standards and Technology (U.S. Dept. of Commerce)
NIWA	National Institute of Water and Atmospheric Research (New Zealand)
NOAA	National Oceanic and Atmospheric Administration (U.S. Dept. of Commerce)
NODC	National Oceanographic Data Center
NPC	NREL Pyrheliometer Comparison
NRC	National Research Council
NREL	National Renewable Energy Laboratory
NRL	Naval Research Laboratory
NSF	National Science Foundation
NSFA	Naval Support Force Antarctica
NSRB	net surface radiation budget
NWR	Niwot Ridge, Colorado, sampling site
NWS	National Weather Service (NOAA)
OAR	Oceanic and Atmospheric Research (NOAA)
OC	organic carbon

OD	outside diameter
OMS	Observations of the Middle Stratosphere
OPP	Office of Polar Programs (NSF)
OTTO	automated flask GC-ECD instrument (not an acronym)
PAN	peroxyacetyl nitrate
PANTHER	PAN and other Trace Hydrohalocarbons Experiment
PAR	photosynthetically active radiation
PBL	planetary boundary layer
PEM Tropics	Pacific Exploratory Mission in the Tropics
PFC	perfluorocarbon
PFR	precision filter radiometer
PMEL	Pacific Marine Environment Laboratory (NOAA)
PMOD	Physikalisch-Meteorologisches Observatorium Davos (World Radiation Center)
POES	Polar Operational Environmental Satellite
POLARIS	Photochemistry of Ozone Loss in the Arctic Region in Summer
POP	persistent organic pollutant
ppb	parts per billion
ppt	parts per trillion
PSA	Palmer Station, Antarctica, sampling site
PSAP	particle soot absorption photometer
PSC	polar stratospheric cloud
PSP	precision spectral pyranometer
PV	photovoltaic
QBO	quasi-biennial oscillation
RAF	radiative amplification factor
RCF	Radiometer Calibration Facility
RITS	Radiatively Important Trace Species
RPS	Raytheon Polar Services
SAFARI	Southern African Fire-Atmosphere Research Initiative
SAGE	Stratospheric Aerosol and Gas Experiment
SASP	Surface Air Sampling Program
SBUV	solar backscatter ultraviolet
SC	sky cover
SCAR	Scientific Committee in Antarctic Research
SD	standard deviation
SEAREX	Sea-Air Exchange Experiment
SEASPAN	SEAREX South Pacific Aerosol Network
SEC	Space Environment Center (NOAA)
SGP	Southern Great Plains (Lamont, Oklahoma)
SH	southern hemisphere
SHADOZ	Southern Hemisphere Additional Ozonesondes
SHEBA	Study of the Heat Budget in the Arctic
SIL	Stable Isotope Laboratory (INSTAAR)
SIO	Scripps Institution of Oceanography (University of California, San Diego)
SMO	Samoa Observatory, American Samoa (CMDL)
SOLVE	SAGE III Ozone Loss and Validation Experiment
SOWER	Soundings of Ozone and Water in the Equatorial Region
SPO	South Pole Observatory, Antarctica (CMDL)
SRF	Solar Radiation Facility (CMDL)
SRM	Standard Reference Material
SRRB	Surface Radiation Research Branch (NOAA)
SST	sea surface temperature
STAR	Solar and Thermal Atmospheric Radiation group (CMDL)
STEP	Solar-Terrestrial Energy Program
SUNY	State University of New York
S-XRF	synchrotron-x-ray fluorescence
SZA	solar zenith angle
TCT	thermal deposition cold trap
TDF	Ushuaia Observatory (near Tierra del Fuego, Argentina), sampling site
TEI	Thermo Environmental Instruments
TEO	Territorial Energy Office
TEXAQS	Texas Air Quality Study

THD	Trinidad Head, California, sampling site
THESEO	Third European Stratospheric Experiment on Ozone
TM3	Tracer Model 3
TOMS	Total Ozone Mapping Spectrometer
TOMS^{3}F	Total Ozone Measurements by Satellites, Sondes, and Spectrophotometers at Fairbanks
TOR	thermal optical reflectance
TRACE-P	Transport and Chemical Evolution over the Pacific
TROICA	Trans-Siberian Observations Into the Chemistry of the Atmosphere
TSI	Thermo Systems Incorporated
UAF	University of Alaska, Fairbanks
UCI	University of California, Irvine
UCSD	University of California, San Diego
UIC	Ukpeagvik Inupiat Corporation (Alaska)
UNEP	United Nations Environmental Programme
UPS	uninterruptible power supply
USAP	U.S. Antarctic Program
USDA	United States Department of Agriculture
USGS	United States Geological Survey
UTC	Universal Time Coordinated
UV	ultraviolet
UVB	ultraviolet B band
VOC	volatile organic compound
VOGNET	Volcano Gas observatory Network
WAS	Whole Air Sampler
WCRP	World Climate Research Program
WEPC	water equivalent precipitation
WERC	Water and Environmental Research Center
WMO	World Meteorological Organization, Geneva, Switzerland
WOCE	World Ocean Circulation Experiment
WOUDC	World Ozone and Ultraviolet Data Centre (Canada)
WRC	World Radiometric Center
WRR	World Radiation Reference
WSA	Sable Island, Canada
WSG	World Standard Group
WVMS	Water Vapor Millimeter-wave Spectrometer
YES	Yankee Environmental Systems